



Kent Academic Repository

Mifsud, Duncan (2023) *On the Astrochemistry of Sulphur Molecules in Interstellar and Solar System Ice Analogues*. Doctor of Philosophy (PhD) thesis, University of Kent,.

Downloaded from

<https://kar.kent.ac.uk/100905/> The University of Kent's Academic Repository KAR

The version of record is available from

<https://doi.org/10.22024/UniKent/01.02.100905>

This document version

UNSPECIFIED

DOI for this version

Licence for this version

CC BY-NC-ND (Attribution-NonCommercial-NoDerivatives)

Additional information

Versions of research works

Versions of Record

If this version is the version of record, it is the same as the published version available on the publisher's web site. Cite as the published version.

Author Accepted Manuscripts

If this document is identified as the Author Accepted Manuscript it is the version after peer review but before type setting, copy editing or publisher branding. Cite as Surname, Initial. (Year) 'Title of article'. To be published in **Title of Journal**, Volume and issue numbers [peer-reviewed accepted version]. Available at: DOI or URL (Accessed: date).

Enquiries

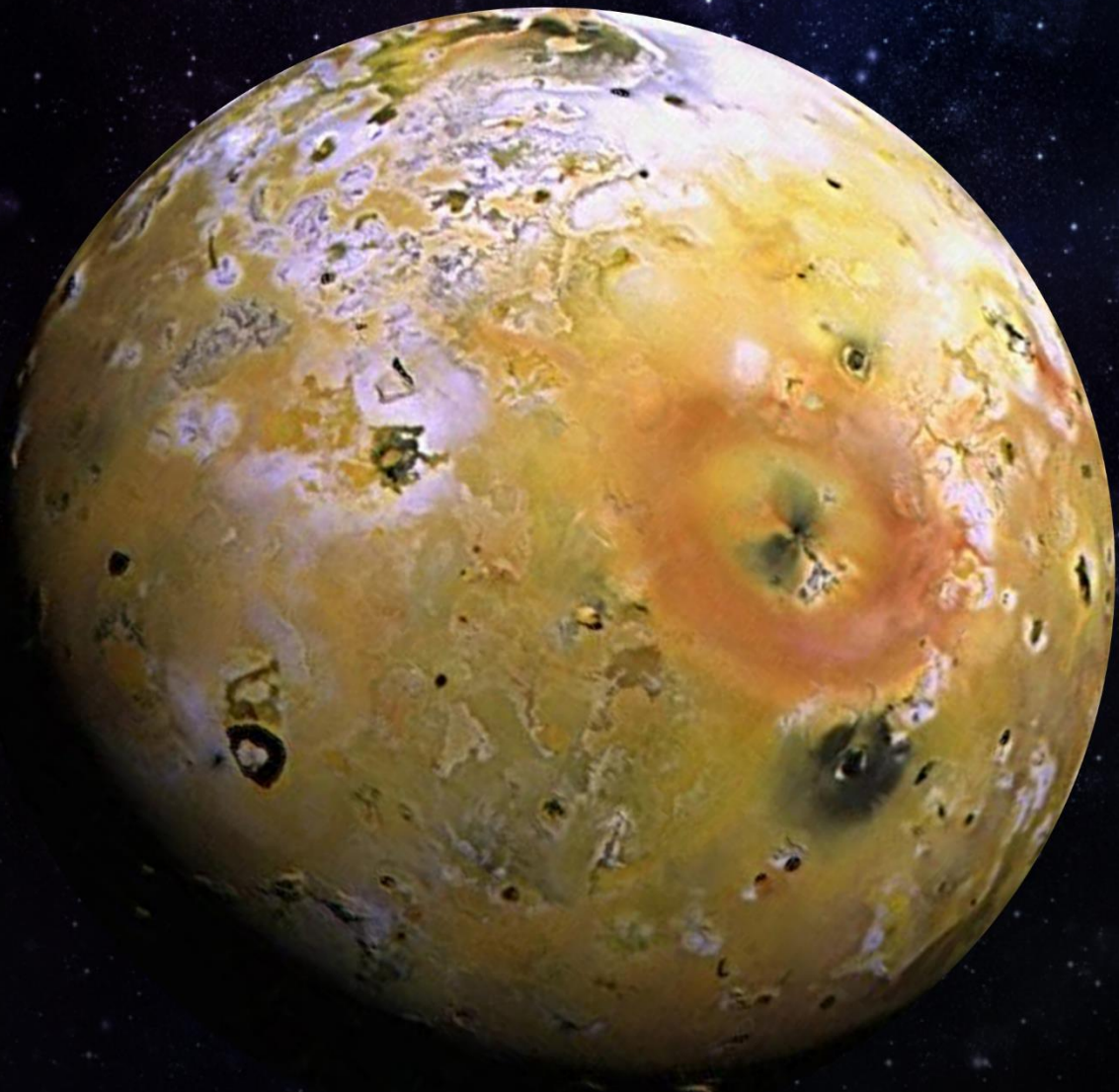
If you have questions about this document contact ResearchSupport@kent.ac.uk. Please include the URL of the record in KAR. If you believe that your, or a third party's rights have been compromised through this document please see our [Take Down policy](https://www.kent.ac.uk/guides/kar-the-kent-academic-repository#policies) (available from <https://www.kent.ac.uk/guides/kar-the-kent-academic-repository#policies>).

On the Astrochemistry of Sulphur Molecules in Interstellar and Solar System Ice Analogues

A thesis presented to the Division of Natural Sciences at the University of Kent in
partial fulfilment of the requirements for the degree of Doctor of Philosophy in Physics

Duncan V. Mifsud

January 2023



To Mum, Pops, and Nanna

for their unconditional love and constant support.

Acknowledgements

A PhD is, quite unsurprisingly, not an easy thing to do; and especially so during a global pandemic. It would therefore be remiss of me to not acknowledge the efforts made by a myriad of wonderful people who made my years as a doctoral scholar happy and memorable ones. In the first instance, I would like to extend my heartfelt thanks to my primary supervisor, Nigel J. Mason OBE, for his constant support. His cheery disposition, evident from our first meeting, and his encouragement for me to develop my own scientific ideas have pushed me to always strive for excellence, and for this I am eternally grateful.

I would also like to express my thanks to Zoltán Juhász; my acting supervisor during my two-and-a-half-year secondment to the Institute for Nuclear Research (Atomki) in Debrecen. I will always have fond memories of our late-night laboratory shifts, as well as our first post-pandemic conference in Visegrád. In truth, I owe a debt of gratitude to the entire academic team at Atomki, namely Péter Herczku, Béla Sulik, Sándor T. S. Kovács, K. K. Rahul, Richárd Rácz, Sándor Biri, and Gergő Lakatos. Together, they helped to create a marvellous working environment at Atomki, in which I felt able to develop my scientific ideas and pursue my research interests. I am especially indebted, however, to Péter Herczku, for not only welcoming me to the laboratory as a true friend, but also for his indispensable aid whenever I was locked up in post-migration quarantine!

I am also very thankful for the help and guidance offered to me by several members of the extended research group. To Sergio Ioppolo, I am grateful for the career guidance offered and for the feedback which allowed me to continually improve upon my work. To Zuzana Kaňuchová, I am grateful for the tips and tricks shown to me on how to analyse data and display results in a clear and concise manner. And finally, to Robert W. McCullough, I am grateful for the education in ion collision physics, as well as for some of the best discussions and debates on Rugby Union I have ever had! I should also like to extend my thanks to the many collaborators with whom I have had the pleasure to work, most notably István Rajta, István Vajda, Tomas A. Field, László Rinyu, Mihály Veres, Sándor Góbi, György Tarczay, Matthias van Ginneken, Giovanni Strazzulla, and Bhala Sivaraman.

To have met all the fantastic postgraduate students at the Centre for Astrophysics and Planetary Science at the University of Kent, as well as those beyond, was truly a privilege, and I am thankful for the friendship that they have shown me over the past few years. I am especially grateful to Perry A. Hailey, whose near psychic ability to determine when I was in need of a pint was crucial to the completion of this thesis. On which note, I would also like to thank the brewers at Somersby Cider, whose creativity and ingenuity continue to inspire and amaze.

Finally, I must thank all my family for their constant love and support, including my nanna Marlene, uncle Arthur, aunty Elaine, and cousins Matthew and Andrew (Dadu). I also wish to thank my girlfriend Bexy for being an absolute bastion of support and for repeatedly making the arduous trip from Canterbury to Debrecen to spend time with me, even at times when work rendered me more than a little cantankerous. Thank you for adding a healthy dose of gaiety to my life! By far my biggest debt of gratitude, however, is owed to my parents Vincent and Nadya. To say that this PhD would not have been possible without them is a massive understatement, and I am incredibly thankful to have had them by my side every step of the way, wherever I was in the world. Parents; take a bow.

We are a way for the Universe to know itself

Carl Sagan

Abstract

Sulphur is the tenth most abundant element in the universe and is known to play many important roles in biochemical, geochemical, and atmospheric processes. However, the astrochemistry of sulphur presents many as yet unresolved problems. In the dense interstellar medium, for instance, there exists a notable paucity of sulphur in both the gas phase as well as within interstellar icy grain mantles, compared to the expected cosmic abundance of the element. Moreover, no conclusive detection of solid interstellar H₂S has yet been made, despite the known efficiency of hydrogenation reactions on the surface of interstellar dust grains. Within the Solar System, solid SO₂ is known to be a component of many icy bodies, including the Galilean moons of Jupiter and several comets, but the mechanism leading to its formation still largely eludes contemporary astronomers, chemists, and spectroscopists.

This thesis probes a number of questions relating to sulphur ice astrochemistry in both interstellar and Solar System environments. It begins with a review of the current state of knowledge of extra-terrestrial sulphur chemistry, before delving into a broader discussion of the chemical characteristics of the cosmos and a brief history of astrochemistry as an independent field of research. A background to the relevant scientific concepts and principles routinely used in laboratory astrochemistry then follows, which includes detailed discussions on molecular structure and symmetry, spectroscopy (with an emphasis on measurements made in the mid-infrared spectral range), and radiation chemistry.

A thorough description of a new experimental facility for ion and electron irradiation studies of astrophysical ice analogues based at the Institute for Nuclear Research (Atomki) is provided, along with various experiments performed to validate the set-up. The results of systematic studies on the mid-infrared absorption spectra of H₂S and SO₂ astrophysical ice analogues, both pure and mixed with H₂O, are then presented and discussed in the context of their applicability to the detection of these sulphur-bearing species in different astrophysical environments. The results of the first ever systematic comparisons of the radiation chemistry and physics of the amorphous and crystalline phases of a number of pure astrophysical ice analogues, including some that bear sulphur atoms, are described in the subsequent chapter. The observed greater radiolytic decay rates of amorphous ices and the more rapid formation of molecular products as a result of their irradiation is discussed both in the context of the differences in the strength and extent of the intermolecular interactions between the amorphous and crystalline phases, as well as in light of the recent discoveries of complex organic molecules in astrophysical environments in which space radiation-induced amorphisation is thought to out-compete thermal crystallisation of ices.

The results of experiments investigating the implantation of high-energy sulphur ions into oxygen-bearing ices as a potential mechanism towards the formation of icy SO₂ on the surfaces of the Galilean moons of Jupiter are also presented, with the analysis of the data demonstrating that this is not likely to be a major contributor towards solid SO₂ on these moons. This contrasts with the results obtained from experiments investigating the irradiation of oxygen-bearing ices deposited on top of elemental sulphur layers, which was shown to result in the formation of a number of volatile sulphur-bearing molecules such as SO₂, CS₂, and OCS. The thesis concludes with a discussion of potential directions for future work, as well as a number of suggestions on improving the present experimental set-up.

Table of Contents

Opening Pages

Dedication.....	i
Acknowledgements.....	ii
Abstract.....	iv
Table of Contents.....	v
List of Figures.....	x
List of Tables.....	xv
List of Physical Variables.....	xvi

Chapter 1: Sulphur in Space

1.1 Sulphur Astrochemistry: An Introduction.....	1
1.2 Thermal Chemistry.....	5
1.3 Photon-Induced Radiation Chemistry.....	5
1.4 Particle-Induced Radiation Chemistry.....	7
1.5 Sulphur Ion Bombardment.....	8
1.6 Thesis Outline and Motivation.....	9

Chapter 2: Molecules in Space: An Introduction

2.1 Astrochemistry: The Chemistry of the Cosmos.....	12
2.2 The Structure and Chemistry of the Interstellar Medium.....	14
2.2.1 <i>Diffuse Interstellar Clouds</i>	16
2.2.2 <i>Dense Interstellar Clouds</i>	21
2.2.3 <i>Giant Molecular Clouds and Bok Globules</i>	27
2.3 The Cosmic Chemistry Cycle.....	27
2.3.1 <i>Setting the Stage for Stellar Birth</i>	28
2.3.2 <i>Planetary Systems</i>	30
2.3.3 <i>Stellar Evolution and Death</i>	31
2.3.4 <i>Comments on the Emergence of Life in the Universe</i>	35
2.4 An Overview of Icy Bodies in the Solar System.....	37
2.4.1 <i>The Inner Terrestrial Planets</i>	37
2.4.2 <i>Ceres and Vesta</i>	38
2.4.3 <i>The Galilean Moons of Jupiter</i>	39
2.4.4 <i>Pluto and Charon</i>	42
2.4.5 <i>Comets</i>	43
2.5 Summary.....	44

Chapter 3: Fundamental Physical Chemistry

3.1	Atomic Theory.....	45
3.1.1	<i>Atomic Structure</i>	45
3.1.2	<i>Assigning Electrons to Atomic Orbitals</i>	47
3.1.3	<i>Atomic Orbital Hybridisation</i>	47
3.1.4	<i>The Formation of Atomic Ions</i>	48
3.2	Molecules.....	49
3.2.1	<i>Valence Bond Theory</i>	49
3.2.2	<i>Molecular Orbital Theory</i>	50
3.2.3	<i>Valence Shell Electron Pair Repulsion Theory</i>	51
3.2.4	<i>Point Group Symmetry</i>	52
3.2.5	<i>Electronegativity and Polarity</i>	55
3.2.6	<i>Isomerism in Molecules</i>	57
3.3	Infrared Spectroscopy.....	58
3.3.1	<i>The Interaction of Matter with Electromagnetic Radiation</i>	58
3.3.2	<i>Quantum Vibration in Molecules as a Ball and Spring Model</i>	62
3.3.3	<i>Infrared Spectroscopic Techniques and Instrumentation</i>	66
3.4	Radiation Chemistry.....	69
3.4.1	<i>Mechanisms of Energy Transfer</i>	69
3.4.2	<i>Summary of Processes in Radiation Chemistry</i>	71
3.5	Summary.....	74

Chapter 4: Experimental Apparatus and Techniques

4.1	Laboratory Astrochemistry Chambers.....	75
4.2	The Ice Chamber for Astrophysics-Astrochemistry (ICA).....	77
4.2.1	<i>The Deposition of Astrophysical Ice Analogues</i>	80
4.2.2	<i>In Situ Analysis</i>	83
4.2.3	<i>Ion Irradiation of Ices: The Atomki Tandetron Accelerator</i>	86
4.2.4	<i>Electron Irradiation of Ices: The Miskolci Egyetem Electron Gun</i>	89
4.3	Typical Experimental Procedures.....	91
4.3.1	<i>Ion Irradiation of Pure Amorphous Methanol Ice</i>	91
4.3.2	<i>Electron Irradiation of Pure Amorphous Methanol Ice</i>	94
4.3.3	<i>Thermal Reactions between Water and Sulphur Dioxide Ices</i>	96
4.4	Limitations of the Experimental Set-Up.....	97
4.5	Software.....	98
4.5.1	<i>The SRIM Programme</i>	99
4.5.2	<i>The CASINO Programme</i>	99
4.6	Summary.....	100

Chapter 5: Systematic Mid-Infrared Spectroscopic Study of H₂S and SO₂ Astrophysical Ice Analogues

5.1	Contextual Introduction.....	101
5.2	An Overview of Previous Laboratory Spectroscopic Studies.....	102
5.2.1	<i>Mid-Infrared Spectroscopy of H₂S Ices</i>	102
5.2.2	<i>Mid-Infrared Spectroscopy of SO₂ Ices</i>	105
5.3	Experimental Methodology.....	108
5.4	Mid-Infrared Spectroscopic Characterisations.....	109
5.4.1	<i>Thermal Annealing of Pure H₂S Ices</i>	109
5.4.2	<i>Thermal Annealing of Pure SO₂ Ices</i>	113
5.4.3	<i>Thermal Annealing of H₂S and SO₂ Ices Mixed with H₂O Ice</i>	118
5.5	Applications to Planetary and Space Chemistry.....	126
5.5.1	<i>Dense Interstellar Clouds</i>	126
5.5.2	<i>Ceres</i>	127
5.5.3	<i>Io and Europa</i>	127
5.6	Summary.....	128

Chapter 6: Constraining the Influence of Solid Phase on the Radiation Chemistry of Astrophysical Ice Analogues

6.1	Contextual Introduction.....	130
6.1.1	<i>CH₃OH Ice</i>	131
6.1.2	<i>N₂O Ice</i>	131
6.1.3	<i>H₂O Ice</i>	132
6.1.4	<i>H₂S and SO₂ Ices</i>	133
6.2	Experimental Methodology.....	133
6.3	Comparative Electron Irradiations of Amorphous and Crystalline Ices.....	136
6.3.1	<i>Amorphous and Crystalline CH₃OH and N₂O Ices</i>	136
6.3.2	<i>Amorphous, Restrained Amorphous, and Crystalline H₂O Ices</i>	143
6.3.3	<i>Amorphous and Crystalline H₂S and SO₂ Ices</i>	151
6.4	Astrochemical Implications.....	158
6.5	Summary.....	160

Chapter 7: The Implantation of Reactive Sulphur Ions into Oxygen-Bearing Ices

7.1	Contextual Introduction.....	162
7.2	Experimental Methodology.....	164
7.3	290 keV S ⁺ Ion Implantation into CO ₂ Ice at 20 and 70 K.....	167
7.4	400 keV S ⁺ Ion Implantation into CO Ice at 20 K.....	171

7.5	400 keV S ⁺ Ion Implantation into O ₂ Ice at 20 K.....	176
7.6	Implications for Astrochemistry and Astrobiology.....	179
	7.6.1 <i>Formation of SO₂ on Europa</i>	179
	7.6.2 <i>Sulphur Chemistry on Trans-Neptunian and Kuiper Belt Objects</i>	181
	7.6.3 <i>On the Non-Detections of OCS and CS₂</i>	181
7.7	Summary.....	182

Chapter 8: Ion Irradiation of Oxygen-Bearing Ices Deposited on Top of Pure Sulphur Residues

8.1	Contextual Introduction.....	184
8.2	Experimental Methodology.....	185
8.3	1 MeV He ⁺ Ion Irradiation of Oxygen-Bearing Ices on Top of Pure Sulphur.....	188
	8.3.1 <i>O₂ Ice on Top of Sulphur at 20 K</i>	188
	8.3.2 <i>CO Ice on Top of Sulphur at 20 K</i>	190
	8.3.3 <i>CH₃OH Ice on Top of Sulphur at 25 K</i>	193
	8.3.4 <i>CO₂ Ice on Top of Sulphur at 20 and 70 K</i>	195
	8.3.5 <i>H₂O Ice on Top of Sulphur at 20 and 70 K</i>	201
8.4	Astrochemical Implications.....	205
8.5	Summary.....	207

Chapter 9: Conclusions and Scope for Future Work

9.1	Thesis Conclusions.....	209
9.2	Scope for Future Work.....	214
	9.2.1 <i>Further Systematic Spectroscopic Characterisations</i>	214
	9.2.2 <i>Radiolytic Formation of Thiols</i>	214
	9.2.3 <i>Reactivity of H₂S Ices</i>	215
	9.2.4 <i>Irradiation of Sulphur-Bearing Minerals</i>	215
	9.2.5 <i>Radiation-Induced Sulphur Isotope Fractionations</i>	216
9.3	Proposed Upgrades to the ICA Set-Up.....	217
	9.3.1 <i>Spectroscopic Range and Removal of Atmospheric Contaminants</i>	217
	9.3.2 <i>Ice Temperatures</i>	218
	9.3.3 <i>Determination of Ice Thicknesses and Optical Parameters</i>	218
	9.3.4 <i>Quadrupole Mass Spectrometry</i>	222
	9.3.5 <i>Improved Simulation of Astrophysical Surfaces</i>	222
9.4	Summary.....	224

Appendices: SRIM and CASINO Calculation Output Graphs

A	SRIM Calculation Output Graphs.....	225
B	CASINO Calculation Output Graphs.....	233

Closing Pages

Publications, Posters, and Presentations.....	236
Biography.....	243
References.....	244

List of Figures

Note that, in the case of long figure captions, an abridged caption (typically the first sentence of the full caption) has been provided.

Chapter 1

1.1	Images of the rhombic (α -) and the monoclinic (β -) polymorphs of S_8 .	2
1.2	A graphical summary of the radiolytic sulphur cycle present on the surface of Europa.	4

Chapter 2

2.1	The relative strengths of the DIBs that characterise interstellar absorption spectra overlaid on a representation of the electromagnetic spectrum.	13
2.2	Barnard 68 is a comparatively small dense interstellar cloud in the constellation Ophiuchus.	16
2.3	The H_2O cycle in diffuse interstellar clouds is mediated almost entirely by gas-phase reactions.	18
2.4	Summary of the surface reaction mechanisms available on an interstellar dust grain.	19
2.5	Plot of the ratio of the number density of a particular species X to that of atomic hydrogen against the column density of atomic hydrogen.	20
2.6	The Horsehead Nebula (also known as Barnard 33) is a dense interstellar cloud about 1375 ly away in the constellation Orion whose PDRs are clearly observable.	22
2.7	A simplified representation of the layered structure of interstellar icy grain mantles.	23
2.8	Summative representation of the five major mechanisms driving molecular formation in astrophysical ices.	25
2.9	A graphical representation of the line-of-sight requirements for observing the molecular components of interstellar icy grain mantles.	27
2.10	Graphical representation of the Cosmic Chemistry Cycle, including the birth and death stages of low mass stars.	28
2.11	Evolution of interstellar icy grain mantles during the birth and evolution of a nearby protostar.	30
2.12	Summary of the evolution of low mass and high mass stellar objects.	32
2.13	A cross-section through a hypothetical red supergiant, showing the ‘onion-like’ structure in which different nucleosynthetic fusion reactions dominate.	34
2.14	Examples of high latitude surface ice deposits on the inner terrestrial planets.	38
2.15	True colour pictures (not to scale) of Ceres and Vesta imaged during the <i>Dawn</i> mission.	39
2.16	Io, Europa, Ganymede, and Callisto. Collectively, these Jovian satellites are referred to as the Galilean moons of Jupiter.	39
2.17	Energy profiles of protons, O^+ ions, and S^+ ions in the vicinity of Europa and Ganymede.	41
2.18	True colour pictures (not to scale) of Pluto and Charon imaged during the <i>New Horizons</i> mission.	44

Chapter 3

3.1	The spherical symmetric $1s$ and $2s$ atomic orbitals.	46
3.2	The directionality of p orbitals is such that the orbital axis is aligned to any of the Cartesian coordinate axes.	46
3.3	The approximate relative energy spacing of atomic orbitals.	47
3.4	The hybridisation of one $2s$ atomic orbital with three $2p$ orbitals yields four sp hybrid orbitals.	48
3.5	Graphical representation of Valence Bond Theory as applied to the carbon-carbon double bond in ethene.	50
3.6	Molecular orbital diagrams for H_2 and He_2 .	51

3.7	Molecular geometries adopted by molecules with central atoms having different coordination numbers and non-bonding (or lone) electron pairs as predicted by VSEPR Theory.	52
3.8	Axes of rotation in a trigonal planar BF_3 molecule.	53
3.9	Mirror planes in relation to the principal axis of rotation in the H_2O molecule.	53
3.10	One S_4 rotation-reflection operation in the CH_4 molecule.	54
3.11	Flow-chart used to determine the point group of a molecule.	55
3.12	Electrostatic potential maps for the non-polar CO_2 and CCl_4 molecules.	56
3.13	The possible stereoisomers of tartaric acid.	57
3.14	Representation of an electromagnetic wave as perpendicularly oscillating electric E and magnetic B fields.	58
3.15	The electromagnetic spectrum.	59
3.16	Energy level diagram depicting the rotational, vibrational, and electronic transitions associated with the absorption of electromagnetic radiation.	60
3.17	The parabolic energy function of quantum harmonic oscillation and the Morse function of quantum anharmonic oscillation.	63
3.18	Visual representations of the fundamental vibrational modes of the H_2O and CO_2 molecules.	65
3.19	Schematic diagram of a Michelson interferometer.	68
3.20	Generic Bragg curve for a heavy projectile ion penetrating a target medium.	71

Chapter 4

4.1	A top-view schematic diagram of the ICA.	77
4.2	Photographs of the sample holder with its heat shield as seen from the front and the rear sides.	78
4.3	A close-up photograph of a ZnSe substrate of the type mounted onto the sample holder.	79
4.4	The geometry of the gold-coated oxygen-free copper sample holder H and clamp plate C around one ZnSe deposition substrate S.	82
4.5	Percentage transmittance of ZnSe substrates of different thicknesses across infrared wavelengths between 2.5-25 μm .	86
4.6	The heat conductance of a ZnSe substrate disc can be approximated by that of a ZnSe rod of cross-sectional area $\sigma = (1.5^2 - 1.2^2) \times (\pi \div 4) = 0.64 \text{ cm}^2$.	87
4.7	Schematic diagram of the controlled ion beam irradiation system (not to scale).	89
4.8	Plots of the measured and modelled electron currents $I(Y)$ as a function of collimator displacement from its nominal position along the vertical axis of the chamber relative to the maximum beam current $I_{\text{max}}(Y)$ measured at zero displacement.	90
4.9	Mid-infrared absorption spectra of an amorphous CH_3OH ice irradiated by a 1 MeV proton beam at 20 K.	92
4.10	Evolution of the CH_3OH column density as measured from the absorption band at 1027 cm^{-1} assuming a band strength constant of $1.61 \times 10^{-17} \text{ cm molecule}^{-1}$ with increasing proton and S^{2+} ion beam dose.	93
4.11	Infrared spectral evolution of a 1 μm CH_3OH ice at different time interval during electron irradiation by a 2 keV beam.	95
4.12	Infrared spectral evolution of a thermally annealed $\text{H}_2\text{O}:\text{SO}_2$ (3:5) mixed ice.	96
4.13	Graphical user interface of the SRIM programme.	99
4.14	Graphical user interface of the CASINO programme.	100

Chapter 5

5.1	Mid-infrared spectra of amorphous and crystalline H_2S ices deposited at temperatures of 20 and 70 K, respectively.	103
5.2	Mid-infrared spectra of amorphous and crystalline SO_2 ices deposited at temperatures of 20 and 100 K, respectively.	106
5.3	Thermal evolution of the H_2S ν_3 band for ices deposited at 20, 40, and 70 K.	110
5.4	Thermal evolution of the H_2S ν_2 band for ices deposited at 20, 40, and 70 K.	112

5.5	Evolution of the H ₂ S ν_s normalised band peak areas for the ices deposited at 20, 40, and 70 K during their thermal annealing.	113
5.6	Thermal evolution of the SO ₂ ν_3 band for ices deposited at 20, 40, 70, and 100 K.	115
5.7	Thermal evolution of the SO ₂ ν_1 band for ices deposited at 20, 40, 70, and 100 K.	116
5.8	Thermal evolution of the SO ₂ $\nu_1 + \nu_3$ combination band for ices deposited at 20, 40, 70, and 100 K.	117
5.9	Evolution of the SO ₂ ν_1 and ν_3 normalised band peaks areas for the ices at 20, 40, 70, and 100 K during their thermal annealing.	118
5.10	Mid-infrared absorption spectrum of a 1:7 H ₂ S:H ₂ O ice prepared by co-deposition of the respective gases at 20 K.	119
5.11	Mid-infrared absorption spectrum of a 1:11 SO ₂ :H ₂ O ice prepared by co-deposition of the respective gases at 20 K.	120
5.12	Mid-infrared absorption spectra of a 1:11 SO ₂ :H ₂ O ice undergoing thermal annealing from deposition at 20 K to sublimation.	122
5.13	Variation in the peak areas of the SO ₃ (ν_3), HSO ₃ ⁻ , and S ₂ O ₅ ²⁻ bands during the thermal annealing of a 1:7 SO ₂ :H ₂ O ice.	123
5.14	A shoulder is apparent on the lower wavenumber flank of the H ₂ S ν_s band throughout the thermal annealing process.	124
5.15	Mid-infrared spectra of a 1:7 H ₂ S:H ₂ O ice undergoing thermal annealing from deposition at 20 K to sublimation.	125

Chapter 6

6.1	Evolution of the H ₂ O mid-infrared stretching modes during the thermal annealing of an ice deposited at 20 K.	134
6.2	Electron-induced decay of CH ₃ OH and N ₂ O ice phases with increasing electron fluence.	138
6.3	The broadening of the double peaked infrared absorption band at about 3200 cm ⁻¹ in crystalline CH ₃ OH ice as a result of electron irradiation is an indication of amorphisation.	140
6.4	Mid-infrared absorption spectra of the unirradiated and 2 keV electron irradiated amorphous and crystalline phases of solid CH ₃ OH and N ₂ O.	141
6.5	Average column densities for the products of amorphous and crystalline CH ₃ OH irradiation by 2 keV electrons.	142
6.6	Average column densities for the products of amorphous and crystalline N ₂ O irradiation by 2 keV electrons.	142
6.7	Mid-infrared spectra of ASW (deposited at 20 K), RAI (deposited at 80 K), Ic (deposited at 130 K), and Ih (deposited at 150 K) H ₂ O ice phases.	143
6.8	The evolution of the broad stretching mode in RAI, Ic, and Ih during the electron irradiation of those phases at 20 K.	144
6.9	The hydroxyl dangling bonds in (micro)porous ASW are visible as two small absorption features (indicated by arrows) at the higher wavenumber end of the H ₂ O stretching mode band in the unirradiated ice.	145
6.10	Spectral identification of H ₂ O ₂ in electron-irradiated (1.3×10^{17} electrons cm ⁻²) H ₂ O ices.	148
6.11	Scatter plot depicting the evolution of the measured H ₂ O ₂ column density with fluence during 2 keV electron irradiation.	149
6.12	Mid-infrared spectra of the amorphous and crystalline phases of H ₂ S and SO ₂ ices at several points during their irradiation by energetic electrons at 20 K.	152
6.13	Decay of amorphous and crystalline H ₂ S column densities normalised to the initially deposited column density during irradiation at 20 K using 2 keV electrons.	153
6.14	Decay of amorphous and crystalline SO ₂ column densities normalised to the initially deposited column density during irradiation at 20 K using 1.5 keV electrons.	154
6.15	Column density of H ₂ S ₂ from amorphous and crystalline H ₂ S ices irradiated using 2 keV electrons at 20 K and column density of SO ₃ from amorphous and crystalline SO ₂ ices irradiated using 1.5 keV electrons at 20 K.	155
6.16	Sulphur budgets of the electron irradiated amorphous and crystalline H ₂ S and SO ₂ ices considered in this study.	156

Chapter 7

7.1	Cartoon summary of the processes considered in this study.	164
7.2	Mid-infrared spectra of condensed CO ₂ before and after the implantation of 290 keV S ⁺ ions at 20 K.	168
7.3	Mid-infrared spectra of condensed CO ₂ before and after the implantation of 290 keV S ⁺ ions at 70 K.	168
7.4	Mid-infrared spectra of condensed CO before and after the implantation of 400 keV S ⁺ ions at 20K.	173
7.5	Mid-infrared spectra of condensed CO before and after the implantation of 400 keV S ⁺ ions at 20 K.	174
7.6	Mid-infrared absorption spectra collected during the implantation of 176 keV S ¹¹⁺ ions into solid CO at 20 K as studied by Lv <i>et al.</i> (2014a).	175
7.7	Mid-infrared spectra of condensed O ₂ before and after the implantation of 400 keV S ⁺ ions at 20 K.	177

Chapter 8

8.1	Photographs of the glass plate acting as a deposition substrate during the preliminary experiment used to determine the deposition time required to prepare a sulphur layer.	186
8.2	Mid-infrared spectra of O ₂ ice deposited on top of a layer of elemental sulphur before and during its irradiation by 1 MeV He ⁺ ions at 20 K.	189
8.3	Column density evolution of SO ₂ formed as a result of the irradiation of O ₂ ice on top of a layer of elemental sulphur using 1 MeV He ⁺ ions.	189
8.4	Mid-infrared spectra of condensed CO on top of a layer of elemental sulphur (<i>black trace</i>) and after (<i>red trace</i>) irradiation by 1 MeV He ⁺ ions at 20 K.	191
8.5	Mid-infrared spectra of CO ice deposited on top of a layer of elemental sulphur before and during its irradiation by 1 MeV He ⁺ ions at 20 K.	192
8.6	Mid-infrared spectra of CH ₃ OH ice deposited on top of a layer of elemental sulphur before and during its irradiation by 1 MeV He ⁺ ions at 25 K.	194
8.7	Column density evolution of CS ₂ formed as a result of the irradiation of CH ₃ OH ice on top of a layer of elemental sulphur using 1 MeV He ⁺ ions.	194
8.8	Mid-infrared spectra of CO ₂ ice deposited on top of a layer of elemental sulphur before and during its irradiation by 1 MeV He ⁺ ions at 20 K.	196
8.9	Column density evolution of SO ₂ formed as a result of the irradiation of CO ₂ ice on top of a layer of elemental sulphur using 1 MeV He ⁺ ions at 20 K.	196
8.10	Mid-infrared spectra of CO ₂ ice deposited on top of a layer of elemental sulphur before and during its irradiation by 1 MeV He ⁺ ions at 70 K.	198
8.11	Column density evolution of SO ₂ formed as a result of the irradiation of CO ₂ ice on top of a layer of elemental sulphur using 1 MeV He ⁺ ions at 70 K.	199
8.12	Column density evolution of SO ₂ formed as a result of the irradiation of CS ₂ ice on top of a layer of elemental sulphur using 1 MeV He ⁺ ions at 70 K.	199
8.13	The major reactions suggested to be taking place within the CO ₂ ice on top of elemental sulphur irradiated by 1 MeV He ⁺ ions at 70 K.	200
8.14	Mid-infrared spectra of H ₂ O ice deposited on top of a layer of elemental sulphur before and during its irradiation by 1 MeV He ⁺ ions at 20 K.	202
8.15	Mid-infrared spectra of H ₂ O ice deposited on top of a layer of elemental sulphur before and during its irradiation by 1 MeV He ⁺ ions at 20 K.	203

Chapter 9

9.1	Optical ray diagram exhibiting the various reflection and refraction processes leading to the detected interference of the helium-neon laser light.	219
9.2	Examples of typical fringe patterns observed during laser interferometry of H ₂ O ices deposited at different temperatures.	220
9.3	Schematic diagram of a process chamber containing an ultrasonic levitator as constructed by Brotton and Kaiser (2013).	223

Appendix A

A.1	SRIM output graphs demonstrating the projectile ion penetration profile of <i>a</i>) 200 keV, <i>b</i>) 400 keV, <i>c</i>) 750 keV, and <i>d</i>) 1 MeV protons impacting an amorphous CH ₃ OH ice.	225
A.2	SRIM output graph demonstrating the projectile ion penetration profile of a 6 MeV S ⁺ ion beam impacting an amorphous CH ₃ OH ice.	226
A.3	SRIM output graph demonstrating the projectile ion penetration profile of a 290 keV S ⁺ ion beam impacting an amorphous CO ₂ ice.	226
A.4	SRIM output graph demonstrating the projectile ion penetration profile of a 290 keV S ⁺ ion beam impacting a crystalline CO ₂ ice.	227
A.5	SRIM output graph demonstrating the projectile ion penetration profile of a 400 keV S ⁺ ion beam impacting a CO ice.	227
A.6	SRIM output graph demonstrating the projectile ion penetration profile of a 400 keV S ⁺ ion beam impacting a crystalline O ₂ ice.	228
A.7	SRIM output graph demonstrating the projectile ion penetration profile of a 1 MeV He ⁺ ion beam impacting a pure elemental sulphur layer.	228
A.8	SRIM output graph demonstrating the projectile ion penetration profile of a 1 MeV He ⁺ ion beam impacting a crystalline O ₂ ice deposited on top of a layer of elemental sulphur.	229
A.9	SRIM output graph demonstrating the projectile ion penetration profile of a 1 MeV He ⁺ ion beam impacting a CO ice deposited on top of a layer of elemental sulphur.	229
A.10	SRIM output graph demonstrating the projectile ion penetration profile of a 1 MeV He ⁺ ion beam impacting an amorphous CH ₃ OH ice deposited on top of a layer of elemental sulphur.	230
A.11	SRIM output graph demonstrating the projectile ion penetration profile of a 1 MeV He ⁺ ion beam impacting an amorphous CO ₂ ice deposited on top of a layer of elemental sulphur.	230
A.12	SRIM output graph demonstrating the projectile ion penetration profile of a 1 MeV He ⁺ ion beam impacting a crystalline CO ₂ ice deposited on top of a layer of elemental sulphur.	231
A.13	SRIM output graph demonstrating the projectile ion penetration profile of a 1 MeV He ⁺ ion beam impacting an amorphous H ₂ O ice deposited on top of a layer of elemental sulphur.	231
A.14	SRIM output graph demonstrating the projectile ion penetration profile of a 1 MeV He ⁺ ion beam impacting an amorphous H ₂ O ice deposited on top of a layer of elemental sulphur.	232

Appendix B

B.1	CASINO output graph demonstrating the projectile electron penetration profile of a 2 keV electron beam impacting an amorphous and crystalline CH ₃ OH ice.	233
B.2	CASINO output graph demonstrating the projectile electron penetration profile of a 2 keV electron beam impacting an amorphous and crystalline N ₂ O ice.	233
B.3	CASINO output graph demonstrating the projectile electron penetration profile of a 2 keV electron beam impacting a H ₂ O ice.	234
B.4	CASINO output graph demonstrating the projectile electron penetration profile of a 2 keV electron beam impacting a H ₂ S ice.	234
B.5	CASINO output graph demonstrating the projectile electron penetration profile of a 1.5 keV electron beam impacting a SO ₂ ice.	235

List of Tables

Note that, in the case of long table headers, an abridged header (typically the first sentence of the full header) has been provided.

Chapter 2

2.1	Summary of the main characteristics of the different ISM phases.	14
2.2	Mechanisms by which gas-phase chemical reactions take place in the ISM.	18
2.3	List of the solid-phase molecules in interstellar and circumstellar media as classified using the system used by Boogert <i>et al.</i> (2015).	26
2.4	Physical and chemical characteristics of the Galilean moons of Jupiter.	42

Chapter 3

3.1	Summary of the symmetry elements characterising different point groups.	54
3.2	Time-scale of events in radiation chemistry.	74

Chapter 4

4.1	List of facilities and set-ups actively performing laboratory studies of astrophysical ice analogues.	76
4.2	Summary of deposition experiments performed to demonstrate that the thicknesses and compositions of the deposited ices are similar across all four deposition substrates.	82
4.3	List of commonly used infrared transparent materials and their transmission ranges and refractive indices.	85

Chapter 5

5.1	Summary of the major mid-infrared absorption features of H ₂ S ice (and of some isotopologues).	104
5.2	Summary of the major mid-infrared absorption features of SO ₂ ice (and of some isotopologues).	107
5.3	Ice densities (ρ) and integrated band strength constants (A_s) used in this study.	108
5.4	Summary of the thermal annealing experiments performed in this study.	109
5.5	Summary of results from selected previous studies on the thermal formation of HSO ₃ ⁻ and S ₂ O ₅ ²⁻ in SO ₂ :H ₂ O mixed ices at cryogenic temperatures.	123

Chapter 6

6.1	Summary of the comparative electron irradiation experiments performed in this study.	135
6.2	List of characteristic mid-infrared absorption bands and their associated band strength constants for the species considered quantitatively in this study.	140

Chapter 7

7.1	List of mid-infrared band positions, their associated integrated band strength constants, and ice densities for CO, CO ₂ , and O ₂ ices.	165
7.2	Summary of the sulphur ion implantations into oxygen-bearing ices performed in this study.	166
7.3	List of oxocarbon molecules present in the CO ice irradiated by 400 keV S ⁺ ions sorted by the wavenumber position of their mid-infrared absorption peaks.	172

Chapter 8

8.1	List of integrated band strength constants (A_s) and densities (ρ) of the ices considered in this study.	188
8.2	List of oxocarbon molecules present in the CO ice on top of a layer of elemental sulphur after irradiation by 1 MeV He ⁺ ions.	192

List of Physical Variables

Term	Meaning	Typical Units
A	Mass number	dimensionless
A_e	Elemental atomic weight	amu
A_s	Integrated band strength constant	cm molecule ⁻¹
A_v	Absorbance	dimensionless
a	Absorptivity	dm ³ g ⁻¹ cm ⁻¹
B	Spectral power density	W Hz ⁻¹
B_0	Stopping number	dimensionless
b	Pathlength	cm
C	Concentration	mol dm ⁻³
D	Number of communicative civilisations	dimensionless
d	Ice thickness	μm
d_{rel}	Relative ice thickness	dimensionless
E	Energy	J or eV
E_b	Energy barrier between adsorption sites	J mol ⁻¹
E_D	Desorption energy	J mol ⁻¹
E_d	Dissociation energy	J mol ⁻¹
f_c	Fraction of intelligent life-forms that become radio-communicative	dimensionless
f_i	Fraction of life-sustaining planets on which intelligent life emerges	dimensionless
f_l	Fraction of planets on which life emerges	dimensionless
f_p	Fraction of stars having orbiting planets	dimensionless
f_v	Volume filling factor	dimensionless
G	Heat conductance	W K ⁻¹
H	Average number of habitable planets per star	dimensionless
I	Radiation power intensity	W cm ⁻³
i	Current density	μA cm ⁻²
$I(Y)$	Current	μA
j	Black body radiant emittance	W m ⁻²
k	Generic constant	various
L	Duration for which intelligent life-forms are radio-communicative	year
l	Gradient	variable
M	Mass	g to kg
m	Molecular mass	amu
N	Column density	cm ⁻²
N_c	Corrected normalised column density	dimensionless
N_{fr}	Number of fringes observed in interferogram	dimensionless
N_n	Normalised column density	dimensionless
N_p	Normalised column density plateau (steady-state) value	dimensionless
n	Particle number density	cm ⁻³
n_e	Expected molecular fragmentation rate	molecules ion ⁻¹
n_0	Amount of substance	mol
P	Transmitted radiant power	W
P_0	Incident radiant power	W
P_a	Absorption band peak area	cm ⁻¹
P_s	Stopping power	eV nm ⁻¹
p	Pressure or partial pressure	Pa
Q	Coulombic charge	C
R_{in}	Rate of influx	s ⁻¹
R^*	Rate of stellar formation	year ⁻¹
r	Internuclear separation	Å to cm
r_{diss}	Rate of molecular dissociation	molecules s ⁻¹
r_{eq}	Equilibrium internuclear separation	Å to cm
r_{ion}	Rate of projectile ion delivery	ions s ⁻¹
S	Sticking coefficient	dimensionless

s	Pumping speed	$\text{m}^3 \text{s}^{-1}$
T	Temperature	K
t	Time	s
T_v	Transmittance	dimensionless
V	Voltage or volume	V or cm^{-3}
V_{av}	Average excitation potential	eV mol^{-1}
v	Velocity	cm s^{-1}
ν_q	Vibrational quantum number	dimensionless
x_a	Anharmonicity constant	dimensionless
Z	Atomic number	dimensionless
α	Area	cm^2
β	Solid angle cone half-angle	degrees
δ	Dose	Gy
ε	Molar attenuation coefficient	$\text{dm}^3 \text{mol}^{-1} \text{cm}^{-1}$
η	Refractive index	dimensionless
θ	Angle of reflection	degrees
κ	Thermal conductivity	$\text{W K}^{-1} \text{cm}^{-1}$
λ	Wavelength	m
μ	Reduced mass	amu
ν	Frequency	Hz
ζ	Wavenumber	cm^{-1}
ρ	Density	g cm^{-3}
ρ_{mol}	Molecular density	molecules cm^{-3}
σ	Cross-sectional area	cm^2
τ	Excited state lifetime	fs to μs
τ_v	Optical depth	dimensionless
Φ	Beam flux	$\text{cm}^{-2} \text{s}^{-1}$
φ	Beam fluence	cm^{-2}
χ	Electronegativity	dimensionless
Ω	Acceptance solid angle	degrees
Ω^0	Central solid angle	degrees
ω	Vibrational frequency	Hz
ω_a	Vibrational frequency of an anharmonic oscillator	cm^{-1}

Term	Physical Constant	Value
c	Speed of electromagnetic radiation <i>in vacuo</i>	$3 \times 10^8 \text{ m s}^{-1}$
e	Euler constant	2.71828
h	Planck constant	$6.63 \times 10^{-34} \text{ J s}$
m_e	Mass of an electron at rest	$9.11 \times 10^{-31} \text{ kg}$
m_p	Mass of a proton	$1.67 \times 10^{-21} \text{ kg}$
N_A	Avogadro constant	$6.02 \times 10^{23} \text{ mol}^{-1}$
M_\odot	Solar mass	$1.99 \times 10^{30} \text{ kg}$
q	Fundamental or Coulombic electric charge	$1.602 \times 10^{-19} \text{ C}$
R	Universal gas constant	$8.314 \text{ J mol}^{-1} \text{ K}^{-1}$
π	Archimedes constant	3.14159
σ_{SB}	Štefan-Boltzmann constant	$5.67 \times 10^{-8} \text{ W m}^{-2} \text{ K}^{-4}$

1 SULPHUR IN SPACE: A LABORATORY PERSPECTIVE

This first chapter of the thesis introduces the key theme of extra-terrestrial sulphur chemistry. Although more complete descriptions of astrochemistry and the tools and techniques used to study solid-phase reactions in astrophysical ice analogues will be provided in subsequent chapters, this chapter will serve to not only introduce the topic of sulphur ice astrochemistry, but also highlight current problems and as yet unanswered questions in the field. The chapter concludes by providing a motivation for answering some of these questions, as well as an outline of how the thesis will set about addressing them.

Note: The majority of the work described in this chapter has been published in peer-reviewed journals or periodicals as: [1] Mifsud *et al.* (2021), *Space Sci. Rev.* **217**, 14.

1.1 Sulphur Astrochemistry: An Introduction

Sulphur is one of the most abundant elements in the Universe. Atomic sulphur has an estimated abundance of 1.32×10^{-5} relative to hydrogen (Asplund *et al.* 2009), while S^+ has a relative abundance of 1.66×10^{-5} (Esteban *et al.* 2004). This cosmic ubiquity of sulphur is the result of its efficient nucleosynthetic formation as a result of silicon burning within high mass stars, or alternatively as a result of the fusion of oxygen nuclei:



The fundamental chemistry of sulphur is similar to that of other chalcogen (group XVI) elements. However, compared to oxygen chemistry, for instance, the chemistry of sulphur is actually more versatile. The comparatively lower electronegativity¹ of sulphur allows it to accommodate a positive charge more easily, while still permitting the formation of hydrogen bonds. Moreover, sulphur is able to exist in several oxidation states between -2 and $+6$, while oxygen is significantly more limited in this regard being able to only exist in oxidation states between -2 and $+2$. Sulphur is also known to exist in multiple stable allotropic forms. Indeed, sulphur is second only to carbon in terms of the number of known allotropes (Greenwood and Earnshaw 1997). These allotropes largely take on the form of chains and rings, with the most stable being the puckered (or crown) structure of S_8 . In addition to the known allotropes, several polymorphs are also known to exist; the most common structures being the α - (rhombic) and the β - (monoclinic) polymorphs of S_8 (Fig. 1.1).

Sulphur is also known to be an active participant in several biochemical, geochemical, and atmospheric systems. From the biochemical standpoint, it is considered to be one of the six elements fundamental to all known life (the others being carbon, hydrogen, oxygen, nitrogen, and phosphorus). It is therefore perhaps not surprising that sulphur may be found in a wide variety of biomolecules, including amino acids, sugars, nucleic acids, and vitamins

¹ A full discussion of the physical and chemical meaning of the term 'electronegativity' will be provided in Chapter 3.

(Beinert 2001). In a geochemical context, terrestrial sulphur cycles are known to cover practically every environmental reservoir, including the biosphere, atmosphere, geosphere, and hydrosphere (Brimblecombe 2013). Other planets in the Solar System are also known to host a rich sulphur chemistry: the atmospheres of Venus and the ice giants Uranus and Neptune are known to contain various sulphur-bearing molecules (Zhang *et al.* 2012, Frandsen *et al.* 2020, Moses *et al.* 2020), while the magnetosphere of the planet Jupiter is known to be richly populated by sulphur ions (Cooper *et al.* 2001).

Despite this extensive and intriguing chemistry, the astrochemistry of sulphur presents several unanswered problems. It has been well established, for instance, that gas-phase sulphur chemistry accounts for its total expected cosmic abundance in diffuse interstellar clouds² (Sofia *et al.* 1994, Jenkins 2009). However, within dense interstellar clouds, there exists an unexpected paucity of sulphur, with the amount of sulphur observed in such regions being two to three orders of magnitude lower than the expected cosmic abundance (Tieftrunk *et al.* 1994, Ruffle *et al.* 1999). This lack of sulphur is largely reflected in the small number of sulphur-bearing molecules that have been detected in interstellar space: as of June 2022, only 33 such molecules have been detected in the gas phase, corresponding to about 12% of all known interstellar molecules (McGuire 2022). About one-third of these sulphur-bearing molecules were detected in the years 2021 and 2022, and the majority of them are simple diatomic or triatomic species with only five complex organic molecules incorporating sulphur having been detected.

Several attempts at investigating this ‘sulphur depletion’ problem have been made. It is commonly assumed that the main mechanism by which sulphur is depleted is the Coulomb-enhanced freeze-out of S^+ onto negatively charged dust grains as diffuse interstellar clouds evolve into translucent ones (Ruffle *et al.* 1999). Caselli *et al.* (1994) investigated the possibility that the resultant sulphur atoms mostly reside on the surface of the dust grains, where they may be rapidly converted to H_2S *via* surface-catalysed hydrogenation reactions. The fact that H_2S has yet to be detected within interstellar icy grain mantles, however, seems to contradict the possibility that H_2S is the most abundant sulphur-bearing molecule in dense interstellar clouds.

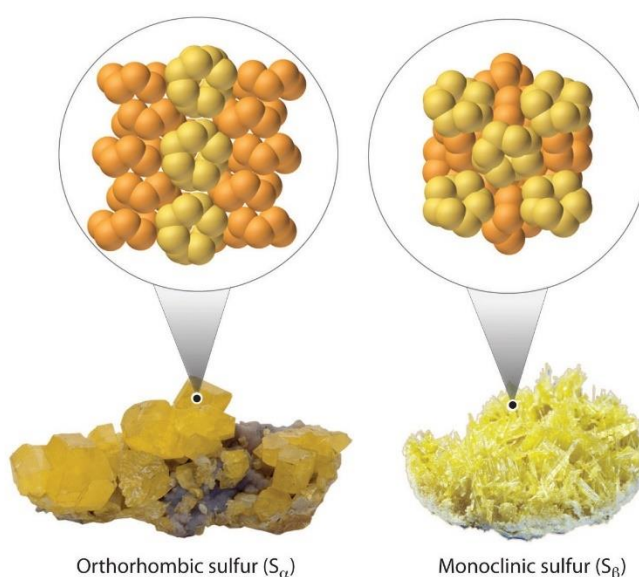


Fig. 1.1: Images of the rhombic (α -) and the monoclinic (β -) polymorphs of S_8 . Image credit: C.P. Chieh.

² Further information on the structure and evolution of interstellar space is provided in the next chapter.

The chemical nature of this depleted sulphur is thus still widely debated. Modelling efforts by Vidal *et al.* (2017) suggested that, depending upon the age of the dense cloud, the majority of sulphur exists either as unobservable atoms in the gas phase or as H₂S within condensed ices. Navarra-Almáida *et al.* (2020) also suggested the dominance of gas-phase sulphur atoms, while combined experimental and theoretical studies by Cazaux *et al.* (2022) proposed that the formation of sulphur-based chains and rings is favourable during the Coulomb-enhanced freeze-out of S⁺. Shingledecker *et al.* (2020) also suggested that solid-phase allotropic forms of sulphur should be a major reservoir of the element within the dense interstellar medium (ISM), along with SO₂ and OCS. The work of Anderson *et al.* (2013) proposed that refractory sulphur allotropes could themselves be a major source of gas-phase atomic sulphur *via* shock-induced dissociation and sputtering. Such residual allotropes were not predicted by the model of Laas and Caselli (2019), who instead proposed that simple organosulphur molecules within the interstellar icy grain mantles should account for a large reservoir of sulphur.

Unanswered questions relating to sulphur astrochemistry are by no means limited to interstellar space. Several sulphur-bearing molecules are known to exist on various Solar System bodies for which no formation mechanism has been widely accepted. Of greatest interest to this thesis is the presence of SO₂ on the surfaces of the icy Galilean moons of Jupiter, but particularly so on Europa. The distribution of SO₂ on the European surface is such that it is significantly more prevalent on the trailing hemisphere, arranged in a ‘bulls-eye’ pattern (Carlson *et al.* 2005, Hendrix *et al.* 2011, Becker *et al.* 2022). This is suggestive of an exogenic source of sulphur, in which sulphur ions (largely S⁺ and S²⁺) from the Jovian magnetosphere preferentially impact and implant into the oxygen-rich surface ices on the European trailing hemisphere, yielding the SO₂ as a primary product.

However, laboratory experiments investigating the implantation of high energy sulphur ions into H₂O ice (the dominant icy species on the surface of Europa) have thus far consistently failed to document the formation of SO₂ (Strazzulla *et al.* 2007, Strazzulla *et al.* 2009, Ding *et al.* 2013). Computational simulations have also reported similar negative results (Anders and Urbassek 2019a, Anders and Urbassek 2019b). Instead, it is H₂SO₄ and its hydrates that are efficiently produced as a result of sulphur ion implantation into H₂O ice. Such results actually tie in well with observations of the surface composition of Europa, where it has been established that H₂SO₄ and its hydrates are not only the dominant sulphur-bearing molecule, but are also arranged in a ‘bulls-eye’ pattern on the trailing hemisphere (Shirley *et al.* 2010, Dalton *et al.* 2012). Later work by Dalton *et al.* (2013) found a very strong correlation between the surface H₂SO₄ abundance and magnetospheric sulphur ion influx which, when combined with the laboratory results described above, has led to the general acceptance of exogenic ion implantation as the primary method for H₂SO₄ formation on the surface of Europa.

More recent studies have looked into the possibility of forming SO₂ as a result of the implantation of reactive sulphur ions into other oxygen-bearing molecular ices known to exist on the surface of Europa, such as CO₂. However, the results of these studies have been seemingly contradictory. After implanting sulphur ions into CO₂ ice at 15 K, Lv *et al.* (2014a) reported the detection of SO₂ and quantified its formation efficiency as being 0.38 molecules ion⁻¹. Based on this value, Lv *et al.* (2014a) estimated that the observed abundance of SO₂ on the surface of Europa could be synthesised within a geologically reasonable time-scale of 2×10⁴ years. However, this estimate relies on the assumption that implantation processes at 15 K are representative of those occurring on the surface of Europa, where temperatures are significantly higher. This assumption was made due to a previous observation in which the yield of CO and CO₂ from H₂O ice into which carbon ions were implanted was found to be independent of temperature (Lv *et al.* 2012). Follow-up studies by Boduch *et al.* (2016), however, did not observe the formation of SO₂ after the

implantation of sulphur ions into CO₂ ice at 16 K. The possibility of forming SO₂ as a result of the implantation of magnetospheric sulphur ions into the various oxygen-bearing surface ices on Europa therefore remains an open question.

The formation of H₂SO₄ hydrates and SO₂ on the surface of Europa are thought to be constituent processes of a wider radiolytic sulphur cycle (Fig. 1.2), in which sulphur is transformed to different molecular forms as a result of its continuous irradiation by magnetospheric ions and electrons (Carlson *et al.* 1999, Carlson *et al.* 2002). The cycle is completed within 4000 years, however long-term imbalances may arise due to a net loss of H₂O *via* the Jeans escape³ of H₂ and O₂. The result of this is an increase in the abundance of sulphur-bearing molecules on the surface, resulting in its darkening. This may be alleviated by the adsorption of H₂O, followed by the oxidation of S_x, which may contribute to surface brightening.

It is therefore clear that sulphur ice astrochemistry, though poorly understood, is potentially rich and may involve the formation and destruction of simple and complex molecules which are of significant relevance to interstellar and Solar System chemistry, as well as the emergence of life in the Universe. In the remainder of this chapter, a concise overview of prior experimental work on: (i) thermal chemistry, (ii) photon-induced radiation chemistry, (iii) particle-induced radiation chemistry, and (iv) sulphur ion bombardment relevant to sulphur ice astrochemistry is provided. These studies have provided key insights into the chemistry of various sulphur-bearing molecules in interstellar and outer Solar System environments, and so serve as an excellent starting point from which key questions to be answered in this thesis may be identified. These questions will be outlined at the end of this chapter, while further details on the structure and chemistry of the icy cosmos, as well as on infrared spectroscopy and radiation chemistry, will be provided in subsequent chapters.

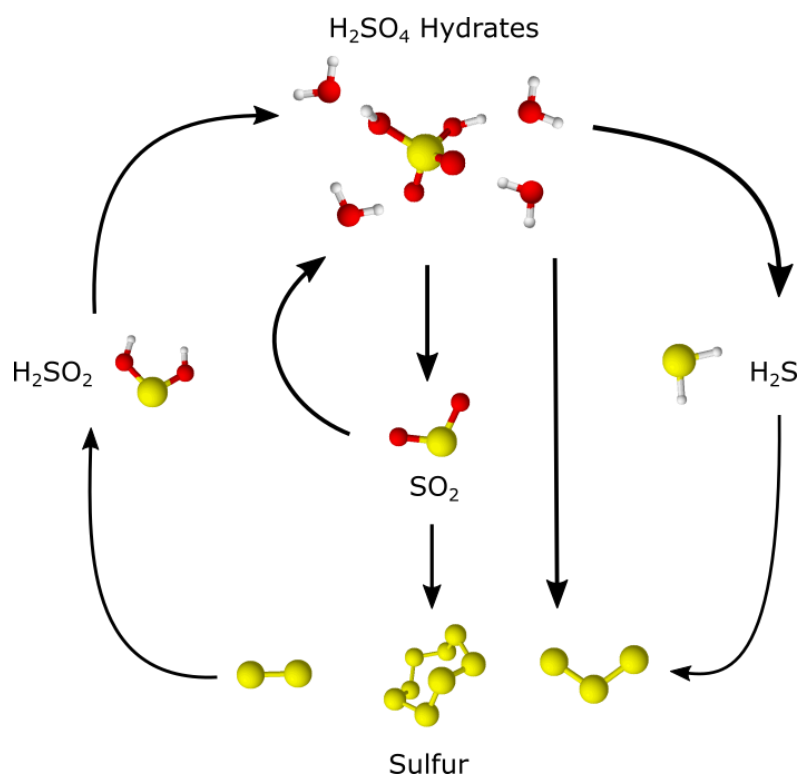
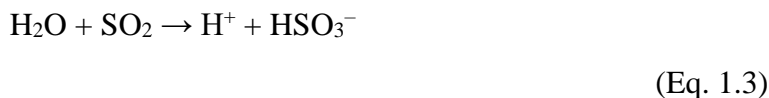


Fig. 1.2: A graphical summary of the radiolytic sulphur cycle present on the surface of Europa. Further information on individual process rates and species lifetimes may be found in the work of Carlson *et al.* (2002).

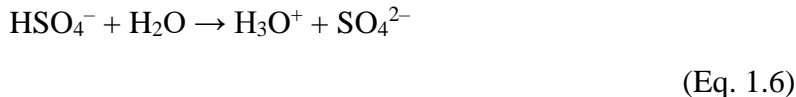
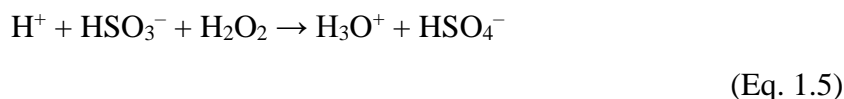
³ *Jeans escape* refers to the loss of gas-phase molecules from an atmosphere or exosphere due to their kinetic energy being sufficiently high as to cause their velocity to exceed the escape velocity of the planet or moon.

1.2 Thermal Chemistry

Cryogenic thermal reactions represent an important yet oftentimes neglected aspect of astrochemical research (Theulé *et al.* 2013). Despite this, however, prior laboratory studies have clearly demonstrated that sulphur ice thermal chemistry is potentially rich and may result in the consumption and production of various molecules of planetary and astrobiological significance. For instance, Kaňuchová *et al.* (2017) found that H₂O:SO₂ ice mixtures deposited at 16 K and thermally annealed to 160 K resulted in the formation of HSO₃⁻ anions, along with a smaller quantity of S₂O₅²⁻ anions.



Work by Bang *et al.* (2017) also showed that thermal reactions between H₂O ice and gas-phase SO₂ molecules may occur at temperatures greater than 90 K. In addition to the formation of HSO₃⁻, Bang *et al.* (2017) documented evidence for the formation of the OH⁻ anion and the SO₂⁻ anion. The results of these studies complemented the previous findings of Loeffler and Hudson (2010), Loeffler and Hudson (2013), and Loeffler and Hudson (2015), who also demonstrated that, when the ice mixture includes H₂O₂, the oxidation of HSO₃⁻ anions to HSO₄⁻ anions is favourable. Further oxidation to SO₄²⁻ anions may be achieved *via* H₂O-mediated deprotonation.



Building on their previous work, Loeffler and Hudson (2016) further showed that the above reaction scheme is also possible if the oxidant is switched from H₂O₂ to O₃. Indeed, analogous gas-phase chemistry is believed to contribute to the loss of O₃ in the atmosphere of the Earth (Erickson *et al.* 1977, Penkett *et al.* 1979). Most recently, the work of Tribbett and Loeffler (2022) showed that oxidation of H₂S ice mixed with O₃ in the presence of H₂O *via* thermal annealing also results in the production of the sulphur oxyanions listed above.

The thermal chemistry of OCS and CS₂ has also been investigated. Mahjoub and Hodyss (2018) found that the nucleophilic addition of CH₃NH₂ to OCS at temperatures exceeding 100 K resulted in the synthesis of NH₄⁺CH₃NHCSO⁻ (methylammonium methylthiocarbamate). This species may be an intermediate in the formation of peptides, and thus is of relevance to astrobiology and prebiotic chemistry. Of similar interest is the refractory species NH₄⁺NH₂CS₂⁻ (ammonium dithiocarbamate), which was shown to be efficiently formed *via* the thermal reaction between CS₂ and NH₃ in a mechanism believed to be analogous to the formation of NH₄⁺NH₂CO₂⁻ (ammonium carbamate) (Frasco 1964, Bossa *et al.* 2008, Methikkalam *et al.* 2016, James *et al.* 2020).

1.3 Photon-Induced Radiation Chemistry

Much of the experimental photon-induced radiation chemistry of sulphur-bearing ices that has been explored has focused on SO₂ and H₂S. The vacuum-ultraviolet photon irradiation of pure SO₂ ice has been shown to yield SO₃ as a primary product (Schriver-Mazzuoli *et al.*

2003a), possibly after the formation of SO₂ dimers (Sodeau and Lee 1980). Irradiation using soft x-rays revealed a similar chemistry (de Souza Bonfim *et al.* 2017), although the observation of an enhanced SO₂ photo-desorption rate at low photon fluences led to the hypothesis that, in the initial stages of irradiation, the fragments arising from the dissociation of SO₂ efficiently recombine to give SO₂ in an electronically excited state. The vacuum-ultraviolet irradiation of H₂O:SO₂ ice mixtures has also been studied, with the dominant product having been shown to be H₂SO₄ along with minor quantities of SO₄²⁻, HSO₄⁻, and HSO₃⁻ (Schriver-Mazzuoli *et al.* 2003a, Hodyss *et al.* 2019). Pilling and Bergantini (2015) extended such results by considering the soft x-ray irradiation of a more complex mixture of H₂O:SO₂:NH₃:CO₂, and found that various sulphur containing products such as monomeric and polymeric SO₃, H₂SO₄ and its hydrates, SO₄²⁻, HSO₄⁻, HSO₃⁻, and also H₂SO₃ were formed alongside other products including CO, O₃, H₂O₂, and the OCN⁻ anion.

The major product of the vacuum-ultraviolet and soft x-ray photon irradiation of H₂S ice is H₂S₂, although significant quantities of S_x ($x = 2-8$) also form efficiently (Harrison *et al.* 1988, Liu *et al.* 1999, Cook *et al.* 2001, Jiménez-Escobar and Muñoz Caro 2011, Jiménez-Escobar *et al.* 2012, Cazaux *et al.* 2022). The efficient production of S_x may go some way to explain the observed depletion of sulphur in dense interstellar clouds, as discussed earlier. It should be noted, however, that a recent investigation by Zhou *et al.* (2020) discovered a wavelength dependence for the quantum yield of HS radicals produced *via* H₂S photo-dissociation. Taking into account the absorption of photons from the interstellar radiation field by H₂S, this result implies that only about 26% of interstellar photo-excitations result in the production of HS radicals. Ice mixtures containing H₂S have also been irradiated with ultraviolet photons in laboratory studies: the irradiation of H₂O:H₂S mixtures resulted in the production of product molecules similar to those sourced from the irradiation of H₂O:SO₂ ices, along with SO₂ itself (Jiménez-Escobar and Muñoz Caro 2011). The irradiations of H₂S ice mixed with CO or CH₃OH have also been considered, and have been shown to result in the formation of various carbon-bearing molecules; most notably OCS and CS₂ (Jiménez-Escobar *et al.* 2014, Chen *et al.* 2015).

Although most of the available literature on the photon-induced radiation chemistry of sulphur-bearing astrophysical ice analogues is concerned with H₂S or SO₂, there have been some attempts to characterise this radiation chemistry in OCS and CS₂ ices. For instance, Ikeda *et al.* (2008) investigated the vacuum-ultraviolet photon irradiation of these species adsorbed to H₂O ice layers, and found that the formation of S₂ *via* the abstraction of sulphur by atomic sulphur is favourable. This work largely built upon the previous efforts of Dixon-Warren *et al.* (1990) and Leggett *et al.* (1990), who also demonstrated similar results. The irradiation of pure CS₂, on the other hand, is known to result in the formation of C₃S₂ (Heymann *et al.* 2000) along with stable refractory carbon-sulphur polymers (Cataldo *et al.* 1995). Similar polymeric products have been observed as a result of the irradiation of CS₂ using gamma rays (Cataldo 2000) and after its sonochemical treatment (Cataldo and Heymann 1998).

An interesting experiment looking into the cryogenic ultraviolet photon irradiation of OCS mixed with various halogen containing species in an argon matrix found that *syn*-halogenocarbonylsulphenyl halides based on X–C(=O)–S–Y backbones (where X and Y are the constituent atoms of the halogen species originally present in the ice) can be produced (Romano *et al.* 2001, Tobón *et al.* 2006). No evidence was observed for the corresponding *anti*-rotamer, however, as this conformational isomer is known to be less stable. When similar experiments were performed using CS₂ instead of OCS, both the *syn*- and *anti*-halogenothiocarbonylsulphenyl halides based on X–C(=S)–S–Y backbones were detected (Tobón *et al.* 2007). Such results clearly demonstrate the possibility of forming complex organic molecules containing sulphur as a result of the irradiation of ices containing only simple molecules, and thus hint at a potentially rich chemistry within astrophysical ices.

Lastly, it should be noted that the photon irradiation of more complex and exotic sulphur-bearing molecules has also been investigated. The irradiation of HSCH₂CN in an argon matrix was studied by Zapała *et al.* (2019), who found that a number of stable isomeric products could be produced. The results of this study are very significant to astrochemistry, since the related compound HSCN has been detected in interstellar space (Halfen *et al.* 2009). Matrix isolation photon irradiation experiments have also been carried out on thienyl substituted molecules, with various new sulphur-containing functional groups being produced (Pharr *et al.* 2012).

1.4 Particle-Induced Radiation Chemistry

In discussing the concept of particle-induced radiation chemistry in sulphur-bearing ices, it is the use of non-reactive charged particles such as ions of noble gases and electrons that shall be considered first. One of the earliest studies in this regard was that of Moore (1984), who demonstrated that the proton irradiation of condensed SO₂ either as a pure ice or mixed with S₈ yielded SO₃ and that, upon post-irradiation thermal annealing, SO₄²⁻ anions could also be observed. This result mirrors the findings of similar experiments conducted using vacuum-ultraviolet photon irradiation.

The irradiation of S_x in H₂O ice using 0.5 MeV electrons was observed to produce H₂SO₄ (Carlson *et al.* 2002), complementing the previous results of Johnston and Donaldson (1971) and Della Guardia and Johnston (1980) who had irradiated colloidal suspensions of sulphur in liquid H₂O. Persistent irradiation is also able to convert SO₄²⁻ anions to SO₂ (Hochanadel *et al.* 1955). Moore *et al.* (2007) would later go on to show that the proton irradiation of H₂O:SO₂ and H₂O:H₂S mixed ices results in the formation of various sulphur oxyanions, along with H₂SO₄ and its hydrates, in a similar fashion to the vacuum-ultraviolet photolysis and thermal chemistry experiments on H₂O:SO₂ ice mixtures discussed previously. Interestingly, when protons were implanted into SO₂ ices at 16 K, no evidence for H₂SO₃ formation was found (Garozzo *et al.* 2008). This outcome is somewhat unexpected, as the analogous process of H₂CO₃ formation as a result of proton implantation into CO₂ ice has been successfully carried out (Brucato *et al.* 1997, Garozzo *et al.* 2008, Strazzulla 2011). Experiments looking into the irradiation of H₂O ice deposited on top of refractory sulphurous residues also failed to produce any of the expected products, such as SO₂ (Gomis and Strazzulla 2008, Strazzulla *et al.* 2009).

In their study, Loeffler *et al.* (2011) considered the proton irradiation of H₂SO₄ along with its monohydrate and tetrahydrate forms. The main products of this irradiation process were SO₂, thiosulphate-based oligomers, and various sulphur oxyanions. However, perhaps the most interesting aspect of this study was the observed radio-resistance of the monohydrate acid compared to that of the pure acid. Moreover, the radiation-induced destruction of the tetrahydrate acid was found to be strongly correlated with temperature, with increased losses at irradiation temperatures of 86 K and below being recorded due to a combination of radiolysis and amorphisation which results in a change in the number of H₂O molecules associated with the acid. Later studies by Loeffler and Hudson (2012) demonstrated that, after low exposure to proton irradiation, amorphised H₂SO₄ could be recrystallised to its original structure *via* thermal annealing with nearly 100% recovery.

When binary ices containing a sulphur-bearing molecule (such as H₂S or SO₂) and a carbon-bearing molecule (such as CO or CO₂) are irradiated using protons, OCS readily forms (Ferrante *et al.* 2008, Garozzo *et al.* 2010). Several scenarios for such a process have been considered, including H₂O-rich and H₂O-free ices as well as mixed and layered ices. The overall yield of OCS has been shown to be dependent upon the nature of the sulphur-bearing and carbon-bearing parent molecules, with H₂S and CO being the most amenable to

OCS formation, likely *via* the direct addition of a radiolytically derived sulphur atom to CO (Ferrante *et al.* 2008). The irradiation of H₂S:CO mixed ices also results in the formation of appreciable quantities of CS₂ (Garozzo *et al.* 2010), which itself displays an interesting radiation chemistry. The radiopolymerisation of CS₂ has already been referred to (Cataldo 2000), however the irradiation of the pure ice using 5 keV electrons has been observed to also produce C₂S₂ and C₃S₂ (Maity *et al.* 2013). Furthermore, the electron irradiation of CS₂:O₂ and CS₂:CO₂ mixed ices has been studied, with various products being formed including OCS, SO₂, and SO₃ (Maity and Kaiser 2013, Sivaraman 2016).

The irradiation of H₂S using charged particles results in the formation of H₂S₂ as the major product (Moore *et al.* 2007), although higher order polysulphanes (H₂S_{*x*}; where *x* > 2) as well as S_{*x*} are also known to be formed (Cazaux *et al.* 2022). The irradiation of more complex ice mixtures containing H₂S has also been considered. For example, Mahjoub *et al.* (2016) and Mahjoub *et al.* (2017) showed that the simultaneous electron irradiation and thermal annealing of a H₂O:CH₃OH:NH₃:H₂S mixed ice results in a great many sulphur-bearing products being formed, including simple molecules such as S_{*x*}, OCS, CS₂, S₂, and SO₂; as well as complex species such as CH₃SCH₃, CH₃S₂CH₃, and CH₃SOOCH₃ (methyl methanesulphinate).

Finally, it must be noted that the charged particle irradiation of ionic solids representative of mineral structures in interstellar grains or on the surfaces of outer Solar System bodies has also been studied. The irradiations of Li₂SO₄, Na₂SO₄, and MgSO₄ have yielded oxide, sulphide, and hydroxide salts, along with SO₂ and O₂ (Sasaki *et al.* 1978, Johnson *et al.* 1998). In the case of Na₂SO₄, irradiation is thought to represent a facile method of sodium loss (Benninghoven 1969, Wiens *et al.* 1997), and may be the mechanism by which atomic sodium is fed into the exosphere of Europa (Brown and Hill 1996).

1.5 Sulphur Ion Bombardment

The implantation of reactive sulphur ions into molecular ices can lead to the formation of new molecules incorporating the projectile sulphur ion. Perhaps the most studied system is the implantation of sulphur ions into H₂O ice. Such implantations have been shown to result in the formation of H₂SO₄ and its hydrates (Strazzulla *et al.* 2007, Strazzulla *et al.* 2009, Ding *et al.* 2013), although no evidence has thus far been found for the formation of other, simpler sulphur-bearing molecules such as H₂S or SO₂. The formation of H₂SO₄ is fairly efficient, though, with a formation efficiency of about 0.65 H₂SO₄ molecules per impinging sulphur ion when 200 keV S⁺ ions are used (Strazzulla *et al.* 2007). Systematic implantations of multiply charged sulphur ions over an energy range of 35-176 keV also further demonstrated that the production of H₂SO₄ and its hydrates is independent of the charge state of the projectile, but is dependent on its energy with greater abundances of the acid being produced when using higher energy sulphur ions (Ding *et al.* 2013).

Lv *et al.* (2014a) showed that the implantation of 176 keV S¹¹⁺ ions into condensed CO at 15 K results in the formation of SO₂ as well as OCS. The implantation of 90 keV S⁹⁺ ions into CO₂ ice under similar experimental conditions was also reported to form SO₂ as a product, but formed CS₂ rather than OCS (Lv *et al.* 2014a). Follow-up studies by Boduch *et al.* (2016), however, did not detect SO₂ as a product after their implantations of 144 keV S⁹⁺ ions into CO₂ ice at 16 K. It should be noted that Boduch *et al.* (2016) made use of ultraviolet absorption spectroscopy as their primary analytical tool, as opposed to the more traditional infrared absorption spectroscopy. As such, they ascribed their non-detection of SO₂ as the result of the abundance of that molecule being less than the detection limit of their instrument, or else due to the fact that the ultraviolet absorption features of SO₂ could have been hidden by the more intense features of SO₃⁻ radical anions, which were detected.

Boduch *et al.* (2016) also did not detect any SO₂ after the implantation of 144 keV S⁹⁺ ions into pure O₂ ice, although the abundance of any SO₂ formed could also have been less than the detection limits of their instrument. It is worth noting that the implantation of such ions into CO₂:NH₃ and H₂O:CO₂:NH₃ ice mixtures in a study by Lv *et al.* (2014b) also did not result in the formation of any sulphur-bearing species, however the fluences used in that study were too low to allow for any significant accumulation of such molecules.

Computational simulations have also been employed to aid in addressing the possibility of forming new sulphur-bearing molecules as a result of the irradiation and implantation of reactive sulphur ions into molecular ices. Anders and Urbassek (2019a) simulated the irradiation of a complex multi-component ice whose composition was relevant to the surface of Europa by a 20 MeV S⁺ ion, and found that this irradiation actually resulted in a net loss of SO₂, which had been initially included in the ice mixture. It should be noted, however, that this simulation did not consider the implantation of the S⁺ ion into the ice, and so any chemistry which may have led to the formation of novel sulphur-bearing species as a result of the incorporation of the sulphur projectile could not be studied. In a second study, Anders and Urbassek (2019b) did consider the implantation of a 20 MeV S⁺ ion into a simpler mixed ice containing H₂O, CH₃OH, CO₂, and NH₃. Although various complex organic molecules were found to form as a result of the irradiative processing of the ice, none incorporated the projectile S⁺ ion. This was likely due to the low fluence of one ion per simulation that was used. Ices of similar compositions were the subject of experimental studies by Ruf *et al.* (2019) and Ruf *et al.* (2021) who, by using an advanced mass spectrometric technique, found that the implantation of sulphur ions into such ices, as well as the organic residues left over after their irradiation using unreactive charged particles, could indeed result in the formation of several thousand organosulphur molecules with molecular weights of up to 900 amu.

1.6 Thesis Outline and Motivation

Throughout this chapter, a review of the available literature on sulphur ice astrochemistry has been provided in the context of sulphur chemistry in interstellar space and the outer Solar System. It is evident that many questions on this topic remain inadequately answered. The motivation behind this thesis is therefore to contribute further experimental results to aid in the elucidation and understanding of sulphur astrochemistry in the condensed phase, perhaps most particularly as it pertains to the simpler molecules H₂S and SO₂; although the astrochemistry of other sulphur-bearing molecules such as OCS and CS₂ is also of interest. Experiments aimed at better understanding the following questions have therefore been performed:

(i) Can improved and higher resolution infrared spectroscopy aid in the detection of H₂S and SO₂ in astrophysical ices?

The only sulphur-bearing molecular species to have been detected in interstellar icy grain mantles are OCS and SO₂. However, these detections remain tentative due to the observation of only one or no convincingly identifiable infrared absorption band (Boogert *et al.* 2015). H₂S has not been identified within interstellar ices, despite its hypothesised presence there based on its cometary abundance (Rubin *et al.* 2020). It is possible that improved and higher resolution infrared absorption spectra of H₂S and SO₂ ices deposited at various temperatures and undergoing thermal annealing may aid in the detection of these species in the ISM and in outer Solar System ices. This is particularly relevant in light of several current and forthcoming space-based observational missions. A thorough and systematic characterisation of the mid-

infrared spectroscopy of H₂S and SO₂ ices, both pure as well as mixed with H₂O, deposited at various temperatures and thermally annealed to sublimation has therefore been performed, the results of which are presented in Chapter 5.

(ii) Is the radiation chemistry of H₂S and SO₂ influenced by changes in the phase of the ice, and how does this compare to other, more often considered species?

Various studies have demonstrated the role of different physical parameters such as temperature or dose in the outcome of the radiation chemistry occurring within ices. However, studies examining the influence of solid phase on the outcome of such processes are rare, in spite of the fact that they may yield important insights into radiation astrochemistry. A thorough investigation of the role of the solid phase of different astrophysical ice analogues on the outcome of their irradiative processing is thus warranted, and has therefore been performed. Results obtained from the comparative electron irradiation of the amorphous and crystalline phases of solid H₂S and SO₂, as well as frozen CH₃OH, N₂O, and H₂O, are presented in Chapter 6.

(iii) Does sulphur ion implantation into oxygen-bearing ices represent a reasonable mechanism by which SO₂ may form?

In the previous sub-section, the chemical results of the implantation of reactive sulphur ions into various oxygen-bearing astrophysical ice analogues were discussed at length. Implantation of such ions into H₂O ices does not result in the formation of SO₂, with H₂SO₄ and its hydrates being efficiently produced instead (Strazzulla *et al.* 2007, Strazzulla *et al.* 2009, Ding *et al.* 2013). Studies investigating the formation of SO₂ as a result of the implantation of sulphur ions into CO or CO₂ ices have reported seemingly conflicting results, perhaps due to the use of different analytical techniques (Lv *et al.* 2014a, Boduch *et al.* 2016). A systematic study investigating the possible formation of SO₂ (and other sulphur-bearing molecules) as a result of the implantation of reactive sulphur ions into O₂, CO, and CO₂ ices at different temperatures has been carried out; the results of which are presented in Chapter 7.

(iv) Can sulphur chemistry (including the formation of SO₂) be induced as a result of the irradiation of oxygen-bearing ices deposited above elemental sulphur layers?

The irradiation of H₂O ice deposited on top of a refractory sulphurous residue has shown little to no evidence for the efficient formation of SO₂ (Gomis and Strazzulla 2008). The idea that sulphur-bearing volatiles (such as SO₂ or H₂S) could be formed as a result of the irradiation of other volatile species deposited onto elemental sulphur or sulphurous residues is an interesting one that may be applied to further understanding sulphur chemistry in interstellar icy grain mantles or on the surface of Europa, but it has not been explored beyond the initial study of Gomis and Strazzulla (2008). A systematic study considering the irradiation of the volatile species O₂, CO, CO₂, CH₃OH, and H₂O deposited as ices onto layers of pure sulphur at different temperatures has thus been performed using a new methodology to prepare the sulphur layers. The results of this study are given in Chapter 8.

The experimental work presented in this thesis throughout Chapters 5-8 relies heavily upon the use of infrared absorption spectroscopy as the primary analytical technique used to understand the radiation chemistry of different astrophysical ice analogues. As such, a discussion on molecular structure and symmetry, infrared spectroscopy, and radiation chemistry will form the basis of Chapter 3, which follows a detailed introduction to the science of astrochemistry provided in Chapter 2. In Chapter 4, a detailed overview of the experimental techniques and apparatus used will be provided. This apparatus, the Ice Chamber for Astrophysics-Astrochemistry (ICA), is a novel and highly versatile scientific

instrument which has been purposefully designed to conduct experiments on the radiation astrochemistry of astrophysical ice analogues and is located at the Institute for Nuclear Research (Atomki), where all the experimental work presented in this thesis was carried out. Finally, a summative conclusion will be presented in Chapter 9, which will also outline potential future directions for research in the field of sulphur ice astrochemistry.

2 MOLECULES IN SPACE: AN INTRODUCTION

This chapter introduces the subject of astrochemistry by providing a contextual history which highlights the major developments in the field and their implications since the first detections of molecules in interstellar space in the 1930s. Descriptions of the chemistry and molecular diversity of icy grain mantles embedded within the interstellar medium and on icy Solar System bodies are also given throughout the chapter.

2.1 Astrochemistry: The Chemistry of the Cosmos

Defining the term *astrochemistry* is not as easy a task as may first appear. It is perhaps natural, upon hearing this term, to imagine the chemistry defining the surfaces and atmospheres of exotic planets orbiting distant stars. If this is the case, however, then how would the underlying principles of astrochemistry differ from those of geochemistry and atmospheric science as applied to a more terrestrial context? Perhaps then, the field is more concerned with chemical reactions occurring within the depths of interstellar space.

However, the idea of active chemistry occurring within interstellar space was an especially challenging concept for astronomers in the early twentieth century, due to the low temperatures and particle number densities which permeate most of the so-called interstellar medium (ISM). Such conditions are insufficient to overcome reaction activation energy barriers. Moreover, it was expected that any chemical bonds that could form would be largely prevented from doing so due to efficient molecular dissociation mediated by the vacuum- and extreme-ultraviolet components of the interstellar radiation field.

Despite such apparent constraints, the first evidence for molecules in the ISM arose in 1937 when Swings and Rosenfeld (1937) suggested that absorption by CH radicals could account for an interstellar absorption line at 4300.3 Å which had been previously observed by Dunham (1937). This suggestion was largely confirmed by the observational work conducted by Adams (1941), as well as the laboratory experiments of McKellar (1940a, 1940b) who found that the absorption lines of CH included one which coincided well with the observed interstellar one. McKellar (1940b) also suggested that other unidentified interstellar absorption lines could be attributed to CN radicals.

Although several of the remaining interstellar absorption lines had yet to be positively identified, McKellar (1941) noted that the sharp nature of four in particular was similar to that of atomic and diatomic species, and that their relative spacing further suggested that they represented a vibrational progression of a photo-ionised molecule. Conversations between Herzberg and Teller would lead them to conclude that CH⁺ radical cations were the most likely candidate, and this was confirmed when the rotational-vibrational spectrum of CH⁺ was measured and was found to contain three vibrational bands which matched three of the interstellar ones exactly (Douglas and Herzberg 1941, Douglas and Herzberg 1942).

Despite this initial progress in the identification of the molecular sources of interstellar absorption lines, comparatively little headway has been made in defining the carriers of many diffuse interstellar bands (DIBs): a series of several hundred absorption features in the near-ultraviolet to mid-infrared spectra of stars as their light passes through diffuse interstellar media. Since their detection in 1922 by Heger (1922), astronomers and spectroscopists have struggled to identify the individual molecular carriers of these bands (Fig. 2.1), although it is believed that large carbon-bearing molecules such as fullerenes and polycyclic aromatic hydrocarbons (PAHs) are the most likely candidates (Herbig 1995, Ehrenfreund 1999).

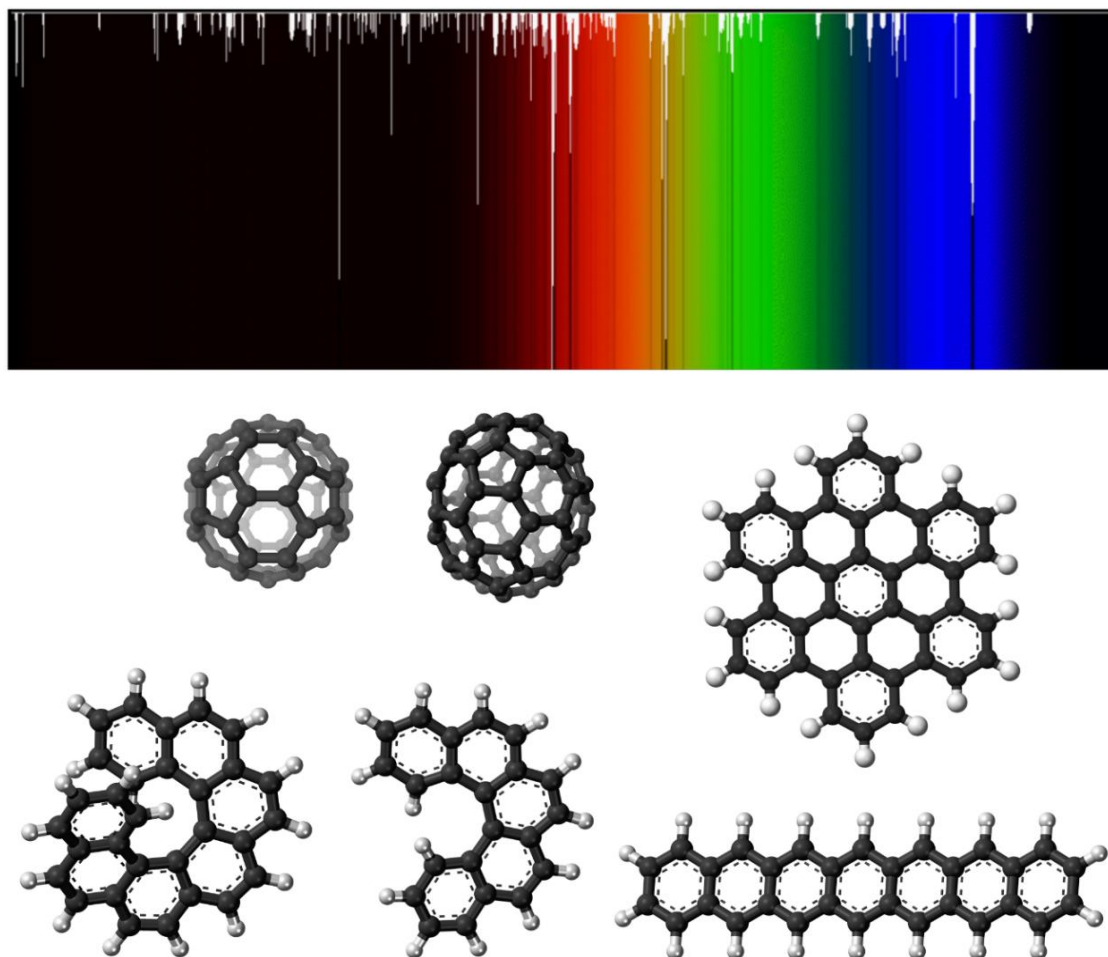


Fig. 2.1: *Above:* The relative strengths of the DIBs that characterise interstellar absorption spectra overlaid on a representation of the electromagnetic spectrum (image credit: NASA). *Below:* Examples of some of the large carbon-rich molecules (including fullerenes and PAHs) thought to be responsible for such absorptions.

Although predicted by many researchers in the preceding decades, the existence of fullerenes was only confirmed in 1985 when Kroto, Smalley, and Curl successfully detected C_{60} and C_{70} in the sooty residue of vaporised carbon (Kroto *et al.* 1985); a discovery for which they were awarded the 1996 Nobel Prize in Chemistry. Shortly after their discovery, the astrochemical significance of fullerenes and their cations as potential carriers of DIBs was recognised (Kroto 1988). In the 1990s, Foing and Ehrenfreund (1994) detected two DIBs with positions very close to two measured absorption bands of the matrix-isolated C_{60}^+ cation, and ascribed the small offset to shifts between the gas- and solid-phase spectra. Although initially disputed (Jenniskens *et al.* 1997), subsequent observational and spectroscopic work has indeed confirmed the status of C_{60}^+ as the carrier of bands at 9348.5, 9365.9, 9428.5, 9577.5, and 9632.7 Å (Campbell *et al.* 2015, Campbell *et al.* 2016, Walker *et al.* 2015, Spieler *et al.* 2017, Lallement *et al.* 2018, Cordiner *et al.* 2019).

This *modus operandi* of comparing laboratory-generated spectra to astronomical observations has been greatly assisted by the advent and development of radio astronomy starting in the mid-twentieth century, and has allowed for the identification of over 270 molecules in the ISM and circumstellar shells, as well as about 70 in extragalactic sources⁴. Interplanetary space missions within our own Solar System, such as probes and landing

⁴ A regularly updated list of molecules identified in such environments is available online in the Cologne Database for Molecular Spectroscopy: <https://cdms.astro.uni-koeln.de/classic/molecules>

modules, have also contributed to our understanding of the chemical processes and molecules on other planets and moons, asteroids, comets, and Kuiper Belt Objects (KBOs).

Interestingly, however, the detection of the most ubiquitous molecule in the cosmos, H_2 , proved to be one of the most challenging. Although its existence in the ISM had been proposed as early as the 1930s (Eddington 1937, Strömberg 1939), this was not confirmed until Carruthers (1970) detected it towards ζ Persei *via* rocket-borne ultraviolet spectroscopy in 1970. The reason for this 30-plus year discrepancy is that H_2 exhibits neither an electric dipole nor a magnetic dipole rotational-vibrational spectrum, making its detection in interstellar media or planetary atmospheres difficult. To overcome this problem, Herzberg (1938) suggested to instead detect the weak electric quadrupole infrared rotational-vibrational spectrum of H_2 , as well as the electric dipole spectrum of its isotopologue HD, with several bands being recorded and identified over the subsequent decades in laboratory experiments (Herzberg 1949, Herzberg 1950a, Herzberg 1950b, Durie and Herzberg 1960). Indeed, it was later discovered that quadrupole emission spectra of H_2 are regularly produced by collisional shocks and ultraviolet excitations in the ISM, with the first recorded instance being the observation of shocked H_2 in the Orion Nebula (Gautier *et al.* 1976).

Such progress in our understanding of cosmic chemistry led Dalgarno (2008) to propose a new definition for *astrochemistry* which is broad enough to include the chemistry occurring in both the ISM as well as stellar and planetary systems: “the study of the formation, destruction, and excitation of molecules in astronomical environments and their influence on the structure, dynamics, and evolution of astronomical objects”. By encompassing all these aspects of space chemistry, this definition highlights the interdisciplinary nature of the field which draws upon expertise from a variety of research areas. Discussions of the chemistry occurring in the ISM and the icy environments of the Solar System are provided in sub-sections 2.2 and 2.3, respectively.

2.2 The Structure and Chemistry of the Interstellar Medium

By conventional standards, the ISM could be considered a near-perfect vacuum due to it having a particle number density a factor of about 10^{19} lower than that of the terrestrial atmosphere at sea-level. The dispersed material contained within the ISM is composed of approximately 99% gas (largely hydrogen and helium, with a trace amount of heavier elements) and 1% carbonaceous or silicate dust grains (van Dishoeck 2014, Millar 2015). The ISM is, however, by no means a homogeneous structure and the material within it may be found in a variety of different physical states. Overall, interstellar baryonic matter may be classified into six distinct phases (Tielens 2005, Draine 2011)⁵, a summary of which is given below and in Table 2.1:

Table 2.1: Summary of the main characteristics of the different phases of the ISM. Data collected from the works of Tielens (2005), Draine (2011), and Millar (2015). Note that f_v refers to the volume filling factor of the ISM and n_{H} is the hydrogen particle number density.

ISM Phase	f_v	T (K)	n_{H} (cm^{-3})	Scale (pc)	State of H
HIM	0.5?	10^5 - 10^7	0.005	20 - 10^3	Ionised
WIM	0.1	10^3 - 10^4	0.3 - 10^4	100 - 10^3	Ionised
WNM	0.4	10^3 - 10^4	0.5	300-400	Atomic
CNM	0.01	100-300	20-50	100-300	Atomic
Diffuse Clouds	0.001	50-100	100	5-70	Mostly Atomic
Dense Clouds	0.0001	7-50	10^3 - 10^6	1-50	Molecular

⁵ A seventh phase, that of cool stellar outflows, has also been proposed but will be omitted from this discussion for the sake of clarity.

(i) Hot Ionised Medium

Also referred to as coronal gas, the hot ionised medium (HIM) is the most tenuous component of the ISM. Gas in the HIM is shock-heated to temperatures of $>10^5$ K by blast-waves caused by supernovae, which also heavily ionise the atoms present there (e.g., H^+ , C^{4+} , O^{6+}).

(ii) Warm Ionised Medium

Also known as H II regions, the warm ionised medium (WIM) is largely composed of hydrogen gas which has been photo-ionised to H^+ by recently formed hot and massive O- or B-type stars. The resultant zone of ionised gas surrounding the star is referred to as a Strömgren Sphere (Strömgren 1939). In addition to the WIM, photo-ionised hydrogen may be found as very distinctive structures known as planetary nebulae⁶. These structures are created when red giant stars undergo rapid mass loss processes later in their lifecycles thus exposing their stellar cores, the radiation from which is able to ionise the outflowing gas.

(iii) Warm Neutral Medium

The warm neutral medium (WNM) is composed of mainly atomic hydrogen gas heated to temperatures of $>10^3$ K. It is known to occupy a significant fraction of the volume of the ISM within the Milky Way Galaxy.

(iv) Cold Neutral Medium

The cold neutral medium (CNM) is also largely composed of atomic hydrogen gas, but at colder temperatures of a few 10^2 K.

(v) Diffuse Interstellar Clouds

Diffuse interstellar clouds are the first true ‘overabundances’ of baryonic matter in the ISM. Although these clouds are not massive enough to collapse under the influence of their own gravity, they are the starting point for the formation of the simplest astrophysical molecules and the main reservoir from which star-forming dense interstellar clouds develop. Diffuse clouds are so named because they are transparent to optical and ultraviolet photons, and the impinging radiation field results in the photo-ionisation of several atoms within the cloud, such as carbon and sulphur. Notably, atomic hydrogen resists ionisation as photons with energies equal to or greater than its ionisation potential (13.6 eV) are absorbed in the WIM surrounding luminous stars.

(vi) Dense Interstellar Clouds

Dense interstellar clouds are gravitationally bound star-forming structures having the highest particle number densities in the ISM. This high density makes the cloud opaque to impinging optical and ultraviolet photons and thus causes the cloud to ‘black out’ background star fields when viewed using ground- or space-based telescopes. Moreover, as the interior of the cloud is shielded from impinging optical and ultraviolet photons, the formation of simple molecules is not prevented by the high rates of photon-induced dissociation which characterise diffuse clouds. Another consequence of this shielding effect is that the temperature of the dense cloud drops significantly to 7-20 K at its cores, allowing much of the molecular material to condense onto the (sub)micron sized dust grains, thus forming an icy mantle. An example of one such dense cloud is shown in Fig. 2.2.

⁶ This name is an unfortunate misnomer as planetary nebulae are unrelated to planets. They were named as such by astronomers in the eighteenth century (including Herschel and de Pellepoix) who noted that their round shape resembled that of planets.

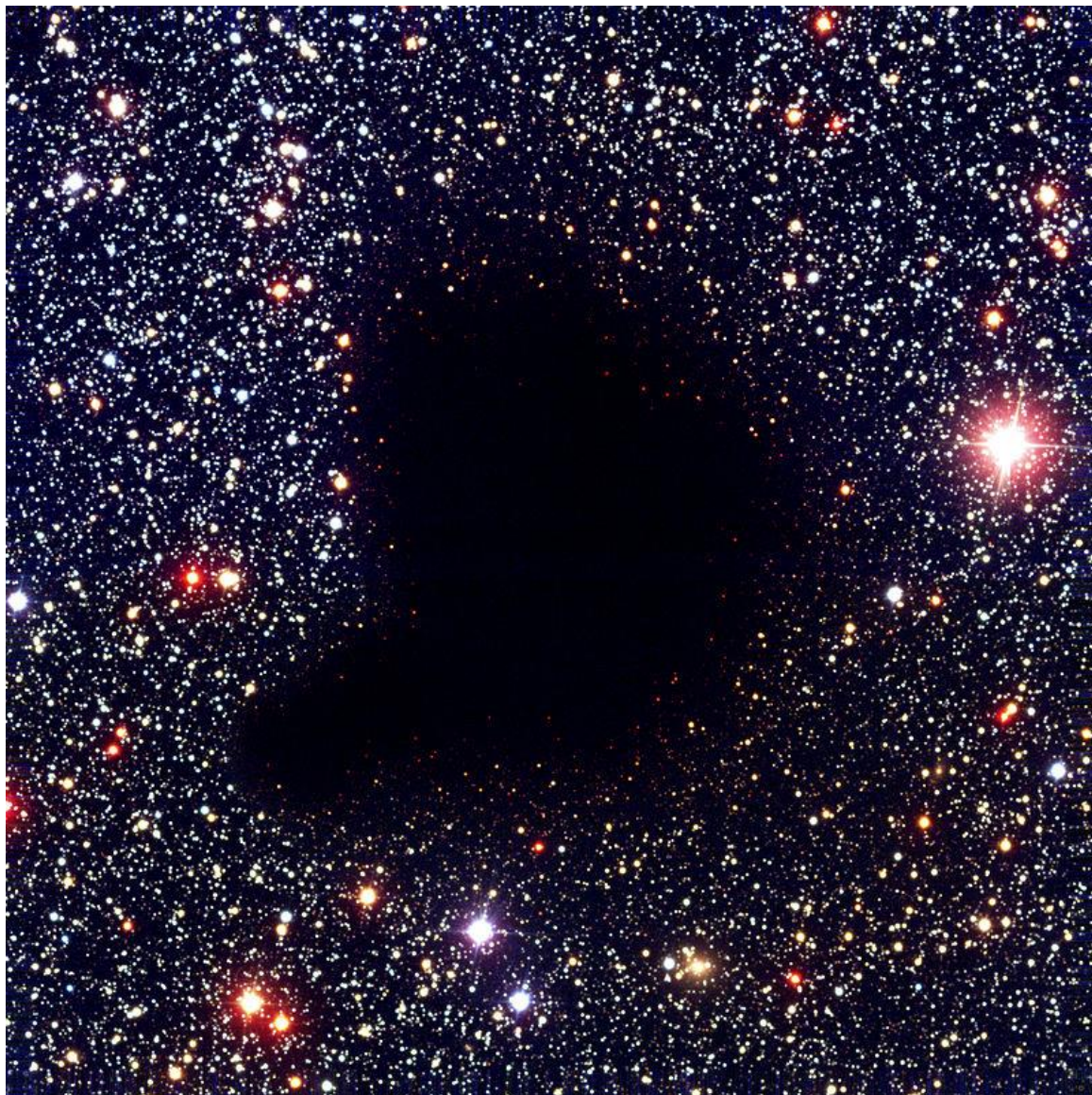


Fig. 2.2: Barnard 68 is a comparatively small dense interstellar cloud in the constellation Ophiuchus. At a distance of only 500 ly⁷ away, it is one of the nearest interstellar clouds. Image credit: ESO.

2.2.1 Diffuse Interstellar Clouds

Although the ISM displays a rich diversity of physical structures, it is the diffuse and dense interstellar clouds and the processes which occur within them that are perhaps the most relevant to astrochemistry. In their review, Arumainayagam *et al.* (2019) identified three milieux for astrochemical reactions leading to the production of molecules in these environments: gas-phase chemistry, reactions catalysed by the bare surfaces of interstellar dust grains, and reactions in icy grain mantles. The nature and complexity of the product molecules arising from each milieu is dependent upon a number of factors, including the astronomical environment in which the reaction is taking place and its physical and chemical characteristics.

⁷ A lightyear (ly) is the distance covered in one year by a photon travelling at the speed of light in a vacuum, and corresponds to 9.46×10^{15} m. Another unit of distance frequently used in astronomy is the parsec (pc), which is the distance at which one astronomical unit (AU; the average distance between the sun and the Earth taken to be 1.50×10^{11} m) subtends an angle of one arcsec. This is equivalent to 3.09×10^{16} m.

As mentioned previously, diffuse interstellar clouds are sufficiently dilute as to be transparent to optical and ultraviolet photons. As such, the gas and dust within the cloud are continuously bathed in the interstellar radiation field, which corresponds to a photon flux of $10^8 \text{ cm}^{-2} \text{ s}^{-1}$ (Habing 1968, Draine 1978). If the diffuse cloud is in the vicinity of a hot and massive star, then this flux would be substantially intensified. This continuous exposure to the interstellar radiation field has important consequences for the chemistry within the cloud.

For instance, it ensures the very high efficiency of photo-desorption processes, thus preventing the condensation of atomic or molecular material onto interstellar dust grains so causing this material, most of which is ionised, to remain in the gas phase. As such, gas-phase reactions are a dominant feature of diffuse interstellar cloud chemistry. These reactions may be sub-divided into at least nine different mechanistic types, as summarised in Table 2.2. Several reviews of the gas-phase chemistry occurring in the ISM are available, particularly on those reactions involving ionised species (Snow and Bierbaum 2008, Smith 2011, Larsson *et al.* 2012, Geppert and Larsson 2013, Millar 2015).

The presence of H_2O in diffuse clouds is dependent on such gas-phase reactions (Hollenbach *et al.* 2012, Yamamoto 2017). The reaction scheme (Fig. 2.3) begins with the OH^+ radical cation, which itself is produced *via* simple ion-molecule or charge transfer reactions. The reaction between OH^+ and H_2 results in the formation of H_2O^+ , which may subsequently react with a further moiety of H_2 to yield H_3O^+ . This species is isoelectronic with neutral NH_3 , and so it resists further hydrogen addition. Instead, it undergoes dissociative recombination to yield either H_2O (~25% of outcomes) or the neutral OH radical (~60% of outcomes). All hydrogenated cations in this reaction scheme have been detected using telescopes, such as the *Atacama Pathfinder Experiment* and the *Herschel Space Observatory* (Yamamoto 2017).

The lack of condensation onto the surfaces of dust grains in diffuse clouds also means that these surfaces, which are very irregularly shaped, are available for catalytic function during gas-grain reactions. Indeed, the formation of H_2 – the most abundant molecule in the cosmos – is reliant upon such surface catalysed reactions (Wakelam *et al.* 2017). A complete description of the properties of (sub)micron sized interstellar dust grains and their roles in gas-grain astrochemistry would go beyond the scope of this thesis, and so only a brief overview of those catalytic mechanisms relevant to molecular synthesis in interstellar clouds is provided here.

Experimental evidence has demonstrated that H_2 formation at the surfaces of dust grains principally occurs *via* three mechanisms: (i) the Eley-Rideal mechanism, (ii) the Langmuir-Hinshelwood mechanism, and (iii) the Harris-Kasemo (or ‘hot atom’) mechanism (Kolasinski 2008, Wakelam *et al.* 2017). Before considering the details of these mechanisms, it is important to note that the influx rate of atomic hydrogen onto an interstellar dust grain is fairly low, and may be calculated using Eq. 2.1:

$$R_{\text{in}} = \frac{v\sigma n_{\text{H}}}{4} \tag{Eq. 2.1}$$

where v is the velocity of an infalling hydrogen atom (cm s^{-1}), σ is the cross-sectional area of the dust grain (cm^2), and n_{H} is the hydrogen atom number density of the cloud (cm^{-3}). For a typical interstellar dust grain for which $\sigma = 10^{-10} \text{ cm}^2$, and assuming $v = 5 \times 10^4 \text{ cm s}^{-1}$, the influx rates in diffuse and dense interstellar clouds are on the order of 10^{-4} and 10^{-2} s^{-1} , respectively (Wakelam *et al.* 2017). Once an infalling hydrogen atom has made contact with the grain surface, it adsorbs such that it may or may not be fully energetically accommodated (i.e., thermalised).

In the Eley-Rideal mechanism, an incoming hydrogen atom reacts directly with an energetically accommodated partner already adsorbed to the surface before it is able to undergo thermalisation itself. The cross-section for this reaction is thus only on the order of atomic dimensions, however the resultant H_2 molecule is likely to leave the surface of the grain with most of the energy gained in the reaction. Conversely, the Langmuir-Hinshelwood mechanism requires two individual hydrogen atoms to thermalise on the surface of the grain and diffuse towards each other *via* thermal hopping or quantum tunnelling.

Table 2.2: Mechanisms by which gas-phase chemical reactions take place in the ISM. Table adapted from Arumainayagam *et al.* (2019).

Number	Reaction Type	Example
1	Cosmic-ray induced ionisation	$\text{H}_2 \rightarrow \text{H}_2^+$
2	Ion-neutral reactions	$\text{H}_2 + \text{H}_2^+ \rightarrow \text{H} + \text{H}_3^+$
3	Neutral-neutral reactions	$\text{H}_2 + \text{OH} \rightarrow \text{H} + \text{H}_2\text{O}$
4	Radiative association	$\text{C}^+ \rightarrow \text{H}_2 \rightarrow \text{CH}_2^+ + h\nu$
5	Dissociative recombination	$\text{H}_3\text{O}^+ + \text{e}^- \rightarrow \text{H} + \text{H}_2\text{O}$
6	Associative detachment	$\text{C}_6\text{H}^- + \text{H} \rightarrow \text{C}_6\text{H}_2 + \text{e}^-$
7	Photo-dissociation	$\text{H}_2\text{O} + h\nu \rightarrow \text{H} + \text{OH}$
8	Photo-ionisation	$\text{H}_2\text{O} + h\nu \rightarrow \text{H}_2\text{O}^+ + \text{e}^-$
9	Photo-detachment	$\text{C}_6\text{H}^- + h\nu \rightarrow \text{C}_6\text{H} + \text{e}^-$

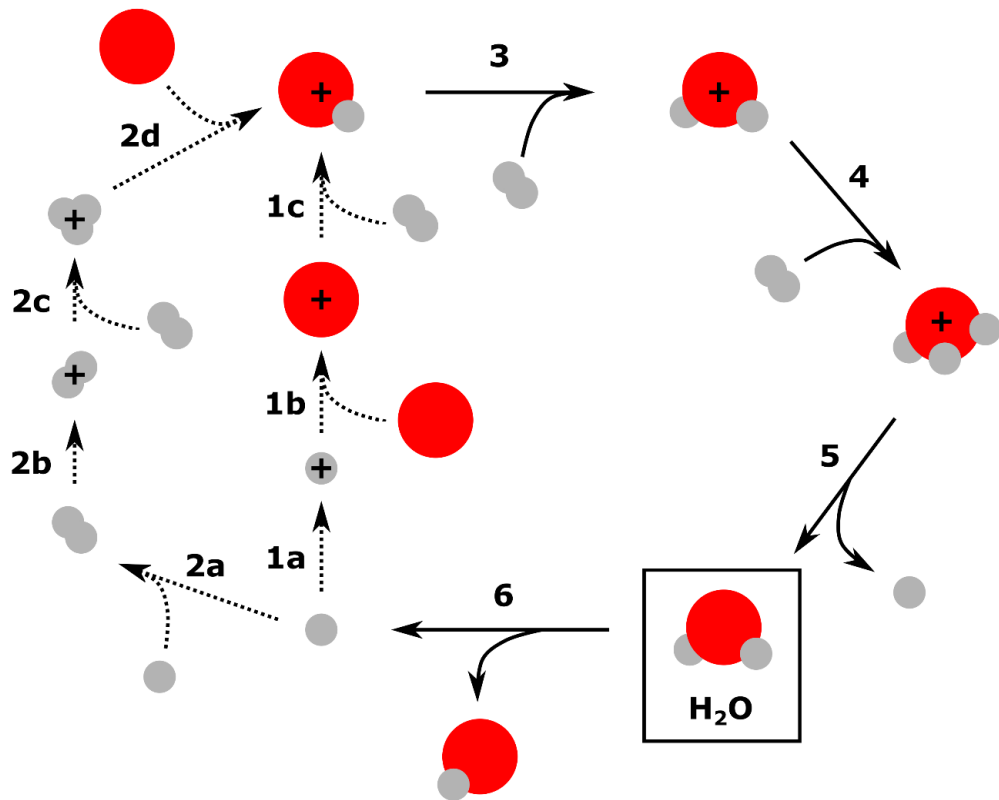


Fig. 2.3: The H_2O cycle in diffuse interstellar clouds is mediated almost entirely by gas-phase reactions. In this scheme, atomic hydrogen may be converted to OH^+ *via* one of two methods: ionisation by cosmic rays produces H^+ (1a) which may undergo charge transfer with atomic oxygen to yield O^+ (1b), the reaction of which with H_2 gives OH^+ (1c). Alternatively, dust grain-catalysed H_2 formation (2a) may be followed by ionisation by cosmic rays (2b) before the resultant H_2^+ reacts with H_2 to yield H_3^+ (2c). Due to the low proton affinity of H_2 , H_3^+ is an excellent proton donor and reacts with atomic oxygen to yield OH^+ (2d). Two successive reactions with H_2 sequentially yield H_2O^+ (3) and H_3O^+ (4), and the dissociative recombination of the latter with an incident electron finally yields H_2O (5). The cycle may be started again by the photo-dissociation of H_2O (6). For the sake of clarity, the emission of atomic hydrogen in reactions (1b), (1c), (2c), (3), and (4), as well as the emission of H_2 in reaction (2d), have been omitted.

Once the atoms come into contact, they react to yield H_2 which may or may not desorb from the grain surface, depending on how the energy gained in the reaction is utilised. The final mechanism under consideration, the Harris-Kasemo mechanism, involves an inbound hydrogen atom sampling the surface of the grain without being thermalised and yielding H_2 through a reaction with a thermalised hydrogen atom adsorbed to the grain surface. A visual summary of these mechanisms is provided in Fig. 2.4.

Although the Eley-Rideal, Langmuir-Hinshelwood, and Harris-Kasemo mechanisms have been described here in the context of H_2 formation from hydrogen atoms, they may be applied equally well to the formation of other species from various radicals and molecules adsorbed to the surface of interstellar dust grains. It is important to note, however, that grain surface reactions between radicals typically proceed with no activation energy barriers, while those involving non-radical species may possess appreciable reaction activation energy barriers (Herbst and van Dishoeck 2009).

Furthermore, the weak binding energies of adsorbate hydrogen (and deuterium) atoms mean these atoms are able to diffuse across the surface of the dust grain at significantly higher rates than heavier adsorbates, which are typically more strongly bound to the surface (Herbst and van Dishoeck 2009). As such, hydrogenation (and deuteration) reactions are very efficient and dominate the chemistry at grain surfaces. Such diffusive chemistry proceeding through Langmuir-Hinshelwood mechanisms is in fact preferred over Eley-Rideal processes, even in the context of non-hydrogenation reactions.

Interestingly, Langmuir-Hinshelwood surface reactions involving non-radical species are characterised by higher activation energy barriers than Eley-Rideal reactions, despite being the preferred catalytic mechanism. This is due to the existence of a linear relationship between the total adsorbate surface binding energy and the reaction activation energy barrier (Baxter and Hu 2002). As two species are adsorbed in the Langmuir-Hinshelwood mechanism and only one is adsorbed in the Eley-Rideal, it is evident that the former should exhibit higher activation energy barriers.

The preference for the diffusive Langmuir-Hinshelwood mechanism derives from the fact that the reaction cross-section of the Eley-Rideal mechanism is on the order of atomic dimensions. Therefore, unless the inbound species is directly above the adsorbate and in the correct relative orientation for reaction, the Eley-Rideal mechanism cannot occur and the inbound species will instead adsorb onto the surface (Baxter and Hu 2002). In contrast, if two diffusing species do not successfully react as per the Langmuir-Hinshelwood mechanism, then it is still possible for them to diffuse across the surface and re-attempt reaction upon making contact at a later point.

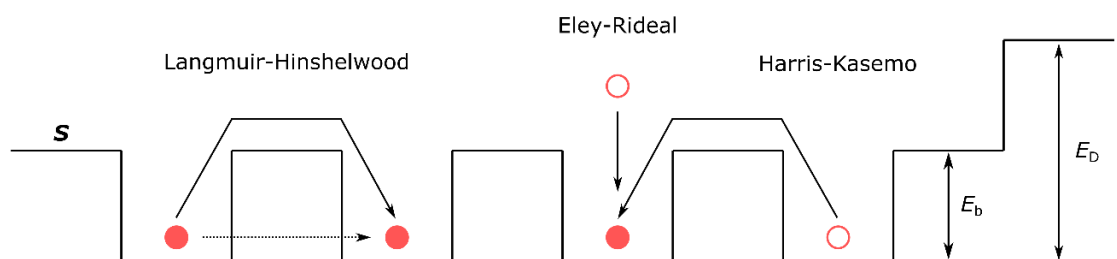


Fig. 2.4: Summary of the surface reaction mechanisms available on an interstellar dust grain. In this image, thermalised species are given as solid circles, while non-thermalised species are represented by hollow circles. S refers to the sticking coefficient of a gas-phase adsorbate, E_b is the energy barrier from one adsorption site to the next, and E_D is the binding (or desorption) energy of an adsorbate to the surface. Image adapted from Herbst and van Dishoeck (2009).

It is at this point that the topic of the existence of molecules in diffuse interstellar clouds should be discussed in more depth. Although continuously impinged upon by the vacuum- and extreme-ultraviolet components of the interstellar radiation field, diffuse interstellar clouds evidently play host to a rich chemistry. Indeed, the earliest molecules to be detected in the ISM (e.g., CH, CH⁺, and CN) were all identified in diffuse interstellar media (McKellar 1940a, McKellar 1940b, McKellar 1941, Douglas and Herzberg 1941, Douglas and Herzberg 1942). For this to be the case, however, it is necessary for the gas-phase and grain surface reactions described above to proceed at rates sufficient to counterbalance molecular destruction *via* photo-dissociation or pre-dissociation.

Diffuse interstellar clouds are not homogeneous structures, and so may offer settings in which the accumulation of molecular material may take place as a result of the predominance of such chemical reactions. Snow and McCall (2006) proposed a classification system in which diffuse clouds may be sub-divided into three types representing an evolutionary progression from the most tenuous cloud to the densest (Fig. 2.5). The classification of diffuse clouds into any of these types is based on the molecular content (or fraction) of the cloud, and not on its mass density or line-of-sight properties.

Diffuse atomic clouds represent the first sub-division of the diffuse ISM, in which matter in the cloud is fully exposed to the interstellar radiation field. As such, nearly all molecules are rapidly destroyed by photo-dissociation and matter exists in the form of neutral or charged atoms. As stated previously, photons with energies equal to or greater than the ionisation potential of atomic hydrogen (13.6 eV) are absorbed in the WIM surrounding luminous stars, and so hydrogen remains in the neutral atomic form while other elements are ionised yielding an abundance of free electrons.

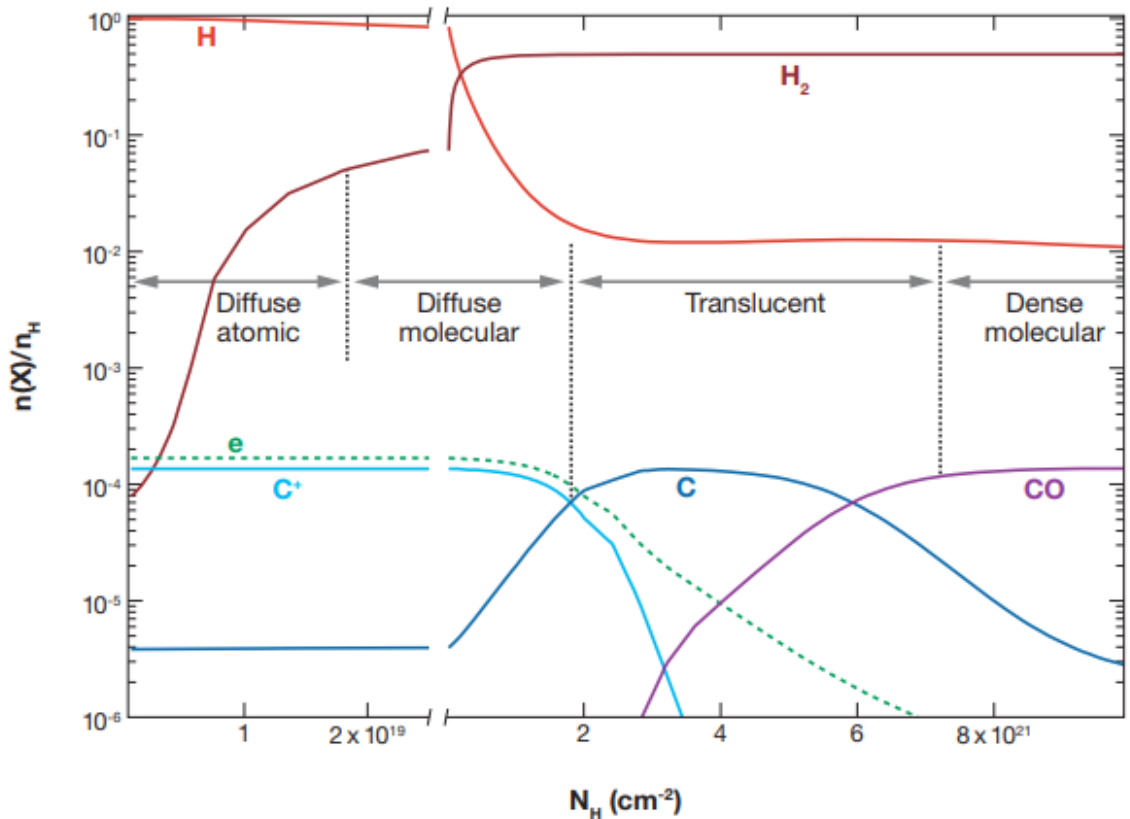


Fig. 2.5: Plot of the ratio of the number density of a particular species X to that of atomic hydrogen against the column density of atomic hydrogen. As can be seen, the fractional content of charged and atomic matter decreases in favour of molecular species on moving from diffuse atomic to dense molecular interstellar clouds. Image reproduced from Snow and McCall (2006).

Diffuse molecular clouds constitute the second sub-division, and are typically surrounded by a region of diffuse atomic gas which attenuates the individual wavelengths of the interstellar radiation field responsible for H₂ dissociation, thus allowing the molecular content of the cloud to increase. However, enough radiation penetrates the cloud so as to ionise other atoms (e.g., carbon and sulphur) and efficiently photo-dissociate other molecules. The presence of H₂ does, however, allow appreciable chemistry to begin *via* the gas-phase reaction mechanisms outlined above (Table 2.2).

The final sub-division of diffuse interstellar clouds are the translucent clouds, which represent an intermediate stage between the diffuse and dense ISM (van Dishoeck and Black 1989, Snow and McCall 2006). In such clouds, enough of the interstellar radiation field is attenuated by surrounding gas-phase material that carbon begins to transition from a charged atomic form to a neutral atom, with some molecular carbon (largely as CO) also being stable. Accompanying this increase in neutral species is a concomitant decrease in the number of free electrons present in the cloud.

2.2.2 Dense Interstellar Clouds

The idea of a natural and evolutionary progression from the most tenuous diffuse atomic clouds to dense molecular ones as pictured in Fig. 2.5 is a good starting point for a discussion of the structure and chemistry of the latter. Dense molecular clouds are formed *via* the aggregation of more diffuse interstellar matter: a more thorough review of the mechanisms behind this process was given by Ballesteros-Paredes *et al.* (2020). Similarly to their diffuse counterparts, dense interstellar clouds are not homogeneous in their structure and are characterised by regions of varying density. As such, they are often described in the literature as having a ‘clumpy’ structure.

Such heterogeneity in the structure of dense quiescent interstellar clouds offers different environments within which molecular formation from the three milieux identified by Arumainayagam *et al.* (2019) may take place. Two such environments which have received significant attention from the research community are the photon-dominated regions (PDRs) at the edge of the cloud, as well as its cold molecular cores. Despite both being associated with the dense ISM, these regions exhibit vastly different chemistries; summaries of which now follow.

PDRs are located at the edges of dense interstellar clouds and are often thought of as denser versions of diffuse interstellar clouds due to their exposure to the far-ultraviolet component of the interstellar radiation field (Fig. 2.6). Perhaps unsurprisingly, photo-dissociation reactions are a major component of PDR astrochemistry and atomic hydrogen is a dominant species in the most exposed regions of the cloud (Hollenbach and Tielens 1997). However, upon exceeding a column density of 10¹⁴ H₂ molecules cm⁻², the cloud becomes opaque to far-ultraviolet photons and so molecular material deeper within the cloud structure is shielded against photo-dissociation.

Their exposure to far-ultraviolet radiation raises the temperature of PDRs to a few 10²-10³ K (Hollenbach and Tielens 1997); considerably higher than those temperatures encountered deeper within the cloud. The combination of increased abundances of H₂, high temperatures, and an intense radiation field allows for new chemical pathways within PDRs as a result of the pumping of excited molecular rotational-vibrational states, thus rendering endothermic processes or reactions with high activation energy barriers more viable. As an example, the gas-phase synthesis of interstellar H₂O in PDRs may proceed *via* a series of neutral-neutral hydrogenation reactions mediated by vibrationally excited H₂. It is important

to note, however, that this non-equilibrium state-to-state chemistry⁸ is typically very selective and depends on which species is in an excited state. For example, although the rotational excitation of H₂ enhances the rate of its reaction with OH, the reaction is not favourable if it is OH which is the excited species.

Located deeper within the structure of the dense cloud, cold molecular cores are characterised by very different conditions to those found in PDRs. In the first instance, these cores constitute the densest and innermost regions of the cloud, and are thus well shielded from the interstellar radiation field which impinges upon PDRs. The attenuation of high energy photons thus results in a dark astrophysical environment devoid of large-scale photo-dissociation processes and temperatures as low as 7-20 K (Steinacker *et al.* 2016).

Under these conditions, astrochemical reactions may still take place *via* gas-phase chemistry or grain surface-catalysed processes, however an additional milieu is available: the cold temperatures within cold molecular cores allow for the development of icy grain mantles as a result of the condensation of atomic and molecular material (except for hydrogen and helium) onto the surfaces of the interstellar dust particles (van Dishoeck 2014, Arumainayagam *et al.* 2019).



Fig. 2.6: The Horsehead Nebula (also known as Barnard 33) is a dense interstellar cloud about 1375 ly away in the constellation Orion whose PDRs are clearly observable. Image credit: ESA.

⁸ This state-to-state chemistry is sometimes also referred to as non-Maxwellian chemistry due to it not meeting the thermodynamic equilibrium requirement of the Maxwell-Boltzmann distribution.

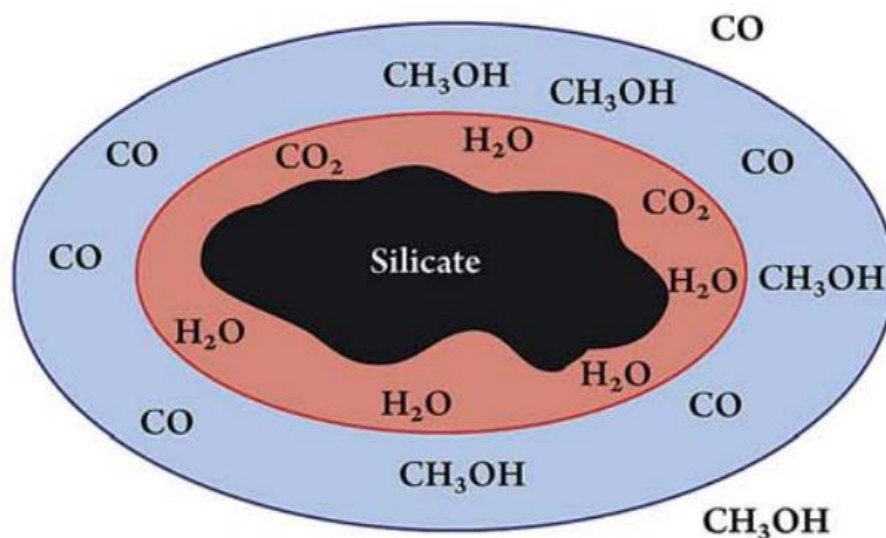


Fig. 2.7: A simplified representation of the layered structure of interstellar icy grain mantles. Note that the thicknesses of the ice layers relative to the dimensions of the dust grain have been exaggerated for the sake of clarity. Image adapted from Herbst and van Dishoeck (2009).

The first molecules to form these icy grain mantles are those resulting from the hydrogenation of heteroatoms adsorbed to the surface of the dust grains *via* the various mechanisms outlined above (Fig. 2.4), such as H_2O , NH_3 , CH_4 , and presumably also H_2S (Hiroaka *et al.* 1995, Ioppolo *et al.* 2008, Hidaka *et al.* 2011, Oba *et al.* 2019, Qasim *et al.* 2020). The formation of these species occurs fairly early on during the lifetime of the dense cloud, and the resultant molecular ice is polar⁹ due to it being dominated by H_2O molecules (Whittet *et al.* 2013). As the cloud evolves further and its density increases to a point where the total gas particle density exceeds 10^{15} cm^{-3} , the majority of the heavier molecular material undergoes a catastrophic condensation onto the dust grains to form a second icy layer (Fig. 2.7). As most of the gas condensing to form this second icy layer is CO , the accreted layer is non-polar in nature (Caselli *et al.* 1999, Pontoppidan 2006).

Interstellar icy grain mantles are thought to be the main reservoir from which many molecular species (including most complex organic molecules¹⁰) in the ISM are sourced, as gas-phase chemistry is thought to be insufficient to account for the total observed abundances of these species (Herbst and van Dishoeck 2009). Indeed, prior laboratory work on the chemistry occurring in these ices has repeatedly demonstrated the formation of complex organic molecules, including those that are relevant to biology such as amino acids and nucleobases (Muñoz Caro *et al.* 2002, Nuevo *et al.* 2007, Nuevo *et al.* 2012, Hudson *et al.* 2008).

Given that the main topic of this thesis is the chemistry occurring within astrophysical ices (including interstellar icy grain mantles), it is worthwhile to discuss the exact mechanisms by which such chemistry occurs in some detail. In total, there are five major mechanisms which drive molecular formation in astrophysical ices, which may be classified as either non-energetic (thermal chemistry and atom or radical additions) or energetic

⁹ A full discussion of the physical and chemical meaning of the term 'polarity' will be provided in the next chapter.

¹⁰ In the context of astrochemistry, a complex organic molecule is defined as one possessing six or more atoms. This differs greatly to the concept of a complex molecule as used in organic chemistry and biochemistry.

(radiation chemistry, photochemistry, and shock chemistry) processes. These mechanisms are summarised in Fig. 2.8 and a description of each now follows:

(i) Thermal Chemistry

Under cryogenic conditions, solid-phase thermal reactions with low activation energy barriers may still take place between closed-shell and electronically stable molecules. Such reactions are actually an important aspect of astrochemistry, and have been shown to lead to the formation of complex organic species and refractory residues. There are four types of thermal reaction which are of particular interest to astrochemistry: acid-base reactions, nucleophilic additions, eliminations, and condensation reactions. A review of thermal chemistry in laboratory astrophysical ice analogues was provided by Theulé *et al.* (2013).

(ii) Atom or Radical Additions

Atom addition reactions (specifically, hydrogenation reactions) have already been invoked to explain the initial formation of the polar layer in interstellar icy grain mantles and its constituent molecules, such as H₂O, NH₃, and CH₄. However, such additions may also take place at the surface of the ice. Indeed, the hydrogenation of condensed CO has been shown to sequentially yield H₂CO and CH₃OH (Watanabe and Kouchi 2002). The reaction of CO with OH radicals is also known to lead to the formation of CO₂ (Ioppolo *et al.* 2011). More complex molecules, such as CH₃CH₂OH and NH₂CH₂COOH (glycine) may also be formed through networks of atom or radical addition reactions (Ioppolo *et al.* 2021, Perrero *et al.* 2022). A review of relevant atom addition processes was provided by Linnartz *et al.* (2015).

(iii) Radiation Chemistry

Astrophysical ices are often found in energetic charged particle (i.e., ion and electron) radiation environments driven by galactic cosmic rays, stellar winds, or giant planetary magnetospheric plasmas. Such energetic processing leads to both structural and chemical changes within the ice, including: ice sputtering, the compaction of microporous structures, the amorphisation of ordered phases, and the radiolytic formation of radicals and molecules (Baragiola 2003, Boduch *et al.* 2015). It is interesting to note that, although many of these astrophysical radiation environments are characterised by fluxes of particles having energies in the range of a few keV to a few MeV (Arumainayagam *et al.* 2019), there is good evidence to suggest that the chemistry occurring in irradiated ices is in fact driven by a cascade of tens of thousands of non-thermal, low energy (<20 eV) secondary electrons (Mason *et al.* 2014, Boyer *et al.* 2016). New molecules may also be formed as a result of the incorporation of implanted reactive ions (e.g., carbon or sulphur ions) into astrophysical ices (Boduch *et al.* 2015). As most of the work presented in this thesis is concerned with the radiation chemistry of astrophysical ice analogues, the physical and chemical effects of ice irradiation will be discussed in much greater detail in the next chapter.

(iv) Photochemistry

Interstellar icy grain mantles are typically found embedded in the cold molecular cores of dense clouds, where the ultraviolet components of the interstellar radiation field should be efficiently attenuated. Despite this, photochemistry still plays an important role in the chemical and molecular evolution of these ices. This is due to the fact that the interaction of galactic cosmic rays (which are not attenuated by the boundaries of the dense interstellar cloud) with gas-phase H₂ results in the emission of a low intensity flux (about 10⁴ photons cm⁻²) of Lyman- α photons that may irradiate the ice (Öberg 2016).

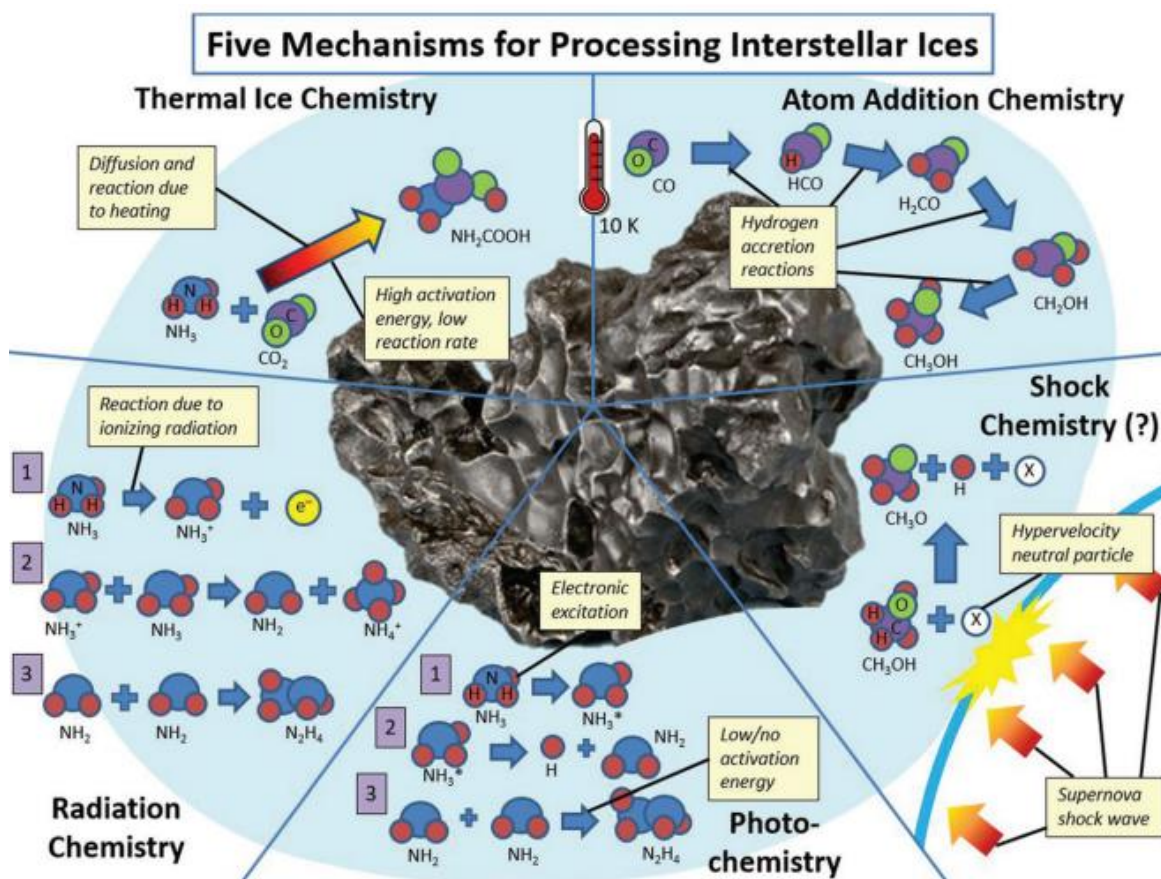


Fig. 2.8: Summative representation of the five major mechanisms driving molecular formation in astrophysical ices: (i) thermal chemistry, (ii) atom or radical addition reactions, (iii) radiation chemistry, (iv) photochemistry, and (v) shock chemistry. Image taken from Arumainayagam *et al.* (2019).

This ultraviolet photon irradiation of interstellar ices is known to efficiently produce radical species whose recombination leads to the formation of new molecules. Indeed, the production of complex organic molecules relevant to biology after ultraviolet photon irradiation of astrophysical ice analogues containing only simple molecules has been well established (Muñoz Caro *et al.* 2002, Nuevo *et al.* 2007, Nuevo *et al.* 2012). Physical restructuring processes within the ice, such as amorphisation, have also been reported in the literature (Kouchi and Kuroda 1990). At first glance, the physical and chemical effects of ultraviolet photon irradiation are similar to those of charged particle irradiation, since molecular ionisation, dissociation, and recombination are possible during both processes. However, several important distinctions also exist. For instance, the absorption of ultraviolet photons by solid-phase molecules is typically a ‘one-off’ event governed by the Grotthuss-Draper Law¹¹ and the Stark-Einstein Law¹². Furthermore, the resultant excitation is governed by the relevant selection rules. Contrastingly, charged particle projectiles may interact with multiple molecules along their track through the solid and the resultant excitations may access optically forbidden states.

¹¹ The Grotthuss-Draper Law states that photons must be absorbed by molecular materials in order to bring about a photochemical reaction.

¹² The Stark-Einstein Law states that, for each photon of light absorbed by a chemical system, no more than one molecule is activated to take part in a photochemical or photophysical process.

(v) **Shock Chemistry**

Shock chemistry is concerned with those processes which elicit molecular formation in astrophysical ices (including interstellar icy grain mantles) as a result of the contact collision of the ice with another body or of its interaction with a magneto-hydrodynamic shock wave. Experimental studies have shown that such processes do lead to the formation of new molecules, including those complex organic species relevant to biology (Goldman *et al.* 2010, Martins *et al.* 2013).

Despite the fact that interstellar icy grain mantles are widely considered to be the molecular factories of the ISM, very few species have been firmly (or even tentatively) detected in astronomical observations of interstellar ices (Boogert *et al.* 2015). This paucity of molecules observed in icy grain mantles contrasts greatly with the large and rapidly growing number of gas-phase molecules known to exist in interstellar and circumstellar media, which currently stands at over 270 (McGuire 2022) and is mainly due to the greater spectroscopic challenges associated with astronomical observations of ices compared to gas-phase molecules.

The detection of gas-phase interstellar molecules is typically achieved *via* the use of rotational spectroscopy. This is advantageous as the separation between rotational quantum levels is small enough such that absorption can take place against the background continuum, thus allowing for the emission signals of these molecules to be studied along any proposed line-of-sight (Fortenberry 2017, Puzzarini and Barone 2020). In the case of observations of interstellar ices, the unambiguous detection of molecules is more complicated due to the fact that the solid phase excludes the possibility of rotational motion, and thus rotational spectroscopy cannot be used in this regard.

Instead, infrared absorption spectroscopy has been traditionally utilised to observe the molecular components of interstellar icy grain mantles (Fig. 2.9). This technique does have a few drawbacks, however, most notably in that an infrared source (e.g., a young stellar object) behind the interstellar ices relative to the line-of-sight of the observer is required in order for the solid-phase molecules to access higher vibrational quantum levels that may be detected, thus greatly reducing the number of astrophysical environments that may be studied (Fig. 2.9). Identifying the individual carriers of interstellar infrared absorptions is also a somewhat difficult task, as molecules with similar structures and functional moieties present similar absorption spectra. Furthermore, the shape and position of these absorption bands are also known to vary significantly depending on several parameters of the ice, such as its thickness, structure, phase, chemical composition, and temperature (Boogert *et al.* 2015). A list of molecules identified in interstellar icy grain mantles is given in Table 2.3.

Table 2.3: List of solid-phase molecules in interstellar and circumstellar media as classified using the system used by Boogert *et al.* (2015). Securely identified molecules are those species for which more than one vibrational mode has been detected which fits well with modelled or laboratory-generated spectra. Likely identified molecules are classified similarly, but on the basis of having only one identifiable band observed in the ISM. Possibly identified molecules, on the other hand, are those species for which a convincing profile fit has not yet been demonstrated.

Securely Identified Molecules	Likely Identified Molecules	Possibly Identified Molecules
H ₂ O	H ₂ CO	HCOOH
CO	OCN ⁻	CH ₃ CH ₂ OH
CO ₂	OCS	HCOO ⁻
CH ₃ OH		CH ₃ CHO
NH ₃		NH ₄ ⁺
CH ₄		SO ₂
		PAH

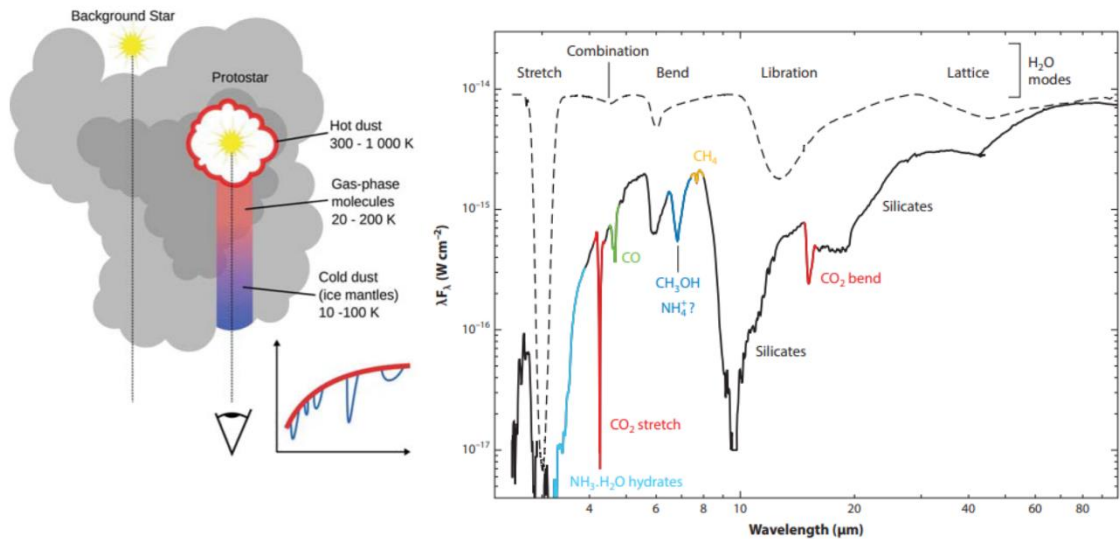


Fig. 2.9: *Left:* A graphical representation of the line-of-sight requirements for observing the molecular components of interstellar icy grain mantles, in which an infrared source such as a young stellar object must be behind the ices from the perspective of the viewer. Image taken from van Dishoeck *et al.* (2013). *Right:* An overview of the most prominent ice and dust absorption features as observed towards the young stellar object AFGL 7009 S. The dashed line trace represents the absorption spectrum of H₂O ice at 10 K. Image adapted from Boogert *et al.* (2015).

2.2.3 Giant Molecular Clouds and Bok Globules

The ‘clumpy’ molecular clouds discussed thus far may themselves be part of a significantly larger structure of molecular gas and ice. Once this larger structure exceeds a mass greater than ten thousand times that of the sun¹³, it is referred to as a Giant Molecular Cloud (GMC). GMCs are truly astronomically large objects, spanning around 600 ly across and having a mass of up to $10^7 M_{\odot}$ (Murray 2011). The overall structure of a GMC contains many diverse sub-structures including filaments, sheets, and irregularly shaped clumps that, as described above, may themselves be considered to be localised dense molecular clouds. GMCs are, however, by no means the largest structure in the cosmos, as they are able to associate with each other to produce molecular cloud complexes. For instance, the Orion molecular cloud complex is composed of two GMCs and a number of older stars somewhat isolated from the molecular gas.

Where GMCs represent some of the largest instances of associated molecular material in the cosmos, Bok globules lie on the opposite end of the size and mass spectrum. These isolated molecular clouds are typically not much greater than 1 ly across and have masses which do not exceed a few $100 M_{\odot}$; although most are smaller and much less massive than this. Barnard 68, shown in Fig. 2.2, is an example of one such Bok globule, having a mass of about $2 M_{\odot}$ and a diameter of just 0.5 ly.

2.3 The Cosmic Chemistry Cycle

An evolutionary progression starting from diffuse interstellar media and progressing to dense molecular cores (as demonstrated in Fig. 2.5) has already been alluded to. This evolution is

¹³ The mass of the sun is often referred to as a solar mass, and is equivalent to 1.99×10^{30} kg. The assigned symbol for the solar mass is M_{\odot} .

in fact part of a greater mechanism through which atomic and molecular material is cycled through various stages associated with the births and deaths of stellar and planetary systems. This cycle is referred to as the Cosmic Chemistry Cycle (Fig. 2.10); the details of which will be discussed in this sub-section. The diffuse interstellar regions described above represent what is perhaps the earliest evolutionary stage of the cycle, and so are a convenient starting point for such a discussion.

2.3.1 Setting the Stage for Stellar Birth

As described above, diffuse interstellar clouds are continuously exposed to the vacuum- and extreme-ultraviolet components of the interstellar radiation field. As such, most matter in these clouds remains in the atomic or ionised state, although a few molecules are produced as a result of gas-phase and surface-catalysed chemistry (e.g., H_2 , CH, and CN) and are able to survive the harsh environment. Aggregation of diffuse interstellar matter proceeds *via* magneto-hydrodynamically assisted gravitational attractions, resulting in a dense molecular cloud (Ballesteros-Paredes *et al.* 2020). As previously stated, the cores of dense molecular clouds are shielded from external low wavelength ultraviolet photons, providing a dark and cold environment in which interstellar icy grain mantles may form.

The edges of a dense cloud do not attenuate galactic cosmic rays, however, and these rays may initiate radiation chemistry within the solid ices. The interaction of these rays with gas-phase H_2 also engenders the production of Lyman- α photons which may initiate ice photochemistry. Of course, other kinds of chemistry (i.e., thermal reactions, atom or radical additions, and shock chemistry) may also result in the formation of molecules in interstellar icy grain mantles (Fig. 2.8). Dense molecular clouds are supported by turbulence and magnetic fields, and so may remain quiescent and stable for a few 10^6 years (van Dishoeck 2014), all the while producing new and increasingly complex molecules within the icy grain mantles.

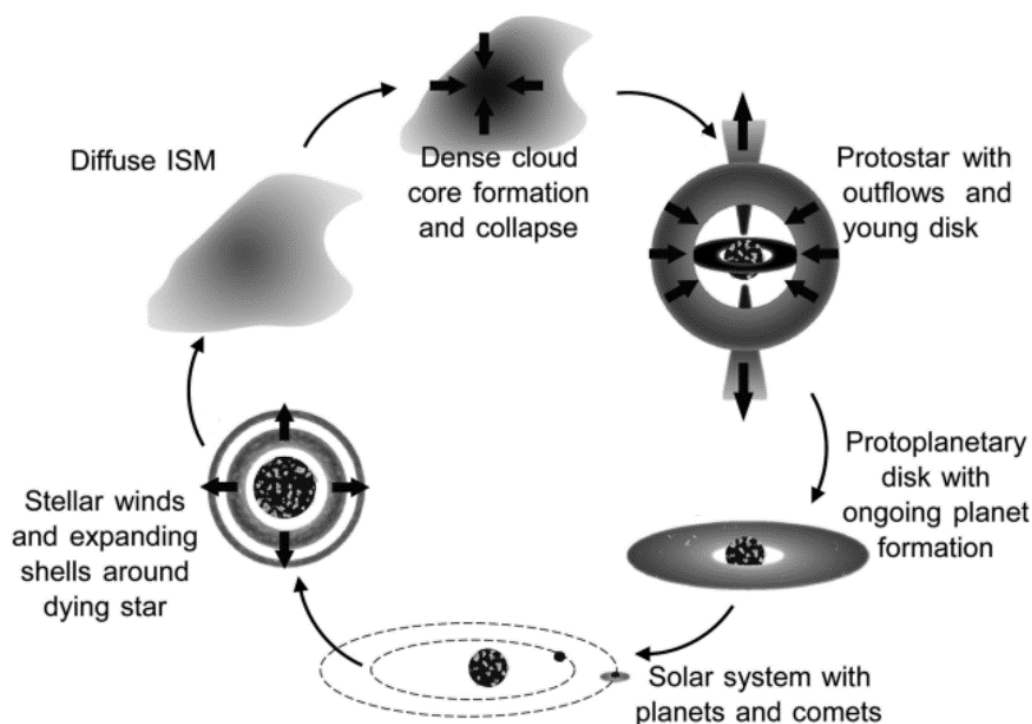


Fig. 2.10: Graphical representation of the Cosmic Chemistry Cycle, including the birth and death stages of low mass stars. Image taken from Öberg (2016).

The stability of dense molecular clouds is, however, not permanent; and eventually gravitational collapse occurs at the densest parts of its cold molecular cores. The accreting material constitutes a protostar, whose internal pressure and temperature continually increase as more and more material is accreted. As much of this material rotates around the growing protostar, the Law of Conservation of Angular Momentum is conserved, and the material begins to take on the shape of a flat disc. Further accretion also occurs *via* channelling by magneto-hydrodynamically mediated funnel flows. Other magneto-hydrodynamic processes at the boundary between the disc and the star emit jets and winds perpendicular to the plane of the disc. These jets and winds may assimilate material in bipolar outflows, as well as create shock waves when interacting with the surrounding dense cloud which can, in turn, drive shock chemistry in interstellar ices further afield.

The increasing temperature of the growing protostar has important consequences for the fate of the icy grain mantles in its vicinity. As the temperature of the cloud begins to increase to 30-50 K, the most volatile icy molecules (e.g., CO and CH₄) begin to sublime. This not only leaves an increased concentration of larger and more complex molecules in the ice, but also promotes their formation through increased thermal reaction rates. As the cloud temperature increases further to values over 100 K, even more molecular material begins to sublime from the icy grain mantles, thus enriching the gas-phase of the cloud in complex organic molecules and leaving only the most refractory of materials and residues (e.g., silicates) in the solid phase. A summary of the evolution of interstellar icy grain mantles as a result of the increased temperatures experienced during protostellar formation is given in Fig. 2.11.

Over the course of approximately 10⁶ years, the circumstellar disc (now referred to as a protoplanetary disc) emerges as the dominant feature around the now optically visible star. At this point, the stellar object is classified as a pre-main sequence star and, although it has acquired practically all of its mass, it has not yet begun nucleosynthetic hydrogen burning at its core¹⁴ (Larson 2003). The protoplanetary disc itself has a high particle number density of around 10¹³ cm⁻³, which allows for frequent collisions to take place. In the inner regions closer to the pre-main sequence star, these collisions take place between materials with high melting points, such as metals and silicates, which results in their coagulation to form larger bodies eventually leading to rocky planets, moons, and asteroids¹⁵ (Lissauer 1993, Blum and Wurm 2008).

At further distances from the young stellar object, temperatures are significantly colder and so volatile materials may remain in the ice phase. Each volatile species (e.g., H₂O, CO, CH₄) has a defined snow line, which represents the distance from the young stellar object at which these species condense from the gas phase. Of course, these snow lines are not static and change during the evolution of the stellar object. Nevertheless, the outer reaches of the protoplanetary disc are inhabited by icy objects which may also accrete into larger structures, such as comets.

At some point during its growth, the pressures and temperatures at the core of the young stellar object will become sufficiently large as to cause the hydrogen atoms (which dominate its chemical composition) to undergo nuclear fusion to helium. The energy that is released as part of this fusion reaction ignites the star, quickly leading to hydrostatic equilibrium in which the energy released by the stellar core is counterbalanced by the inward force of gravitational collapse. In this stable state, the stellar object is referred to as a main sequence star.

¹⁴ Theory does predict, however, that some limited fusion of ²H (deuterium) with ¹H will occur to yield ³He.

¹⁵ It is important to note that much of our understanding of planetary formation is still incomplete and the discussions presented in this thesis represent the most accepted scientific view.

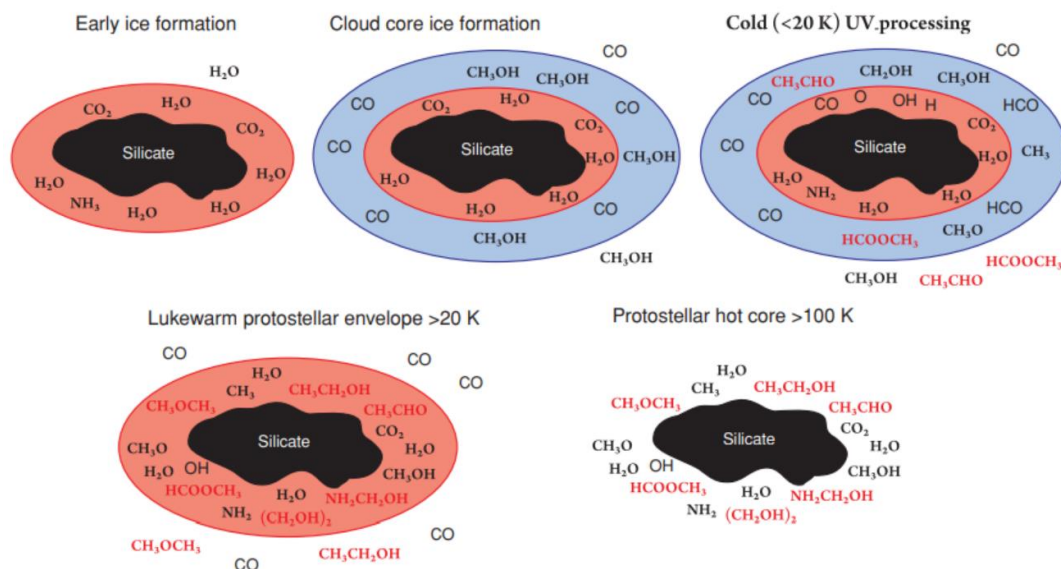


Fig. 2.11: Evolution of interstellar icy grain mantles during the birth and evolution of a nearby protostar. Image taken from Öberg *et al.* (2010).

2.3.2 Planetary Systems

A planetary system with a star in the main sequence stage and a selection of rocky, gaseous, and icy worlds and bodies is a prime setting for advanced chemistry in a variety of environments. The ignition of the star floods much of the planetary system with infrared, visible, and ultraviolet photons; with peak emission wavelength and flux varying from star to star depending on its mass and luminosity. Such photons may drive photochemistry within the planetary system, thus leading to new and possibly more complex molecules. Thermal chemistry may also be induced by the heat emitted by the star, although this is perhaps more limited to those bodies whose orbits either maintain them or bring them in occasional proximity to the star.

In low mass stars, the high temperatures of the upper stellar atmosphere allow particles with small masses (such as protons and electrons) and trace amounts of heavier atoms and ions to be thermally accelerated away from the star, thus generating a stellar wind. The loss of mass *via* stellar winds is not significant for low mass stars, such as the sun; although this contrasts greatly with the mass loss for high mass stars, which could be as high as 50% during their main sequence stage (Lamers and Cassinelli 1999). In this latter case, the stellar winds are driven directly by the radiation pressure of photons emitted by the star.

The emitted stellar winds generate a radiation environment which could also engender significant and productive chemistries potentially leading to the formation or destruction of complex organic molecules. The interaction of various component bodies of the planetary system with stellar wind radiation is expected to result in their physical and chemical alteration, as discussed previously for interstellar icy grain mantles. Such irradiation may be attenuated somewhat by differentiated planetary-like bodies with an active internal dynamo, as this allows for the establishment of a local magnetosphere which inhibits radiation chemistry from playing a major role at the surface of the body.

The formation of such magnetospheres around giant planetary objects may, however, actually increase the relative importance of radiation chemistry on the surfaces of any orbiting satellites. In our own Solar System, for instance, several of the Jovian and Saturnian moons orbit within the giant magnetospheres of their host planets, and are thus exposed to continuous bombardment by charged particles leading to radiation-induced chemical and

structural alterations to their surfaces. The ions and electrons which populate these magnetospheres are typically sourced from molecular ejection processes occurring on the orbiting moons, such as volcanic eruptions or emission plumes (Jia *et al.* 2010). The ejected molecules are then dissociated and ionised within the magnetosphere. Interestingly, the thickness of the surface material of these moons (which is on the order of a few to a few tens of km) allows for reactive magnetospheric ions to undergo implantation in the surface, after which they may be incorporated into newly formed molecules. Such a process will be explored in significantly more detail at several points in this thesis.

As the planetary system evolves further and many new worlds emerge, various new environments arise within which chemical reactions may take place. Earth is an exemplary planetary laboratory to showcase such environments: the gas-phase reactions within the atmosphere, for instance, may lead to the formation of molecules which may influence surface temperatures or planetary albedos, while the presence of expansive H₂O bodies (such as rivers, lakes, and oceans) not only allows for marine chemistry, but also for geological processes such as dissolution and sedimentation. Geological activity in the form of tectonic motion or volcanism may also give rise to new molecules and minerals. Although a complete description of planetary chemistry would go well beyond the scope of this thesis, this brief overview perhaps goes some way to demonstrating the various environments which may contribute to the chemical complexity of a planetary system.

2.3.3 Stellar Evolution and Death

The nuclear fusion reactions occurring at the core of stellar objects which convert hydrogen to helium are a defining characteristic of a main sequence star. However, the mechanisms by which such reactions occur (as well as the ultimate fate of the star once all hydrogen in its core has been exhausted) differ depending upon the mass of the star (Fig. 2.12). For stars with masses $<1.4 M_{\odot}$, the dominant reaction pathway followed is the proton-proton (p-p) chain, in which the net consumption of four protons produces a single ${}^4\text{He}$ nucleus¹⁶:



Red dwarfs represent the least massive ($M < 0.8 M_{\odot}$) main sequence stars and undergo nuclear fusion at very slow rates. The smallest red dwarfs ($M < 0.35 M_{\odot}$) are fully convective and so do not allow helium to accumulate in the core, thus prolonging hydrogen burning even further. It is thought that no red dwarfs have yet left the main sequence stage, and that they may endure for a few 10^{12} years (Adams *et al.* 2004). The fact that the lifespan of a red dwarf exceeds the present age of the Universe presents an observational challenge when considering the fate of such stars. Given that such a star is not sufficiently massive as to allow for helium burning, however, it has been suggested that they will simply undergo a prolonged cooling process involving a progressive evolution to a blue dwarf, followed by a white dwarf, and finally a black dwarf.

¹⁶ ${}^4\text{He}$ nuclei are often referred to as α -particles.

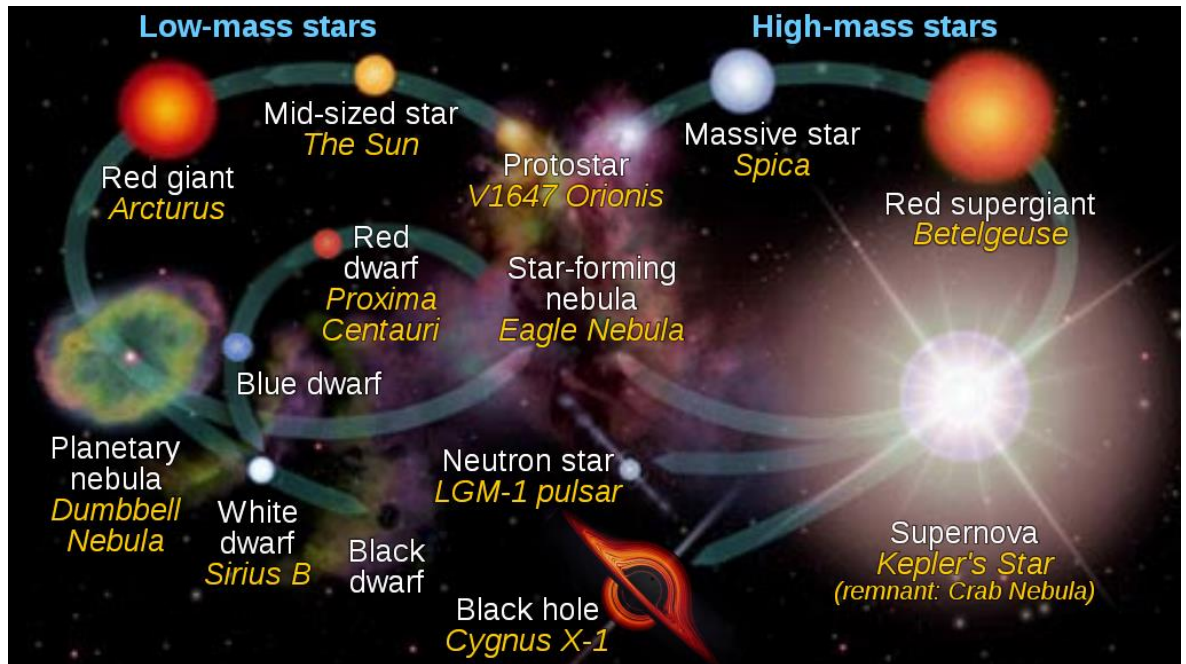


Fig. 2.12: Summary of the evolution of low mass (*left*) and high mass (*right*) stellar objects. Examples of each object are provided in yellow italics. Image credit: NASA.

Stellar objects with masses ranging between $0.8-8 M_{\odot}$ are considered to be mid-sized stars and, despite having an identical ultimate fate to red dwarfs, they undergo a significantly more complex evolution (Ryan and Norton 2010). The increased mass and density of their cores do not permit convective flow, and there is therefore no transfer of material into or out of the core. Once the limited hydrogen in the core has been fully fused to helium, hydrogen fusion begins to take place within a layer (or ‘shell’) just outside the core. The additional energy emitted by this fusion increases the temperature of the star, causing it to expand and become a subgiant. As nuclear fusion continues to take place in the hydrogen shell, the star is further warmed and thus expands significantly more; eventually becoming a red giant.

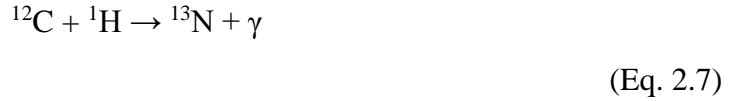
Once in the red giant phase, the gravitational force at the surface of the star will be sufficiently weak as to be overcome by the energy emitted by the nuclear fusion processes occurring deeper within. The result of this is that the star will shed its outer layers in a mass loss process. Deeper within the structure of the star, the continuous nucleosynthetic creation of helium in the shell neighbouring the core eventually increases the pressure in the core sufficiently as to ignite helium fusion to carbon in a sequence of nuclear fusion reactions termed the triple alpha process:



The energy produced by helium burning is initially mostly absorbed by the core, which results in its expansion. This in turn slows down hydrogen fusion to helium in overlaying shells, thereby decreasing the total energy production of the star and causing it to contract (although it is still significantly larger than it was as a main sequence stellar object). As carbon begins to accumulate in the core, the outer layers of the star once again heat up and expand; resulting in a second, more extensive mass shedding. Overall, helium burning is not

a particularly stable process, with rates of fusion and energy output varying substantially on very short time-scales (Rose 1967). The star may therefore undergo a series of tremendous paroxysms, each accompanied by yet another loss of mass. Eventually, the stellar core will exhaust its helium supply. Mid-sized stars are not massive enough to trigger carbon fusion, and so energy production ceases.

By this point, the star will have shed its outer layers leaving only the dense and hot core behind. The structure of the core at this point is consistent with that of a white dwarf and, since no more energy may be produced *via* nuclear fusion reactions, it will simply cool over time; eventually becoming a black dwarf. Although expanding away, the shed layers will remain in close proximity to the white dwarf for a few 10^3 years, and the interaction of the ionising radiation emitted by the latter with the receding gas results in the production of a planetary nebula; reference to which was made in sub-section 2.2. It should be noted that, for stars with masses exceeding $1.4 M_{\odot}$, the dominant hydrogen fusion mechanism occurring within the stellar core shifts from the p-p chain to the carbon-nitrogen-oxygen (CNO) cycle. Unlike the p-p chain, in which all participating nuclei other than the product ${}^4\text{He}$ are consumed, the CNO cycle is a catalytic process in which various isotopes of nitrogen, carbon, and oxygen promote the fusion of four protons:



The evolution of high mass ($>8 M_{\odot}$) stellar objects initially follows a similar pathway to that of mid-sized stars. Once carbon accumulates in the core of the latter, however, fusion reactions cease as the density and temperature of the core are not high enough to trigger carbon ignition. High mass stars, on the other hand, are sufficiently massive as to raise the density and temperature of their cores to the point where carbon fuses to neon, while helium fusion to carbon begins to occur in the overlaying shell and a new shell fusing hydrogen to helium is formed over that. The star thus begins to take on an ‘onion-like’ structure, in which distinct layers of nucleosynthetic fusion processes are present (Fig. 2.13). The continuous heating of the core as a result of its contraction results in the sequential burning of neon to oxygen and magnesium, and oxygen to silicon¹⁷; with each overlaying shell progressing by one nucleosynthetic fusion step each time.

¹⁷ A smattering of other elements is also produced by these fusion reactions. For instance, carbon burning also yields sodium and magnesium, while oxygen burning yields sulphur, phosphorus, and magnesium.

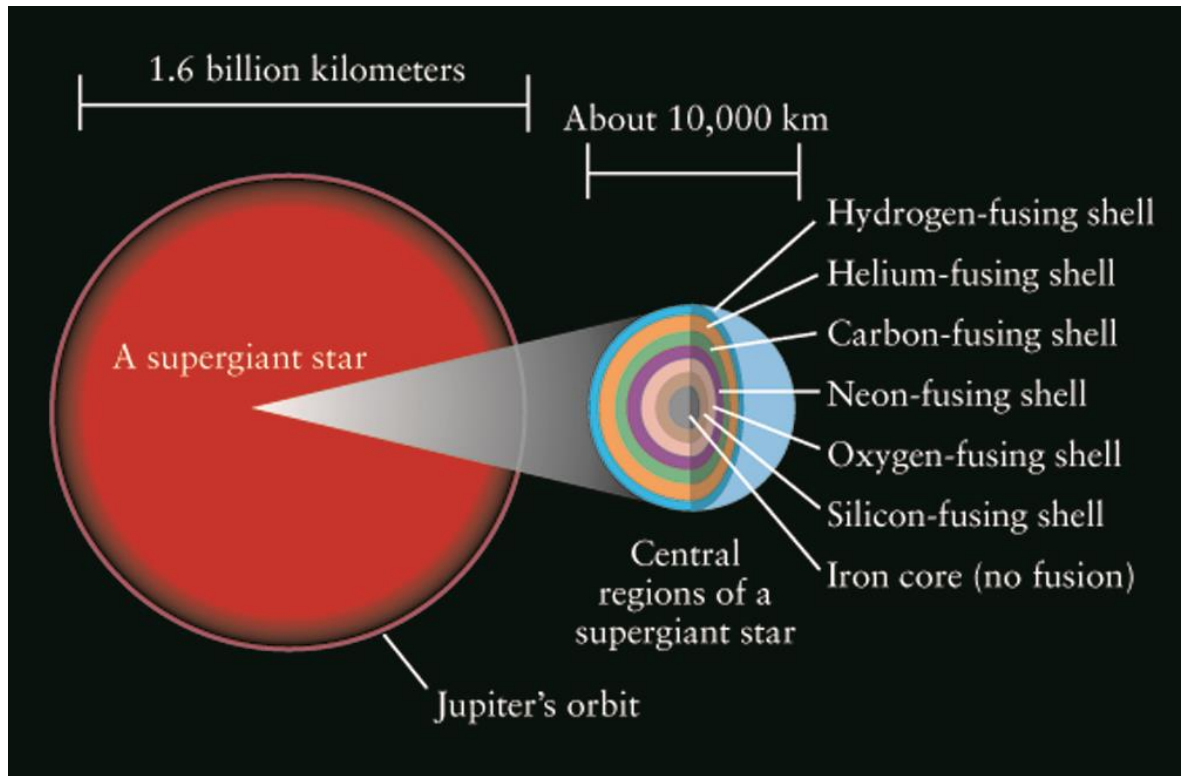


Fig. 2.13: A cross-section through a hypothetical red supergiant, showing the ‘onion-like’ structure in which different nucleosynthetic fusion reactions dominate. Image credit: D. Pogosyan.

During the fusion of hydrogen in their cores, high mass stellar objects are typically blue main sequence stars. However, as their temperature is raised during nuclear fusion, the outer layers are heated resulting in the expansion of the star; at which point it is termed a red supergiant (or in the case of especially massive stars, a red hypergiant). As the core switches from one fusion reaction to the next, the outer layers respond by contracting and expanding much in the same way as for mid-sized stars, thus allowing the high mass star to cycle between the red supergiant and blue supergiant phases.

Eventually, silicon burning becomes the dominant nuclear fusion process occurring within the core. Among the various elements formed as a result of this process (such as sulphur, nickel, chromium, titanium, argon, and calcium) is iron. Unlike all other nucleosynthetic fusion reactions before it, however, the fusion of iron (as ^{56}Fe) results in a net loss of energy (Ryan and Norton 2010). Moreover, iron is able to act as a sink for any free electrons, thus virtually eliminating the electron degeneracy pressure of the core¹⁸. The combined sudden¹⁹ loss of fusion-induced energy release and electron degeneracy pressure means that there is no force left to counterbalance the inward gravitational force, and so the core collapses with the outer core regions crashing into the inner ones with a velocity that is a significant fraction of the speed of light.

As the core collapses it becomes incredibly denser, and so the force of gravity it exerts on the outer layers of the star causes them to begin falling inwards rapidly. However, shockwaves generated by the collapse of the core move outward, slowing down the infalling material. Additionally, the collapse of the core emits a large number of neutrinos which

¹⁸ *Electron degeneracy pressure is a special case of the more general quantum degeneracy pressure, in which the Pauli Exclusion Principle prohibits the existence of two electrons from simultaneously occupying the same quantum state. This is manifested as a pressure against the compression of matter into small volumes.*

¹⁹ *On average, most high mass stars are expected to completely exhaust the supply of silicon in their cores within a matter of a few days.*

collide with the infalling material, forcing it to reverse its course and explode outwards as a supernova. Supernovae are among the most violently energetic events that may occur in the Universe; so much so that further nucleosynthesis is induced resulting in the production of large quantities of new, heavier elements.

Eventually, the collapse of the core creates the conditions necessary for electron capture by protons to become spontaneous, thus generating an abundance of neutrons. Indeed, by the time the core has collapsed to a diameter of approximately 20 km, it is composed almost entirely of neutrons. From this point onwards, the ultimate fate of the stellar core is determined by the initial mass of the star: for stars with masses between 8-20 M_{\odot} , the gravitational force causing the inwards collapse of the core is not large enough to overcome the neutron degeneracy pressure²⁰ of the core, and so the collapse comes to an abrupt halt (Heiselberg and Pandharipande 2000, Heger *et al.* 2003). The shockwave emanating from this halt contributes to the supernova explosion of the outer stellar layers, while the core remains behind as a neutron star.

In the case of more massive stars, however, the gravitational force of the collapsing core will readily overcome its neutron degeneracy pressure, allowing the collapse to proceed further. As the core continues to shrink in size, the force of gravity it exerts correspondingly increases until it reaches a point where it is so strong that the escape velocity for an object at the boundary of the core exceeds the speed of light in a vacuum ($c = 3 \times 10^8 \text{ m s}^{-1}$). At this point, no object (including light) can escape the gravitational influence of the collapsed core, which is now termed a black hole.

Whether a high mass stellar object ends its life as a neutron star or a black hole is largely immaterial to the Cosmic Chemistry Cycle, as supernovae are associated with the formation of both of these astronomical bodies. As mentioned previously, these supernovae are incredibly energetic and are able to blast out atoms and nuclei of the various elements formed during stellar nucleosynthesis (as well as those formed during the explosive nucleosynthesis associated with the supernova itself), thus enriching the chemical composition of the surrounding ISM. Over time, the material in the ISM may coalesce to form a diffuse molecular cloud (Fig. 2.12), thus re-initiating the cycle.

2.3.4 Comments on the Emergence of Life in the Universe

As has been highlighted above, the Cosmic Chemistry Cycle creates various astrophysical environments which provide the elements and conditions necessary for the generation of molecules of a prebiotic nature. It has already been mentioned, for instance, that the processing of interstellar icy grain mantles has been shown to lead to the formation of amino acids and nucleobases, among other species (Muñoz Caro *et al.* 2002, Nuevo *et al.* 2007, Hudson *et al.* 2008, Nuevo *et al.* 2012). It is hypothesised that the seeding of so-called 'habitable worlds' with these prebiotic molecules could therefore contribute to the emergence of life.

The seemingly inherent ability of the Universe to synthesise prebiotic molecules, as well as the tremendously large number of planets thought to exist (which could be as large as a few 10^{24} planets) implies that, not only should life itself be fairly ubiquitous throughout the cosmos, but that a reasonable number of these lifeforms should have evolved and advanced sufficiently to have become intelligent and even possibly radio-communicative. In an effort to stimulate discussions on the scientific factors which may need to be considered when contemplating the existence of extra-terrestrial life and the potential to communicate

²⁰ Neutron degeneracy pressure is similar in concept to electron degeneracy pressure, but requires a greater gravitational collapse to be overcome.

with it, the Drake Equation (Burchell 2006) was proposed to estimate the number of communicative civilisations in our galaxy, D :

$$D = R_* f_p H f_l f_i f_c L \quad (\text{Eq. 2.13})$$

where R_* is the rate of star formation in the galaxy, f_p is the fraction of those stars that are orbited by planets, H is the average number of habitable planets per orbited star, f_l is the fraction of habitable planets on which life does actually emerge, f_i is the fraction of life-sustaining planets on which intelligent life evolves, f_c is the fraction of those lifeforms that are able to develop a technology with which they may release detectable signs of their existence into space, and L is the duration for which they do so.

It is evident that the Drake Equation, although containing some physical parameters that may be easily quantified due to their having a sound theoretical or observational basis, also contains many parameters for which only a speculative value may be assigned. For instance, stellar formation rates have been constrained to be about two stars per year (Robitaille and Whitney 2010), while microlensing surveys suggest that practically all stars in the galaxy have at least one orbiting planet (Cassan *et al.* 2012). However, the remaining parameters in the equation are based on our (fairly poor) understanding of the emergence and evolution of life, intelligence, and civilisation. As such, the Drake Equation may yield widely varying results depending on the assumptions made when assigning values to these latter parameters. It is possible to assume, for instance, that 0.2 planets per orbited star are habitable and that 10% of these will go on to host life. By further assuming that all life will at some point become intelligent and that 25% of these intelligent lifeforms can develop the technology to emit detectable signs of their existence into space for a period of at least 10^6 years, then the number of civilisations within our galaxy with which contact may be made is as high as 10,000 (Eq. 2.13). However, no evidence of any extra-terrestrial life (let alone intelligent life) has been encountered thus far²¹.

Several explanations have been proposed to explain the lack of evidence for the existence of extra-terrestrial life. It has been proposed, for instance, that intelligent life may not arise frequently, and that any intelligent civilisation that does emerge does not exist for long enough either to develop the technology to emit evidence of their presence into space or for such emitted signals to be detected by other civilisations. Alternatively, the so-called Rare Earth Hypothesis posits that the number of essential properties required by a planet in order for it to be deemed habitable are so many in number that it is actually H which is the limiting factor in the Drake Equation, and thus renders $D \ll 1$ (Ward and Brownlee 2000).

The existence and emergence of extra-terrestrial life in the cosmos remains an open question in the field of astrobiology; and one which is intimately linked with the chemistry leading to the formation of prebiotic molecules discussed throughout this chapter. Although a more complete review of astrobiology would go beyond the scope of this thesis, it is of importance to note that further investigations into the tolerances of extremophilic organisms are continually changing our understanding of biology and pushing the limits on which environments may be classified as habitable. Indeed, recent work has highlighted the ability of various organisms to survive astrophysical conditions (Mastascusa *et al.* 2014), including hyper-velocity impacts (Traspas Muña and Burchell 2021). This has highlighted the need to further characterise the chemistry of diverse astrophysical settings, including those which traditionally have been regarded as being inhospitable to life.

²¹ *The apparent contradiction between the lack of evidence for extra-terrestrial life and the high estimates for its existence has come to be known as the Fermi Paradox.*

2.4 An Overview of Icy Bodies in the Solar System

Thus far, the discussion of astrophysical ices has been largely restricted to interstellar icy grain mantles. However, ices are also abundant within planetary systems. Indeed, within our own Solar System, molecular ices are thought to exist on the surface of virtually every celestial body with the notable exception of Venus. The five mechanisms by which solid-phase astrochemical reactions may occur (Fig. 2.8) are all viable in Solar System ices (Arumainayagam *et al.* 2019). For instance, radiation chemistry may be driven by the solar wind or planetary magnetospheric plasmas; while the emission of heat and ultraviolet and optical photons from the sun results in appreciable thermal chemistry and photochemistry. This sub-section will provide a very brief overview of selected icy bodies within the Solar System; images of which are given in Figs. 2.14-2.18.

2.4.1 The Inner Terrestrial Planets

Being the closest planet to the sun, Mercury regularly experiences very high temperatures at its surface, which may be as high as 700 K at the equator (Vasavada *et al.* 1999). Despite this, evidence for the existence of surface ices emerged in the early 1990s as a result of extensive observational work (Harmon and Slade 1992, Slade *et al.* 1992, Paige *et al.* 1992, Butler *et al.* 1993). These ices are principally composed of H₂O and exist within shallow and permanently shadowed craters towards the north pole. These craters are not directly exposed to sunlight, and so the temperature within them does not exceed 130 K (Ingersoll *et al.* 1992, Salvail and Fanale 1994), thus preventing the sublimation of the ice. The exact source of these H₂O ice deposits is not known, although the current favoured hypothesis suggests that they are remnants of impacts with H₂O-bearing interplanetary dust particles, asteroids, or comets (Ernst *et al.* 2018, Frantseva *et al.* 2022).

Orbiting at a considerably further distance from the sun and having a permanent (albeit thin) atmosphere, the existence of surface ices on Mars is perhaps less surprising than on Mercury. Indeed, H₂O ices have been detected at various latitudes across the planetary surface (Titus *et al.* 2003, Vincendon *et al.* 2010), although the most famous of these are certainly the two permanent polar ice caps. Although these ice caps are largely composed of solid H₂O, they are best known for their role in cycling CO₂ between the surface and the atmosphere (Hess *et al.* 1979). During the winter months, the polar regions become cold enough for a significant proportion of the atmosphere (which is largely composed of CO₂) to condense onto the surface, resulting in a thin veneer of CO₂ atop the H₂O polar ice caps. With the arrival of spring, the surface temperatures rise causing the CO₂ to sublimate back into the atmosphere. This seasonal cycle is accompanied by the transportation of large quantities of dust and H₂O vapour, which give rise to clouds and other nephological phenomena.

The last of the inner terrestrial planets on which surface ice is known to exist is our own home: the Earth. The presence of large open bodies of liquid H₂O at its surface and an evolved hydrological cycle explains why the dominant icy species is H₂O. Surface H₂O ice mainly exists as snow, glaciers, ice sheets, and permafrost at high latitudes, particularly in polar regions. Environmental transformations of this surface ice have been linked to various planetary-scale climatological effects, such as altered ocean currents, changes in sea-levels, and increased carbon exchange (Dobinski 2006). It is interesting to note that the solid phase adopted by H₂O ice on the surface of the Earth differs to that thought to exist in astrophysical settings: the higher temperatures and pressures associated with the former favour the adoption of a hexagonal crystalline phase, while amorphous H₂O ices (or, to a more limited extent, the meta-stable cubic crystalline phase) are more commonly encountered in the latter (van Dishoeck *et al.* 2013).

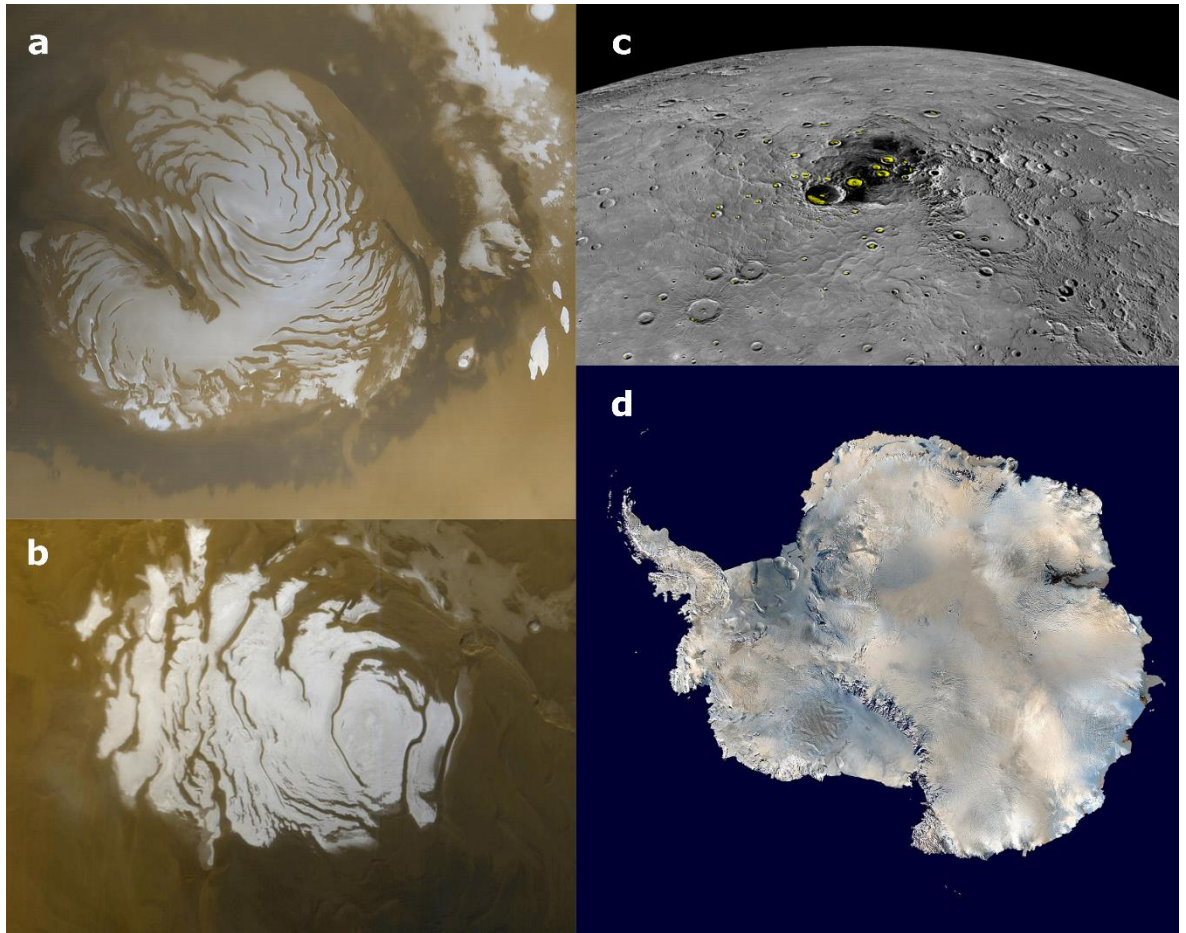


Fig. 2.14: Examples of high latitude surface ice deposits on the inner terrestrial planets, such as the (a) northern and (b) southern polar ice caps on Mars, (c) ice deposits (indicated in yellow) within permanently shadowed crater regions near the north pole of Mercury, and (d) the Antarctic ice sheet on Earth. Image credits: NASA.

2.4.2 Ceres and Vesta

Ceres and Vesta are respectively the largest and second-largest objects in the main asteroid belt. Being sufficiently massive for its own gravity to maintain it as a spheroid in hydrostatic equilibrium, Ceres is officially classified as a dwarf planet; thereby making Vesta the largest true asteroid. Interestingly, Vesta is thought to have a differentiated internal structure (Consolmagno *et al.* 2015), meaning it is possibly the only known remaining protoplanet of the kind that formed the inner terrestrial planets through gravitational accretion.

The surface compositions of Ceres and Vesta are believed to be fairly depleted in ices, although geomorphological evidence has suggested that the subsurface of Ceres is likely a mixture of silicate minerals and H₂O ice (Schmidt *et al.* 2017) while exposed surface H₂O ice is likely preserved in cold traps such as high latitude permanently shadowed craters (Hayne and Aharonson 2015, Platz *et al.* 2017). In the case of Vesta, H₂O ice is almost certainly restricted to the polar regions where it is buried beneath a few tens of cm of surface regolith (Stubbs and Wang 2012).

An interesting spectroscopic feature of the Cererian surface is an ultraviolet absorption edge at about 4000 Å which has traditionally been attributed to a ferric oxide intervalence charge transfer transition in phyllosilicate minerals (Johnson and Fanale 1973). On the basis of laboratory ultraviolet-visible spectroscopy experiments, Hendrix *et al.* (2016) have suggested that this absorption edge may have some contribution from allotropic sulphur of the form S_x and SO₂ surface ices. The presence of sulphur-bearing molecular ices on the

surface of Ceres implies the existence of geothermal activity on the dwarf planet, which is consistent with additional evidence of some geologically young surface features (Sori *et al.* 2018). However, this interpretation has been disputed more recently by Roth (2018) on the basis that, under the pressure and temperatures conditions that characterise the Cererian surface, both S_x and SO_2 would sublimate at too rapid a rate for their accumulation to occur.

2.4.3 The Galilean Moons of Jupiter

As the largest planet in the Solar System, it is perhaps unsurprising that Jupiter is orbited by a great many natural satellites. Of its approximately 80 known moons, the best studied are the four so-called Galilean moons²²: Io, Europa, Ganymede, and Callisto. These moons are amongst the largest in the Solar System, with Ganymede itself being larger (although significantly less massive) than the planet Mercury. The Galilean moons are all tidally locked to Jupiter, resulting in the same face being turned towards the host planet at all times. Moreover, a 4:2:1 Laplacian orbital resonance exists between Io, Europa, and Ganymede.

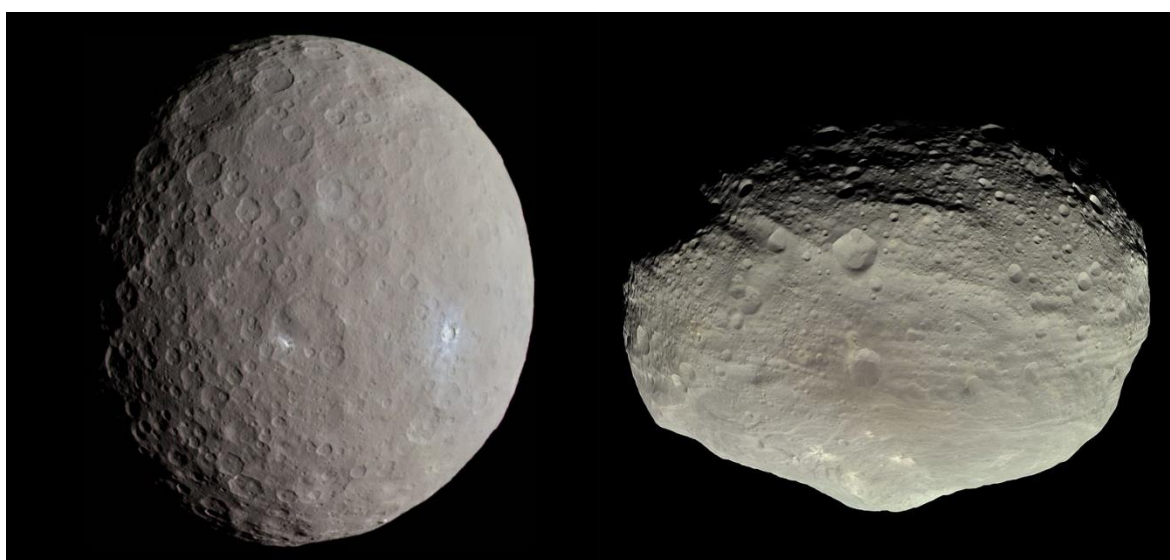


Fig. 2.15: True colour pictures (not to scale) of Ceres (*left*) and Vesta (*right*) imaged during the *Dawn* mission. Image credits: NASA.

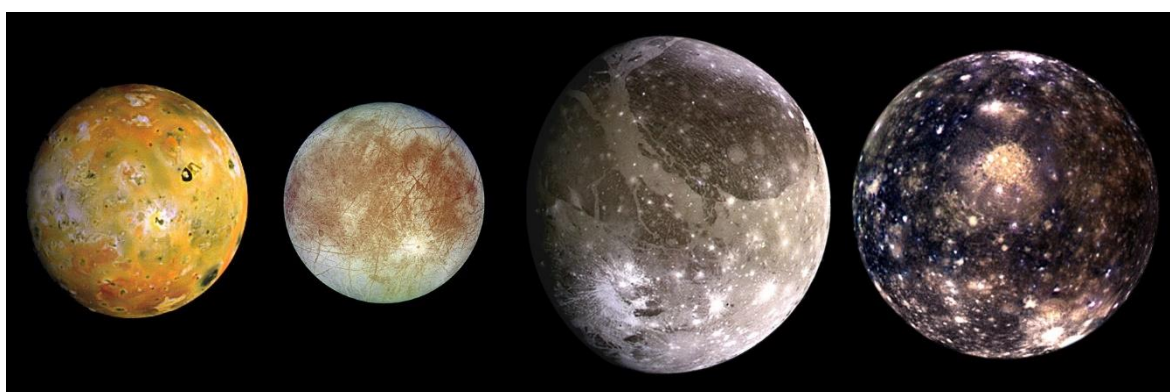


Fig. 2.16: *Left to right:* Io, Europa, Ganymede, and Callisto. Collectively, these Jovian satellites are referred to as the Galilean moons of Jupiter. Image credit: NASA and DLR.

²² These moons are known as the Galilean moons in honour of Galileo Galilei, who was the first to unambiguously identify them in the early seventeenth century.

Io, the innermost of the Galilean moons, is the most geologically active object in the Solar System, with over 400 active volcanoes on its surface (Lopes *et al.* 2004). This extreme volcanism is driven by the large tidal forces that the moon experiences during its orbit of Jupiter, which distorts its shape causing frictional heating of its interior in a process known as tidal flexing. The orbital resonance and resultant gravitational interactions with Europa and Ganymede maintain Io in an elliptical orbit, thus ensuring a continually changing degree of distortion in the shape of the latter and the persistent melting of subsurface silicate rock (Tyler *et al.* 2015). Volcanism on Io is also a significant contributor to the composition of the Jovian magnetosphere (Yoneda *et al.* 2010, Yoshikawa *et al.* 2017, Yoshioka *et al.* 2018). Molecular volcanic ejecta such as SO₂ and H₂S are efficiently dissociated and ionised in the magnetosphere, thus populating it with energetic protons, oxygen ions, sulphur ions, and electrons (Cooper *et al.* 2001).

Unlike the other Galilean moons, Io is not an icy world. Rather, it is a dense moon having an iron or FeS₂ (iron sulphide) core surrounded by a silicate crust and mantle, with around 10% of the latter being molten due to tidal flexing (Kerr 2010). The surface of Io is covered by frosts of SO₂ and S_x sourced from volcanic ejecta, with smaller quantities of H₂S and SO₂Cl₂ also thought to be present (Tosi *et al.* 2020). Analogously to the Martian poles discussed earlier, daily condensation and sublimation cycles of Ionian surface SO₂ frosts are thought to drive the existence and composition of a tenuous exosphere (Bagenal and Dols 2020). During the day, when temperatures are warmer, the exosphere is largely composed of SO₂ sourced from sublimating surface frosts, along with trace quantities of SO, S₂, NaCl, and KCl. However, as temperatures drop during the night or during an eclipse, much of this exosphere collapses due to the condensation of the SO₂.

Despite being the smallest of the Galilean moons, Europa has arguably generated the most excitement among the planetary science community. The reason for this is the fact that the moon is believed to host a subsurface global H₂O ocean which is rich in mineral salts lying above a silicate mantle (Carr *et al.* 1998, Kivelson *et al.* 2000). This ocean is kept in the liquid phase by tidal flexing, which may also possibly drive active hydrothermal vents at the ocean-mantle interface (Goodman *et al.* 2004, Bland and Elder 2022). The presence of a warm ocean containing various mineral salts and free energy sources has made Europa a prime candidate to host the emergence and continued sustenance of extra-terrestrial life (Chyba and Phillips 2002).

The habitability of the European subsurface global ocean may also be enhanced as a result of its interactions with the icy surface (Orlando *et al.* 2005, Howell and Pappalardo 2018), although the extent of these interactions has been the subject of intense debate (Billings and Kattenhorn 2005). Due to the orbit of Europa being within the giant Jovian magnetosphere, the surface of the moon is continually bombarded by energetic charged particles (i.e., ions and electrons). Since the surface is mostly composed of H₂O, its irradiation results in the formation of a large number of oxidants such as OH and O₂ which, if transported to the subsurface ocean, could act as an additional driver of chemical disequilibrium (Chyba and Hand 2001, Boduch *et al.* 2011). The irradiation of the surface is also thought to sustain a tenuous exosphere of O₂ (Ip 1996).

Ganymede, the largest of the Galilean moons (and indeed, the largest moon in the Solar System), is a fully differentiated body with an active magnetosphere of its own generated by an iron-rich liquid core (Hauck *et al.* 2006). The surface of the moon is composed mainly of H₂O ice, with a smattering of other minor component species such as CO₂ and SO₂ also present (McCord *et al.* 1998a). The observation of hydrated mineral salts such as those of MgSO₄ and possibly also Na₂SO₄ at the surface suggests the existence of a subsurface ocean from whence they originate (McCord *et al.* 2001a), similarly to Europa. Contrastingly, however, it has been suggested that Ganymede may have a series of layered H₂O oceans separated by different phases of H₂O ice, with the lowest liquid layer being in contact with

the silicate mantle (Vance and Brown 2013, Vance *et al.* 2014). Like their European counterparts, the Ganymedean subsurface oceans have been identified as one of the most promising possible habitats for extra-terrestrial life.

The fourth and outermost of the Galilean moons, and the only one to not participate in the Laplacian orbital resonance characteristic of the system, is Callisto. The Callistoan surface is a very heavily cratered mixture of rock and H₂O ice, with minor quantities of CO₂ and SO₂ ices also present. It is thought that a salty subsurface ocean exists beneath the icy surface (Khurana *et al.* 1998, Zimmer *et al.* 2000). Beyond this, however, little else is certain with respect to the internal structure of Callisto. Measurements of the moment of inertia by the *Galileo* orbiter suggest that the interior is a largely undifferentiated mass of rock and ice coalescing around a small silicate core (Anderson *et al.* 1998, Kuskov and Kronrod 2005). However, the idea of a satellite as large as Callisto failing to differentiate as a result of global melting during its formation is challenging, and has not been borne out realistically by numerical simulations (Monteux *et al.* 2014). As such, many questions regarding the internal structure of the moon remain presently unanswered.

The Galilean moon system provides what is arguably one of the most interesting Solar System settings for the study of radiation astrochemistry of solid ices. All four moons orbit within the giant Jovian magnetosphere which, as discussed previously, is populated by charged particles sourced from the dissociation and ionisation of molecular volcanic ejecta from Io (Fig. 2.17). Therefore, the icy surfaces of these moons are continually bombarded by these charged projectiles resulting in various physical and chemical changes. Such changes may include, for instance, the erosion or sputtering of surface ices, the development and sustenance of tenuous exospheres, ice compaction and amorphisation, the formation of new molecules as a result of radiolytic chemistry, and even the formation of molecules as a result of the incorporation of implanted reactive ions (Baragiola 2003, Johnson *et al.* 2004, Strazzulla 2011, Boduch *et al.* 2015).

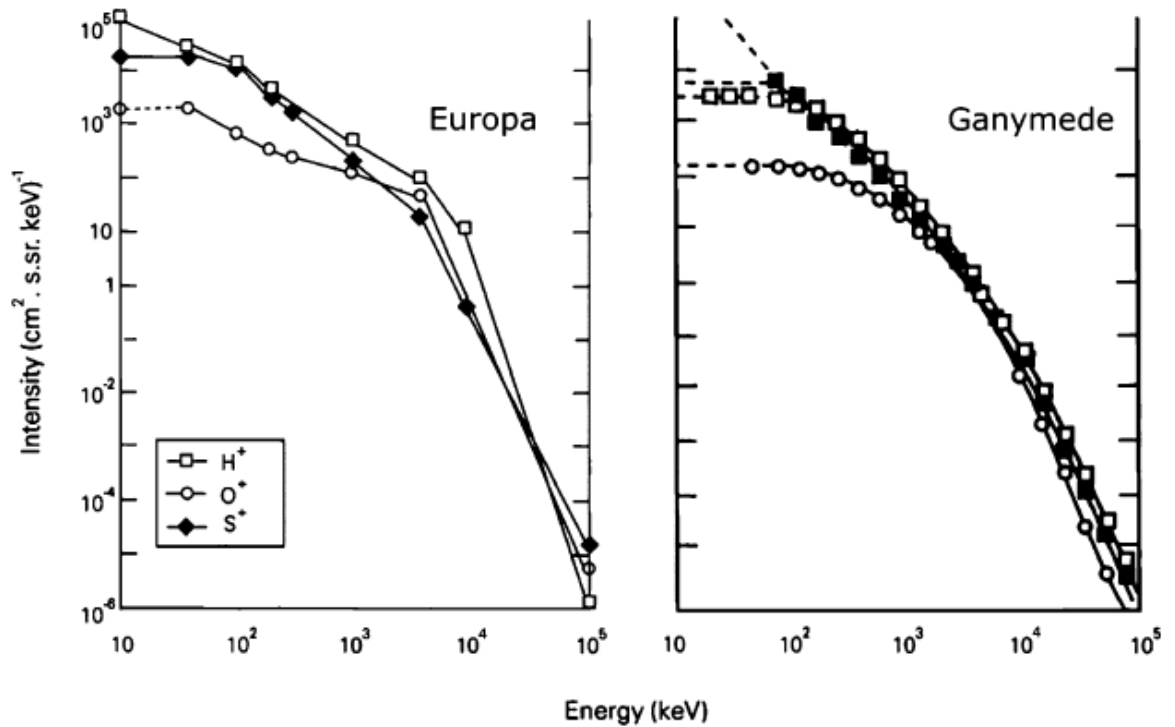


Fig. 2.17: Energy profiles of protons, O⁺ ions, and S⁺ ions in the vicinity of Europa and Ganymede. Figure produced using data originally published by Ip *et al.* (1997) and Ip *et al.* (1998).

It should be noted that the trailing hemispheres of the Galilean moons are preferentially exposed to magnetospheric ion and electron irradiation, due to the fact that the giant Jovian magnetosphere rotates significantly faster than the orbital periods of the moons. Such a hemispherical dichotomy in irradiation regimes carries important implications for radiation chemical networks present at the icy surfaces, and the radiation-induced formation (or indeed destruction) of particular molecules may therefore be promoted on the more heavily irradiated trailing hemispheres. Further information on the charged particle fluxes and radiation doses at each Galilean moon, as well as information on other physical characteristics, is given in Table 2.4.

Table 2.4: Physical and chemical characteristics of the Galilean moons of Jupiter. Data amalgamated from Schubert *et al.* (1981) McCord *et al.* (1998a), Delitsky and Lane (1998), Cooper *et al.* (2001), Johnson *et al.* (2004), Dalton *et al.* (2010), and Ashkenazy (2019).

Parameter	Io	Europa	Ganymede	Callisto
Diameter (km)	3643	3122	5262	4821
Mass (10^{20} kg)	894	480	1482	1076
Density (g cm^{-3})	3.528	3.014	1.942	1.834
Average Albedo	0.62	0.68	0.44	0.19
Surface Temperature (K)	90-130	46-125	70-152	80-165
Surface Radiation Dose (Sv day^{-1})	36	5.4	0.08	1×10^{-4}
Particle Energy Flux ($\text{keV cm}^{-2} \text{s}^{-1}$)	1.0×10^9	7.8×10^{10}	5.4×10^9	2.2×10^8
UV (<280 nm) Energy Flux ($\text{keV cm}^{-2} \text{s}^{-1}$)	4.0×10^{10}	4.0×10^{10}	4.0×10^{10}	4.0×10^{10}
UV (<207 nm) Energy Flux ($\text{keV cm}^{-2} \text{s}^{-1}$)	7.6×10^8	7.6×10^8	7.6×10^8	7.6×10^8
Major Component of Exosphere	SO ₂	O ₂	O ₂	CO ₂
Exospheric Surface Pressure (mbar)	4.0×10^{-8}	1.0×10^{-12}	1.2×10^{-11}	7.4×10^{-12}
Molecular Surface Constituents	SO ₂ , S _x , SO ₂ Cl ₂	H ₂ O, CO ₂ , H ₂ SO ₄ , SO ₂	H ₂ O, CO ₂ , SO ₂ , O ₃	H ₂ O, CO ₂ , SO ₂
Mantle Composition	Silicate	Silicate	Silicate	Rock / Ice?
Core Composition	Fe / FeS ₂	Fe-Ni	Fe-Ni / FeS ₂	Silicate?

2.4.4 Pluto and Charon

Although formerly the ninth planet of the Solar system, Pluto is now classified as a dwarf planet. It is located in the Kuiper Belt: a circumstellar disc of icy objects left over from the formation of the Solar System whose orbit is beyond that of Neptune²³. Being so far from the sun, the surface of Pluto is characterised by temperatures that are sufficiently low as to allow for the condensation of many otherwise volatile species. Indeed, the main component of the Plutonian surface is N₂ ice, with CH₄ and CO ices also present in trace amounts (Owen *et al.* 1993, Pavithraa *et al.* 2017). It has also been hypothesised that a subsurface liquid H₂O ocean exists beneath these surface ices, formed as a result of heating during the decay of radioactive elements (Kimura and Kamata 2020).

Charon is the largest moon of Pluto and, being fully one-eighth the mass of its host body, is sufficiently massive as to influence the orbital dynamics of the Plutonian system by causing the barycentre to be shifted outside Pluto, thus causing Pluto and Charon to seemingly orbit each other. Unlike the Plutonian surface, the surface of Charon is dominated by H₂O ice (Grundy *et al.* 2016). Interestingly, however, the surface is characterised by a

²³ Objects which orbit the sun at an average distance greater than that of Neptune are referred to as trans-Neptunian objects.

stark trend in albedo, with polar regions being significantly darker than equatorial ones. This is thought to be the result of sublimating molecular ices escaping Pluto and transferring to Charon where they subsequently re-condense at the polar regions during the Charonian winter (Tucker *et al.* 2015, Hoey *et al.* 2017). Solid-phase astrochemical reactions driven by the interaction of these ices with the solar wind and ultraviolet photons result in the formation of new molecules, including refractory organic tholins²⁴. As temperatures rise with the arrival of spring, volatile molecules sublime and escape Charon, leaving the tholins behind (Raut *et al.* 2022). Over several millions of years, these tholin residues accumulate, causing a darkening of the polar regions. It should be noted that tholins have also been detected on the surface of Pluto (Fayolle *et al.* 2021).

2.4.5 Comets

Comets are small Solar System bodies originating in either the Kuiper Belt or the Oort Cloud (the latter being a large spherical distribution of icy objects extending outwards from the Kuiper Belt). The nucleus of a comet, which may range in size from <1 km to a few tens of km across, is primarily composed of a loose agglomeration of dust and ice which has often been likened to a ‘dirty snowball’. Having been stored in the outer Solar System for extended time-scales, comets are regarded to be amongst the most pristine and unaltered icy bodies in the Solar System (Caselli and Ceccarelli 2012). Indeed, observational work has indicated that the molecular composition of comets is fairly consistent with those of interstellar icy grain mantles observed across various dense molecular clouds (Ehrenfreund and Charnley 2000).

Gravitational perturbations in the outer Solar System may set comets in motion in an eccentric orbit around the sun. As they approach perihelion, the temperature of the comet begins to gradually rise resulting in the sublimation and ionisation of the volatile ices within the nucleus. This results in the formation of an extremely thin exosphere-like structure of bound gas around the cometary nucleus known as the coma, as well as of two tails, one composed of emitted ionised gas and the other of dust particles. Comets represent one of the best studied astrochemical environments due to the various processes which may drive chemistry within the icy nucleus. For instance, the interaction of high energy galactic cosmic rays with the comet may engender radiation chemistry. Similar radiation chemistry may also be mediated by lower energy charged components of the solar wind as the comet approaches perihelion in its orbit around the sun. This portion of the orbit in which the comet increases its proximity to the sun is also likely characterised by more extensive thermal chemistry and photochemistry.

Much effort has been devoted to the study of cometary chemistry, since it is known that collisions between comets and planetary-like bodies may result in the delivery of new material to the latter, including large quantities of H₂O and, possibly, prebiotic organic molecules (Chyba 1990, Blank *et al.* 2001). Such collisions are commonplace in the Solar System, perhaps best exemplified by the collision of comet D1993/F2 (Shoemaker-Levy) with Jupiter in 1994. Closer to home, cometary impacts are known to have influenced the geological and climatic development of Earth (Shoemaker 1983, Covey *et al.* 1994). Indeed, dendrochronological evidence has tentatively suggested that the impact of a small cometary body with the Earth may have occurred as recently as 536 AD (Rigby *et al.* 2004).

²⁴ *Tholins are those complex polymer-like organic compounds (usually composed of extensive networks of carbon, nitrogen, and oxygen) formed as a result of the irradiation of mixtures of simple compounds. Although not formed naturally on Earth, they are ubiquitous on the surfaces of icy outer Solar System bodies where they contribute to an apparent reddening of the surface. In the presence of H₂O, tholins may act a starting feedstock for the initiation of more complex prebiotic chemistry.*

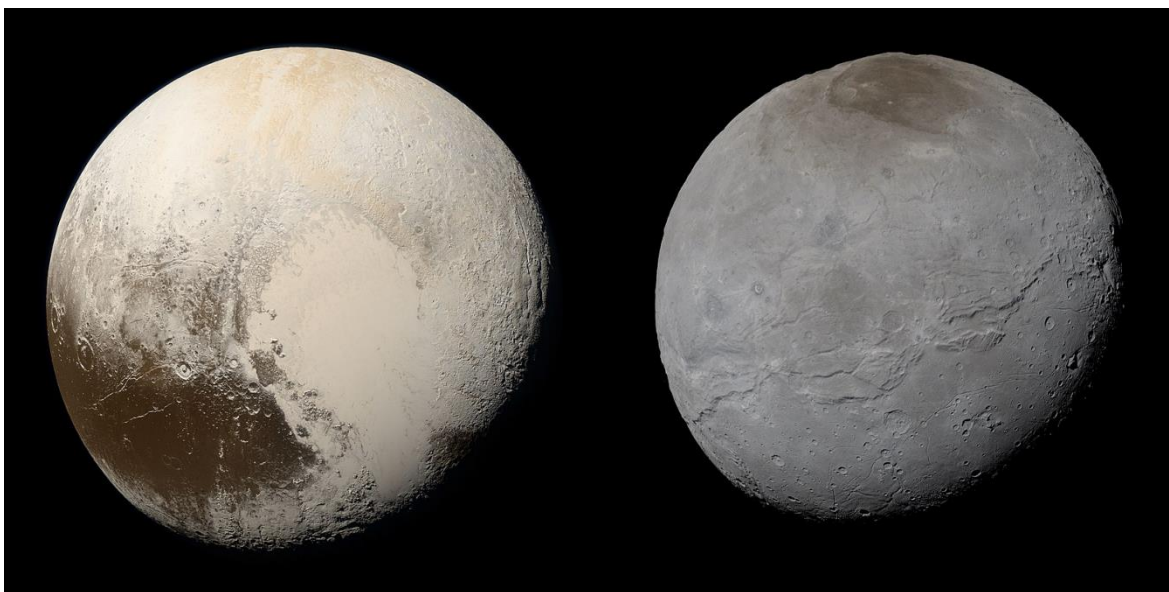


Fig. 2.18: True colour pictures (not to scale) of Pluto (*left*) and Charon (*right*) imaged during the *New Horizons* mission. Image credits: NASA.

2.5 Summary

In this chapter, a detailed overview of the study of astrochemistry has been provided with a particular focus on the chemical composition and evolution of the icy cosmos. The chapter begins with a description of astrochemistry in a historical context, highlighting a few major discoveries and achievements in the century since the first evidence for the existence of molecules in interstellar space came to light. A thorough discussion of the heterogeneous structure of the ISM is then provided, with a particular focus on the physical characteristics of and chemistry occurring within diffuse and dense interstellar clouds. The five mechanisms by which chemistry may occur in astrophysical ices (i.e., thermal chemistry, atom addition reactions, radiation chemistry, photochemistry, and shock chemistry) have also been discussed in the context of the Cosmic Chemistry Cycle, which allows for the evolution of more and more complex molecular material after each iterative cycle. Finally, the chapter concludes by providing an overview of selected icy bodies in the Solar System, including the inner terrestrial planets, Ceres and Vesta, the Galilean moons of Jupiter, Pluto and Charon, and comets.

3 FUNDAMENTAL PHYSICAL CHEMISTRY

This chapter provides the theoretical basis for many of the techniques and principles used in this thesis. It begins with a detailed description of atomic and molecular structure, including the common theories used to describe chemical bonding. It continues with a description of the electromagnetic spectrum, which then naturally leads to a discussion of the principles of spectroscopy, with particular attention paid to infrared absorption spectroscopy. The chapter then concludes with an introductory description of the interaction of matter with ionising radiation in the form of charged particles.

3.1 Atomic Theory

The concept of an indivisible fundamental particle from which all matter in the Universe could be derived can be traced back at least 2,500 years to the Ancient Greek philosophers Leucippus and Democritus²⁵ (De Ley 1968). Indeed, the Greek word *ἄτομον* ('*atomon*'), from which we derive the modern word *atom*, translates to 'uncuttable' or 'indivisible'. Much progress has been made with regards to our understanding of the nature of atoms since these ancient ideas were first put forward; most notable is the fact that atoms are now not thought to be the base particle of nature, and are themselves composed of constituent particles. Nevertheless, atoms represent the smallest unit of baryonic matter that may participate in chemical reactions and processes. The most important property of atoms to chemistry (and thus, by extension, to this thesis) is their ability to join together to form molecules and salts. Before the properties of such molecules can be considered, however, a brief discussion of the structure of atoms must be presented.

3.1.1 Atomic Structure

Atoms are composed of a central, dense structure termed the nucleus. Within the nucleus are a number of positively charged (protons) and electrostatically neutral (neutrons) sub-atomic particles; collectively referred to as nucleons. All atoms of a specific element are defined by a characteristic number of protons, which is indicated by the atomic number, Z . The number of neutrons contained within an atom of a specific element may vary, however, and atoms of the same element possessing a different number of neutrons are termed isotopes. Atoms are also described by their mass number A , which indicates the total number of nucleons contained within the atom. The weighted average mass of the naturally occurring isotopes of a given element is referred to as the elemental atomic weight, A_e .

Surrounding the atom at relatively large distances are small, negatively charged sub-atomic particles called electrons. The Bohr Model of the atom, built on the principles of classical mechanics, suggested that electrons orbit the nucleus similarly to planets orbiting a star, with the energy of an electron being related to its distance from the nucleus. Such a model cannot be correct, however, as an electron in orbit would emit electromagnetic radiation and the resultant energy loss from the system would cause the electron to spiral into the nucleus, thus destabilising the atomic structure. Furthermore, the Bohr Model is at

²⁵ It should be noted that preambles to the concept of atomism can be found in the works of the Ancient Indian philosopher Uddalaka Aruni, who lived approximately 300 years before Leucippus and Democritus.

odds with the Heisenberg Uncertainty Principle, as it simultaneously and precisely defines the position and momentum of the orbiting electron.

The distribution of electrons in an atom can be more accurately represented using a quantum mechanical model. The behaviour of specific electrons in an atom can be described mathematically using a wave equation, the solutions to which are termed wavefunctions. By plotting the square of a wavefunction in three-dimensional space, the volume of space around the nucleus that an electron is most likely to occupy can be defined. This space is referred to as an atomic orbital, and usually takes on the shape of a sphere, a dumbbell, or a teardrop (Figs. 3.1 and 3.2). The lowest energy solution to the wave equation (i.e., the atomic orbital) is spherically symmetric with the atomic nucleus at its centre and is therefore termed the $1s$ orbital. The next higher energy wavefunction is also spherically symmetric, however it is more diffuse and contains a region in which the electron density probability is zero at which the algebraic sign of the wavefunction (i.e., whether it is positive or negative) changes. This orbital is termed the $2s$ orbital.

After the $2s$ atomic orbital, the wave equation has three degenerate solutions: the $2p_x$, $2p_y$, and $2p_z$ atomic orbitals. These orbitals are dumbbell-shaped with nodes representing a change in the algebraic sign of the wavefunction between the two lobes. A p orbital is characterised by its directionality in space since the orbital axis may be aligned along any of the Cartesian x , y , or z coordinate axes (hence the sub-script labels). The third set of wavefunctions furnish the $3s$ and $3p$ atomic orbitals, which are similar in shape to, but more diffuse than their lower energy counterparts and have two nodes. Still higher atomic orbitals are characterised by increasing diffusivity and numbers of nodes as well as different shapes. These are, however, not as important to astrochemistry and so will not be discussed here.

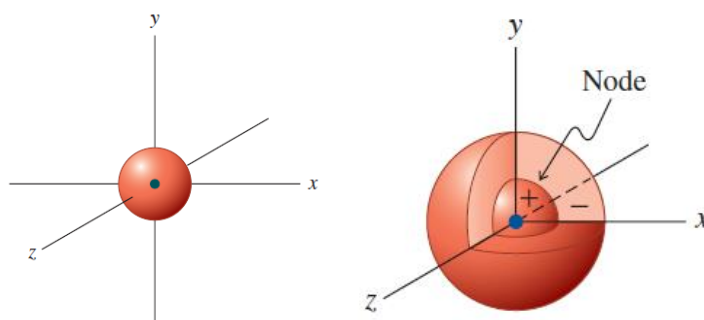


Fig. 3.1: The spherically symmetric $1s$ (left) and $2s$ (right) atomic orbitals. Note the presence of a node in the latter at which point the algebraic sign of the wavefunction changes. Image taken from Vollhardt and Schore (2011).

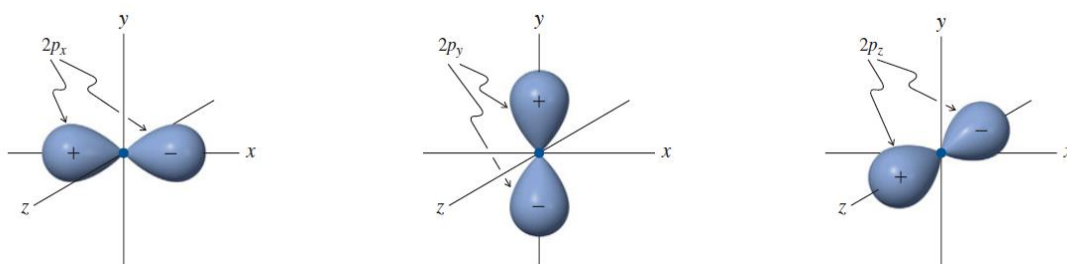


Fig. 3.2: The directionality of p orbitals is such that the orbital axis is aligned to any of the Cartesian coordinate axes. Note the presence of a node in these $2p$ orbitals as well as the change of the algebraic sign of the wavefunction on moving from one lobe to the next. Image taken from Vollhardt and Schore (2011).

3.1.2 Assigning Electrons to Atomic Orbitals

The electrons in an atom will be accommodated in the atomic orbitals as described above, with each orbital hosting a maximum of two electrons. The electron configuration adopted is such that the overall energy of the system is minimised; this represents the so-called ‘ground state’ of the atom. This lowest energy electron configuration may be predicted on the basis of three rules. The first rule is the Aufbau Principle, which states that the lowest energy orbitals are fully occupied first. A graphical representation of the approximate relative energies of atomic orbitals is given in Fig. 3.3. The second rule is the Pauli Exclusion Principle, which mandates that two electrons accommodated within the same atomic orbital possess opposite quantum spins. Lastly, in the case of degenerate orbitals (such as the $2p_x$, $2p_y$, and $2p_z$ orbitals), Hund’s Rule states that these orbitals are occupied by electrons of parallel spins until they are all half-full.

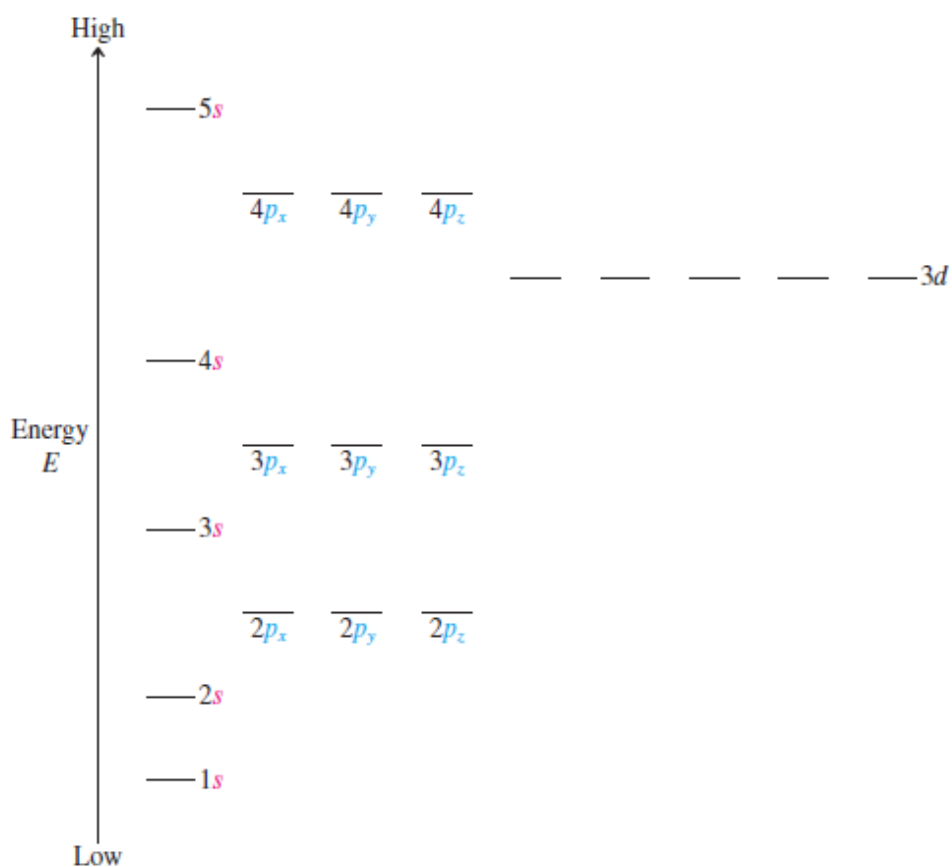


Fig. 3.3: The approximate relative energy spacing of atomic orbitals. Image taken from Vollhardt and Schore (2011).

3.1.3 Atomic Orbital Hybridisation

Consider, for a moment, an atom of carbon which has six electrons arranged in an electron configuration of $1s^2, 2s^2, 2p^2$. Despite this electron configuration being the one resulting from the application of the Aufbau Principle, the Pauli Exclusion Principle, and Hund’s Rule, it is not the configuration adopted for chemical bonding. Instead, the $2s$ and some (or all) of the $2p$ orbitals undergo hybridisation to yield sp orbitals (Fig. 3.4). The number of hybrid orbitals yielded as a result of this process is equal to the number of atomic orbitals consumed, and any remnant $2p$ orbitals not involved in hybridisation are arranged orthogonal to the resultant hybrid orbitals.

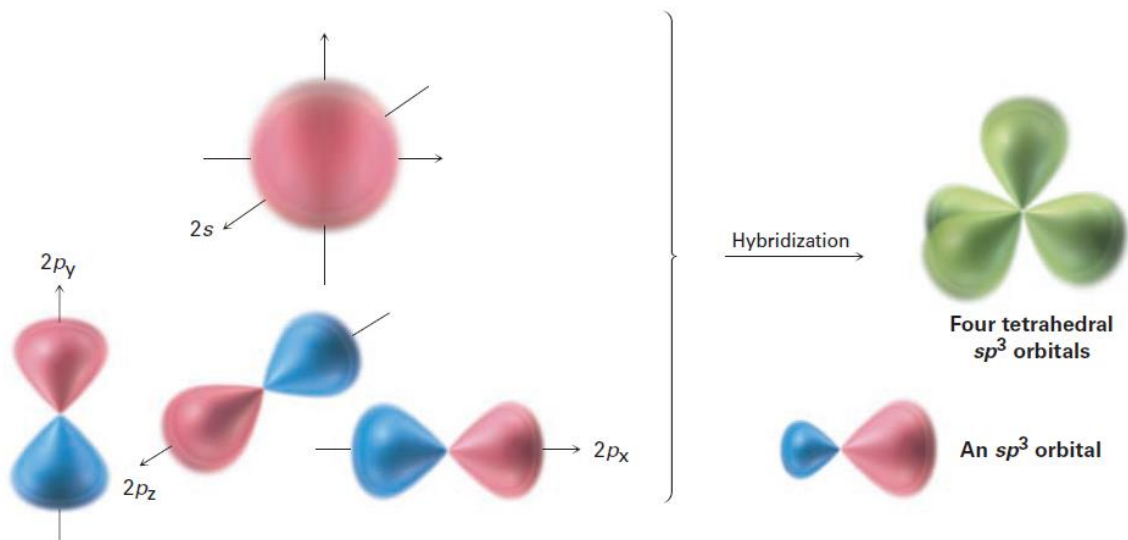


Fig. 3.4: The hybridisation of one $2s$ atomic orbital with three $2p$ orbitals yields four sp hybrid orbitals. Since three $2p$ orbitals were consumed in the hybridisation process, the resultant orbitals are termed sp^3 hybrids. Image taken from McMurry (2012).

The drive behind hybridisation is the interference between the atomic orbitals being consumed: during hybridisation, constructive interference occurs between the $2s$ orbital and the $2p$ orbital lobe having the same algebraic sign, while destructive interference occurs between the $2s$ orbital and the $2p$ orbital lobe having opposite algebraic signs. The result is a sp hybrid orbital which is asymmetric and highly oriented in one direction (Fig. 3.4). The larger lobe of the hybrid orbital is able to participate in the formation of stronger chemical bonds than the original unhybridised orbitals, thus explaining the favourability of the process. It should be noted that hybridisation is not limited to carbon atoms, and that the process can also occur in nitrogen, oxygen, phosphorus, and sulphur.

3.1.4 The Formation of Atomic Ions

The addition or removal of electrons from electrostatically neutral atoms respectively creates negatively charged (anions) and positively charged (cations) ions that may exhibit different chemical properties to the neutral atoms from which they were derived. The ease with which an atom may undergo ionisation to yield either a cation or an anion is quantified *via* its ionisation potential or its electron affinity, respectively. The ionisation potential of an atom is defined as the potential difference corresponding to the energy (in electron volts) that is just sufficient to ionise a gas molecule. The electron affinity of an atom is defined as the energy required to abstract an electron from a negatively charged ion to yield a neutral atom.

The electron configuration of neutral atoms plays a major role in determining the magnitude of their ionisation potentials and electron affinities. Atoms and ions are more stable when their highest energy atomic orbitals are fully occupied by electrons. A smaller, but still significant, increase in the stability of the atom or ion may also be conferred by the highest energy atomic orbital being half-filled with electrons. Therefore, electron loss processes which contribute to the creation of such electron configurations will have much smaller ionisation potentials than those leading to their disruption. To exemplify, the ionisation potentials of atomic lithium, carbon, nitrogen, and neon are 5.4, 11.2, 14.5, and 21.6 eV, respectively (Lide 2004). The low ionisation potential of lithium reflects the fully

occupied highest energy atomic orbital in Li^+ , while the higher values for nitrogen and neon are due to their respective half-full and full highest energy atomic orbitals. Analogous comparisons may be made for the electron affinities of different atoms.

It should be noted that, in general, second ionisation potentials and second electron affinities are highly endothermic processes due to the need to overcome the attractive force between the cation and associated electron in the one case, and the need to overcome the repulsive force between the anion and an incoming electron in the other. Of course, the same is true for all higher order ionisation potentials and electron affinities, with significantly larger energy inputs required for each successive ionisation.

3.2 Molecules

It has been empirically determined that those atoms or ions that possess eight electrons in their highest energy electron shell²⁶, such as the noble gases, are especially stable. This phenomenon, known as the Octet Rule, is the driver behind atomic bonding as atoms seek to lose, gain, or share electrons in an effort to take on the electron configuration of a noble gas and thus lower the total energy content of the system. For instance, alkali metals will readily donate their s electron to a halogen atom, which will accommodate the donated electron in a p orbital. In this way, the resultant alkali metal cation and halide anion achieve a noble gas-like electron configuration and may be held together in an ionic compound (or salt) by Coulombic interactions.

However, it is very challenging to add or remove multiple electrons to or from an atom due to the large input of energy required to overcome the electrostatic interactions generated after the first ionisation of the atom. As such, elements such as carbon or nitrogen, which require the addition or removal of multiple electrons to achieve a noble gas-like electron configuration, tend to achieve this by instead sharing their valence electrons with other atoms through the formation of covalent bonds. The number of covalent bonds an atom tends to form is equal to the number of electrons it must gain in order to achieve a valence octet. The neutral collection of atoms held together by covalent bonds is termed a molecule. The formation of molecules as a result of covalent bonding is described by two models: (i) Valence Bond Theory and (ii) Molecular Orbital Theory, descriptions of which now follow.

3.2.1 Valence Bond Theory

Valence Bond Theory states that a covalent bond is formed when an atomic orbital containing an unpaired electron overlaps with the orbital of another atom that also contains an unpaired electron. This results in the pairing of the electrons in the overlapping orbitals, which are now attracted to both nuclei thus bonding the two atoms together. The head-on overlap of two orbitals allows for a large degree of orbital mixing, thus forming strong covalent bonds known as σ -bonds. Orbital overlap may also occur laterally; however, this results in the formation of a weaker type of covalent bond known as π -bonds (Fig. 3.5).

²⁶ *Electron shells are organisational units centred around the atomic nucleus that contain various orbitals of differing geometries and energies. The electron shell in which an atomic orbital is located is indicated by the number in the orbital name. For instance, the 2s and 2p atomic orbitals are all in the second electron shell.*

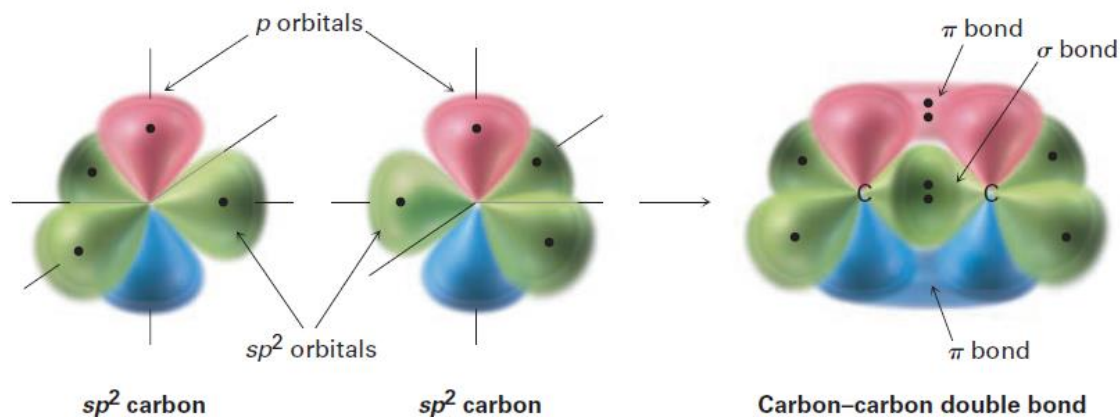


Fig. 3.5: Graphical representation of Valence Bond Theory as applied to the carbon-carbon double bond in C_2H_4 . The head-on overlap of two sp^2 hybrid orbitals results in the formation of a strong σ -bond, while the lateral overlap of the p orbitals results in a weaker π -bond. Image taken from McMurry (2012).

Valence Bond Theory is thus largely defined by electrostatic interactions between electrons and nuclei. As such, there exists an optimum internuclear separation at which the energy content of the system is at a minimum. If the nuclei are too far away from one another, then the atomic orbitals will not overlap thus precluding the formation of a covalent bond. Conversely, if they are too close together, then the energy of the system will increase dramatically due to electrostatic repulsion between the two positively charged nuclei. The optimum distance is referred to as the covalent bond length, and the energy content of the system (which must be supplied to break the covalent bond) is termed the bond energy.

3.2.2 Molecular Orbital Theory

Molecular Orbital Theory describes the formation of covalent bonds as being the result of a linear mathematical combination of atomic orbitals to yield molecular orbitals. Similarly to atomic orbitals, molecular orbitals describe the region of space around a molecule where electrons are likely to be found. The linear combination of atomic orbitals may occur in two ways. Firstly, the in-phase, or additive, combination of the orbitals leads to the production of a new, lower energy molecular orbital in which the electron density in the space between the atomic nuclei is strongly reinforced. This molecular orbital is referred to as a bonding molecular orbital, and its occupancy by electrons is the prime contributor to the formation of the covalent bond. On the other hand, the out-of-phase, or subtractive, combination of the atomic orbitals results in a new, higher energy molecular orbital containing a node in the space between the two nuclei, which may thus repel each other. This molecular orbital is referred to as an antibonding molecular orbital.

The favourability of covalent bond formation may be described through the use of molecular orbital diagrams (Fig. 3.6). Consider the potential for bond formation between two hydrogen atoms, each with an electron configuration of $1s^1$. Additive combination of the orbitals leads to the formation of a σ_{1s} bonding molecular orbital, while their subtractive combination yields the σ_{1s}^* antibonding molecular orbital. Each of these molecular orbitals, like the atomic orbitals from which they were derived, are able to accommodate a maximum of two electrons. However, since the total system contains two electrons, both of these may be housed within the σ_{1s} bonding molecular orbital, thus decreasing the total energy of the system.

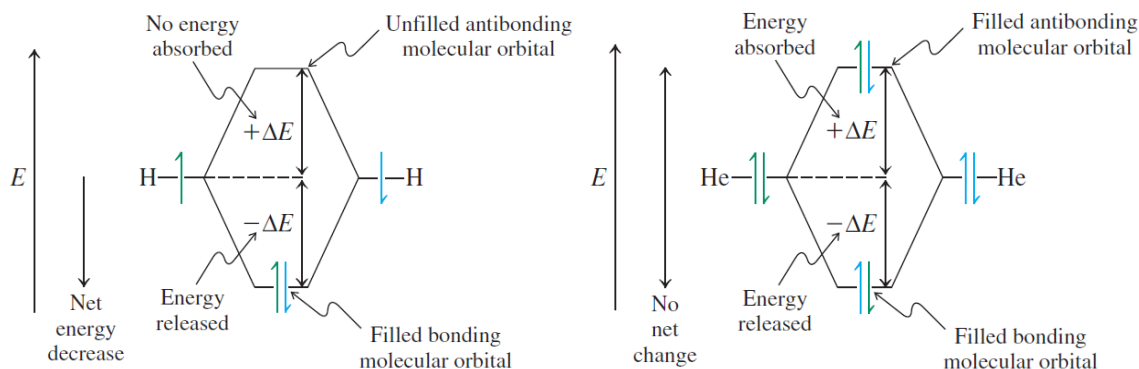


Fig. 3.6: Molecular orbital diagrams for H_2 (left) and He_2 (right). Image taken from Vollhardt and Schore (2011).

Compare this to the molecular orbital diagram of the hypothetical molecule He_2 . The linear combination of the helium $1s$ orbitals would also result in the production of a σ_{1s} bonding molecular orbital and a σ_{1s}^* antibonding molecular orbital. However, in this case, there are four electrons in the system, meaning that the bonding and antibonding molecular orbitals must each accommodate two electrons. As there is no net decrease in the energy content of the system, the formation of a covalent bond between two helium atoms is thus not favoured. More complex molecular orbital diagrams for heavier atoms containing more electrons may also be drawn (Housecroft and Sharpe 2012); however, a fuller explanation of such bonding systems would go beyond the scope of this thesis.

3.2.3 Valence Shell Electron Pair Repulsion Theory

The nominal geometry adopted by a molecule is controlled by the repulsion between electron pairs situated on the central atom in the molecule. This statement forms the premise of the Valence Shell Electron Pair Repulsion (VSEPR) Theory, which states that molecules adopt specific geometries so as to minimise the repulsion between electron pairs on central atoms (Fig. 3.7). Moreover, VSEPR Theory proposes that the repulsion between two non-bonding electron pairs is greater than that between two bonding electron pairs. To begin with, consider the simplest case wherein a central atom in a molecule has no non-bonding electron pairs and a coordination number of two; that is to say it is bonded to two other atoms, as in the case of CO_2 . The geometry that minimises the repulsion between sets of bonded electrons is a linear one, as this keeps the two $\text{C}=\text{O}$ bonds as far apart in space as possible.

This idea that sets of bonded electrons should be maintained as far apart as possible in the lowest energy molecular geometry can be extended to molecules whose central atom has a higher coordination number. In CH_4 , in which the central carbon atom has a coordination number of four and no non-bonding electron pairs, the adopted geometry is a tetrahedral one with $\text{H}-\text{C}-\text{H}$ bond angles of 109.5° . In the case of H_2O , the central oxygen atom has a coordination number of four which includes two pairs of non-bonding electrons. These four electron densities (i.e., the two bonds and the two lone pairs) are also arranged in a tetrahedral structure, but as the non-bonding electron pairs do not contribute to the overall molecular geometry, the actual shape of a H_2O molecule appears to be angled or bent. Furthermore, the non-bonding electron pairs are able to repel other electron densities more strongly than the covalent bonds: each non-bonding electron pair reduces nearby bond angles by about 2.5° , and thus the $\text{H}-\text{O}-\text{H}$ bond angle is 104.5° .

















CN	Number of Lone Electron Pairs							
	0	e.g.	1	e.g.	2	e.g.	3	e.g.
2	 linear	CO ₂						
3	 trigonal planar	BCl ₃ SO ₃	 angled	SO ₂ NO ₂ ⁻ O ₃	 linear	O ₂		
4	 tetrahedral	CH ₄ SO ₄ ²⁻	 trigonal pyramidal	NH ₃	 angled	H ₂ O	 linear	HCl
5	 trigonal bipyramidal	PCl ₅	 bisphenoidal (seesaw)	SF ₄	 T-shaped	ClF ₃	 linear	I ₃ ⁻
6	 octahedral	SF ₆	 square pyramidal	ClF ₅	 square planar	ICl ₄ ⁻		
7	 pentagonal bipyramidal	IF ₇						

Fig. 3.7: Molecular geometries adopted by molecules with central atoms having different coordination numbers and non-bonding (or lone) electron pairs as predicted by VSEPR Theory. Image credit: Merck.

3.2.4 Point Group Symmetry

Although molecules may be categorised by their geometries, it is often more useful to categorise them in terms of their symmetry into so-called ‘point groups’. Molecules may be assigned to different point groups by assessing the validity of various symmetry operations. Symmetry operations are defined as those operations (such as rotations, inversions, or reflections) which leave the molecular structure in a configuration that is indistinguishable from, and superimposable on, the original structure. All symmetry operations are carried out with respect to a defined point, line, or plane which is termed the symmetry element. The number and nature of the symmetry elements present within the structure of a given molecule thus allow the molecule to be classified into a specific point group. This is of importance, as different point groups are associated with different molecular properties. There are a total of five symmetry operations, a description of each of which now follows.

(i) **Rotation about a n -fold axis of symmetry**

The rotation about a n -fold symmetry axis is denoted using the symbol C_n , in which the angle of rotation is $360^\circ / n$, where n is a simple integer. Considering the trigonal planar BF_3 molecule, two axes of rotation are present (Fig. 3.8): one perpendicular to the plane of the molecule (C_3 rotation axis) and one through a B–F bond (C_2 rotation axis). The principal axis of rotation is that with the highest order; in this case the C_3 rotation axis. Linear molecules such as CO_2 possess a C_∞ axis of rotation through the bond axis.

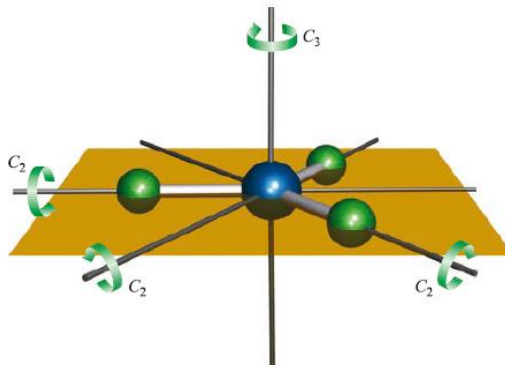


Fig. 3.8: Axes of rotation in a trigonal planar BF_3 molecule. Image taken from Housecroft and Sharpe (2012).

(ii) **Reflection through a plane of symmetry (mirror plane)**

If reflection of all parts of a molecule through a plane produces a configuration indistinguishable from that of the original, then the plane is a symmetry element. The reflection operation is given the symbol σ . Reflection operations may be divided into three sub-types, depending on the relation of the principal axis of rotation to the mirror plane. If the principal axis of rotation is contained within the mirror plane, then the plane is of the σ_v type; while if it is orthogonal to the mirror plane, then the plane is of the σ_h type. The BF_3 molecule contains this latter type of mirror plane (Fig. 3.8), while the H_2O molecule contains the former type (Fig. 3.9). The third type of plane, the σ_d type, is the special case wherein the mirror plane contains the principal axis of rotation but also bisects the angle between two C_2 rotation axes.

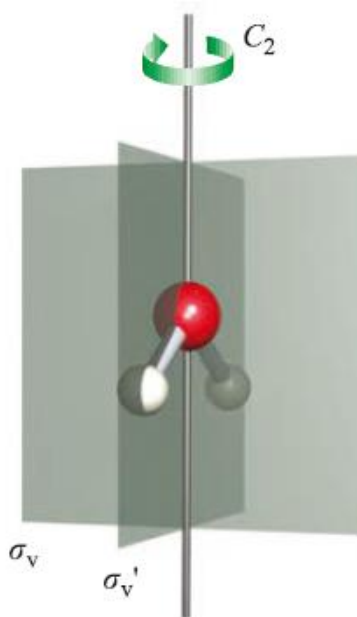


Fig. 3.9: Mirror planes in relation to the principal axis of rotation in the H_2O molecule. Image taken from Housecroft and Sharpe (2012).

(iii) **Reflection through a centre of symmetry (inversion centre)**

The centre of a molecule may be a symmetry element known as the inversion centre if reflection of all parts of the molecule through this point produces an indistinguishable configuration from that of the original. The inversion symmetry element is given the symbol i .

(iv) **Improper rotation about a n -fold axis**

If rotation about an axis followed by reflection through a plane yields an identical molecular configuration as that of the original, then the symmetry operator is called a n -fold improper rotation and the element is given the symbol S_n , where n refers to the same n used to define the rotation angle as $360^\circ / n$. The CH_4 molecule possesses three S_4 axes, and the operation of one S_4 rotation-reflection is shown in Fig. 3.10.

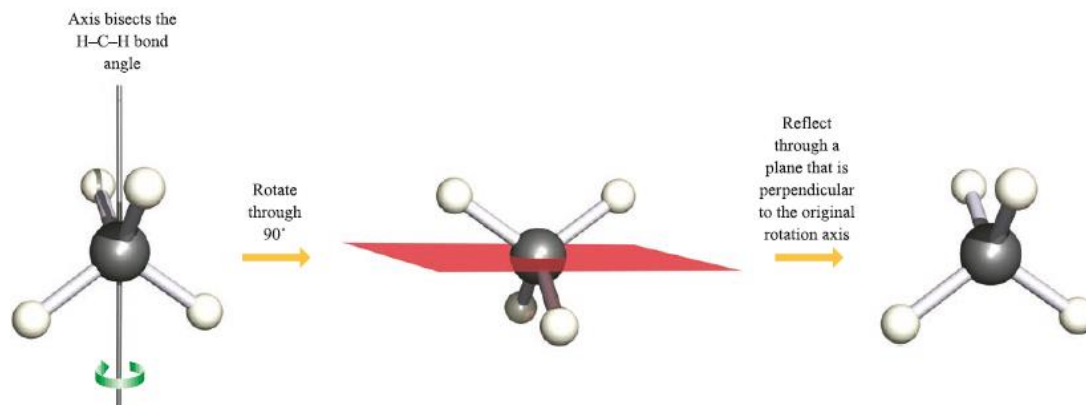


Fig. 3.10: One S_4 rotation-reflection operation in the CH_4 molecule. Image taken from Housecroft and Sharpe (2012).

(v) **Identity operator**

The identity operator is given the symbol E , and it effectively identifies the molecular configuration leaving it unchanged. All objects may be operated upon by the identity operator.

Table 3.1 summarises the main point groups and their symmetry elements, while the flow-chart in Fig. 3.11 presents a systematic methodology by which molecules may be assigned to the different point groups.

Table 3.1: Summary of the symmetry elements characterising different point groups. Table adapted from Housecroft and Sharpe (2012).

Point Group	Symmetry Elements
C_s	E , one σ plane
C_i	E , inversion centre
C_n	E , one (principal) n -fold axis
C_{nv}	E , one (principal) n -fold axis, n σ_v planes
C_{nh}	E , one (principal) n -fold axis, one σ_h plane, one S_n -fold axis coincident with the C_n axis, i if $n = 2, 4$, or 6
D_{nh}	E , one (principal) n C_2 axes, one σ_h plane, n σ_v planes, one S_n -fold axis, i if $n = 2, 4$, or 6
D_{nd}	E , one (principal) n -fold axis, n C_2 axes, n σ_v planes, one S_n -fold axis, i if $n = 3$ or 5
T_d	Tetrahedral geometry
O_h	Octahedral geometry
I_h	Icosahedral geometry

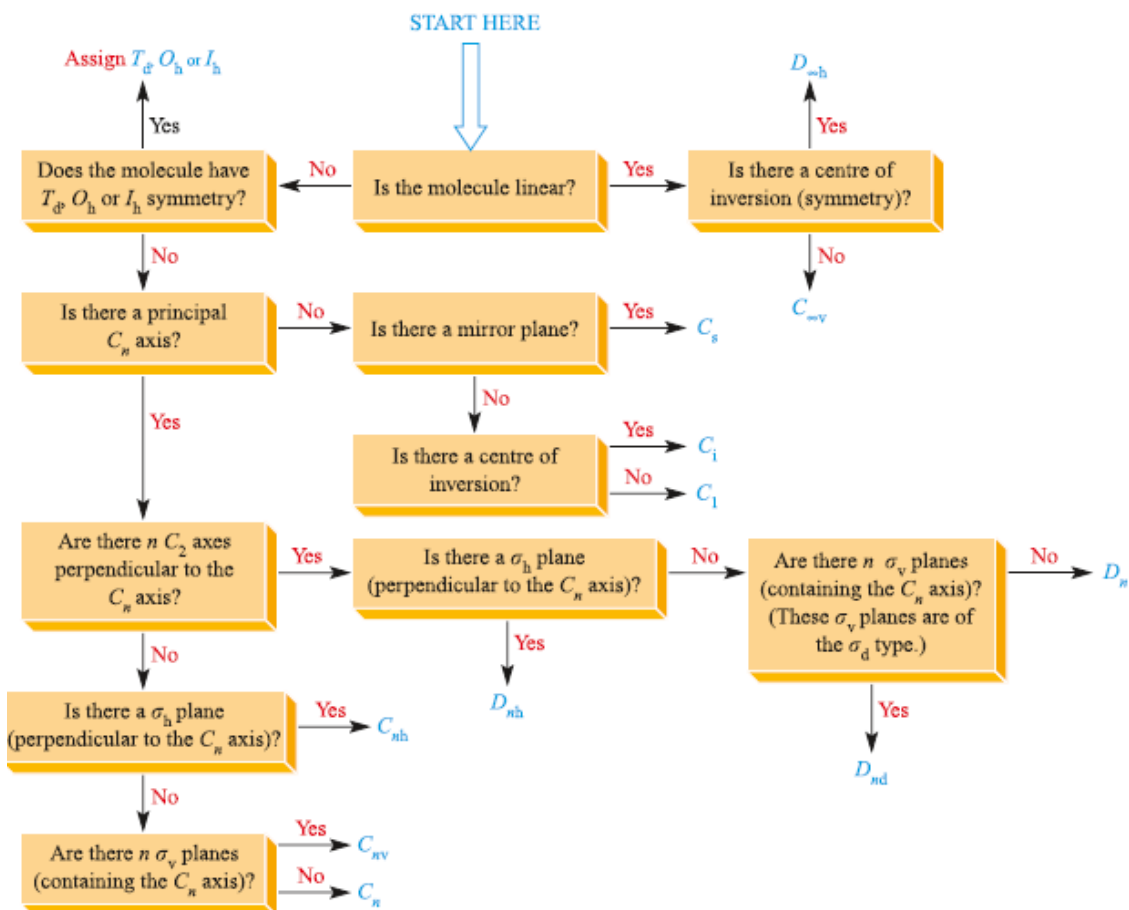


Fig. 3.11: Flow-chart used to determine the point group of a molecule. Image taken from Housecroft and Sharpe (2012).

3.2.5 Electronegativity and Polarity

Electronegativity is defined as the ability of an atom to attract shared electrons in a chemical bond towards it, thus distorting the electron distribution around the molecule towards that atom. Smaller atoms with more protons in their nucleus (i.e., those situated towards the top-right of the periodic table) are more electronegative, while larger atoms with fewer protons (i.e., those at the bottom-left of the periodic table) are less electronegative. The most and least electronegative elements are fluorine and caesium²⁷, respectively.

There are many methods by which the electronegativity of an atom may be quantified, but the most commonly used is the Pauling Scale which defines the difference in the electronegativity χ of two generic elements A and B in terms of the dissociation energies E_d of the A–A, B–B, and A–B bonds:

$$|\chi_A - \chi_B| = (\text{eV})^{-\frac{1}{2}} \sqrt{E_d(\text{AB}) - \frac{E_d(\text{AA}) + E_d(\text{BB})}{2}} \quad (\text{Eq. 3.1})$$

where the term in eV is included to ensure that the electronegativity χ remains dimensionless.

²⁷ Although francium is a larger atom than caesium, its electronegativity is slightly greater due to the increased contribution of relativistic quantum effects.

Since only differences in electronegativity are defined by Eq. 3.1, it is necessary to first select an arbitrary reference point so as to construct a scale. Hydrogen was selected for this purpose on the basis of its ability to covalently bond with a large number of elements. The electronegativity of hydrogen was set at 2.10, although this was later amended to 2.20 (Allred 1961). As such, the electronegativity of each element may be calculated based solely on thermodynamic information on the dissociation energies of just two types of covalent bond formed by the element.

The difference in electronegativity between two elements linked in a chemical bond is of direct relevance to the electrostatic properties of the molecule. As previously mentioned, atoms that are more electronegative are able to more strongly attract the electrons shared in a chemical bond, thus distorting the electron distribution in the molecule towards these atoms. This skewed electron distribution results in the formation of a dipole moment along the axis of the bond towards the more electronegative atom due to the formation of a partial negative charge on the electronegative atom and a partial positive charge on the atom to which it is bonded. The bond is thus said to be polarised. The extent of bond polarisation dictates the type of bond formed between two atoms: if $|\chi_A - \chi_B| < 0.5$, then the bond is considered to be a typical non-polar covalent bond, whilst if $|\chi_A - \chi_B| > 1.8$, then the bond is sufficiently polarised for complete charge transfer to take place resulting in an ionic bond. Finally, if $0.5 < |\chi_A - \chi_B| < 1.8$, then the covalent bond is a polar one.

Molecules may contain multiple polar bonds each with their own directed dipole moment. Since dipole moments are vector quantities, these may be geometrically added to give an overall molecular dipole. If this molecular dipole is non-zero, as in the case of CH_3Cl or CH_3OH , then the molecule itself is considered to be a polar molecule. However, if dipole moments within a molecule are of an equal magnitude but opposite direction, then they will cancel out. If all dipole moments within a molecule are cancelled out, as in the case of CO_2 , then the molecule itself is non-polar despite it containing polar covalent bonds. Examples of such scenarios are given in Fig. 3.12. Given the evident geometrical considerations which must be taken into account when deciding whether a molecule is polar or not, it is perhaps unsurprising that molecular symmetry must also be considered. Indeed, only those molecules belonging to the C_n , C_{nv} , and C_s point groups may be polar. However, it should be noted that molecules belonging to the C_n or C_{nv} point groups cannot have a molecular dipole in the direction perpendicular to the symmetry axis.

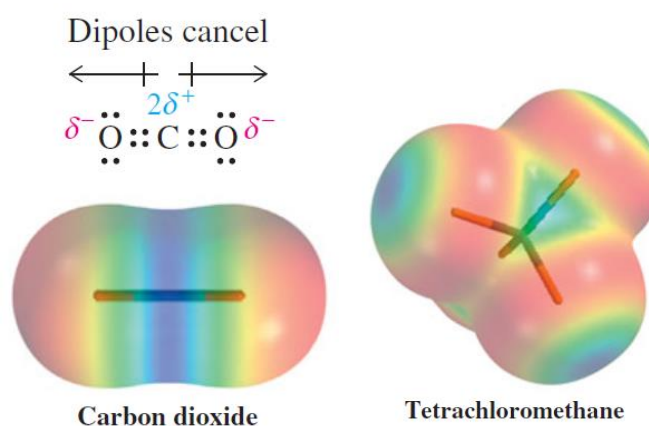


Fig. 3.12: Electrostatic potential maps for the non-polar CO_2 (left) and CCl_4 (right) molecules, in which higher electron densities around more electronegative atoms are indicated in red and lower electron densities around less electronegative atoms are indicated in blue. Although both molecules contain polar bonds, the individual dipole moments cancel each other out resulting in an overall non-polar molecule. Images taken from Vollhardt and Schore (2011).

3.2.6 Isomerism in Molecules

Isomers are polyatomic molecules or ions that contain the same number of atoms of each element, but have distinct arrangements of those atoms in space. There are two main types of isomerism: structural isomerism (sometimes referred to as constitutional isomerism) and stereoisomerism (sometimes referred to as spatial isomerism). In structural isomerism, the bonds between atoms differ resulting in the two isomeric molecules having different skeletal structures, different functional groups, or different positions of the major functional group. Examples of such structural isomers are *n*- and *i*-butane forms of C₄H₁₀, CH₃CH₂OH and CH₃OCH₃, and CH₃(CH₂)₂OH and CH₃CH(OH)CH₃ (propyl and isopropyl alcohol).

Stereoisomers contain the exact same bonding system (and thus, by extension, the same functional groups) but their structures are non-superimposable on one another. Stereoisomers can be divided into two sub-classes: enantiomers and diastereomers. Enantiomers are non-superimposable mirror image structures that oftentimes contain an asymmetric carbon atom bonded to four unique systems. Asymmetric carbon atoms endow molecules with a property known as chirality. Chiral systems are able to rotate the plane of incident polarised light. As enantiomers represent two mirror images, the individual structures rotate the plane of this polarised light by an equal amount but in opposite directions. Many molecules relevant to biology are chiral, and biological systems seem to have developed a distinct preference for a particular enantiomeric structure (Globus and Blandford 2020).

The class of diastereomers constitutes all non-superimposable non-mirror image stereoisomers, such as *cis*- and *trans*-isomers or conformational isomers. Diastereomeric structures are often encountered in molecules containing more than one asymmetric carbon atom. If such a molecule contains *k* asymmetric centres, then it may exhibit a maximum of 2^{*k*} stereoisomers (including enantiomers and diastereomers but excluding conformational isomers). Note that this is the maximum number of stereoisomers that may be exhibited, but many molecular structures actually exhibit fewer. Consider, for instance, the structure of tartaric acid (Fig. 3.13). This molecule contains two asymmetric carbon atoms, and should thus exhibit a maximum of four stereoisomers. Indeed, the molecule may exhibit two non-superimposable mirror images representing a pair of enantiomers. However, on examining the remaining two structures, it is possible to note that they are they present the same spatial structure offset by a rotation of 180°. Given that they are the same structure, which is referred to as the meso form, tartaric acid only exhibits three stereoisomers.

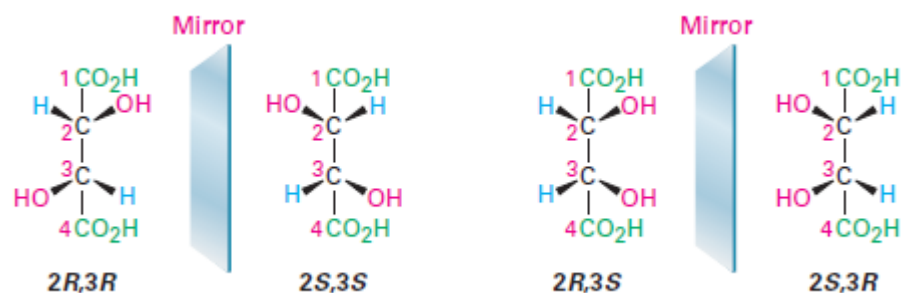


Fig. 3.13: The possible stereoisomers of tartaric acid. Note that the prefixes *R*- and *S*- refer to the configuration of bonding systems around the asymmetric carbon atom. On the left, the *2R*-,*3R*- and *2S*-,*3S*- stereoisomers are mirror images and thus represent a pair of enantiomers. On the right, the *2R*-,*3S*- and *2S*-,*3R*- isomers are in fact the same structure offset by a rotation of 180°: this structure corresponds to the meso form. Thus, the meso form is diastereomeric with respect to the enantiomers. Image taken from Vollhardt and Schore (2011).

It should also be noted that meso forms are not chiral molecules, and thus do not rotate the plane of incident polarised light. By examining the meso structure of tartaric acid (Fig. 3.13), this lack of chirality may be understood in terms of the fact that the two asymmetric carbon atoms are bonded to the same chemical systems but in the opposite configuration. They therefore rotate the plane of incident polarised light by an equal but opposite amount, thus cancelling out the effects of one another. The identification of a meso compound may be achieved by assessing the symmetry of a molecule: if a diastereomeric structure contains a mirror plane or a centre of inversion, then it is an achiral meso form.

3.3 Infrared Spectroscopy

Infrared spectroscopy represents the main analytical tool used throughout this thesis. Accordingly, the underlying principles of this technique and the practicalities of its application to the observation and study of astrophysical ices will be discussed. In order to fully understand this topic, it is necessary to first describe the quantised method by which matter interacts with electromagnetic radiation.

3.3.1 The Interaction of Matter with Electromagnetic Radiation

Electromagnetic radiation propagates as two mutually perpendicular electric and magnetic transverse (i.e., sinusoidal) waves which oscillate in phase (Fig. 3.14). The velocity of this propagation in a vacuum is constant at $c = 3 \times 10^8 \text{ m s}^{-1}$. This velocity may be related to the wavelength (defined as the distance between adjacent wave peaks) λ and its frequency (defined as the number of oscillations per unit time) ν through the equation:

$$c = \lambda\nu \quad (\text{Eq. 3.1})$$

Furthermore, the energy E of the electromagnetic wave may be given as:

$$E = h\nu \quad (\text{Eq. 3.2})$$

where h is the Planck constant which is equal to $6.63 \times 10^{-34} \text{ J s}$ (or alternatively, $4.14 \times 10^{-15} \text{ eV s}$). It is on the basis of its energy that electromagnetic radiation is classified into the various components of the so-called electromagnetic spectrum (Fig. 3.15). Infrared radiation lies within a wavelength range of between approximately 1 mm and 750 nm, corresponding to a frequency range of between 300 GHz and 400 THz.

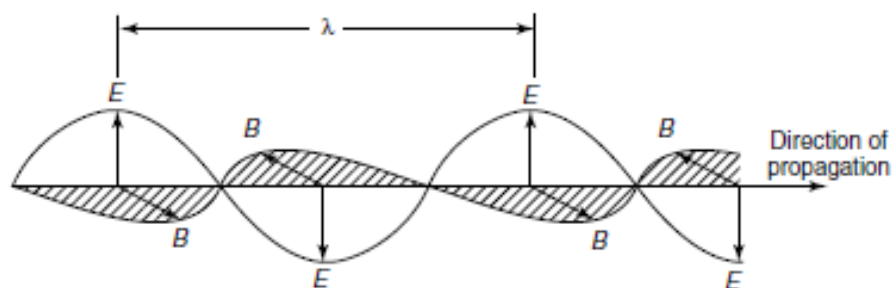


Fig. 3.14: Representation of an electromagnetic wave as perpendicularly oscillating electric E and magnetic B fields. Image taken from Stuart (2004).

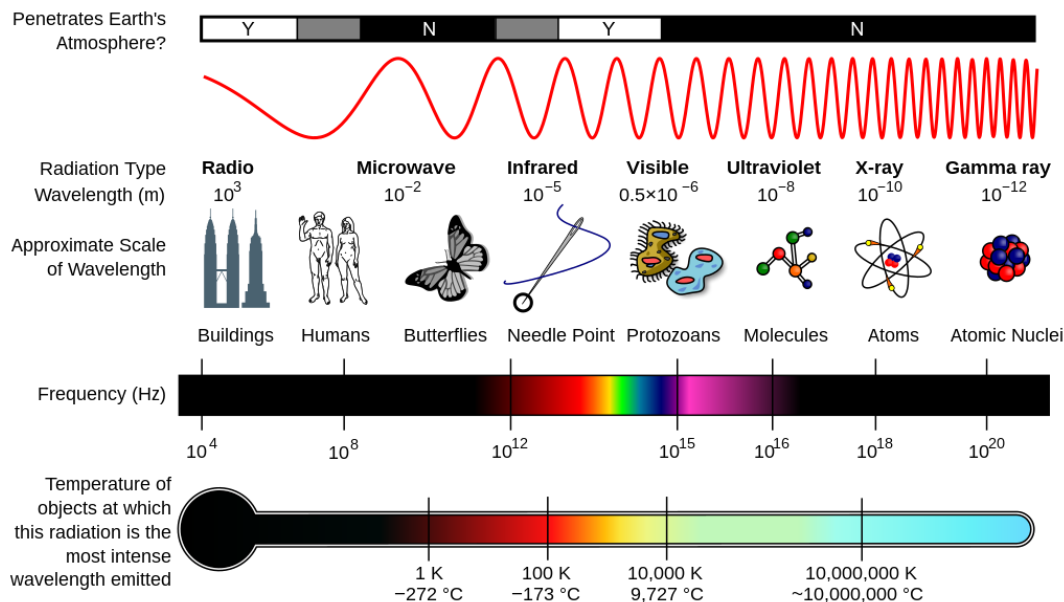


Fig. 3.15: The electromagnetic spectrum. Image credit: NASA.

The interaction of electromagnetic radiation with matter (specifically, molecules) is at the heart of the underlying theory of spectroscopy. There are three basic processes by which molecules may absorb incident radiation and, in all cases, the molecule is raised to a higher internal energy level in a process termed excitation, with the increase in energy being equal to the energy absorbed. It is very important to note that these three types of molecular internal energy are quantised; that is to say that they exist at discrete energy levels rather than as an energy continuum (Fig. 3.16). As such, for a successful excitation to occur, the absorbed energy must be of a definite wavelength matching the quantised energy discrepancy between the ground and excited states.

The lowest energy of excitation is that causing rotational excitation of the molecule and corresponds to wavelengths in the microwave region of the electromagnetic spectrum. As discussed in Chapter 2, rotational spectroscopy is the most widely used technique in the detection of gas-phase interstellar molecules (Fortenberry 2017, Puzzarini and Barone 2020). Solid materials, such as the ices of interest to this thesis, are rotationally constrained, and thus rotational spectroscopy is of little to no use to the detection of interstellar molecules within icy grain mantles or the laboratory study of astrophysical ice analogues. The second type of energy excitation is that of vibrational excitation, which corresponds to the absorption of energy in the infrared region of the electromagnetic spectrum. It is this type of quantised energy excitation that will be the focus of the discussion in this sub-section. Lastly, the third type of excitation is the promotion of electrons from lower energy molecular orbitals to higher energy ones. These transitions correspond to the absorption of energy in the visible and ultraviolet regions of the electromagnetic spectrum.

The lifetimes of molecular excited states are typically very short, ranging from a few fs to a few μ s, and the molecules thus rapidly undergo de-excitation and return to the ground state. This process may be a radiationless one, in which the energy initially absorbed is lost as heat during collisions. Radiative de-excitations, such as fluorescence or phosphorescence, may also occur (Wells 1972), although a fuller description of these processes would go beyond the scope of this thesis.

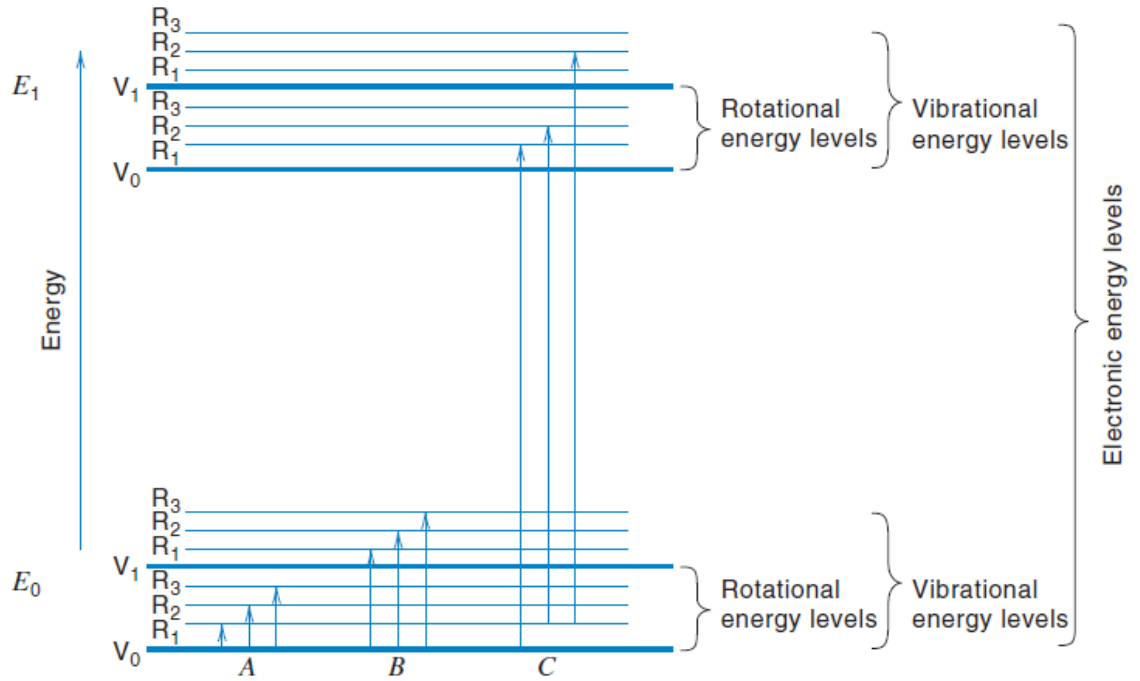


Fig. 3.16: Energy level diagram depicting the rotational, vibrational, and electronic transitions associated with the absorption of electromagnetic radiation. Image taken from Christian *et al.* (2014).

The absorption of monochromatic radiation by a sample is quantitatively described by the Bouguer-Lambert-Beer Law, more commonly referred to as Beer's Law. Consider a beam of electromagnetic radiation of initial power P_0 incident upon an absorbing material of concentration C and pathlength b . Assuming the radiation is not fully attenuated by the absorbing material, then it will transmit through the material emerging with a radiant power P . The transmittance T_v of the material may thus be defined as:

$$T_v = \frac{P}{P_0} \quad (\text{Eq. 3.3})$$

It is perhaps evident that the absorption of electromagnetic radiation is dependent upon the number of molecules available to absorb the radiation and the pathlength through which the radiation must travel. Empirical studies in the eighteenth and nineteenth centuries demonstrated that the power of the transmitted radiation decreases exponentially with respect to both concentration and pathlength. As such, the transmittance of the absorbing sample may also be expressed as:

$$T_v = 10^{-k_1 b} = 10^{-k_2 C} \quad (\text{Eq. 3.4})$$

where k_1 and k_2 are two constants. An equation may thus be formed which expresses T_v in terms of both b and C by combining the two constants into a new constant a which is termed the absorptivity of the sample:

$$T_v = 10^{-abC} \Rightarrow -\log(T_v) = abC \quad (\text{Eq. 3.5})$$

Multiplying the absorptivity of the sample by its molecular weight yields a new constant intrinsic to the absorbing sample called the molar attenuation coefficient ϵ . Furthermore, the absorbance A_v of the absorbing sample may be defined as being equivalent to $-\log(T_v)$, and thus:

$$A_v = \epsilon b C \quad (\text{Eq. 3.6})$$

Moreover, the optical depth τ_v of the absorbing sample may be defined as:

$$\tau_v = -\ln(T_v) = \frac{-\log(T_v)}{\log(e)} \approx 2.303 A_v \quad (\text{Eq. 3.7})$$

where e is the Euler constant which is approximately 2.71828. The practical application of this equation will be explained in the next chapter.

It is interesting to note that, although the quantised nature of vibrational transitions predicts that absorptions in infrared spectra should appear as discrete and narrow lines, it is in fact absorption bands that are observed in typical spectra. Many factors may contribute to this broadening of the absorptions, including molecular collisions, the Doppler Effect, and the lifetime of the excited states. Each of these types of broadening is discussed below:

(i) Collisional Broadening

Collisional broadening occurs in gases and liquids wherein molecules are constantly in motion. The frequent collisions between the molecules results in a slight perturbation of their quantised energy levels. In gases, collisional broadening increases proportionally with the total pressure p , while in solutions it increases proportionally with concentration C . The effect of collisional broadening is significantly reduced in solids due to the restriction of molecular motion.

(ii) Doppler Broadening

Doppler broadening is a consequence of the Doppler Effect, in which a shift in the frequency of radiation occurs as the radiation source moves towards or away from a target. In gases and liquids, molecules are constantly in motion with some moving towards and some moving away from the source of electromagnetic radiation. The result is a broadening of the absorption features which increases with molecular velocity.

(iii) Lifetime Broadening

Lifetime broadening is a consequence of the Heisenberg Uncertainty Principle. If an excited state exists for a limited lifetime τ , then an uncertainty in the energy levels of the system δE will exist such that:

$$\delta E \approx \frac{h}{2\pi\tau} \quad (\text{Eq. 3.8})$$

where π is the Archimedes constant which is approximately 3.14159. Since all excited states have finite lifetimes before their decay, they all suffer from lifetime broadening.

3.3.2 Quantum Vibration in Molecules as a Ball and Spring Model

During the discussion of Valence Bond Theory, it was mentioned that there exists an optimum internuclear separation between two covalently bonded atoms at which the energy content of the system is at a minimum. This separation is termed the equilibrium distance r_{eq} and any attempts to distort the molecular bond *via* compressing it or extending it is resisted by the electrostatic interactions involving the nuclei and electrons. The compression and extension of a covalent bond may be compared to that of a spring. Indeed, this analogy may be further developed by assuming that the bond obeys Hooke's Law and thus:

$$F = -k(r - r_{\text{eq}}) \quad (\text{Eq. 3.9})$$

$$E = \frac{1}{2}k(r - r_{\text{eq}})^2 \quad (\text{Eq. 3.10})$$

where F is the restoring force, E is the energy of the system, r is the internuclear separation, and k is a constant.

This model of a vibrating diatomic molecule as two balls (the atoms) joined by a spring (the covalent bond) is called the Simple Harmonic Oscillator Model and, while it is only an approximation, it serves as an excellent starting point for a more detailed discussion of infrared spectroscopy. A plot of the energy of the diatomic system as a function of internuclear separation yields a parabolic curve with a minimum point (more specifically, a zero point) at $r = r_{\text{eq}}$ (Fig. 3.17). Elastic bonds, like springs, are associated with oscillatory frequencies dependent upon the mass of the diatomic system and the force constant, but are independent of the extent of compression or extension. This frequency ω is given as:

$$\omega = \frac{1}{2\pi} \sqrt{\frac{k}{\mu}} \quad (\text{Eq. 3.11})$$

where μ is the reduced mass of the diatomic system, which is defined as the ratio of the product of the masses of the constituent atoms to their sum. As previously noted, molecular vibrational energy is quantised, and the allowed vibrational energies for a given system may thus be calculated by solving the Schrödinger Equation for a quantum harmonic oscillator:

$$E\psi = -\frac{\hbar^2}{8\pi^2\mu} \frac{d^2}{dr^2} \psi + \frac{1}{2}\mu\omega^2 r^2 \psi \quad (\text{Eq. 3.12})$$

where ψ represents a vibrational wavefunction. Solving this equation yields:

$$E_v = \left(v_q + \frac{1}{2}\right) h\omega \quad (\text{Eq. 3.13})$$

where v_q is known as the vibrational quantum number which may be any non-negative integer value.

The vibrational energy levels of a quantum harmonic oscillator are typically expressed in the more spectroscopically useful units of inverse wavelengths expressed in cm^{-1} , more commonly referred to as wavenumbers ξ . Therefore:

$$\xi = \left(v_q + \frac{1}{2} \right) \frac{\omega}{c}$$

(Eq. 3.14)

Interestingly, when $v_q = 0$ is substituted into Eq. 3.13, then it is evident that the vibrational energy of the molecular system is non-zero. This implies that a diatomic molecule (and, indeed, all molecules) can never have zero vibrational energy and therefore the atoms cannot be at rest relative to one another. This so-called zero-point energy is a fundamental property of each molecule, depending only upon the strength of the covalent bond and the mass of the constituent atoms.

The quantum nature of vibrational excitation leads to the simple selection rule:

$$\Delta v_q = \pm 1$$

(Eq. 3.15)

It should also be emphasised, however, that such vibrational excitation can only occur if the diatomic molecule interacts with infrared radiation and if the vibration results in a change in the net dipole moment of the molecule. Therefore, in the case of diatomic molecules, infrared spectra are only observable for heteronuclear diatomic molecules, since homonuclear diatomic molecules exhibit neither a normal dipole moment nor can they exhibit an induced one. Applying the selection rule yields:

$$\xi_{v_q \rightarrow v_q \pm 1} = \left| \left(v_q + 1 + \frac{1}{2} \right) \frac{\omega}{c} - \left(v_q + \frac{1}{2} \right) \frac{\omega}{c} \right| = \frac{\omega}{c}$$

(Eq. 3.16)

irrespective of the initial value of v_q .

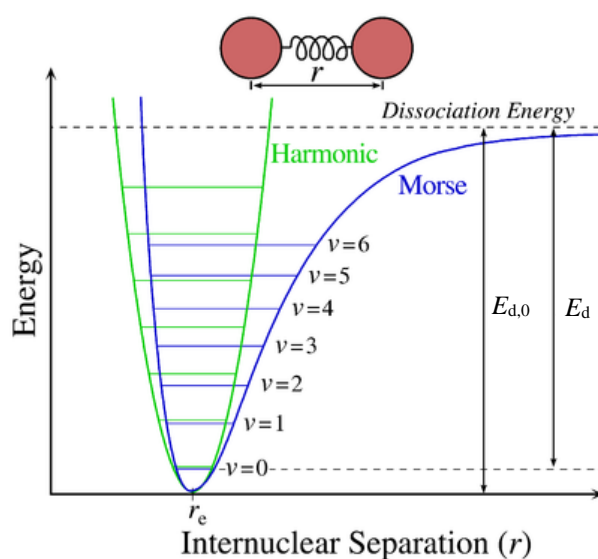


Fig. 3.17: The parabolic energy function of quantum harmonic oscillation (*green*) and the Morse function of quantum anharmonic oscillation (*blue*). Note that the energy spacing between vibrational energy levels is even in the case of the former, but not in the case of the latter. E_d refers to the bond dissociation energy, while $E_{d,0}$ refers to the sum of the bond dissociation energy and the molecular zero-point energy. Image credit: P. Kelly.

This result implies that quantised vibrational energy levels in simple harmonic systems are equally spaced, and that transitions between any two neighbouring levels involve equal energy changes. However, real molecules do not strictly follow the laws of simple harmonic motion since real covalent bonds, although elastic, are not so homogeneous as to obey Hooke's Law. If the bond is extended beyond a reasonable limit, for instance, then it will break resulting in the dissociation of the molecule into its constituent atoms. The energy profile of molecules undergoing anharmonic compressions and extensions as a function of internuclear separation is known as the Morse function (Fig. 3.17), and it is fitted by the empirical formula:

$$E = E_d \left[1 - e^{k(r_{eq}-r)} \right]^2 \quad (\text{Eq. 3.17})$$

where k is a constant specific to a molecule.

Starting from this energy relation and solving the Schrödinger Equation, the allowed vibrational energy levels for a quantum anharmonic oscillator are given to be:

$$\xi = \omega_a \left[1 - x_a \left(v_q + \frac{1}{2} \right) \right] \left(v_q + \frac{1}{2} \right) \quad (\text{Eq. 3.18})$$

where ω_a is the frequency of an anharmonic oscillator expressed in cm^{-1} , and x_a is the corresponding anharmonicity constant which, for bond stretching vibrations, is a small and positive value.

The selection rule for the anharmonic oscillator is:

$$\Delta v_q = \pm 1, \pm 2, \pm 3, \dots \quad (\text{Eq. 3.19})$$

This selection rule is similar to that of the harmonic oscillator, but with the possibility of larger excitations involving transitions across multiple levels. However, theory predicts that such transitions are of rapidly diminishing probability (Banwell 1983). Furthermore, Boltzmann distribution calculations have demonstrated that, at room temperature or below, the populations of the $v_q > 1$ states are fairly negligible. As such, the major vibrational transitions of importance are the $v_q = 0 \rightarrow v_q = 1$ (this is known as the fundamental absorption and is the most intense), $v_q = 0 \rightarrow v_q = 2$ (this is the first overtone and has a weak intensity), and $v_q = 0 \rightarrow v_q = 3$ (this is the second overtone and has an almost negligible intensity) transitions.

Thus far, the discussion on the quantised nature of molecular vibrational energy levels has been restricted to diatomic molecules. However, this theory may be easily extended to polyatomic systems: consider, to start with, a molecule containing N atoms whose position may be described *via* the three Cartesian coordinates. The molecule therefore has a total of $3N$ coordinate values, which are more commonly referred to as the degrees of freedom. The translational motion of the molecule as a whole can be described by the movement of its centre of mass which requires three degrees of freedom. Moreover, the molecule may rotate in a manner that may be resolved into components about two (in the case of linear molecules) or three (in the case of non-linear molecules) perpendicular axes. Thus, the molecule is left with $3N - 5$ (if linear) or $3N - 6$ (if non-linear) degrees of freedom which correspond to the

fundamental degrees of vibrational freedom. As long as the molecule is acyclic, $N - 1$ of these degrees of vibrational freedom are bond stretching modes, while the remainder is a bending mode.

Taking H_2O as an example; the molecule is non-linear and composed of three atoms, and there therefore exist $3N - 6 = 3$ vibrational modes, of which two are stretching modes and one is a bending mode (Fig. 3.18). If a rotation of the vibrating H_2O molecule by 180° about its C_2 axis yields an identically vibrating molecule, then the vibrational mode is said to be symmetric. The symmetric stretching mode (ν_1) therefore occurs when both O–H bonds extend and compress in phase with one another. The bending mode (ν_2) is also a symmetric vibration, and results from the increase or decrease of the H–O–H bond angle as a result of the ‘bending’ of the O–H bonds away from or towards each other. The final vibrational mode is the asymmetric stretch (ν_3); so-named because a rotation of the vibrating H_2O molecule by 180° about its C_2 axis yields a molecule vibrating in anti-phase with the vibrational motion of the original.

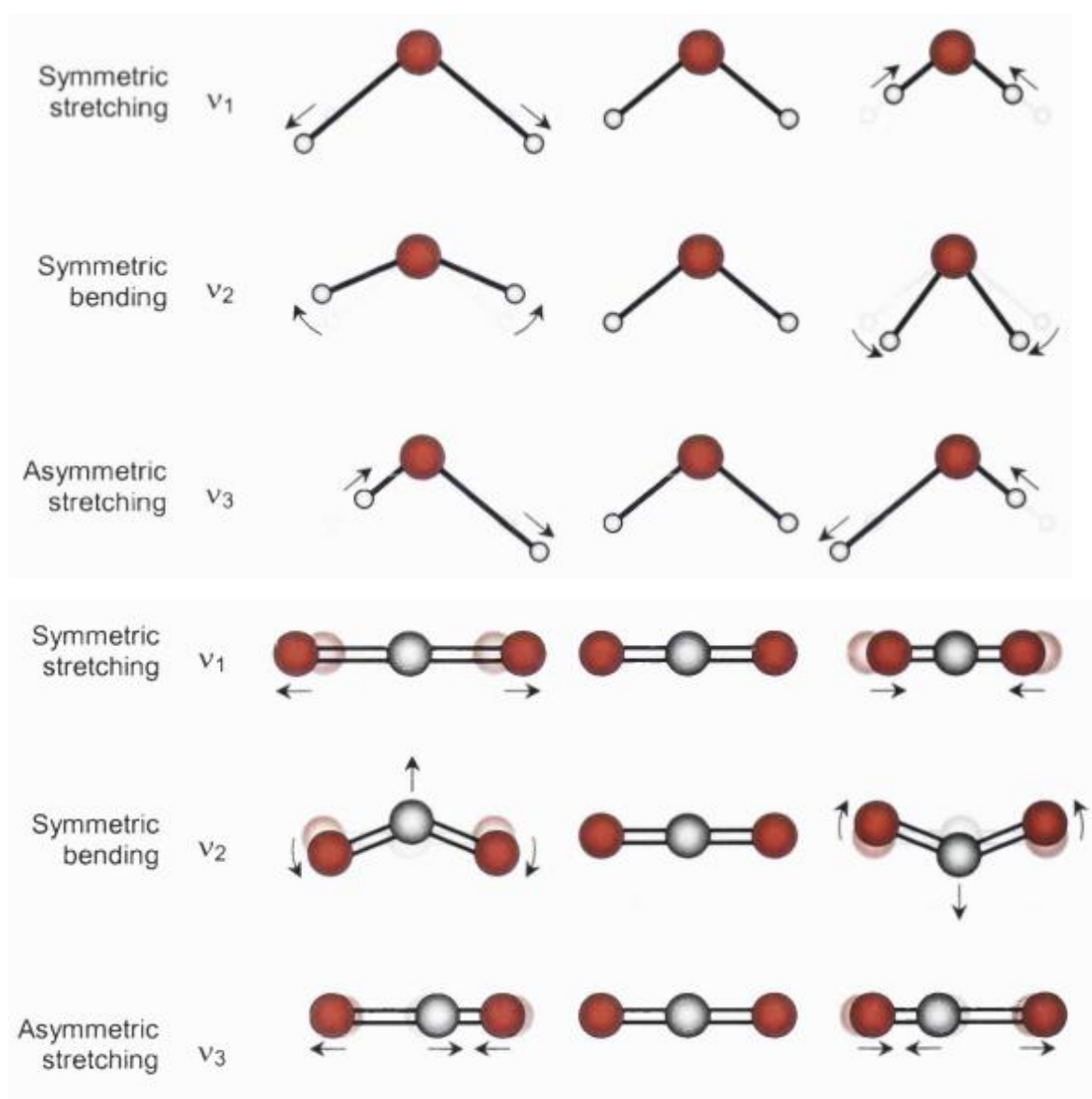


Fig. 3.18: Visual representations of the fundamental vibrational modes of the H_2O (*above*) and CO_2 (*below*) molecules. Image taken from Dawes (2003).

Taking CO_2 as another example; this molecule is also composed of three atoms but is linear and thus possesses $3N - 5 = 4$ vibrational modes. Three of these modes correspond to the symmetric (ν_1) and asymmetric (ν_3) stretching modes and the symmetric bending (ν_2) mode. The fourth mode is an additional bending mode which vibrates in a perpendicular plane to that of the original bending mode (ν_2). Being identical in all respects other than the orientation of the vibrational motion, these two modes are degenerate but must nonetheless be considered as distinct vibrational modes. Indeed, it is always in the degeneracy of a bending mode that the extra vibrational mode of a linear molecule over a non-linear one is to be found. It is important to note at this point that the bending of H_2O cannot occur in a plane perpendicular to the one depicted in Fig. 3.18, as this would constitute a rotation rather than a vibration. As a molecule approaches linearity this rotation degenerates into a vibration and the molecule therefore loses one degree of rotational freedom in exchange for one degree of vibrational freedom.

It may be intuitive to assume that the infrared spectra of molecules are characterised by $3N - 5$ (linear) or $3N - 6$ (non-linear) absorption bands corresponding to the individual fundamental vibrational modes. This, however, is an over-simplification which relies on two assumptions: firstly, that the vibration is simple harmonic, and secondly that each vibrational mode is independent of all others. It has already been discussed that quantised molecular vibration is anharmonic in nature and thus transitions across multiple levels are possible leading to the appearance of overtone bands in infrared absorption spectra whose intensities progressively decline with increasing transition energy. Furthermore, the selection rules now permit the appearance of combination and difference bands in the infrared absorption spectra of molecules. The former bands arise from the addition of two or more fundamental vibrational modes or overtones (e.g., $\nu_1 + \nu_2$ or $2\nu_1 + \nu_2$) whereas the latter bands arise from the subtraction of fundamental or overtone modes (e.g., $\nu_1 + \nu_2 - \nu_3$ or $2\nu_1 - \nu_2$). In either case, however, the intensities of these bands are normally small.

The assumption that each vibrational mode in a molecule is independent of all others breaks down in the case of accidental degeneracy, in which two individual vibrational modes have similar energies. One example of this exists in the CO_2 absorption spectrum, where the ν_1 and $2\nu_2$ mode modes are located at 1330 cm^{-1} and 1334 cm^{-1} , respectively²⁸. In cases where fundamental and overtone bands are accidentally degenerate, they are often observed to be of similar intensities. This is unexpected, as it is well-known that overtone bands are less intense than fundamental ones. However, being of similar energies, these vibrational modes may undergo resonance in which the band due to the overtone vibration gains intensity at the expense of that due to the fundamental vibrational mode. This phenomenon is referred to as Fermi resonance, and is more likely to occur in the infrared absorption spectra of complex molecules possessing many fundamental vibrational modes.

3.3.3 Infrared Spectroscopic Techniques and Instrumentation

To conclude this sub-section on infrared spectroscopy, the operation and design of a typical infrared spectrophotometer will be discussed. Overall, there are four main instrumental components that should be described:

²⁸ Neither of these bands is visible in the infrared spectrum of CO_2 , as the vibrations to which they correspond do not result in a change in the dipole moment of the molecule. They are, however, visible in Raman spectra of CO_2 .

(i) The Source

The source of infrared radiation is usually some form of filament maintained at red- or white-heat by an electric current.

(ii) The Optical Path and Monochromator

The infrared spectroscopic beam is guided by mirrors silvered on their surfaces, and is focused to the point where the sample is to be placed. It is important to note that glass mirrors or lenses cannot be used for guiding or focusing purposes, as glass absorbs over infrared wavelengths. For this reason, rotatable monochromator prisms used to produce specific frequencies of infrared light are constructed out of infrared transparent materials (e.g., ZnSe, NaCl, KBr, CsI). These prisms have been gradually superseded by rotatable gratings as these offer much better resolution.

(iii) The Detector

There are two main types of detector that are widely in use: thermal detectors and photoconductors. The first of these types is sensitive to the heating effect caused by incident infrared radiation, and can thus relate the increased temperature of the detector to the increased transmittance (or, conversely, the decreased absorbance) of the sample at a particular wavelength. Thermocouples and bolometers fall into this class of detector. Photoconductors are a specific type of semiconductor which, when irradiated with electromagnetic radiation, promote electrons to a conduction band thus increasing their electrical conductivity. Therefore, the increased transmittance of a sample can be related to increased conductivity. Photoconductive materials specific to infrared light include PbS, InSb, and $\text{Hg}_x\text{Cd}_{(1-x)}\text{Te}$.

(iv) The Sample

The sample to be analysed is typically held in a container or on a substrate made of a material which is transparent to infrared light. Pure liquids are typically pressed between two plates made of NaCl or KBr, while solutions are held in cuvettes. Gas samples are held in long glass cells (ranging in length from a few cm to >1 m) closed at their ends with infrared transparent windows. Samples that are solid under ambient temperature and pressure conditions may be analysed as a Nujol mull or in a KBr disc. This thesis will explore the infrared absorption spectroscopy of solids, but will use another technique involving the deposition of a solid onto an infrared transparent substrate at cryogenic temperatures. This technique will be explained more fully in the next chapter.

Although infrared absorption spectroscopy may be carried out in a variety of ways (e.g., transmission, specular or diffuse reflectance, attenuated total reflectance, photoacoustic), the operation of most modern spectrophotometers is underpinned by the interferometric principles of the Fourier-transform. The most commonly used interferometer in Fourier-transform infrared (FTIR) spectroscopy is the Michelson interferometer (Fig. 3.19), which consists of two perpendicular mirrors, one of which is held stationary while the other is able to oscillate in the plane perpendicular to the stationary mirror. A semi-reflecting structure known as a beam-splitter bisects the planes of these two mirrors. If a collimated beam of monochromatic infrared radiation is passed through an ideal beam-splitter, then 50% of the radiation is reflected to one of the mirrors while the remaining 50% is transmitted to the other mirror. The two beams are then reflected from these mirrors, returning to the beam-splitter where they recombine. The oscillating mirror introduces an optical pathlength

difference between the two beams, meaning that they are able to interfere constructively or destructively. The beam which then emerges from the interferometer perpendicular to the input beam is then read by the detector.

The detector therefore records radiation that is alternating in power intensity, I . This power intensity, which is a function of pathlength b , is related to the spectral power density B at a particular wavenumber ξ through the equation:

$$I(b) = \int_0^{+\infty} B(\xi) \cos(2\pi b\xi) d\xi \quad (\text{Eq. 3.20})$$

which is one-half of the so-called Fourier-transform equation pair, the other being:

$$B(\xi) = \int_{-\infty}^{+\infty} I(b) \cos(2\pi b\xi) db \quad (\text{Eq. 3.21})$$

These two equations are interconvertible *via* the application of a Fourier-transform. The detector is able to record the variation in the power intensity of the incident radiation as a function of the difference in pathlength, which produces an interference pattern. The typical experiment to obtain a FTIR absorption spectrum is thus to produce interferograms of the detected beam with and without a sample in its the pathway, and subsequently perform Fourier-transforms to obtain the spectra of the source with and without sample absorptions, respectively. The ratio of these spectra corresponds to a double-beam dispersive spectrum. The major advantage of FTIR absorption spectroscopy is the speed of the computational algorithm used to perform the Fourier-transform, which allows multiple scans of an absorbing sample to be acquired thus greatly improving the signal-to-noise ratio.

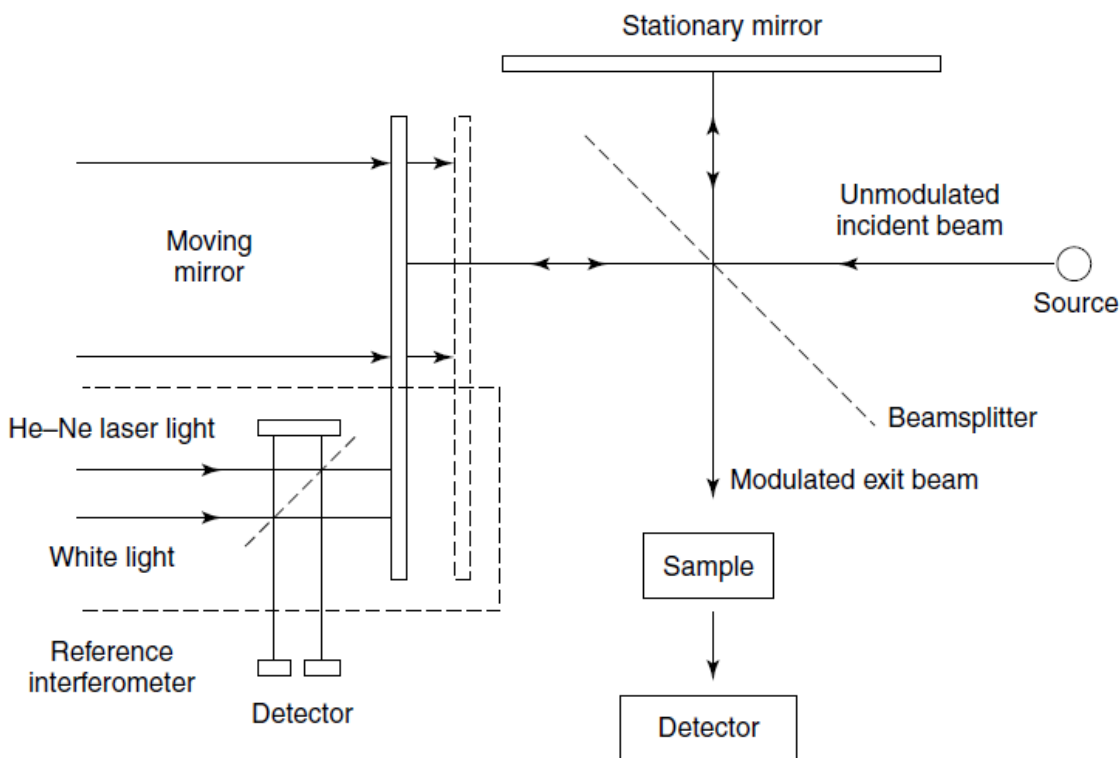


Fig. 3.19: Schematic diagram of a Michelson interferometer. Image taken from Stuart (2004).

3.4 Radiation Chemistry

The interaction between radiation, which may be considered to be either electromagnetic waves or charged particles, with solid matter and the physical, physico-chemical, and chemical effects it engenders is at the heart of this thesis. Indeed, the importance of radiation chemistry in astrochemical reactions has already been extensively discussed in the previous chapter. This sub-section is therefore devoted to providing a description of the mechanisms that transfer energy from charged particles to molecular matter, as well as the resultant chemical evolution of the latter.

3.4.1 Mechanisms of Energy Transfer

In general, energy is transferred from projectile charged particles to target molecules *via* electrostatic interactions with the electrons of the latter, although exceptions are found at low or very high velocities (Mozumder 1999). The absorption of this energy by a target molecule results in its excitation to a higher electronic quantum state; however, if the energy transfer is sufficiently large as to exceed the ionisation potential of the molecule, then ionisation to yield a mono-positively charged molecular radical cation occurs in competition with neutral dissociation. When large energy transfers occur, the emitted (i.e., secondary) electrons acquire significant kinetic energies, thus themselves becoming projectile charged particles and transferring energy to nearby molecules in a similar fashion to that of the primary irradiating particle. Therefore, higher generations of electrons are successively produced as long as the supply of energy lasts. From the perspective of the irradiated molecular target, however, the process is very rapid and the molecules experience a cascade of electrons of a given spectral character (Mason *et al.* 2014, Boyer *et al.* 2016).

The loss of energy from a projectile charged particle as it traverses a target molecular medium is usually quantified by the stopping power P_s of the medium toward a penetrating charged particle. The stopping power is defined simply as the energy loss suffered by the particle per unit pathlength. The most commonly cited theories of stopping power are those that concern heavy charged particles that are fast but not ultra-relativistic (Mozumder 1999). Under such conditions, the interaction of the irradiating particle and the target medium is purely electrostatic, and energy loss occurs through inelastic collisions with the electrons on the target molecules. For this reason, the stopping power in this scenario is commonly referred to as electronic stopping power.

The simplest mathematical treatment of electronic stopping power to consider is Bohr's Theory, which takes a classical view of inelastic collisions. A quantum mechanical treatment of electronic stopping power is given by Bethe's Theory (Mozumder 1999); however, for the purposes of this thesis a brief discussion of Bohr's Theory will suffice. The collision between an irradiating charged particle and a target molecule may be described in terms of the classical impact parameter, which is defined as the distance of closest approach between the incident particle and a molecule-bound electron where there is zero interaction. The electronic stopping power at this point is thus given as:

$$P_s = \frac{4\pi Z^2 q^4 n}{m_e v^2} B_0$$

(Eq. 3.22)

where q is the fundamental or Coulombic electric charge (1.602×10^{-19} C), m_e is the mass of an electron at rest (9.11×10^{-31} kg), Z and v are respectively the atomic number and velocity of the charged projectile, n is the molecular density of the target medium, and B_0 is the stopping number given as:

$$B_0 = Z \ln \left(\frac{2m_e v^2}{V_{av}} \right) \quad (\text{Eq. 3.23})$$

where V_{av} is the average excitation potential of a molecule in the target.

Bohr's Theory therefore provides a reasonably straightforward method of estimating the electronic stopping power of a fast, heavy projectile charged particle. However, the contribution of electronic stopping to the retardation and energetic degradation of a projectile decreases at lower velocities. Consider a positively charged ion approaching a molecular target. As the ion nears its target within a few tens of Å, it begins to abstract electrons from the neutral molecular target in a process termed resonant neutralisation (Arnaud *et al.* 1997, Winter and Aumayr 1999). The initially captured electron is usually lost fairly quickly, but is replaced by another abstracted electron. Cycles of capture and loss proceed until it is energetically unfavourable to lose electrons, thus eventually neutralising the charged projectile ion to a hollow atom in which inner electron orbitals are unoccupied. Decay of the transient hollow atoms occurs *via* radiative electron cascade or Auger electron emission, although time constraints mean that it is often the case where only a few electrons are able to de-excite to the inner shells before impact with the molecular target occurs (Hermann *et al.* 1994).

The cross-sections for these electron abstraction and loss processes are dependent upon a high inverse power of the velocity of the projectile, and are thus negligible at high velocities. However, at lower velocities, their contribution to the stopping power is significantly greater. Thus, at lower velocities, it is the so-called nuclear stopping power, in which the projectile charged particle loses energy through elastic interactions with the nuclei of the target medium, that is the dominant degradation mechanism. The total stopping power of an irradiation process is usually simply defined as the sum of its electronic (inelastic) and nuclear (elastic) stopping power contributions. It should be noted, however, that electronic and nuclear stopping are not the only two mechanisms by which a charged projectile may lose energy. For instance, a charged particle that is decelerated as a result of its deflection by another charged particle will emit electromagnetic radiation. This process, termed bremsstrahlung, is usually significant only when the charged particle is travelling at very high velocities (including ultra-relativistic ones), corresponding to energies of about 1 GeV and 100 MeV for ions and electrons, respectively (Mozumder 1999). Another mechanism of energy loss is the Cerenkov Effect²⁹, although this practically never dominates over other mechanisms.

The rate of energy loss (i.e., the stopping power) of the projectile charged particle naturally defines its range within the target medium. However, it would be incorrect to assume that the stopping power is constant across the entire track the projectile takes through the target medium. Indeed, plots of stopping power against pathlength demonstrate that the maximum loss of energy from a heavy projectile occurs just before it comes to rest within

²⁹ The Cerenkov Effect is the emission of a blue-white light by an electron that exceeds the group velocity of light in a transparent medium.

the target medium. This is logical and follows from the inverse square relation between stopping power and velocity, such as that described by Eq. 3.22. An example of such a plot, which is more commonly referred to as a Bragg curve, is given in Fig. 3.20 and clearly depicts the maximum stopping power (the so-called Bragg peak) just before the projectile comes to rest.

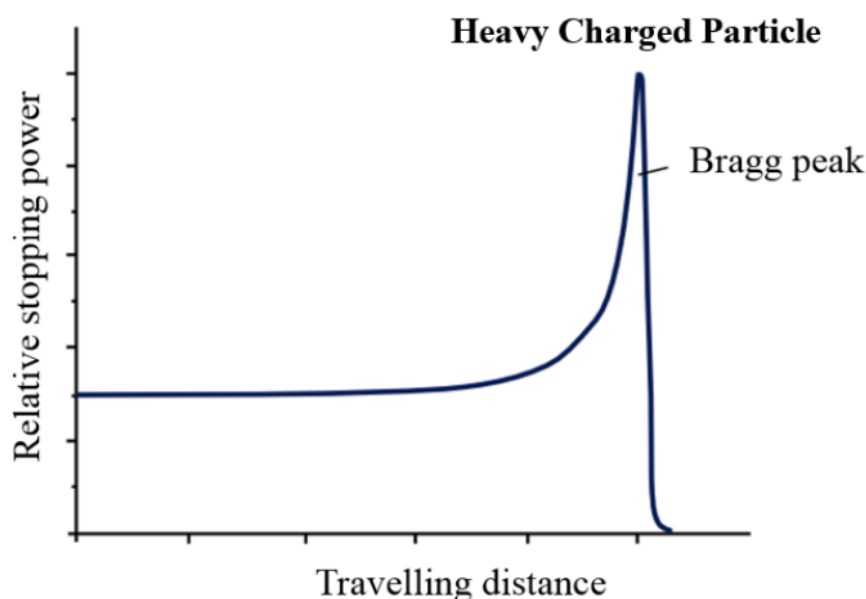


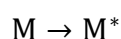
Fig. 3.20: Generic Bragg curve for a heavy projectile charged ion penetrating a target medium. Image taken from Grdanovska (2015).

3.4.2 Summary of Processes in Radiation Chemistry

Reference has already been made to several of the processes which characterise radiation chemistry³⁰ in the previous chapter (Table 2.2). It is, however, worthwhile to delve into these processes in more detail, as these processes constitute important mechanistic steps in the reaction schemes of irradiated solid ices and are thus highly relevant to this thesis. There are seven main processes that should be considered, a brief description of each of which now follows:

(i) Excitation, Ionisation, and Dissociation

A molecule may gain energy from a projectile charged particle thus resulting in its excitation to higher electronic quantum states.



(Eq. 3.24)

If the absorbed energy is greater than the ionisation potential of the molecule, then an electron is lost to yield a mono-positively charged cation. This cation may be

³⁰ It is important to remember that radiation chemistry need not necessarily be triggered by the collision of an energetic charged particle with a target medium. Various high-energy components of the electromagnetic spectrum, such as γ -rays, x-rays, and vacuum-ultraviolet photons are also able to trigger radiation chemistry but are more limited due to their penetration depth being defined by the optical properties of the target medium as well as the application of the relevant photon absorption selection rules.

neutralised by combining with an incident electron. The resultant neutral species is typically in a highly excited state that rapidly decays to a lower state of excitation.



If the absorbed energy exceeds the bond dissociation energy of any of the covalent bonds in the molecular structure, then homolytic dissociation of that bond will take place to yield two neutral radicals. If the molecule existed in an excited state prior to its dissociation, then one of the resultant fragments may remain in an excited state.

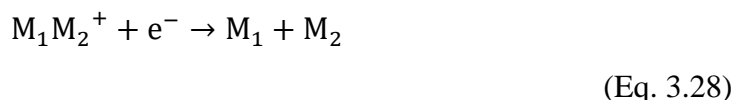


(ii) Ion-Neutral and Neutral-Neutral Reactions

The ionised and neutral species resulting from the ionisation and dissociation of molecules absorbing radiation may themselves partake in a wide variety of chemical reactions, producing second generation molecules which may themselves be charged or electrostatically neutral.

(iii) Ion Recombination

Ions may be neutralised by their combination with an electron or their interaction with a species of the opposite electrostatic charge (Eq. 3.26). An interesting special case of ion recombination is that of dissociative recombination, in which the combination of an electron with a mono-positively charged molecular cation results in the dissociation of the latter to yield two neutral species.



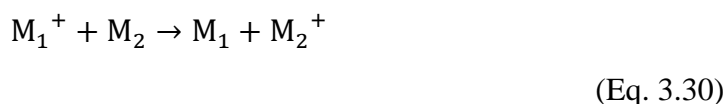
(iv) Non-Radiative Energy Transfer

The electronic energy of an excited molecule may be transferred to another, as long as the energy required to excite the second molecule (i.e., that which is initially in the ground state) is less than or equal to that of the first.



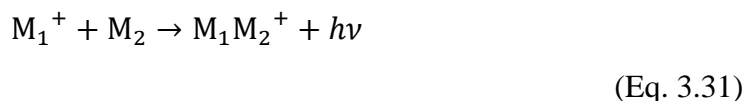
(v) Charge Transfer

Charge transfer may occur when a mono-positively charged molecular cation abstracts an electron from a nearby neutral molecule, as long as the ionisation potential of the second molecule (i.e., that which is initially neutral) is less than or equal to that of the first in its neutral state.



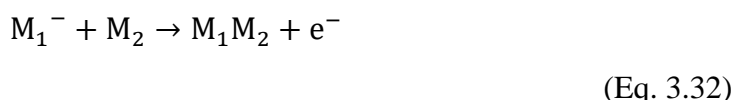
(vi) Radiative Association

Radiative association occurs when a neutral species combines with an ion, thereby yielding a larger ion and emitting electromagnetic radiation in the process.

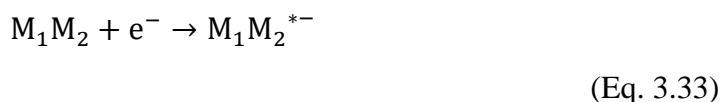


(vii) Detachment

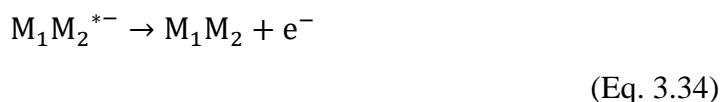
Detachment processes involve negatively charged anions that are usually in an electronically excited state. For instance, associative detachment involves the combination of a mono-negatively charged molecular anion with a neutral species, emitting an electron in the process.



The capture of an electron by a neutral molecule results in the production of an excited and transient mono-negatively charged molecular anion.



This electronically excited molecular anion may subsequently undergo one of three processes. In the first instance, it may eject the electron and return to the ground state. This is termed electron auto-detachment.



Alternatively, the excited molecular anion may simply decay to the ground state. This is an especially favourable process if the anion is a chemically stable species.



Finally, dissociative electron attachment may cause the molecular anion to fragment:



The processes described above all take place on very rapid time-scales, although the extent of their rapidity does vary somewhat. The time period between the absorption of incident radiation and the ultimate chemical effect is often segregated into five stages. In ascending order of time-scale these are: (i) the physical stage, (ii) the physico-chemical stage, (iii) the chemical stage, (iv) the biochemical stage, and (v) the biological stage. Table 3.2 summarises the major events occurring in each of these stages, although it is important to note that only the first three stages are of importance in the context of this thesis.

Table 3.2: Time-scale of events in radiation chemistry. Table adapted from Mozumder (1999). The physical, physico-chemical, chemical, biochemical, and biological stages are defined as ranging over $-\log(t)$ values of 18 to 12, 16 to 8, 14 to -3 , 3 to -4 , and -2 to -8 , respectively. Note that time t is measured in seconds.

$-\log(t)$	Event
18	Projectile electrons traverse molecules.
17	Projectile protons traverse molecules and energy loss to fast secondary electrons.
16	Energy loss to electronic states.
14	Fast ion-molecule reactions and induced molecular vibration.
13	Fast molecular dissociations.
12	Electron thermalisation.
8	Secondary reactions (e.g., intertrack reactions) and charge neutralisation in low viscosity media.
0	Radiative lifetime of triplet states.
-3	Charge neutralisation in high viscosity media.
-4	Formation, evolution, and reaction of secondary radical species.
-8	Large-scale cell damage and long-term biological effects.

3.5 Summary

This chapter provides an overview of the fundamental chemistry and physics that is required to discuss the work performed in this thesis and in the interpretation of experimental results presented. Detailed descriptions of atomic theory, including the quantised nature of atomic orbitals, were followed by a discussion on the theories of the chemical bond, particularly Valence Bond Theory and Molecular Orbital Theory. An introduction to molecular geometry and symmetry was also provided, and provided a basis for a detailed discussion on infrared absorption spectroscopy, which will serve as the major analytical tool for the experimental work described in later chapters. The discussion on infrared spectroscopy included the quantised nature of vibrational excitations in molecules, as well as the treatment of molecular vibration as both a harmonic and an anharmonic oscillator. The chapter concludes with a brief introduction to the radiation chemistry mediated by projectile charged particles, including a mathematical discussion on Bohr's Theory of Stopping Power.

4 EXPERIMENTAL APPARATUS AND TECHNIQUES

This chapter provides an overview of the experimental apparatus and techniques used in conducting the experiments described throughout this thesis. In particular, it provides a detailed description of the Ice Chamber for Astrophysics-Astrochemistry; a custom-built apparatus located at the Institute for Nuclear Research (Atomki) in Debrecen, Hungary. This description begins with a discussion of the layout of the chamber as well as the physical conditions (such as pressure and substrate temperature) within it, before continuing on to a discussion of the ice preparation and processing methodologies used. The chapter concludes with brief discussions on the limitations of the current set-up and some relevant software packages used for data collection and analysis.

Note: The majority of the work described in this chapter has been published in peer-reviewed journals or periodicals as: [1] Herczku *et al.* (2021), *Rev. Sci. Instrum.* **92**, 084501; and [2] Mifsud *et al.* (2021), *Eur. Phys. J. D: Atom. Mol. Opt. Plasma Phys.* **75**, 182.

4.1 Laboratory Astrochemistry Chambers

The study of the composition, structure, and chemistry of astrophysical ices in the laboratory relies on the use of high-vacuum or ultrahigh-vacuum chambers that contain one or more substrates or surfaces that may be cooled to cryogenic temperatures. The essential concept is to prepare an ice on these cooled substrates *via* the condensation of gases or vapours that are dosed into the chamber and to subsequently process the ice in a manner meaningful to astrochemistry as was described in Chapter 2 (Fig. 2.8). The structural and chemical changes in the ice that are induced by this processing may be qualitatively or quantitatively followed *in situ* using various spectrophotometric, spectrometric, or microscopic techniques, with the most commonly used being infrared, terahertz, vacuum-ultraviolet, and ultraviolet-visible absorption spectroscopies, quadrupole mass spectrometry, and transmission electron microscopy. *Ex situ* analysis of any refractory residues left over after the completion of the experiment and the exposure of the substrate to ambient conditions *via* chromatographic and other spectrometric methods is also becoming increasingly popular.

Perhaps the first such astrochemistry chamber that was specifically designed to study the energetic processing of interstellar ice analogues was that developed at the Leiden Observatory in the Netherlands by Hagen, Allamandola, and Greenberg in the 1970s (Hagen *et al.* 1979). This apparatus consisted of a high-vacuum chamber within which astrophysical ice analogues could be prepared on a substrate cooled to 10 K. Simulation of the Lyman- α irradiation of ices occurring within dense interstellar clouds was achieved using ultraviolet lamps, and structural and chemical changes were monitored using infrared absorption spectroscopy. Since this time, many other dedicated astrochemistry chambers have been commissioned in laboratories all over the world, each offering a somewhat unique method of preparing, processing, or monitoring astrophysical ice analogues. A catalogue of some of these facilities is provided in Table 4.1, although this is far from complete.

Table 4.1: List of facilities and set-ups actively performing laboratory studies of astrophysical ice analogues.

Facility Name	Location	Reference
Ice Chamber for Astrophysics-Astrochemistry (ICA)	Debrecen, Hungary	This thesis
Versatile Ice Zigzag Sublimation Set-Up for Laboratory Astrochemistry (VIZSLA)	Budapest, Hungary	Bazsó <i>et al.</i> (2021)
Portable Astrochemistry Chamber (PAC)	Milton Keynes, United Kingdom	James <i>et al.</i> (2020)
University of Sussex Surface Science Laboratory	Brighton, United Kingdom	Salter <i>et al.</i> (2021)
ICE-RIG Set-Up	Edinburgh, United Kingdom	Frankland <i>et al.</i> (2015)
Laboratorio di Astrofisica Sperimentale	Catania, Italy	Baratta <i>et al.</i> (2015)
Friedrich Schiller University of Jena Astrophysics Laboratory	Jena, Germany	Fulvio <i>et al.</i> (2017)
ASTRID-2 Synchrotron Facility	Aarhus, Denmark	Hertel and Hoffmann (2011)
Surface Reaction Simulation Device (SURFRESIDE ²)	Leiden, Netherlands	Ioppolo <i>et al.</i> (2013)
CRYOPAD Set-Up	Leiden, Netherlands	Fuchs <i>et al.</i> (2006)
Laboratory Ice Surface Astrophysics Experiment (LISA)	Nijmegen, Netherlands	Noble <i>et al.</i> (2020)
Planetary Analogues Laboratory for Light, Atmosphere, and Surface Simulations (PALLAS)	Utrecht, Netherlands	ten Kate and Reuver (2016)
Chambre d'Analyse par Spectroscopie Infrarouge des Molécules Irradiées (CASIMIR)	Caen, France	Seperuelo Duarte <i>et al.</i> (2009); Augé <i>et al.</i> (2016)
Irradiation des Glaces Interstellaires et Astrophysiques (IGLIAS)	Caen, France	Augé <i>et al.</i> (2018)
Vers de Nouvelles Synthèses (VENUS)	Paris, France	Congiu <i>et al.</i> (2020)
Volatile Analysis from the Heating of Interstellar or Cometary Ice Analogues (VAHIIA)	Marseille, France	Abou Mrad <i>et al.</i> (2014)
Spectrophotometer with Variable Incidence and Emergence (SHINE)	Grenoble, France	Brissaud <i>et al.</i> (2004)
Spectrophotometer with Change Angles for the Detection of Weak Signals (SHADOWS)	Grenoble, France	Potin <i>et al.</i> (2018)
Interstellar Astrochemistry Chamber (ISAC)	Madrid, Spain	Muñoz Caro <i>et al.</i> (2010)
INFRA-ICE Machine	Madrid, Spain	Santoro <i>et al.</i> (2020)
Cryogenic High-Vacuum Chamber at the Instituto de Estructura de la Materia	Madrid, Spain	Zanchet <i>et al.</i> (2013)
Laboratory for Characterisations of Astrophysical Ices at Alcoy	Alicante, Spain	Satorre <i>et al.</i> (2008, 2013)
Keck Machine	Honolulu, United States	Jones and Kaiser (2013)
SPACE-CAT ² Facility	Cambridge, United States	Lauck <i>et al.</i> (2015)
Sublimation of Laboratory Ices Millimetre/Submillimetre Experiment (SubLIME)	Greenbelt, United States	Yocum <i>et al.</i> (2019)
Goddard Astrochemistry Laboratory	Greenbelt, United States	Moore and Hudson (2000)
STARK Chamber	Campinas, Brazil	Pilling and Bergantini (2015)
National Synchrotron Radiation Research Centre	Hsinchu, Taiwan	Lu <i>et al.</i> (2005, 2008, 2013); Kuo <i>et al.</i> (2007)
Laboratory Set-Up for Surface Reactions in Interstellar Environments (LASSIE)	Sapporo, Japan	Hidaka <i>et al.</i> (2004)

Among these facilities is the Ice Chamber for Astrochemistry-Astrophysics (ICA; pronounced *it-sah* in the Hungarian style); a permanent end-station located at the Institute for Nuclear Research (Atomki) in Debrecen, Hungary. The ICA is among the youngest of those facilities listed in Table 4.1, having only been fully commissioned in the autumn of 2019. The construction, development, and continued operation of the ICA is the result of a successful collaboration between academic and research staff from Atomki, the University of Kent, Queen Mary University of London, Queen’s University Belfast, and the Slovak Academy of Sciences; with additional support received from the University of Miskolc. This thesis is therefore the first (likely, of many) to describe experimental work which made use of the ICA to better understand problems in astrophysical chemistry.

4.2 The Ice Chamber for Astrophysics-Astrochemistry (ICA)

The ICA set-up (Fig. 4.1) is comprised of a spherical decagon ultrahigh-vacuum compatible chamber (Kimball Physics) having an inner diameter of 160 mm. The chamber possesses ten DN-40 CF ports on its side wall evenly separated from one another by an angle of 36° . Two additional DN-160 CF ports are located at the top and bottom of the chamber. The chamber may be pumped down to an operational pressure of a few 10^{-9} mbar *via* the combined use of a dry rough vacuum pump (Edwards nXDS10i) and a turbomolecular pump (Leybold Turbovac TMP 151), both of which are connected through the lower DN-160 CF port. This pressure is measured by an ionisation gauge (Pfeiffer Vacuum PBR260) attached directly to the side of the chamber at one of the DN-40 CF ports.

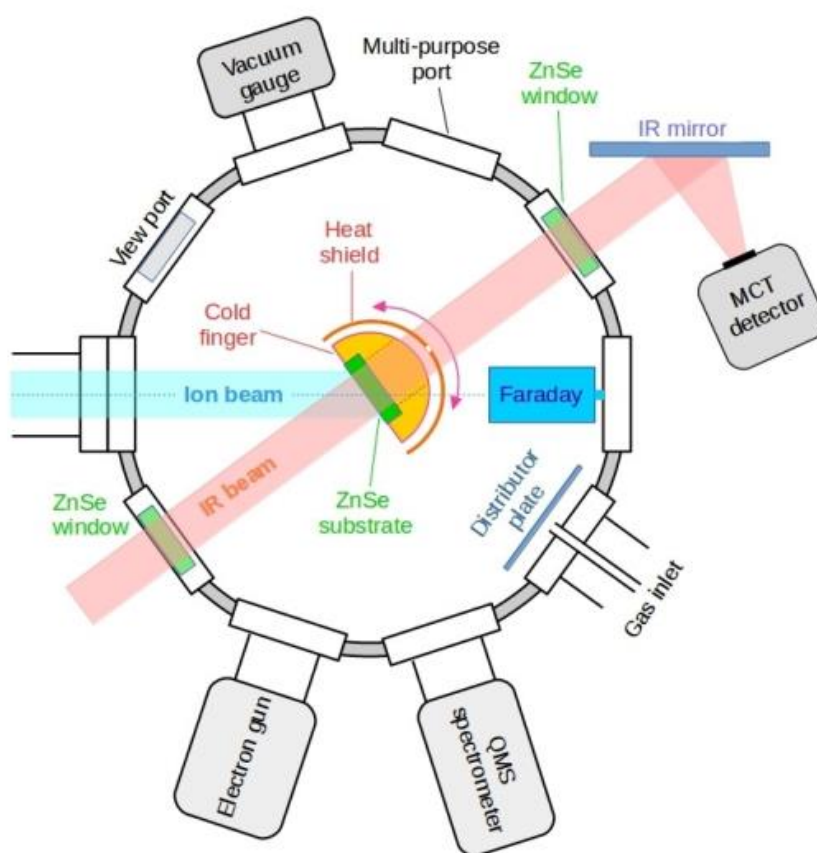


Fig. 4.1: A top-view schematic diagram of the ICA arranged for Fourier-transform mid-infrared transmission absorption spectroscopy. Although the sample holder and heat shield are rotatable, irradiation and thermal annealing experiments are nominally performed as depicted, with the infrared beam pathway orthogonal to the substrate surfaces and ion and electron beams impacting at angles of 36° .

At the centre of the chamber is a gold-coated oxygen-free high-conductivity copper sample holder which allows a maximum of four substrate discs to be mounted onto it (Fig. 4.2). The sample holder and substrates may be rotated to face any of the DN-40 CF ports by means of a 360° rotation stage, and can also be manipulated along the vertical axis of the chamber using a z -linear manipulator with a 50.8 mm stroke. Moreover, the sample holder and the substrate discs may be cooled to a minimum temperature of 20 K using a closed-cycle helium cryostat (Leybold Coolpower 7/25 with a Leybold Coolpak 4000 compressor unit), which is connected to the chamber *via* the upper DN-160 CF port. In order to reach such a low temperature, the sample holder is partially surrounded by a gold-coated oxygen-free copper heat shield (Fig. 4.2). The inclusion of this heat shield in the set-up design is required due to the small diameter of the chamber: at cryogenic temperatures, the walls of the chamber act as black bodies and thus radiate heat to the sample holder in accordance with the Štefan-Boltzmann Law:

$$j = \sigma_{\text{SB}} T^4 \quad (\text{Eq. 4.1})$$

where j is the black body radiant emittance corresponding to the total energy radiated per unit surface area of the black body across all wavelengths per unit time, T is temperature, and σ_{SB} is the Štefan-Boltzmann constant ($5.67 \times 10^{-8} \text{ W m}^{-2} \text{ K}^{-4}$). The heat shield thus acts to absorb this radiated heat, allowing the sample holder and substrates to be cooled to 20 K.

The substrates mounted into the sample holder are ZnSe discs (Crystran) having a diameter of 15 mm and a thickness of 3 mm (Fig. 4.3). The choice of ZnSe as a substrate material is a convenient one, as not only is it transparent to most infrared wavelengths (more details on the spectroscopic component of the ICA are provided later on in this chapter), but it also exhibits remarkable thermal conductivity properties: at 20 K, the thermal conductivity of ZnSe is in excess of $6 \text{ W K}^{-1} \text{ cm}^{-1}$ (Bijalwan *et al.* 1983). To compare, this thermal conductivity is greater than that of room temperature copper, which is about $4 \text{ W K}^{-1} \text{ cm}^{-1}$. As such, it is reasonable to assume that the cooling of the sample holder also results in the efficient cooling of the ZnSe substrate discs.



Fig. 4.2: Photographs of the sample holder with its heat shield as seen from the front (*left*) and rear (*right*) sides. In these photographs, three ZnSe substrates are mounted onto the sample holder with the fourth position being used as a 9.6 mm diameter collimator. This collimator, along with a Faraday cup positioned opposite to an incident charged particle beam, allows for the determination of beam homogeneity.

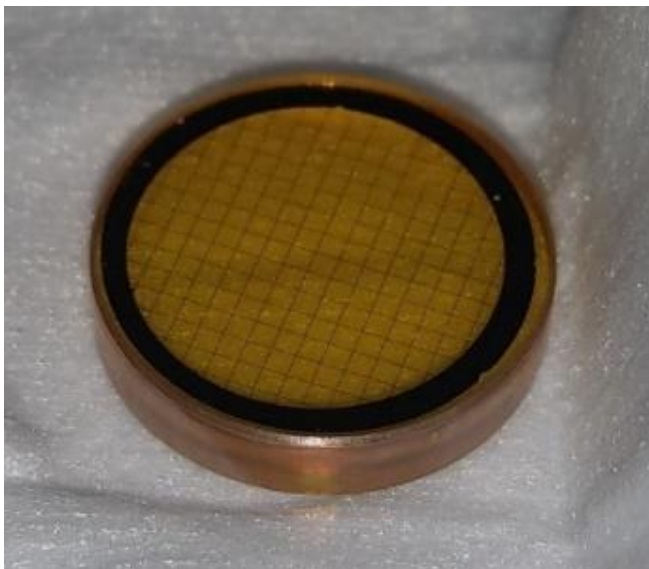


Fig. 4.3: A close-up photograph of a ZnSe substrate of the type mounted onto the sample holder (diameter = 15 mm and thickness = 3 mm).

It is important to consider the possibility of the deposition substrate charging up or emitting sparks when high ion or electron beam currents (>100 nA) are used during the irradiation of deposited astrophysical ice analogues (a fuller discussion of which will be provided later in the chapter). To avoid this, the ZnSe substrate discs are covered by a metallic mesh (Fig. 4.3) composed of a thin (5 nm) layer of chromium evaporated onto the surface of the substrate, on top of which is a thicker (250 nm) layer of gold. The width of the mesh lines is $20\ \mu\text{m}$ and their separation from one another is 0.8 mm. The presence of the gold mesh has been empirically shown to have a negligible contribution to the infrared transmittance properties of the ZnSe substrate discs.

The temperature across the sample holder is measured using two uncalibrated silicon diodes (Lake Shore DT-670B-CO) positioned at opposite ends of the sample holder and connected to a cryogenic temperature controller (Lake Shore model 335), with accurate temperature measurements being made with a proportional-integral-differential controller. The actual measured temperatures of the ZnSe substrates were validated by performing controlled warmings of pure CO and N₂O ices and comparing the temperatures at which phase changes and sublimation were spectroscopically observed with well-established literature values (Acharyya *et al.* 2007, Hudson *et al.* 2017). The experimentally measured temperatures were found to match those in the literature within 1 K. The temperature of the sample holder and the substrates can be regulated by setting an equilibrium between heating and cooling using an internal $25\ \Omega / 100\ \text{W}$ cartridge heater (HTR-25-100). Such an arrangement allows for an operational temperature range of 20-300 K and controlled heating rates of $0.1\text{-}10\ \text{K min}^{-1}$.

The chamber contains a number of attachments to its side wall which will be mentioned and discussed throughout the remainder of this chapter. Of particular novelty, however, is the presence of an optical viewport which allows users to look into the chamber during the deposition, irradiation, or thermal annealing of astrophysical ice analogues (Fig. 3.1). This optical viewport is simply a glass window attached to one of the DN-40 CF ports and allows for quick assessments of the status of the sample holder, of the presence of any visible residues on the substrates, or the occurrence of any sparking due to the accumulation of charge during ion or electron irradiation.

4.2.1 The Deposition of Astrophysical Ice Analogues

Astrophysical ice analogues are prepared on the substrates *via* the background deposition of dosed gases and vapours introduced into the main chamber from a dosing line through a fine regulating all-metal needle valve (LewVac). This dosing line is independently connected to a second dry rough vacuum pump (Pfeiffer ACP-28-40G) that maintains a background pressure of a few 10^{-3} mbar. This pressure is monitored by a mass-independent capacitive manometer gauge (Edwards ASG2). The dosing line has several inflow valves that may be connected to external gas bottles or glass vials containing liquids. Gases are thus directly introduced into the evacuated dosing line, whilst liquids are first de-gassed using the standard liquid nitrogen freeze-pump-thaw technique before their vapours are passed into the dosing line. The introduction of gases and vapours into the dosing line typically raises its internal pressure to a few mbar.

Once the desired pure or mixed gases have equilibrated within the dosing line, they are dosed into the main chamber at a typical chamber pressure of 8×10^{-6} mbar. A distributor (scattering) plate mounted in front of the inlet tube (Fig. 4.1) reduces the pressure inhomogeneity within the chamber during gas injection so as to produce roughly the same ice thickness on all deposition substrates (Table 4.2). It should be noted that, the sample holder presents holes of diameter 12 mm and length 25 mm behind all four mounted deposition substrates in line with a wide slit opening in the heat shield (Fig. 4.2). This ensures that most of the gas dosed into the main chamber is deposited onto the front side of the deposition substrates, and that the amount deposited on the rear side (which would not be processed by ionising radiation) is minimised. This is discussed further below.

Consider, to begin with, the sticking of a generic gas-phase molecule to an equally generic surface. The probability of a successful sticking event is quantified by the so-called sticking coefficient S , which is defined as the ratio of successful sticking events to the total number of collision events between the incident gas-phase molecule and the cold surface. The sticking coefficient is highly dependent upon a number of microscopic parameters such as the geometry of the incident molecule, its energy, orientation, and angle of incidence as well as several macroscopic parameters such as the composition, structure, and temperature of the cold surface and the pressure of the gas. When preparing an ice in the ICA, dosed gas-phase molecules will first stick to the ZnSe substrate; however, once the first few molecular layers of a homogeneous, single-component ice have been deposited, then the material compositions of the depositing gas-phase and cold surface are identical. Under such conditions, the sticking coefficient may be assumed to be large and, indeed, is taken to be unity at 20 K. Of course, this may not necessarily be the case for mixed, multi-component gases, but the similarities between the gas phase and cold surface may be determined experimentally by controlling the stoichiometric ratio of the components of the dosed gas phase and simultaneously measuring the composition of the deposited ice *via* infrared spectroscopy.

In order to model the thickness ratio of the ices deposited on the front and rear sides of a deposition substrate, a sticking coefficient of unity is assumed as a first approach: as such, if a molecule collides with a cold surface, then it successfully sticks to that surface. Moreover, at deposition pressures $< 10^{-4}$ mbar, gas-phase molecules may be assumed to interact only with the surfaces of the chamber and do not collide with one another. Therefore, the only molecules that successfully stick to the substrate are those that make contact with it having not previously collided with any other cold surface. Accordingly, the deposition yield at a point \mathbf{r} on the substrate is proportional to the acceptance solid angle $\Omega(\mathbf{r})$, which is in

turn determined by the geometry of the cold sample holder. The effective deposited thickness is thus proportional to the average solid angle, given by the following equation:

$$\bar{\Omega} = \frac{1}{\alpha} \int_{\alpha} d\vec{r} \Omega(\vec{r}) \quad (\text{Eq. 4.2})$$

where α is the area of the deposition substrate illuminated by the infrared spectroscopic beam.

Given the geometry of the ICA sample holder (Fig. 4.4), the calculation of the average solid angles for the front and rear sides of the deposition substrates is a lengthy but straightforward process. Such calculations show that the average solid angles for these two sides are very different, and so the relative thickness d_{rel} of ice deposited on the rear side of the substrate (assuming $S = 1$) may be given as:

$$d_{\text{rel}} = \frac{d_{\text{rear}}}{d_{\text{rear}} + d_{\text{front}}} = \frac{\bar{\Omega}_{\text{rear}}}{\bar{\Omega}_{\text{rear}} + \bar{\Omega}_{\text{front}}} = 0.039 \quad (\text{Eq. 4.3})$$

Note that this relative thickness may be fairly accurately estimated from the ratio of the central ($\mathbf{r} = 0$) solid angles Ω^0 . For the rear side of the substrate, this is calculated using the average length of the hole within the sample holder, which is 24.7 mm:

$$\Omega_{\text{rear}}^0 = 2\pi(1 - \cos(\beta_{\text{rear}})) = 2\pi\left(1 - \frac{24.7}{\sqrt{24.7^2 + 6^2}}\right) = 0.178 \quad (\text{Eq. 4.4})$$

$$\Omega_{\text{front}}^0 = 2\pi(1 - \cos(\beta_{\text{front}})) = 2\pi\left(1 - \frac{2}{\sqrt{2^2 + 7.5^2}}\right) = 4.664 \quad (\text{Eq. 4.5})$$

$$d_{\text{rel}} = \frac{\Omega_{\text{rear}}^0}{\Omega_{\text{rear}}^0 + \Omega_{\text{front}}^0} = \frac{0.178}{0.178 + 4.664} = 0.037 \quad (\text{Eq. 4.6})$$

where β is the half-angle of the relevant solid angle cone.

These calculations demonstrate that only about 4% of the total ice that is monitored spectroscopically is deposited on the rear side of the substrate and is thus unavailable for ion- or electron-induced radiation chemistry. It should be noted, however, that this value represents a lower bound for d_{rel} , which may be larger if the sticking coefficient is in fact smaller. For instance, a numerical simulation revealed that, if $S = 0.5$ (i.e., only half of collisions result in a successful sticking event) and assuming that non-sticking events result in specular reflection, d_{rel} rises to 9.4%. In any case, however, it is reasonable to state that, in most cases where the sticking coefficient is high (i.e., $S > 0.5$), the thickness of the ice deposited on the rear side of the substrate is <10% of the total deposited thickness. At the highest sticking coefficients (i.e., $S \approx 1$), this thickness is anticipated to be <5%.

Table 4.2: Summary of deposition experiments performed to demonstrate that the thicknesses and compositions of deposited ices are similar across all four deposition substrates. The target thickness for the pure CH₃OH ice was 0.5 μm, while for CH₃OH:CO ices the target thickness was 0.75 μm with a compositional target of 40% CH₃OH. The techniques used to measure these parameters are described later on in this chapter. Note that, although ice thicknesses are slightly lower at substrate 4 compared to the other substrates, this is not problematic as this substrate is generally replaced by a 9.6 mm diameter collimator for charged particle beam homogeneity determination.

ZnSe Substrate	CH ₃ OH Ice Thickness (μm)	CH ₃ OH:CO Ice Thickness (μm)	CH ₃ OH:CO Ice Composition
1	0.47	0.74	36:64
2	0.51	0.77	38:62
3	0.49	0.76	39:61
4	0.41	0.64	41:59

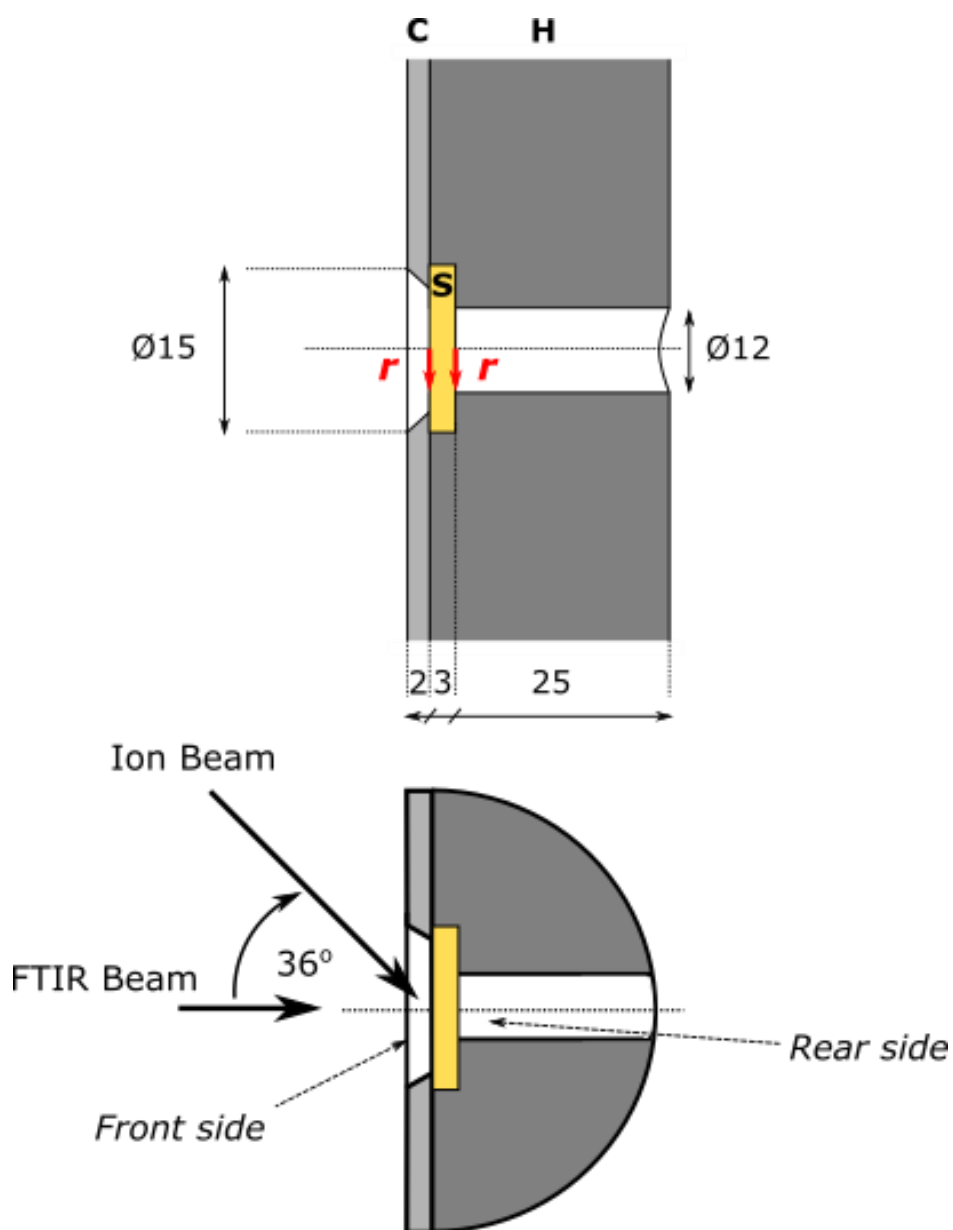


Fig. 4.4: The geometry of the gold-coated oxygen-free copper sample holder H and clamp plate C around one ZnSe deposition substrate S. All parts of the sample holder are assumed to have been cooled to the same temperature. Length values presented in this figure are given in mm.

Background deposition of ices is only suitable if the molecular species to be deposited is a gas or liquid under standard temperature and pressure conditions. If the deposition of a compound that is a refractory solid at standard temperature and pressure conditions is required, then this may be achieved by attaching an effusive evaporator (Createc OLED-40-10-WK-SHM) to the multi-purpose port opposite the electron gun (Fig. 4.1). This evaporator is composed of a tantalum heating wire held in proximity to a glass test-tube. The test-tube may be heated to a temperature between 50 and 800 °C (although optimum temperature control is achieved at <500 °C), and the temperature may be regulated by setting an equilibrium between the heating induced by the tantalum wire and a cooling effect induced by an in-built running-water jacket.

The effusive evaporator is itself mounted onto a linear manipulator such that it may be pushed into or withdrawn from the chamber. This allows for the nozzle to be manually positioned within a few mm of the ZnSe deposition substrate when depositing a refractory sample. As such, all depositions which make use of the effusive evaporator approximate a direct deposition technique. Once the desired sample has been prepared on the ZnSe substrate, a custom-built copper shutter placed in front of the nozzle is closed and the evaporator is withdrawn, thus precluding further deposition of the refractory species which may otherwise still evaporate into the chamber due to the evaporator remaining warm for some time after the deposition process has been completed.

4.2.2 *In Situ* Analysis

As has been mentioned several times throughout this thesis, the primary analytical technique used is that of Fourier-transform mid-infrared (FTIR) transmission absorption spectroscopy. A detailed discussion on the underlying principles of spectroscopy was provided in Chapter 3, where it was stated that the optical depth τ_v of an absorbing sample may be related to its absorbance A_v through the equation:

$$\tau_v = -\ln(T_v) = \frac{-\log(T_v)}{\log(e)} \approx 2.303 A_v \quad (\text{Eq. 4.7})$$

In Chapter 2, the concept of molecular column density was alluded to, and this may be related to the optical depth of an absorbing sample through the relation:

$$N = \frac{1}{A_s} \int \tau_v \, d\xi \quad (\text{Eq. 4.8})$$

where A_s is the integrated band strength constant of the infrared absorption band over which Eq. 4.8 is integrated and ξ refers to wavenumbers. Substituting the value for τ_v given in Eq. 4.7 into Eq. 4.8 yields:

$$N = \frac{2.303}{A_s} \int A_v \, d\xi \quad (\text{Eq. 4.9})$$

However, integrating over an infrared absorption band with respect to wavenumbers is equivalent to measuring the peak area P_a of that band, and thus:

$$N = 2.303 \times \frac{P_a}{A_s} \quad (\text{Eq. 4.10})$$

Thus, the abundance of a deposited ice may be quantified through its column density, which itself may be calculated fairly simply by measuring the peak area of a characteristic infrared absorption band and knowing the integrated band strength constant for that band. Once the column density of a deposited ice is known, the thickness of the ice d may be approximated through the equation:

$$d = 10^4 \times \frac{Nm}{\rho N_A} \quad (\text{Eq. 4.11})$$

where m is the molecular mass, ρ is the mass density of the ice, and N_A is the Avogadro constant (6.02×10^{23} molecules mol^{-1}). The factor 10^4 is included in Eq. 4.11 so as to express d in units of μm . Eq. 4.11 may be rather straightforwardly extended to the calculation of the total thickness of a multi-component ice by calculating the thickness contribution of each individual component in the manner described above and subsequently adding these contributions together. It should be noted, however, that many values for A_s quoted in the literature are valid only for pure ices at a given temperature, and so their use in determining the column density (and, by extension, thickness contribution) of a molecular component in a mixed ice introduces uncertainties that may be as high as 50% (Kaňuchová *et al.* 2017).

In light of this, many astrochemical research groups have elected to instead determine the thickness of a deposited ice *via* an interferometric technique using light from a helium-neon laser (Goodman 1978). This technique is based on monitoring the variation in intensity of the laser beam, which is reflected off the substrate surface at a particular angle. During ice deposition, the laser intensity varies sinusoidally due to interference of the laser light reflected at the ice-vacuum and ice-substrate boundaries. The ice thickness is then calculated using the following equation:

$$d = \frac{\lambda N_{\text{fr}}}{2\eta \cos(\theta)} \quad (\text{Eq. 4.12})$$

where λ is the wavelength of the laser light *in vacuo* (632.8 nm), N_{fr} is the number of constructive interference pattern repetitions observed during ice deposition, η is the refractive index of the ice, and θ is the angle of the light within the ice (see Chapter 9 for more details). Unfortunately, the ICA is not currently equipped with the ports necessary to make use of laser light interferometry as an ice thickness determination technique. Nevertheless, approximations of the ice thickness *via* spectroscopic measurements of the column density (as described above) are still useful in an experimental context.

Qualitative and quantitative infrared spectroscopic measurements are performed using a Thermo Nicolet Nexus 670 FTIR spectrophotometer arranged as depicted in Fig. 4.1, wherein the infrared spectroscopic beam is maintained orthogonal to the plane of the sample holder and deposited ices. The spectrophotometer has a spectral range of $4000\text{-}650 \text{ cm}^{-1}$ ($2.5\text{-}15.4 \mu\text{m}$) and offers a maximum resolution of 0.5 cm^{-1} , although spectra are nominally collected with a lesser resolution of 1 cm^{-1} . The transmitted infrared spectroscopic beam is detected using a liquid nitrogen-cooled $\text{Hg}_x\text{Cd}_{(1-x)}\text{Te}$ (MCT) photoconductive detector

placed outside the main chamber in a small external container. A purge box continuously passes purified dry air through this MCT detector chamber so as to prevent against intense absorptions by infrared active air constituents whose concentration in the atmosphere may vary (e.g., H₂O or CO₂).

At this point, it is important to comment briefly on the motivation for selecting ZnSe as the material for the deposition substrates, given the existence of a number of alternative materials that are also commonly used to produce infrared transparent windows or substrates, a list of which is provided in Table 4.3. It is evident from the data provided in Table 4.3 and Fig. 4.5 that ZnSe exhibits good transmittance properties across mid-infrared wavelengths even when the substrate is as thick as 1 cm and, moreover, has a wider transmission range than other commonly used materials such as Si or ZnS. Additionally, ZnSe exhibits a number of other advantageous properties, such as its insolubility in most solvents, including H₂O. This makes it preferable to substrates made from alkali metal halides (e.g., LiF, NaCl, KBr, or CsI) since, although these materials have a significantly wider transmission range across infrared wavelengths, they are all very sensitive to moisture and will readily dissolve in the presence of H₂O. As such, ZnSe represents a very good choice of substrate material for the infrared spectroscopic analysis of realistic astrophysical ice analogues, which are often rich in H₂O.

The ICA is also equipped with a quadrupole mass spectrometer (QMS; Pfeiffer QME200) that allows for a mostly qualitative monitoring of the gas-phase composition of the main chamber. This is most relevant during the ion irradiation and thermal annealing of astrophysical ice analogues, wherein molecules may respectively sputter or desorb from the bulk ice. The QMS presently attached to the chamber is able to detect sputtered or desorbed molecules with a molecular mass of up to 200 amu at a mass resolution of 1 amu, and is able to function efficiently at chamber pressures of up to about 5×10^{-5} mbar.

Table 4.3: List of commonly used infrared transparent materials and their transmission ranges and refractive indices. Table adapted from Schrader (1995).

Optical Material	Transmission Range (10 ⁴ cm ⁻¹)	Refractive Index	Comments
SiO ₂ (quartz)	8.33-0.22	1.6	Sensitive to HF
SiO ₂ (fused silica)	8.33-0.22	1.5	-
Si (silicon)	0.83-0.07	3.5	Limit on purity
Al ₂ O ₃ (sapphire)	7.14-0.15	1.7	Good strength
MgF ₂	9.09-0.13	1.4	-
CaF ₂	7.69-0.08	1.4	Sensitive to NH ₄ ⁺ salts
ZnSe	2.22-0.05	2.4	Insoluble in most solvents
ZnS	1.00-0.07	2.2	Insoluble in most solvents
LiF	8.33-0.11	1.3	Sensitive to acids
NaCl	4.76-0.04	1.5	Soluble in H ₂ O and alcohols
KBr	4.00-0.02	1.5	Soluble in H ₂ O and alcohols
CsI	4.00-0.01	1.8	Soluble in H ₂ O
Se (amorphous selenium)	0.60-0.04	2.2	Soft
Ge	0.55-0.04	4.1	-
C (diamond)	4.00-0.01	2.4	Good strength

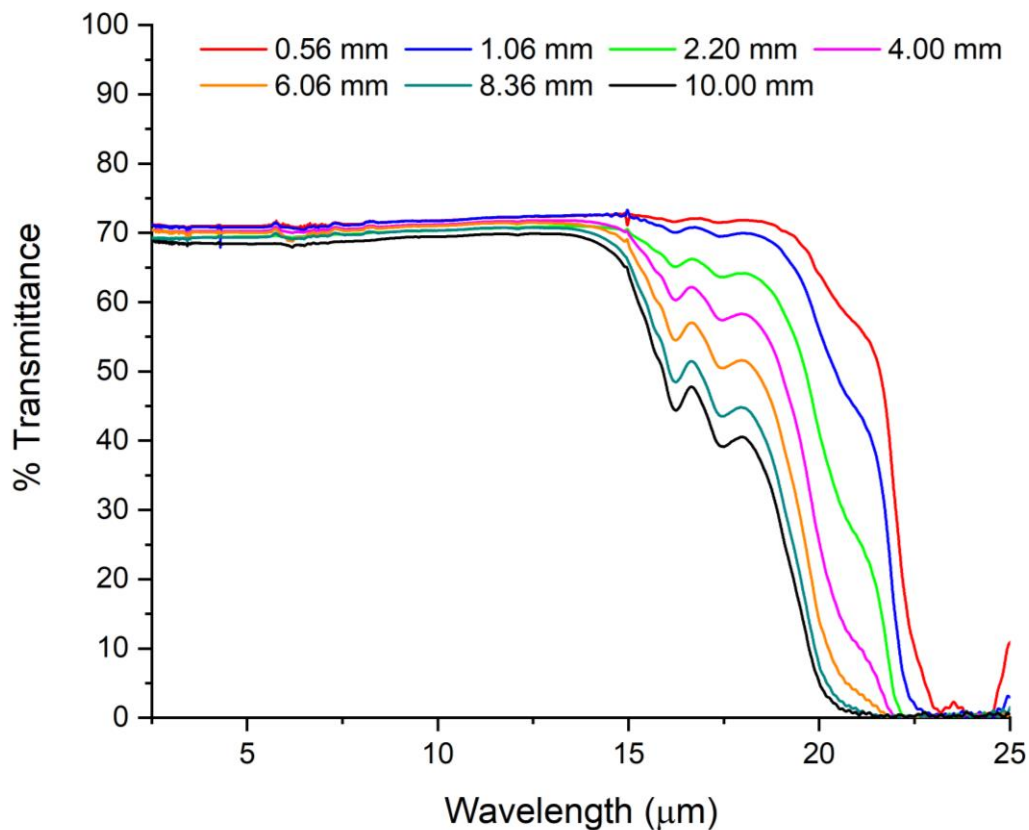


Fig. 4.5: Percentage transmittance of ZnSe substrates of different thicknesses across infrared wavelengths between 2.5-25 μm (4000-400 cm^{-1}). Data courtesy of Crystran.

4.2.3 Ion Irradiation of Ices: The Atomki Tandetron Accelerator

One of the major advantages of the ICA apparatus is its status as a permanent end-station on one of the beamlines at the Atomki Tandetron Laboratory (Rajta *et al.* 2018, Biri *et al.* 2021), which therefore allows the regular performance of mid- to high energy ion irradiations of astrophysical ice analogues. Although the use of particle accelerators in astrochemical research goes back over 40 years (Brown *et al.* 1978), their use is still somewhat of a rarity due to the high costs associated with their construction and maintenance (Strazzulla and Brunetto 2017). Nonetheless, ion irradiation experiments are an important aspect of laboratory astrochemistry as they are able to simulate various radiation chemical processes occurring within interstellar and Solar System ices.

The Atomki Tandetron accelerator is equipped with two multi-cusp ion sources for proton and helium ion beams and a caesium sputtering ion source for ion beams of heavier elements. The terminal voltage of the accelerator can be set in the range 0.085-2 MV and has a typical stability of 200 V hr^{-1} . Testing has revealed, for instance, that a terminal voltage of 1 MV was found to vary within just 50 V over a time range in excess of five hours, with a ripple of 15 V. As such, the Tandetron accelerator is capable of delivering very stable ion beams to the ICA chamber. For proton beams, the available energy range is 0.2-4 MeV, while for heavier ion beams, this energy range is determined by the available terminal voltage range, the relation between which is given as:

$$E_{\text{beam}} = q[V_{\text{ext}} + V_{\text{term}}(k + 1)] \tag{Eq. 4.13}$$

where q is the fundamental electric charge, V_{ext} is the ion beam extraction voltage, V_{term} is the terminal voltage (which, as previously mentioned, may be set between 0.085 and 2 MV), and k is the positive integer charge of the projectile ion. Thus, for example, a He^+ ion beam for which the extraction voltage is 20 kV has an available energy range of between 190 keV and 4.02 MeV.

Aside from providing stable ion beams, the accelerator is also able to provide fairly high beam currents of at least 200 μA in the case of protons and at least a few μA for heavier ion projectiles. Although such currents are available, the ion beam currents actually used for ice irradiation experiments typically do not exceed a few hundred nA, as higher current densities may induce unwanted heating of the deposition substrate and the ices. It is useful, therefore, to estimate an upper bound for the heating effect induced by ion irradiation and, for this purpose, the irradiation of an ice at 20 K by a 1 MeV ion beam having a beam current of 1 μA is considered. Such an ion beam has a power dissipation of 1 W. If the heat conductance of a ZnSe deposition substrate G can be approximated by that of a ZnSe rod (Fig. 4.6) having a cross-sectional area $\sigma = 0.64 \text{ cm}^2$ and a length $b = 0.8 \text{ cm}$ (corresponding to the maximum heat transfer pathlength through the substrate), then it would be given as:

$$G = \frac{\kappa\sigma}{b}$$

(Eq. 4.14)

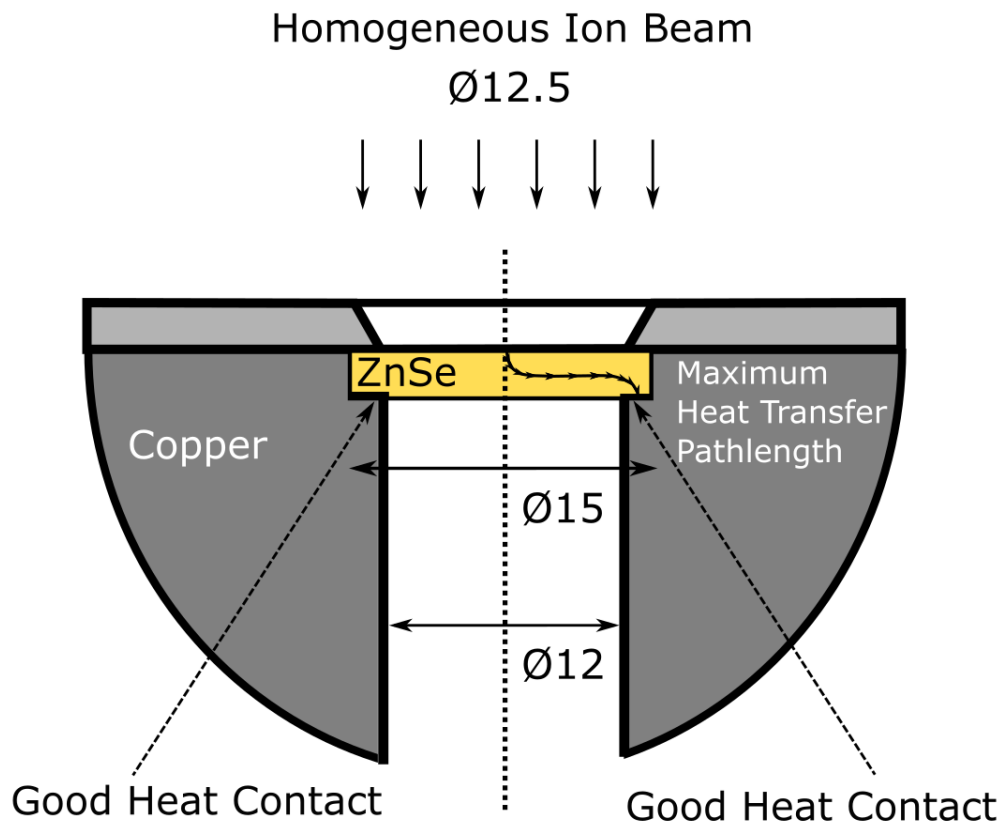


Fig. 4.6: The heat conductance of a ZnSe substrate disc can be approximated by that of a ZnSe rod of cross-sectional area $\sigma = (1.5^2 - 1.2^2) \times (\pi \div 4) = 0.64 \text{ cm}^2$. The maximum heat transfer pathlength is indicated in the diagram, and represents the approximate maximum distance from the centre of the front side of the substrate to the furthest point of good heat contact with the copper sample holder (about 0.8 cm).

where κ is the thermal conductivity of ZnSe at 20 K, which is known to be $6 \text{ W K}^{-1} \text{ cm}^{-1}$ (Bijalwan *et al.* 1983). The heat conductance is thus simply calculated to be 4.8 W K^{-1} . The maximum temperature increase experienced by the substrate and deposited ice as a result of their irradiation by an ion beam is therefore given as the ratio of the power dissipation of the beam to the heat conductance. As such, for a 1 MeV ion beam with a current of $1 \mu\text{A}$, this corresponds to only 0.21 K. However, as previously stated, the beam currents typically used for an ion irradiation experiment do not exceed a few hundred nA, and so the maximum power dissipation of the beam is on the order of 100 mW. Hence, maximum heating induced by irradiation practically always corresponds to a temperature increase of less than 0.1 K.

A stable and homogeneous current density at the surface of the deposited astrophysical ice analogue is required to accurately monitor any induced structural or chemical changes in the ice *via* infrared spectroscopy (Fig. 4.7). For this reason, an ion beam scanner consisting of x - and y -deflector pairs as well as high-voltage ramp generators with minimum frequencies of 25 and 600 Hz in the x - and y -directions, respectively, are applied along the ion beam pathway so as to provide homogeneous irradiation of the ice target. The resultant nominal scanned area is around $25 \times 25 \text{ mm}$. The beam is then passed through a circular collimator of diameter 14 mm, and the emergent circularly shaped ion beam can then be viewed on a quartz probe using a high-definition camera.

During irradiation, the beam current is continuously monitored using a Faraday cup (labelled I_{mon} in Fig. 4.7) placed in the path of the incident ion beam having a second collimator at its base through which the ion beam may be channelled towards the deposited ice. This second collimator reduces the diameter of the ion beam to 12.5 mm. The true deposited current is measured by means of a movable reference Faraday cup (labelled I_{ref} in Fig. 4.7). The homogeneity of the ion beam may be frequently checked during irradiation by rotating the sample holder so that it is orthogonal to the beam pathway and using a 9.6 mm diameter collimator mounted on the sample holder (labelled C_2 in Fig. 4.7) as shown in Fig. 4.2, together with a final Faraday cup (labelled F_3 in Fig. 4.7). Geometrical constraints require the current measured by this latter Faraday cup to be approximately half that measured by the movable reference Faraday cup for all homogeneous ion beams.

The extent of the irradiation of an astrophysical ice analogue is quantified by means of the beam flux Φ and the charged particle fluence φ . Using the series of Faraday cups available along the ion beam pathway (Fig. 4.7), it is possible to measure the total Coulombic charge Q deposited on the sample during a given irradiation step of duration t . Knowing this value, it is relatively straightforward to calculate the ion fluence:

$$\varphi_{\text{ion}} = \int \Phi_{\text{ion}} dt = \frac{Q}{\alpha k q} \quad (\text{Eq. 4.15})$$

where α is the irradiated area (which, in the case of the ICA, corresponds to 1.13 cm^2), k is the positive integer charge of the projectile, and q is the fundamental electric charge. An alternative method of quantifying the extent of irradiation (which will not be used frequently throughout this thesis) is the absorbed radiation dose δ , which is given as:

$$\delta = \frac{\varphi P_s}{\rho} \quad (\text{Eq. 4.16})$$

where P_s is the stopping power of the charged projectile and ρ is the density of the target astrophysical ice analogue. Although usually expressed in units of Gy, the dose absorbed by an irradiated material may also sometimes be expressed in units of eV per small molecule (e.g., eV per 16 amu).

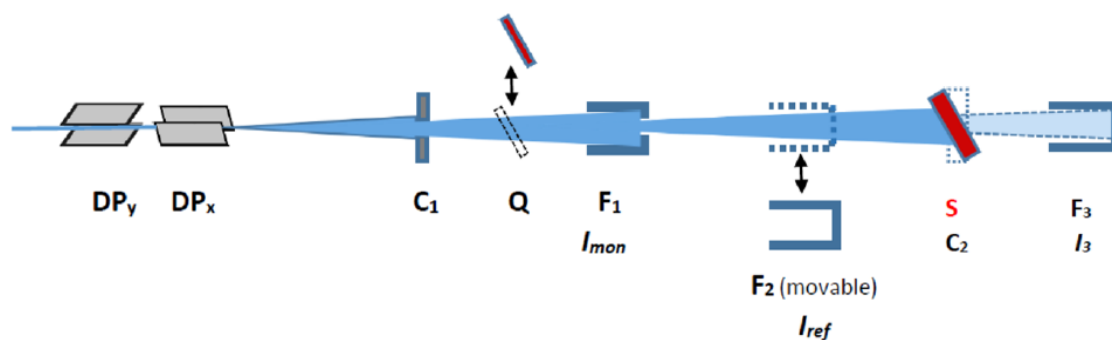


Fig. 4.7: Schematic diagram of the controlled ion beam irradiation system (not to scale). Once the beam passes through deflector pairs DP_y and DP_x , the collimator C_1 defines a circularly shaped beam having a diameter of 14 mm which may be then viewed on the quartz probe Q . The beam current (I_{mon}) is measured by Faraday cup F_1 with a second collimator reducing the beam diameter to 12.5 mm. The movable reference Faraday cup F_2 allows for the ion beam current (I_{ref}) to be measured just before it impacts the sample holder and substrates S . The beam homogeneity can be confirmed using the collimator C_2 and a final Faraday cup F_3 .

4.2.4 Electron Irradiation of Ices: The Miskolci Egyetem Electron Gun

The ICA is equipped with an electron gun (Kimball ELG-2A) which is directly attached to one of the DN-40 CF flanges on its side wall. The arrangement of the experimental set-up is such that the sample holder and deposition substrates may be maintained orthogonal to the pathway of the infrared spectroscopic beam, while both ion and electron irradiations may be performed with incident projectiles impacting the deposited astrophysical ice analogues at angles of $\pm 36^\circ$ to the normal (Fig. 4.1). In principle, the gun is able to emit electrons with kinetic energies ranging between 5 eV and 2 keV; however, since the ICA is not designed to reduce the influence of any external magnetic field within the chamber to zero, in practice only electrons with energies of 1-2 keV may be used reliably. The inclusion of the electron gun in the ICA is the result of a successful long-term collaboration with its proprietors at the University of Miskolc, who have kindly agreed for the gun to be incorporated into the set-up on a long-term basis.

In order to quantitatively assess the radiation chemistry of a deposited ice subjected to an incident energetic electron beam, it is necessary to have knowledge of both the current density distribution at the surface of the ice as well as the electron beam flux. In the case of ion beams delivered by the Tandetron accelerator, this information is gleaned through the use of a series of collimators and Faraday cups along the pathway of the beam (Fig. 4.7). To characterise the profile homogeneity of the electron beam, the 9.6 mm diameter collimator mounted onto the sample holder is used in tandem with a Faraday cup which is attached to the multi-purpose DN-40 CF port directly opposite to the position of the electron gun (Fig. 4.1). The sample holder is first rotated to directly face the electron beam pathway, after which the electron beam is transmitted through the collimator and the current is measured by the Faraday cup as a function of the vertical position of the collimator Y as it is displaced from its nominal position in fine steps. The zero value for the x , y , and Y coordinates at the surface of a deposited ice is defined by the passage of the axis of the electron beam through

the plane of its surface. The experimentally measured current values $I_{\text{measured}}(Y)$ may then be compared to model calculations:

$$I_{\text{model}}(Y) = \iint_{x^2+y^2 \leq R_c^2} dx dy i(x, y - Y) \quad (\text{Eq. 4.17})$$

where R_c is the radius of the collimator (4.8 mm) and $i(x, y)$ is the hypothetical current density in the plane of the deposited ice surface.

A unique solution for the model function current density $i(x, y)$ does not exist when compared to the measured values and so, in the strictest sense, this cannot be considered a fit. However, given reasonable and few-parameter $i(x, y)$ functions, an approximation of the shape and uniformity of the electron beam may be obtained. An example of this for a 2 keV electron beam is shown in Fig. 4.8, which demonstrates that the measured current intensity data match the current density function for a modelled homogeneous and cylindrical beam of diameter 8.4 mm very well.

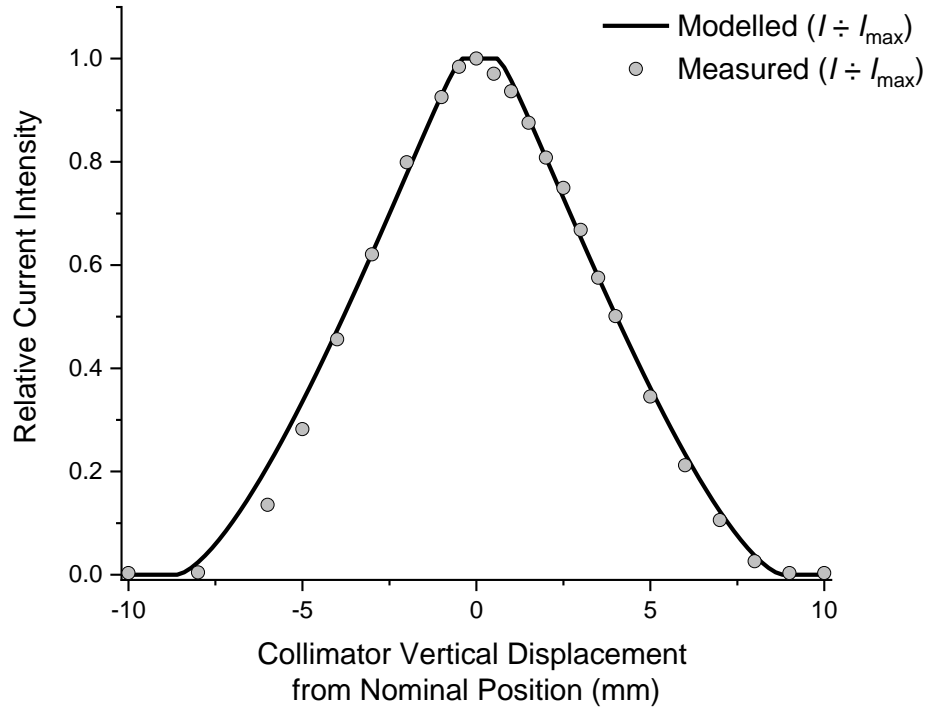


Fig. 4.8: Plots of the measured (*dots*) and modelled (*line*) electron currents $I(Y)$ as a function of collimator displacement from its nominal position along the vertical axis of the chamber relative to the maximum beam current $I_{\text{max}}(Y)$ measured at zero displacement. The modelled beam depicted in this plot is a homogeneous and cylindrical one with a diameter of 8.4 mm.

It should be noted, however, that Fig. 4.8 represents a rather special electron beam focusing condition which cannot be performed in all cases. Sharp focusing to a beam diameter of <3 mm, however, is possible at all beam energies and so, in general, a uniform electron beam density is ensured by sweeping the focused electron beam in the x and y directions using sawtooth-shaped voltages applied to the deflection electrodes of the electron gun. In such cases, the uniformity of the beam current density may also be determined from the measured profile by using Eq. 4.17 and a straightforward algorithm. Electron beam

sweeping is the preferred option if beam homogeneity is important. Conversely, if an accurate value of the beam flux is required, then a beam spot diameter of <9.6 mm (as depicted in Fig. 4.8) is the optimum choice.

The characterisation of the electron beam profile allows for the beam spot area α incident on the target astrophysical ice analogue during irradiation to be defined. This value, along with the maximum beam current $I_{\max}(Y)$ that is measured at a collimator displacement of $Y = 0$ and the fundamental electric charge q , may be used to quantify the electron beam flux:

$$\phi = \frac{I_{\max}(Y)}{\alpha q} \quad (\text{Eq. 4.18})$$

In order to ensure that a constant flux is used throughout an electron irradiation experiment, the beam current is measured on the Faraday cup opposite to the electron gun prior to each irradiation and is compared to the current emitted by the filament, which is displayed on the digital power supply. This displayed current is then continuously monitored throughout the irradiation process. Test runs have repeatedly demonstrated that the beam currents emitted by the filament and measured by the Faraday cup are stable, with the ratio between the two varying by less than 1% over a time range of five hours.

4.3 Typical Experimental Procedures

As has been explained in detail throughout the previous sub-section, the ICA has been designed to facilitate the ion irradiation, electron irradiation, and thermal annealing of deposited astrophysical ice analogues so as to simulate the chemical and structural changes that solid ices may undergo in interstellar and Solar System environments. In this sub-section, summaries of validation experiments performed after the initial commissioning of the set-up are provided. In particular, the ion and electron irradiations of amorphous CH_3OH ice at 20 K, as well as the thermally induced cryogenic chemistry occurring between H_2O and SO_2 ices, are described. These processes have been described at length in the literature, and so represent ideal experiments for the practical validation of the ICA apparatus.

4.3.1 Ion Irradiation of Pure Amorphous Methanol Ice

The ion irradiation of frozen CH_3OH has been previously studied in some detail (Moore *et al.* 1996, Palumbo *et al.* 1999, Brunetto *et al.* 2006, de Barros *et al.* 2011a), and has revealed that CH_3OH is efficiently radiolysed to yield a plethora of new molecular products; the most abundant being CO , CO_2 , H_2CO , and CH_4 . To reproduce these results, pure amorphous CH_3OH ices having a thickness of about 2 μm were prepared in the ICA *via* the background deposition of the vapour at 20 K. Once deposited, a pre-irradiation mid-infrared spectrum of the ice was acquired (1 cm^{-1} resolution; 128 scans), following which it was exposed to an ion beam. In total, five irradiation experiments were performed using different ion beams: four proton beams with energies of 200 keV, 400 keV, 750 keV, and 1 MeV, as well as a 6 MeV S^{2+} ion beam. Additional spectra were acquired at regular intervals during the irradiation process so as to monitor any radiation-induced changes within the ice.

Considering first the proton irradiated CH₃OH ices: the exposure of the ices to the ion beams resulted in a gradual decrease in the peak areas of the CH₃OH infrared absorption bands along with the appearance and progressive growth of several new absorption features caused by the formation of new molecules (Fig. 4.9). In total, six new molecules including the closed-shell species CO, CO₂, H₂CO, and CH₄ along with the radical species HCO and CH₂OH were detected in the acquired infrared spectra, thus agreeing well with previously published data (Moore *et al.* 1996, Palumbo *et al.* 1999, Brunetto *et al.* 2006, de Barros *et al.* 2011a). Comprehensive work by Bennett *et al.* (2007) and Schmidt *et al.* (2021) has revealed much of the mechanistic chemistry leading the formation of these products. Initial fragmentation of the CH₃OH molecule is thought to proceed either *via* the loss of hydrogen to yield CH₃O or CH₂OH radicals or alternatively *via* the loss of oxygen to directly yield CH₄. The formation of CH₄ may also occur *via* hydrogen abstraction by CH₃; another radiolytic fragment of CH₃OH. The subsequent loss of hydrogen from CH₃O or CH₂OH yields H₂CO, which may then undergo an additional dehydrogenation step to yield HCO.

The remaining products, CO and CO₂, are second-generation products since their formation is dependent upon the consumption of stable molecular species produced by the fragmentation of CH₃OH. The formation of CO may take place as a result of the loss of hydrogen from either H₂CO or HCO, with the former process being favoured (Bennett *et al.* 2007, Schmidt *et al.* 2021), whereas CO₂ is most efficiently formed as a result of the reaction between CO and OH which proceeds *via* a HO-CO intermediate complex (Goumans *et al.* 2008, Ioppolo *et al.* 2011).

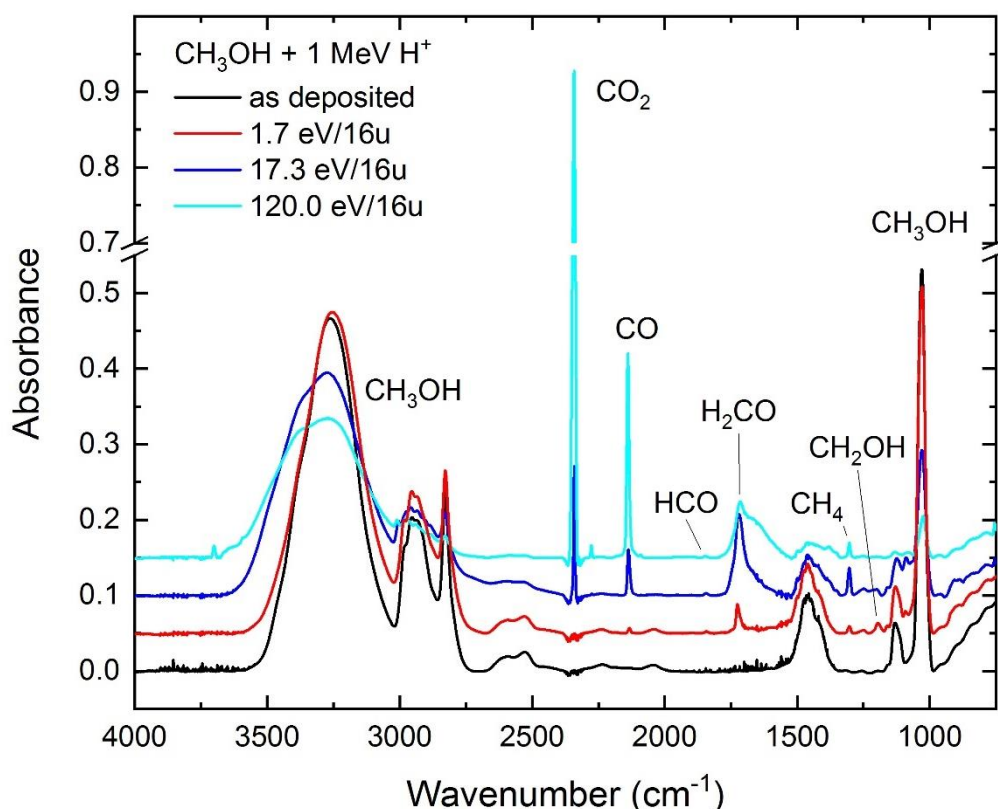


Fig. 4.9: Mid-infrared absorption spectra of an amorphous CH₃OH ice irradiated by a 1 MeV proton beam at 20 K. Note that spectra have been vertically offset for clarity.

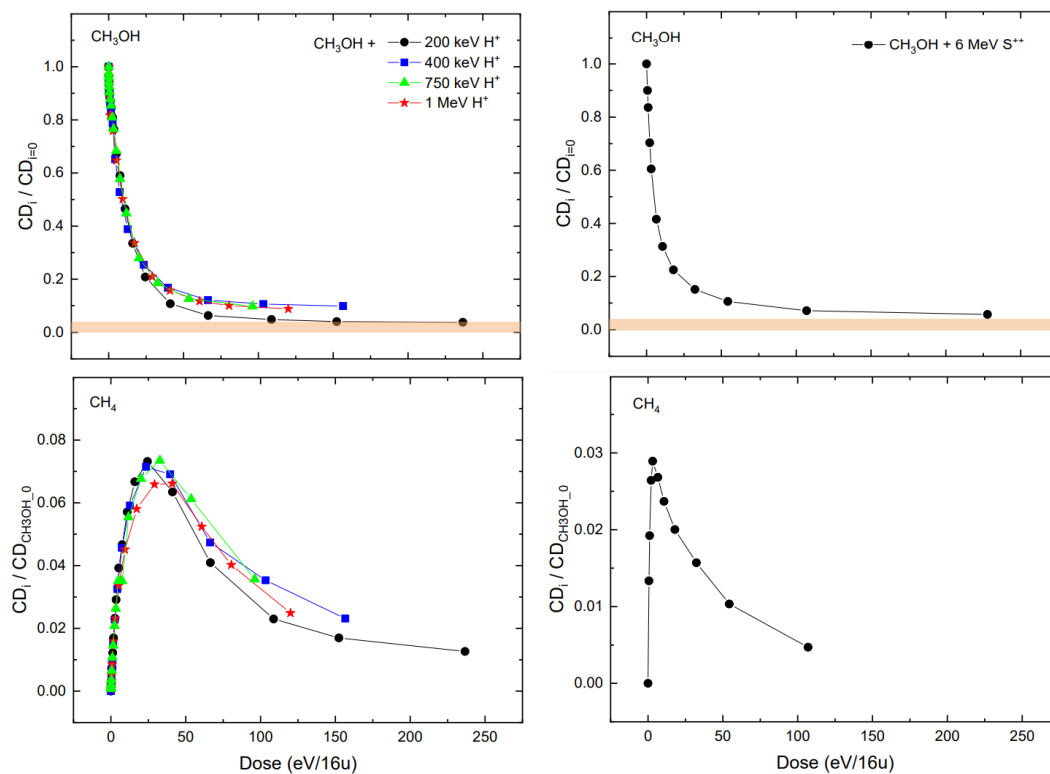


Fig. 4.10: *Top panels:* Evolution of the CH₃OH column density as measured from the absorption band at 1027 cm⁻¹ assuming a band strength constant of 1.61×10⁻¹⁷ cm molecule⁻¹ (Luna *et al.* 2018) with increasing proton (*left*) and S²⁺ (*right*) ion beam dose. *Bottom panels:* Evolution of the CH₄ column density as measured from the absorption band at 1300 cm⁻¹ assuming a band strength constant of 8×10⁻¹⁸ cm molecule⁻¹ (Mejía *et al.* 2013) with increasing proton (*left*) and S²⁺ (*right*) ion beam dose. Note that all column densities are reported relative to the initial column density of CH₃OH that was deposited. The horizontal bars in the upper panels indicate the lower bound value of CH₃OH deposited on the rear side of the ZnSe substrates.

An interesting result of the proton irradiation of CH₃OH ice is the observation that the decay of the column densities of the parent molecule as a function of the absorbed dose was well replicated across all proton energies (Fig. 4.10). This is likely due to the fact that the penetration depths of all the incident protons considered here lie in the range 3-32 μm³¹, and so exceed the thickness of the CH₃OH ice in all cases. As such, it is likely that energy loss from the incident charged particle was still within the linear regime and that different results may be expected from experiments using either lower proton energies or significantly thicker ices. The evolution of the column density of CH₄ as a function of dose was also analysed. The reason for selecting this molecule is the fact that it possesses the most well-defined absorption band of all first-generation products in the acquired infrared spectra (Fig. 4.10). The analysis demonstrated that the radiolytic formation of CH₄ peaks after a dose of 30 eV per 16 amu is supplied in all irradiation experiments irrespective of proton energy, likely due to the linear energy loss of the projectile particles. Beyond this dose, the CH₄ column density declined as it was consumed in the formation of second-generation products.

The radiolysis of CH₃OH ice induced by 6 MeV S²⁺ ions was found to be qualitatively similar to that induced by the proton beams, in that all product species recorded after irradiation using the latter were also documented after irradiation using the former. One notable difference between the proton irradiations and the S²⁺ ion irradiation was the fact that the decay of the CH₃OH ice column density was noted to be significantly more rapid in

³¹ Details on the computational software used to compute the penetration depths of incident ions and electrons are given later in this chapter.

the case of the latter. Similarly, the radiolytic formation of CH₄ peaks at a considerably lower radiation dose before beginning to decay. It is difficult to pinpoint a single reason for this observation as there exist a number of possible contributing factors. One possibility, for instance, is that although the implantation of the incident 6 MeV S²⁺ ions is negligible, the stopping power may not be within the linear regime and thus leads to a more rapid depletion of CH₃OH and, consequentially, a more rapid build-up and subsequent consumption of CH₄. Alternatively, it is possible that since a sulphur ion is significantly more massive than a proton, the sputtering yield occurring during S²⁺ ion irradiation was greater than that occurring during proton irradiation. Such sputtering would cause the ejection of CH₃OH and product molecules from the bulk ice and, therefore, lead to a comparatively quicker decay of these species. Indeed, QMS signals ascribed to CH₃OH and several closed-shell molecular products (including CH₄) were detected during the 6 MeV S²⁺ ion irradiation, indicating that ice sputtering occurred to at least some extent.

4.3.2 Electron Irradiation of Pure Amorphous Methanol Ice

The radiation chemistry of pure CH₃OH ice initiated by high energy electrons has also been studied extensively (Bennett *et al.* 2007, Jheeta *et al.* 2013, Sullivan *et al.* 2016, Schmidt *et al.* 2021), and is qualitatively similar to that induced by ion irradiation. In this sub-section, the results of the electron irradiation of condensed CH₃OH using the ICA apparatus are described. A CH₃OH ice of thickness 1 μm was prepared *via* the background deposition of the vapour at 20 K. Once deposited, a pre-irradiation mid-infrared spectrum of the ice was collected (1 cm⁻¹ resolution; 128 scans), after which it was exposed to a 2 keV electron beam of flux $\Phi = 4.2 \times 10^{14}$ electrons cm⁻² s⁻¹ for 30 minutes (corresponding to a total delivered fluence of $\varphi = 7.6 \times 10^{17}$ electrons cm⁻²), with additional mid-infrared spectra being collected at several intervals.

The electron irradiation of the CH₃OH ice resulted in decreases in the peak areas of its characteristic absorption bands, as well as the appearance of new absorption features due to the formation of new molecules (Fig. 4.11). Overall, all the closed-shell molecular products observed after ion irradiation of amorphous CH₃OH (i.e., CO, CO₂, H₂CO, and CH₄) were also formed after electron irradiation. The mechanistic routes towards the formation of these molecules are anticipated to be similar to those described for their formation *via* the ion irradiation of CH₃OH since, as explained previously, this radiation chemistry is largely mediated by the emission of a cascade of low energy (<20 eV), non-thermal secondary electrons (Mason *et al.* 2014, Boyer *et al.* 2016).

The penetration depths of the projectile electrons used for irradiation experiments with the ICA are typically on the order of a few tens to a few hundreds of nm, depending upon the kinetic energy of the electrons and the density of the target ice. Such penetration depths are small, and thus electrons are efficiently implanted into all but the thinnest of ices. During the analysis of data acquired from electron irradiation experiments, it is preferable to correct for that volume of the target ice beyond the penetration depth of the incident electrons which experiences no radiation chemistry but is still spectroscopically observable. The density of amorphous CH₃OH prepared at 20 K is 0.636 g cm⁻³ (Luna *et al.* 2018), and the maximum penetration depth of an incident 2 keV electron is approximately 220 nm. Given that the total thickness of the ice deposited in this experiment was about 1 μm, it is necessary to correct for the unirradiated volume of the ice, which accounts for over three-quarters of the total ice volume.

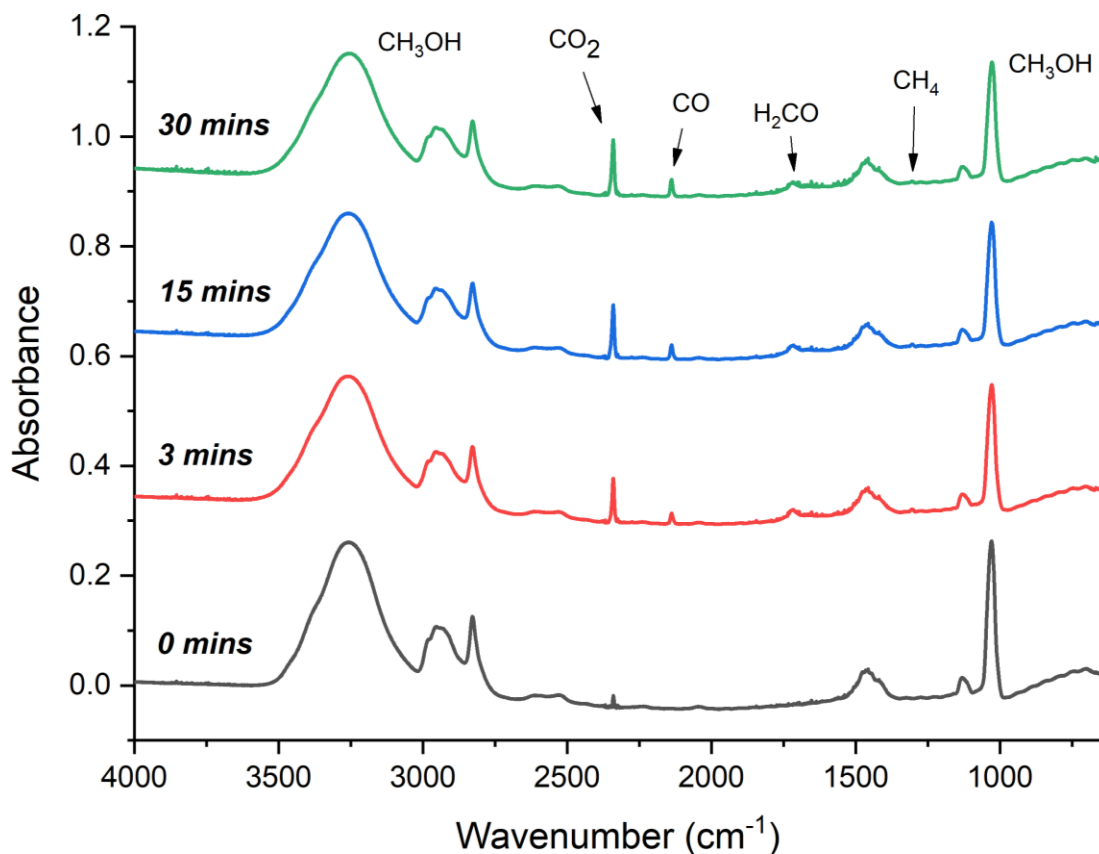


Fig. 4.11: Mid-infrared spectral evolution of a 1 μm CH_3OH ice at different time intervals during electron irradiation by a 2 keV beam having a flux $\Phi = 4.2 \times 10^{14}$ electrons $\text{cm}^{-2} \text{s}^{-1}$. The absorption bands attributed to CO , CO_2 , H_2CO , and CH_4 have been indicated by arrows. Note that spectra have been vertically offset for clarity.

Throughout this thesis, a parent molecular column density correction factor will often be used when discussing the results obtained from electron irradiation experiments. The use of this correction factor thus excludes as much as possible the diluting influence of that volume of the ice which does not partake in radiation chemistry but is still observed in the acquired mid-infrared spectra. The corrected normalised column density N_c is given as:

$$N_c = \frac{N_n - N_p}{1 - N_p} \quad (\text{Eq. 4.19})$$

where N_n is the measured column density normalised to that which was initially deposited and N_p refers to the plateau or asymptotic value that the normalised molecular column density of the parent species reaches after prolonged irradiation as a result of its rates of radiation-induced destruction and formation being equal (i.e., the so-called ‘steady state’). If an electron irradiation is not performed for long enough for the steady state to be achieved, then an approximation for N_p may be found by fitting an exponential decay function to a plot of normalised parent ice molecular column density against fluence and subsequently calculating the normalised column density at an appropriately high fluence value (e.g., 10^{20} electrons cm^{-2}) using this fitted function.

4.3.3 Thermal Reactions between Water and Sulphur Dioxide Ices

Thermal chemistry at cryogenic temperatures represents an important aspect of interstellar and Solar System astrochemistry, and may lead to the formation of complex molecules of potential relevance to biology (Theulé *et al.* 2013). The temperatures of astrophysical ice analogues and the ZnSe deposition substrate discs onto which they were prepared may be controlled in the range of 20-300 K, and thus the ICA set-up may be conveniently exploited to probe thermal chemistry in these ices. To validate such studies, an experiment aiming to characterise the thermal chemistry in a mixed H₂O:SO₂ ice was performed. Although this chemistry has been well explored by previous studies (Moore *et al.* 2007, Kaňuchová *et al.* 2017), the experiment presented here made use of a hitherto unconsidered ice mixture stoichiometry.

A mixed H₂O:SO₂ ice of compositional stoichiometry 3:5 and thickness 3 μm was prepared on a ZnSe substrate *via* background co-deposition of H₂O vapour and SO₂ gas at 20 K. Once deposited, a pre-annealing mid-infrared spectrum was acquired (1 cm⁻¹ resolution; 128 scans), following which the ice was thermally annealed to 160 K at a rate of 2 K min⁻¹. Additional mid-infrared absorption spectra were collected at 20 K intervals. Results demonstrated that, as the ice mixture was warmed, new absorption features appeared at around 1040 cm⁻¹ and 956 cm⁻¹ (Fig. 4.12) which are ascribed to the formation of HSO₃⁻ and S₂O₅²⁻, respectively (Pichler *et al.* 1997, Zhang and Ewing 2002). The mechanistic steps leading to the formation of these products (which were already provided in Chapter 1) are given as:

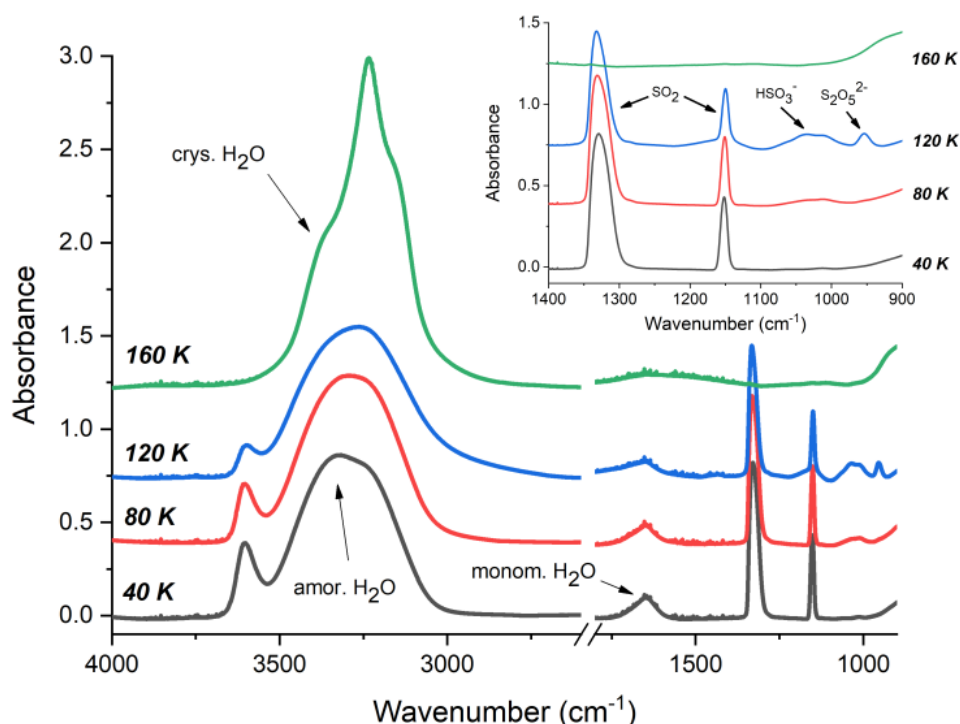
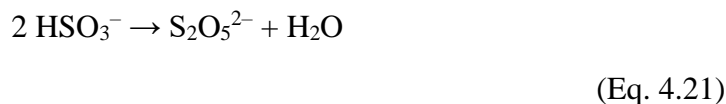
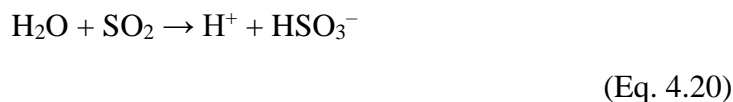


Fig. 4.12: Mid-infrared spectral evolution of a thermally annealed H₂O:SO₂ (3:5) mixed ice. As the ice is warmed, thermal reactions between H₂O and SO₂ are promoted leading to the formation of HSO₃⁻ and S₂O₅²⁻, whose infrared absorption bands are more clearly visible in the inset. At 160 K, all sulphur-bearing molecules seem to have sublimated from the bulk ice. The thermally induced restructuring of the H₂O ice from an amorphous solid at 20 K to a hexagonal crystalline phase at 160 K is also evident in these spectra. Note that increases in the absorbance values at low wavenumbers (<1000 cm⁻¹) in the 160 K spectrum are due to changes in the high temperature background profile that are not taken into account by the background spectrum that was used which was measured at 20 K.



The absorption band due to HSO_3^- was first observed at 40 K, and continued to grow in size with increasing temperature, representing an increase in the overall abundance of this species within the bulk ice. The first traces of the $\text{S}_2\text{O}_5^{2-}$ band were observed later at 80 K: this is logical, as the formation of this species requires the accumulation of HSO_3^- as a first step, as per Eqs. 4.20 and 4.21. Further increases in the temperature of the ice result in the growth of the absorption bands for both these product molecules up until a temperature of 120 K in the case of HSO_3^- and 140 K in the case of $\text{S}_2\text{O}_5^{2-}$. At higher temperatures, the absorption band peak areas for these molecules begin to decrease due to their sublimation. By the time a temperature of 160 K was reached, no spectroscopic evidence could be detected for the presence of SO_2 , HSO_3^- , or $\text{S}_2\text{O}_5^{2-}$ in the bulk ice (Fig. 4.12).

4.4 Limitations of the Experimental Set-Up

Although the ICA set-up is certainly a versatile one that may be utilised to gain a deeper understanding of the radiation and thermal chemistry of interstellar and Solar System ices, as with all such astrochemical simulation systems, it does have its limitations. A summary of these limitations now follows:

(i) Simulating Astrophysical Time-Scales

There exists no method by which the time-scales over which astrochemical reactions and processes occur may be simulated in the laboratory. Such processes may take place over 10^4 - 10^6 years, whereas typical laboratory experiments are performed over a period of a few hours. It is typically assumed the outcome of much of the chemistry is independent of the time-scale over which it takes place, and that the morphologies of ices prepared in the laboratory are similar to those grown in actual astrophysical environments over geological or astronomical time-scales. However, the validity of such assumptions is unknown.

(ii) Simulating Astrophysical Pressures

The base pressure of the ICA is on the order of a few 10^{-9} mbar, which could be as much as a factor of 10^7 greater than those pressures actually encountered in the ISM. Although some other experimental astrochemistry facilities are able to offer better base pressures of 10^{-10} or 10^{-11} mbar (Table 4.1), no facility has yet adequately reproduced interstellar pressure levels in the laboratory.

(iii) Simulating Interstellar Dust Grain Surfaces

Although the ICA seeks to replicate the chemistry occurring on the surfaces of interstellar dust grains (as well as outer Solar System bodies), the laboratory surface analogue is quite poor. Although flat and polished ZnSe discs of the type used in the ICA as deposition substrates are convenient from a spectroscopic perspective, they do not mimic well the composition or morphology of interstellar dust grains, which are thought to be carbonaceous or silicate-based and are highly irregularly shaped (van Dishoeck 2014, Millar 2015). Moreover, interstellar dust grains are (sub)micron sized,

and are thus likely to present significantly smaller cross-sections for ice condensation than are the ZnSe substrate discs used in the ICA, despite the more irregular morphology of the former. It should be noted that there have been recent attempts at circumventing this problem by levitating small dust particle analogues in an ultrasonic trap (Mason *et al.* 2008, Brotton and Kaiser 2013, Dangi and Dickerson 2021), although more development of this technique is required.

(iv) **Incomplete Knowledge on the Composition of Astrophysical Ices**

The paucity of securely identified interstellar molecules in the ice phase (as compared with the large number of known gas-phase species) has already been discussed in the context of the relevant observational constraints (Table 2.3). This lack of information on the chemical diversity of interstellar ices makes it difficult to gauge the applicability of experiments conducted using laboratory set-ups. For instance, experiments looking into the processing of an icy mixture of complex molecules may demonstrate that significant chemistry of interest to the emergence of life or to the formation of planetary systems is possible under interstellar conditions; however, if such a mixture does not actually exist in the ISM, then this chemistry is not applicable to such an environment. Similar arguments may be made with regards to the chemistry of outer Solar System objects, although the compositions of such bodies are typically better defined.

(v) **Temperature-Programmed Desorption Studies**

The ICA set-up is not designed to perform quantitative temperature-programmed desorption (TPD) studies, primarily due to the background deposition technique used to prepare astrophysical ice analogues since this technique results in the condensation of volatile gases and vapours on any cold surface within the chamber. However, TPD experiments of irradiated ices may still be performed if certain precautions are taken. In particular, only one ZnSe deposition substrate should be mounted onto the sample holder and exposed to the ion or electron beam, thus excluding the simultaneous desorption of product species from multiple sources during the TPD. In this scenario, kinetic infrared spectroscopic monitoring of the single substrate during TPD may yield reliable quantitative information regarding the composition of the ice, whilst qualitative measurements of the gas-phase using the QMS may be made alongside control experiments to account for the sublimation of non-irradiated icy material from other cold surfaces within the chamber.

4.5 Software

Although the work described in this thesis is experimental in its nature, it has been assisted through the use of various software packages. In this sub-section, a brief description of two of these packages that were used to calculate the stopping power and penetration depths of projectile charged particles in target astrophysical ices is provided. The first of these freely available software packages is the *Stopping and Range of Ions in Matter* (SRIM) programme³² (Ziegler *et al.* 2010) which was used in ion irradiation experiments, while the second is the *Monte Carlo Simulation of Electron Trajectory in Solids* (CASINO) programme³³ (Drouin *et al.* 2007) which was used in electron irradiation experiments.

³² The SRIM programme may be downloaded online: <http://www.srim.org/>

³³ The CASINO programme may be downloaded online: <https://www.gegi.usherbrooke.ca/casino/index.html>

4.5.1 The SRIM Programme

The SRIM programme is primarily used to determine the stopping power and penetration depth of ions after their collision with a given target material. The programme utilises a quantum mechanical treatment of ion-atom collisions, which is subsequently extended to molecular targets *via* the Köln Core and Bond Model. This model determines the stopping power of projectiles in molecular targets by superimposing the relevant nuclear and electron stopping interactions. Once the programme has been initialised, a target compound may be defined by specifying the nature of the atoms present in the desired molecular target and their relative stoichiometries, as well as the density of the target (Fig. 4.13). The characteristics of the ion beam used must then be defined, including the nature of the ion, its energy, the angle at which it makes contact with the target, and the total number of projectile ions simulated. The programme can then run a simulation that yields the stopping power and penetration depth of the projectile ions.

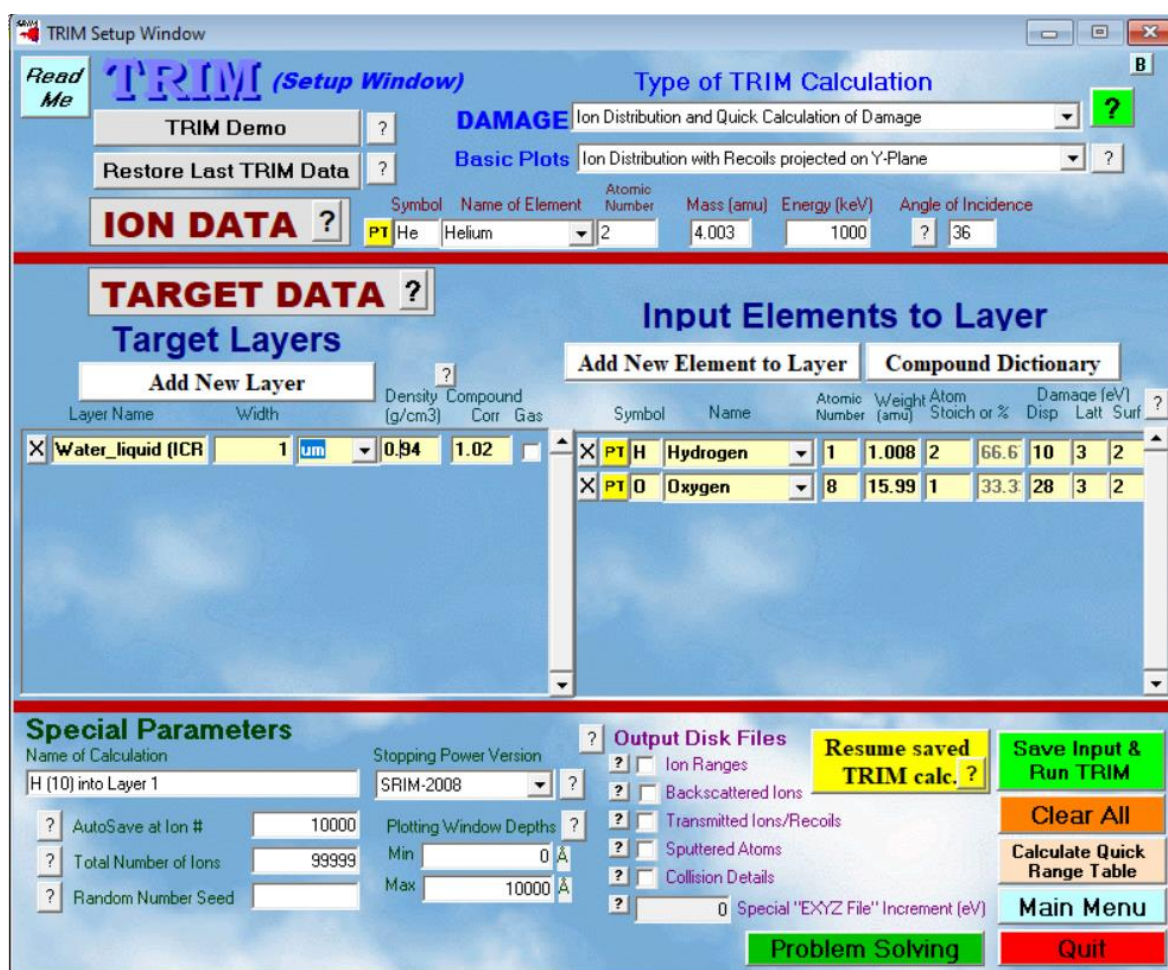


Fig. 4.13: Graphical user interface of the SRIM programme (specifically, the *Transmission and Range of Ions in Matter* or TRIM sub-package). This image depicts the parameter input set-up for a 1 MeV He⁺ ion beam impacting a H₂O target ice of density 0.94 g cm⁻³ and thickness 1 μm at 36° to the normal. Note that a default of 99,999 ions is considered by the simulation, although this may be reduced if necessary.

4.5.2 The CASINO Programme

The CASINO programme makes use of Monte Carlo simulations to calculate the trajectories of electrons through a given target material. This is calculated by considering only elastic collisions between the incident electrons and the atomic nuclei in the target material based on the total cross-section for each chemical element in a given region, with the atom

responsible for electron deviation in regions characterised by multiple elements being determined using the total cross-section ratio. Electron energy loss events are thus grouped into a continuous energy loss function. The calculations are repeated until the deviated incident projectile electron has an energy <50 eV. Once the programme has been initialised, a molecular target material may be defined by stipulating the nature of the atoms present, their relative stoichiometries, and the density of the target (Fig. 4.14). The characteristics of the electron beam used must then be inputted, such as its energy, the angle with which it makes contact with the target material, and the number of electrons to be simulated. A simulation is then run to yield the total penetration depth and energy dissipation of the projectile electrons.

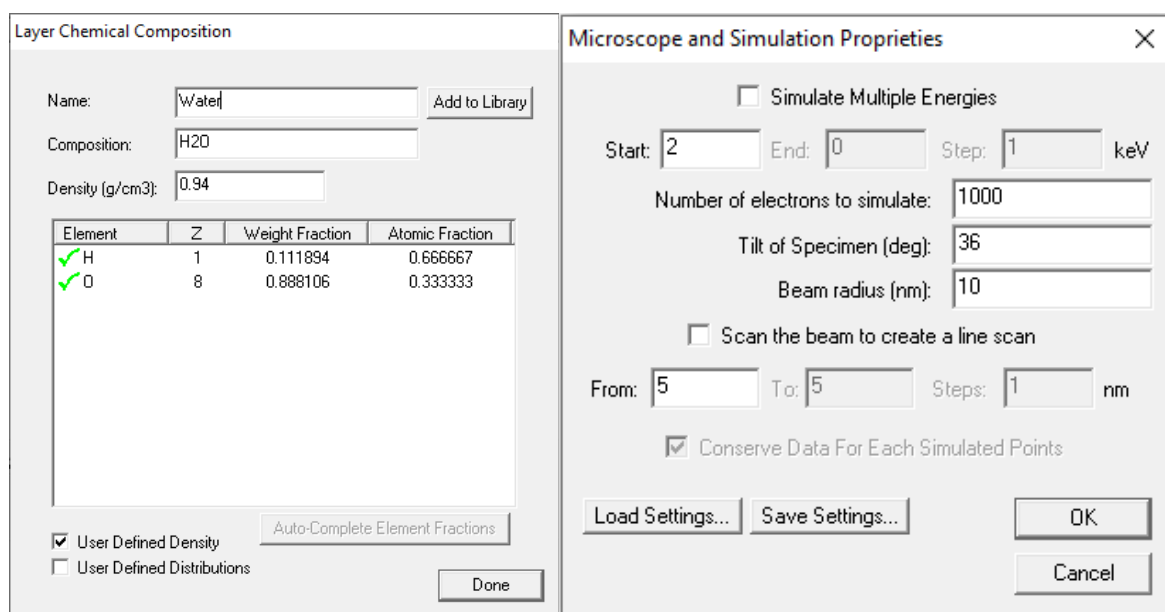


Fig. 4.14: Graphical user interface of the CASINO programme. *Left:* The characteristics of a molecular target (in this case, H₂O) must first be defined. *Right:* Subsequently, the physical parameters of the electron beam are then inputted. In this case, a 2 keV beam impacting the target material at an angle of 36° to the normal has been defined. Note that a default of 1000 electrons is considered by the simulation, although this may be altered if necessary.

4.6 Summary

This chapter provides a detailed technical description of the laboratory apparatus and experimental methodologies used for the work described in this thesis. It begins with a brief overview of the use of high-vacuum and ultrahigh-vacuum chambers in the study of the chemical processing of astrophysical ice analogues, before delving into a deeper discussion of the ICA facility. The configuration of the set-up and the instruments used for *in situ* analysis are described in some detail, as is the method of preparing astrophysical ice analogues onto ZnSe deposition substrates *via* the background deposition of dosed gases or vapours or the effusive evaporation of refractory solids. The chapter also includes a comprehensive description of the Atomki Tandatron particle accelerator and the Miskolci Egyetem electron gun used to provide stable and homogeneous ion and electron beams, respectively. The results of experiments performed to calibrate and validate the ICA are also presented in this chapter, namely: (i) the ion and (ii) electron irradiations of pure amorphous CH₃OH ice at 20 K, and (iii) the thermally induced chemistry between H₂O and SO₂ ices at cryogenic temperatures. The chapter concludes with brief discussions of the limitations of the ICA apparatus as well as the computational software packages used to support the experimental work.

5 SYSTEMATIC MID-INFRARED SPECTROSCOPIC STUDY OF H₂S AND SO₂ ASTROPHYSICAL ICE ANALOGUES

This chapter presents the results of a thorough and systematic investigation looking to characterise the mid-infrared spectra of pure H₂S and SO₂ astrophysical ice analogues deposited at various temperatures and thermally annealed to sublimation. A similar characterisation of the mid-infrared spectra of H₂S:H₂O and SO₂:H₂O mixed ices has also been performed. The acquisition of resolved and well characterised mid-infrared spectra is critical to confirming the detections of molecular species in interstellar icy grain mantles, and also plays an important role in detections made within the Solar System. The chapter concludes by discussing possible uses for the data collected in light of the recently launched *James Webb Space Telescope*, as well as forthcoming interplanetary missions such as the *Europa Clipper* and the *Jupiter Icy Moons Explorer*.

Note: The majority of the work described in this chapter has been published in peer-reviewed journals or periodicals as: [1] Mifsud *et al.* (2023), *Astrophys. Space Sci.* to be submitted; [2] Mifsud *et al.* (2023), *Astrophys. Space Sci.* to be submitted.

5.1 Contextual Introduction

The use of molecular spectroscopy as a key tool for the identification of molecules in extra-terrestrial environments was discussed in Chapter 2. Rotational emission spectra have been a highly effective tool for the determination of the chemical composition of the gas phase of the ISM (Fortenberry 2017, McGuire 2022); however, in the condensed phase rotational motion is restricted and thus infrared absorption spectroscopy using stellar objects along the line of sight of observation as the infrared source must be used instead (Fig. 2.9). This technique has allowed for the identification of about 15 individual molecules within the dense ISM (Boogert *et al.* 2015; Table 2.3).

The recent launch of the *James Webb Space Telescope* on Christmas Day 2021 will provide an unprecedented opportunity to probe the chemical composition of interstellar icy grain mantles, as well as icy bodies in the outer Solar System, with extremely sensitive mid-infrared spectroscopic measurements (Kalirai 2018). In combination with measurements made by other telescopes working in this spectral range, such as the *Spitzer Space Telescope* and the *Infrared Space Observatory*, it is anticipated that much will be revealed with regards to astrochemical processes occurring in the solid phase within dense interstellar clouds, circumstellar discs, icy moons, and comets. However, in order to correctly interpret spectroscopic data acquired by such telescopes, it is necessary to have laboratory generated spectra with which to compare against.

In this chapter, a thorough and systematic mid-infrared spectroscopic characterisation of pure H₂S and SO₂ ices deposited at various cryogenic temperatures and thermally annealed to sublimation is provided. Additionally, mid-infrared spectra of their mixtures with H₂O ice deposited at 20 K and thermally annealed to total sublimation of the ice are presented. The need for more spectroscopic data on sulphur-bearing astrophysical ice analogues was highlighted in Chapter 1, and is reflective of a comparatively incomplete understanding of sulphur ice astrochemistry. As was mentioned in that chapter, there exists an as yet unexplained apparent depletion of sulphur (compared to its expected cosmic abundance) in the dense ISM (Tieftrunk *et al.* 1994, Ruffle *et al.* 1999).

At present, the only sulphur-bearing molecules to have been detected in interstellar icy grain mantles are SO₂ and OCS (Boogert *et al.* 1997, Palumbo *et al.* 1997), and measured column densities suggest that their combined contribution to the sulphur budget of dense interstellar regions could be less than 10% (van der Tak *et al.* 2003). Furthermore, the detection of these molecules in interstellar icy grain mantles is still considered to be fairly tentative due to a lack of multiple matching infrared bands between observational and laboratory data (Boogert *et al.* 2015). The lack of a convincing detection of condensed H₂S in dense interstellar clouds is also somewhat surprising, particularly in light of the apparent ease by which atoms may be hydrogenated on the surface of dust grains (Linnartz *et al.* 2015), as well as the fact that it has been recognised to be among the most abundant sulphur-bearing species in the icy nuclei of comets (Rubin *et al.* 2020).

More thoroughly characterised infrared spectra may also be of use in further understanding sulphur ice astrochemistry within the Solar System. For example, Hendrix *et al.* (2016) suggested that the observed ultraviolet-visible reflectance spectra of the dwarf planet Ceres between 320-400 nm could be approximated fairly well by laboratory spectra of phyllosilicate minerals (such as montmorillonite) intermixed with solid SO₂ and S_x. Such an interpretation carries intriguing implications for the Cererian surface and near-subsurface, as it is suggestive of sustained geothermal activity leading to the active outgassing of sulphurous species. Such an interpretation has, however, been met with some resistance. Firstly, none of the infrared bands attributable to SO₂ was detected by the *Visible and Infrared* (VIR) spectrometer aboard the *Dawn* mission (Stephan *et al.* 2018). Although such a non-detection is not supportive of the idea of widespread SO₂ ices across the surface of Ceres, it does not necessarily exclude its presence since these bands could be obscured by dark surface material or could be blended with spectral features assigned to carbonate minerals (De Sanctis *et al.* 2016). However, a further challenge exists in the volatility of SO₂ under Cererian surface conditions. At 201 K, the surface temperature of Ceres is sufficiently high as to drive sublimation and loss of SO₂ without significant re-condensation (Zhang and Paige 2009), and would thus lead to surface patches of SO₂ that are far too small to produce measurable spectral features in global reflectance spectra (Roth 2018).

The laboratory generation of resolved mid-infrared spectra of H₂S and SO₂ ices under various thermal annealing and deposition conditions, as well as of their mixtures with H₂O ice, will thus aid in further defining the sulphur content and chemistry of the icy cosmos. In the following sub-section, a brief review of previous relevant work is provided. This is followed by a description of the experimental methodology used for the study presented in this chapter, with a full discussion of the results obtained and their implications for sulphur ice astrochemistry in the context of future observational work being given in the subsequent sub-sections. The chapter then concludes with a summary of the key points of the study.

5.2 An Overview of Previous Laboratory Spectroscopic Studies

5.2.1 Mid-Infrared Spectroscopy of H₂S Ices

The laboratory mid-infrared spectroscopy of H₂S ice has been extensively studied, with the most comprehensive recent investigations probably being those of Fathe *et al.* (2006) and Hudson and Gerakines (2018). The most dominant feature in the mid-infrared spectrum of the amorphous ice at 20 K (Fig. 5.1) is a broad stretching band ν_s centred about 2548 cm⁻¹ comprised of both the symmetric (ν_1) and asymmetric (ν_3) stretching modes, while a less intense but nonetheless prominent bending (ν_2) mode has been reported at 1168 cm⁻¹ (Fathe *et al.* 2006, Hudson and Gerakines 2018). The positions of these absorption bands are in reasonably good agreement with those reported by previous works (Table 5.1).

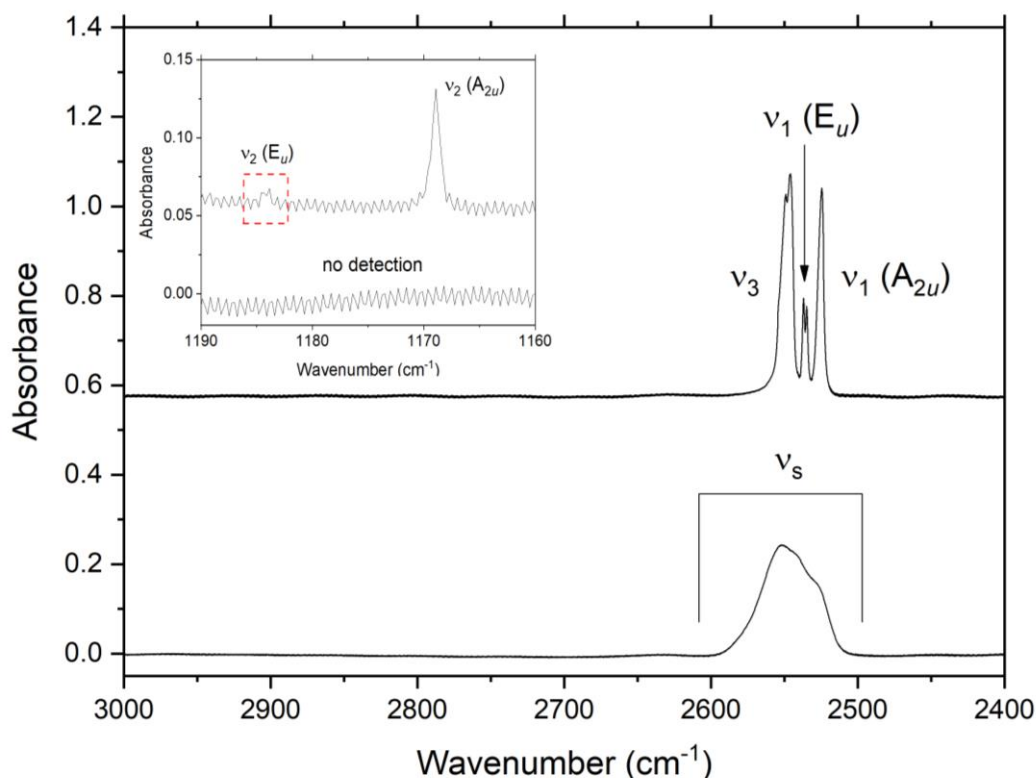


Fig. 5.1: Mid-infrared spectra of amorphous (*below*) and crystalline (*above*) H₂S ices deposited at temperatures of 20 and 70 K, respectively. The spectra, collected at 0.5 cm⁻¹ resolution, show the strong ν_1 , ν_3 , and ν_s absorption bands along with the weaker ν_2 band (inset). Note that the spectra are vertically offset for clarity. The estimated thicknesses of the amorphous and crystalline ices were 0.92 and 0.69 μm , respectively.

The phase chemistry of solid H₂S is particularly interesting, as multiple crystalline phases are known to exist under cryogenic and ambient pressure conditions. These phases are designated using numbers, and are termed phases I, II, and III and are characterised by ambient pressure transition temperatures of 126.2 (I \rightarrow II) and 103.5 K (II \rightarrow III) (Fathe *et al.* 2006 and references therein). The higher temperature phases I and II are orientationally disordered; that is to say they are ordered with respect to sulphur atoms, but not with respect to hydrogen atoms and thus display broad ν_s bands which are only slightly narrower than those of the amorphous phase. This contrasts greatly with the ordered phase III, which exhibits a narrower ν_s band in which individual vibrational modes emerge as distinct substructures (Fig. 5.1). Moreover, both the ν_1 mode and the ν_2 mode are observed to undergo splitting due to the existence of two unique sulphur atoms but three unique S–H bonds in the eight-molecule unit cell (Fitch and Cockcroft 1990, Cockcroft and Fitch 1990): this non-equivalence results in the splitting of a number of the vibrational modes (Zeng and Anderson 2001).

Under conditions relevant to astrochemistry (i.e., cryogenic temperatures and high to ultrahigh vacuum pressures), the only crystalline phase of importance is phase III (hereafter referred to simply as the H₂S crystalline phase), which may be obtained as a result of the thermal annealing of the amorphous ice to temperatures greater than 60 K. The spectra of both the amorphous and crystalline phases exhibit a number weaker combination bands, including several that involve rotational (also referred to as librational) and translational lattice modes (Fig. 5.1, Table 5.1). It is worth noting that no overtone bands appear in the mid-infrared spectral region and that higher energies in the near-infrared must be accessed to observe these bands (Ferraro and Fink 1977).

Table 5.1: Summary of the major mid-infrared absorption features of H₂S ice (and of some isotopologues). Band peak positions for selected ices investigated in this study (amorphous ice at 20 K and crystalline ice at 70 K) are also included for comparative purposes.

Mode	Assignment	Band Position (cm ⁻¹)								This Work	
		Reference 1	Reference 2	Reference 3	Reference 4	Reference 5	Reference 6	Reference 7	Reference 8	Amorphous	Crystalline
ν _s	¹ H ₂ ³² S	2548	-	-	-	-	-	-	2548	2551.0	-
	² H ₂ ³² S	1853	-	-	-	-	-	-	-	-	-
ν ₁	¹ H ₂ ³² S (A _{2u})	-	2525	2523	2523	2523	2526	2523.5	-	-	2524.5
	¹ H ₂ ³² S (E _u)	-	2536	2532	2532	2532	2535	2533.5	-	-	2535.7
	² H ₂ ³² S (A _{2u})	-	1832	1835	1835	-	-	1832.0	-	-	-
	² H ₂ ³² S (E _u)	-	1840	1843	1843	-	-	1840.0	-	-	-
ν ₂	¹ H ₂ ³² S	1168	-	-	-	-	-	-	1168	-	-
	¹ H ₂ ³² S (A _{2u})	-	1169	1171	1171	1171	1169	1170.0	-	-	1168.8
	¹ H ₂ ³² S (E _u)	-	1184	1186	1186	1186	1184	1185.0	-	-	1183.9
	¹ H ² H ³² S	-	-	1026	-	-	-	1028.0	-	-	-
	² H ₂ ³² S (A _{2u})	-	846	847	847	-	-	846.0	-	-	-
	² H ₂ ³² S (E _u)	846	856	857	857	-	-	856.5	-	-	-
	² H ₂ ³² S	-	860	-	-	-	-	-	-	-	-
ν ₃	¹ H ₂ ³² S	-	2548	2544	2544	2544	2547	2545.0	-	-	2545.7
	² H ₂ ³² S	-	1852	1854	1854	-	-	1854.0	-	-	-
ν _s + ν ₂	¹ H ₂ ³² S	3704	-	-	-	-	-	-	-	3712.8	-
	² H ₂ ³² S	2693	-	-	-	-	-	-	-	-	-
ν _s + ν _R	¹ H ₂ ³² S	2715	-	-	-	-	-	-	-	-	-
ν _s + ν _T	¹ H ₂ ³² S	2642	-	-	-	-	-	-	-	2635.7	-
	² H ₂ ³² S	1942	-	-	-	-	-	-	-	-	-
ν ₁ + ν ₂	¹ H ₂ ³² S	-	3682	-	-	-	3683	-	-	-	3694.5
	² H ₂ ³² S	-	2671	-	-	-	-	-	-	-	-
ν ₂ + ν ₃	¹ H ₂ ³² S	-	3694	-	-	-	3695	-	-	-	-
	² H ₂ ³² S	-	2687	-	-	-	-	-	-	-	-
ν ₃ + ν _R	¹ H ₂ ³² S	-	2722	-	-	-	2720	-	-	-	-
ν ₃ + ν _T	¹ H ₂ ³² S	-	2636	-	-	-	2635	-	-	-	2628.1
	² H ₂ ³² S	-	1938	-	-	-	-	-	-	-	-

Reference 1: Fathe *et al.* (2006) for an amorphous ice at 10 K

Reference 2: Fathe *et al.* (2006) for a crystalline ice at 70 K

Reference 3: Reding and Hornig (1957) for a crystalline ice at 63 K

Reference 4: Miller and Leroi (1968) for a crystalline ice at 80 K

Reference 5: Ferraro and Fink (1977) for a crystalline ice at 62 K

Reference 6: Ferraro *et al.* (1980) for a crystalline ice at 89 K

Reference 7: Anderson *et al.* (1977) for a crystalline ice at 18 K

Reference 8: Hudson and Gerakines (2018) for an amorphous ice at 16 K

The mid-infrared spectra of mixed H₂S:H₂O ices have also been investigated in laboratory experiments (Moore *et al.* 2007, Jiménez-Escobar and Muñoz Caro 2011, Oba *et al.* 2018). The analysis of these spectra is somewhat challenging, due to the significantly lower cross-sections of the H₂S infrared modes compared to those of H₂O, as well as the fact that several of the H₂S vibrational modes coincide with the strong H₂O combination and overtone bands. Therefore, otherwise prominent H₂S absorption features may be difficult to detect in dilute H₂S:H₂O mixed ices: for instance, Moore *et al.* (2007) described the spectrum of a 5 µm-thick 1:30 H₂S:H₂O mixed ice at 86 K as being dominated by the broad absorption features of amorphous H₂O. Nevertheless, it is possible to extract quantitative information from such spectra. For example, Jiménez-Escobar and Muñoz Caro (2011) noted that, when trapped within a matrix of solid H₂O at 7 K, the position of the H₂S ν_s band does not vary compared to pure H₂S; however, its band profile does change and a significant increase in the band broadness occurs with its full-width at half-maximum (FWHM) almost doubling.

5.2.2 Mid-Infrared Spectroscopy of SO₂ Ices

The low temperature mid-infrared spectroscopy of condensed SO₂ (Fig. 5.2) was studied by Schriver-Mazzuoli *et al.* (2003b), who have arguably provided the most detailed spectroscopic analysis of this ice to date. In the condensed phase, amorphous SO₂ presents three distinct fundamental absorption bands associated with the symmetric stretching (ν_1), bending (ν_2), and asymmetric stretching (ν_3) modes respectively located at 1145.8, 520.1, and 1315.5 cm⁻¹ at 30 K (Schriver-Mazzuoli *et al.* 2003b). These values match fairly well with those reported by older studies (Table 5.2). Thermal annealing of an amorphous SO₂ ice induces its crystallisation at temperatures above 70 K, resulting in the visible narrowing of the ν_1 and ν_3 bands and the development of band sub-structures attributable to various SO₂ isotopologues and LO-TO splitting³⁴ of the ³²S¹⁶O₂ bands (Barbe *et al.* 1971, Brooker and Chen 1991, Schriver-Mazzuoli *et al.* 2003b). The presence of a number of weaker higher frequency combination and overtone bands (Table 5.2) was reported by Schmitt *et al.* (1995) and Nash and Betts (1995).

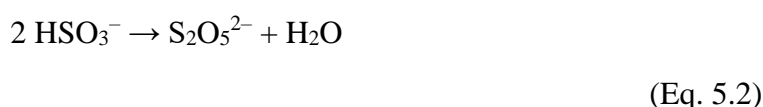
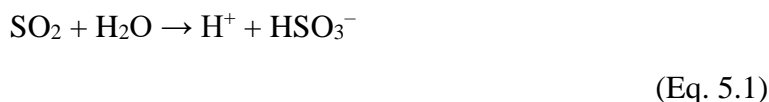
The matrix-isolation spectroscopy of SO₂ diluted in a number of infrared inactive species (e.g., N₂ and Ar) has also been carried out with the aim of determining the structure of the dimer (Wierzejewska-Hnat *et al.* 1994, Schriver-Mazzuoli *et al.* 1995). From the perspective of molecular astrophysics, however, the most relevant ice mixture containing SO₂ is that also containing H₂O due to the cosmic ubiquity of the latter species (Öberg 2016). Schriver-Mazzuoli *et al.* (2003b) reported the presence of two absorption bands at 3627.6 and 3553.0 cm⁻¹ in a 10:1 SO₂:H₂O ice which they attributed to the presence of (SO₂)_x(H₂O)_y aggregates not trapped in the SO₂ lattice that possibly arose as a result of the heterogeneous freezing of the condensing gas mixture. This identification complemented that of Salama *et al.* (1990), who observed two bands at about 3623 and 3559 cm⁻¹ in H₂O:H₂S:SO₂ ice mixtures ranging in composition from 1:3:100 to 1:30:1000.

Although these results are certainly of academic interest, spectroscopic measurements of SO₂:H₂O ices richer in H₂O are likely to be of greater relevance to interstellar and Solar

³⁴ Phonons may result from long-range collective vibrations in a solid lattice. Phonons are quantised vibrations in which lattice molecules vibrate at a single frequency. Optical phonons occur when molecules are moving out of phase within the lattice, and may propagate either parallel (longitudinal optical; LO) or perpendicular (transverse optical; TO) to the direction of the incident infrared field. This is manifested as a splitting of a number of infrared absorption bands.

System chemistry. Such ices were studied by Schriver-Mazzuoli *et al.* (2003b), who showed that a reasonably intense absorption band (at least, compared to the stretching modes of H₂O) exists at 3609.7 cm⁻¹ in a 1:5 SO₂:H₂O ice at 15 K and attributed this to the formation of hydrogen bonds between SO₂ and H₂O molecules. This feature was also observed at 3609.2 cm⁻¹ in the validation experiments performed for the ICA apparatus (Fig. 4.12), for which a 5:3 SO₂:H₂O ice deposited at 20 K was studied.

Furthermore, as has already been described in Chapters 1 and 4, the thermal annealing of a mixed SO₂:H₂O ice initiates a cryogenic thermal reaction which results in the step-wise conversion of SO₂ to HSO₃⁻ and then to S₂O₅²⁻ (Kaňuchová *et al.* 2017):



In the presence of oxidants such as O₃ or H₂O₂, oxidation of the sulphur takes place to yield HSO₄⁻ and SO₄²⁻ (Loeffler and Hudson 2010, Loeffler and Hudson 2013, Loeffler and Hudson 2015, Loeffler and Hudson 2016). The oxidation of SO₂ to SO₃ may be induced as a result of the irradiation of the pure ice by ultraviolet photons, ions or electrons (Moore 1984, Schriver-Mazzuoli *et al.* 2003a, Garozzo *et al.* 2008, de Souza Bonfim *et al.* 2017), as discussed in Chapters 1 and 2. When similar irradiations of mixed SO₂:H₂O ices are performed, various oxidised forms of sulphur (such as HSO₃⁻, HSO₄⁻, SO₄²⁻, SO₂²⁻, and polymeric SO₃ chains) are yielded as products (Schriver-Mazzuoli *et al.* 2003a, Moore *et al.* 2007, Kaňuchová *et al.* 2017, Hodyss *et al.* 2019).

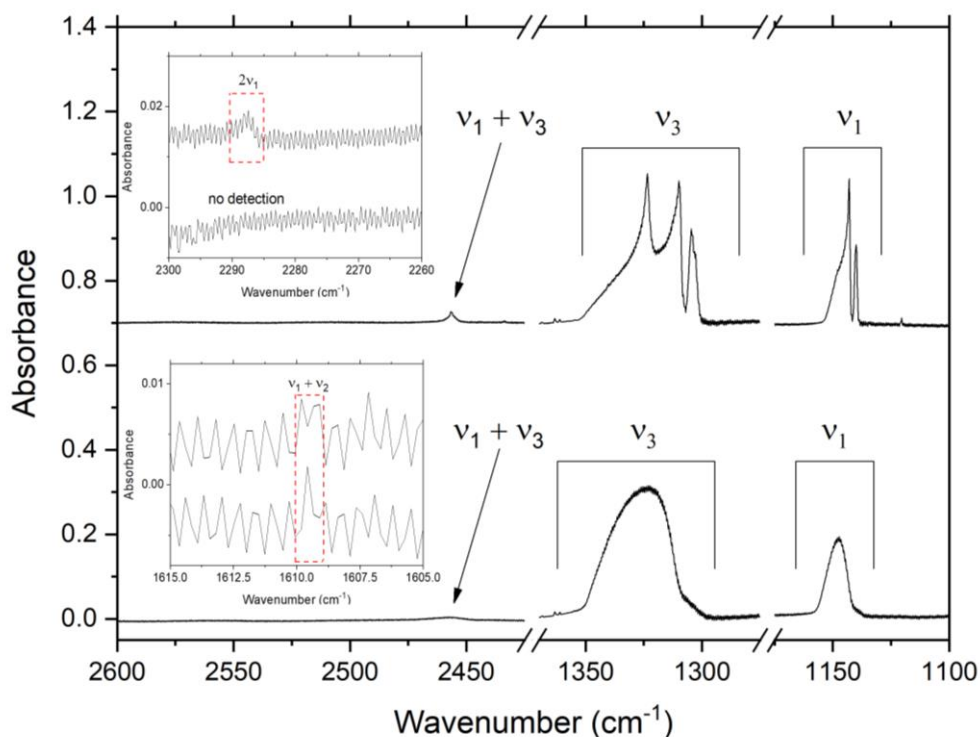


Fig. 5.2: Mid-infrared spectra of amorphous (*below*) and crystalline (*above*) SO₂ ices deposited at temperatures of 20 and 100 K, respectively. The spectra, collected at 0.5 cm⁻¹ resolution, show the strong ν₁, ν₃, and ν₁ + ν₃ absorption bands along with the weaker ν₁ + ν₂ and 2ν₁ modes (insets). Note that the spectra are vertically offset for clarity. The estimated thicknesses of the amorphous and crystalline ices were 0.48 and 0.31 μm, respectively.

Table 5.2: Summary of the major mid-infrared absorption features of SO₂ ice (and of some isotopologues). Band peak positions for selected ices investigated in this study (amorphous ice at 20 K and crystalline ice at 100 K) are also included for comparative purposes.

Mode	Assignment	Band Position (cm ⁻¹)								This Work	
		Reference 1	Reference 2	Reference 3	Reference 4	Reference 5	Reference 6	Reference 7	Reference 8	Amorphous	Crystalline
v ₁	³² S ¹⁸ O ¹⁶ O	-	-	-	-	1122	1121	1120.6	1121.5	-	1120.5
	³⁴ S ¹⁶ O ₂	-	1140.1	1140.5	1140.0	1141	1140	1140.4	-	-	1140.0
	³² S ¹⁶ O ₂ A ₁ (TO)	1145.8	1142.8	1147.0	1143.0	1144	1144	1144.8	-	1147.5	1142.8
	³² S ¹⁶ O ₂ A ₁ (LO)	-	-	1160.0	1150.0	1148	-	-	1148.0	-	1149.1
v ₂	³² S ¹⁸ O ¹⁶ O	-	-	-	-	-	-	514.3	-	-	-
	³⁴ S ¹⁶ O ₂	-	-	517.0	-	-	517	-	-	-	-
	³² S ¹⁶ O ₂ A ₁ (TO)	520.1	520.8	525.0	522.7	524	521	522.0	525.4	-	-
	³² S ¹⁶ O ₂ A ₁ (LO)	-	-	546.0	530.0	542	528	-	533.1	-	-
v ₃	³⁶ S ¹⁶ O ₂	-	-	-	-	-	-	1288.0	-	-	-
	³² S ¹⁸ O ¹⁶ O	-	1302.8	-	1302.8	-	-	-	-	-	1302.8
	³⁴ S ¹⁶ O ₂	-	1304.5	1304.0	1304.3	1304	1303	1302.8	1305.8	-	1304.8
	³² S ¹⁶ O ₂ B ₁ (TO)	1315.5	1310.8	1313.0	1310.1	1312	1310	1315.2	1316.4	-	1311.9
	³² S ¹⁶ O ₂ B ₂ (TO)	-	1321.6	1327.0	1323.3	1324	1322	1323.2	1329.6	1323.7	1323.3
	³² S ¹⁶ O ₂ B ₂ (LO)	-	-	1358.0	1345.0	1341	1334	-	-	-	1342.4
v ₁ + v ₂	³² S ¹⁶ O ₂	1607.6	1611.3	-	-	-	-	-	-	1609.7	1609.7
v ₁ + v ₃	³⁴ S ¹⁶ O ₂	-	2433.7	-	2433.7	-	2432	2433.5	2435.5	-	2433.8
	³² S ¹⁶ O ₂	2455.8	2456.2	2457.4	2456.2	-	2455	2456.5	2456.7	2457.4	2456.7
v ₂ + v ₃		-	-	-	-	-	-	-	1850.1	-	-
2v ₁ + v ₃	³² S ¹⁶ O ₂	-	3584.5	-	-	-	-	-	-	-	-
2v ₁	³⁴ S ¹⁶ O ₂	-	2273.9	-	2273.9	-	-	2274.3	-	-	-
	³² S ¹⁶ O ₂	2288.4	2287.4	2288.2	2287.4	-	2287	2288.0	2289.7	-	2287.4

Reference 1: Schriver-Mazzuoli *et al.* (2003b) for an amorphous ice at 30 K

Reference 2: Schriver-Mazzuoli *et al.* (2003b) for a crystalline ice at 90 K

Reference 3: Anderson and Campbell (1977) for a crystalline ice at 20 K

Reference 4: Khanna *et al.* (1988) for a crystalline ice at 90 K

Reference 5: Anderson and Savoie (1965) for a crystalline ice at 77 K

Reference 6: Giguère and Falk (1956) for a crystalline ice at 98 K

Reference 7: Barbe *et al.* (1971) for a crystalline ice at 77 K

Reference 8: Nash and Betts (1995) for a crystalline ice at 80 K

5.3 Experimental Methodology

The mid-infrared spectra of the pure H₂S and SO₂ ices and their mixtures with H₂O were investigated using the ICA. The pure ices were prepared *via* the background deposition of the relevant gases by first introducing the gas (H₂S = 99.5%; SO₂ = 99.8%; both Linde) into the dosing line before leaking it into the main chamber at a pressure of a few 10⁻⁶ mbar, thus allowing the ice to form as a result of gas condensation on the ZnSe substrate which had been pre-cooled to the desired temperature. Once the desired ice had been prepared, it was thermally annealed at a rate of 2 K min⁻¹ with mid-infrared spectra (0.5 cm⁻¹ resolution; 256 scans) acquired at 10 K intervals until complete sublimation of the ice was recorded.

To deposit the mixed H₂S:H₂O and SO₂:H₂O ices, a glass vial of H₂O was attached to the dosing line and the liquid was de-gassed using several cycles of the standard freeze-pump-thaw technique; after which H₂O vapour and either H₂S or SO₂ gas were introduced into the dosing line in the desired stoichiometric ratio. The mixed gases were then dosed into the main chamber at a pressure of a few 10⁻⁶ mbar to allow for their co-deposition at 20 K. The thermal annealing of the mixed ices was similar to that of the pure ices, with mid-infrared spectra being collected at 10 K intervals until sublimation of the ice was observed.

As described in detail in Chapter 4, the amount of ice deposited in a given experiment may be quantitatively assessed *via* the mid-infrared spectra collected just after the deposition of the ice prior to commencing the thermal annealing process. The molecular column density of a deposited species N is given as:

$$N = 2.303 \times \frac{P_a}{A_s} \quad (\text{Eq. 5.3})$$

where P_a is the peak area of a characteristic absorption band and A_s is the integrated band strength constant for that band. Knowing the deposited column density, it is possible to calculate the thickness of the ice (or, in the case of a mixed ice, the contribution of a particular component to the total thickness) d through the equation:

$$d = 10^4 \times \frac{Nm}{\rho N_A} \quad (\text{Eq. 5.4})$$

where m is the molecular mass, ρ is the mass density of the ice, and N_A is the Avogadro constant. A list of ice densities and integrated band strength constants used throughout this study is given in Table 5.3, while a summary of all the experiments performed as part of this study is given in Table 5.4. It should be noted that the work of Yarnall and Hudson (2022a) demonstrated that the integrated band strength constants of amorphous H₂S and SO₂ intermixed with H₂O are not significantly different to those of the pure ices, and may thus be used equally well in experiments considering either pure or mixed ices.

Table 5.3: Ice densities (ρ) and integrated band strength constants (A_s) used in this study.

Species	A_s (10 ⁻¹⁷ cm molecule ⁻¹)	ρ (g cm ⁻³)	References
SO ₂	0.73 (v ₁) and 4.20 (v ₃)	1.395 (amor.) and 1.893 (crys.)	Yarnall and Hudson (2022a, 2022b)
H ₂ S	1.69 (v _s)	0.944 (amor.) and 1.224 (crys.)	Yarnall and Hudson (2022a, 2022b)
H ₂ O	20.00 (v _s)	0.940	Gerakines <i>et al.</i> (1995)

Table 5.4: Summary of the thermal annealing experiments performed in this study, including information on the deposition temperature of the ices ($T_{\text{deposition}}$) and their column densities (N) and thicknesses (d).

Ice	Experiment	$T_{\text{deposition}}$ (K)	N (10^{17} molecules cm^{-2})	d (μm)
H ₂ S	1	20	6.25	0.48
	2	40	5.71	0.43
	3	70	6.34	0.36
SO ₂	4	20	5.58	0.31
	5	40	15.30	0.92
	6	70	9.54	0.57
	7	100	11.56	0.69
H ₂ S:H ₂ O (1:7)	8	20	1.41:10.32	0.41
SO ₂ :H ₂ O (1:11)	9	20	1.60:18.61	0.71

5.4 Mid-Infrared Spectroscopic Characterisations

5.4.1 Thermal Annealing of Pure H₂S Ices

As demonstrated in Fig. 5.1, the most prominent mid-infrared absorption band of amorphous H₂S is the ν_s band located at about 2551 cm^{-1} , which is split into a number of distinct and individual sub-structures in the crystalline phase corresponding to the ν_1 (A_{2u}), ν_1 (E_u), and ν_3 vibrational modes. A much weaker ν_2 mode was also observed at lower wavenumbers of about 1169 cm^{-1} . A few higher energy combination bands were also observed (Table 5.1), but proved too weak for a reliable spectroscopic analysis to be performed. As such, the following discussion is dedicated to the evolution of the ν_s and ν_2 bands during the thermal annealing of H₂S ices deposited at different temperatures.

Fig. 5.3 depicts the stretching modes of H₂S ices deposited at 20, 40, and 70 K and annealed to sublimation. For the ice deposited at 20 K, the ν_s band initially presents as a broad, featureless, and asymmetric absorption feature that peaks at 2551.0 cm^{-1} . However, upon thermal annealing, the contribution of individual sub-structures becomes more apparent. At 30 K, the band peak remains at 2551.0 cm^{-1} but a second peak is visible at 2526.3 cm^{-1} : these bands respectively correspond to the ν_3 and ν_1 (A_{2u}) modes. Further thermal annealing to 50 K results in the appearance of a third peak at 2536.1 cm^{-1} , which is attributed to the ν_1 (E_u) band. Despite emerging as individual sub-structures, these three absorption features remain relatively broad at 50 K. However, thermal annealing to 60 K and above results in the splitting of the ν_3 and the ν_1 (E_u) bands. As explained earlier, this splitting is the result of the existence of two unique sulphur atoms but three unique S–H bonds in the crystalline H₂S unit cell (Fitch and Cockcroft 1990, Cockcroft and Fitch 1990, Zeng and Anderson 2001). At 80 K, the absorbance of the composite band decreases slightly and the ν_3 , ν_1 (E_u), and ν_1 (A_{2u}) bands respectively blue-shift by 0.5, 0.8, and 1.4 cm^{-1} compared to their positions at 70 K. This is likely due to minor sublimation of the ice to the gas phase at this higher temperature, which causes changes in the structure of the ice due to bulk or surface desorption. Full sublimation was recorded by 90 K.

The appearances of the ν_3 , ν_1 (E_u), and ν_1 (A_{2u}) bands for the ice deposited at 40 K are somewhat different to those observed in the H₂S ice deposited at 20 K and subsequently thermally annealed to 40 K (Fig. 5.3). Firstly, the bands in the former ice are well-defined and have undergone visible splitting, whilst those in the latter ice are still broad and have yet

to undergo any splitting of the band peaks. This indicates that the deposition of a H₂S ice at 40 K results in the formation of a more structurally ordered (i.e., crystalline) solid than does the deposition of the ice at 20 K followed by thermal annealing to 40 K. It should be noted, however, that upon thermal annealing of the ice deposited at 40 K to higher temperatures, the absorbance of these bands increases thus suggesting that the deposited ice is not wholly crystalline and undergoes further structural re-organisation at higher temperatures. Once again, a slight decrease in absorbance and a blue-shift in the band positions (1.1, 0.8, and 1.1 cm⁻¹ for the ν_3 , ν_1 (E_u), and ν_1 (A_{2u}) bands, respectively) were observed at 80 K due to minor losses to sublimation. The ice was recorded to have fully desorbed from the deposition substrate by 90 K.

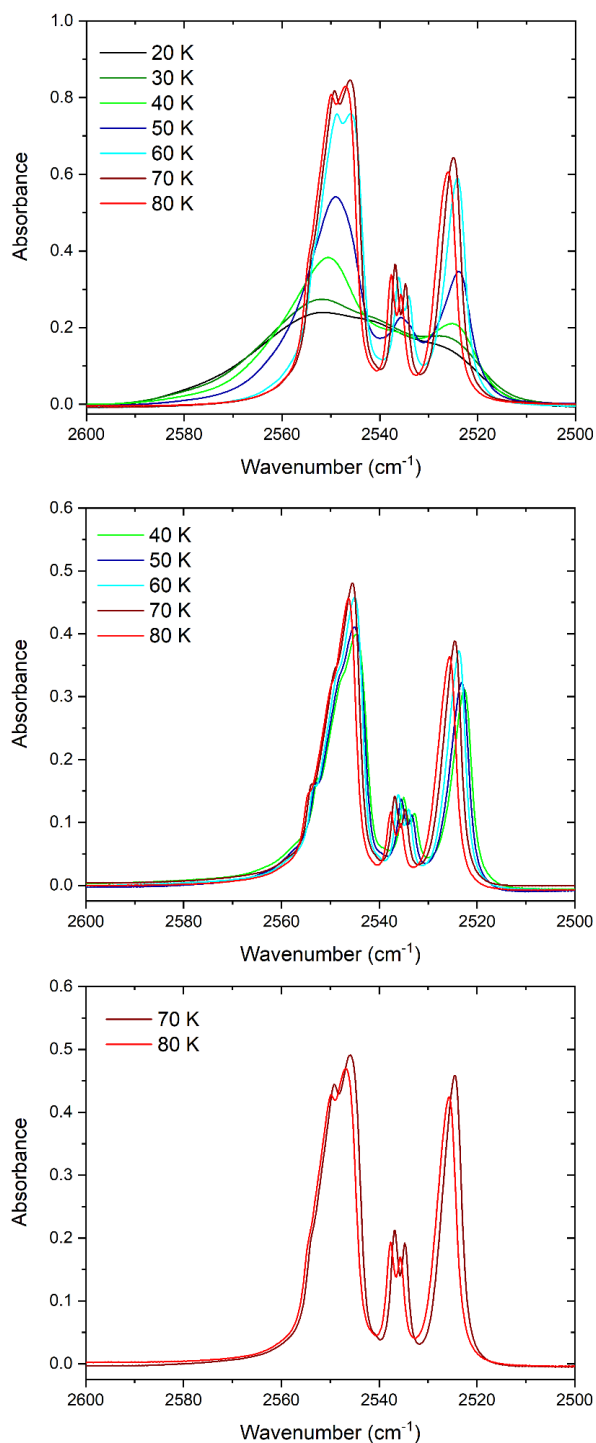


Fig. 5.3: Thermal evolution of the H₂S ν_s band for ices deposited at 20, 40, and 70 K. The band undergoes splitting to its individual ν_3 , ν_1 (E_u), and ν_1 (A_{2u}) bands under the influence of thermal annealing.

It is important to note the appearance of a small shoulder on the larger ν_3 band whose exact position varies between 2552.7 and 2554.6 cm^{-1} during the thermal annealing of the H_2S ice deposited at 40 K. The precise nature of this shoulder is uncertain, as it is not known whether this shoulder is merely the result of more extensive splitting of the ν_3 mode, is caused by a different vibrational mode altogether (perhaps one due to an isotopologue), or is an unaccounted-for artefact produced during the rendering of the spectroscopic data. This small shoulder is also apparent in the spectra of the thermally annealed H_2S ices deposited at 20 or 70 K (Fig. 5.3), although it is significantly weaker in these cases. No further attempt to characterise this shoulder has been made, but it is suggested that a future dedicated study should investigate this matter.

Lastly, the H_2S ice deposited at 70 K appears to be fully crystalline, due to the clearly visible emergence of the individual band sub-structures upon deposition as well as the clear splitting each individual band undergoes. Upon thermal annealing to 80 K, blue-shifts of 0.7, 1.0, and 1.0 cm^{-1} are respectively observed in the peak positions of the ν_3 , ν_1 (E_u), and ν_1 (A_{2u}) bands; similar to the blue-shifts reported for the ices deposited at 20 and 40 K. At higher temperatures, the ice efficiently sublimates and has totally desorbed from the deposition substrate by 90 K.

The evolution of the ν_2 mode of H_2S ices deposited at 20, 40, and 70 K and subsequently thermally annealed to sublimation is presented in Fig. 5.4. For the ice deposited at 20 K, it is possible to note that no ν_2 mode is visible either upon deposition nor upon thermal annealing to 30 K. At 40 K, a weak and broad absorption feature attributable to the ν_2 (A_{2u}) mode begins to emerge against the background at 1169.0 cm^{-1} . By 50 K, this absorption mode is clearly visible and at 60 K, a second band attributable to the ν_2 (E_u) mode emerges at 1184.1 cm^{-1} . These bands remain visible in the spectrum upon further thermal annealing until sublimation of the ice occurs at around 90 K. Such findings complement the previous observations made on the thermal evolution of the ν_s band and suggest that significant restructuring of the solid phase occurs at about 40 K, although at this temperature the ice is still likely to be largely amorphous as evidenced by the lack of a ν_2 (E_u) mode in Fig. 5.4. At 50 K, the ice has adopted a significantly more structured solid phase and by a temperature of 60 K, the ice is likely to be largely crystalline as indicated by the extensive band splitting of the ν_1 (E_u) and ν_3 modes along with the clear appearance of the ν_2 (E_u) mode at this temperature.

Interestingly, when deposited at 40 K, the H_2S ice clearly exhibits both the ν_2 (A_{2u}) mode and the ν_2 (E_u) mode (Fig. 5.4), thus contrastingly strongly with the mid-infrared spectral appearance of the ice deposited at 20 K and thermally annealed to 40 K. When deposited at 40 K, the H_2S ice appears to be already extensively structurally ordered and thus largely crystalline: this is evidenced by the fact that not only are the ν_2 (A_{2u}) and the ν_2 (E_u) modes both present and clearly identifiable, but also by the fact that the ν_3 , ν_1 (E_u), and ν_1 (A_{2u}) bands are also identifiable and have undergone splitting. Therefore, it is evident that a more crystalline H_2S solid may be achieved by depositing the ice at a given temperature than would otherwise be achieved by depositing it at a lower temperature and subsequently performing thermal annealing. Lastly, it is important to note that, as implied by the appearances of the ν_3 , ν_1 (E_u), and ν_1 (A_{2u}) bands, the ν_2 (A_{2u}) and the ν_2 (E_u) bands also suggest that the H_2S ice deposited at 70 K is likely wholly crystalline.

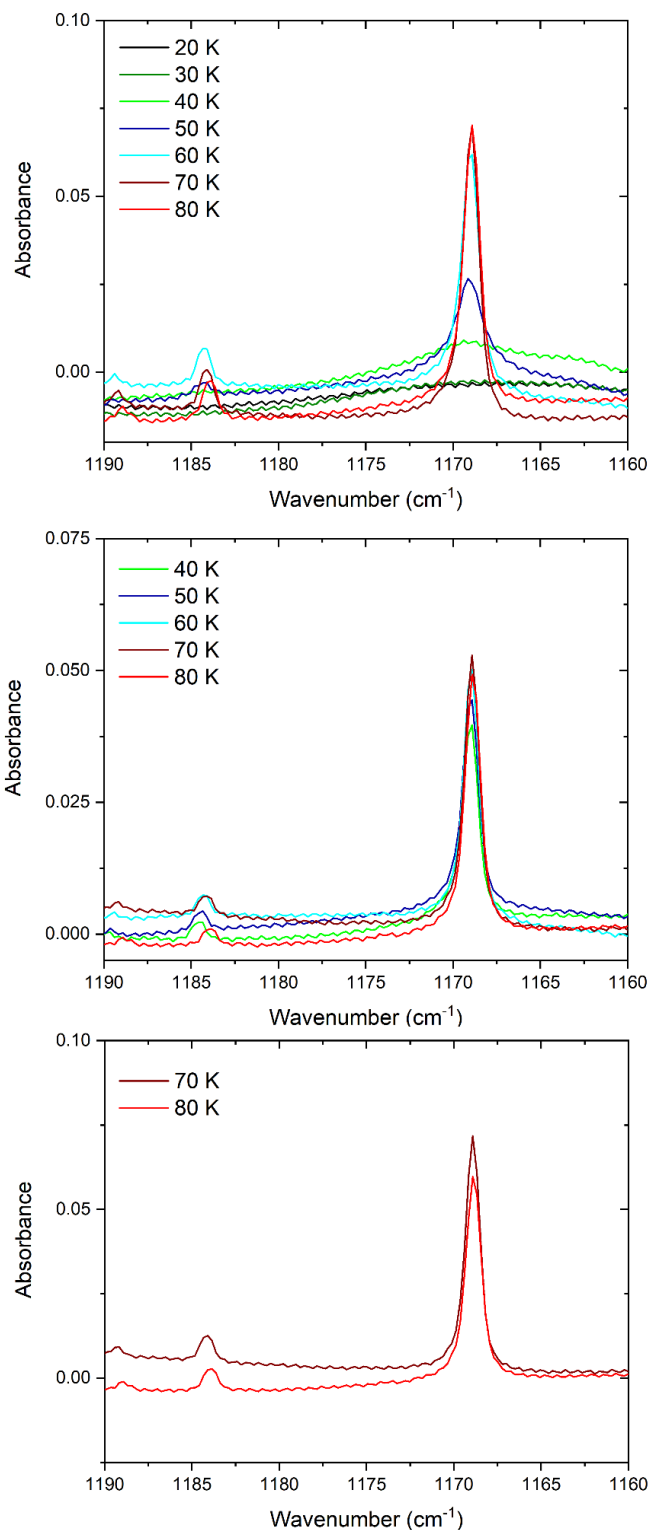


Fig. 5.4: Thermal evolution of the H₂S ν_2 band for ices deposited at 20, 40, and 70 K. The ν_2 (A_{2u}) and ν_2 (E_u) bands become more conspicuous under the influence of thermal annealing.

To further quantify the analysis of the H₂S mid-infrared spectra presented in Figs. 5.3 and 5.4, an assessment of the changes in the normalised peak area of the stretching modes (including all higher temperature emergent sub-structures) induced by thermal annealing has been performed. This analysis is summarised in Fig. 5.5. Traditionally, the broadness of a mid-infrared absorption band has been gauged through its FWHM; however, the quantification of this parameter as well as changes in its value as a result of thermal annealing

of the ices considered in this study is complicated by the many sub-structures that emerge as a result of the structural reorganisation and crystallisation of the ices which would require the fitting of multiple Gaussian curves to measure, thus potentially introducing large uncertainties. The analysis of the normalised peak areas that have been corrected using a linear baseline thus circumvents this problem entirely and may still provide useful quantitative information to observational astrochemists interested in the thermal histories of various astrophysical environments. It should be noted that no attempt was made to perform such an analysis for the ν_2 bands due to their small absorbance values, which would have resulted in significant uncertainties in the measured band peak areas.

Different trends were observed for the variations in the stretching mode band peak areas of the ices deposited at 20, 40, and 70 K. In the case of the ice deposited at 20 K, it is clear that thermal annealing results in the growth of the normalised band peak area as the ice undergoes restructuring to a more crystalline phase. This band peak area reaches a maximum of over 30% greater than that of the initially deposited ice at a temperature of 60 K, which is sustained at 70 K, before declining slightly at 80 K due to minor losses caused by sublimation. The trend observed for the ice deposited at 40 K is more difficult to explain. At first, it is perhaps intuitive to suggest that the band peak area declines slightly upon thermal annealing to 50 K before recovering to its original peak area at 60 K and subsequently declining further at 70 and 80 K. Although this may very well be the observed trend, it is important to note that the measured band peak area does not vary by more than 9% of the original normalised value and so the observed scatter in the data may be due to uncertainties associated with the measurement of the band peak area. Lastly, it is possible to note that the band peak area of the ice deposited at 70 K appears to decrease by approximately 10% upon thermal annealing to 80 K, which could be indicative of minor sublimation of the ice to the gas phase.

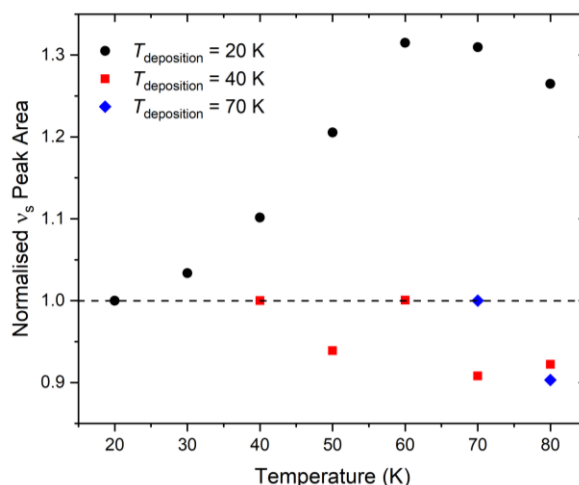


Fig. 5.5: Evolution of the H_2S ν_s normalised band peak areas for the ices at 20, 40, and 70 K during their thermal annealing. The limits of integration during measurement were as follows: $\nu_s = 2610\text{-}2500\text{ cm}^{-1}$.

5.4.2 Thermal Annealing of Pure SO_2 Ices

As shown in Fig. 5.2, the most prominent mid-infrared absorption features of SO_2 ice are the symmetric (ν_1) and asymmetric (ν_3) stretching fundamental bands, along with the $\nu_1 + \nu_3$ combination band. These bands are therefore the most relevant from the perspective of observational astrochemistry, and thus the spectroscopic analysis presented in this subsection will focus on these absorption bands. Unfortunately, the ν_2 mode is located beyond

the spectral range of the ICA set-up at about 520 cm^{-1} , and thus it is not possible to carry out any analysis on this absorption band. A dedicated future study on the influence of temperature on the appearance and profile of the $\text{SO}_2\text{ } \nu_2$ mode using alternative instrumentation is thus warranted.

The evolution of the appearance of the ν_3 mode as a result of the thermal processing of pure SO_2 ices deposited at 20, 40, 70, and 100 K is shown in Fig. 5.6. For the ice deposited at 20 K, the band initially presents itself as a broad quasi-symmetric structure which does not vary much in its profile upon thermal annealing to 60 K. Upon warming to 70 K, the majority of the band remains essentially broad and featureless but does begin to show signs of structural ordering in the form of a distinct sub-structure at 1304.8 cm^{-1} attributable to the $^{34}\text{S}^{16}\text{O}_2$ isotopologue (Table 5.2). At 80 K, the absorbance of this sub-structure increases and other, higher energy sub-structures also begin to emerge from the broad band as a result of more extensive crystallisation of the ice. In particular, two intense features at 1311.9 and 1323.3 cm^{-1} become visible, respectively attributed to the $^{32}\text{S}^{16}\text{O}_2$ B_1 (TO) and the $^{32}\text{S}^{16}\text{O}_2$ B_2 (TO) modes. Further annealing to 90 K causes all three bands to reach their maximum absorbance value, which largely persists to 100 K at which temperature a small band at 1302.6 cm^{-1} attributed to the $^{32}\text{S}^{18}\text{O}^{16}\text{O}$ isotopologue could be identified.

The ice deposited at 40 K exhibits a similar trend upon its thermal annealing (Fig. 5.6), although a number of subtle differences are evident. For instance, an increase in the absorbance of the broad component of the band was noted upon warming to 60 K, likely due to the compaction of the initially microporous ice; such a process is known to be induced in an astrophysical ice analogue upon its thermal annealing or its irradiation using ultraviolet photons or charged particles (e.g., Palumbo 2006). Compaction of the SO_2 ice should also have resulted during the thermal annealing of the SO_2 ice deposited at 20 K; however, no significant increase in the absorbance of the broad band was recorded at 60 K. It is speculated that this may have been due to a more gradual compaction of the ice deposited at 20 K over a larger temperature range.

Another difference between the data collected for the ν_3 band of the ices deposited at 20 and 40 K lies in the profile of the band at 70 K. For the former ice, this band was still largely broad and featureless with a small sub-structure due to the $^{34}\text{S}^{16}\text{O}_2$ isotopologue being recorded. However, upon thermal annealing of the SO_2 ice deposited at 40 K to 70 K, the ν_3 band presents a structured profile with intense sub-structures attributable to the $^{32}\text{S}^{16}\text{O}_2$ B_1 (TO) and the $^{32}\text{S}^{16}\text{O}_2$ B_2 (TO) modes, as well as the $^{34}\text{S}^{16}\text{O}_2$ isotopologue, being observed. It is therefore possible to state that the thermal annealing of a SO_2 ice to 70 K results in a more extensive crystallisation if the ice was deposited at 40 K compared to 20 K. Further thermal annealing of the ice deposited at 40 K causes all emergent sub-structures to increase in their absorbances, which peak at 90 K.

Finally, the ν_3 bands of the ices deposited at 70 and 100 K all present profiles containing sub-structures with intensities that do not vary much over the process of thermal annealing. These ices do, however, exhibit more evident bands attributed to the $^{32}\text{S}^{18}\text{O}^{16}\text{O}$ isotopologue at about 1303 cm^{-1} (Fig. 5.6). It should be noted that the transition from the peak of the $^{32}\text{S}^{16}\text{O}_2$ B_2 (TO) mode at 1323 cm^{-1} to the baseline appears to include an emergent shoulder at 1342 cm^{-1} : this is due to the contribution of the $^{32}\text{S}^{16}\text{O}_2$ B_2 (LO) band at this wavenumber. It should be noted that all ices demonstrated a decrease in the peak areas of their sub-structures at 110 K irrespective of their deposition temperature, likely due to some minor sublimation of the ice to the gas phase. Indeed, by the point the deposition substrates were warmed to 120 K, all the SO_2 ice had sublimated.

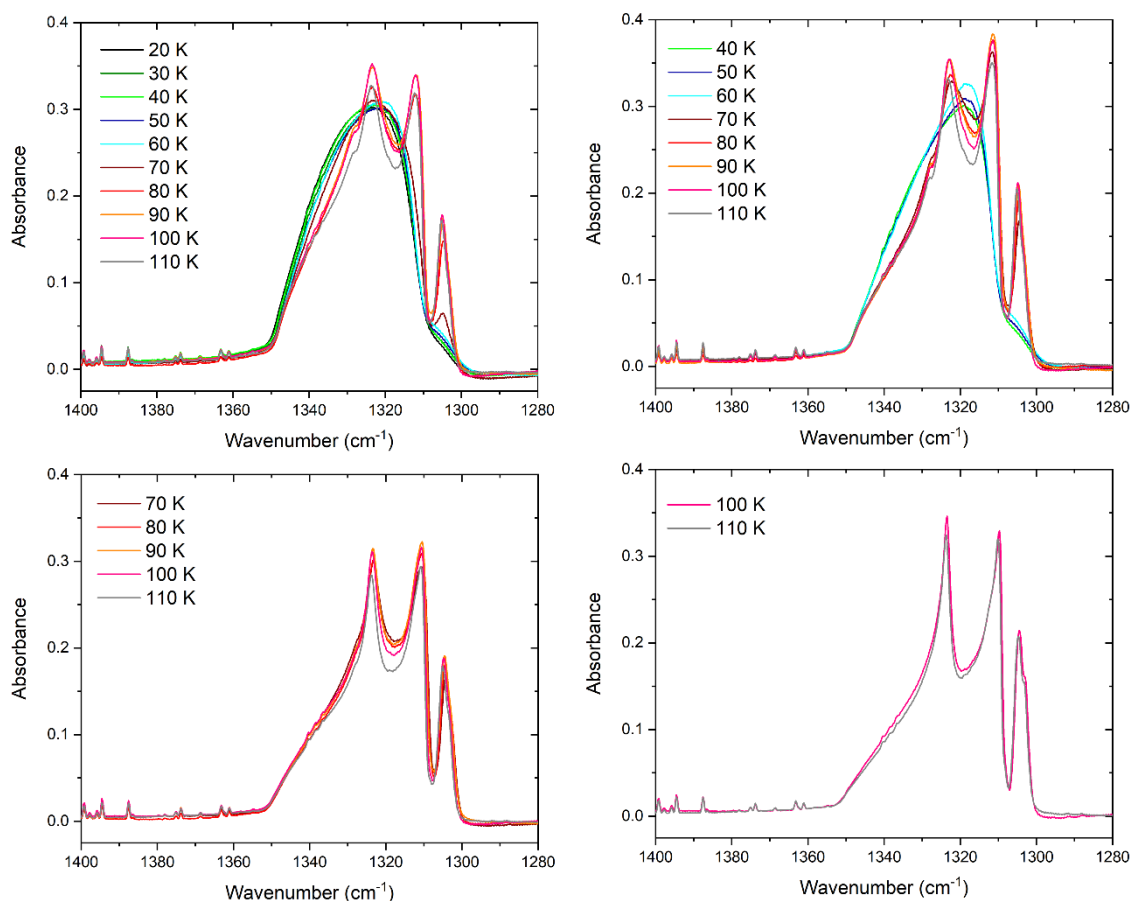


Fig. 5.6: Thermal evolution of the SO_2 ν_3 band for ices deposited at 20, 40, 70, and 100 K. The band splits into a number of component features under the influence of thermal annealing, such as the $^{34}\text{S}^{16}\text{O}_2$, $^{32}\text{S}^{16}\text{O}_2$ B_1 (TO), $^{32}\text{S}^{16}\text{O}_2$ B_2 (TO), $^{32}\text{S}^{18}\text{O}^{16}\text{O}$, and the $^{32}\text{S}^{16}\text{O}_2$ B_2 (LO) ν_3 bands.

The variations in the profile of the ν_1 mode during the thermal annealing of the pure SO_2 ices deposited at 20, 40, 70, and 100 K are given in Fig. 5.7; it is apparent that these variations mirror and complement the spectroscopic findings with regards to the ν_3 band. For example, no significant changes in the band shape or structure were noticed upon thermally annealing the ice deposited at 20 K to 60 K. Once it was warmed to 70 K, however, the emergence of distinct sub-structures attributable to the $^{32}\text{S}^{18}\text{O}^{16}\text{O}$ and $^{34}\text{S}^{16}\text{O}_2$ isotopologues were observed. Moreover, a shift towards lower wavenumbers is apparent in the broader component of the band, indicative of a restructuring of the solid lattice. By 80 K, the ν_1 band appears as several distinct sub-structures which persist upon further thermal annealing. Aside from the sub-structures attributed to the $^{32}\text{S}^{18}\text{O}^{16}\text{O}$ and $^{34}\text{S}^{16}\text{O}_2$ isotopologues, a distinct band with a sharp peak at about 1143 cm^{-1} due to the $^{32}\text{S}^{16}\text{O}_2$ A_1 (TO) mode is present. This band does not sharply decay to the baseline at higher wavenumbers, but rather a shoulder is present at about 1149 cm^{-1} indicative of the contribution from the $^{32}\text{S}^{16}\text{O}_2$ A_1 (LO) mode at this wavenumber.

The ν_1 band of the pure SO_2 ice deposited at 40 K displays a qualitatively similar response to thermal annealing to the ν_3 band: a slight increase in the absorbance of the broad band was also noted on thermal annealing to 60 K, likely due to the same compaction process described previously. Once again, however, the thermal annealing of the SO_2 ice deposited at 40 K to 70 K resulted in a significantly more ordered solid structure than did the analogous

annealing of the SO₂ ice deposited at 20 K, as demonstrated by the emergence of the band contributions from the ³⁶S¹⁸O¹⁶O and ³⁴S¹⁶O₂ isotopologues as well as the ³²S¹⁶O₂ A₁ (TO) and ³²S¹⁶O₂ A₁ (LO) modes. This may therefore be regarded as further evidence of a more complete crystallisation of solid SO₂ thermally annealed to 70 K if it was initially deposited at higher temperatures. The absorbances of all emergent sub-structures continued to increase upon additional thermal annealing to 100 K, and only decreased thereafter due to minor sublimation of the ices. By 120 K, however, the ice had fully desorbed.

Lastly, the ν_1 bands of the SO₂ ices deposited at 70 and 100 K appear to indicate an ice that is, to a large degree, crystalline in structure. The bands themselves are well resolved with all aforementioned sub-structures being clearly identifiable, and do not significantly vary with increased temperatures aside from a small decrease in absorbance at 110 K due to some minor sublimation of the ice (Fig. 5.7). Such observations complement well the trends observed with regards to the ν_3 bands of these ices.

An analysis of the evolution of the weaker $\nu_1 + \nu_3$ combination band as a result of the thermal annealing of pure SO₂ ices deposited at 20, 40, 70, and 100 K has also been performed (Fig. 5.8). This mid-infrared analysis once again complements those findings with regards to the ν_1 and ν_3 fundamental bands. At 20 K, this band appears as a single broad absorption feature which does not change much upon thermal annealing to 60 K. At 70 K, however, the band takes on a narrower profile whose absorbance value increases marginally upon further thermal annealing. The appearance of a satellite band at around 2434 cm⁻¹ is evident at 80 K and is ascribed to the ³⁴S¹⁶O₂ isotopologue.

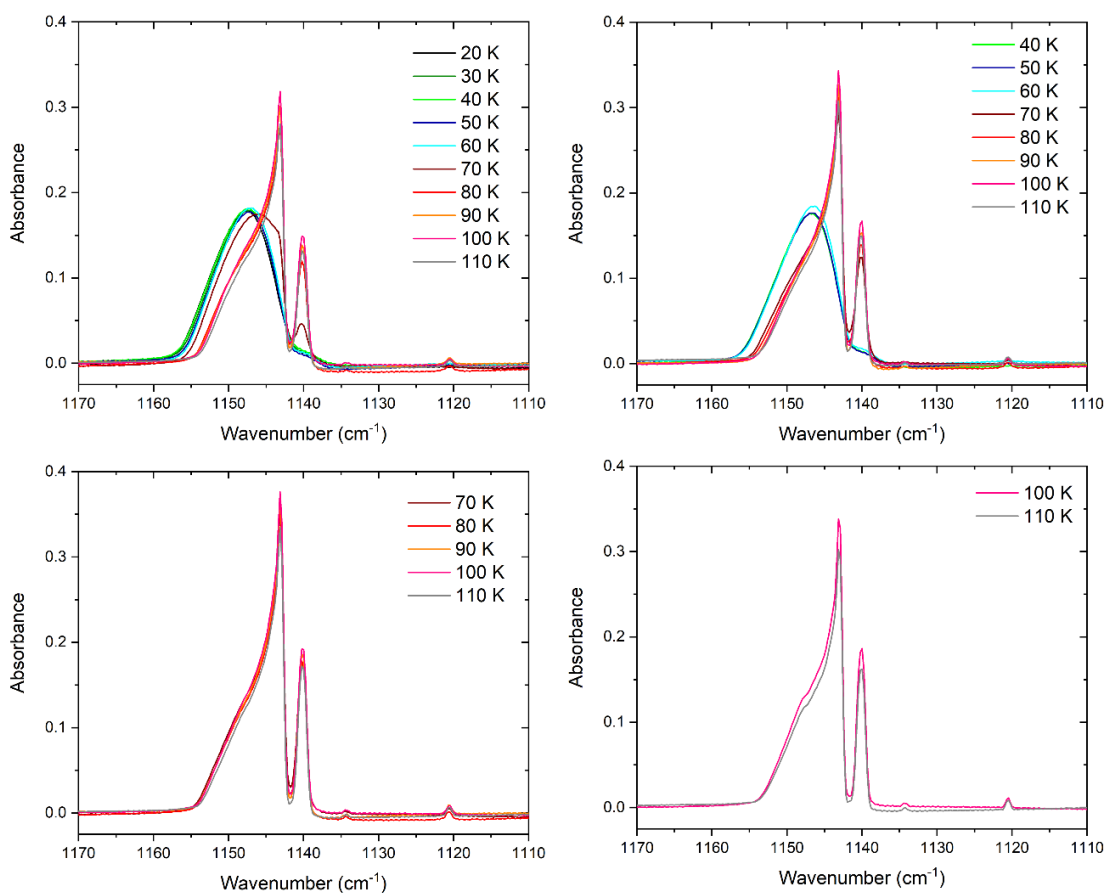


Fig. 5.7: Thermal evolution of the SO₂ ν_1 band for ices deposited at 20, 40, 70, and 100 K. A number of individual contributor bands emerge under the influence of thermal annealing, such as the ³⁶S¹⁸O¹⁶O, ³⁴S¹⁶O₂, ³²S¹⁶O₂ A₁ (TO), and ³²S¹⁶O₂ A₁ (LO) ν_1 bands.

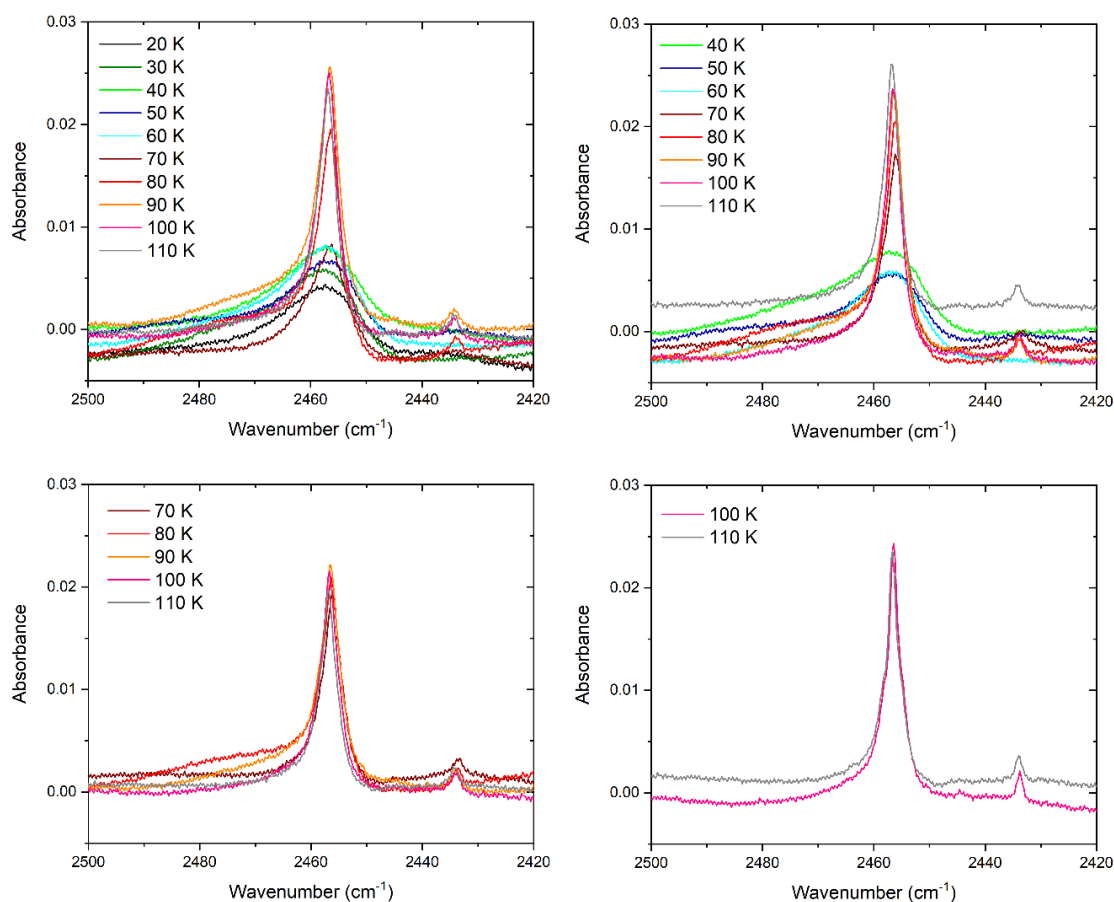


Fig. 5.8: Thermal evolution of the SO_2 $\nu_1 + \nu_3$ band for ices deposited at 20, 40, 70, and 100 K. Thermal annealing results in the emergence of a band attributed to the $^{34}\text{S}^{16}\text{O}_2$ isotopologue.

The $\nu_1 + \nu_3$ combination band of the SO_2 ice deposited at 40 K also follows a similar trend, but the absorbance of the band structure observed at 70 K is greater than in the case of the ice deposited at 20 K, thus further evidencing a more extensive structural ordering of the SO_2 ice at 70 K if it was deposited at 40 K rather than 20 K. Interestingly, however, the satellite band due to $^{34}\text{S}^{16}\text{O}_2$ is not yet fully developed when the ice deposited at 40 K is annealed to 70 K and only becomes appreciably conspicuous at 80 K. This suggests that the ice is likely not wholly crystalline at 70 K, although significant restructuring to a more ordered phase has certainly occurred by this point.

Lastly, the ices deposited at 70 and 100 K exhibit narrow and well-defined $\nu_1 + \nu_3$ combination bands as well as developed and conspicuous satellite bands ascribed to the $^{34}\text{S}^{16}\text{O}_2$ isotopologue. These bands do not significantly change in their absorbance value nor do they radically vary in terms of the appearance of their profile with further thermal annealing and so this suggests that these ices are probably overwhelmingly crystalline in structure. As with all other SO_2 absorption bands investigated in this study, a slight decrease in the $\nu_1 + \nu_3$ combination band absorbance was registered at 110 K due to a small amount of ice sublimation to the gas phase.

The characterisations of the responses of the SO_2 ice ν_1 , ν_3 , and $\nu_1 + \nu_3$ mid-infrared absorption bands to thermal annealing of the ice when deposited at various temperatures that have been described here have demonstrated that, with the exception of the $^{32}\text{S}^{16}\text{O}_2$ A_1 (TO) ν_1 mode (for which an average red-shift of 4.7 cm^{-1} was recorded between 20 and 100 K),

the positions of all bands and their sub-structures remained largely invariant with increasing temperature. Indeed, in most cases, the maximum band peak position shift was much less than 1 cm^{-1} and thus approaches the experimental uncertainty.

As a final analytical consideration, the changes in the normalised band peak area of the ν_1 and ν_3 mid-infrared absorption bands have been assessed, and these changes are summarised in Fig. 5.9. Considering first the observed trends for the ν_3 band, it is clear that the band peak area does not change by more than 15% of the normalised value throughout the thermal annealing experiments, regardless of the deposition temperature of the SO_2 ice. Moreover, a similar trend is apparent amongst all the ices considered: after a small decrease in the normalised band peak area between 20-40 K (which may be due to uncertainties in the band peak area measurement), a gradual increase is registered until it peaks at 90 K, after which the band peak area declines again, possibly due to increased sublimation effects at these higher temperatures. Conversely, no discernible trends were recorded for the normalised band peak areas of the ν_1 band. It should be noted, however, that aside from the measured band peak areas at 110 K for the SO_2 ices deposited at 70 and 100 K, the maximum change in the ν_1 band peak area was very small at less than 8% of the normalised value. As such, it is possible that the seemingly random scatter observed in the data for this absorption band (Fig. 5.9) is simply the result of uncertainties in the measurement of the band peak areas.

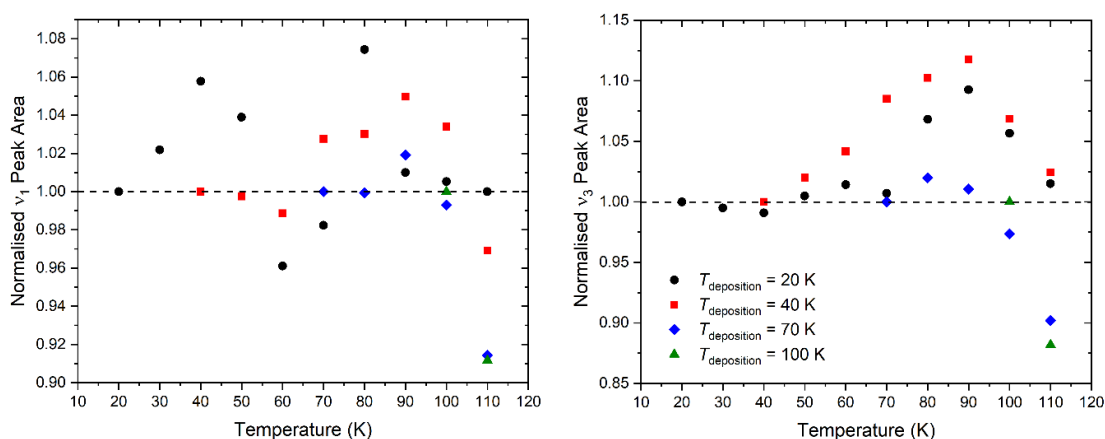


Fig. 5.9: Evolution of the SO_2 ν_1 (left) and ν_3 (right) normalised band peak areas for the ices at 20, 40, 70, and 100 K during their thermal annealing. The limits of integration during measurement were as follows: $\nu_1 = 1160\text{-}1115 \text{ cm}^{-1}$; $\nu_3 = 1360\text{-}1290 \text{ cm}^{-1}$.

5.4.3 Thermal Annealing of H_2S and SO_2 Ices Mixed with H_2O Ice

Up until this point in this chapter, only mid-infrared characterisations of pure H_2S and SO_2 ices have been considered. Although such spectroscopic information is certainly valuable from an analytical point of view, and may be applied to the search for such icy species in various astrophysical environments, astrophysical ices are rarely pure. Indeed, most ices are anticipated to be composed of a mixture of various simple inorganic species, refractory residues, minerals, and also potentially a few complex organic molecules (Öberg 2016, Minissale *et al.* 2022). Of these various species, however, the most prevalent ice in the cosmos is H_2O (Klinger 1983, van Dishoeck *et al.* 2013, Öberg 2016). For this reason, it is important to characterise the mid-infrared spectra of H_2S and SO_2 ices mixed with H_2O in a stoichiometric ratio in which H_2O is dominant (Table 5.4) during thermal annealing from deposition at 20 K to total sublimation of the ice mixture.

The mid-infrared spectra of the H₂S:H₂O and SO₂:H₂O ice mixtures upon their deposition at 20 K are respectively shown in Figs. 5.10 and 5.11. Considering first the mixed SO₂:H₂O mixed ice, it is possible to note that, for the stoichiometric composition considered, the SO₂ ν_1 and ν_3 bands are prominent and respectively peak at 1154.0 and 1331.4 cm⁻¹, thus indicating a significant blue-shift compared to the positions of these bands in the pure SO₂ ice at 20 K (1147.5 and 1323.7 cm⁻¹; Table 5.2). No other SO₂ absorption bands were observed in the mid-infrared spectrum (Fig. 5.10), most likely because they are sufficiently weak as to be obscured by the intense absorptions of H₂O.

One particularly interesting feature in the spectrum depicted in Fig. 5.11 is the apparent shoulder to the H₂O stretching modes centred at 3595.3 cm⁻¹. This shoulder is attributed to the formation of hydrogen bonds between the SO₂ and H₂O molecules in the ice mixture. Previous work has demonstrated that this feature is very sensitive to the stoichiometric composition of the ice: for example, in the thermal annealing experiments performed as part of the validation of the ICA which involved the warming of a 5:3 SO₂:H₂O ice from 20 K (Chapter 4), this band was found to not appear as a shoulder but rather as a distinct peak centred at 3609.2 cm⁻¹ (Fig. 4.12). Similar results were reported by Moore *et al.* (2007) who investigated a 1:3 SO₂:H₂O ice deposited at 86 K. Interestingly the mid-infrared spectrum of a 1:30 SO₂:H₂O mixed ice as reported by Moore *et al.* (2007) shows no evidence of this band, thus highlighting the rarer occurrence of hydrogen bonding between SO₂ and H₂O molecules. Systematic work by Schriver-Mazzuoli *et al.* (2003b) investigating SO₂:H₂O ice mixtures of various stoichiometric compositions demonstrated that, not only is such hydrogen bonding ubiquitous in ices with a high enough SO₂ content, but that small (SO₂)_x(H₂O)_y aggregates are also able to form in ices which are very rich in SO₂.

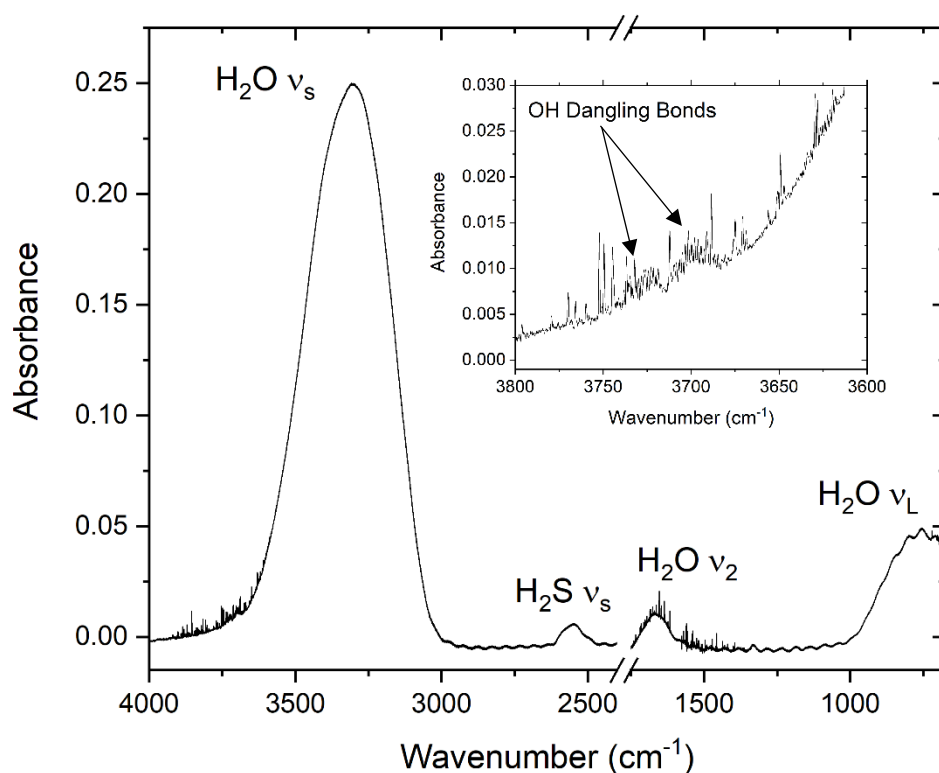


Fig. 5.10: Mid-infrared absorption spectrum of a 1:7 H₂S:H₂O ice prepared by co-deposition of the respective gases at 20 K. The estimated ice thickness was 0.41 μm . Sinusoidal patterns in the spectrum of the deposited ice are caused by interference of infrared light reflected in the substrate-ice-vacuum optical system.

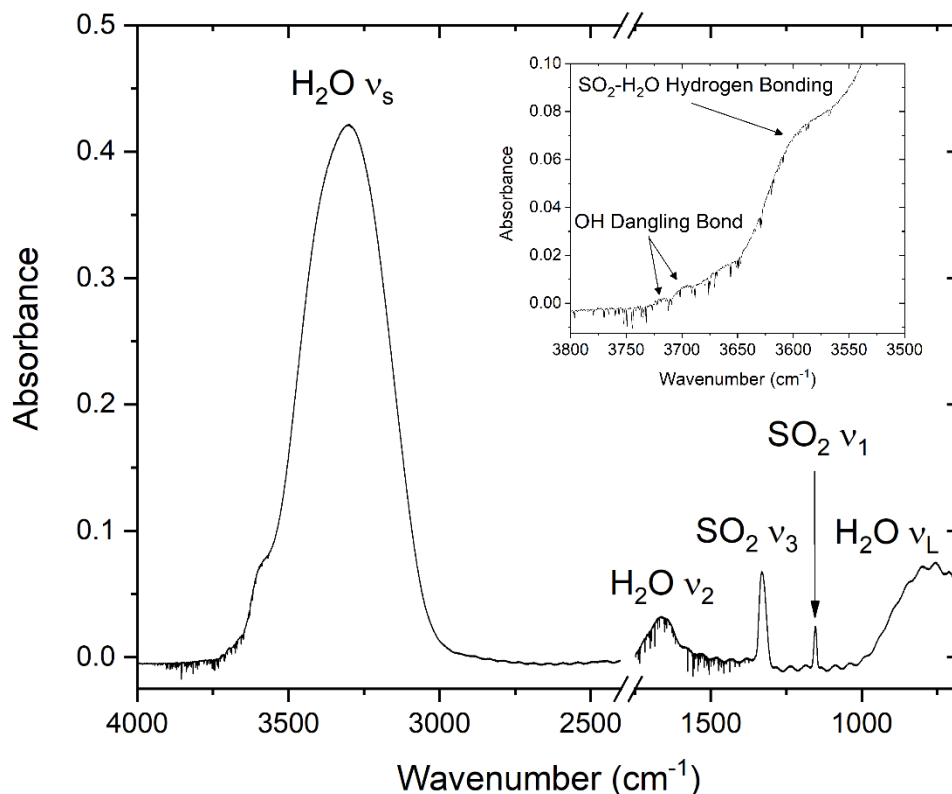


Fig. 5.11: Mid-infrared absorption spectrum of a 1:11 SO_2 : H_2O ice prepared by co-deposition of the respective gases at 20 K. The estimated ice thickness was $0.71 \mu\text{m}$. Sinusoidal patterns in the spectrum of the deposited ice are caused by interference of infrared light reflected in the substrate-ice-vacuum optical system.

It should be noted that, upon its preparation at 20 K, the mixed SO_2 : H_2O ice is porous as evidenced by the two small mid-infrared absorption bands centred at 3701.0 and 3721.0 cm^{-1} caused by hydroxyl dangling bonds (Jenniskens and Blake 1994, Palumbo 2006). Porous or microporous ice structures play important roles in solid-phase astrochemistry as these (micro)pores offer routes through which thermally or radiolytically derived radicals and ions may migrate, thus allowing for more extensive and substantial chemical reaction networks. Thermal and radiation chemical processes are, however, known to induce compaction of the ice and thus reduce ice porosity significantly (Palumbo 2006, Bossa *et al.* 2012). Indeed, during the thermal annealing of the mixed ice (Fig. 5.12) the peak areas of these hydroxyl dangling bonds were observed to diminish rapidly until no evidence for them could be observed at 40 K.

The disappearance of these hydroxyl dangling bonds suggests that restructuring processes are able to take place within the ice even at low temperatures. Aside from pore closing and ice compaction, a phase change occurs at 40-50 K in which the H_2O ice transitions from one with high true density to one with a lower true density (Collings *et al.* 2003a and references therein; note that true density refers only to the density of the H_2O molecules and excludes any empty space in the porous structure). Unfortunately, changes in the mid-infrared spectrum of H_2O indicative of this particular phase transition are difficult to identify, and may manifest in different ways in ices accreted from the vapour phase (Hagen *et al.* 1981, Jenniskens *et al.* 1995). It is important to recognise that this phase change is not necessarily associated with changes in the porosity of the ice and, indeed, experimental evidence has suggested that porous ices that have been thermally annealed retain at least some degree of porosity even at comparatively elevated temperatures (Isokoski *et al.* 2014).

Perhaps the most obvious indicator of large-scale restructuring occurring within the ice are the changes observed in the appearance of the strong H₂O stretching modes (Fig. 5.12). As the ice was thermally annealed, a gradual red-shifting of the band peak position to lower wavenumbers, accompanied by the development of a more resolved structure, could be observed. Such changes are indicative of the thermodynamically favourable crystallisation of the amorphous ice to the cubic phase. This cubic phase appears to be achieved at a temperature of 120 K. Further annealing to higher temperatures results in this mid-infrared absorption band adopting a radically different appearance characteristic of the hexagonal crystalline phase at a temperature of 150 K. At 160 K, the absorbance of the H₂O mid-infrared absorption bands decreased significantly, likely due to notable losses caused by sublimation of the molecular ice to the gas phase, and total sublimation of the ice was recorded at 170 K.

In contrast to those of the H₂O ice, the mid-infrared absorption bands of the SO₂ component of the mixed ice did not exhibit any indications of crystallisation during thermal annealing, with the bands remaining fairly broad and not undergoing any splitting in contrast to the observations made during the thermal evolution of the pure SO₂ ice. As such, it is reasonable to assume that the SO₂ in the mixed ice either remained in a structurally disordered amorphous state throughout the thermal annealing process, or else was initially too dilute to form intermolecular interactions. However, such a result should not be misconstrued as implying that the SO₂ did not undergo any physical changes during thermal annealing: indeed, an examination of the shoulder attributed to the hydrogen bonding between SO₂ and H₂O molecules revealed that this feature progressively declined with increasing temperature, until it disappeared entirely just beyond 110 K, thus indicating fewer intermolecular interactions between the SO₂ and H₂O molecules within the bulk ice (Fig. 5.12). Interestingly, and despite this observation, the SO₂ ν_1 and ν_3 absorption bands remained clearly visible in the mid-infrared spectra up to a temperature of 140 K, suggesting that the SO₂ component of the ice did not suffer significant losses to sublimation. These observations may be interpreted as indirect evidence of thermally induced segregation of the ice mixture resulting in SO₂ molecules preferentially associating with other SO₂ molecules rather than H₂O molecules. Similar processes have been previously reported in other thermally annealed ice mixtures, such as H₂O and CO₂ (Isokoski *et al.* 2014) as well as CO and N₂ (Nguyen *et al.* 2018).

Lastly, it is important to recall that the thermal annealing of a mixed SO₂:H₂O ice promotes cryogenic thermal reactions within the ice structure that yield sulphur oxyanions (Bang *et al.* 2017, Kaňuchová *et al.* 2017). As shown in the inset of Fig. 5.12, the thermal annealing of the mixed SO₂:H₂O ice results in the formation of two new absorption bands: a broad bimodal peak ranging between 1100.0-983.1 cm⁻¹ and peaking at 1066.0 and 1011.2 cm⁻¹, together with a separate and smaller band at 954.5 cm⁻¹. The presence of these bands has been ascribed to the formation of HSO₃⁻ and S₂O₅²⁻, respectively, as per Eqs. 1.3 and 1.4. The positions of these bands are in excellent agreement with those reported by other studies (Table 5.5). It is interesting to consider the temperature at which the HSO₃⁻ and S₂O₅²⁻ absorption bands appear and how this relates to the stoichiometric composition of the ice. In this present investigation, the first diagnostic traces of the HSO₃⁻ band could be observed at 110 K, but were significantly stronger at 120 K. This latter temperature was also the first temperature at which the S₂O₅²⁻ mid-infrared band was observed (Fig. 5.12). The later (i.e., higher temperature) emergence of the S₂O₅²⁻ mid-infrared band compared to the HSO₃⁻ band is logical, since the formation of the former species requires a sufficient build-up of the latter within the ice.

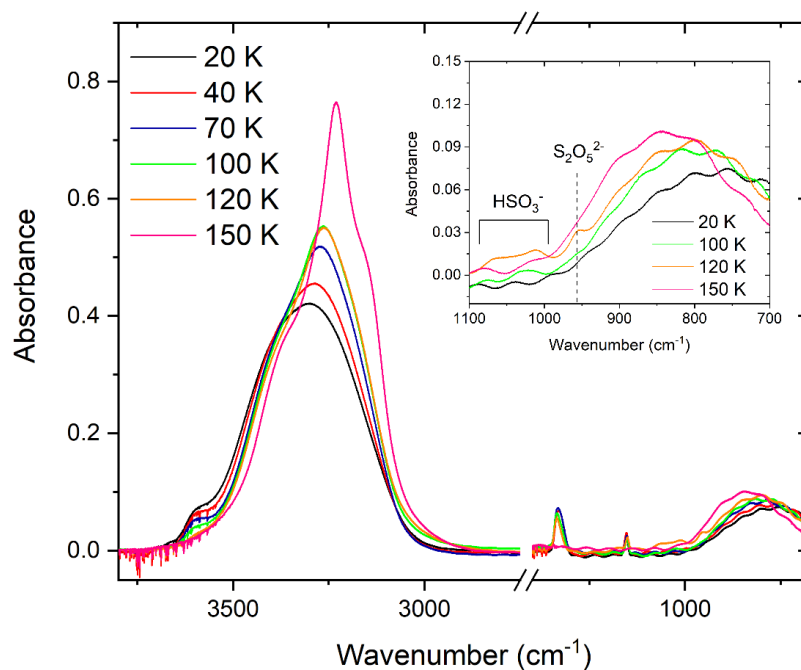


Fig. 5.12: Mid-infrared absorption spectra of a 1:11 $\text{SO}_2\text{:H}_2\text{O}$ ice undergoing thermal annealing from deposition at 20 K to sublimation. Sinusoidal patterns in the spectrum of the deposited ice are caused by interference of infrared light reflected in the substrate-ice-vacuum optical system. However, this interference pattern does not preclude the identification of the HSO_3^- and $\text{S}_2\text{O}_5^{2-}$ bands.

It should be noted that, at a stoichiometric ratio of 1:11, the mixed $\text{SO}_2\text{:H}_2\text{O}$ ice considered in this study was relatively sulphur-poor. Therefore, it is likely that the thermal chemistry leading to the formation of HSO_3^- and $\text{S}_2\text{O}_5^{2-}$ was only kinetically feasible at higher temperatures that allow for significant diffusion of molecules and ions within the solid ice structure, thus explaining why these product species were only identified in the mid-infrared spectra collected above 110 K. This idea is substantiated by the results of Kaňuchová *et al.* (2017) and from the ICA validation experiments described in Chapter 4, where the formation of HSO_3^- and $\text{S}_2\text{O}_5^{2-}$ was observed at temperatures of 80 and 100 K, respectively, for ices that were more evenly composed of SO_2 and H_2O having stoichiometric compositions of 1:1, 1:3, and 5:3 (Table 5.5). Moreover, in their study, Kaňuchová *et al.* (2017) also considered the thermal annealing of a H_2O -poor $\text{SO}_2\text{:H}_2\text{O}$ mixed ice having a stoichiometric composition of 10:1. Their results mirrored the ones reported in this present investigation, with mid-infrared bands for HSO_3^- and $\text{S}_2\text{O}_5^{2-}$ only being observed at 120 K likely due to the increased diffusion of the relevant precursor molecules and ions through the solid ice at this elevated temperature.

It is difficult to estimate the efficiency of the conversion of SO_2 to these sulphur oxyanions, since the integrated band strength constants for HSO_3^- and $\text{S}_2\text{O}_5^{2-}$ have not been reported in any previous experimental or computational study. In an effort to provide a more quantitative analysis of this process, the integrated linear baseline-corrected band areas for these products, as well as for the parent SO_2 species, have been plotted as a function of ice temperature (Fig. 5.13). It is possible to note that the band peak area of SO_2 largely declines throughout the thermal annealing process, with the greatest losses observed to begin beyond 30 K. At 140 K, however, there is an unexpected increase in the band peak area. The cause of this increase is not definitively known; however, it is tentatively suggested that it may be due to some small-scale structural ordering of the SO_2 ice which would have undergone extensive segregation from the H_2O ice by this temperature, as discussed previously.

Table 5.5: Summary of results from selected previous studies on the thermal formation of HSO_3^- and $\text{S}_2\text{O}_5^{2-}$ in $\text{SO}_2:\text{H}_2\text{O}$ mixed ices at cryogenic temperatures.

Study	Band Position (cm^{-1})		$\text{SO}_2:\text{H}_2\text{O}$ Ratio
	HSO_3^-	$\text{S}_2\text{O}_5^{2-}$	
This investigation	1066.0, 1011.2	954.4	1:11
ICA validation (Chapter 4)	~1040	956	5:3
Moore <i>et al.</i> (2007)	1035, 1011	958	1:3
	~1065	-	1:30
Loeffler and Hudson (2010)	1034, 1013	958	1:6
Kaňuchová <i>et al.</i> (2017)	1065, 1036	-	10:1
	1036, 1011	950	1:1
	1037, 1011	958	1:3

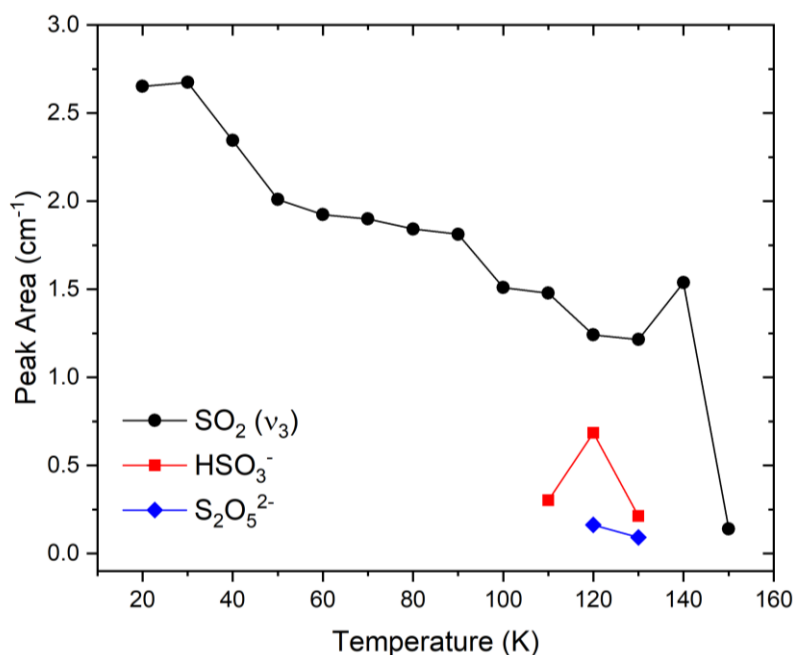


Fig. 5.13: Variation in the peak areas of the $\text{SO}_2 (\nu_3)$, HSO_3^- , and $\text{S}_2\text{O}_5^{2-}$ bands during the thermal annealing of a 1:7 $\text{SO}_2:\text{H}_2\text{O}$ ice. Note that uncertainties in the measurement of the band peak areas may be quite large due to the effects of the sinusoidal interference pattern present in the spectra. The limits of integration were as follows: $\text{SO}_2 (\nu_3) = 1175\text{-}1140 \text{ cm}^{-1}$; $\text{HSO}_3^- = 1100\text{-}980 \text{ cm}^{-1}$; $\text{S}_2\text{O}_5^{2-} = 980\text{-}935 \text{ cm}^{-1}$.

Beyond 140 K, the SO_2 sublimates efficiently and only traces are observable at 150 K. The higher temperature sublimation of solid SO_2 when mixed with H_2O compared to that of the pure SO_2 ice is in line with previous literature concerned with the thermal desorption of volatiles (Minissale *et al.* 2022). The mid-infrared absorption band of HSO_3^- is first apparent at 110 K and subsequently increases in peak area until it reaches a maximum at 120 K. It is at this latter temperature that the mid-infrared absorption band of $\text{S}_2\text{O}_5^{2-}$ is first detected. Further thermal annealing results in a decline in the peak areas of both absorption bands, and they are observed to have disappeared by 140 K, most likely due to their sublimation from the ice.

Considering now the mid-infrared spectrum of the mixed 1:7 $\text{H}_2\text{S}:\text{H}_2\text{O}$ ice deposited at 20 K shown in Fig. 5.10, it is possible to note that it is only the ν_s band of the H_2S ice component that is visible and that the less intense ν_2 mode is not apparent. Compared to the

pure H₂S ice (Fig. 5.1), the ν_s band is red-shifted by 1.5 cm⁻¹ in the mixed ice where it is located at 2549.5 cm⁻¹. It is interesting to note that the apparent shift in the ν_s band position in the mixed H₂S:H₂O ice is less significant than and in the opposite direction to the analogous shifts of the SO₂ ν_1 and ν_3 bands in the mixed SO₂:H₂O ice. It is also interesting to note that the ν_s band of the H₂S ice mixed with H₂O is seemingly characterised by a shoulder (Fig. 5.14) at about 2500 cm⁻¹ (± 10 cm⁻¹) which was not present in the spectra of the pure H₂S ices (Fig. 5.10), although this is difficult to confidently identify against the sinusoidal background and thus may simply be a persistent artefact within the spectral data. The remainder of this discussion will assume that this absorption feature is indeed a band, although further experimental work is strongly recommended to confirm this.

Based on prior assignments by Nelander (1978) and Barnes *et al.* (1984), this shoulder has been tentatively ascribed to the doubly hydrogen bonded system H₂O···HSH···OH₂. The presence of such a structure in this ice would not be surprising, as not only is H₂S known to weakly participate in hydrogen bonding (Lowder *et al.* 1970, Das *et al.* 2018), but it is also a much stronger acid than H₂O (H₂S $pK_a = 7$; H₂O $pK_a = 14$; Perrin 1982, Silverstein and Heller 2017) and thus more able to act as the proton donor in the hydrogen bond system. This shoulder appears to be present throughout the thermal annealing process right up until the sublimation of the H₂S component of the ice at a temperature of just over 100 K. Therefore, if this band is truly attributable to the H₂O···HSH···OH₂ system as is suspected, then its presence throughout the thermal annealing process implies that the H₂S did not undergo segregation from the H₂O ice, unlike what was observed for the SO₂:H₂O ice mixture. Although the exact reason for this difference is not entirely understood, it is to be acknowledged that ice segregation as a consequence of thermal annealing is known to be dependent upon the molecular components of the mixed ice and their initial stoichiometric composition (Boogert 2019).

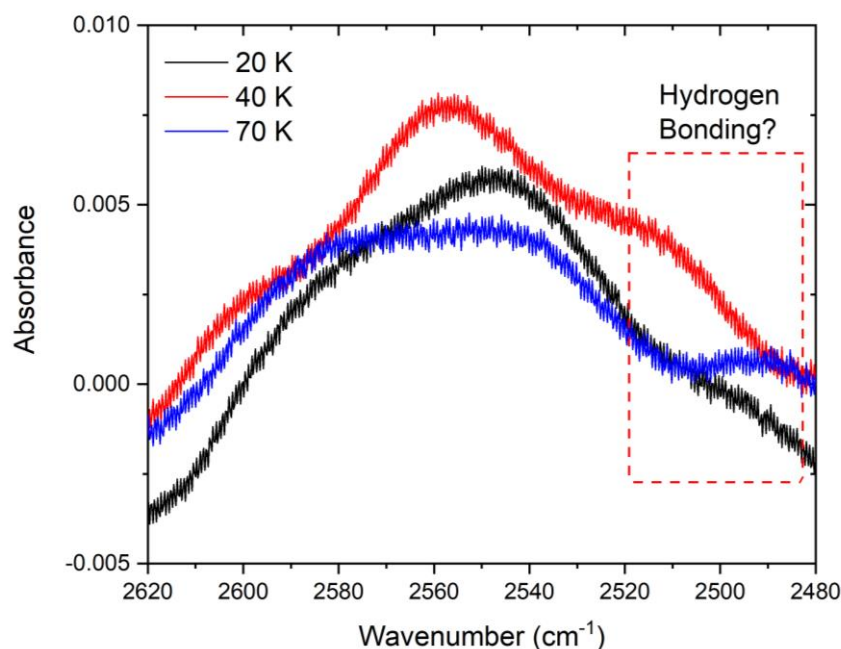


Fig. 5.14: A shoulder is apparent on the lower wavenumber flank of the H₂S ν_s band throughout the thermal annealing process. This band has been tentatively attributed to the hydrogen bonded system H₂O···HSH···OH₂. It is important to recognise that this absorption feature is weak, and may be an artefact of the sinusoidal background present in the spectral data.

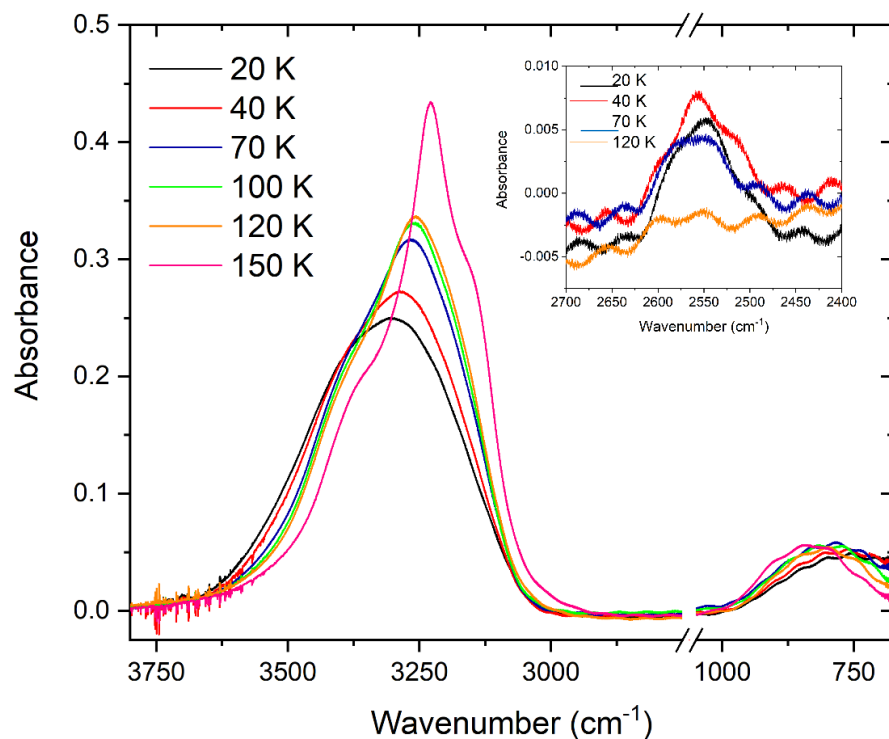


Fig. 5.15: Mid-infrared spectra of a 1:7 H₂S:H₂O ice undergoing thermal annealing from deposition at 20 K to sublimation. The inset depicts the possible presence of a shoulder due to H₂O⋯HSH⋯OH₂ hydrogen bonding. Sinusoidal patterns in the spectrum of the deposited ice are caused by interference of infrared light reflected in the substrate-ice-vacuum optical system.

The mid-infrared spectra collected during the thermal annealing of the 1:7 H₂S:H₂O ice are shown in Fig. 5.15. Upon its deposition at 20 K, the H₂S:H₂O ice was found to be porous as evidenced by the presence of hydroxyl dangling bonds positioned at 3698.6 and 3723.2 cm⁻¹ (Fig. 5.11). These dangling bonds are approximately located at the same position as those in the SO₂:H₂O mixed ice and, indeed, the decline in the peak areas of these bands as a result of thermal annealing was found to be very similar in both mixed ices, with no evidence for the hydroxyl dangling bonds being present at temperatures of 40 K and above. As discussed previously, the absence of these bands should not necessarily be interpreted as the complete and total compaction of the ice (Isokoski *et al.* 2014).

Thermal annealing of the H₂S:H₂O ice resulted in various changes in the appearance of the mid-infrared spectra (Fig. 5.15). The changes in the H₂O mid-infrared absorption bands were virtually identical to those observed during the thermal annealing of the SO₂:H₂O ice, with phase changes from amorphous to cubic crystalline and then to hexagonal crystalline being observed at 120 and 150 K, respectively. At 160 K, the absorbance of the H₂O absorption bands decreased due to increased sublimation of the ice to the gas phase, and total sublimation was recorded by 170 K.

Regarding the thermal evolution of the H₂S ν_s band, this absorption feature presents as a fairly broad band upon deposition at 20 K, and largely remains so up to 60 K indicating that the H₂S ice remains amorphous across this temperature range. At 60 K, however, it is evident that the band begins to take on more of a bimodal structure which becomes somewhat more evident at higher temperatures and persists until sublimation occurs at a temperature just beyond 100 K (Fig. 5.15). Such a change suggests that, although the H₂S component of the mixed ice never achieves a truly crystalline phase, some limited degree of restructuring to a more ordered (perhaps polycrystalline) phase has taken place.

Lastly, it is important to comment on the fact that the thermal annealing of the H₂S:H₂O mixed ice did not initiate any cryogenic thermal reactions, in contrast to the thermal annealing of the SO₂:H₂O mixed ice. Such a result is in agreement with the prior work of Moore *et al.* (2007). A more recent study has demonstrated that the oxidation of H₂S to SO₂ and various sulphur oxyanions *via* the thermal annealing of a H₂S:H₂O mixed ice is in fact possible only if an oxidant (such as O₃) is initially included as an additional component of the ice mixture (Tribbett and Loeffler 2022). However, such a consideration is beyond the scope of this present investigation.

5.5 Applications to Planetary and Space Chemistry

In the previous sub-sections, the results of an extensive and systematic study of the mid-infrared spectroscopy of SO₂ and H₂S astrophysical ice analogues deposited at various cryogenic temperatures and processed *via* thermal annealing were described and compared to previously published literature. In this section, the relevance of such results to sulphur astrochemistry in the ISM and the icy Solar System will be discussed. It should be noted that the aim of this sub-section is not to compare the laboratory generated data presented in this chapter with data collected from actual observational missions, but rather to provide a series of brief discussions highlighting those astrophysical environments where sulphur chemistry is thought to play an important role. Such a discussion may aid observational astrochemists in selecting targets for future study and thus address as yet unanswered questions in the field of sulphur ice astrochemistry.

5.5.1 Dense Interstellar Clouds

As has been described in both Chapter 1 as well as the introduction of this chapter, there is a noticeable paucity of sulphur in the dense ISM (Tieftrunk *et al.* 1994, Ruffle *et al.* 1999). Thus far, only SO₂ and OCS have been detected in interstellar icy grain mantles (Boogert *et al.* 1997, Palumbo *et al.* 1997) and even then, these detections are regarded as being tentative due to the lack of multiple matching infrared bands between observational and laboratory data (Boogert *et al.* 2015). Therefore, it is necessary to understand the various molecular forms that sulphur may adopt in these regions. Recent work has proposed that this apparent depletion of sulphur may be induced by the Coulomb-enhanced freeze-out of sulphur cations onto negatively charged interstellar dust grains, at which point they polymerise and catenate to give sulphur-bearing rings and chains (Cazaux *et al.* 2022).

Computational studies have offered some further insight into the molecular composition of interstellar sulphur, although diverse and sometimes conflicting results have been reported: Vidal *et al.* (2017), for instance, proposed that H₂S is the dominant sulphur-bearing molecule in interstellar icy grain mantles while atomic sulphur dominates the gas phase of the dense ISM. Laas and Caselli (2019), on the other hand, concluded that the majority of sulphur exists as organo-sulphur molecules in the condensed phase, while Shingledecker *et al.* (2020) suggested that the major sulphur-bearing species are in fact sulphur residues along with SO₂ and OCS.

Despite it never having been unambiguously observed, it is nonetheless anticipated that H₂S would be one of the most abundant sulphur-bearing molecules of interstellar icy grain mantles. This expectation is based on its detection and abundance within the nuclei of

comets (Rubin *et al.* 2020) which are believed to be quasi-pristine catalogues of the pre-stellar molecular inventory of dense interstellar clouds, as well as the apparently efficient hydrogenation reactions that may take place on the surfaces of interstellar dust grains (Linnartz *et al.* 2015). It is hoped that the recent launch of the *James Webb Space Telescope* will aid in not only detecting H₂S, but also confirm the detections of SO₂ and OCS and thus shed further light on the sulphur depletion problem that has characterised the chemistry of the dense ISM for several decades. The spectroscopic characterisations presented in this chapter may prove useful in this regard.

5.5.2 Ceres

There is currently an ongoing debate as to the possible presence of SO₂ and S_x on the surface of the innermost of the dwarf planets; Ceres. Based on laboratory generated spectroscopic data, Hendrix *et al.* (2016) proposed that phyllosilicate minerals such as montmorillonite intermixed with SO₂ ice and S_x could explain the ultraviolet-visible reflectance spectrum of Ceres as measured by the *Hubble Space Telescope*. Such a finding has profound implications for the Cererian subsurface environment, which is thought to harbour a briny ocean (Castillo-Rogez 2020), since the presence of sulphurous species at the surface supports the idea that Ceres is home to ongoing geothermal activity. The presence of a briny ocean with geothermal energy sources could therefore make Ceres of significant astrobiological interest.

However, the presence of sulphur-bearing volatiles at the surface of the dwarf planet has been challenged by Roth (2018), who argued that, at 201 K, the surface temperature of Ceres is too high to permit any reasonable accumulation of SO₂ to the extent that would be needed to be detected by the *Hubble Space Telescope* (Zhang and Paige 2009). Such an interpretation is consistent with the non-detection of SO₂ by the VIR Spectrometer aboard the *Dawn* mission (Stephan *et al.* 2017). Such a non-detection is not conclusive evidence of the absence of SO₂ at the surface of Ceres, however, as the relevant infrared bands may be obscured by dark surface materials or could be blended with spectral features assigned to carbonate minerals (De Sanctis *et al.* 2016). The spectroscopic characterisations presented in this chapter could therefore be of use to future measurements of the Cererian surface composition by the *James Webb Space Telescope*, whose increased sensitivity may produce results that could aid in either confirming or firmly rejecting the presence of sulphur-bearing volatiles there; or to the possible future surface lander mission proposed by Castillo-Rogez *et al.* (2022).

5.5.3 Io and Europa

Sulphur chemistry is a key component of the surface chemistry of the Galilean moons of Jupiter. For example, SO₂ is the principal constituent of the surface ices of Io; and its rapid sublimation during the Ionian day results in the formation of a tenuous SO₂ exosphere (Bagenal and Dols 2020; Table 2.4). During the night-time, when surface temperatures cool, the exosphere collapses and the SO₂ surface ices are replenished as a result of re-condensation. Although there is scientific consensus as to the predominance of SO₂ ices on the surface of Io (Douté *et al.* 2001), the observation of H₂S on the surface of this moon has proven to be somewhat more controversial.

Observational investigations have detected the presence of a broad infrared reflectance feature at about 2551 cm⁻¹ (Nash and Howell 1989, Salama *et al.* 1990), whose position and

profile would agree with that of the amorphous H₂S ν_s band. However, this identification has been met with some scepticism since H₂S ice should be crystalline at the temperatures that characterise the surface of Io (Schmitt and Rodriguez 2003), and the reflectance feature should thus exhibit splitting in its structure as shown in Fig. 5.3. Interestingly, the results presented in this chapter demonstrate that the thermal annealing of a H₂S:H₂O ice mixture in which H₂S is the minor component does not result in the formation of crystalline H₂S (Figs. 5.14 and 5.15). Rather, the H₂S either remains amorphous or adopts a polycrystalline structure which is maintained right up until its sublimation at just over 100 K.

If it can be assumed that a similar outcome to that observed in thermally annealed H₂S:H₂O ice would be observed as a result of the thermal annealing of a H₂S:SO₂ ice in which SO₂ was the dominant species, then the results presented here suggest that the Ionian surface infrared reflectance feature at 2551 cm⁻¹ could indeed be due to the presence of H₂S. Future studies are planned to test the validity of this assumption. It is important to note, however, that H₂S ice would be very unstable under the conditions that characterise the surface of Io and would thus be expected to efficiently sublime into the gas phase. However, the ubiquitous volcanism on Io could, in principle, deliver sufficient quantities of H₂S to the surface to allow it to have a residence time that is sufficiently long for it to be observed using various observation techniques.

Orbiting Jupiter slightly further out is Europa: a moon with its own enigmatic surface chemistry. SO₂ ice has been detected on the surface of Europa (Lane *et al.* 1981, Noll *et al.* 1995), although there remain several questions as to its source. As the orbit of Europa lies within the giant Jovian magnetosphere, it has been hypothesised that the sulphur ions that populate the magnetospheric plasma may implant into the surface of the moon, whereupon they react with oxygen-bearing ices (e.g., H₂O or CO₂) to yield SO₂ (experiments investigating such reactions in more systematic detail are the focus of Chapter 7). Indeed, such an exogenous mechanism was suggested to be part of a wider radiolytic sulphur cycle occurring at the surface (Carlson *et al.* 1999). However, laboratory experiments have thus far failed to yield any convincing evidence as to the efficacy of this mechanism (Strazzulla *et al.* 2007, Ding *et al.* 2013). Alternative endogenous sources, such as venting from the subsurface ocean, have therefore also been proposed (McKinnon and Zolensky 2003).

In any case, it is likely that many of the questions relating to sulphur ice astrochemistry on the surfaces of the Galilean moons of Jupiter, including those discussed briefly here, will be addressed by the forthcoming *Jupiter Icy Moons Explorer* and *Europa Clipper* missions (Grasset *et al.* 2013, Phillips and Pappalardo 2014). The former mission is due to be launched in the spring of 2023, and will include the *Moons and Jupiter Imaging Spectrometer* (MAJIS); a visible and infrared imaging spectrograph operating over the 0.5-5.5 μm range. Therefore, the infrared spectroscopic characterisations presented in this chapter may prove useful to interpreting the data collected by this mission and, by extension, further understanding the intricate sulphur chemistry occurring on the surfaces of the Galilean moons.

5.6 Summary

In this chapter, the results of an extensive mid-infrared spectroscopic characterisation of pure H₂S and SO₂ astrophysical ice analogues deposited at various temperatures and thermally annealed to sublimation, as well as of mixed H₂S:H₂O and SO₂:H₂O ices deposited at 20 K and thermally annealed to total sublimation of the ice, have been presented. It is anticipated

that the results presented here will be of use in the interpretation of data collected by the recently launched *James Webb Space Telescope*, as well as by forthcoming interplanetary missions such as the *Europa Clipper* and *Jupiter Icy Moons Explorer* missions.

In the case of the pure H₂S ices, sublimation was noted to take place before reaching a temperature of 90 K. The temperature at which spectroscopic indicators of crystallinity were observed was found to be dependent upon the temperature of deposition: for the ice deposited at 20 K, crystallisation was recorded at a temperature of 60 K, while the ice deposited at 40 K already exhibited many spectroscopic signatures of crystallinity, such as the splitting of the broad ν_s band into its constituent infrared modes. For the pure SO₂ ices, complete sublimation was found to have taken place by 120 K. Moreover, the band peak positions do not vary throughout the thermal annealing process, aside from a red-shift in the band peak of the ν_1 mode of about 4.7 cm⁻¹ upon crystallisation of the ice. The temperature of crystallisation was found to be dependent upon the temperature of deposition, similarly to the case of H₂S. For the ice deposited at 20 K, only small infrared signatures of crystallinity could be observed at 70 K, while ices deposited at higher temperatures were practically fully crystalline when annealed to this temperature.

An investigation of the thermal annealing of the H₂S:H₂O and SO₂:H₂O mixed ices also revealed several interesting results. In both ices, only the most intense infrared absorption features could be identified and, moreover, the sublimation temperatures of the sulphur-bearing molecules were found to be elevated when compared to the pure ices, in agreement with previous results. Infrared absorption features attributable to hydrogen bonding systems were also observed in the spectra of both mixed ices, and were used to indirectly infer the segregation of SO₂ and H₂O during the thermal annealing of the mixed ice; no evidence for such thermally induced segregation was observed for the H₂S:H₂O ice. When mixed with H₂O ice, both H₂S and SO₂ remain largely amorphous (or, perhaps, polycrystalline) throughout the thermal annealing process right up to their sublimation from the bulk ice. It is interesting to note that the mid-infrared absorption features of SO₂ in the mixed ice were blue-shifted compared to the pure ice, while those of H₂S in the mixed ice were red-shifted. Lastly, evidence was demonstrated of thermally induced chemistry in the SO₂:H₂O ice which yielded a number of sulphur oxyanions. Conversely, no evidence for thermally induced chemistry was observed during the thermal annealing of the H₂S:H₂O ice.

6 **CONSTRAINING THE INFLUENCE OF SOLID PHASE ON THE RADIATION CHEMISTRY OF ASTROPHYSICAL ICE ANALOGUES**

This chapter is dedicated to an investigation of the role of the solid phase of an astrophysical ice analogue in determining the outcome of its radiation chemistry. Constraining the influence of various physical and chemical parameters (e.g., temperature or ice composition) on the radiation chemistry of solids has been a fundamental aspect of astrochemical research; however, experiments systematically comparing ices of an identical composition but different phase have been lacking in the literature. This chapter presents the results of the electron irradiation of the amorphous and crystalline phases of various molecules of differing structures, polarities, functional moieties, and intermolecular interactions, namely CH₃OH, N₂O, H₂O, H₂S, and SO₂. The chapter will then close with a discussion of the implications of the results obtained on molecular formation in different astrophysical environments where thermal or radiation processes may dominate over one another.

Note: The majority of the work described in this chapter has been published in peer-reviewed journals or periodicals as: [1] Mifsud *et al.* (2022), *Phys. Chem. Chem. Phys.* **24**, 10974; [2] Mifsud *et al.* (2022), *Eur. Phys. J. D: Atom. Mol. Opt. Plasma Phys.* **76**, 87; [3] Mifsud *et al.* (2022), *Front. Chem.* **10**, 1003163.

6.1 **Contextual Introduction**

The characterisation of the effect of varying various experimental parameters on the outcome of the radiation chemistry of astrophysical ice analogues is of vital importance, particularly in light of the fact that it has been established for some time now that the irradiation of low temperature ices using charged particles (i.e., ions and electrons) or ultraviolet photons may lead to the formation of complex organic molecules relevant to biology (Muñoz Caro *et al.* 2002, Neuvo *et al.* 2007, Hudson *et al.* 2008, Nuevo *et al.* 2012).

Several laboratory investigations have sought to further understand the dependence of this radiation astrochemistry on parameters such as temperature. For instance, Sivaraman *et al.* (2007) investigated the formation of O₃ as a result of the electron irradiation of pure O₂ ices at different temperatures and found that, although the addition of radiolytically derived supra-thermal oxygen atoms to O₂ to yield O₃ is a temperature-independent process, the loss of available atoms to do so due to their recombination to recycle O₂ is greater at higher temperatures. Therefore, the yield of O₃ after irradiation at lower temperatures is noticeably greater. The influence of temperature on the radiation chemistry of astrophysical ice analogues has been a popular theme in the literature. However, one experimental parameter that has received considerably less attention is that of the phase of the molecular ice being irradiated. Only a handful of studies have directly compared the radiation chemistry of different phases of an astrophysical ice analogue (Orlando and Sieger 2003, Grieves and Orlando 2005, Zheng *et al.* 2007), and these studies have all considered the electron irradiation of amorphous and cubic crystalline D₂O. The results of these studies have demonstrated that the formation of D₂, O₂, and D₂O₂ was significantly more rapid in the amorphous case. This observation was attributed to the increased ability of radiolytically generated radicals to diffuse through the solid structure in the amorphous ices due to their increased structural defects and porosities.

Nevertheless, there currently exists a gap in the literature with regards to comparative irradiations of the various phases of molecular ices. The aim of the work presented in this chapter, therefore, is to investigate whether there exist any differences in the outcome of the electron irradiation of the amorphous and crystalline phases of selected molecular ices of astrophysical interest (including a number of sulphur-bearing species) that can be ascribed solely to the difference in solid phase. The selected molecules are CH₃OH, N₂O, H₂O, H₂S, and SO₂. Such a selection includes some of the most common ices in the cosmos (e.g., H₂O and CH₃OH) and represents each of the biogenic elements with the notable exception of phosphorus. A brief description of the phase chemistry of each of these ices as well as their astrophysical relevance now follows.

6.1.1 CH₃OH Ice

CH₃OH ices are ubiquitous within the icy cosmos, having been detected on Solar System objects such as comets and centaurs (Bockelée-Morvan *et al.* 1991, Eberhardt *et al.* 1994, Cruikshank *et al.* 1998) as well as around young stellar objects in interstellar space (Pontopiddan *et al.* 2003, Penteado *et al.* 2015, An *et al.* 2017). Their presence in such settings is thought to arise from chemical processes within icy grain mantles in dense interstellar clouds, such as sequential hydrogenation reactions of CO and H₂CO (Hudson and Moore 1999, Watanabe and Kouchi 2002, Wada *et al.* 2006, Chuang *et al.* 2016) or the radiolysis of carbon-bearing H₂O-rich ices (Fuchs *et al.* 2009, Qasim *et al.* 2018).

Although the literature contains a great number of publications concerned with the radiation chemistry of pure CH₃OH ices, few make explicit reference to the phase of the ice their experiments are concerned with. This is perhaps unexpected, as the phase chemistry of CH₃OH at low temperatures and pressures has actually been studied extensively for nearly a century. As a solid ice, CH₃OH may exist as an amorphous structure up to a temperature of 128 K, after which it undergoes crystallisation (Parks 1925). Two crystalline phases are known: a low temperature α -phase that persists to about 160 K (Lucas *et al.* 2005, Gálvez *et al.* 2009), and a high temperature β -phase that persists until liquification at the triple point temperature of 175.61 K (Carlson and Westrum 1971). X-ray and neutron diffraction studies have shown that both the α - and the β -phases exhibit orthorhombic symmetry with four molecules per unit cell (Tauer and Lipscomb 1952, Torrie *et al.* 1989, Torrie *et al.* 2002). The main distinctions between the phases are the orientation of the hydrogen bond chains linking adjacent molecules, and the space group to which they belong: the α -phase belongs to the $D_4^2-P2_12_12_1$ space group while the β -phase belongs to the $D_{2h}^{17}-Cmcn$ space group (Lucas *et al.* 2005).

6.1.2 N₂O Ice

N₂O has been detected in interstellar settings such as stellar nurseries and towards low mass protostars (Ziurys *et al.* 1994, Ligterink *et al.* 2018). The presence of N₂O ice, although yet to be confirmed, is expected on the surfaces of outer Solar System moons and dwarf planets where N₂ and O₂ ices are known to co-exist in radiation environments driven by giant planetary magnetospheres or the solar wind (Ponciano *et al.* 2008, Boduch *et al.* 2012, Ioppolo *et al.* 2020).

Solid N₂O may exist as one of two phases under high-vacuum conditions: an amorphous phase which dominates at temperatures below 30 K and a crystalline phase that

exists at higher temperatures and which adopts a $Pa3$ structure (Kuchta *et al.* 1992, Hudson *et al.* 2017). Interestingly, the phase adopted by a N_2O ice is not only determined by the temperature at which it was prepared, but also by its rate of condensation from the gas phase. Hudson *et al.* (2017) demonstrated that faster deposition rates are conducive to the formation of a partially or wholly crystalline N_2O ice. This crystalline phase has oftentimes been described as a ‘disordered crystal’ due to the fact that the lack of inversion symmetry in the N_2O molecule allows for more than one possible orientation of the weak molecular dipole parallel to the body diagonals of the unit cell. Such a description should not be misconstrued as implying a lack of structure, however, as the crystalline phase is still characterised by an ordering of the constituent N_2O molecules.

6.1.3 H_2O Ice

H_2O ice is among the most ubiquitous materials in the cosmos (Öberg 2016). On planet Earth, H_2O ice is largely found as snow, glaciers, or permafrost, and their environmental transformations have been linked to various planetary-scale climatological effects, such as altered ocean currents, changes in sea-levels, and increased carbon exchange (Dobinski 2006). Beyond Earth, H_2O ice has been detected in a great number of astrophysical settings, including dense interstellar clouds (Chiar *et al.* 2011), circumstellar discs (Honda *et al.* 2009), comets (Davies *et al.* 1997, Sunshine *et al.* 2006), outer Solar System moons (Chyba and Phillips 2002, Brown *et al.* 2006), rocky Solar System planets (Paige *et al.* 1992, Vincendon *et al.* 2010), and Kuiper Belt Objects (Brown *et al.* 2012).

In spite of the low temperatures and ultrahigh-vacuum conditions associated with such astrophysical environments, these H_2O ices display a rich phase chemistry. Condensation of gaseous H_2O at the 10-20 K temperatures encountered within the cores of dense interstellar clouds results in the formation of amorphous solid water (ASW); a polymorphic and metastable phase whose crystallisation to a more ordered structure occurs spontaneously over extended time-scales (Baragiola 2003). The crystallisation of ASW may also be induced *via* thermal annealing, with two crystalline phases forming sequentially: a cubic ice (Ic) is the first, low temperature crystalline phase encountered which, upon further warming, is irreversibly converted to a stable hexagonal ice (Ih).

It has already been mentioned that, upon preparation *via* condensation at 10-20 K, ASW exists as a high-density polymorph which is transformed to another polymorph having a lower true density upon thermal annealing to 40-50 K (Baragiola 2003, Collings *et al.* 2003a). As the ice is warmed to higher temperatures, it begins to crystallise on a local scale *via* the nucleation of small regions, thus leaving the majority of the ice in an amorphous state. Although still technically an amorphous ice, this phase is regarded as somewhat distinct to ASW due to its higher degree of crystallinity and has thus been termed the restrained amorphous ice (RAI) phase (Jenniskens and Blake 1994). RAIs have been observed under various experimental temperature and pressure conditions, including at temperatures as low as 77 K (Kolesnikov *et al.* 1999). Further annealing of the ice results in its crystallisation to Ic at temperatures of 120-140 K (Ehrenfreund and Fraser 2003), although just prior to this there exists a glass transition to a viscous liquid which is thermodynamically distinct from liquid H_2O (McMillan and Los 1965). Additional warming of the Ic phase results in an irreversible reorganisation of the ice to the stable Ih phase at a temperature of about 150 K.

Both the Ic and Ih crystal structures consist of tetrahedrally coordinated H₂O molecules arranged as puckered six-membered rings. The distinction between these crystal structures lies in the stacking order of the hexagonal bilayers which form the lattice, resulting in the Ic and Ih crystals adopting *I4₁md* and *Cmc2₁* space groups, respectively (Jackson *et al.* 1997, Hirsch and Ojamäe 2004, Raza *et al.* 2011). An additional H₂O ice phase that is relevant to astrophysics is that of hyper-quenched glassy water (HGW), which is an amorphous ice phase formed as a result of the rapid cooling of liquid H₂O and is commonly seen on the surfaces of icy outer Solar System moons following meteoritic impacts (Johari *et al.* 1987).

6.1.4 H₂S and SO₂ Ices

The phase chemistries and astrophysical relevance of H₂S and SO₂ ices were discussed at length throughout Chapter 5, and so only a brief overview is given here. Solid H₂S is known to exhibit a number of stable crystalline phases under low temperature and ambient pressure conditions (Fathe *et al.* 2006), but it is the crystalline phase III (hereafter simply referred to as the crystalline H₂S phase) that is of importance under conditions relevant to molecular astrophysics. This phase is orthorhombic, having eight molecules per unit cell and adopting the *Pbcm* space group. SO₂ may also exist as an orthorhombic crystalline solid under conditions relevant to astrophysics, but in this case the *Aba2* space group is adopted and there are only two molecules per unit cell (Schriver-Mazzuoli *et al.* 2003b).

Although sulphur is one of the most abundant elements in the cosmos and is of importance in both a biochemical and a geochemical context, much remains unknown with respect to its chemistry in interstellar and outer Solar System settings. The sulphur depletion problem in the dense ISM has already been discussed at length and, although it has not yet been definitively detected within the solid phase, icy H₂S is anticipated to play an important role in the depletion of sulphur in these regions as a result of the formation of large amounts of sulphur atoms and S_x as a result of the irradiation of H₂S by galactic cosmic rays and ultraviolet photons. SO₂ has been detected within both the dense ISM as well as on the surfaces of several outer Solar System bodies such as the Galilean moons of Jupiter (Boogert *et al.* 1997, Carlson *et al.* 1999). However, the precise chemical mechanisms leading to its formation in these settings remain widely debated.

6.2 Experimental Methodology

The experimental work was performed using the ICA apparatus. The preparation of the astrophysical ice analogues was achieved *via* background deposition by allowing the relevant gas or vapour into a dosing line before dosing it into the main chamber at a pressure of a few 10⁻⁶ mbar. This deposition pressure was reduced to a few 10⁻⁷ mbar in the case of the preparation of the amorphous N₂O samples, due to the known dependence of the phase adopted by this ice upon deposition rate (Hudson *et al.* 2017). In the case of CH₃OH (VWR, VLSI grade) and H₂O (de-ionised), the liquid was first de-gassed in a glass vial using the liquid nitrogen freeze-pump-thaw technique before directing the vapour into the dosing line. For N₂O, H₂S, and SO₂ (respectively 99.5%, 99.5%, and 99.8% purity; all Linde), the gas was introduced directly into the dosing line without any additional preparation.

All amorphous ices were prepared by deposition at 20 K. Careful consideration was needed in order to determine the deposition temperature of the crystalline phases of the ices,

due to the complexity of the phase chemistry in some cases. The results of Chapter 5 allowed for the deposition temperatures of crystalline H₂S and SO₂ to be determined, and these were selected to be 60 and 90 K, respectively. A temperature of 60 K was also selected for the preparation of the crystalline N₂O ices, on the basis of previously published work by Hudson *et al.* (2017). With regards to CH₃OH, it was decided that only the α -phase would be investigated as part of this study, due to the high sublimation rates of solid CH₃OH at the deposition temperatures required to prepare the β -phase under high-vacuum conditions. The preparation of α -crystalline CH₃OH was thus achieved by depositing the ice at 140 K.

Given that H₂O may exhibit a number of different solid phases under conditions relevant to astrophysics, it was necessary to first perform a trial experiment to accurately assess the deposition temperatures required to prepare these phases. A 0.25 μm -thick ASW sample was prepared by deposition at 20 K and subsequently thermally annealed to 110 K at a rate of 1 K min⁻¹ with mid-infrared spectra collected at 10 K intervals, and thereafter at a slower rate of 0.33 K min⁻¹ with spectra being collected at 5 K intervals until sublimation was observed at 165 K. The identification of the phase of H₂O present at a given temperature was achieved *via* comparisons with previously published spectra (Hornig *et al.* 1958, Bertie and Whalley 1964, Whalley, 1977, Bergren *et al.* 1978, Hagen *et al.* 1981, Hagen and Tielens 1982, La Spisa *et al.* 2001).

Thermal annealing of the deposited ASW ice resulted in its crystallisation. As the ice was warmed, observed changes in the acquired mid-infrared spectra indicated a gradual transition to the Ic phase. Such spectroscopic indications could be seen at temperatures as low as 80 K; however, this temperature is far too low to expect full crystallisation to Ic to have occurred and so it is suggested that the observed spectroscopic signatures of crystallinity are more likely to be instead indicative of a RAI phase, in which pockets of crystalline ice are surrounded by a largely amorphous structure. Further annealing of the ices resulted in more extensive crystallisation, with the strongest spectroscopic signatures of the Ic phase being observed over the 130-140 K temperature range. Beyond 140 K, spectroscopic changes indicated a morphological change to the Ih phase which was complete by the time a temperature of 145 K was reached. Continued warming of the ice resulted in sublimation-induced losses, and full desorption of the ice from the deposition substrates occurred by 165 K. Fig. 6.1 summarises the main phase changes induced in the ice as a result of thermal annealing.

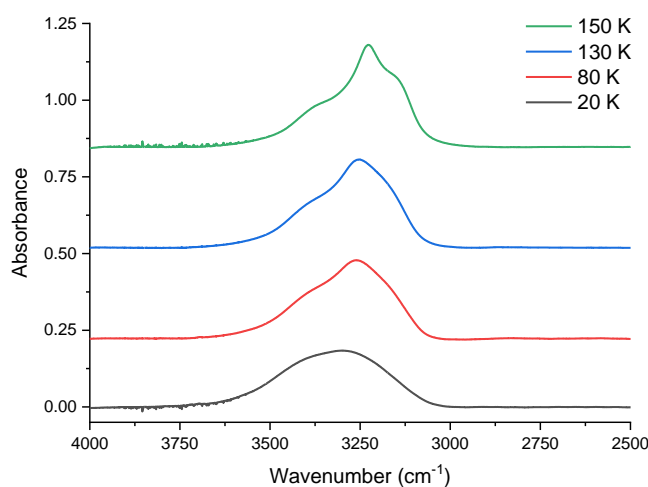


Fig. 6.1: Evolution of the H₂O mid-infrared stretching modes during the thermal annealing of an ice deposited at 20 K. Shown in the figure (*bottom to top*) are the appearances of these modes for the ice in the ASW (20 K), RAI (80 K), Ic (130 K), and Ih (150 K) phases. Note that spectra are offset vertically for clarity.

Table 6.1: Summary of the comparative electron irradiation experiments performed in this study. Note that the penetration depth referred to in the last column refers to the maximum penetration depth of a 2 keV electron impacting each ice target at an angle of 36° to the normal as calculated using the CASINO software, with the exception of the SO₂ ices for which the electron beam energy was 1.5 keV.

Irradiation	Ice	Phase	N (molecules cm ⁻²)	d (μm)	$T_{\text{deposition}}$ (K)	Penetration Depth (μm)
6.3.1 Ice 1	CH ₃ OH	Amorphous	1.3×10^{18}	1.08		
6.3.1 Ice 2	CH ₃ OH	Amorphous	1.1×10^{18}	0.95		
6.3.1 Ice 3	CH ₃ OH	Amorphous	1.2×10^{18}	0.98		
<i>Average</i>			1.2×10^{18}	<i>1.00</i>	20	0.22
6.3.1 Ice 4	CH ₃ OH	Crystalline	1.5×10^{18}	1.20		
6.3.1 Ice 5	CH ₃ OH	Crystalline	1.1×10^{18}	0.88		
6.3.1 Ice 6	CH ₃ OH	Crystalline	1.1×10^{18}	0.87		
<i>Average</i>			1.2×10^{18}	<i>0.98</i>	140	0.19
6.3.1 Ice 7	N ₂ O	Amorphous	2.9×10^{17}	0.17		
6.3.1 Ice 8	N ₂ O	Amorphous	2.8×10^{17}	0.16		
<i>Average</i>			2.9×10^{17}	<i>0.17</i>	20	0.13
6.3.1 Ice 9	N ₂ O	Crystalline	5.8×10^{17}	0.27		
6.3.1 Ice 10	N ₂ O	Crystalline	6.1×10^{17}	0.28		
<i>Average</i>			5.9×10^{17}	<i>0.28</i>	60	0.11
6.3.2 Ice 1	H ₂ O	ASW	7.4×10^{17}	0.23	20	
6.3.2 Ice 2	H ₂ O	RAI	6.5×10^{17}	0.21	80	
6.3.2 Ice 3	H ₂ O	Ic	6.6×10^{17}	0.21	130	
6.3.2 Ice 4	H ₂ O	Ih	6.8×10^{17}	0.22	150	
<i>Average</i>			6.8×10^{17}	<i>0.22</i>		0.18
6.3.3 Ice 1	H ₂ S	Amorphous	7.1×10^{17}	0.33		
6.3.3 Ice 2	H ₂ S	Amorphous	6.5×10^{17}	0.30		
6.3.3 Ice 3	H ₂ S	Amorphous	7.7×10^{17}	0.36		
<i>Average</i>			7.1×10^{17}	<i>0.33</i>	20	0.16
6.3.3 Ice 4	H ₂ S	Crystalline	5.8×10^{17}	0.27		
6.3.3 Ice 5	H ₂ S	Crystalline	6.4×10^{17}	0.29		
6.3.3 Ice 6	H ₂ S	Crystalline	7.6×10^{17}	0.35		
<i>Average</i>			6.6×10^{17}	<i>0.31</i>	60	0.16
6.3.3 Ice 7	SO ₂	Amorphous	3.1×10^{17}	0.17		
6.3.3 Ice 8	SO ₂	Amorphous	2.5×10^{17}	0.14		
6.3.3 Ice 9	SO ₂	Amorphous	2.9×10^{17}	0.16		
<i>Average</i>			2.8×10^{17}	<i>0.16</i>	20	0.07
6.3.3 Ice 10	SO ₂	Crystalline	2.6×10^{17}	0.15		
6.3.3 Ice 11	SO ₂	Crystalline	2.2×10^{17}	0.12		
6.3.3 Ice 12	SO ₂	Crystalline	2.8×10^{17}	0.16		
<i>Average</i>			2.6×10^{17}	<i>0.14</i>	90	0.07

In order to constrain any potential phase dependence of the radiation chemistry of H₂O astrophysical ice analogues, a total of four ice phases were investigated: (i) one ASW formed by slow deposition of H₂O vapour at 20 K, (ii) one RAI formed by deposition at 80 K, (iii) one Ic formed by deposition at 130 K, and (iv) one Ih formed by deposition at 150 K. The deposition temperatures of all the amorphous and crystalline ices investigated in this study are summarised in Table 6.1. Following their deposition, all crystalline ices were cooled to 20 K prior to irradiation. The irradiation of all ices at the same temperature ensured that no differences in the observed radiation chemistry between different ice phases of the same species could be due to increased radical mobility in the ice matrix at elevated temperatures.

Once deposited, all ices were irradiated using 2 keV electron beams with the exception of the SO₂ ices, which were irradiated using a 1.5 keV electron beam, with mid-infrared absorption spectra (1 cm⁻¹ resolution; 128 scans) being acquired at several points throughout the irradiation processes. In all cases, projectile electrons impacted the target ices at an angle of 36° to the normal over a nominal area of around 0.9 cm². Prior to commencing each

irradiation, the beam current, flux, and profile homogeneity were determined using the method outlined in Chapter 4. CASINO simulations were also performed so as to determine the maximum electron penetration depth in the amorphous and crystalline phases of each astrophysical ice analogue (Table 6.1). Furthermore, the experimental protocol used involved multiple irradiations for each solid ice phase so as to ensure good repeatability of the experiment.

6.3 Comparative Electron Irradiations of Amorphous and Crystalline Ices

In this sub-section, the results of the comparative electron irradiations of the amorphous and crystalline phases of the ices listed in Table 6.1 are described and discussed in the context of their relevance to molecular astrophysics and astrochemistry. To facilitate this discussion, the experiments have been divided into three groups depending upon the processing of the raw data acquired during experimentation. In the first group, the results obtained from the irradiations of amorphous and crystalline CH₃OH and N₂O are discussed. This is followed by a discussion of the observations made during the electron irradiation of the four phases of H₂O that were investigated. The final group of results that shall be discussed in this sub-section is that comprised of the observations made during the electron irradiation of the amorphous and crystalline phases of H₂S and SO₂.

6.3.1 Amorphous and Crystalline CH₃OH and N₂O Ices

The irradiation of the amorphous and crystalline phases of solid CH₃OH and N₂O were conducted using 2 keV electrons. CASINO simulations revealed that the penetration depths of the impinging electrons were significantly less than the total thickness of the deposited ices, particularly in the case of the CH₃OH ices (Table 6.1). This means that there exists an ‘active’ zone towards the surface of the ice in which the physical, physico-chemical, and chemical effects of electron irradiation are manifested. It is therefore preferable to correct for the ‘inactive’ zone which is observed spectroscopically but does not play host to any radiation chemistry or physics so as to better illustrate the radiation chemistry and physics occurring within the ‘active’ zone of the ice.

A description of the correction factor used has already been given in Chapter 4, and so only a brief overview is provided here. The measured column density N is first normalised to the initially deposited column density of the ice to yield the dimensionless variable N_n . This is then converted to the corrected normalised column density N_c by use of the equation:

$$N_c = \frac{N_n - N_p}{1 - N_p} \tag{Eq. 6.1}$$

where N_p refers to the plateau or asymptotic value that the normalised molecular column density of the ices reaches after prolonged irradiation (i.e., the so-called ‘steady state’).

To calculate N_p , a plot of N_n as a function of fluence was generated for each irradiated ice and fitted with an exponential decay function. From the equation of this decay function, the N_n value that would be reached after suppling a hypothetical fluence of 10^{20} electrons

cm^{-2} (four orders of magnitude greater than what was actually supplied) was calculated and was assumed to be equal to N_p . This assumption was justified by the fact that the value for N_n calculated for a hypothetical fluence of 10^{19} electrons cm^{-2} was equal to that for 10^{20} electrons cm^{-2} (i.e., N_p) in all cases. It is important to note that this correction factor has only been applied to the CH_3OH and N_2O parent ice column densities, and not to any measurements of the column densities of radiolytically derived product molecules.

As shown in Fig. 6.2, the radiolytic decay rate of CH_3OH was found to be significantly more rapid in the case of the amorphous ice compared to the crystalline one. Conversely, the radiolytic decay trends of the amorphous and crystalline N_2O ices were observed to be more similar to each other, although that of the amorphous phase was still more rapid than that of the crystalline one. Upon supplying an electron fluence of 8.9×10^{15} electrons cm^{-2} , the CH_3OH column density in the 'active' zone of the amorphous ice dropped to an average 25% of its original value, while for the crystalline ice this value, on average, only dropped to 67%. This phase-dependent decay of CH_3OH was apparent throughout the irradiation of the ices, with the amorphous ice requiring a fluence of 2.7×10^{16} electrons cm^{-2} for the 'active' zone column density to drop below 10% of its initial value, while triple this fluence was required to observe this effect in the crystalline phase. Conversely, the average decay trends for amorphous and crystalline N_2O were more similar (Fig. 6.2), with 44% and 52% of the N_2O in the 'active' zone remaining after a fluence of 1.3×10^{16} electrons cm^{-2} had been respectively delivered to the amorphous and crystalline phases.

These observations may be rationalised in terms of the differences in the structure and energetics of the different ice phases of CH_3OH and N_2O and, by extension, their stability against radiolytic decay. In general, crystalline ices benefit energetically from their lattice energy, defined as the energy input required to disrupt the regular ordering of their structure (Jenkins 2005). As such, it is intuitive to expect slower rates of radiolytic decay for the crystalline ices when compared to the amorphous ones, due to the need for the projectile electrons to expend a portion of their energy on overcoming this lattice energy. Such a consideration goes some way to qualitatively explaining why the decay rate of an irradiated amorphous ice is faster than that of its crystalline counterpart, but does not explain why there exists a much larger discrepancy between the decay rates of amorphous and crystalline CH_3OH ice compared to N_2O ice.

In order to explain these differences in decay rates, it is necessary to discuss the intermolecular bonding present within the different ice phases of CH_3OH and N_2O . In the case of the former, the regularity of the crystal lattice permits an extensive array of hydrogen bonds which confers an additional degree of stability to the ice. This network of hydrogen bonds would require an increased supply of energy to be overcome, with some of the kinetic energy of the projectile electrons being used for this purpose. The amorphous phase is not characterised by this extensive hydrogen bonding network, and so there is more available energy which may be used for driving electron-induced radiolytic dissociation of this phase, leading to a more rapid initial depletion of CH_3OH parent molecules. It should be noted that, although some hydrogen bonding in CH_3OH is expected in the amorphous phase, this would not have the stabilising effect of the extensive lattice found in the crystalline phase, particularly in light of the fact that hydrogen bonding in CH_3OH is a cooperative phenomenon in which the presence of a hydrogen bond in the array strengthens subsequent hydrogen bonds *via* electrostatic effects (Kleeberg and Luck 1989, Sum and Sandler 2000).

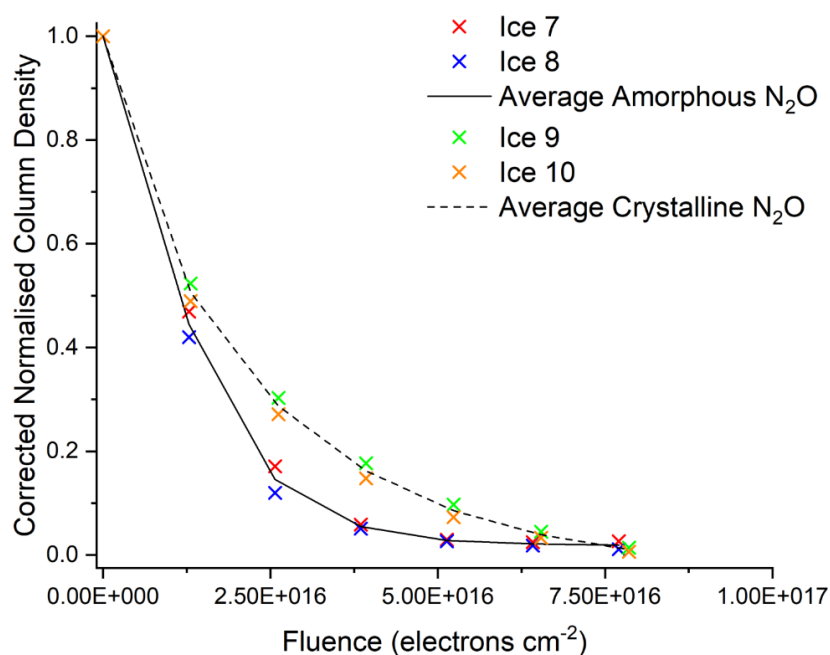
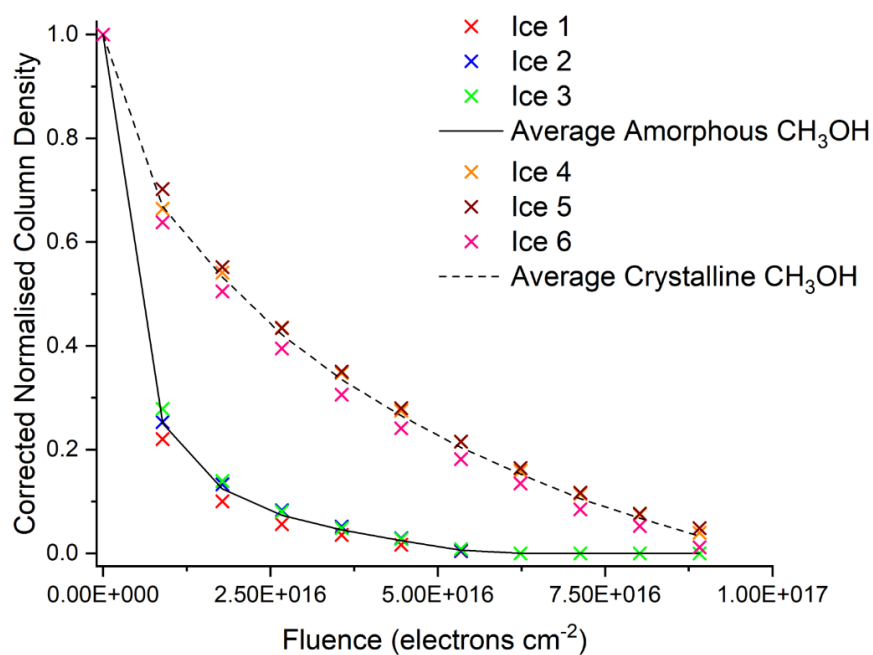


Fig. 6.2: Electron-induced decay of CH₃OH (*above*) and N₂O (*below*) ice phases with increasing electron fluence. Error bars have been omitted from the figure, as the uncertainty in column density is expected to be significantly less than the 30-50% uncertainty associated with the integrated band strength constant used to calculate it.

The need to overcome the hydrogen bonding network implies that the irradiation of the crystalline CH₃OH ice should result in a degree of localised amorphisation of the ice in the ‘active’ zone into which the projectile electrons penetrate (Hudson and Moore 1995). This was observed in the acquired mid-infrared spectra, particularly in the broad absorption band related to the O–H stretching modes centred at around 3200 cm⁻¹ (Fig. 6.3). In the unirradiated crystalline ice, this band presents as a double peaked structure consisting of a defined, narrow higher wavenumber peak and a broad lower wavenumber peak. Conversely,

this band appears as a very broad single peaked structure in the pure amorphous phase. Upon the onset of electron irradiation of the crystalline CH₃OH ice (and particularly so after fluences of 4.5×10^{16} electrons cm⁻² were delivered), however, this band was observed to broaden. The effect of this broadening is most visible in the narrower, higher wavenumber constituent peak (Fig. 6.3) and represents a localised transition to a less ordered ice structure. Once the hydrogen bonding network has been disrupted, radiolytic dissociation of the CH₃OH molecules may take place more efficiently.

Given such results, the next point to consider is perhaps the possibility of a charged projectile not having sufficient energy to overcome the lattice energy or disrupt the hydrogen bonding network and thus not induce any significant radiolytic dissociation of the CH₃OH crystalline phase that would otherwise occur in the amorphous phase. A similar scenario was considered by Bag *et al.* (2013), who demonstrated that CH₂⁺ molecular ions with kinetic energies <8 eV fired towards a D₂O target ice exhibited hydrogen-deuterium exchange reactions when the ice was amorphous, but not when it was crystalline. In terms of electrons as projectiles, although previous studies using lower energies (2.5-20 eV) have been performed, these have typically been performed on an amorphous target ice (e.g., Boyer *et al.* 2016, Sullivan *et al.* 2016). It would therefore be interesting to study the differences between the radiolysis of amorphous and crystalline CH₃OH ices when using a series of lower energy (<20 eV) electrons with the aim of reproducing the results of Bag *et al.* (2013) and of this present study.

The average radiolytic decay trends of the amorphous and crystalline N₂O ices were observed to be significantly more similar than those of the amorphous and crystalline CH₃OH (Fig. 6.2). Although the crystalline N₂O ice does benefit from its lattice energy, there is no hydrogen bonding network present to further stabilise it against radiolytic decay. Instead, the dominant intermolecular interactions between adjacent N₂O molecules are weak dipole interactions and van der Waals forces. The large-scale orientation of molecular dipoles in the regular crystalline lattice confers an additional degree of stability against radiolytic decay; however, since dipole interactions are weaker than hydrogen bonds, this increase in the resistance of crystalline N₂O ice to radiolytic decay is not as great as that of the crystalline CH₃OH ice compared to its amorphous phase. Once again, it is acknowledged that some limited clustering due to orientation of dipoles is expected in the amorphous ice, particularly due to the known existence of gas-phase N₂O dimers, trimers, and tetramers (Miller and Pederson 1997, Miller and Pederson 1998, Dehghani *et al.* 2007). Such molecular clusters are preserved during condensation and, indeed, the structure of the slipped parallel dimer (or an extension thereof) is thought to be key to the so-called ‘spontelectric’ (i.e., spontaneously electric) properties of condensed N₂O (Plekan *et al.* 2017).

These results therefore provide quantitative indications of the increased resistance to radiation induced decay of the crystalline ices compared to their amorphous phases. This resistance is the result of the crystalline lattice energy, as well as more extensive intermolecular forces of attraction in the regular crystalline lattice that must be overcome before molecular dissociation may take place. Stronger and more long-ranging intermolecular interactions, such as the hydrogen bonding network in crystalline CH₃OH, are able to provide greater resistance than weaker ones, such as the molecular dipole interactions in N₂O. As such, it is possible to conjecture that the difference in the radiolytic decay trends of amorphous and crystalline ice phases would be minimised for those molecular species that are non-polar and should be more pronounced for those that exhibit very strong and extensive hydrogen bonding networks in their crystalline phases.

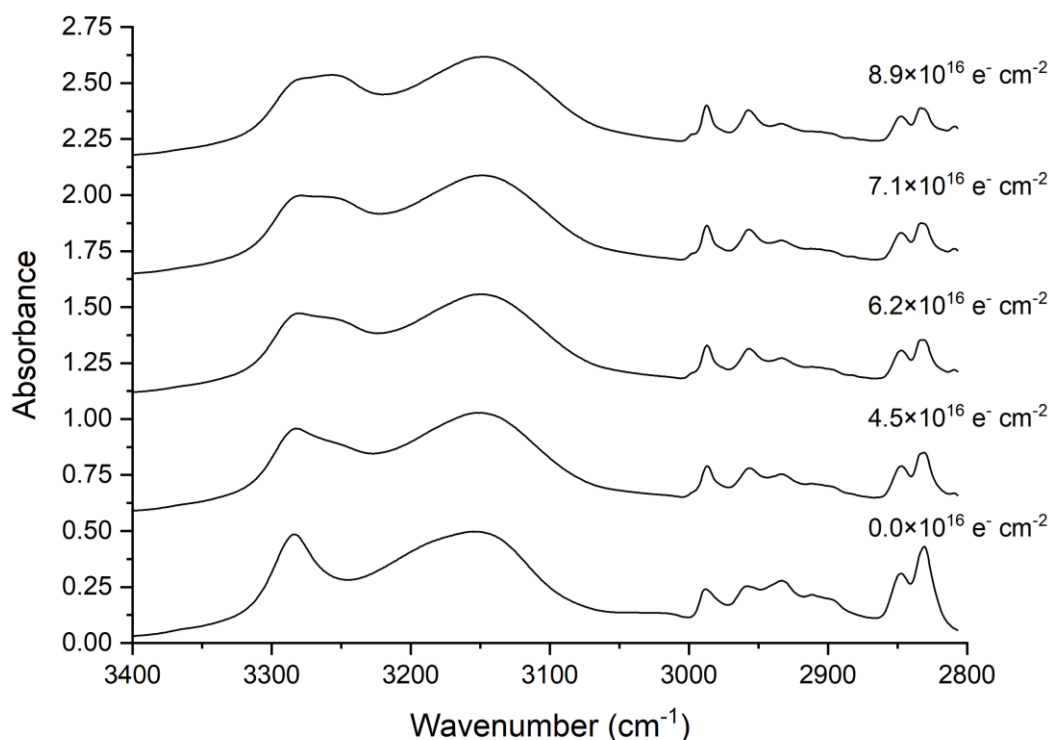


Fig. 6.3: The broadening of the double peaked absorption band at about 3200 cm^{-1} due to the O–H stretching modes in crystalline CH_3OH ice as a result of electron irradiation is an indication of amorphisation. This broadening is most evident in the higher wavenumber constituent peak. Note that spectra are vertically offset for clarity.

In this study, an analysis of the formation of radiation products after the electron irradiation of amorphous and crystalline CH_3OH and N_2O ices has also been performed. Although the formation of many new species in the electron irradiated ices is evident (Fig. 6.4), this discussion shall be limited to those species that present well-defined and unambiguous absorption bands in the mid-infrared spectra that can thus be easily analysed quantitatively. In the case of the electron irradiated CH_3OH ices these are CO , CO_2 , H_2CO , and CH_4 ; while for the electron irradiated N_2O ices these are NO_2 , N_2O_4 , and O_3 (Table 6.2).

Table 6.2: List of characteristic mid-infrared absorption bands and their associated band strength constants (A_s) for the species considered quantitatively in this study. The data have been collected from Sivaraman *et al.* (2008) and Luna *et al.* (2018).

Species	Mid-Infrared Band Position (cm^{-1})	A_s ($10^{-17}\text{ cm molecule}^{-1}$)
CH_3OH (amorphous)	1027 (ν_8)	1.61
CH_3OH (crystalline)	1027 (ν_8)	1.28
CO	2138 (ν_1)	1.10
CO_2	2343 (ν_3)	11.80
H_2CO	1725 (ν_4)	0.96
CH_4	1300 (ν_4)	0.80
N_2O (amorphous)	1283 (ν_1)	1.20
N_2O (crystalline)	1283 (ν_1)	0.98
NO_2	1614 (ν_3)	0.62
N_2O_4	1261 (ν_{12})	0.51
O_3	1039 (ν_3)	1.40

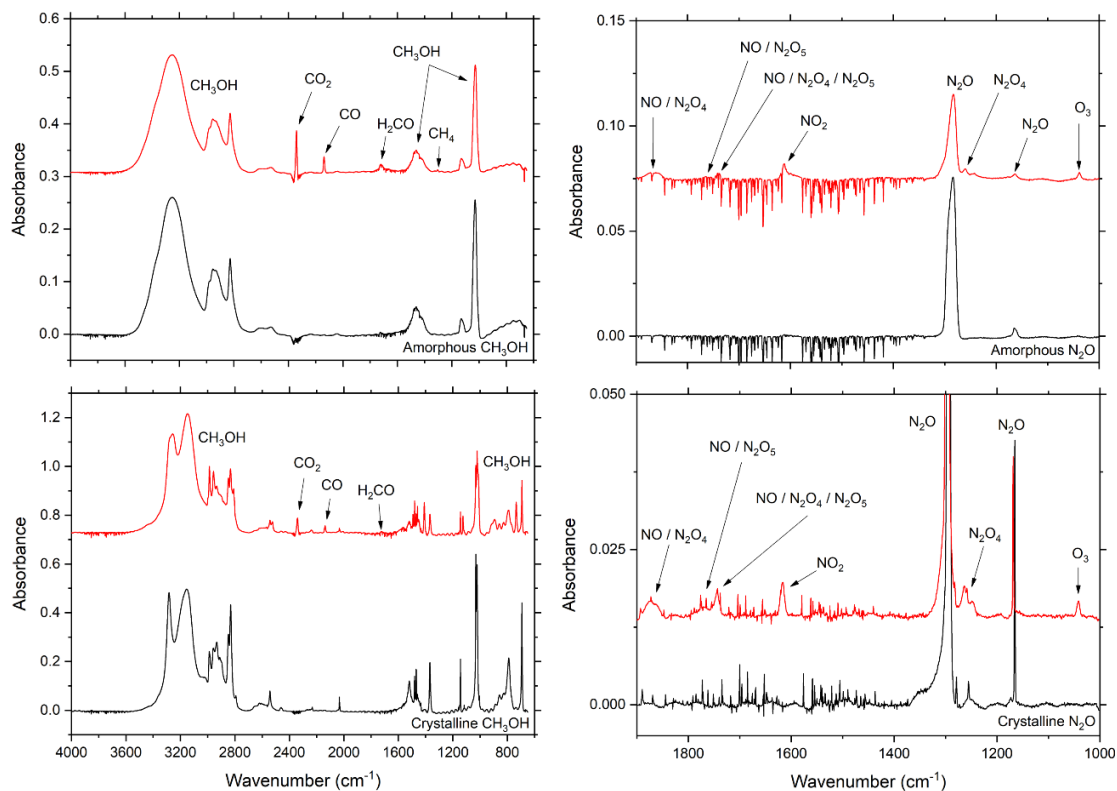


Fig. 6.4: Mid-infrared absorption spectra of the unirradiated (*black traces*) and 2 keV electron irradiated (*red traces*) amorphous and crystalline phases of solid CH₃OH and N₂O. In these spectra, the delivered fluences to the irradiated ices were 8.9×10^{16} and 1.3×10^{16} electrons cm⁻² for the CH₃OH and N₂O ices, respectively. Note that spectra displayed in the same panel are vertically offset for clarity.

For both molecular species, the formation of products as a result of electron irradiation was greater after irradiation of the amorphous phase compared to the crystalline phase by a factor of 1.25-3 at peak production, depending upon the product considered (Figs. 6.5 and 6.6). Although it is perhaps intuitive to consider this to be the result of a more rapid dissociation of the parent molecular species in the amorphous phase, an additional contributing cause for this observation are the differences in porosities and structural defects between amorphous and crystalline ices.

At 20 K, radicals formed as a result of the radiolytic dissociation of the parent species are mobile within the ice matrix, and may therefore diffuse and react with other radicals and molecules to form new species. In amorphous ices, the increase in porosity and structural defects compared to the corresponding crystalline phases allows for these radicals to diffuse more easily through the solid matrix (Grieves and Orlando 2005, Isokoski *et al.* 2014, Stechauner and Kozeschnik 2014). As such, any recycling reactions leading back to the formation of the parent species are not favoured due to the precursor radicals having migrated away from each other and thus no longer being present at the site of their formation. With competition from such recycling reactions being lessened, reactions leading to the formation of new product molecules are favoured leading to a greater abundance of these species in the irradiated amorphous ices.

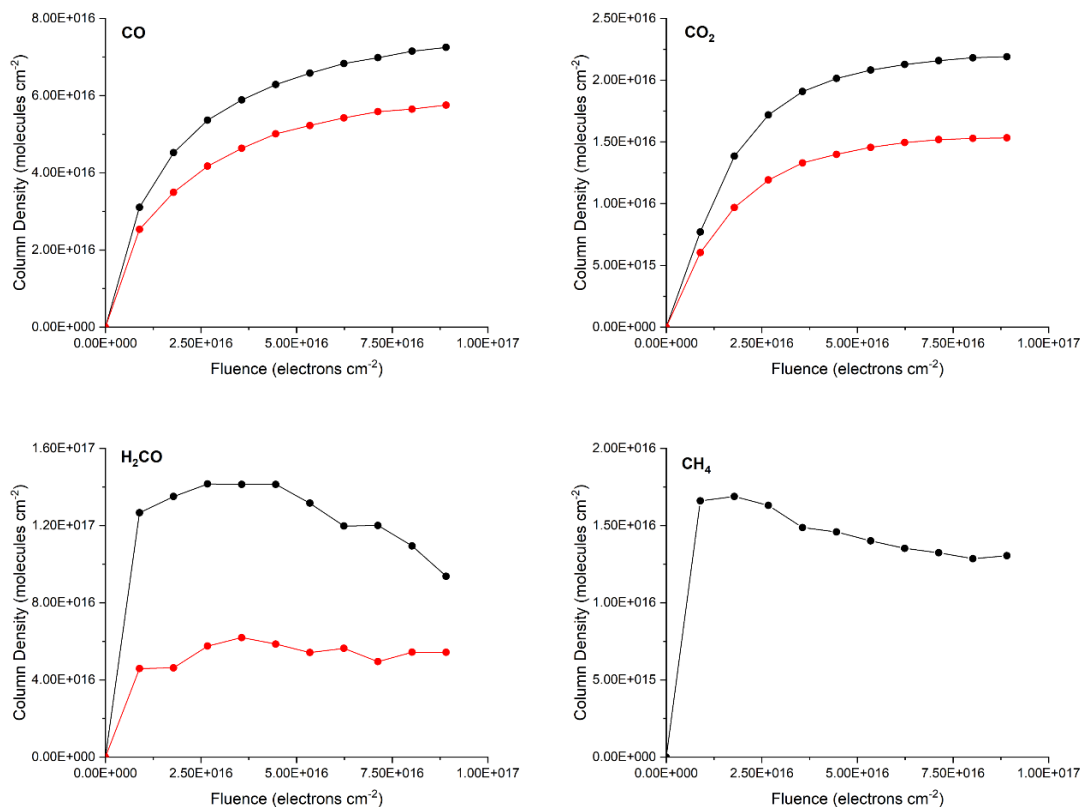


Fig. 6.5: Average column densities for the products of amorphous (*black traces*) and crystalline (*red traces*) CH_3OH irradiation by 2 keV electrons. Although CH_4 was detected in the post-irradiative crystalline CH_3OH mid-infrared spectra, the observed quantities were below the limit of quantitation. Note that lines joining data points are not fits and are plotted solely to guide the eye.

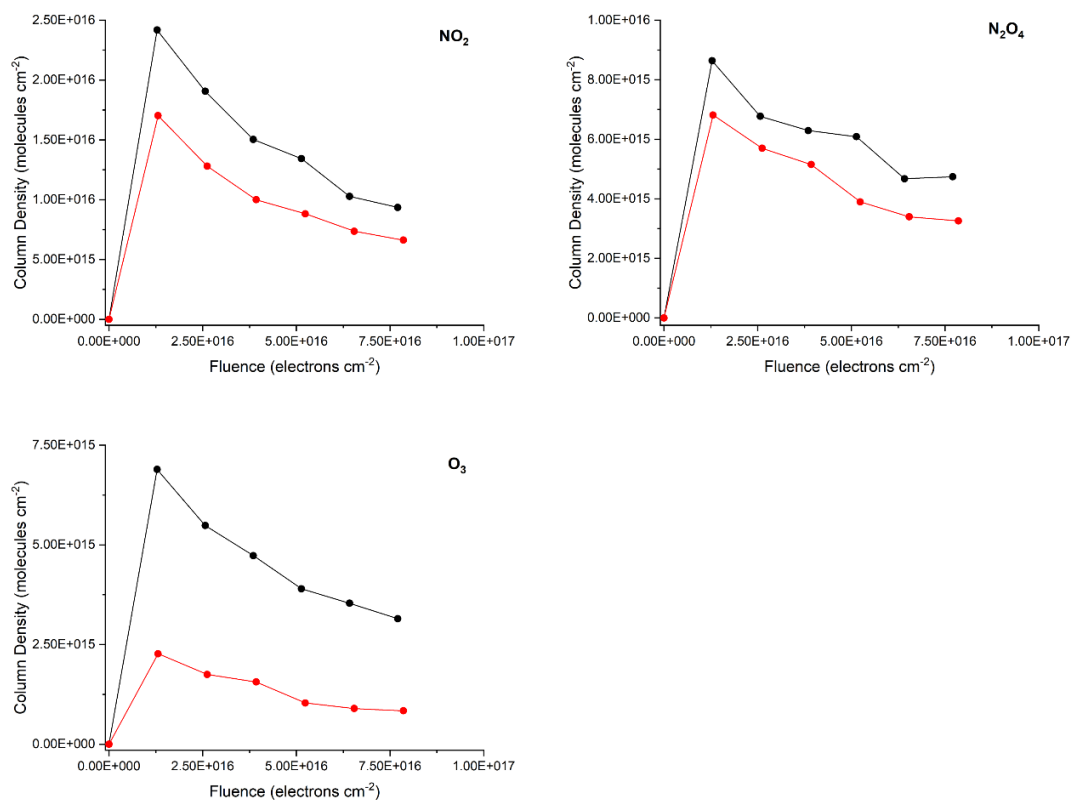


Fig. 6.6: Average column densities for the products of amorphous (*black traces*) and crystalline (*red traces*) N_2O irradiation by 2 keV electrons. Note that lines joining data points are not fits and are plotted solely to guide the eye.

6.3.2 Amorphous, Restrained Amorphous, and Crystalline H₂O Ices

The comparative electron irradiations of the ASW, RAI, Ic, and Ih phases of H₂O have also been studied, although it must be noted that no correction factors have been applied to any measured molecular column densities due to the fact that the thicknesses of the deposited ices are comparable to the penetration depths of the 2 keV electrons (Table 6.1). The mid-infrared spectra of the various H₂O ice phases, both before and after irradiation, are shown in Fig. 6.7. In the pre-irradiative spectra, several of the vibrational modes of the H₂O molecule are visible, including the ν_2 mode centred at about 1655 cm⁻¹ and the librational (ν_L) mode observed at 764 cm⁻¹ in ASW and at 819 cm⁻¹ in RAI, Ic, and Ih (Hagen *et al.* 1981, Hagen and Tielens 1982, Zheng *et al.* 2006a, Zheng *et al.* 2007). A weaker absorption band at 2206 cm⁻¹ is attributed to either the $3\nu_L$ overtone or the $\nu_L + \nu_2$ combination band.

The broad absorption feature at 3250 cm⁻¹ is caused by the stretching modes of the H₂O molecule. The shape of this band changes noticeably on going from ASW to RAI to Ic to Ih (Figs. 6.1 and 6.7). In ASW, the band presents as a very broad, single peaked structure centred at about 3272 cm⁻¹. On transitioning to RAI, the band adopts a narrower profile due to the presence of crystallites within the structure, although additional features are difficult to identify. In the Ic phase, however, shoulders at 3152 and 3399 cm⁻¹ are visible that have been ascribed to the ν_3 and ν_1 modes, respectively (Hagen *et al.* 1981, Hagen and Tielens 1982, Zheng *et al.* 2006a, Zheng *et al.* 2007). In the mid-infrared spectrum of Ih, these contributions are still better resolved and the band appears as a multi-peaked structure.

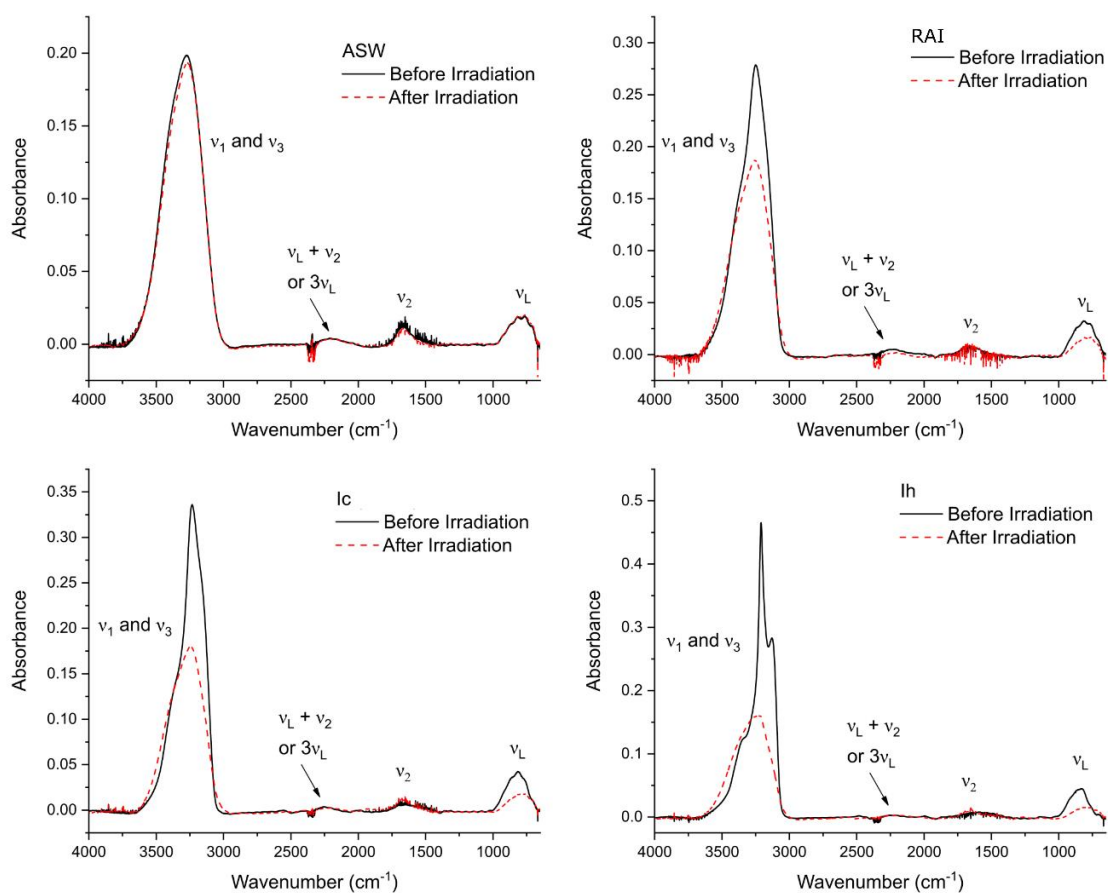


Fig. 6.7: Mid-infrared spectra of ASW (deposited at 20 K), RAI (deposited at 80 K), Ic (deposited at 130 K), and Ih (deposited at 150 K) H₂O ice phases before (*black trace*) and after (*red trace*) irradiation using a fluence of 1.3×10^{17} electrons cm⁻² at 20 K. Prominent vibrational modes have been labelled.

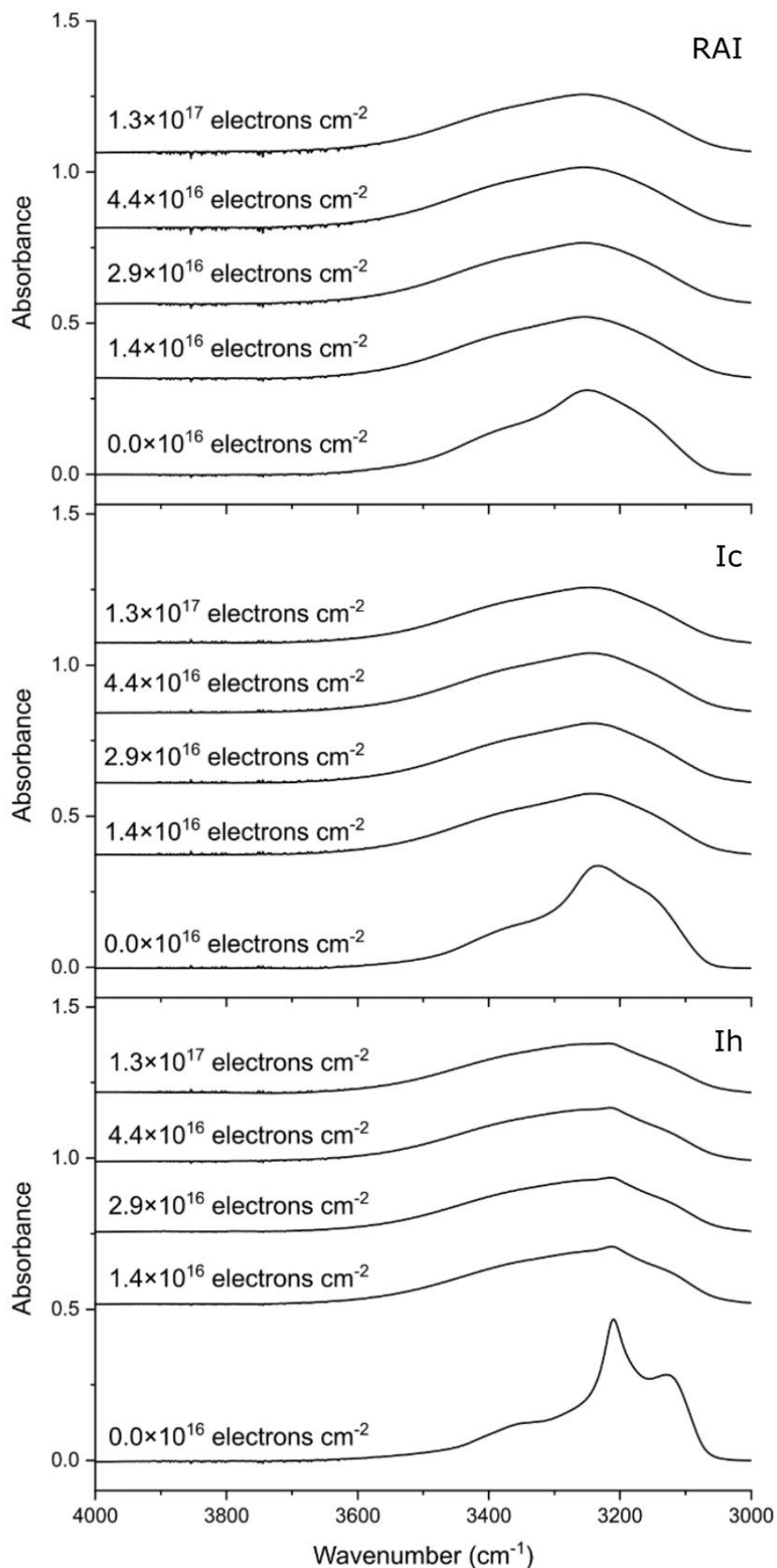


Fig. 6.8: The evolution of the broad stretching mode in RAI, Ic, and Ih during the electron irradiation of those phases at 20 K. The bands for the Ih, Ic, and (to a lesser extent) RAI were observed to undergo increased broadening as a result of electron-induced amorphisation of the ices. This amorphisation is suggested to be more rapid in the cases of RAI and Ic, for which all spectroscopic signatures of crystallinity were lost after an electron fluence of 1.4×10^{16} electrons cm^{-2} was supplied. The Ih phase appeared to be more resistant to radiation-induced amorphisation, with crystallinity only having been deemed to be lost after a fluence of 4.4×10^{16} electrons cm^{-2} was supplied. Note that spectra are vertically offset for clarity.

The onset of electron irradiation results in a noticeable change in the appearance of the mid-infrared spectra of the H₂O ice phases (Fig. 6.7). Perhaps the most evident of these is the change in the appearance of the broad stretching mode. When RAI and the crystalline ices (Ic and Ih) are irradiated, this band changes from a narrower, structured, and partially split one to one which is broader and essentially featureless; similar to that of ASW. This is indicative of an efficient radiation-induced amorphisation process (Palumbo 2006, van Dishoeck *et al.* 2013). When directly comparing these amorphised phases, it is possible to note that the amorphisation of RAI and Ic occurs more rapidly than that of Ih as virtually all spectroscopic features associated with crystallinity in these ices are lost after a fluence of 1.4×10^{16} electrons cm^{-2} has been delivered. In the case of Ih, however, some small and identifiable peaks within the broader band persist until a fluence of 4.4×10^{16} electrons cm^{-2} , after which point the band adopts a broad and featureless structure similar to that of ASW. The progress of the amorphisation process, as observed from changes in the shape and structure of the broad band associated with the stretching modes, is depicted in Fig. 6.8.

In contrast, the electron irradiation of ASW does not appear to result in any significant change to the appearance of the broad stretching mode. However, one minor change which was noted was the disappearance of two small absorption features at 3722 and 3698 cm^{-1} after the onset of irradiation (Fig. 6.9). These peaks are attributed to the hydroxyl dangling bonds in (micro)porous ASW (Rowland *et al.* 1991). The disappearance of these bands occurs early on during irradiation, with their complete absence being recorded at an electron fluence of 1.4×10^{16} electrons cm^{-2} , and is attributed to a collapse of the ice pore structure leading to the compaction of the ice (Palumbo 2006).

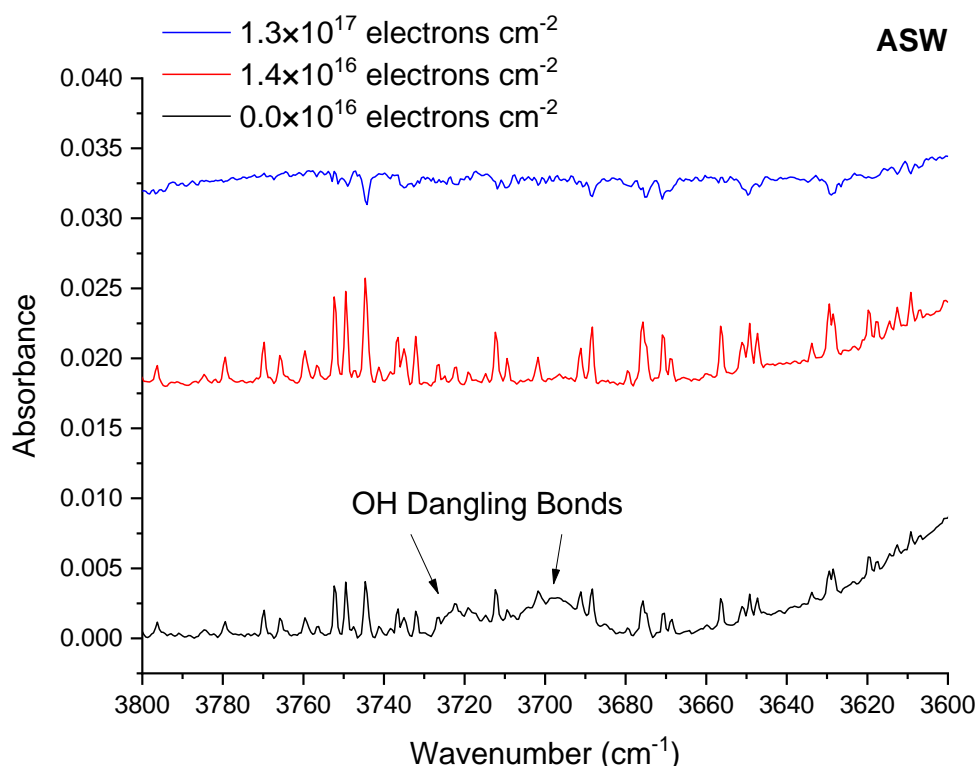


Fig. 6.9: The hydroxyl dangling bonds in (micro)porous ASW are visible as two small absorption features (indicated by arrows) at the higher wavenumber end of the H₂O stretching mode band in the unirradiated ice (*black trace; bottom*). Once an electron fluence of 1.4×10^{16} electrons cm^{-2} was supplied (*red trace; middle*), these peaks disappeared indicating radiation-induced compaction of the ice, and remained absent up to the end of irradiation after a fluence of 1.3×10^{17} electrons cm^{-2} had been supplied (*blue trace; top*). Note that spectra are vertically offset for clarity.

The mid-infrared spectra depicted in Figs. 6.7 and 6.8 clearly show that electron irradiation of the H₂O crystalline ice phases, as well as the RAI sample, results in their amorphisation. This is seen through the broadening of various absorption features, but particularly the stretching mode located at approximately 3250 cm⁻¹. Several other studies have reported similar results (Kouchi and Kuroda 1990, Strazzulla *et al.* 1992, Moore and Hudson 1992, Leto and Baratta 2003, Famá *et al.* 2010). The work of Leto and Baratta (2003) investigated the amorphisation of Ic induced by Lyman- α ultraviolet photon irradiation and compared this with amorphisation induced by 30 keV proton irradiation, and found that the latter was approximately twice as rapid.

The results presented in this thesis also allow for comparisons to be drawn; in this case between the amorphisation of Ic and Ih. As stated previously, complete amorphisation of the crystalline ice was observed spectroscopically after an electron fluence of 1.4×10^{16} electrons cm⁻² was delivered to the Ic phase. However, the Ih phase was observed to be somewhat more resistant to amorphisation, which was not fully observed until a fluence of 4.4×10^{16} electrons cm⁻² had been delivered. This is not unexpected, as the Ih phase is a stable crystalline phase while the Ic phase is only meta-stable with respect to Ih (Mayer and Hallbrucker 1987). This therefore suggests that the radiation-induced phase transition from crystalline to amorphous, which is unachievable solely by cooling (Baragiola 2003), is easier in the case of Ic.

The electron irradiation of Ic has also been studied in a series of papers by Zheng and co-workers (Zheng *et al.* 2006a, Zheng *et al.* 2006b, Zheng *et al.* 2007), in which 0.1 μ m-thick ices were irradiated using 5 keV electrons to a fluence of 3.6×10^{17} electrons cm⁻². Although ice amorphisation was reported in these studies, the process was not as complete as was observed in the results presented here (Figs. 6.7 and 6.8), with several features of crystallinity still clearly visible even at the end of their irradiation experiments. The reason for this is likely relatively mundane: the electron beam used in the experiments presented in this thesis was scanned over a much larger area of the target ice, meaning that there was a significantly lower proportion of unirradiated crystalline H₂O ice that was spectroscopically observed in the data presented here.

One interesting factor of crystalline H₂O ice amorphisation which has not been considered by the present study but should nonetheless be discussed is the temperature dependence of this process. Earlier studies have revealed that the irradiation of crystalline ices at lower temperatures leads to a greater extent of amorphisation (Strazzulla *et al.* 1992, Moore and Hudson 1992, Mastrapa and Brown 2006). Indeed, the results of Zheng *et al.* (2006a), who investigated the temperature dependence of product formation as a result of the electron irradiation of Ic, attest to this, as the most extensive amorphisation-induced changes in the Ic mid-infrared absorption bands were visible at 12 K, while no such changes could be observed after irradiation of Ic at 90 K. Previous works have yet to demonstrate the amorphisation of crystalline H₂O ice as a result of electron irradiation at irradiation temperatures greater than 70 K. The reason for this is not fully understood and constitutes an interesting avenue for potential future investigation.

Irradiation of ASW using 2 keV electrons did not result in any major changes in the shape or appearance of its mid-infrared absorption bands (Fig. 6.7), other than minor band intensity decreases due to the radiolytic conversion of ASW to other molecules, such as H₂O₂. However, the two hydroxyl dangling bond peaks at 3722 and 3698 cm⁻¹ which are typically associated with (micro)porosity were noted to disappear as a result of electron irradiation (Fig. 6.9). This observation has been interpreted as being the result of compaction

of the ice. It is well known that ASW accreted from the vapour phase is a (micro)porous structure; however, the extent of this porosity is dependent upon several parameters, including the temperature and the rate of ice deposition (Palumbo 2006).

Indeed, this becomes increasingly apparent when comparing the mid-infrared spectra of unirradiated ASW presented in Figs. 6.7 and 6.9 to that of Palumbo (2006), who accreted 0.25 μm -thick ASW ices at 15 K from the vapour phase. Although the thicknesses of those ices were similar to the ones deposited in this study, those of Palumbo (2006) displayed more prominent hydroxyl dangling bond absorption bands, suggesting a greater extent of (micro)porosity within the ice structure compared to those considered here. This is not unexpected, as previous studies have shown that the porosity of ASW is greater in ices accreted at lower temperatures (Berland *et al.* 1995, Brown *et al.* 1996). It should also be noted that the angle of H₂O deposition also influences the porosity of the condensed ice (Stevenson *et al.* 1999, Kimmel *et al.* 2001, Dohnálek *et al.* 2003); however, this is not believed to have caused the increased ice porosity of Palumbo (2006) as both that study and this present one made use of a background deposition technique.

In addition to the physical re-structuring of the ice, electron irradiation also resulted in the formation of new chemical products. Previous studies have extensively demonstrated the formation of H₂ and O₂ as a result of the charged particle and ultraviolet photon irradiation of H₂O astrophysical ice analogues (Bahr *et al.* 2001, Gomis *et al.* 2004, Grieves and Orlando 2005, Loeffler *et al.* 2006, Zheng *et al.* 2006a, Zheng *et al.* 2006b, Zheng *et al.* 2007, Yabushita *et al.* 2013). However, these molecular products are infrared inactive and so could not be observed *via* mid-infrared spectroscopy. The formation of H₂O₂, however, is observable through its characteristic $\nu_2 + \nu_6$ combination band at around 2866 cm^{-1} (Moore and Hudson 2000, Baragiola *et al.* 2005). The symmetric bending (ν_2) and asymmetric bending (ν_6) modes were not observed. No spectroscopic evidence for the formation of O₃ or HO₂ was observed either, although this should not necessarily be interpreted as these species being absent from the ice as they may have been present at concentrations below the spectroscopic limit of detection (which is on the order of a few 10^{15} molecules cm^{-2}).

The abundance of H₂O₂ present in each H₂O astrophysical ice analogue after irradiation using 2 keV electrons was noted to differ between phases (Figs. 6.10 and 6.11). The production of H₂O₂ as a function of electron fluence was followed by measuring its column density *via* integration of the peak area of the combination band at 2866 cm^{-1} and taking A_s to be 5.7×10^{-17} cm molecule^{-1} (Loeffler *et al.* 2006). H₂O₂ production was highest as a result of the irradiation of ASW, while column densities observed after the irradiation of the RAI phase were lower (Fig. 6.11). The electron irradiation of the Ic and Ih phases resulted in a similar abundance of H₂O₂ which was lower than that produced as a result of the irradiation of ASW or RAI (Fig. 6.11). By comparing the initial column densities of H₂O present before the irradiation of each phase with the column density of H₂O₂ at the end of irradiation after a fluence of 1.3×10^{-17} electrons cm^{-2} had been supplied, it was possible to deduce that 0.32%, 0.21%, 0.16%, and 0.14% of the H₂O was converted to H₂O₂ as a result of the electron irradiation of ASW, RAI, Ic, and Ih, respectively.

The results presented here appear to constitute the first truly systematic and comparative study of the electron-induced production of H₂O₂ from multiple solid phases of H₂O. The mechanistic chemistry occurring within the ice as a result of electron irradiation is complex and different radiolytic products are the result of following different chemical pathways. Electron irradiation of a H₂O molecule results in the radiolytic abstraction of either a hydrogen atom or an oxygen atom to yield OH or H₂, respectively.

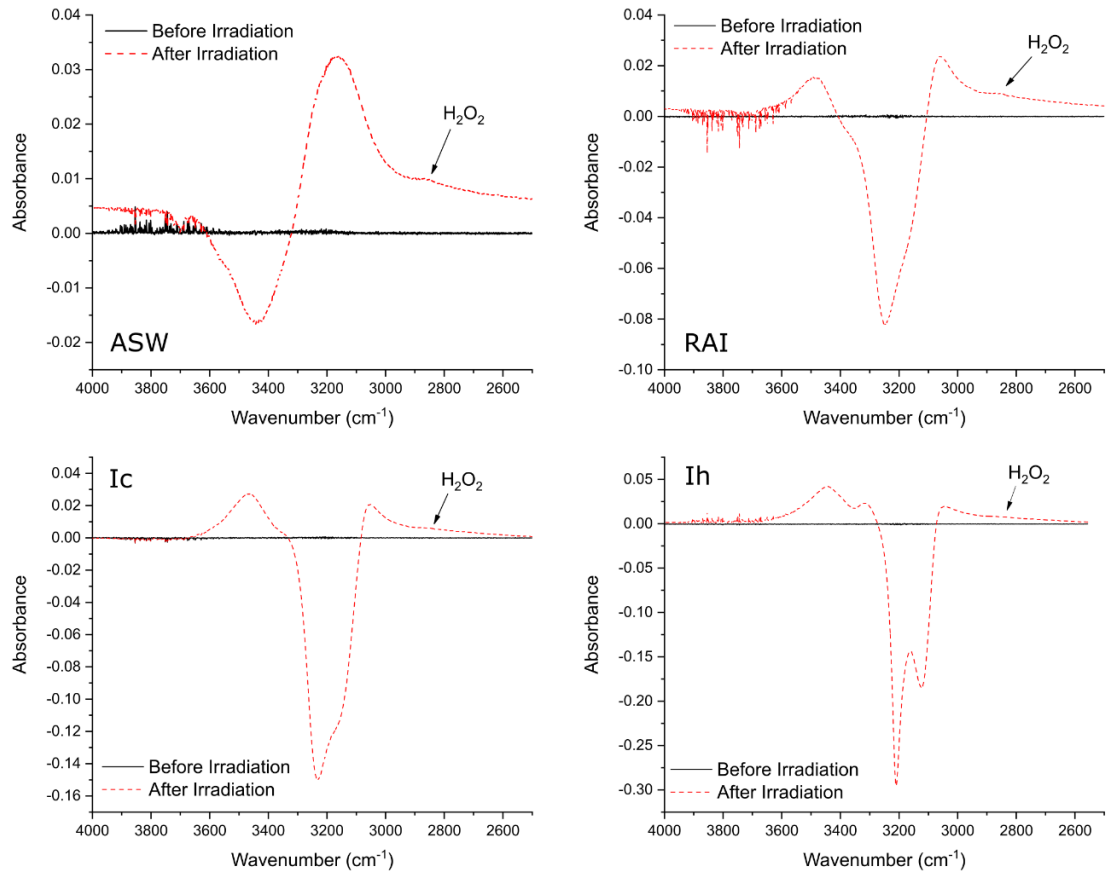
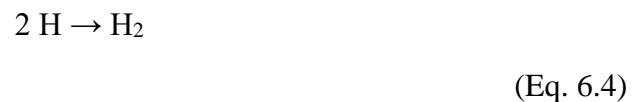


Fig. 6.10: Spectral identification of H_2O_2 in electron-irradiated (1.3×10^{17} electrons cm^{-2}) H_2O ices. In these difference spectra, the spectrum of the ice prior to any irradiation was used as a background, meaning radiolytic decay of the H_2O ice is seen as negative absorptions of its characteristic absorption bands while the formation of product molecules is seen as more accentuated positive absorptions. Note that positive shifts associated with the H_2O stretching modes can also be seen in these spectra, and are due to a combination of changes in the physical structure of the ice (such as amorphisation or compaction) which cause a change in the shape of the absorption band, as well as the appearance of the ν_5 asymmetric stretching and ν_1 symmetric stretching modes of H_2O_2 which are also in this region (Giguère and Harvey 1959).



Abstracted hydrogen and oxygen atoms may combine to yield their respective homonuclear diatomic molecules, H_2 and O_2 , or the heteronuclear OH radical:



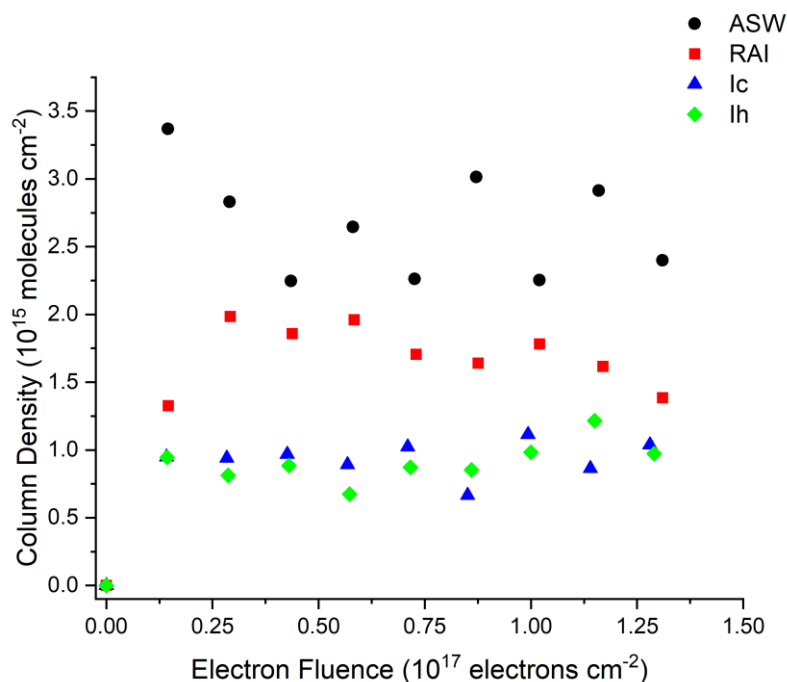
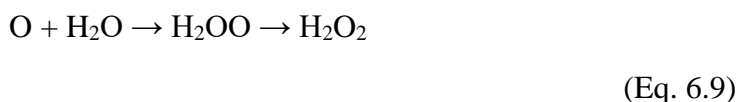


Fig. 6.11: Scatter plot depicting the evolution of the measured H_2O_2 column density (calculated using a linear baseline applied to the H_2O_2 absorption bands highlighted in the spectra shown in Fig. 6.10) with fluence during 2 keV electron irradiation. Error bars have been omitted from the figure, as the uncertainty in column density is expected to be significantly less than the 30-50% uncertainty associated with the integrated band strength constant used to calculate it.

The production of H_2O_2 largely occurs as a result of addition reactions between these atoms and radicals. For instance, the combination of two OH radicals may directly yield H_2O_2 . It is important to note, however, that at a temperature of about 10 K, where radicals are immobile within the bulk ice, this combination reaction can only occur if the OH radicals initially possess the correct geometry with respect to one another, where the distance between oxygen atoms in separate radicals is minimised (Zheng *et al.* 2006a). At higher temperatures, such as the 20 K irradiation temperature used in this present study, radicals are mobile and so the relative geometry of the combining OH radicals is likely to be of lesser importance.

The formation of H_2O_2 may also occur as a result of the reaction of an oxygen atom with a H_2O molecule. Two barrierless reaction pathways are available (Ge *et al.* 2006, Zheng *et al.* 2006a): the first is direct insertion of the electronically excited oxygen atom into the molecular structure of H_2O , thus directly yielding H_2O_2 . The second route involves addition of the oxygen atom to the H_2O molecule producing an oxywater intermediate H_2OO , which then rearranges *via* hydrogen atom migration to form H_2O_2 .



As may be seen in Fig. 6.11, the chemical productivity of H₂O in terms of radiolytic H₂O₂ production was highest for the ASW phase, and proceeded to decrease by a factor of about two on moving to the RAI phase, and again by a factor of about two on moving to the Ic phase, which itself had a similar H₂O₂ productivity to the Ih phase. As such, it may be stated that there is a decrease in the production rate of H₂O₂ on transitioning from less ordered to more ordered ice phases. Similar trends for O₂ and H₂ production were observed by Zheng *et al.* (2007) who made use of QMS to detect the formation of these products in electron irradiated ASW and Ic. Such results are further evidence that the phase of an astrophysical ice analogue has a direct influence on its radiolytic chemical productivity.

The increased H₂O₂ radiolytic productivity of less ordered H₂O ice phases is attributed to a combination of at least four factors. Firstly, the microporous nature of ASW means that the OH radicals and hydrogen atoms formed as a result of radiolytic dissociation of the H₂O molecule may migrate into empty spaces left by the micropores (Isokoski *et al.* 2014). Once there, hydrogen atoms may combine with one another to produce H₂ which may either desorb from the ice or remain trapped as a gas within the pores to form a clathrate-like structure. Either way, the reduction in the number of free hydrogen atoms renders the recombination reaction to recycle H₂O less probable, meaning there are more free OH radicals in the ASW phase available to produce H₂O₂. Similarly, the dissociation of H₂O to yield an oxygen atom and H₂ would allow for the former to contribute to the increased production of H₂O₂ *via* Eqs. 6.8 and 6.9.

A second factor which may play a role in the greater abundance of H₂O₂ in electron irradiated ASW compared to the more ordered phases is the increased presence of structural defects in the former compared to the latter. Some of these defects, such as L-type Bjerrum defects, create conditions amenable to the production of H₂O₂. Bjerrum defects occur in H₂O ices when, rather than a hydrogen bonding network containing intermolecular interacting hydrogen and oxygen atoms being present, a H₂O molecule is rotated about its oxygen atom such that two hydrogen atoms (D-type defect) or two oxygen atoms (L-type defect) face one another (Bjerrum 1952). As such, L-type defects present ideal geometrical conditions for the direct linkage of two radiolytically produced OH radicals through their oxygen atoms so as to yield H₂O₂. The contribution of such defects to the production of H₂O₂ is likely to be greater at lower temperatures where OH radicals are immobile, as discussed previously.

Thirdly, ASW does not benefit from the stabilising effect of lattice energies, unlike in the case of the crystalline ices. Chemistry resulting from the irradiation of the crystalline ice phases requires that this lattice energy is first overcome before any molecular radiolysis leading to the generation of radicals can occur. The data presented in Fig. 6.11 is supportive of this interpretation, as it suggests that more H₂O₂-producing radicals are formed in ASW than in any of the other ices. In the RAI, small pockets of crystallinity reduce the efficiency of radical formation as some of the energy of the projectile electrons must be expended upon overcoming the lattice energy of these small, structurally ordered regions. The H₂O₂ production resulting from the irradiation of the Ic and Ih phases is the lowest amongst the phases considered, and is likely reflective of the more significant lattice energies of these ices that must be overcome before radiolytic chemistry may take place.

Fourthly (and following on from the discussion relating to the difference between the rates of radiolytic decay of amorphous and α -crystalline CH₃OH), it is likely that the presence of an extensive hydrogen bonding network in crystalline H₂O ice phases also contributes to their lower H₂O₂ productivities. In Ic and Ih, this hydrogen bonding network extends throughout the entirety of the crystal lattice and thus adds an extra element of

stability to the structure. During electron irradiation, a portion of the kinetic energy of the incident electrons must be used to overcome the stabilising effect of hydrogen bonding before radiolytic dissociation of the H₂O molecules may take place. Such a disruption would result in a localised amorphisation characterised by increased ice defects (such as Bjerrum defects), as evidenced by the spectra presented in Fig. 6.8. In the ASW phase, hydrogen bonding is significantly less extensive and so there is more energy to be imparted by the incident electrons to drive radiolytic chemistry. However, the ASW phase derived from the irradiation of the crystalline phases cannot be as chemically productive as the ASW phase accreted directly from vapour, since not only must a portion of the kinetic energy of the projectile electrons be spent on disrupting the extensive hydrogen bonding initially present, but the ASW phase produced *via* radiation-induced amorphisation is likely to be compact (and thus, lacking micropores). Indeed, the mid-infrared spectra of electron irradiated Ic and Ih ices do not exhibit any peaks attributable to hydroxyl dangling bonds (Fig. 6.8).

6.3.3 Amorphous and Crystalline H₂S and SO₂ Ices

To continue with the full characterisation of the differences in the radiation chemistry of astrophysical ice analogues of differing phases, as well as in the spirit of the central theme of this thesis (i.e., sulphur ice astrochemistry), electron irradiations of the amorphous and crystalline phases of pure H₂S and SO₂ ices have also been considered. The mid-infrared spectra of these ices, both before and after irradiation by energetic electrons (2 keV in the case of H₂S and 1.5 keV in the case of SO₂) at different fluences, are shown in Fig. 6.12.

The onset of electron irradiation brings about noticeable changes in the appearances of the spectra of the pristine ices. Perhaps the most prominent of these is the significant broadening of the crystalline ice absorption bands, which also lose their split structures. This is due to radiation-induced amorphisation, which has been well documented in several ice species, including those considered in this study. It is interesting to note that, even at the end of the irradiation process once a fluence of 8×10^{16} electrons cm⁻² was delivered to the crystalline ices, the appearances of their absorption bands were still not identical to those of the deposited amorphous ices. Indeed, small signs of crystallinity (e.g., the presence of shoulders or shifted band peak positions) were still observable in the spectra of the crystalline ices at the end of the irradiation process. As such, these irradiated ices are likely largely amorphous but with some small degree of remnant structural order. The irradiation of molecular ices initiates a rich chemistry leading to the formation of new species: previous studies have established that irradiated H₂S ices efficiently yield H₂S₂ as well as higher order polysulphanes (H₂S_{*x*} where *x* > 2) in addition to S_{*x*} (Shingledecker *et al.* 2020, Cazaux *et al.* 2022). In the experiments presented here, the formation of H₂S₂ was observed through the development of its vibrational stretching modes which appear as a broad shoulder on the lower wavenumber end of the analogous H₂S absorption bands at about 2500 cm⁻¹ (Fig. 6.12; Moore *et al.* 2007). The chemistry leading to the formation of H₂S₂ (as well as higher order polysulphanes) is thought to be mediated by HS radicals formed *via* the radiolytic dissociation of the parent H₂S molecules:



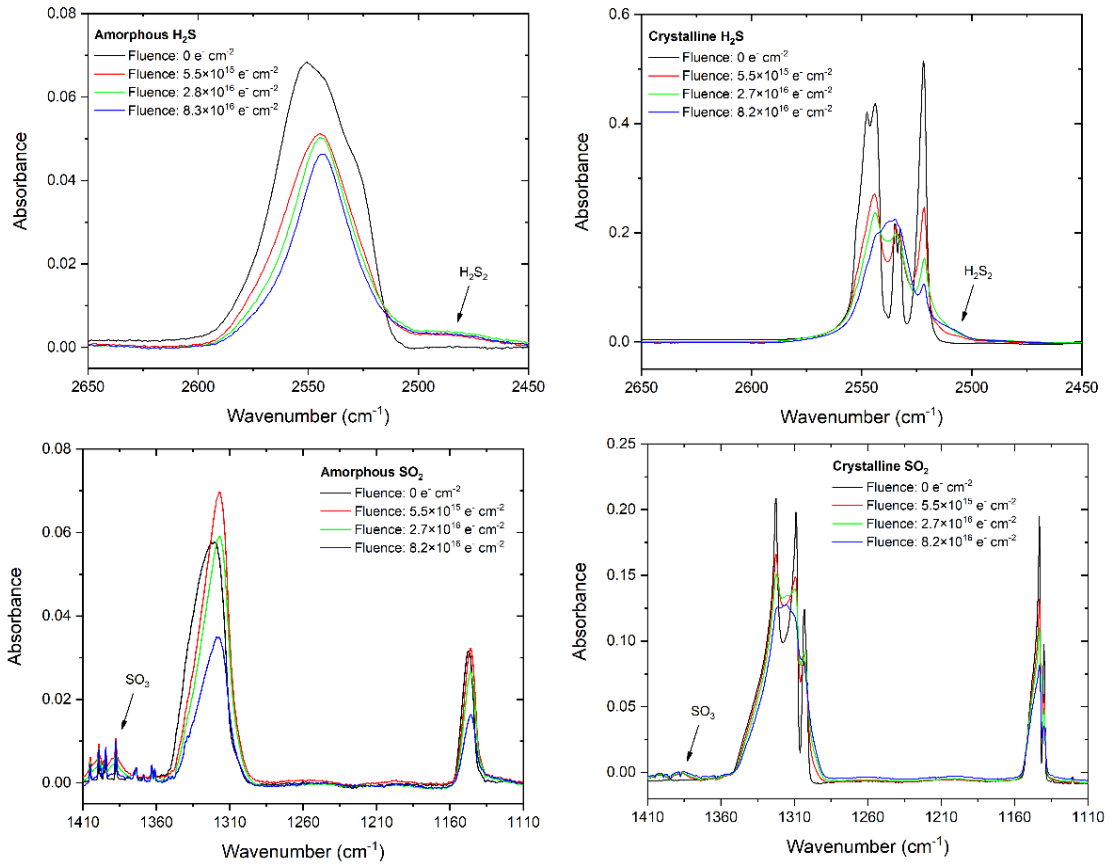
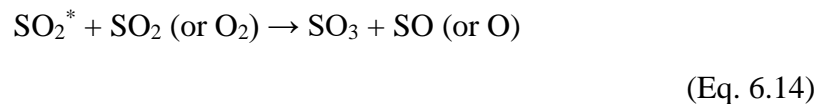


Fig. 6.12: Mid-infrared spectra of the amorphous and crystalline phases of H₂S and SO₂ ices at several points during their irradiation by energetic electrons at 20 K. Note that the fine structures coincident with the SO₃ absorption band in the spectrum of the electron irradiated amorphous SO₂ ice are caused by instabilities in the purge of the detector. Moreover, the initial increase in the intensity of the amorphous SO₂ ν₃ mode is likely caused by the radiation-induced compaction of the porous ice.

The irradiation of the SO₂ ice phases was also observed to lead to the formation of new molecules; in particular SO₃ which was observed through its ν₃ mode at 1388 cm⁻¹ (Guldan *et al.* 1995). SO₃ formation in irradiated SO₂ ices has been studied extensively and is believed to be the result of the dissociation of the latter species to yield free oxygen atoms which may then bond with other SO₂ molecules (Moore *et al.* 2007). It should be noted, however, that earlier studies by Pilling and Bergantini (2015) and de Souza Bonfim *et al.* (2017) have demonstrated that electronically excited SO₂ may also abstract oxygen atoms from either an adjacent SO₂ molecule or from a O₂ molecule; the latter having likely been formed as a result of the double ionisation of the SO₂ parent molecule followed by electron neutralisation as described recently by Wallner *et al.* (2022):



Differences in the parent molecule decay trends and in the abundance of molecular products observed after irradiation were noted between the studied amorphous and crystalline ice phases. Considering first the decay trends of the amorphous and crystalline H₂S ices: it was noted that the rate of decay of the crystalline phase was slower than that of the amorphous phase (Fig. 6.13), similarly to the cases of CH₃OH and N₂O described previously. H₂S is capable of forming hydrogen bonds between adjacent molecules (Das *et al.* 2018), although these are significantly weaker than those formed in alcohols: the hydrogen bond strengths in pure CH₃OH and H₂S are 6.3 and 1.0 kcal mol⁻¹, respectively (Pellegrini *et al.* 1973, Bhattacharjee *et al.* 2013). As such, it is perhaps unsurprising that the difference in the decay trends of the amorphous and crystalline CH₃OH ices (Fig. 6.2) is much greater than that of the corresponding H₂S ices. Indeed, the comparative decay profiles of the amorphous and crystalline H₂S ices are more similar to those of the N₂O ices than those of the CH₃OH ices despite the likely presence of an extensive hydrogen bonding network in crystalline H₂S.

Such an observation is wholly consistent with the previous results reported for CH₃OH and N₂O. Although an extensive hydrogen bonding network is likely to be present in the irradiated crystalline H₂S ices, it is composed of very weak intermolecular bonds that are easily overcome. As such, the intermolecular bonding in crystalline H₂S could be thought of as a strong interaction between orientationally ordered dipole moments, similar to the case of the crystalline N₂O ice and thus explaining the similarity in the observed decay trends for the crystalline and amorphous phases of these ices (Figs. 6.2 and 6.13). Therefore, in real terms, it is the intermolecular interactions of the ordered molecular dipoles, coupled with the quasi-negligible strength of the hydrogen bonding network, in addition to the characteristic lattice energy that stabilises the crystalline H₂S ice phase against radiolytic decay compared to the amorphous phase. This is because a proportion of the kinetic energy of the incident projectile electrons is required to overcome these energetic factors before radiation-induced molecular dissociation may take place in the crystalline phase.

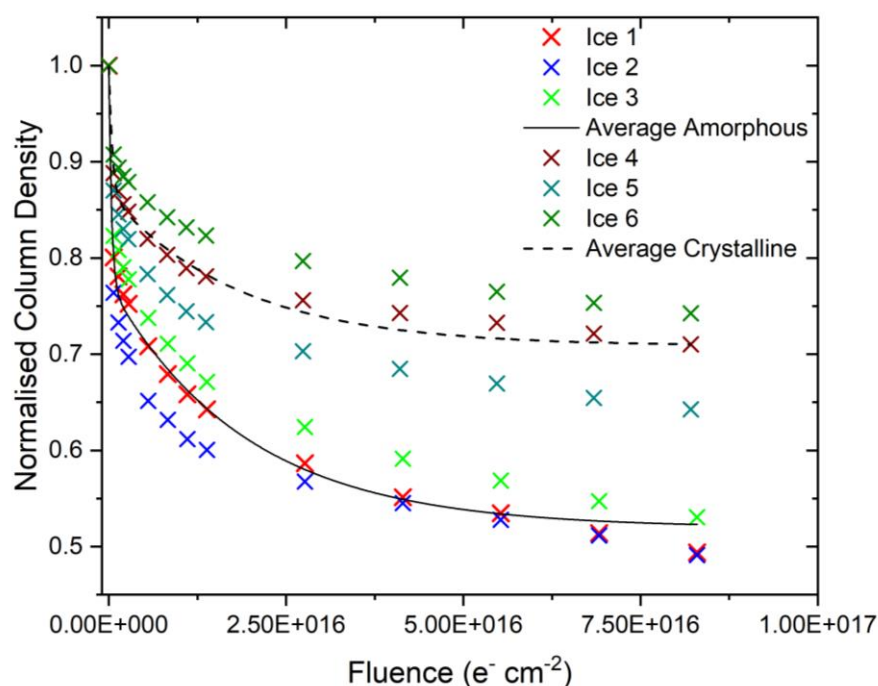


Fig. 6.13: Decay of amorphous and crystalline H₂S column densities normalised to the initially deposited column density during irradiation at 20 K using 2 keV electrons. Note that the average decay trends are fitted by two exponential decay functions joined at a fluence of 1.4×10^{15} electrons cm⁻².

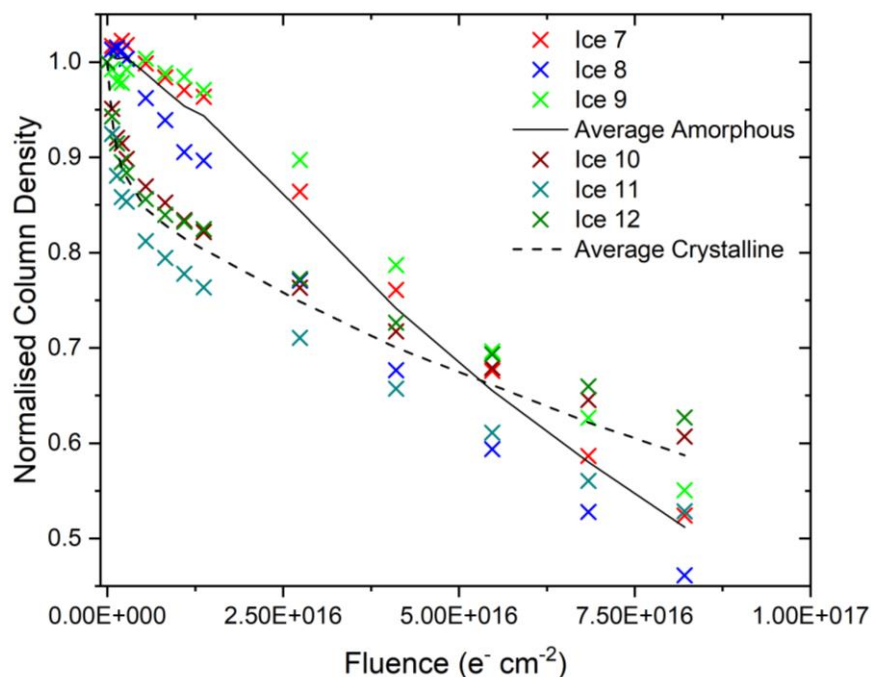


Fig. 6.14: Decay of amorphous and crystalline SO₂ column densities normalised to the initially deposited column density during irradiation at 20 K using 1.5 keV electrons. Note that the average decay trends are not fits and are plotted solely to guide the eye.

The radiation-induced decay trends of amorphous and crystalline SO₂ (Fig. 6.14) are, however, significantly different to those of H₂S and the other ices considered in this study. The decay trends of the crystalline SO₂ ice initially exhibits the anticipated profile of a rapid exponential decay. However, once a fluence of about 1.4×10^{16} electrons cm⁻² is exceeded, the normalised column density declines significantly more slowly. Perhaps even more surprising is the fact that the amorphous SO₂ normalised column density (with respect to the initial SO₂ column density deposited) does not really vary at low electron fluences, having an average normalised column density of 0.97 after a fluence of 8.2×10^{15} had been delivered. For comparison, by the point this fluence had been delivered to the crystalline SO₂ ice, its average normalised column density had decreased to 0.83. However, similarly to the case of the crystalline SO₂ ice, once a fluence of about 1.4×10^{16} electrons cm⁻² had been delivered, the normalised column density was observed to undergo a slow exponential-like decay. Interestingly, beyond a delivered fluence of 1.4×10^{16} electrons cm⁻², the rate of decay of the amorphous SO₂ is apparently greater than that of the crystalline SO₂ and, indeed, the average decay trends cross one another at a fluence of about 5.3×10^{16} electrons cm⁻² (Fig. 6.14).

Providing an exact reason for the observed amorphous SO₂ decay trends is a challenging task. Measurements of the photo-desorption of SO₂ molecules from an amorphous ice induced by soft x-rays allowed de Souza Bonfim *et al.* (2017) to suggest that, at low fluences, the recombination of fragments produced by the dissociation of SO₂ to yield electronically excited SO₂ may be a favourable process, thus largely precluding the net dissociation of SO₂ within the ice. It is also possible that the irradiation of the amorphous SO₂ ice resulted in its compaction, which may cause an increase in the integrated band strength constant A_s of the measured band. Similar results were observed during the ion irradiation of various porous ices, for which A_s may very rapidly fluctuate (either increase

or decrease) as a result of the compaction of the ice (Mejía *et al.* 2015a). It is not possible to discount either of these possible explanations based on the available evidence.

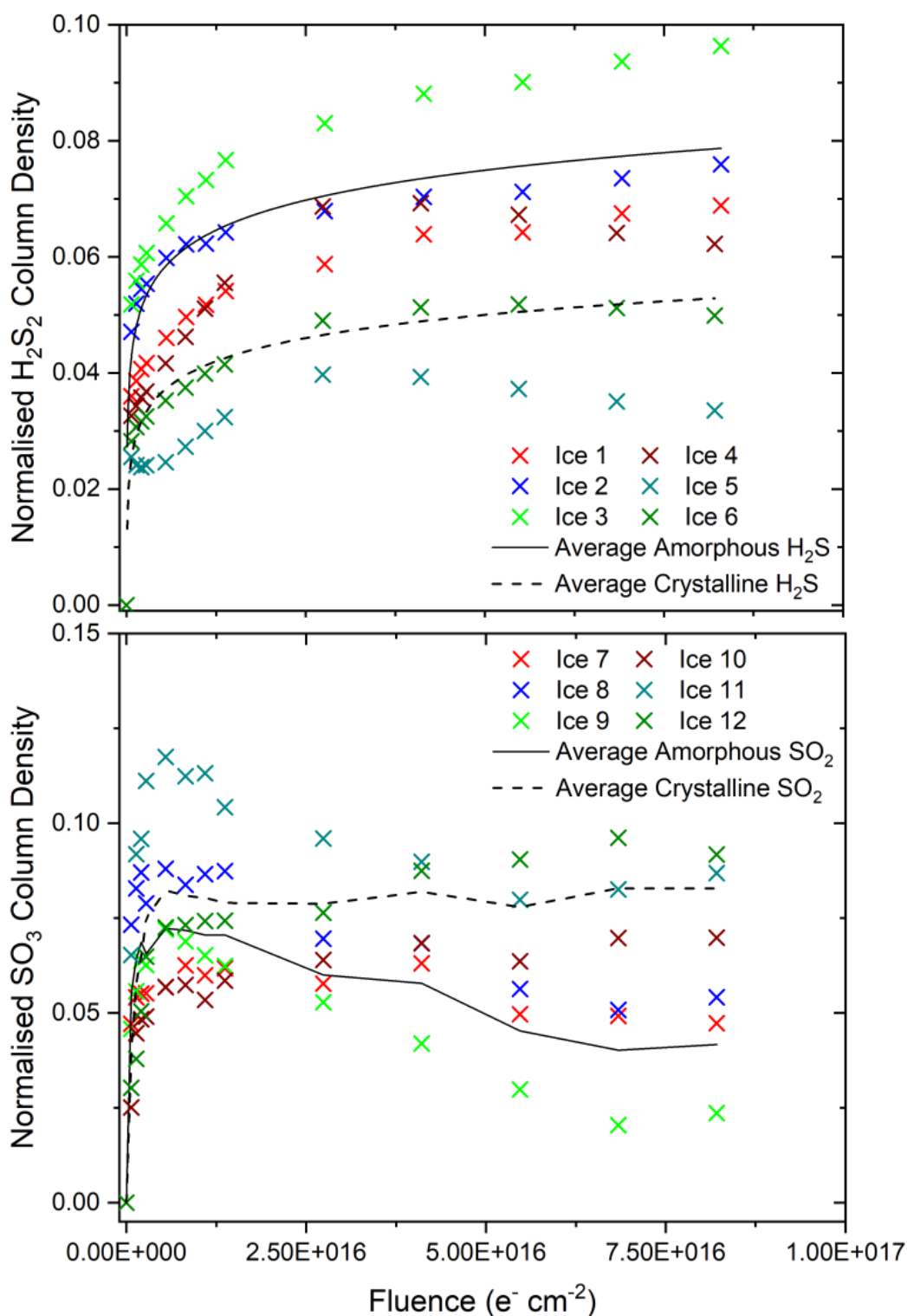


Fig. 6.15: Above: Column density of H₂S₂ from amorphous and crystalline H₂S ices irradiated using 2 keV electrons at 20 K. Below: Column density of SO₃ from amorphous and crystalline SO₂ ices irradiated using 1.5 keV electrons at 20 K. Column densities have been normalised to the initially deposited column density of the parent molecular ice. Note that in the case of H₂S₂ the average trends are fitted by logarithmic functions while in the case of SO₃ the average trends are not fits and are plotted solely to guide the eye.

As a final analytical consideration, an attempt has been made to establish the sulphur budget of the electron irradiation processes presented in this study. The possible chemical transformations of H₂S and SO₂ to infrared inactive species, such as atomic sulphur or S_x have already been extensively discussed in Chapter 1 (Shingledecker *et al.* 2020, Cazaux *et al.* 2022), and so it is useful to quantify how much of the initially deposited H₂S or SO₂ ice ends up in such a form as a result of its irradiation. As depicted in Fig. 6.12, the only major infrared active products of H₂S and SO₂ irradiation were H₂S₂ and SO₃, respectively. The column densities of these product molecules have been quantified throughout the irradiation processes by measuring the peak areas of their primary absorption bands (Fig. 6.15). In performing such a quantitative assessment, the integrated band strength constant (A_s) for the H₂S₂ absorption band at 2500 cm⁻¹ was taken to be 2.4×10^{-17} cm molecule⁻¹ (Cazaux *et al.* 2022). The integrated band strength constant of SO₃ has yet to be defined by any dedicated experimental or computational study, and so the example of de Souza Bonfim *et al.* (2017) has been followed, in which it is assumed that this value for A_s is equal to that of the SO₂ v₃ mode which is 1.47×10^{-17} cm molecule⁻¹ (Garozzo *et al.* 2008).

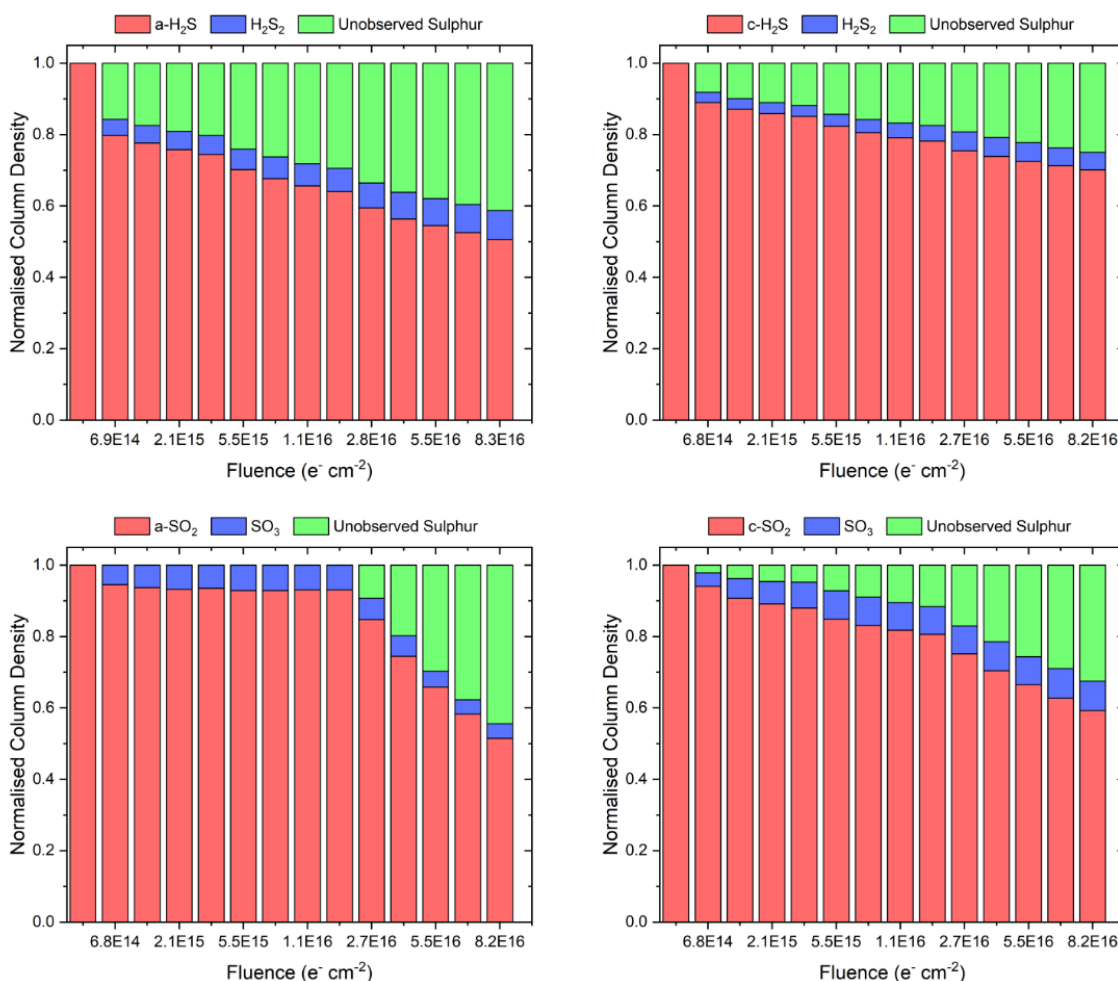


Fig. 6.16: Sulphur budgets of the electron irradiated amorphous and crystalline H₂S and SO₂ ices considered in this study. The quantity of unobserved sulphur represents an upper bound for the abundance of atomic sulphur or S_x formed as a result of irradiation, since it is not certain how many (if any) sulphur-containing molecules were sputtered or desorbed from the bulk ice, although this is anticipated to be a very small quantity. Note that the notations “a-” and “c-” used in the caption indicate whether the irradiated ice was amorphous or crystalline.

As expected, the yield of H₂S₂ from the irradiated amorphous H₂S ice is greater than that from the irradiated crystalline H₂S, commensurate with the increased decay rate of the former compared to the latter. Conversely, the electron irradiation of the crystalline SO₂ ice proved to be more conducive to the formation of SO₃ than did the irradiation of the amorphous phase. This is as expected for the low-fluence regime of the irradiation process (up to a fluence of about 5.3×10¹⁶ electrons cm⁻²), due to amorphous SO₂ ice possibly resisting radiolytic decay. However, the greater abundance of SO₃ in the irradiated crystalline ices persists even beyond this fluence, despite the more rapid decay of amorphous SO₂ after this point. It should be noted, however, that after peaking at a fluence of about 5.5×10¹⁵ electrons cm⁻², the SO₃ column density within the irradiated amorphous SO₂ ice also declines slightly (Fig. 6.15). The concomitant loss of SO₂ and SO₃ ice during its irradiation suggests that sulphur is either being converted into a form that is not infrared active or else is being desorbed or sputtered from the bulk ice. In either case, however, there is a fraction of the initially deposited sulphur that remains unobserved in the ice.

The sulphur budgets of each of the irradiated ices considered in this study are shown in Fig. 6.16. It is possible to note that a loss of sulphur is observed upon supplying an initial electron fluence of 6.9×10¹⁴ electrons cm⁻² in all of the ices apart from the amorphous SO₂ ice, and that the quantity of unobserved sulphur as a fraction of that initially deposited continually grows during irradiation. In the case of the amorphous SO₂ ice, unaccounted for sulphur is only registered after a fluence of 2.7×10¹⁶ electrons cm⁻² has been supplied, possibly due to the resistance of SO₂ to radiolytic dissociation as discussed earlier (de Souza Bonfim *et al.* 2017).

Although it is possible that electron irradiation resulted in the sputtering or desorption of the parent ice species, this process is very likely to have been only a relatively minor one. Previous work has shown, for example, that the reactive desorption of H₂S upon its formation as a result of the hydrogenation of HS on the surface of an interstellar ice analogue has a probability of 3% per hydrogenation event (Oba *et al.* 2018, Oba *et al.* 2019, Furuya *et al.* 2022). From the perspective of the experimental study presented here, this is a very small probability as the hydrogenation of HS to recycle H₂S is one among several reaction pathways that could be followed in an electron irradiated H₂S ice, but is clearly not a major reaction as the depletion of H₂S shown in Fig. 6.13 would have otherwise not been observed. Therefore, if the electron-induced sputtering or desorption of sulphur-bearing molecules from the bulk ice is assumed to be negligible, then the fractions of unobserved sulphur shown in Fig. 6.16 represent the sulphur present in an infrared inactive form, such as atomic sulphur or, more likely, residues composed of various allotropes of S_x (Gomis and Strazzulla 2008).

The data presented here therefore suggest an important point with regards to the production of such residues from pure H₂S and SO₂ ices: it is apparent that the irradiation of amorphous ices results in a greater abundance of sulphur residues or refractories than does the irradiation of crystalline ices. It should be noted, however, that the conversion of observable molecular sulphur to unobservable residues is very efficient in each of the considered ices, with the amorphous H₂S, crystalline H₂S, amorphous SO₂, and crystalline SO₂ ices respectively showing 41%, 25%, 44%, and 32% conversion of the initially deposited sulphur to residues at the end of irradiation (Fig. 6.16).

6.4 Astrochemical Implications

The irradiation experiments discussed throughout this chapter simulate the processing that interstellar icy grain mantles undergo as a result of their interaction with galactic cosmic rays, or of Solar System ices as a result of their interaction with the solar wind or giant planetary magnetospheric plasmas. Such astrophysical environments are known to allow for the cycling of molecular material through different solid phases *via* thermally induced crystallisation and space radiation-induced amorphisation. For instance, although ices in dense quiescent interstellar clouds are believed to be principally amorphous, those in stellar accretion discs are more likely to be crystalline (Poteet *et al.* 2011).

The results presented in this chapter imply that crystal lattice energies are not sufficient to explain the increased resistance to radiolytic decay of crystalline ices, and that strong and long-ranging intermolecular interactions (such as the hydrogen bonding in CH₃OH and H₂O) will confer a greater resistance than weaker interactions (such as the dipole interactions in N₂O and the very weak hydrogen bonding in H₂S). This interpretation of the results has implications for assessing the survivability and residence times of different molecules in various astrophysical radiation environments, and thus highlights the need for both experimental and modelling work in this area of research to take into account the phase of the molecular ice under consideration.

These results have also demonstrated that, irrespective of the nature, strength, or extent of the intermolecular bonds present within a molecular ice, the amorphous phase is typically more chemically productive than the crystalline phase (with the notable special case of SO₂, for which it is possible that the amorphous phase is somewhat resistant to radiolytic decay at low electron fluences). This has been largely attributed to the increased porosity and presence of structural defects within such ices, as well as their lack of stabilising lattice energies or long-ranging strong intermolecular bonding systems, that allow for radicals to be formed and migrate away from the site of their formation more easily, thus promoting the formation of radiolytic products.

The formation of complex organic molecules as a result of the irradiation of an interstellar ice which has been crystallised as a result of thermal processing (e.g., during stellar birth and evolution) is thus likely to be less productive than in the analogous amorphous ice. Therefore, it is possible that the formation of complex organic species may occur to a greater extent in the earliest stages of dense interstellar cloud evolution (i.e., before stellar birth and evolution begin) or in those areas of the dense cloud that are not influenced by the thermal emission of young stellar objects. This idea is not unreasonable, particularly in light of the recent spate of discoveries of complex organic molecules in the pre-stellar cloud TMC-1 (Burkhardt *et al.* 2021, Lee *et al.* 2021a, Lee *et al.* 2021b, Cernicharo *et al.* 2021).

Within the Solar System, radiation processing by planetary magnetospheres or the solar wind would be expected to amorphise ices present on icy moons, comets, and Kuiper Belt Objects. However, these celestial bodies also experience warming and increased temperatures as a result of approaching perihelion during their orbit around the sun or as a result of internal heating processes. Such warming could crystallise ices present on these bodies. Thus, an equilibrium is set in which ice phases are amorphous (or largely so) when radiation processes dominate, and largely crystalline when thermal processes dominate. The three icy Galilean moons of Jupiter provide an intriguing case study of this: H₂O ice has been observed to be largely amorphous on the surface of Europa, where temperatures are

comparatively low but the Jovian magnetospheric plasma flux is fairly high; but crystalline on the surface of Callisto where surface temperatures are higher (Rothard *et al.* 2017). On Ganymede, which possesses its own magnetosphere and where temperatures are intermediate between those on the surfaces of Europa and Callisto, ASW dominates at polar regions while crystalline phases are more common at equatorial regions which are shielded from impinging Jovian magnetospheric ions by the Ganymede magnetosphere (Hansen and McCord 2004). Therefore, the efficiency of molecular production *via* radiation chemistry is expected to vary in time (depending on the position of the body in its orbit around the sun) and across different regions of these celestial bodies. It is anticipated that the recently launched *James Webb Space Telescope* will allow researchers to map out the degree of crystallinity of interstellar and outer Solar System ices in unprecedented detail, thus permitting the influence of solid phase on the outcome of various astrochemical reactions and processes to be further explored.

The present study has also demonstrated that, under the influence of ionising radiation, crystalline ice phases readily amorphise. However, the results observed during the 2 keV electron irradiation of the different H₂O ice phases have also shown, for the first time, that the Ih phase is more resistant to radiation-induced amorphisation than is the Ic phase by a fluence factor of about three. Such an observation is undoubtedly a reflection of the metastability of the Ic phase relative to the Ih phase. With respect to the irradiated H₂S and SO₂ ice phases, the results presented here indicate that if these ices are present within interstellar icy grain mantles, then their processing by galactic cosmic rays could readily contribute towards the formation of sulphur residues in the dense ISM. Since these residues are mid-infrared inactive, their efficient formation could perhaps explain in part the sulphur depletion problem in dense interstellar clouds. Moreover, the results suggest that such processes are likely to be more efficient when the cloud is either fairly young (i.e., it is still in the pre-stellar stage) or in those regions of the cloud that are not in proximity to heat sources thus allowing the molecular constituents of the icy grain mantles to remain in an amorphous phase.

The results obtained from the electron irradiations of the H₂S and SO₂ ice phases are also applicable to outer Solar System chemistry, particularly in the cases of the Galilean moon Io and of comets. SO₂ is the dominant molecular component of the surface ices and exosphere of Io (Douté *et al.* 2001). Surface temperatures on Io undergo quotidian cycles between 90-130 K, thus allowing for cycles of sublimation and condensation of the surface SO₂ frosts to be maintained (Bagenal and Dols 2020). During the Ionian day, warmer temperatures cause the sublimation of much of the surface SO₂ ice, resulting the formation of a tenuous exosphere. At night, however, lower temperatures drive the collapse of much of the exosphere and the condensation of the SO₂ to surface ices.

Given that Io orbits within the giant Jovian magnetosphere, its surface is continually exposed to ionising radiation in the form of energetic ions and electrons. The flux of 0.1-52 keV electrons at the surface of Io was given by Frank and Paterson (1999) to be 3.1×10^8 electrons cm⁻² s⁻¹, meaning that the fluence delivered in the experiments described in this chapter would be delivered to the Ionian surface within 8.5 years. The temperature conditions at the surface of Io would lead one to assume that SO₂ is naturally found in the crystalline phase and that, therefore, the radiation-induced formation of SO₃ should be reasonably efficient (Fig. 6.15). However, the observed results also suggest that the prolonged irradiation of crystalline SO₂ ice at 20 K results in its amorphisation, reducing the comparative yield of SO₃ in favour of refractory sulphur residues (Fig. 6.16). Such residues

may contribute to the distinct colouration of Io (Carlson *et al.* 2007). It should be noted, however, that the extrapolation of radiation-induced amorphisation results acquired at low temperatures to higher ones may not be appropriate. As has been previously discussed, although the amorphisation of crystalline H₂O is known to occur efficiently as a result of its electron irradiation at 20 K, this process has never been reported at temperatures greater than 70 K. The efficiency of the radiation-induced crystalline SO₂ ice amorphisation process at various temperatures (including those relevant to the surface of Io) should therefore be explored in future experiments.

Finally, it is important to note that the results obtained during the electron irradiations of H₂S and SO₂ in this present study are also applicable to the chemistry occurring within the icy nuclei of comets. The recent *Rosetta* mission to comet 67P/Churyumov-Gerasimenko revealed the presence of a number of sulphur-bearing molecules within its icy nucleus, including H₂S, SO₂, SO, OCS, CS₂, and S₂ (Rubin *et al.* 2020). As the comet approaches perihelion in its orbit around the sun, thermally induced crystallisation processes begin to out-compete space radiation-induced amorphisation. Consequently, the formation of sulphur residues *via* the irradiation of the H₂S and SO₂ cometary ice components by the solar wind may decrease slightly in line with the results presented in Fig. 6.16.

6.5 Summary

This chapter details the results of the first truly systematic comparative study of the radiation astrochemistry of ices of different phases. It has been shown that not only is the crystal lattice energy of a crystalline ice a stabilising factor against its radiolytic decay when irradiated by energetic electrons, but that the type and extent of intermolecular bonding present within the crystalline ice are also contributing factors to the stability of an ice undergoing irradiation. For example, the difference in the decay rates of α -crystalline and amorphous CH₃OH is significantly greater than that between the crystalline and amorphous phases of N₂O, and this has been attributed to the stabilising effect of the strong and extensive hydrogen bonding network in the crystalline phase of the former species. Such a significant difference was not seen between the decay rates of the electron irradiated amorphous and crystalline phases of H₂S, despite the fact that hydrogen bonding is known to occur in this species. This is due to the fact that hydrogen bonds between successive H₂S molecules are known to be extremely weak, and thus the intermolecular interaction between such molecules may be approximated as being a strong interaction between adjacent dipoles. This trend of a faster depletion of the amorphous phase of an ice when subjected to ionising radiation was not observed during the electron irradiation of amorphous and crystalline SO₂ ice, for which it is possible that the amorphous phase resists decay *via* the recombination of radicals to form electronically excited SO₂.

The results presented in this chapter have important implications for interstellar and Solar System ice astrochemistry. These may be summarised as three major points: firstly, they demonstrate that the radiolytic decay of an ice and thus, by extension, its lifetime in an astrophysical radiation environment, may differ depending on the phase that the ice adopts. Such a consideration has not been adopted by either the experimental or the modelling communities, and thus should be taken into account during future studies so as to ensure as accurate a simulation of astrophysical radiation chemistry as possible. Secondly, these results show that the irradiation of an amorphous ice is typically more productive than that of a crystalline ice due to various factors including the increased presence of structural

defects and pores, as well as the weaker and less extensive intermolecular forces of attraction characterising the former phase. As such, it is possible that the irradiation of an astrophysical ice may be more chemically productive in those astrophysical regions in which radiation-induced amorphisation out-competes thermally induced crystallisation. Such an idea is not unreasonable, particularly in light of the discovery of several complex organic molecules in pre-stellar dense molecular clouds as described above. Thirdly, the results of the electron irradiation of H₂S and SO₂ demonstrate the relatively facile formation of infrared inactive sulphur-bearing refractories and residues. Such a discovery may prove to be important in the further elucidation of the sulphur depletion problem in dense interstellar clouds. Future studies more closely investigating these residues are planned.

7 THE IMPLANTATION OF REACTIVE SULPHUR IONS INTO OXYGEN-BEARING ICES

The interaction of high energy reactive sulphur ions with oxygen-bearing ices such as H₂O, CO₂, CO, and O₂ is of inherent interest to the surface chemistry of the Galilean moon system of Jupiter, due to the orbit of these moons within the sulphur-rich giant Jovian magnetosphere and the known presence of these icy species on their surfaces. The presence of SO₂ on the surfaces of these moons has often been attributed to the implantation and subsequent reaction of magnetospheric sulphur ions with these oxygen-bearing species; however, there currently exists little to no conclusive laboratory evidence that is able to confirm this. This chapter describes a systematic investigation of the implantation of high-energy S⁺ ions into CO₂, CO, and O₂ ices at different temperatures in an effort to evaluate this mechanism as a possible source of SO₂ on the surfaces of Europa, Ganymede, and Callisto, and elsewhere in the outer Solar System.

Note: The majority of the work described in this chapter has been published in peer-reviewed journals or periodicals as: [1] Mifsud *et al.* (2022), *Geophys. Res. Lett.* **49**, e2022GL100698; [2] Mifsud *et al.* (2023), *Icarus* to be submitted.

7.1 Contextual Introduction

The discovery of SO₂ ice on the surface of the Galilean moon Europa by the *International Ultraviolet Explorer* spacecraft (Lane *et al.* 1981) opened up many new interesting lines of research regarding the surface chemistry of the icy moon. Europa represents one of the most promising potential extra-terrestrial abodes of life, due largely to the fact that it is thought to be home to a subsurface global ocean which is thought to be both warm and rich in mineral salts and organic matter (Kargel *et al.* 2000, Chyba and Phillips 2002, Johnson and Sundqvist 2018, Johnson *et al.* 2019). Therefore, characterising the surface chemistry of Europa, as well as any potential interactions of this chemistry with the subsurface ocean, is of great importance in constraining the potential habitability of this outer Solar System environment.

SO₂ is one of a number of oxidants (such as O₂, CO₂, SO₄²⁻, and H₂O₂) known to exist on the surface of Europa (Johnson *et al.* 2003, Hand *et al.* 2007, Li *et al.* 2022), and may thus be an important participant in life-sustaining redox chemistry occurring in the putative subsurface ocean (Hesse *et al.* 2022). There is thus a strong motivation behind understanding how it comes to exist as an ice on the surface of Europa. It has been suggested that SO₂ may be released within the ocean as a result of ongoing hydrothermal activity, after which it is delivered upwards to the surface where it is outgassed and subsequently condenses to form an ice (Carlson *et al.* 2009). However, such a mechanism would hypothetically yield a fairly uniform distribution of SO₂ on the European surface. This is not observed, and instead the abundance of surface SO₂ is restricted to the trailing hemisphere of the moon where it is arranged in a ‘bulls-eye’ pattern (Hendrix *et al.* 2011, Becker *et al.* 2022).

The apparent preferential formation of SO₂ on the trailing hemisphere of Europa and the ‘bulls-eye’ pattern in which it is arranged is suggestive of a formation mechanism that involves the participation of the giant Jovian magnetosphere. The orbital period of Europa is approximately 85 hours; significantly longer than that of the Jovian magnetosphere which, due to its co-rotation with Jupiter, is about 10 hours. As such, the trailing hemisphere of Europa undergoes preferential irradiation as the ions and electrons that populate the rotating

magnetosphere impinge onto this side of the moon. Furthermore, it is known that the giant Jovian magnetosphere is rich in sulphur ions (Ip *et al.* 1997, Ip *et al.* 1998, Fig. 2.17). These sulphur ions are sourced from the neighbouring moon Io which, as the most volcanically active body in the Solar System, emits around one tonne of sulphur-containing volcanic ejecta per second (Thomas *et al.* 2004). Some of these ejected molecules are dissociated and ionised within the magnetosphere, whereafter they may interact with the surfaces of the other moons in the Galilean system. Lastly, it should be noted the ‘bulls-eye’ pattern into which SO₂ is arranged is known to be produced by asymmetries in the fluxes of magnetospheric ions and electrons that drive radiation chemistry and physics (Johnson *et al.* 2004).

It is perhaps therefore not surprising that, over the past few decades, many researchers have attributed the presence of SO₂ on the surface of Europa to the implantation of reactive magnetospheric sulphur ions into the surface. These implanted sulphur ions were proposed to subsequently react with the various oxygen-bearing ices and materials (e.g., O₂, CO₂, H₂O) on the European surface to yield SO₂ as a product. However, laboratory experiments have thus far failed to demonstrate such a reaction. The implantation of reactive sulphur ions into H₂O ice, which represents the dominant ice on Europa, has been conclusively shown to yield H₂SO₄ and its hydrates, rather than SO₂ (Strazzulla *et al.* 2007, Strazzulla *et al.* 2009, Ding *et al.* 2013). Furthermore, the yields of these H₂SO₄ hydrates were noted to increase with increasing projectile sulphur ion energy (Ding *et al.* 2013). Computational studies making use of molecular dynamics simulations based on a reactive potential have also found no evidence of an efficient reaction mechanism by which sulphur ion implantations yield SO₂ as a primary product (Anders and Urbassek 2019a, Anders and Urbassek 2019b).

The surface of Europa is also host to a number of other oxygen-bearing ices, such as CO₂ and O₂ (Johnson *et al.* 2003, Hansen and McCord 2008). This knowledge has motivated more recent experimental studies to consider the implantation of sulphur ions into such materials as possible alternative sources of SO₂. Lv *et al.* (2014a) performed experiments that demonstrated that such implantations into pure CO and CO₂ ices at 15 K did indeed yield SO₂, and proposed that a geologically reasonable time-scale of 2×10^4 years is sufficient to produce the amount of SO₂ observed on Europa. However, this estimation relied on the assumption that sulphur ion implantation experiments carried out at 15 K are representative of analogous processes occurring on the surface of Europa, which is characterised by significantly higher temperatures (Table 2.4, Ashkenazy 2019). Follow-up studies by Boduch *et al.* (2016) did not detect SO₂ after the implantation of sulphur ions into pure CO₂ ices at 16 K, clearly contrasting with the previous results of Lv *et al.* (2014a). It should be noted, however, that Boduch *et al.* (2016) made use of ultraviolet absorption spectroscopy as their product detection method, and it is therefore possible that the formation of any SO₂ was masked by the stronger absorptions of sulphur oxyanions which were detected after sulphur ion implantation. Nevertheless, it is evident that the question of a possible exogenic sulphur source for SO₂ on the surface of Europa remains an open one.

An experimental attempt has therefore been made to address the possibility of SO₂ formation as a result of the high-fluence ($>10^{16}$ ions cm⁻²) reactive sulphur ion implantation into carbon oxide ices (i.e., CO and CO₂), as well as O₂ ice (Fig. 7.1). Experiments were nominally carried out at 20 K; although the implantations into CO₂ ice were also performed at 70 K so as to determine any potential influence of temperature on the formation of SO₂ and thus extend the results of previous studies (Lv *et al.* 2014a, Boduch *et al.* 2016). The results of these experiments are discussed in the context of the surface chemistry of outer Solar System objects, with particular reference made to the case of Europa.

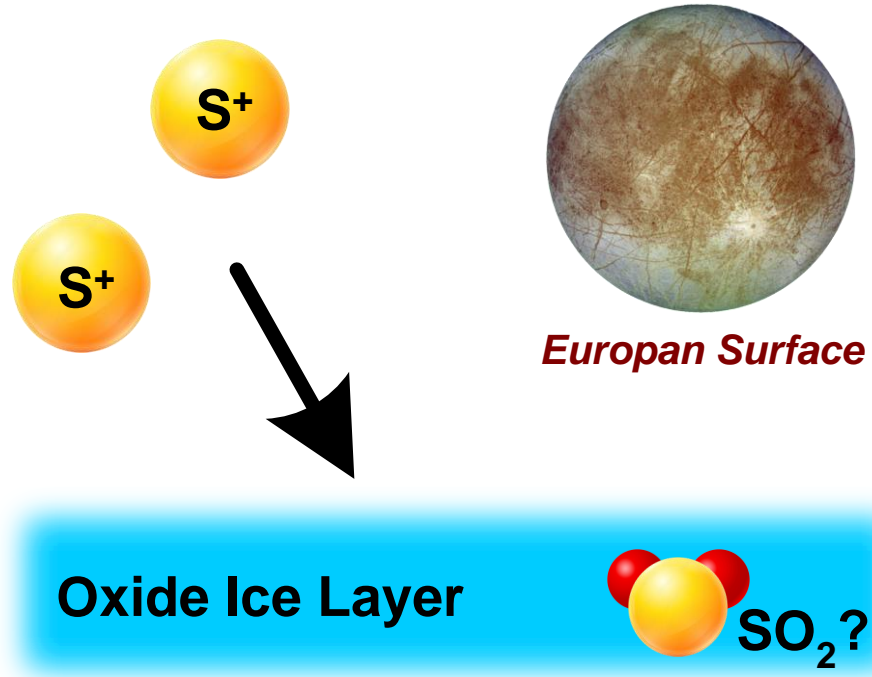


Fig. 7.1: Cartoon summary of the processes considered in this study. The feasibility of the formation of SO_2 as a result of the implantation of high-energy reactive sulphur ions has been considered, and the results discussed in the context of the surface chemistry of Europa and other outer Solar System objects.

7.2 Experimental Methodology

The sulphur ion implantation experiments were performed using the ICA apparatus. Pure ices were prepared *via* the background deposition of the relevant gases (O_2 purity = 99.995%; CO purity = 99.97%; CO_2 purity = 99.995%; all Linde) at a chamber pressure of a few 10^{-6} mbar. The deposition of the ices was followed *in situ* using Fourier-transform mid-infrared transmission absorption spectroscopy over a spectral range of $4000\text{-}650\text{ cm}^{-1}$ (1 cm^{-1} resolution; 128 scans), and the deposited ice column densities and thicknesses could be quantified by using Eqs. 7.1 and 7.2, as described in previous chapters:

$$N = 2.303 \times \frac{P_a}{A_s} \quad (\text{Eq. 7.1})$$

$$d = 10^4 \times \frac{Nm}{\rho N_A} \quad (\text{Eq. 7.2})$$

where P_a is the peak area of a characteristic absorption band, A_s is the integrated band strength constant for that band, m is the molecular mass, ρ is the mass density of the ice, and N_A is the Avogadro constant. A list of ice densities and integrated band strength constants used in this study is provided in Table 7.1.

The most prominent infrared absorption bands of the CO and CO_2 ices are related to their stretching and asymmetric stretching modes at 2139 and 2343 cm^{-1} , respectively (Isokoski *et al.* 2013, Smith *et al.* 2021). However, these absorption bands saturate fairly quickly during ice deposition; indeed, saturation occurs before the ices reach a suitable

thickness for ion implantations to be carried out. Therefore, the less intense absorption bands related to the ^{13}CO stretching and $^{13}\text{CO}_2$ asymmetric stretching modes respectively located at 2092 and 2282 cm^{-1} were instead used to quantify the column densities and thicknesses of the deposited ices. To do this, a mid-infrared spectrum of the ice was acquired just prior to the saturation of the intense ^{12}CO or $^{12}\text{CO}_2$ modes and the $^{12}\text{CO}:^{13}\text{CO}$ or $^{12}\text{CO}_2:^{13}\text{CO}_2$ column density ratios were measured. Continued deposition then resulted in the saturation of the ^{12}CO stretching or $^{12}\text{CO}_2$ asymmetric stretching modes, after which the measured ^{13}CO or $^{13}\text{CO}_2$ column densities were used in combination with the experimental isotopologue abundance ratio to determine the total molecular column densities of the deposited ices as well as their thicknesses. A similar approach was previously employed by Lv *et al.* (2014a).

The deposition of the O_2 ice was somewhat more challenging, due to the fact that O_2 is an infrared inactive species. However, a reasonable estimate of the deposition rate of this molecule could be obtained from the fact that its molecular mass, molecular geometry, and pumping speed are all similar to those of CO . As such, it was assumed that depositing an O_2 ice at the same chamber pressure and for the same duration as was done for the CO ice would result in a similar deposited column density. Given that the density of O_2 ice is known (Table 7.1), the thickness could then be easily calculated. All ices were deposited to a thickness of about 3 μm , which is greater than the penetration depths of the sulphur ions used in these experiments as calculated using the SRIM programme (Ziegler *et al.* 2010) thus ensuring implantation of the projectile ions. Once an ice was deposited to this thickness, a pre-irradiation mid-infrared spectrum was acquired after which the ice was exposed to a sulphur ion beam with additional spectra acquired at pre-defined fluence steps until a total fluence of $>10^{16}$ ions cm^{-2} was implanted. A summary of the sulphur ion implantation experiments performed is provided in Table 7.2.

However, during sulphur ion implantation it was noted that sputtering resulted in a gradual thinning of the ice. To compensate for this sputtering, a simultaneous deposition-irradiation method was used. In this method, after initial deposition of the target ice to a thickness of 3 μm , the ices were irradiated by the sulphur ion beam with concurrent background deposition of more ice at a chamber pressure of about 10^{-5} mbar. Both irradiation and deposition were halted during mid-infrared spectral acquisition. In spite of the possibility of the ion beam interacting with gas-phase CO , CO_2 , or O_2 resulting in molecular dissociation and the subsequent incorporation of the resultant fragments and radicals into the depositing ice, the use of this simultaneous deposition-irradiation method is not anticipated to impact the chemical evolution of the ices any differently to what would be expected under standard ion implantation conditions (in which sequential ion irradiation and ice deposition steps would be utilised to counter ice thinning caused by sputtering). Evidence supporting this claim now follows.

Table 7.1: List of mid-infrared band positions, their associated integrated band strength constants (A_s), and ice densities (ρ) for CO , CO_2 , and O_2 ices. Data collected from Gerakines *et al.* (1995), Freiman and Jodl (2004), and Satorre *et al.* (2008).

Molecule	Mid-Infrared Band Position (cm^{-1})	A_s (10^{-17} cm molecule^{-1})	ρ (g cm^{-3})
CO	2139 (^{12}CO ν_s)	1.1	0.80
	2092 (^{13}CO ν_s)	1.3	
CO ₂	2343 ($^{12}\text{CO}_2$ ν_3)	7.6	0.98 (20 K) / 1.48 (70 K)
	2282 ($^{13}\text{CO}_2$ ν_3)	7.8	
O ₂	-	-	1.54

Table 7.2: Summary of the sulphur ion implantations into oxygen-bearing ices performed in this study.

Experiment	Target Ice	Temperature (K)	S ⁺ Ion Energy (keV)	Implantation Depth (μm)	Fluence Delivered (10 ¹⁶ ions cm ⁻²)
1	CO ₂	20	290	0.66	1.01
2	CO ₂	70	290	0.44	1.25
3	CO	20	400	1.13	1.11
4	O ₂	20	400	0.62	1.01

The expected number n_e of gas-phase molecules undergoing fragmentation as a result of their collision with projectile sulphur ions (molecules ion⁻¹) is given as:

$$n_e = \sigma b \rho_{\text{mol}} \quad (\text{Eq. 7.3})$$

where σ is the fragmentation cross-section of the molecule (cm² ion⁻¹), b is the pathlength of the ion in the chamber before it collides with the ice layer (cm), and ρ_{mol} is the molecular gas density (molecules cm⁻³). This latter term may be calculated by first considering the Ideal Gas Law, which gives the ratio of the amount of gas present n_0 (mol) to its volume V (m³) to be:

$$\frac{n_0}{V} = \frac{p}{RT} = 4 \times 10^{-7} \text{ mol m}^{-3} \quad (\text{Eq. 7.4})$$

where p is the gas pressure (Pa; 10⁻⁵ mbar = 10⁻³ Pa), R is the molar gas constant (8.314 J K⁻¹ mol⁻¹) and T is the temperature of the gas which is assumed to be 298 K (i.e., room temperature). Converting this value to the molecular gas density ρ_{mol} may be achieved by multiplying by the Avogadro constant (6.02×10²³ molecules mol⁻¹):

$$\rho_{\text{mol}} = N_A \frac{n_0}{V} = 2.4 \times 10^{17} \text{ molecules m}^{-3} = 2.4 \times 10^{11} \text{ molecules cm}^{-3} \quad (\text{Eq. 7.5})$$

Assuming that $\sigma = 10^{-15}$ cm² ion⁻¹ (Mejía *et al.* 2015b) and taking $b = 20$ cm (known from the geometry of the ICA) and substituting into Eq. 7.3, a value of 4.8×10⁻³ molecules ion⁻¹ may be calculated for n_e . Consider now the rate of ion delivery to the ICA chamber, r_{ion} (ions s⁻¹): this may be determined by taking the ratio of the nominal sulphur ion beam current (~100 nA) to the Coulombic charge of the projectile ions ($Q = 1.602 \times 10^{-19}$ C). This yields a value of 6.2×10¹¹ ions s⁻¹ for r_{ion} . The rate of molecular dissociation of the gas-phase molecules, r_{diss} (molecules s⁻¹) is therefore:

$$r_{\text{diss}} = n_e r_{\text{ion}} = 3 \times 10^9 \text{ molecules s}^{-1} \quad (\text{Eq. 7.6})$$

The pumping speed of the turbomolecular pump maintaining the vacuum in the ICA is 400 L s⁻¹ (equivalent to 0.4 m³ s⁻¹). Such a value is valid for N₂; however, the pumping speed s of the gases under consideration in this study is estimated to be 90% of this value and is thus 0.36 m³ s⁻¹. By once again making use of the Ideal Gas Law, the partial pressure of those molecules undergoing dissociation due to interaction with the sulphur ion beam may be given as:

$$p = \frac{r_{\text{diss}}RT}{sN_{\text{A}}} = 3.4 \times 10^{-11} \text{ Pa} = 3.4 \times 10^{-13} \text{ mbar}$$

(Eq. 7.7)

Following Dalton's Law of Partial Pressures, the ratio of the total number of gas-phase molecules in the chamber at any one time to the number of dissociated gas-phase molecules is in excess of 10^7 . As such, it is highly unlikely that the fragments formed by molecular interaction with the sulphur ion beam contribute in any significant way to the radiation chemistry and physics occurring within the irradiated bulk ice (for which the column density is well in excess of 10^{18} molecules cm^{-2}) even if all the fragments formed were to deposit and be incorporated into the ice (a scenario which in of itself is unlikely, since at least some of the fragments should be pumped out of the chamber by the turbomolecular and dry rough vacuum pumps before they can condense). Therefore, it may be concluded that the simultaneous deposition-irradiation method used in this study was suitable for studying the possible formation of SO_2 as a result of sulphur ion implantation into CO_2 , CO , and O_2 ices.

7.3 290 keV S^+ Ion Implantation into CO_2 Ice at 20 and 70 K

The implantation of 290 keV S^+ ions into pure CO_2 ices at 20 and 70 K was investigated with the aim of determining whether such a mechanism could account for the formation of SO_2 on the cold surface of Europa. CO_2 ice is a minor component of the European surface (Hansen and McCord 2008), having an estimated abundance of 0.036% by number relative to H_2O (Hand *et al.* 2007), which is the dominant species at the surface of Europa. As such, it is likely that the surface CO_2 ice interacts with incident magnetospheric sulphur ions to at least some extent. The fluxes of keV-MeV sulphur ions vary between 2×10^6 and 10^8 ions $\text{cm}^{-2} \text{ s}^{-1}$, depending on the location on the surface of Europa (Dalton *et al.* 2013). Therefore, a fluence of 10^{16} ions cm^{-2} as was supplied in this study could be expected to be delivered to the European surface within 160 years.

The implantation of 290 keV S^+ ions into CO_2 ice at 20 K resulted in the appearance of several new absorption features in the mid-infrared spectrum (Fig. 7.2). In particular, two new bands are apparent at 1336 and 1150 cm^{-1} . These bands are in reasonably good agreement with the positions of the asymmetric and symmetric stretching modes of SO_2 that were measured in Chapter 5 (Table 5.2), and thus the appearances of these bands have been attributed to the formation of SO_2 within the irradiated CO_2 ice. These absorption bands are, however, fairly small and are located in a region of the spectrum where several other, stronger absorption bands are also present. In light of this, two control experiments have been performed so as to be confident in the detection of SO_2 . Firstly, the wavenumber peak positions of these bands have been compared with those of SO_2 in an unirradiated $\text{CO}_2:\text{SO}_2$ (6:1) ice mixture (Fig. 7.2), and a very good agreement (within 1 cm^{-1}) with the suspected SO_2 band positions in the irradiated ice was found. Secondly, a control experiment was performed in which a similar fluence of 300 keV He^+ ions was implanted into pure CO_2 ice at 20 K under similar experimental conditions. After the implantation of He^+ ions, any absorption bands due to molecules formed as a result of the incorporation of the sulphur ion projectile should be absent, while all other bands produced as a result of the energetic processing of the ice would still be present. This outcome was indeed observed, with the bands at 1336 and 1150 cm^{-1} not being observed at any point during the implantation of the He^+ ions.

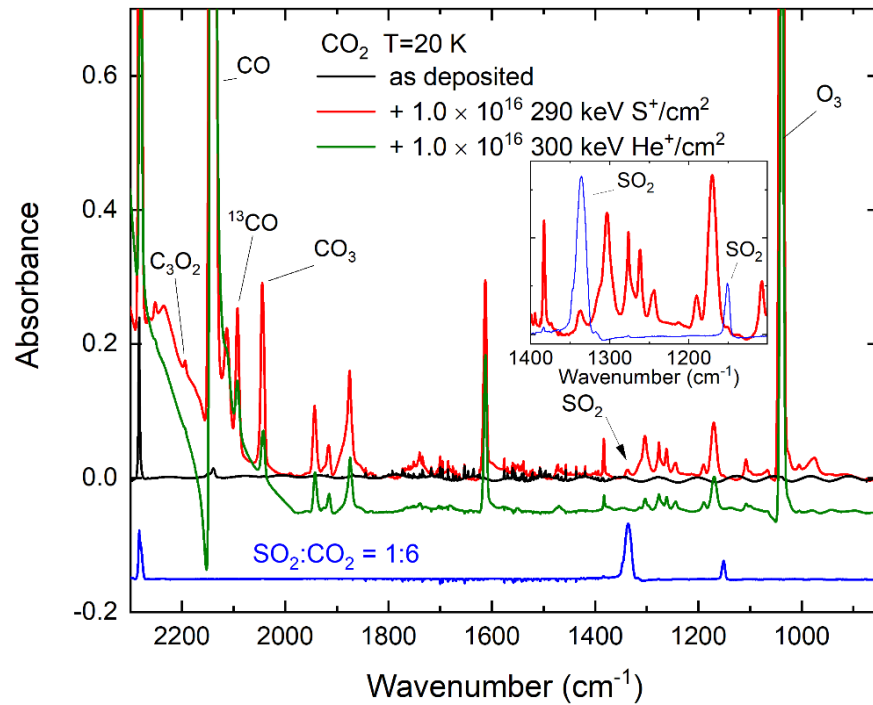


Fig. 7.2: Mid-infrared spectra of condensed CO₂ before (*black trace*) and after (*red trace*) the implantation of 290 keV S⁺ ions at 20 K. Also shown are the mid-infrared spectra acquired during control experiments, including an unirradiated CO₂:SO₂ (6:1) ice mixture at 20 K (*blue trace*) and a CO₂ ice after the implantation of 300 keV He⁺ ions at 20 K (*green trace*). Note that the spectra of the irradiated ices are difference spectra yielded after the subtraction of the ‘as deposited’ spectra. Note also that some spectra are vertically shifted for clarity. Sinusoidal patterns in the spectrum of the deposited ice are caused by interference of infrared light reflected in the substrate-ice-vacuum optical system.

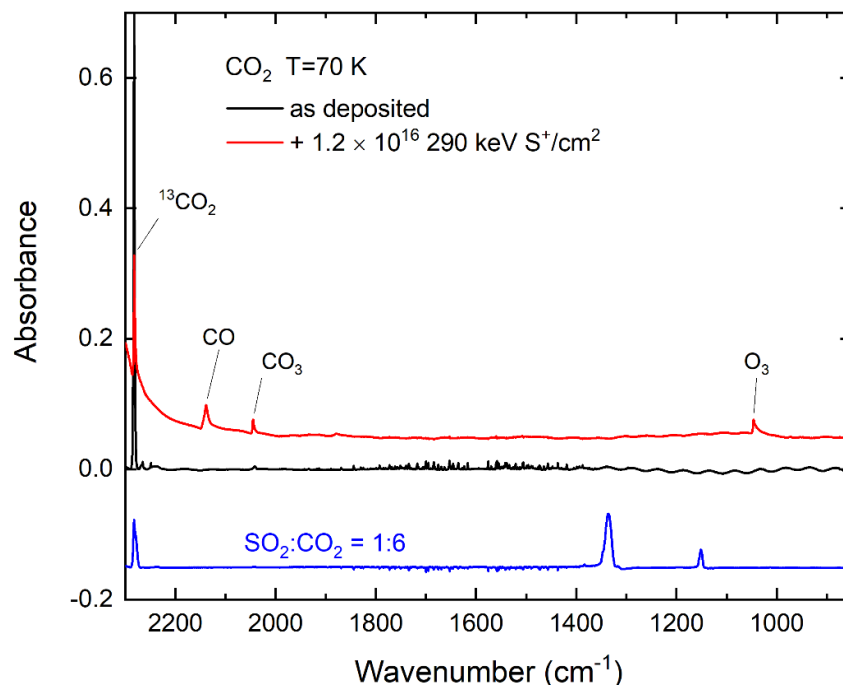


Fig. 7.3: Mid-infrared spectra of condensed CO₂ before (*black trace*) and after (*red trace*) the implantation of 290 keV S⁺ ions at 70 K. Also shown is the mid-infrared spectrum of an unirradiated CO₂:SO₂ (6:1) ice mixture at 20 K (*blue trace*). Note that the spectrum of the irradiated ice is a difference spectrum yielded after the subtraction of the ‘as deposited’ spectrum. Note also that some spectra are vertically shifted for clarity. Sinusoidal patterns in the spectrum of the deposited ice are caused by interference of infrared light reflected in the substrate-ice-vacuum optical system.

It is acknowledged that the implantation of 10^{16} He⁺ ions cm⁻² in a CO₂ ice at 20 K results in a different dose administered to the ice than does the implantation of 10^{16} S⁺ ions cm⁻². It is thus possible to make the argument that perhaps the absence of the bands at 1336 and 1150 cm⁻¹ after the implantation of 10^{16} He⁺ ions cm⁻² may have been due to the simple fact that the bands may simply not have been strong enough to detect. However, this proposed explanation can be rebutted by considering and comparing the radiation doses administered to the CO₂ ice after implantation of the He⁺ and S⁺ ions. Consider first the number of CO₂ molecules in a volume whose dimensions equal an area of 1 cm² and a thickness of 1 Å. This can be found from the density of the ice ($\rho = 0.98$ g cm⁻³) and the relative molecular mass of CO₂ ($m = 44$ amu):

$$\frac{\rho}{m_p \times m} = \frac{0.98 \text{ g cm}^{-3}}{1.67 \times 10^{-24} \text{ g} \times 44} \quad (\text{Eq. 7.8})$$

where m_p corresponds to the mass of a proton (1.67×10^{-24} g). If $1 \text{ cm} = 10^8 \text{ \AA}$, then:

$$\frac{0.98 \text{ g cm}^{-3}}{1.67 \times 10^{-24} \text{ g} \times 44} = \frac{0.98 \text{ g} (\text{cm}^{-2} (10^8 \text{ \AA})^{-1})}{1.67 \times 10^{-24} \text{ g} \times 44} = \frac{0.98 \times 10^{-8} \text{ g cm}^{-2} \text{ \AA}^{-1}}{1.67 \times 10^{-24} \text{ g} \times 44} \quad (\text{Eq. 7.9})$$

Arithmetically solving Eq. 7.9 gives a molecular density of 1.33×10^{14} CO₂ molecules cm⁻² Å⁻¹. The stopping powers of 290 keV S⁺ and 300 keV He⁺ ions in CO₂ ice were calculated using the SRIM software (Ziegler *et al.* 2010) and found to be 4.33 and 9.74 eV Å⁻¹, respectively. These stopping powers may be expressed in units of eV cm² per CO₂ molecule by dividing the values given by the SRIM simulation by the molecular column density:

$$P_{s, \text{ sulphur}} = \frac{4.33 \text{ eV \AA}^{-1}}{1.33 \times 10^{14} (44 \text{ amu}) \text{ cm}^{-2} \text{ \AA}^{-1}} = 3.25 \times 10^{-14} \text{ eV cm}^2 \text{ molecule}^{-1} \quad (\text{Eq. 7.10})$$

$$P_{s, \text{ helium}} = \frac{9.74 \text{ eV \AA}^{-1}}{1.33 \times 10^{14} (44 \text{ amu}) \text{ cm}^{-2} \text{ \AA}^{-1}} = 7.30 \times 10^{-14} \text{ eV cm}^2 \text{ molecule}^{-1} \quad (\text{Eq. 7.11})$$

Given that a fluence of approximately 10^{16} ions cm⁻² was delivered in both the sulphur and helium ion implantation experiments, it is possible to calculate the administered dose by simply multiplying this fluence by the stopping powers given in Eqs. 7.10 and 7.11. The total doses administered to the ices during 290 keV S⁺ and 300 keV He⁺ ion implantation are therefore 325 and 730 eV per CO₂ molecule, respectively. Although a higher dose of energy was imparted to the CO₂ ice during He⁺ ion implantation, the bands that were attributed to SO₂ were never observed during the irradiation process, even at doses comparable to those administered during S⁺ ion implantation. Thus, it is reasonable to assume that these bands do not appear during He⁺ ion implantation because they are the result of the formation of a molecule that incorporated the sulphur ion projectile.

It should be noted that other sulphur-bearing molecules, such as SO and S₂O, also present mid-infrared absorption features in the vicinity of 1150 cm⁻¹ (Hopkins and Brown

1975). However, these species are not likely to be the carriers of the bands shown in Fig. 7.2 due to their inherent instability. SO, for instance, is a very unstable molecule that has only been isolated in inert matrices at very low temperature (Hopkins and Brown 1975). Indeed, the recent work of Góbi *et al.* (2021) demonstrated that the reaction between hydrogen atoms and SO is favourable at temperatures as low as 3 K in a *para*-hydrogen matrix. The CO₂ ices considered in this study are certainly not inert matrices due to the energy deposited within the ices during sulphur ion implantation which results in the formation of a plethora of radical species. At 20 K, the temperature is sufficiently high as to allow for the diffusion of these radicals, thus ensuring the rapid oxidation of SO to SO₂ (Rolfes *et al.* 1965, Herron and Huie 1980, Baklouti *et al.* 2004). The S₂O molecule is also very unstable, and previous literature has shown multiple efficient dissociation pathways that would have more than likely dominated within the irradiated CO₂ ices such as: thermal decomposition, dissociative electron attachment, pre-dissociation followed by cleavage of the S–S bond, and disproportionation (Dudley and Hoffmann 2003, Steudel and Steudel 2004, Field *et al.* 2005, Navizet *et al.* 2010).

The mechanistic chemistry leading to the formation of SO₂ is presumed to proceed after the neutralisation of the implanted sulphur ion. As the ion traverses the ice it dissipates energy into its surroundings resulting in the dissociation of CO₂ to CO and an oxygen atom (Pilling *et al.* 2022). The neutralised sulphur ion may then react with one such oxygen atom to produce SO (Tevault and Smardzewski 1978). Alternatively, SO may result from the abstraction of an oxygen atom from a surviving CO₂ molecule by the neutralised sulphur ion (Froese and Goddard 1993). SO is then rapidly oxidised to SO₂ as discussed above.

In contrast, when the implantation of 290 keV S⁺ ions was performed at 70 K, no SO₂ was detected among the radiation products (Fig. 7.3). Indeed, the mid-infrared spectrum of the CO₂ ice into which S⁺ ions had been implanted shows significantly fewer absorption bands than does its 20 K counterpart (Fig. 7.2). One striking difference is the size of the absorption band attributed to the asymmetric stretching mode of O₃ located at about 1041 cm⁻¹ (Chaabouni *et al.* 2000). In the 20 K spectrum, this band is very intense and is indicative of the efficient formation of O₃ in the irradiated CO₂ ice. In the 70 K spectrum, however, this band is significantly smaller, suggesting an inefficient O₃ formation pathway. It is this observation that gives an insight into why the formation of SO₂ as a result of S⁺ ion implantation into condensed CO₂ is favourable at 20 K, but not at 70 K.

The energetic processing of CO₂ by ions, electrons, and ultraviolet photons is known to yield several oxygen-bearing products, including O₃ (Sivaraman *et al.* 2013, Martín-Doménech *et al.* 2015). The formation of this radiolytic product is, however, dependent upon the prior synthesis of O₂ within the ice which then furnishes O₃ upon the barrierless addition of a supra-thermal oxygen atom (Sivaraman *et al.* 2007). In the 20 K experiment, the O₂ is stable within the ice as the experimental temperature is lower than its sublimation temperature, and so O₃ formation may occur efficiently. Indeed, O₃ is one of the major products of this ion implantation process (Fig. 7.2). In the 70 K experiment, however, it is evident that O₂ sublimation from the ice is fairly efficient (Jones *et al.* 2014), thus effectively depleting the ice of its oxygen content. The result of this is that there are fewer oxygen atoms available within the bulk ice that may react with the implanted sulphur ion to yield SO₂, thus explaining the absence of this latter species at 70 K. Previous studies have suggested that otherwise volatile solid-phase molecules such as O₂ may be stabilised at temperatures beyond their sublimation point *via* their encapsulation within clathrate-like structures (Hand *et al.* 2006). It is possible to speculate that, in the experiments considered in this study, any

such CO₂-based clathrate-like structures may not have been sufficiently stable to retain O₂ due to the fact that CO₂ itself is also a fairly volatile species. The presence of a radiolytically-derived tenuous O₂ exosphere on Europa (Milillo *et al.* 2016) is consistent with this interpretation.

These results build upon and extend the previous findings of Lv *et al.* (2014a) and Boduch *et al.* (2016). In their study, Lv *et al.* (2014a) implanted multiply charged sulphur ions into condensed CO and CO₂ at 15 K, and recorded the formation of SO₂ in each ice. Based on their reported SO₂ formation efficiency of 0.38 molecules ion⁻¹ for the implantation of 90 keV S⁹⁺ ions into CO₂ ice, Lv *et al.* (2014a) suggested that the observed abundance of SO₂ on Europa could be formed within a geologically reasonable time-scale of 2×10⁴ years. However, this result was not reproduced by the later study of Boduch *et al.* (2016), who did not observe any SO₂ in the ultraviolet absorption spectra of CO₂ into which 144 keV S⁹⁺ ions had been implanted at 16 K. This non-detection was ascribed to one of two reasons: either the accumulated column density of SO₂ formed as a result of ion implantation was below the spectroscopic detection limits of their instrument, or else the absorption bands attributable to SO₂ were masked by the intense absorptions of sulphur oxyanions such as SO₃⁻.

The results of this present investigation suggest that, although the formation of SO₂ as a result of sulphur ion implantation into CO₂ ice is indeed possible at low temperatures (15-20 K), this is not true for higher temperatures more representative of the surface of Europa, such as the 70 K temperature considered here. This is actually somewhat of an unexpected result, as other ion implantation processes in which the implanted ion is incorporated into an oxygen-bearing product molecule have been shown to be unaffected by changes in the experimental temperature (Lv *et al.* 2012, Ding *et al.* 2013). It is possible to conclude, therefore, that sulphur ion implantation into CO₂ ices at the surface of Europa is not an efficient mechanism by which the SO₂ observed on the surface may form. This result is also consistent with the lack of correlation in the spatial distributions of SO₂ and CO₂ ices on Europa (Hansen and McCord 2008).

7.4 400 keV S⁺ Ion Implantation into CO Ice at 20 K

The implantation of reactive sulphur ions into CO ice has also been studied. CO is not known to be on the surface of Europa or, in fact, on any of the icy Galilean moons (McCord *et al.* 1997). However, it is of much greater importance in the context of the chemistry occurring on the surfaces of icy bodies further out in the Solar System, such as trans-Neptunian and Kuiper Belt objects. In these regions, temperatures are significantly colder (30-50 K), thus allowing for the condensation and accumulation of the most volatile molecules whose chemistry consequently plays a dominant role in the surface evolution of these celestial bodies (Young *et al.* 2020). Regions in the outer Solar System are also host to a rich radiation chemistry mediated by the solar wind, of which sulphur is a known component (Giammanco *et al.* 2007). Based on measurements of the solar wind S/O ratio at 1 AU by von Steiger *et al.* (2010), Ruf *et al.* (2019) were able to determine that a flux of 1.58 sulphur ions cm⁻² s⁻¹ is expected in the outer Solar System at 50 AU.

Recent studies have demonstrated that the implantation of reactive sulphur ions into simple ice mixtures relevant to trans-Neptunian and Kuiper Belt objects results in the synthesis of a plethora of complex organic molecules, a reasonable percentage of which incorporate the projectile sulphur ion (Ruf *et al.* 2019, Ruf *et al.* 2021). However, the

formation of other volatile species (in particular, SO₂) on these icy Solar System objects as a result of sulphur ion implantation remains somewhat unexplored. This therefore provides a prime motivation for studying the implantation of sulphur ions into a relevant volatile oxygen-bearing ice, such as CO.

The implantation of 400 keV S⁺ ions into CO ice resulted in the appearance of several new mid-infrared absorption bands, many of which clustered in the 2400-2000 cm⁻¹ wavenumber range associated with the C=O bond stretching modes of various molecules (Fig. 7.4). Based on previous assignments by various studies (Strazzulla *et al.* 1997, Gerakines and Moore 2001, Trottier and Brooks 2004, Loeffler *et al.* 2005, Palumbo *et al.* 2008, Lv *et al.* 2014a), it has been possible to ascribe these bands to a number of species including cumulene dioxides (of the type C_xO₂ where $x > 1$), radical oxocarbon molecules (of the type C_xO where $x > 1$), as well as CO₂ and CO₃ (Table 7.3). It is presumed that the radiation chemistry that leads to the formation of these species begins with the homolytic dissociation of the CO molecule to yield free, supra-thermal carbon and oxygen atoms:



These free carbon atoms are subsequently able to react with surviving CO molecules to begin a catenation reaction sequence yielding sequentially larger radical oxocarbon molecules. The growth of these radicals by sequential carbon atom addition may be quenched *via* the addition of a free oxygen atom at the radical terminus, which results in the formation of a closed-shell, unsaturated cumulene dioxide species. An example of such a reaction sequence for the formation of C₃O₂ *via* the sequential formation of C₂O and C₃O is shown in Eqs. 7.13-7.15 below:



Table 7.3: List of oxocarbon molecules present in the CO ice irradiated by 400 keV S⁺ ions sorted by the wavenumber position of their mid-infrared absorption peaks.

Formula	Molecule		Mid-Infrared Band Position (cm ⁻¹)
		Name	
¹² CO ₂		Carbon dioxide	2343
¹³ CO ₂		Carbon dioxide	2282
C ₃ O		Tricarbon monoxide	2247
C ₃ O ₂		Tricarbon dioxide (carbon suboxide)	2242
C ₅ O ₂		Pentacarbon dioxide	2221
¹² CO		Carbon monoxide	2139
C ₇ O ₂		Heptacarbon dioxide	2122
¹³ CO		Carbon monoxide	2092
C ₅ O ₂		Pentacarbon dioxide	2059
CO ₃		Carbon trioxide	2044
C ₃		<i>Catena</i> -tricarbon	2019
C ₂ O		Dicarbon monoxide	1990

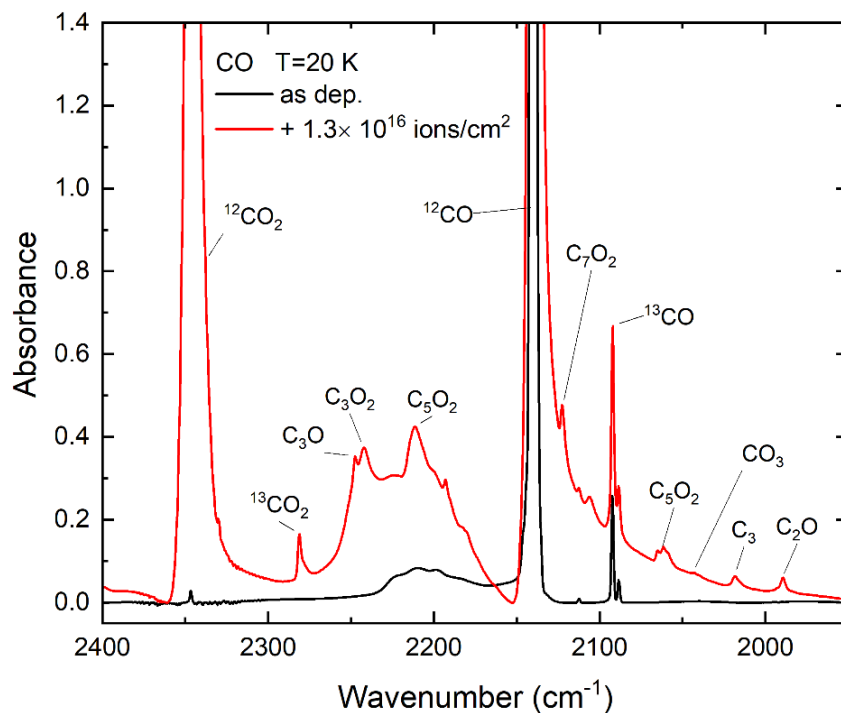


Fig. 7.4: Mid-infrared spectra of condensed CO before (*black trace*) and after (*red trace*) the implantation of 400 keV S⁺ ions at 20 K.

It must be realised, however, that the formation of cumulene dioxides and radical oxocarbons as shown in Fig. 7.4 requires a greater supply of the carbon atoms sourced from CO dissociation than of the oxygen atoms. As such, additional processes must exist which consume the remaining oxygen atoms. Of these processes, perhaps the most efficient is the formation of CO₂ as a result of the addition of a supra-thermal oxygen atom to CO; a process which has been described at some length in the literature (Loeffler *et al.* 2005, de Barros *et al.* 2011b). The addition of oxygen atoms to these CO₂ molecules results in the synthesis of CO₃ (Sivaraman *et al.* 2013); a minor quantity of which was observed in the processed CO ice (Fig. 7.4). Lastly, the formation of O₃, noted by the appearance of its asymmetric stretching mode at about 1040 cm⁻¹ (Chaabouni *et al.* 2000), could also act as a sink for nascent oxygen atoms in this experiment (Fig. 7.5).

A closer examination of the data shown in Fig. 7.5 reveals that a small absorption feature is present at about 1335 cm⁻¹. The position of this absorption band coincides well with that of the asymmetric stretching mode of solid SO₂ diluted in CO, as confirmed by performing a control experiment in which the mid-infrared absorption spectrum of a CO:SO₂ (30:1) ice mixture was recorded and the positions of the SO₂ asymmetric stretching mode in the unirradiated ice mixture were compared to the position of the small absorption feature in the mid-infrared spectrum of the irradiated pure CO ice, with good agreement (within 1.5 cm⁻¹) being found. It should be noted that the identification of solid SO₂ in an irradiated ice is usually made on the basis of the detection of both the asymmetric stretching mode and the symmetric stretching mode. However, as the intensity of the asymmetric stretching mode is much greater than that of the symmetric stretching mode, it is possible to argue that SO₂ was indeed formed in the CO ice as a result of the implantation of 400 keV S⁺ ions after a delivered fluence of 10¹⁶ ions cm⁻², but that the abundance formed was too low for the symmetric stretching mode to become evident against the background continuum.

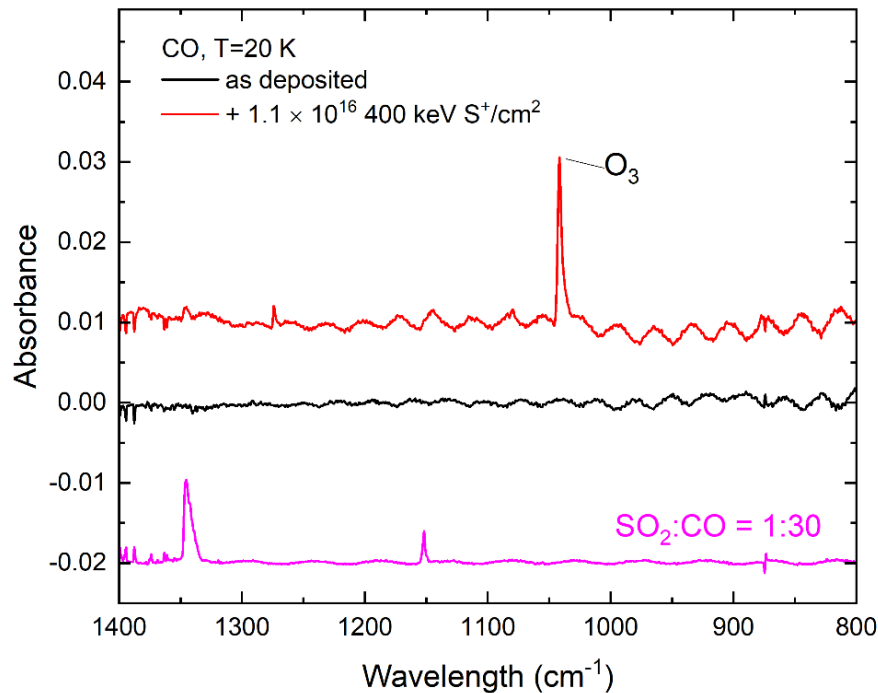


Fig. 7.5: Mid-infrared spectra of condensed CO before (*black trace*) and after (*red trace*) the implantation of 400 keV S⁺ ions at 20 K. Also shown is the mid-infrared spectrum of an unirradiated CO:SO₂ (30:1) ice mixture at 20 K (*pink trace*). Note that the spectrum of the irradiated ice is a difference spectrum yielded after the subtraction of the ‘as deposited’ spectrum. Note also that spectra are vertically shifted for clarity. Sinusoidal patterns in the spectra of the ices are caused by interference of infrared light reflected in the substrate-ice-vacuum optical system.

Indeed, the results of Lv *et al.* (2014a) would seem to support such an interpretation, as their experiments determined that the emergence of the SO₂ symmetric stretching mode at about 1150 cm⁻¹ only appeared in a CO ice into which 176 keV S¹¹⁺ ions had been implanted after a fluence of 1.9×10¹⁶ ions cm⁻² had been delivered (Fig. 7.6): almost twice the total fluence delivered in this present investigation (Table 7.2). Nevertheless, this interpretation should be treated with a large degree of caution due to certain inconsistencies between the data reported here in this present investigation and the results obtained by Lv *et al.* (2014a). Looking at the evolution of the SO₂ mid-infrared absorption features as a result of the implantation of reactive sulphur ions into CO ice as reported by Lv *et al.* (2014a), it is possible to note that they did not observe the appearance of the asymmetric stretching mode prior to that of the symmetric stretching mode (Fig. 7.6), as has been suggested to possibly occur in this present study. Rather, it seems that both the asymmetric and the symmetric stretching modes appear in their mid-infrared spectrum simultaneously.

Moreover, there is somewhat of a discrepancy between the relative intensities of these features in their mid-infrared spectrum compared to those reported for the pure SO₂ ice (Fig. 7.6) or the CO:SO₂ (30:1) ice shown in Fig. 7.5. In these two latter spectra, the intensity of the SO₂ asymmetric stretching (ν₃) mode at about 1335 cm⁻¹ is always greater than that of the symmetric stretching mode at about 1150 cm⁻¹. However, the bands that were attributed to these vibrational modes by Lv *et al.* (2014a) are of approximately equal intensity, and thus do not match the expected profile of the mid-infrared absorption bands of SO₂. It is therefore entirely possible that these bands are not due to SO₂ at all, and may be caused by the formation of one or more unrelated molecules. Since Lv *et al.* (2014a) did not provide any additional evidence for the presence of SO₂ in their ice (such as the appearance of a peak

at a mass-to-charge ratio of 64 in quadrupole mass spectra collected during post-irradiative temperature-programmed desorption experiments), the formation of SO₂ as a result of sulphur ion implantation into CO ice at 20 K in both their study as well as in the present investigation must be regarded as tentative or inconclusive at best.

If it were assumed that the assignment of the bands reported in Fig. 7.6 by Lv *et al.* (2014a) is correct, and their calculated SO₂ formation efficiency of 0.2 molecules per ion is accurate, then the maximum formation rate of SO₂ on CO-rich trans-Neptunian and Kuiper Belt objects as a result of their interaction with the solar wind would be approximately 10⁷ molecules cm⁻² per year, if it is also assumed that all the impinging sulphur ions implant into CO surface ice. Further assuming that the flux of sulphur ions present in the solar wind at 50 AU has not varied since the formation of these outer Solar System objects, and that any SO₂ formed on their surfaces as a result of sulphur ion implantation is completely preserved and not destroyed by further irradiative processing, the amount of SO₂ on the surfaces of these objects would only be on the order of about 5×10¹⁶ molecules cm⁻². Given the number of assumptions of questionable reasonableness made in calculating this fairly modest surface abundance, as well as the known multi-component surface compositions of icy objects in the outer Solar System, it is most probably safe to assume that sulphur ion implantation into CO ice does not represent a reasonable SO₂ formation mechanism on these objects.

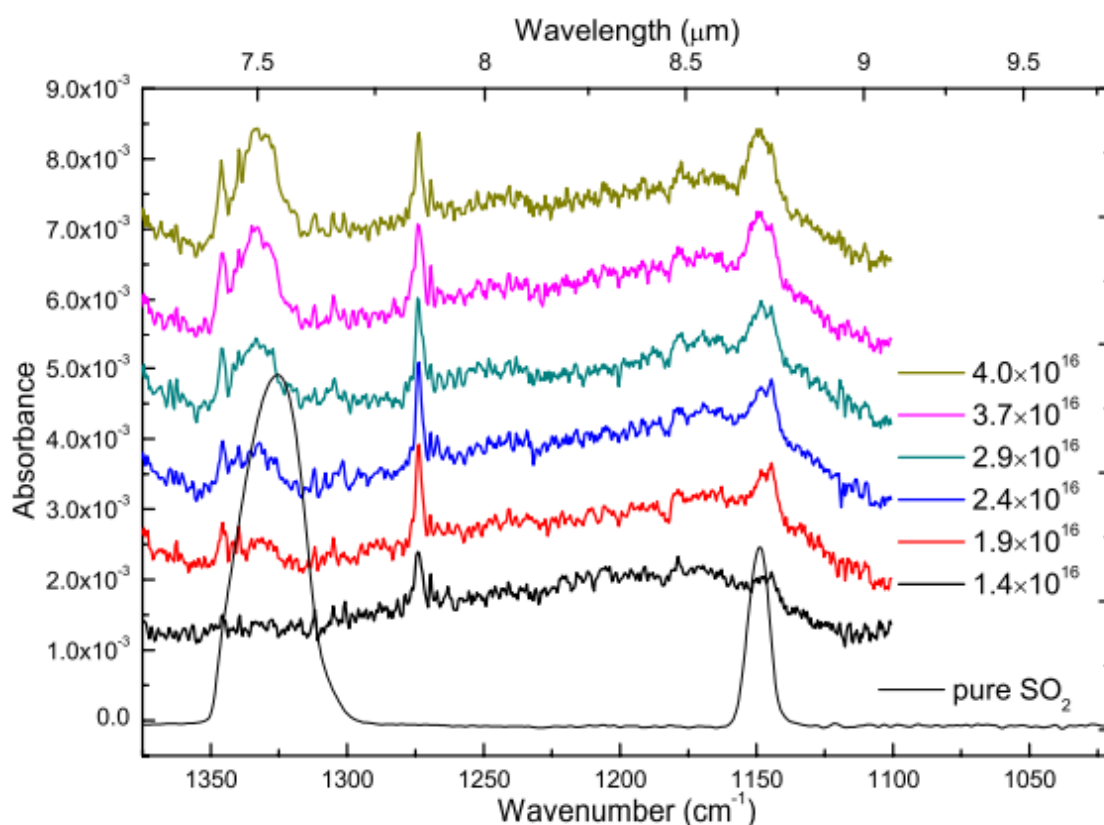


Fig. 7.6: Mid-infrared absorption spectra collected during the implantation of 176 keV S¹¹⁺ ions into solid CO at 20 K as studied by Lv *et al.* (2014a). It is possible to note that the absorption bands ascribed to SO₂ do not clearly appear in the spectrum until a fluence of at least 1.9×10¹⁶ ions cm⁻² has been supplied to the ice. However, it is also possible to note that the relative intensities of these bands do not match that of either the pure SO₂ ice (as shown in this figure and throughout Chapter 5) nor the CO:SO₂ (30:1) ice shown in Fig. 7.5. Given the lack of additional evidence for the assignment of these bands, the detection of SO₂ must therefore be regarded as tentative at best. Image reproduced from Lv *et al.* (2014a).

The lack of a convincing detection of SO₂ after the implantation of 400 keV S⁺ ions into solid CO at 20 K, even after a fluence of 10¹⁶ ions cm⁻² had been supplied to the ice (Fig. 7.5), contrasts strongly with the result reported for the analogous implantation process into CO₂ ice, where some SO₂ was indeed found among the radiolysis products (Fig. 7.2). Although the exact reason for this discrepancy cannot be stated with any certainty, it is possible to put forward a hypothesis based on the state of oxidation of the two target ices in question. The CO₂ molecule is comparatively oxygen-rich (two out of three of the constituent atoms are oxygen), resulting in a carbon atom with an oxidation state of +4. Conversely, the CO molecule is poorer in oxygen resulting in a carbon atom with an oxidation state of just +2. As such, the irradiation of solid CO results in the release of fewer free oxygen atoms than does the analogous irradiation of solid CO₂, meaning oxidised product molecules (such as SO₂) are less likely to form as a result of the ensuing radiation chemistry. This interpretation is consistent with the significantly lower yield of O₃ formed after the irradiation of CO (Fig. 7.5) compared to that formed after the irradiation of CO₂ (Fig. 7.2).

7.5 400 keV S⁺ Ion Implantation into O₂ Ice at 20 K

The implantation of reactive sulphur ions into pure O₂ ice represents perhaps the simplest potential chemical route towards the formation of SO₂. The presence of O₂ on various outer Solar System bodies on which SO₂ is also known to be present, including the Galilean moons Europa (Johnson *et al.* 2003) and Ganymede (Migliorini *et al.* 2022), as well as comets such as 67P/Churyumov-Gerasimenko (Luspay-Kuti *et al.* 2018), has been well-established and thus the formation of the latter species as a result of the implantation of reactive sulphur ions into the former should be studied. However, thus far, this process has only been previously studied using ultraviolet absorption spectroscopy (Boduch *et al.* 2016). Although certainly a useful analytical technique, this region of the electromagnetic spectrum is not ideally suited for molecular identification. As such, the results presented here constitute the first investigation of sulphur ion implantation into a low-temperature O₂ ice using mid-infrared spectroscopy, thus allowing for the more secure identification of radiolytic product molecules.

As with the implantations into the CO and CO₂ ices outlined in the previous subsections, the implantation of 400 keV S⁺ ions into O₂ ice at 20 K results in the formation of new absorption bands. The most prominent of these bands is that at about 1040 cm⁻¹ attributable to O₃. The formation of O₃ as a result of the irradiative processing of solid O₂ has been studied thoroughly (Famá *et al.* 2002, Bennett and Kaiser 2005, Sivaraman *et al.* 2007, Ennis *et al.* 2011), and thus will only be discussed very briefly in this thesis. The radiolytic synthesis of O₃ proceeds *via* a two-step reaction sequence first involving the homolytic molecular dissociation of O₂ to supra-thermal oxygen atoms followed by the addition of one such atom to O₂. Such an addition reaction has been considered to be either energetically barrierless (Bennett and Kaiser 2005, Sivaraman *et al.* 2007), or else as having a small activation energy barrier of <0.5 eV (Ioppolo *et al.* 2008).



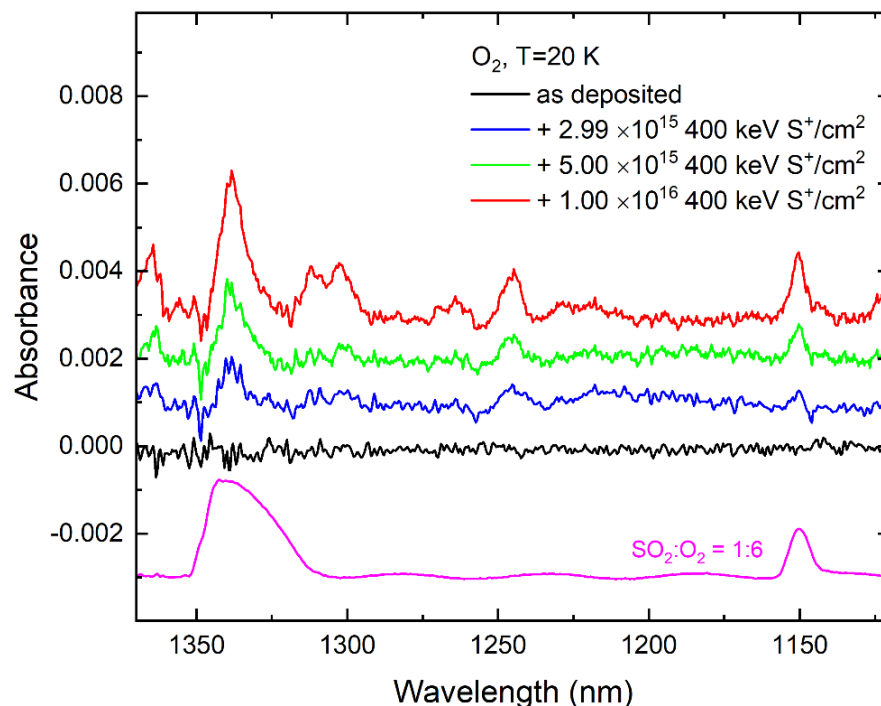


Fig. 7.7: Mid-infrared spectra of condensed O₂ before (*black trace*) and after the implantation of 400 keV S⁺ ions at 20 K (*blue, green, and red traces*). Also shown is the mid-infrared spectrum of an unirradiated O₂:SO₂ (6:1) ice mixture at 20 K (*pink trace*). Note also that spectra are vertically shifted for clarity.

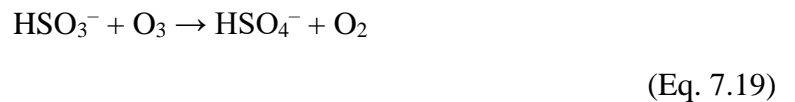
Of particular interest is the appearance of two absorption features at about 1343 and 1150 cm⁻¹ which begin to appear after a fluence of about 3×10^{15} S⁺ ions cm⁻² and continue to increase in absorbance with increasing fluence (Fig. 7.7). The intensity of the absorption band that appears at 1343 cm⁻¹ is consistently greater than that of the band at 1150 cm⁻¹ throughout the ion implantation process. The positions and relative profiles of these bands are therefore in agreement with the asymmetric and symmetric stretching modes of SO₂ and, indeed, a comparison with a control spectrum of an unirradiated O₂:SO₂ (6:1) mixed ice demonstrated a good degree of similarity. As such, the bands that appear at 1343 and 1150 cm⁻¹ in the O₂ ice as a result of the implantation of reactive sulphur ions can be safely attributed to the formation of SO₂.

The observed formation of SO₂ after the implantation of 400 keV S⁺ ions into O₂ ice at 20 K (as depicted in Fig. 7.7) contrasts strongly with the results of Boduch *et al.* (2016), who studied the implantation of 144 keV S⁹⁺ ions into O₂ ice at 16 K using ultraviolet absorption spectroscopy but did not detect the formation of SO₂. Instead, the main sulphur-bearing product reported by that study was the SO₃⁻ radical anion which presented a strong and broad absorption band centred at about 255 nm. This band may have possibly obscured any ultraviolet absorption bands attributable to SO₂, such as that expected at about 276 nm (Holtom *et al.* 2006, Mason *et al.* 2006). Nevertheless, the results of this investigation clearly demonstrate that sulphur ion implantation into O₂ ice at cold (15-20 K) temperatures does indeed result in the formation of solid SO₂.

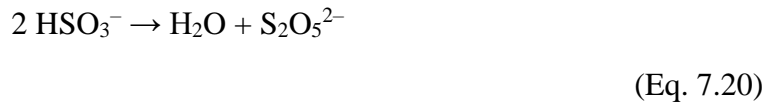
However, it is to be noted that this formation mechanism is likely to be of limited applicability to outer Solar System sulphur chemistry, such as that occurring on the surfaces of the icy Galilean moons of Jupiter, due various temperature constraints. It is important to note that the surface temperatures of these moons and many other outer Solar System objects are considerably higher than that of the sublimation temperature of pure O₂ (which is about

30 K; Collings *et al.* 2003b). As such, the existence of pure surface patches of O₂ on these objects is unlikely; rather, O₂ would need to be encapsulated within clathrate-like structures involving molecules that are significantly less volatile, such as H₂O. Indeed, clathrate hydrates of O₂ are known to be particularly stable (Mayer and Hallbrucker 1989, Hallbrucker and Mayer 1990), and have been invoked to explain the presence of icy O₂ on the surface of Europa (Hand *et al.* 2006). However, the inclusion of H₂O within the ice mixture may reduce the efficiency of SO₂ formation as a result of sulphur ion implantation, particularly in light of the efficiency of the competing formation of H₂SO₄ and its hydrates (Strazzulla *et al.* 2007, Strazzulla *et al.* 2009, Ding *et al.* 2013). Therefore, further work on the efficiency of SO₂ formation as a result of sulphur ion implantation into H₂O:O₂ mixed ices would need to be performed in order to determine the applicability of the results of this present study to the surface chemistry of the Galilean moons of Jupiter.

Moreover, it is likely that any yield of SO₂ as a result of sulphur ion implantation into a H₂O:O₂ mixed ice would be highly dependent on the temperature of the irradiation process. This is due to the fact that the major product of O₂ irradiation is O₃, which is a potent oxidant that is able to oxidise SO₂ to HSO₄⁻ in the presence of H₂O (Loeffler and Hudson 2016). The reaction sequence for this oxidation process is thought to be similar to that occurring in the atmosphere of the Earth (Erickson *et al.* 1977, Penkett *et al.* 1979):



Although it should be recalled that the HSO₃⁻ intermediate species may also be consumed in the formation of S₂O₅²⁻ (Kaňuchová *et al.* 2017):



The SO₂ consumption chemistry outlined above has been reported to be especially efficient at temperatures of 50-120 K, which are relevant to the surfaces of the icy Galilean moons (Moore *et al.* 2007, Loeffler and Hudson 2010, Loeffler and Hudson 2016, Kaňuchová *et al.* 2017). Thus, it is possible that any SO₂ that could form as a result of sulphur ion implantation into H₂O:O₂ mixed ices would be either consumed by neighbouring H₂O molecules in the production of HSO₃⁻ and S₂O₅²⁻, or would be efficiently oxidised to HSO₄⁻ by the copious amounts of O₃ produced as a result of the interaction of O₂ with ionising radiation. Thus, when considering the existence of H₂O, SO₂, and O₃ ices in an astrophysical environment characterised by temperatures greater than ~50 K, it may be stated that the presence of two of these species should exclude the third. Indeed, this kind of molecular distribution has been observed on several icy outer Solar System objects: SO₂ has been detected on the leading hemisphere of Callisto (McCord *et al.* 1998b, Hibbitts *et al.* 2000), while O₂ (the radiolytic precursor to O₃) has thus far only been observed on the trailing hemisphere (Spencer and Calvin 2002). Furthermore, SO₂ was detected to be among the most abundant sulphur-bearing species in the icy nucleus of comet 67P/Churyumov-Gerasimenko (Calmonte *et al.* 2016), while no evidence for the presence of O₃ could be found (Altwegg 2018).

7.6 Implications for Astrochemistry and Astrobiology

The main aim of this chapter was to determine whether or not the implantation of reactive sulphur ions into various oxygen-bearing ices at cryogenic temperatures represents a feasible mechanism for SO₂ formation. Such studies are of inherent interest to astrochemistry and planetary science, and so this sub-section will be devoted to a detailed discussion of the applicability of the results presented throughout this chapter to the solid-phase sulphur chemistry of astrophysical environments, with a particular focus on the outer Solar System.

7.6.1 Formation of SO₂ on Europa

The presence of SO₂ on the European surface has been the subject of a number of publications (e.g., Noll *et al.* 1995, McCord *et al.* 1998a, Hendrix *et al.* 2011, Becker *et al.* 2022) since its initial detection by Lane *et al.* (1981). Despite this, the method by which it forms remains elusive. As discussed in Section 7.1., the ‘bulls-eye’ pattern of SO₂ on Europa tentatively suggests an exogenic source of sulphur and it has been proposed that the implantation of Jovian magnetospheric sulphur ions into the surface ice of Europa yields the observed SO₂. Previous experimental studies have not supported this hypothesis: the implantation of reactive sulphur ions into H₂O surface ice analogues has been found to efficiently yield H₂SO₄ and its hydrates instead (Strazzulla *et al.* 2007, Strazzulla *et al.* 2009, Ding *et al.* 2013), with no evidence for the formation of SO₂ having been reported thus far.

The results of this present investigation reveal that SO₂ formation as a result of the implantation of sulphur ions into CO₂ ice, another component of the European icy surface (McCord *et al.* 1998a), is also improbable due to the demonstrated temperature dependence of this process (Figs. 7.2 and 7.3). Such a result is consistent with the lack of spatial correlation between the distributions of CO₂ and SO₂ on the surface of Europa (Hansen and McCord 2008). Moreover, although O₂ is also known to be present on the surface of Europa (Hand *et al.* 2006), and the present results suggest that sulphur ion implantation could represent a possible formation route towards SO₂ at 20 K, it has been proposed that such a reaction would not be efficient at contributing to SO₂ synthesis at higher temperatures relevant to Europa due to the increasingly dominant role of competing thermal and radiolytic reactions. As such, it appears that the results of this and previous experimental studies suggest that the implantation of hot sulphur ions from the Jovian giant magnetosphere into the surface ices of Europa does not constitute an effective contributor to the formation of SO₂ there, and so alternative mechanisms should be considered instead.

The ‘bulls-eye’ pattern in which SO₂ is distributed on the European surface is, however, still indicative of the participation of magnetospheric sulphur ions in the synthesis of SO₂. Moreover, the close spatial correlation of SO₂ and H₂SO₄ hydrates hints at a related synthetic chemistry. Indeed, an early study by Hochenadel *et al.* (1955) demonstrated that the irradiation of concentrated H₂SO₄ solution yielded SO₂, and a similar result was more recently observed by Loeffler *et al.* (2011) for condensed H₂SO₄ and its hydrates at low temperatures. Therefore, it is reasonable to suggest that the implantation of sulphur ions from the Jovian magnetosphere into the European H₂O surface ices efficiently yields H₂SO₄ hydrates which, upon further irradiation, are then decomposed to yield SO₂. Such a mechanism would satisfactorily explain the lower surface abundance of SO₂ compared to H₂SO₄ hydrates (Carlson *et al.* 2009), the spatial correlation of these species, and the experimentally determined improbability of SO₂ formation as a direct result of exogenic sulphur ion implantation.

Of course, other mechanisms could also contribute to the presence of SO₂ on Europa. The irradiation of sulphate minerals thought to exist on Europa and Ganymede, such as mirabilite (Na₂SO₄·10H₂O), thenardite (Na₂SO₄), or epsomite (MgSO₄·7H₂O), could result in their decomposition and the concomitant release of SO₂ (McCord *et al.* 1999, McCord *et al.* 2001a). Experimental work by Johnson *et al.* (1998) and McCord *et al.* (2001b) revealed that although mirabilite and epsomite are fairly stable against radiation-induced decay, a small amount of SO₂ may possibly be yielded as a result of their decomposition in the warmest regions of Europa (i.e., at about 130 K). Interestingly, the analogous experimental irradiation of Li₂SO₄ does not yield SO₂, but rather Li₂SO₃, Li₂S, and S_x are the major sulphur-bearing products (Sasaki *et al.* 1978).

An alternative source of surface SO₂ could be its endogenous delivery from the global subsurface ocean. Hydrothermal activity has long been postulated to occur at the boundary of the ocean and the underlying silicate mantle (Barge and White 2017, and references therein), and would likely result in the degassing of sulphurous molecules such as SO₂ to the ocean (Kargel *et al.* 2000). Modelling work has suggested that the upwelling of SO₂ may result in its delivery to upward-propagating cracks in the surface ice that are filled with H₂O, after which exsolution of the SO₂ (along with other gaseous species dissolved in the ocean) results in its delivery to the surface *via* explosive cryovolcanism (Stevenson 1982, Crawford and Stevenson 1988, Fagents *et al.* 2000). An endogenous source of SO₂ carries many implications with regards to the habitability of Europa, since terrestrial hydrothermal vents are not only known to harbour life, but are also suspected of having played a key role in the origins of life on Earth (Martin *et al.* 2008, Sojo *et al.* 2016).

However, this mechanism of SO₂ delivery to the European surface does not fully explain its observed surface distribution, which is known to be significantly enhanced on the trailing hemisphere (Carlson *et al.* 2009). If uniform hydrothermal degassing followed by exsolution were the primary source of surface SO₂, then the abundance of this species on the surface would not be expected to vary from region to region. Moreover, strong spatial correlations between the surface distributions of SO₂ and other species likely to have been degassed from the silicate mantle (such as CO₂) would be expected to be observed, which has not been the case (Hansen and McCord 2008). Although such observations could partially be explained by inhomogeneities in the thickness of the icy crust leading to thicker surface ices on the leading hemisphere, this hypothesis is merely speculative.

Finally, Becker *et al.* (2022) have recently suggested that cold (sub-keV) sulphur ions sourced from the Jovian magnetosphere could generate the SO₂ observed on the surface of Europa as a result of their implantation into the oxygen-bearing ices there. Such a process has yet to be considered experimentally, as all previous work has been concerned with hot (>10 keV) sulphur ion implantation. In reality, hot sulphur ions are able to access both the trailing and the leading hemisphere of Europa (Cassidy *et al.* 2013), while cold sulphur ions preferentially impinge upon the trailing hemisphere due to their smaller gyroradii (Cassidy *et al.* 2013, Addison *et al.* 2021). If the implantation of these lower energy sulphur ions into European surface ices does indeed result in a different sulphur radiation chemistry compared to that of hot sulphur ion implantation by efficiently producing SO₂, then that would neatly account for its observed surface distribution. Experimental work should therefore be conducted to confirm or refute the feasibility of this proposed mechanism.

7.6.2 Sulphur Chemistry on Trans-Neptunian and Kuiper Belt Objects

Trans-Neptunian and Kuiper Belt object surface ice chemistry is anticipated to be dominated by volatile species; principally CO, N₂, and CH₄ (Cruikshank *et al.* 1993, Brown *et al.* 1995, Cruikshank *et al.* 1997). As such, the implantation of sulphur ions into CO ice described earlier in this chapter is a good analogue for the interaction of sulphur ions within the solar wind with these celestial objects. The results of this study have been interpreted in light of previous experimental efforts on the subject (Lv *et al.* 2014a), and it has been determined that sulphur ion implantation into CO ice likely does not represent an appreciable mechanism for the formation of SO₂.

However, such a result need not necessarily imply that sulphur chemistry as a result of ion implantation is not possible on trans-Neptunian or Kuiper Belt objects. Previous work by Ruf *et al.* (2019) and Ruf *et al.* (2021) has revealed that, although the implantation of reactive sulphur ions into mixed ices whose composition is relevant to these objects does not yield SO₂ (or, at least, its formation was not reported), a plethora of organosulphur molecules is produced with over 1100 individual species having been detected by mass spectrometry. Since no sulphur-bearing species were observed after the implantation of 400 keV S⁺ ions into solid CO (Fig. 7.5), the question as to the molecular form the implanted sulphur adopts remains unanswered. However, it is possible that the implanted sulphur is incorporated into refractory organosulphur molecules whose individual abundances were too low to be detected *via* mid-infrared absorption spectroscopy.

7.6.3 On the Non-Detections of OCS and CS₂

One striking observation made during the implantation of sulphur ions into the CO and CO₂ considered here is the non-detection of either OCS or CS₂ in the irradiated ices. The detection of OCS in astrophysical environments carries important astrobiological implications, due to the known role of this molecule in the catalysis of amino acid oligomerisation to give peptides (Leman *et al.* 2004). Given that Europa is considered to be a prime candidate host for extra-terrestrial life (Chyba and Phillips 2002), it is important to define the chemical formation pathways (or lack thereof) of any molecules that could participate in prebiotic chemistry. Detailed studies by Ferrante *et al.* (2008) demonstrated that the formation of OCS from irradiated CO ices mixed with sulphur-containing molecules is more efficient than the analogous formation from irradiated CO₂ ices. Such a result was later corroborated by Lv *et al.* (2014a), who did not observe OCS formation after the implantation of reactive sulphur ions into CO₂ ice at 15 K but did observe it after implantation into CO ice.

In this present investigation, no evidence could be found for the formation of OCS after the implantation of sulphur ions into either CO or CO₂ ice at any studied temperature. In the mid-infrared range, pure OCS presents an absorption band at about 2045 cm⁻¹ which is attributed to the asymmetric stretching of its C=O bond; however, this band is known to experience large shifts in its position of up to 30 cm⁻¹ when OCS is a component of a mixed ice (Ferrante *et al.* 2008, Garozzo *et al.* 2010, Sivaraman 2016). Indeed, an absorption band at the approximately correct position was observed in the CO₂ and CO ices into which sulphur ions were implanted at 20 K (Figs. 7.2 and 7.4); however, this band was attributed to CO₃, which also presents an absorption feature in this region of the mid-infrared spectrum.

Identifying whether the band at approximately 2045 cm⁻¹ is caused by OCS or CO₃ may be achieved through an analysis of its FWHM. OCS presents a broad absorption feature

whose FWHM varies between 15-20 cm^{-1} depending on the composition of the ice (Ferrante *et al.* 2008). Conversely, the FWHM for the CO_3 band is significantly smaller at 5-8 cm^{-1} (Ferrante *et al.* 2008, Lv *et al.* 2014a). Given that the bands observed in Figs. 7.2 and 7.4 did not have a FWHM exceeding 7 cm^{-1} , these bands were attributed to the presence of CO_3 . Moreover, it should be noted that the band attributed to CO_3 in the present experiments was weak in the case of the ion-implanted CO ice but strong in the case of the ion-implanted CO_2 ice, which agrees well with previous literature data on the abundance of CO_3 formed after the irradiation of CO and CO_2 ices (Satorre *et al.* 2000, Trottier and Brooks 2004, Jamieson *et al.* 2006, Bennett *et al.* 2010, Sivaraman *et al.* 2013). Conversely, such an observation is not in agreement with the formation of OCS after sulphur ion implantation into these ices, which has been demonstrated by Lv *et al.* (2014a) after implantation into CO ice but not CO_2 ice, thus effectively ruling out OCS as the cause of the observed absorption band.

CS_2 is another molecule of great interest to prebiotic chemistry and astrobiology, due in part to the known polymerisation and oligomerisation processes in which this molecule partakes as a result of its radiation processing, photo-processing, or its sonochemical treatment (Cataldo 1995, Cataldo and Heymann 1998, Heymann *et al.* 2000, Cataldo 2000, Cataldo and Heymann 2001). The resultant carbon- and sulphur-rich oligomers and polymers may therefore act as a backbone for the production of larger macromolecules with multiple functional groups that may be relevant to biology (Rushdie and Simoneit 2005). Moreover, and similarly to OCS, CS_2 is also known to catalyse the formation of peptides in aqueous solutions (Leman *et al.* 2015), and may thus play a key role in the formation of biomolecules in extra-terrestrial settings.

Although previous studies have considered the radiation chemistry of pure and mixed CS_2 astrophysical ice analogues (Cataldo 2000, Maity and Kaiser 2013, Sivaraman 2016), less attention has been paid to its radiolytic formation from other carbon- and sulphur-bearing species. Lv *et al.* (2014a) noted that the implantation of sulphur ions into CO_2 ice at 15 K resulted in a small abundance of CS_2 being produced, although none was detected as a result of similar implantations into CO ice. The results of this present investigation offer no real evidence for the formation of CS_2 as a result of the implantation of sulphur ions into either ice (Figs. 7.2 and 7.4). It should be noted that the work of Lv *et al.* (2014a) was only able to calculate an upper limit to the formation efficiency of CS_2 as a result of sulphur ion implantation into condensed CO_2 , which was determined to be 0.027 molecules per impinging ion. As such, a maximum of 2.7×10^{14} CS_2 molecules cm^{-2} could have formed in the present CO_2 experiment; an abundance which is below the spectroscopic limit of detection of the apparatus. It is therefore possible to conclude that the implantation of sulphur ions into carbon oxide ices is likely not a reasonable mechanism for the formation of CS_2 in astrophysical environments.

7.7 Summary

This chapter discusses the results obtained from a series of systematic sulphur ion implantation experiments into a number of oxygen-bearing ices at cryogenic temperatures; namely, CO at 20 K, CO_2 at 20 and 70 K, and O_2 at 20 K. The motivation behind this work was to determine whether or not such implantation processes could lead to the formation of SO_2 and, if so, whether such a process could account for the observation of SO_2 on the surface of Europa and elsewhere in the Solar System.

The implantation of reactive sulphur ions into CO₂ ice revealed that small quantities of SO₂ could indeed be formed at 20 K, but that this synthesis is temperature-dependent and does not occur at the more Europa-relevant temperature of 70 K. This result, combined with the observed lack of spatial correlation in the distribution of CO₂ and SO₂ on the surface of Europa (Hansen and McCord 2008), would suggest that sulphur ion implantation into CO₂ ices does not contribute to the observed SO₂ on Europa. Previous results have also shown that the implantation of sulphur ions into H₂O ice, which represents the dominant icy species on Europa, does not yield SO₂ as a product (Strazzulla *et al.* 2007, Strazzulla *et al.* 2009, Ding *et al.* 2013). Alternative sources of surface SO₂ must therefore be considered instead, and some possible formation routes have been discussed herein.

The implantation of sulphur ions into CO ice at 20 K did not result in the formation of SO₂; rather, the formation of cumulene dioxides and oxocarbon radicals, together with CO₂ and CO₃, dominated the radiation chemistry occurring within the ice. The lack of sulphur-bearing product molecules raises the question as to final molecular form of the implanted sulphur ions and, based on the previous results of Ruf *et al.* (2019) and Ruf *et al.* (2021), it is speculated that low abundances of refractory organosulphur molecules or even sulphur residues may have been produced. The analogous implantation process into O₂ ice did result in the formation of SO₂; however, there exist several problems regarding the applicability of this result to the sulphur chemistry occurring on, for example, the icy surface of Europa. This is due to volatility of pure O₂ ice, which would efficiently sublime at temperatures such as those that characterise the surface of Europa. Moreover, the primary product of O₂ irradiation, O₃, is hypothesised to deplete any nascent SO₂ as a result of the oxidation of the latter in the presence of H₂O (Loeffler and Hudson 2016). The chapter concludes with a thorough description of the applicability of the results obtained to the sulphur radiation chemistry that is thought to characterise the surfaces of the icy Galilean satellites of Jupiter and trans-Neptunian and Kuiper Belt objects, as well as a brief commentary on the non-detections of the prebiotically relevant molecules OCS and CS₂.

8 ION IRRADIATION OF OXYGEN-BEARING ICES DEPOSITED ON TOP OF PURE SULPHUR RESIDUES

In the previous chapter, routes towards the formation of SO₂ and other sulphur-bearing molecules as a result of the implantation of sulphur ions into oxygen-bearing ices were explored, with the aim of applying the results obtained to the radiation chemistry occurring on the surfaces of the Galilean satellites of Jupiter and other outer Solar System objects. In this chapter, an alternative mechanism is investigated, that of the irradiation of oxygen-bearing ices deposited on top of pure elemental sulphur. This mechanism has only been very briefly considered in previous works, and only for H₂O ice deposited at 80 K on top of a sulphur residue. This chapter presents details of a new and more efficient method of generating the required elemental sulphur layer and the results of a systematic investigation of the 1 MeV He⁺ ion irradiation of H₂O, CH₃OH, CO₂, CO, and O₂ ices on top of elemental sulphur at different temperatures.

Note: The majority of the work described in this chapter has been published in peer-reviewed journals or periodicals as: [1] Mifsud *et al.* (2023), *Icarus* to be submitted; [2] Mifsud *et al.* (2023), *Earth Planet. Sci. Lett.* to be submitted.

8.1 Contextual Introduction

The possible contributions of refractory residues to the formation of new molecules have been rarely studied in astrochemical experiments, which are more often concerned with chemical reactions and physical processes taking place within ices representative of those found on interstellar dust grains or outer Solar System bodies. However, many such residues are composed of reactive elements that are known to readily form molecules that could form part of an astrophysical ice, such as carbon, nitrogen, or sulphur (Ehrenfreund and Sephton 2006, Gomis and Strazzulla 2008, Rahul *et al.* 2020). Indeed, some previous experimental work has demonstrated that the irradiation of H₂O ice deposited on top of hydrogenated carbon grains by ions or ultraviolet photons yields CO and CO₂ (Mennella *et al.* 2004, Gomis and Strazzulla 2005, Mennella *et al.* 2006), thus evidencing the transfer of atoms from a refractory residue to a volatile product.

Such reactions may be particularly important in the context of sulphur astrochemistry, as refractory sulphur is hypothesised to be widespread across the cosmos (Kama *et al.* 2019). In the ISM, for instance, nano-inclusions of FeS minerals such as octahedral iron(II) sulphide or hexagonal troilite in silicate dust grains have been invoked to partially explain the observed depletion in sulphur (Köhler *et al.* 2014), which was previously described in detail in Chapter 1. Polysulphanes of the type H₂S_{*x*} (*x* > 2) and S_{*x*} are also thought to be a component of interstellar icy grain mantles, most likely at the grain-ice interface (Druard and Wakelam 2012, Cazaux *et al.* 2022). On Europa, elemental sulphur and sulphur-based residues were proposed to partially account for features in the ultraviolet-visible spectra on both the leading and trailing hemispheres (McEwen 1986, Nelson *et al.* 1986, Spencer *et al.* 1995). Although questions were initially raised regarding the possibility of S₈ existing on Europa due to the known efficiency of its sublimation under surface conditions (Nash 1987), Steudel *et al.* (1986) and Steudel and Eckert (2003) demonstrated that the irradiation of S₈ could open the molecular ring and lead to the production of longer chains and rings that are stable against sublimation and whose ultraviolet-visible spectra are consistent with those of both Io and Europa (Hapke and Graham 1989, Carlson *et al.* 2009).

Despite the potentially key role of elemental sulphur and sulphur-bearing residues in the radiation chemistry occurring in the ISM and the outer Solar System, there have only been a few previous experimental studies that have considered this chemistry. Moore (1984) had previously reported remnant polymeric SO₃, S₈, and sulphates after warming an irradiated SO₂ ice, whilst Gomis and Strazzulla (2008) produced a sulphur residue by depositing SO₂ ice on a cold substrate at 16 K and subsequently irradiating it with 200 keV He⁺ and Ar⁺ ions, before warming the ice to room temperature so as to affect the sublimation of the volatile components. The remnant sulphur-rich residue was then re-cooled to 80 K and a layer of H₂O ice was deposited on top of it, before further irradiation was carried out using 200 keV He⁺ ions (Gomis and Strazzulla 2008). The results of that study found little in the way of efficient SO₂ formation as a result of this energetic processing.

Although H₂O is the dominant ice in the cosmos (Klinger 1983, van Dishoeck *et al.* 2013), other oxygen-bearing ices, such as O₂, CO, CO₂, and CH₃OH, are also known to exist on the surfaces of outer Solar System objects and in interstellar icy grain mantles. It is, therefore, necessary to investigate the potential for the formation of volatile sulphur-bearing molecules (such as SO₂, CS₂, or OCS) as a result of the irradiation of oxygen-bearing ices deposited on top of sulphur-rich residues. There are, however, certain disadvantages to the experimental methodology used by Gomis and Strazzulla (2008) to prepare the refractory sulphur-rich residue, mainly relating to the amount of residue that is produced.

In their work, Gomis and Strazzulla (2008) initially deposited a SO₂ ice with a column density of up to a few 10¹⁸ molecules cm⁻² which was then irradiated to produce various new product molecules, including the residue. However, their analysis revealed that the majority of the ice remained as SO₂ even at the end of their irradiations, with some SO₃ also being observed in the acquired mid-infrared spectra. The majority of sulphur atoms was therefore still locked away in volatile molecules at the end of the irradiation process, and were thus lost to sublimation upon warming the ice to room temperature. The remnant sulphur-rich residue therefore likely did not contain a significant amount of sulphur, thus greatly limiting the number of sulphur-bearing product molecules that could be formed as a result of the irradiation of the H₂O ice on top of this residue. Moreover, it is very likely that the sulphur-rich residue was not purely composed of sulphur, as some oxygen atoms may have been incorporated into the residue during its formation as a result of the irradiation of the SO₂ ice.

It is thus desirable to be able to produce a thicker residue composed purely of sulphur. In this chapter, a new method of generating this solid layer based on the effusive evaporation of elemental sulphur followed by its condensation at cryogenic temperatures is described. This technique was then used to investigate the 1 MeV He⁺ ion irradiations of O₂, CO, CO₂, and H₂O ices on top of a sulphur layer at 20 K, with the aim of searching for sulphur-bearing volatile product molecules. Furthermore, the irradiations of H₂O and CO₂ ices on sulphur layers at 70 K, as well as the irradiation of CH₃OH ice on top of sulphur at 25 K, were also studied. The results are interpreted in the context of the production of sulphur-bearing volatiles in interstellar icy grain mantles, as well as on icy Solar System bodies such as comets and Europa.

8.2 Experimental Methodology

Prior to beginning the main experimental work, a preliminary experiment for the preparation of the sulphur layer using the effusive evaporator was performed so as to determine the required temperature to which elemental sulphur (pharmaceutical grade, 99.95% purity)

needed to be heated to deposit the residue. A glass test tube was filled with approximately 10 g of sulphur and was then loaded into the evaporator. The evaporator was then attached to a stainless steel four-way cross in the centre of which was a suspended glass plate which was to serve as the deposition substrate for this preliminary experiment. An optical viewport was installed on the port opposite the evaporator to allow for the observation of the glass plate at all times, while the remaining ports on the four-way cross (i.e., those above and below the plane of the ports containing the evaporator and viewport) were sealed off using blank flanges.

Previous experience on the preparation of refractory pyrene residues using the effusive evaporator demonstrated that temperatures of 50-80 °C could be used for the slow deposition of carbon-based refractories. Therefore, the sulphur was heated to a temperature of 78 °C and allowed to deposit onto the glass plate. After approximately two hours of deposition, a thin sulphur layer became visible (Fig. 8.1), at which point deposition was halted. The thickness of the deposited sulphur layer was estimated to be in the range of a few 0.1 mm based on the fact that this is the smallest thickness generally visible to the naked eye (Yanoff and Duker 2009) and that deposition was stopped immediately after the appearance of the layer. A sulphur layer having a thickness of a few μm was required for the irradiation experiments. Assuming that the actual thickness of the sulphur layer deposited over two hours in the preliminary experiment lay in the range of 0.1-0.5 mm, then a similar deposition lasting only five minutes should produce a sulphur layer with a thickness of 4-20 μm . For the purposes of this thesis, it has been assumed that the lower bound value of 4 μm is the thickness of the sulphur layer produced *via* effusive evaporation of the powder at 78 °C for five minutes.

The He^+ ion irradiation experiments were performed using the ICA set-up with the effusive evaporator attached to the multi-purpose port shown in Fig. 4.1. Once the ICA had been evacuated to a base pressure of a few 10^{-9} mbar and the ZnSe substrates cooled to the desired deposition temperature (i.e., 20, 25, or 70 K), the sample holder and substrates were turned to directly face the effusive evaporator and sulphur layers of thickness 4 μm were prepared by heating elemental sulphur to 78 °C for five minutes. After these five minutes had elapsed, the copper shutter in front of the evaporator nozzle was closed so as to preclude any further deposition of the sulphur.

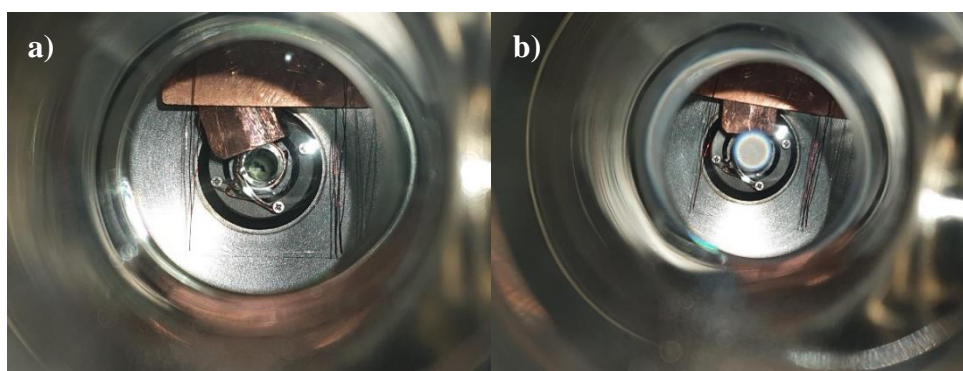


Fig. 8.1: Photographs of the glass plate acting as a deposition substrate during the preliminary experiment used to determine the deposition time required to prepare a sulphur layer. The photographs were taken through the optical window of the four-way cross, with the effusive evaporator located directly opposite (indeed, the copper shutter of the evaporator is visible in the photographs). Panel *a*) shows the glass plate before the preliminary deposition began, with no sulphur being visible. Panel *b*) shows the glass plate after the deposition of sulphur at 78 °C for about two hours. Note that the apparent rotation of the image between panels *a*) and *b*) is merely the result of having rotated the camera between taking the photographs.

Once the sulphur layer had been successfully deposited, the sample holder and deposition substrates were rotated to face the mid-infrared spectroscopic beam. The various allotropes of elemental sulphur (of the type S_x) only present infrared absorption features at wavenumbers $<550\text{ cm}^{-1}$ (Trofimov *et al.* 2009), which are not accessible using the current apparatus and thus any acquired spectra would have simply appeared as a flat line with oscillatory interference caused by the change in pathlength of the infrared spectroscopic beam that is not taken into account by collected background spectra of the pure ZnSe deposition substrates. Therefore, a new set of background spectra (1 cm^{-1} resolution; 128 scans) were taken after the deposition of the sulphur layers.

Pure ices were then prepared on top of the sulphur layers *via* the background deposition of the relevant gases or vapours (O_2 purity = 99.995%; CO purity = 99.97%; CO_2 purity = 99.995%; all Linde; VLSI grade CH_3OH from VWR; de-ionised H_2O) at a chamber pressure of a few 10^{-6} mbar. In the case of the CH_3OH and H_2O ice depositions, the liquid samples from which the vapours were sourced were first de-gassed using the standard liquid nitrogen freeze-pump-thaw technique before their vapours were passed into the dosing line and subsequently dosed into the main chamber. The growth of the ices was followed *in situ* using Fourier-transform mid-infrared transmission absorption spectroscopy over a spectral range of $4000\text{-}650\text{ cm}^{-1}$ (1 cm^{-1} resolution; 128 scans), and the deposited ice column densities and thicknesses could be quantified using Eqs. 8.1 and 8.2, as described in previous chapters:

$$N = 2.303 \times \frac{P_a}{A_s} \quad (\text{Eq. 8.1})$$

$$d = 10^4 \times \frac{Nm}{\rho N_A} \quad (\text{Eq. 8.2})$$

where P_a is the band area of a characteristic absorption band, A_s is the integrated band strength constant for that band, m is the molecular mass, ρ is the mass density of the ice, and N_A is the Avogadro constant. A list of ice densities and integrated band strength constants used in this study is given in Table 8.1. It should be noted that Eqs. 8.1 and 8.2 cannot be used to determine the deposited column density and thickness of O_2 ice, as O_2 is inactive in the mid-infrared spectral region. Instead, it was assumed that the deposition rate of O_2 is similar to that of CO based on the similarities in the molecular geometry, molecular mass, and pumping speed of the molecules; and so, depositing an O_2 ice at the same chamber pressure and for the same duration as was done for the CO ice would result in a similar deposited column density, from which the ice thickness could be determined based on the known density of O_2 ice (Table 8.1).

Once an ice had been successfully prepared on top of the sulphur layer at the desired temperature, it was exposed to a 1 MeV He^+ ion beam with mid-infrared spectra being collected at several intervals during irradiation until a total fluence of 10^{15} ions cm^{-2} was delivered. The acquired mid-infrared spectra were used to determine whether sulphur-bearing molecules such as SO_2 , OCS, or CS_2 formed as a result of the radiation chemistry occurring at the interface of the sulphur layer and the ice. The choice of helium ions as the projectile particle was based on two factors: firstly, given the calculated penetration depths of a 1 MeV He^+ ion in the irradiation experiments performed in this study (Ziegler *et al.* 2010), it is likely that the projectile ions may have implanted into the sulphur layer. By

making use of He⁺ ions as the projectile, any chemical modifications of the sulphur layer *via* reaction with the implanted particle could be precluded due to the inert nature of the neutral helium atom. Secondly, He⁺ ions are a known constituent of galactic cosmic rays (Simpson 1983, Mewaldt 1994), and thus are of astrophysical and astrochemical relevance.

Table 8.1: List of integrated band strength constants (A_s) and densities (ρ) of the ices considered in this study. Note that, with exception of S₈, the implantation depth refers to a 1 MeV He⁺ projectile ion traversing an ice of defined thickness (CO = 0.20 μm ; CO₂ at 20 K = 0.07 μm ; CO₂ at 70 K = 0.05 μm ; CH₃OH = 1.30 μm ; H₂O at 20 K = 1.20 μm ; H₂O at 70 K = 1.00 μm ; O₂ = 0.20 μm) deposited over a 4 μm sulphur layer in each case, as occurred in this study. In the case of S₈, the implantation depth refers to a 1 MeV He⁺ ion traversing a sulphur layer of thickness 4 μm . Data taken from Gerakines *et al.* (1995), Greenwood and Earnshaw (1997), Freiman and Jodl (2004), Satorre *et al.* (2008), and Luna *et al.* (2018).

Molecule	Mid-Infrared Band Position (cm ⁻¹)	A_s (10 ⁻¹⁷ cm molecule ⁻¹)	ρ (g cm ⁻³)	Implantation Depth (μm)
S ₈ (sulphur)	-	-	2.07	2.9
CO	2139 (v _s)	1.1	0.80	3.0
CO ₂	2343 (v ₃)	7.6	0.98 (20 K) / 1.48 (70 K)	3.0 (20 K) / 2.9 (70 K)
CH ₃ OH	1027 (v ₈)	1.6	0.64	3.5
H ₂ O	3250 (v _s)	20.0	0.93 (20 K) / 0.94 (70 K)	3.3 (20 K) / 3.1 (70 K)
O ₂	-	-	1.54	2.9

8.3 1 MeV He⁺ Ion Irradiation of Oxygen-Bearing Ices on Top of Pure Sulphur

This sub-section details the results obtained after the 1 MeV He⁺ ion irradiation of different oxygen-bearing ices deposited on top of a pure elemental sulphur layer and includes a comparative discussion of the spectroscopic observations that were recorded. In total, seven irradiation experiments involving five different ices have been carried out: (i) O₂ at 20 K; (ii) CO at 20 K; (iii) CH₃OH at 25 K; (iv and v) CO₂ at both 20 and 70 K; and (vi and vii) H₂O at both 20 and 70 K.

8.3.1 O₂ Ice on Top of Sulphur at 20 K

The irradiation of pure O₂ ice deposited on top of a layer of elemental sulphur represents what is arguably one of the most straightforward chemical systems from which SO₂ may be produced. Indeed, mid-infrared absorption features at about 1335 and 1150 cm⁻¹ were observed to develop during the irradiation of the ice by 1 MeV He⁺ ions (Fig. 8.2). These bands have been respectively attributed to the asymmetric and symmetric stretching modes of SO₂ on the basis of the excellent agreement of their wavenumber positions with those of a reference O₂:SO₂ (6:1) ice, as well as their exhibiting the expected SO₂ spectral profile in which the band due to the asymmetric stretching mode has a greater intensity than that due to the symmetric stretching mode. By making use of an integrated band strength constant of 1.47×10⁻¹⁷ cm molecule⁻¹ for the asymmetric stretching mode (Garozzo *et al.* 2008), the column density of SO₂ could be tracked throughout the irradiation process (Fig. 8.3). It was found that SO₂ forms fairly early on during irradiation, with the first observation of the asymmetric stretching mode being made after a fluence of just 4.2×10¹⁴ ions cm⁻² was delivered. The SO₂ column density continued to grow throughout irradiation, until it eventually plateaued at 1.2×10¹⁶ molecules cm⁻² after a He⁺ ion fluence of just over 10¹⁵ ions cm⁻² had been delivered (Fig. 8.3).

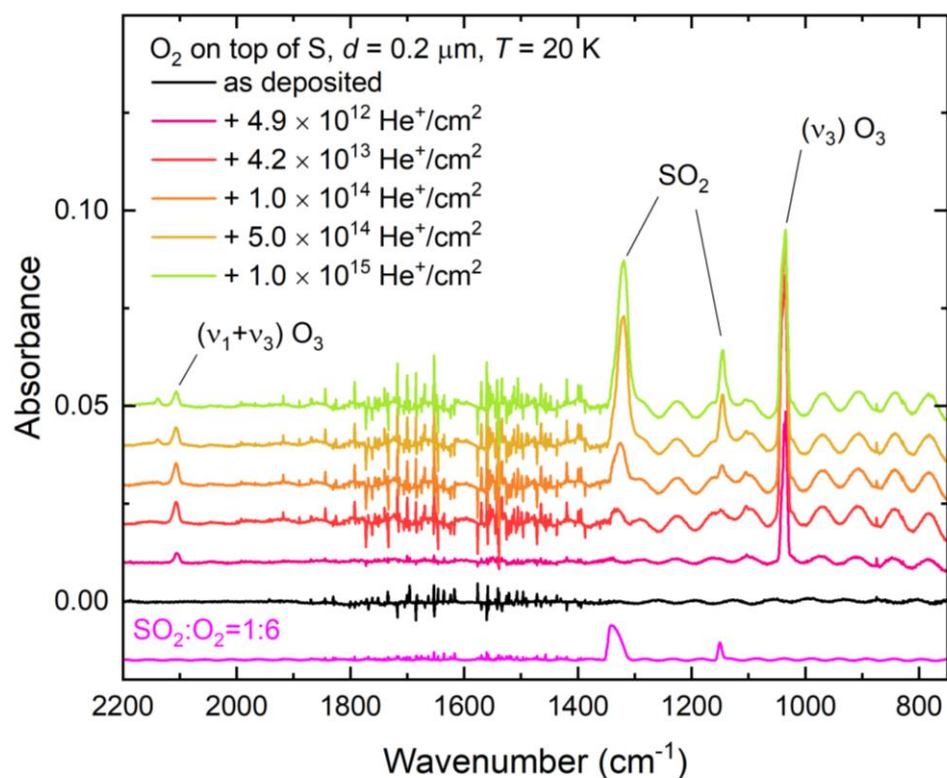


Fig. 8.2: Mid-infrared spectra of O_2 ice deposited on top of a layer of elemental sulphur before and during its irradiation by 1 MeV He^+ ions at 20 K. Included in the figure is the spectrum of an unirradiated $\text{O}_2:\text{SO}_2$ (6:1) ice for comparative purposes. Note that spectra are vertically shifted for clarity. Sinusoidal patterns in the spectra are caused by interference of infrared light reflected in the substrate-ice-vacuum optical system.

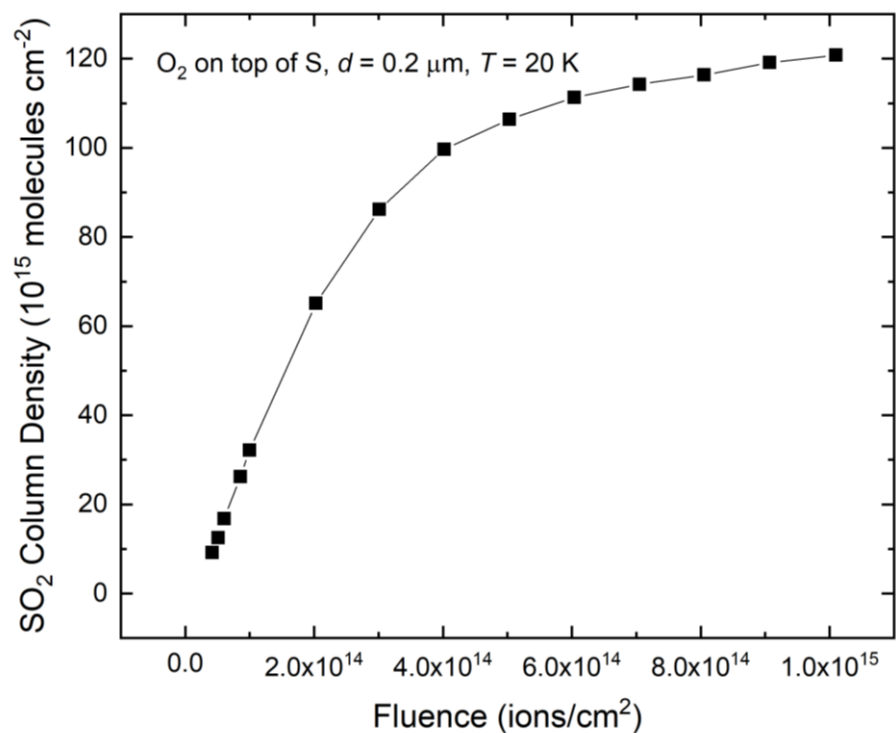


Fig. 8.3: Column density evolution of SO_2 formed as a result of the irradiation of O_2 ice on top of a layer of elemental sulphur using 1 MeV He^+ ions. Note that the column density was calculated through measurement of the band attributed to the SO_2 asymmetric stretching mode using an integrated band strength constant of $1.47 \times 10^{-17} \text{ cm molecule}^{-1}$ (Garozzo *et al.* 2008).

This result may be compared to that obtained after the implantation of 400 keV S⁺ ions into O₂ ice at 20 K, which was discussed in Chapter 7. Both processes lead to the formation of SO₂; however, the irradiation of the ice deposited on top of elemental sulphur was clearly more productive in this regard as may be inferred through the larger SO₂ band areas in Fig. 8.2 compared to those in Fig. 7.7. This may be attributed to the larger number of sulphur atoms available for SO₂ formation during the He⁺ ion irradiation experiment, where many sulphur atoms may react with radiolytically derived oxygen atoms at the interface of the O₂ ice with the elemental sulphur layer to yield SO₂. Conversely, the number of sulphur atoms available for SO₂ formation in the S⁺ ion implantation experiment was limited to the fluence of ions that was actually implanted into the target O₂ ice and subsequently underwent neutralisation which, at just 1.01×10^{16} ions cm⁻², was likely several orders of magnitude less than the number produced in this present experiment.

Oxygen atoms that are produced as a result of the radiolytic dissociation of O₂ along the track of the projectile He⁺ ion but that are far away from the ice-sulphur interface cannot partake in reactions leading to the formation of SO₂. Instead, it is more likely that O₃ will be the dominant radiolysis product in these regions of the ice. Indeed, the formation of O₃ as a result of the 1 MeV He⁺ ion irradiation of the O₂ ice was confirmed through the appearance in Fig. 8.2 of its asymmetric and combination ($\nu_1 + \nu_3$) bands approximately located at 1040 and 2110 cm⁻¹, respectively (Chaabouni *et al.* 2000). As was described in Chapters 1 and 7, the co-existence of solid SO₂ and O₃ is dependent upon the absence of any H₂O in the ice, as otherwise a series of cryogenic thermal reactions leading to the production of various sulphur oxyanions, including HSO₃⁻, HSO₄⁻, and S₂O₅²⁻ (Loeffler and Hudson 2016, Kaňuchová *et al.* 2017), would be triggered. None of these species was detected as a result of the irradiation processes studied here (Fig. 8.2).

Any appreciable formation of SO or S₂O as a result of the irradiation of O₂ ice deposited on top of elemental sulphur is fairly unlikely due to the inherent instability of these species under the conditions of the experiment. As was described in Chapter 7, SO is rapidly oxidised unless maintained in an inert matrix at low temperatures (Rolfes *et al.* 1965, Hopkins and Brown 1975, Herron and Huie 1980, Baklouti *et al.* 2004), whereas S₂O is readily dissociated *via* various chemical pathways including thermal decomposition, dissociative electron detachment, pre-dissociation followed by cleavage of the S–S bond, and disproportionation (Dudley and Hoffmann 2003, Steudel and Steudel 2004, Field *et al.* 2005, Navizet *et al.* 2010). It is, however, entirely possible that the radiation chemistry induced by the projectile He⁺ ions resulted in the interconversion of various allotropic forms of sulphur. For instance, it is possible that ring-opening or chain-breaking reactions of larger or unstable allotropes, such as S₁₂ or S₂₀, may lead to the formation of smaller allotropes such as S₂ or S₃ (Zysman-Colman *et al.* 2008). Alternatively, oligomerisation and polymerisation reactions involving sulphur atoms sourced from the irradiation of the deposited layer may produce larger allotropes (Mahjoub *et al.* 2017). Unfortunately, this sulphur chemistry is very difficult to elucidate due to the fact that the infrared absorption bands of most allotropic forms of sulphur are located beyond the spectral range accessible with ICA set-up (Trofimov *et al.* 2009).

8.3.2 CO Ice on Top of Sulphur at 20 K

The 1 MeV He⁺ ion irradiation of CO ice on top of a layer of elemental sulphur at 20 K resulted in the formation of several new products, as evidenced by the appearance of many

new absorption features in the mid-infrared spectra of the ice acquired during irradiation (Figs 8.4 and 8.5). As was the case after the implantation of sulphur ions into CO ice, many of the new absorption bands observed here were clustered in the 2400-2000 cm^{-1} wavenumber range and are associated with the C=O bond stretching modes of various oxocarbon species (Strazzulla *et al.* 1997, Gerakines and Moore 2001, Trottier and Brooks 2004, Loeffler *et al.* 2005, Palumbo *et al.* 2008, Lv *et al.* 2014a). Indeed, most of the oxocarbon radicals and cumulene dioxides detected after the implantation of 400 keV S^+ ions into CO ice at 20 K (Table 7.3) were also detected after the He^+ ion irradiation of CO deposited on top of a sulphur layer (Table 8.2), with the notable exceptions of CO_3 , C_3 , and C_2O .

However, it should be noted that the abundances of the oxocarbon species produced as a result of the 1 MeV He^+ ion irradiation of the CO ice were significantly less than those produced after 400 keV S^+ ion implantation, as may be deduced by comparing the areas of the relevant absorption bands (Figs. 7.4 and 8.4). This may be due to the fact that the implantation of the S^+ ions resulted in all of the kinetic energy of the projectile being deposited within the ice. This was not the case for the He^+ ions, which traversed the 0.2 μm ice thickness and were subsequently implanted a further 2.8 μm into the sulphur layer. As such, the Bragg peak (and, consequently, the majority of the deposited energy) was located deep within the sulphur layer at a point which could not have engendered CO radiolytic chemistry. Given that the mid-infrared absorption bands of CO_3 , C_3 , and C_2O are all weaker than the bands of the other detected oxocarbon species, it is therefore possible that the energy deposited into the CO ice by the impinging He^+ ions was not sufficient to generate enough of these species to be detected by the spectroscopic instrumentation available at the ICA.

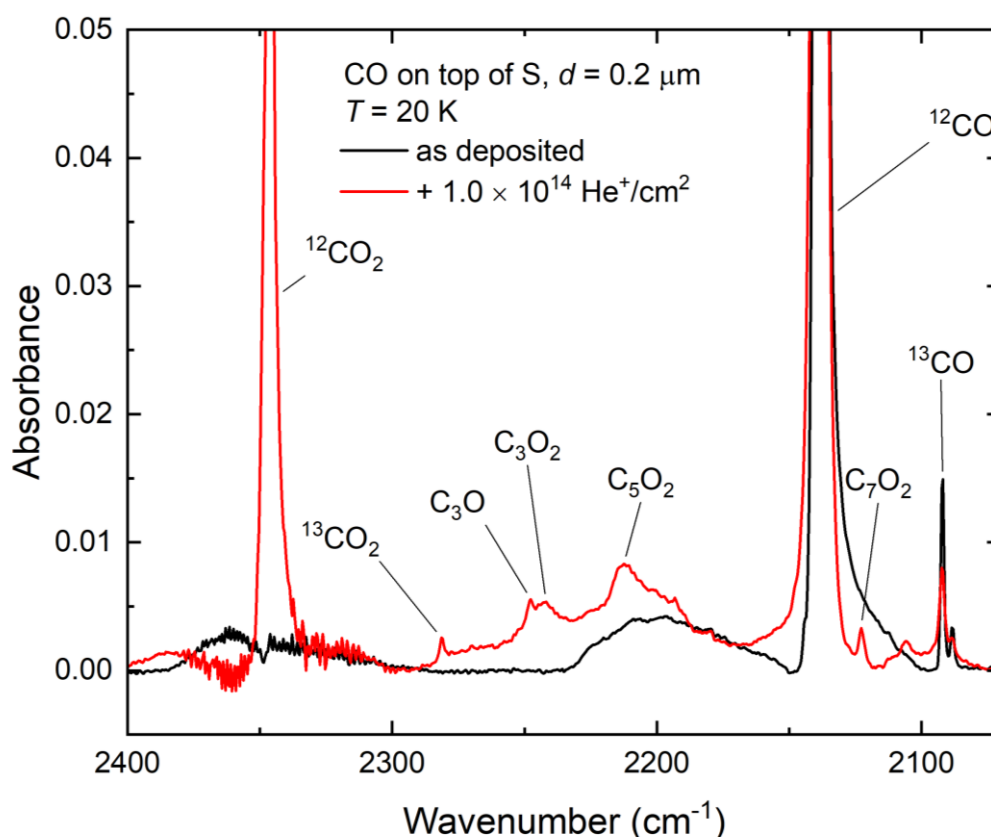


Fig. 8.4: Mid-infrared spectra of condensed CO on top of a layer of elemental sulphur before (*black trace*) and after (*red trace*) irradiation by 1 MeV He^+ ions at 20 K.

Table 8.2: List of oxocarbon molecules present in the CO ice on top of a layer of elemental sulphur after irradiation by 1 MeV He⁺ ions sorted by the wavenumber position of their mid-infrared absorption band peaks.

Formula	Molecule		Mid-Infrared Band Position (cm ⁻¹)
		Name	
¹² CO ₂		Carbon dioxide	2346
¹³ CO ₂		Carbon dioxide	2281
C ₃ O		Tricarbon monoxide	2247
C ₃ O ₂		Tricarbon dioxide (carbon suboxide)	2242
C ₅ O ₂		Pentacarbon dioxide	2211
¹² CO		Carbon monoxide	2138
C ₇ O ₂		Heptacarbon dioxide	2122
¹³ CO		Carbon monoxide	2092

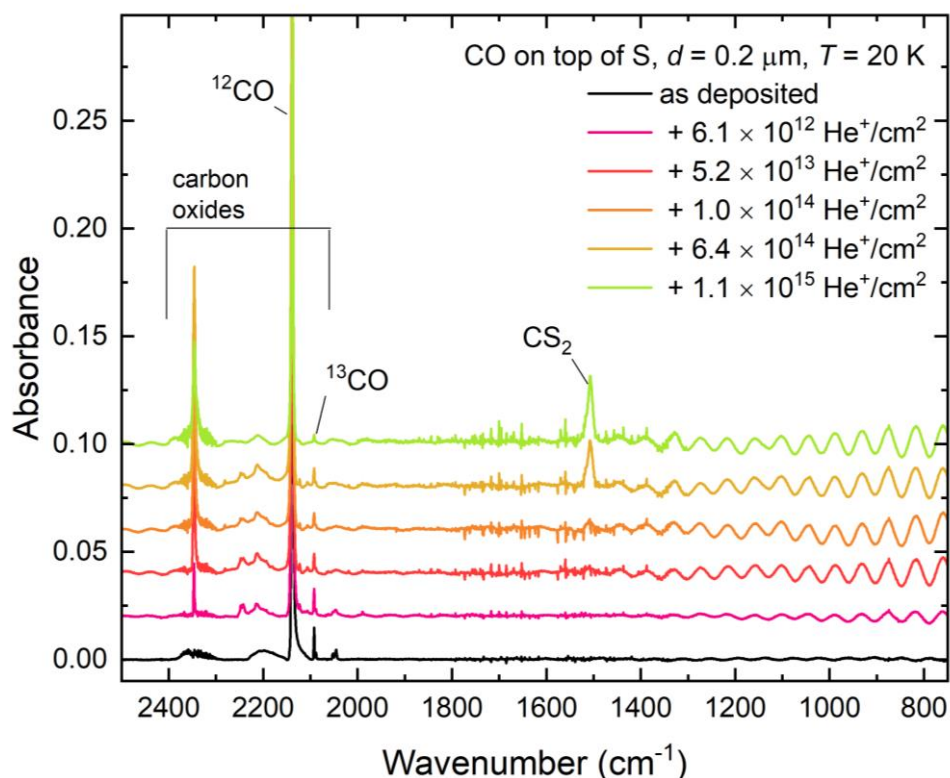


Fig. 8.5: Mid-infrared spectra of CO ice deposited on top of a layer of elemental sulphur before and during its irradiation by 1 MeV He⁺ ions at 20 K. Note that spectra are vertically shifted for clarity. Sinusoidal patterns in the spectra are caused by interference of infrared light reflected in the substrate-ice-vacuum optical system.

Interestingly, no SO₂ was observed to form as a result of the irradiation of CO ice deposited on top of elemental sulphur (Fig. 8.5). Instead, the major product of irradiation was determined to be CS₂ due to the appearance of a single, strong absorption band at 1509 cm⁻¹ attributed to its ν₃ mode (Jiménez-Escobar *et al.* 2014). It should be noted that the exact wavenumber position of the CS₂ ν₃ mode has been known to vary somewhat depending on the composition of the molecular ice. For instance, Sivaraman (2016) measured its position to be 1511 cm⁻¹ in a mixed CS₂:CO₂ ice deposited at 85 K, while Ferrante *et al.* (2008) measured it to be 1524 cm⁻¹ for CS₂ produced as a result of the irradiation of a H₂S:CO mixed ice by 800 keV protons at 10 K. Moreover, no O₃ was noted to form as a result of the 1 MeV He⁺ ion irradiation of CO deposited on top of elemental sulphur, meaning that other sinks for oxygen atoms produced *via* the radiolytic dissociation of CO (such as, for example, the formation of CO₂) must have been more favourable.

The lack of any mid-infrared spectroscopic features attributable to O₃ in Fig. 8.5 contrasts strongly with its seemingly efficient formation as a result of the implantation of 400 keV S⁺ ions into CO at 20 K (Fig. 7.5). The discrepancy between these two results may be understood in terms of the availability of O₂ molecules in each ice: in the S⁺ ion implantation experiment, a CO ice having an initial thickness of 3 μm was deposited, while in the He⁺ ion irradiation experiment a significantly thinner CO ice having a thickness of just 0.2 μm was prepared. As such, a greater column density of O₂ could be produced and react with radiolytically derived oxygen atoms in the S⁺ ion implantation experiment than in the He⁺ ion irradiation experiment. Indeed, a large abundance of O₂ is a necessary prerequisite for O₃ formation *via* the irradiation of CO ice, due to the many known reactions which efficiently compete for oxygen atoms, such as the formation of CO₂, oxocarbon radicals, and cumulene dioxides (Trottier and Brooks 2004).

Finally, the non-detection of SO₂ after the He⁺ ion irradiation of CO ice on top of a layer of elemental sulphur at 20 K has important implications for its tentative but inconclusive detection after the implantation of S⁺ ions into condensed CO at the same temperature: the presence of a thick sulphur layer below the CO ice should have resulted in a greater availability of sulphur atoms during He⁺ ion irradiation compared to the number delivered during S⁺ ion implantation into a CO ice, and thus any resultant sulphur chemistry should have been more extensive in the former irradiation compared to the latter. However, He⁺ ion irradiation of CO ice deposited on top of a layer of sulphur does not result in the formation of any SO₂ (Fig. 8.5); rather, CS₂ is the dominant sulphur-bearing radiolysis product. Therefore, it is very likely that SO₂ would not form as a result of the implantation of reactive sulphur ions into CO ice and that the band at about 1335 cm⁻¹ in Fig. 7.5 that was tentatively assigned to SO₂ is really caused by the formation of another unidentified species. By extension, it is also possible that the detection of SO₂ by Lv *et al.* (2014a) in their experiments on the implantation of sulphur ions into CO ice at 15 K may be incorrect; indeed, such a misidentification would explain the similarity in the intensity of the bands that they attributed to the asymmetric and symmetric stretching modes of SO₂ (Fig. 7.6), which has not been observed in either the pure SO₂ ices or any ice mixture involving SO₂ studied throughout this thesis.

8.3.3 CH₃OH Ice on Top of Sulphur at 25 K

The 1 MeV He⁺ ion irradiation of CH₃OH ice represents the only energetic processing of a complex organic oxygen-bearing ice deposited on top of a layer of elemental sulphur that was considered in this study. The mid-infrared spectrum of CH₃OH ice deposited on top of sulphur at 25 K is practically identical to that of the amorphous ice deposited on a ZnSe substrate at 20 K as shown in Fig. 6.4. After being processed by 1 MeV He⁺ ions, a number of new absorption bands were evident in the acquired mid-infrared spectra (Fig. 8.6). Many of these bands are attributed to molecules formed as a direct result of the radiolytic decomposition of CH₃OH and were also observed after the irradiation of pure CH₃OH by proton beams of various energies (Chapter 4) and 2 keV electrons (Chapter 6). Among these molecules were CO and CO₂ (as well as their isotopologues ¹³CO and ¹³CO₂), whose absorption bands were respectively detected at 2136 and 2344 cm⁻¹ (¹³C isotopologues: 2098 and 2274 cm⁻¹). The formation of CH₄ was also confirmed due to the appearance of its ν₄ mode at 1302 cm⁻¹. Interestingly, the abundances of these species peaked in the ice after a He⁺ ion fluence of about 6×10¹⁴ ions cm⁻² was delivered, and thereafter began to decrease as a result of their own radiolytic decomposition (Fig. 8.6).

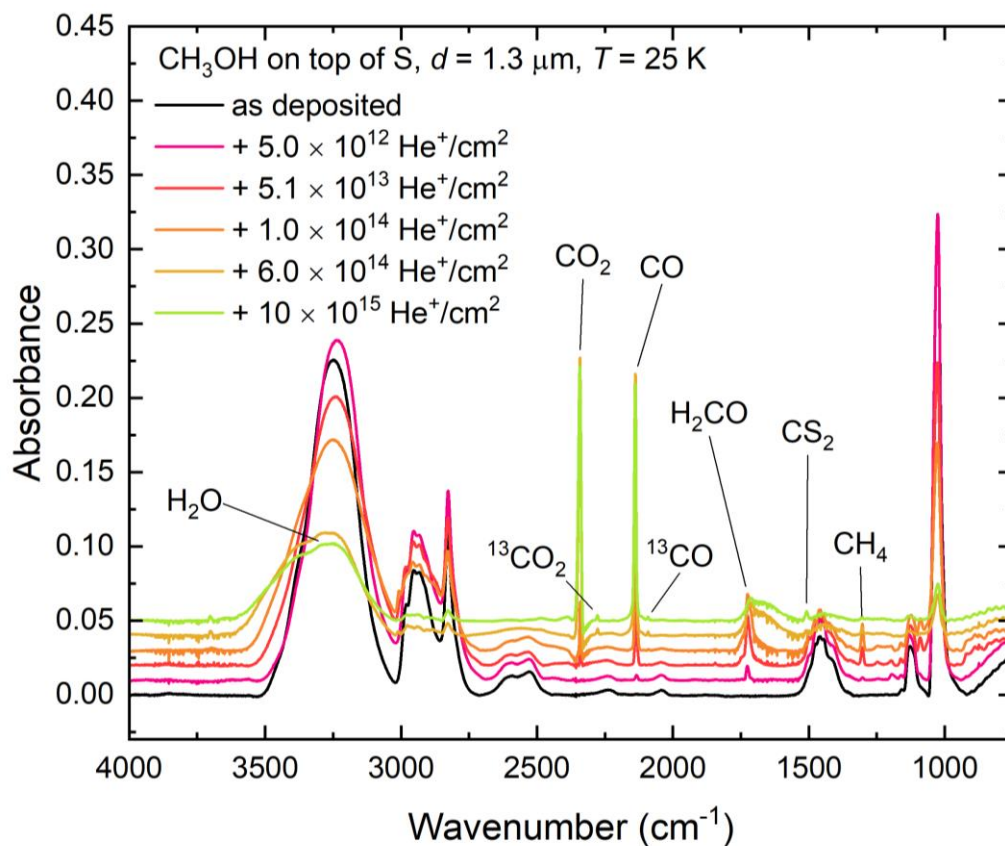


Fig. 8.6: Mid-infrared spectra of CH₃OH ice deposited on top of a layer of elemental sulphur before and during its irradiation by 1 MeV He⁺ ions at 25 K. Note that spectra are vertically shifted for clarity.

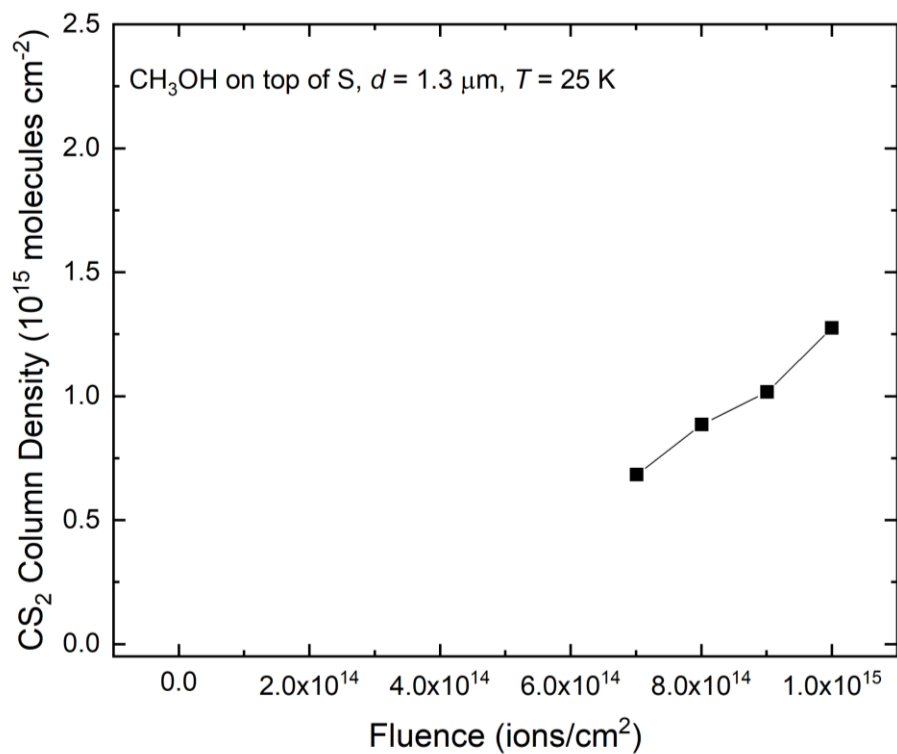


Fig. 8.7: Column density evolution of CS₂ formed as a result of the irradiation of CH₃OH ice on top of a layer of elemental sulphur using 1 MeV He⁺ ions. Note that the column density was calculated through measurement of the CS₂ asymmetric stretching mode at 1509 cm⁻¹ using an integrated band strength constant of $9.1 \times 10^{-17} \text{ cm molecule}^{-1}$ (Pugh and Rao 1976).

During the course of the irradiation experiment, it was noted that not only did the CH₃OH stretching mode band decrease in its absorbance (commensurate with its radiolytic decay), but it was also observed to broaden and the band peak also blue-shifted from 3237 to 3255 cm⁻¹. Additionally, a higher wavenumber shoulder to this peak attributable to the stretching modes of H₂O was observed to develop at 3388 cm⁻¹ (Hagen *et al.* 1981). This shoulder was first apparent after a He⁺ ion fluence of 10¹⁴ ions cm⁻² and continued to grow thereafter, highlighting the favourable formation of H₂O as a result of the radiolytic decomposition of CH₃OH. The detection of H₂O in the irradiated ice was confirmed by the observation of its broad ν_2 mode at 1671 cm⁻¹ (Hagen *et al.* 1981).

The radiolytic decay of CH₃OH also led to the formation of H₂CO, which was detected *via* the observation of its ν_2 mode at 1725 cm⁻¹ (Bouilloud *et al.* 2015). The formation of H₂CO occurred fairly early on during the irradiation process as a result of the double dehydrogenation of CH₃OH (Hiroshi *et al.* 1968), with the strong ν_2 mode being evident in the acquired mid-infrared spectra at a delivered He⁺ ion fluence of just 5×10¹² ions cm⁻² (Fig. 8.6). The band area of the H₂CO ν_2 mode in the irradiated ice continued to grow until a fluence of 10¹⁴ ions cm⁻², after which it began to subside. The decline of the H₂CO mid-infrared absorption band is coincident with the increase in the area of the H₂O ν_2 mode in the same spectral region (Fig. 8.6), pointing to a possibly related radiation chemistry. This agrees well with the results of López-Islas *et al.* (2019), who successfully demonstrated that the reaction between H₂CO and OH radicals (which may have been sourced from the direct radiolysis of CH₃OH in the present experiment) efficiently yields H₂O.

Despite the fact that CH₃OH is classified as a complex organic molecule, and that three different atoms (hydrogen, carbon, and oxygen) were available to partake in radiation-driven reactions with the underlying sulphur layer, the sulphur chemistry resulting from the 1 MeV He⁺ ion irradiation of the system was found to be somewhat limited. Indeed, the only sulphur-bearing product molecule detected in the acquired mid-infrared spectra was CS₂ (Fig. 8.6), whose formation was deduced as a result of the appearance of its ν_3 mode at 1509 cm⁻¹. No spectroscopic evidence was found for the formation of any other volatile sulphur-bearing molecules, such as H₂S, SO₂, or OCS. By taking the integrated band strength constant for the CS₂ band at 1509 cm⁻¹ to be 9.1×10⁻¹⁷ cm molecule⁻¹ (Pugh and Rao 1976), the column density evolution of this molecule as a function of projectile He⁺ ion fluence could be plotted (Fig. 8.7). CS₂ was only detected after a fluence of 7×10¹⁴ ions cm⁻² was delivered, but the measured column density continued to increase until the end of the irradiation process. It is possible to speculate that sulphur chemistry would have become more prevalent at higher projectile ion fluences, at which point most of the larger molecules and radicals within the ice would have likely been broken down into smaller fragments (or possibly to single atoms) with which the sulphur atoms produced in the underlying layer may have reacted efficiently to yield new sulphur-bearing species.

8.3.4 CO₂ Ice on Top of Sulphur at 20 and 70 K

The 1 MeV He⁺ ion irradiation of CO₂ ice deposited on top of a layer of elemental sulphur was investigated at two temperatures (20 and 70 K) so as to complement the previous study investigating the chemistry arising from the implantation of 400 keV S⁺ ions into solid CO₂ at these temperatures (Chapter 7). At 20 K, the irradiation process resulted in the formation of a number of new product molecules, including two that contained sulphur atoms. Aside from CO₂ itself, the most prominent mid-infrared absorption bands in the acquired spectra

were caused by the products formed as a result of the radiolysis of CO₂ (Sivaraman *et al.* 2013, Martín-Doménech *et al.* 2015); namely CO, CO₃, and O₃ (Fig. 8.8). Moreover, mid-infrared absorption features attributable to SO₂ and CS₂ were also detected.

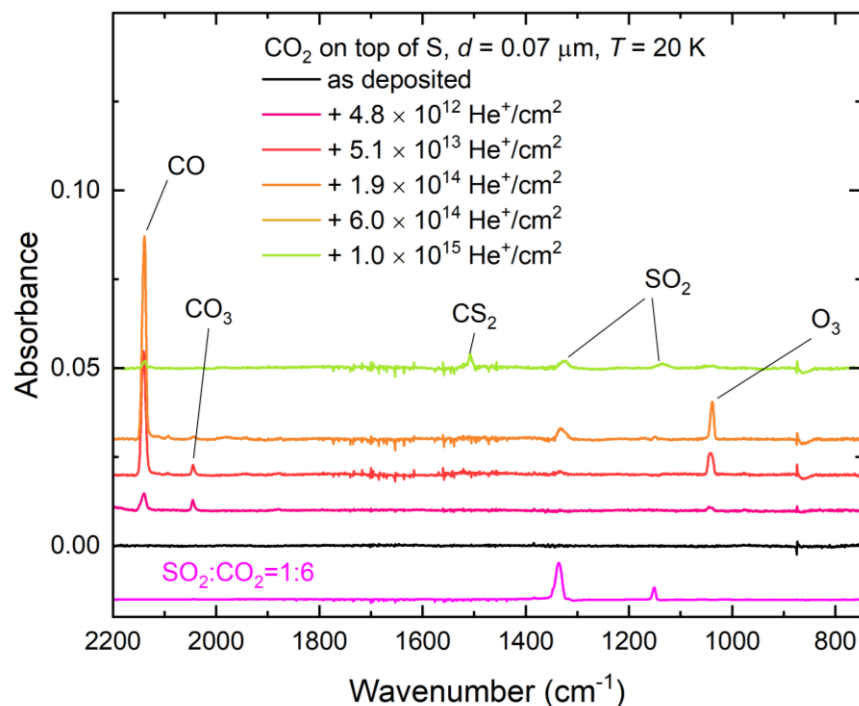


Fig. 8.8: Mid-infrared spectra of CO₂ ice deposited on top of a layer of elemental sulphur before and during its irradiation by 1 MeV He⁺ ions at 20 K. Included in the figure is the spectrum of an unirradiated CO₂:SO₂ (6:1) ice for comparative purposes. Note that spectra are vertically shifted for clarity.

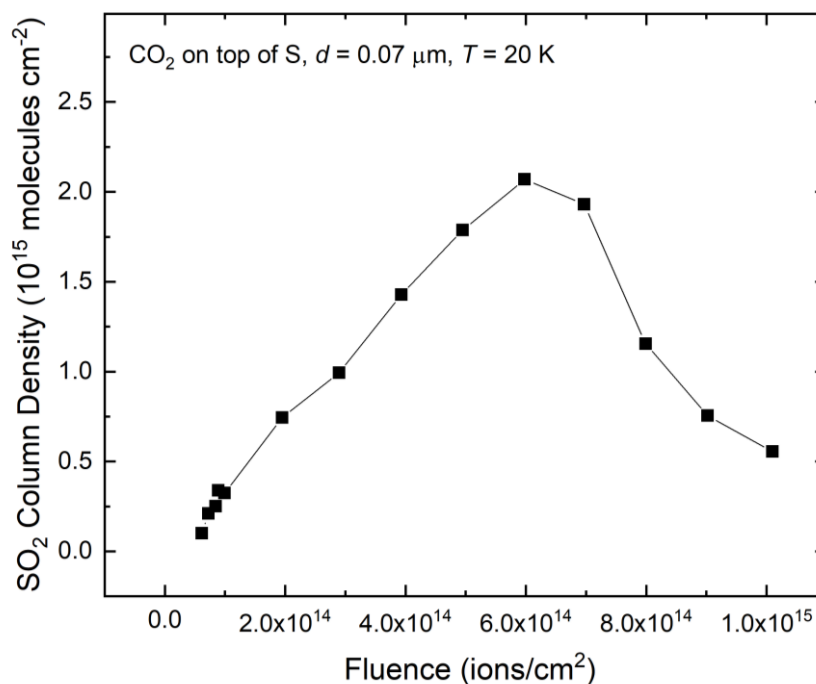


Fig. 8.9: Column density evolution of SO₂ formed as a result of the irradiation of CO₂ ice on top of a layer of elemental sulphur using 1 MeV He⁺ ions at 20 K. Note that the column density was calculated through measurement of the asymmetric stretching mode at 1327 cm⁻¹ using an integrated band strength constant of 1.47 × 10⁻¹⁷ cm molecule⁻¹ (Garozzo *et al.* 2008).

It is possible to note that, under prolonged irradiation beyond a delivered He^+ ion fluence of around 6×10^{14} ions cm^{-2} , the abundances of all the product molecules in the irradiated ice begin to decrease, as inferred from the decreasing absorbances of their mid-infrared absorption bands (Fig. 8.8). Specifically examining the column density evolution of the sulphur-bearing product species as a function of fluence, it was found that the column density of SO_2 steadily increased until a He^+ ion fluence of 6×10^{14} ions cm^{-2} , after which point it began to decrease (Fig. 8.9). A similar column density evolution analysis initially could not be performed for CS_2 , due to the presence of a number of fine structures coincident with its absorption band in the mid-infrared absorption spectrum that would have introduced very large uncertainties in the measurement of the CS_2 band area (Fig. 8.8). These fine structures are the result of absorption by gas-phase H_2O in the pathlength leading up to the external MCT detector, which is not maintained under vacuum.

The reason for the apparent decrease in the abundance of product molecules upon prolonged irradiation by He^+ ions is not immediately clear. It is possible to speculate that continued irradiation resulted in the formation of carbon-sulphur polymers that did not present notable absorptions in the mid-infrared spectral range. Indeed, previous research has documented the efficient formation of complex polymeric structures after the irradiation of CS_2 which present very weak or difficult to observe absorptions in the mid-infrared spectral range (Cataldo 1995, Cataldo and Heymann 2001). It is therefore possible that such polymerisation processes took place in the present experiment at higher projectile ion fluences, and that the formation of the resultant carbon- and sulphur-rich polymers consumed many of the volatile molecular species observed in the mid-infrared spectra (Fig. 8.8).

The features of the mid-infrared spectra collected during the 1 MeV He^+ ion irradiation of CO_2 on top of sulphur at 20 K contrast strongly with those of the analogous experiment conducted at 70 K (Fig. 8.10). Perhaps the most evident difference is that, at this higher temperature, the irradiation of the ice results in a higher abundance of the sulphur-bearing products SO_2 and CS_2 , whose column densities continued to grow throughout the irradiation process (Figs. 8.11 and 8.12). Comparing the spectra shown in Figs. 8.8 and 8.10, it is possible to note that the higher temperature irradiation also resulted in lower yields of CO , CO_3 , and O_3 . It is therefore possible to conclude that the sustained formation of sulphur-bearing products as a result of the irradiation of CO_2 on top of a sulphur layer is more efficient at higher temperatures.

This trend is opposite to that observed during the implantation of 400 keV S^+ ions into CO_2 ice (Chapter 7), wherein SO_2 formation was recorded at 20 K but not at 70 K. In that experiment, SO_2 was the only sulphur-bearing product observed and was suggested to have formed as a result of the reaction of the neutralised sulphur ion with atomic oxygen produced by the decomposition of CO_2 to sequentially yield SO and SO_2 (Rolfes *et al.* 1965, Tevault and Smardzewski 1978, Herron and Huie 1980). At 70 K, however, it was proposed that much of the oxygen content of the ice would have been diminished due to the combination of oxygen atoms to yield O_2 , which would have then efficiently sublimated from the ice. This reduced oxygen content would have precluded the efficient formation of SO_2 at 70 K.

Clearly, however, this mechanistic chemistry does not explain the observed formation of both CS_2 and SO_2 as a result of the He^+ ion irradiation of CO_2 ice on top of sulphur and their greater formation efficiencies at 70 K compared to 20 K (Figs. 8.8-8.12). Given that the initial abundances of both CO_2 and elemental sulphur were similar in both the 20 K and the 70 K experiments, the difference in the results between these two experiments must be caused by different reaction pathways being favoured at these two temperatures. It is known

that radicals are increasingly mobile within solid matrices as temperatures are raised (e.g., Kusumoto *et al.* 2019), and thus it is likely that sulphur atoms produced by the dissociation of the deposited allotropic sulphur can move throughout the ice matrix to a much greater extent at 70 K than at 20 K. Indeed, the increased mobility of sulphur atoms in an ice matrix at higher temperatures has already been demonstrated (Khriachtchev *et al.* 1999, Kiljunen *et al.* 2000). The comparatively high concentration of sulphur atoms intermixed with CO₂ ice promotes the direct reaction between these species to yield SO and CO, as was previously described by Froese and Goddard (1993). Being an inherently unstable species, SO rapidly oxidises to yield SO₂ (Rolfes *et al.* 1965, Tevault and Smardzewski 1978, Herron and Huie 1980).

The reaction between atomic sulphur and CO₂ would contribute to the abundance of CO within the ice (Froese and Goddard 1993), and thus it would be intuitive to assume that the CO abundance in the 70 K irradiation experiment would be greater than that in the 20 K experiment. This is not observed (Fig. 8.10); instead, CO is consumed *via* the reaction with sulphur atoms to produce OCS (Hawkins *et al.* 1985, Ferrante *et al.* 2008), which was detected through its broad absorption band centred at 2031 cm⁻¹. The position of this band is in relatively good agreement with that reported by Sivaraman (2016), who measured its position at 2035 cm⁻¹ after the irradiation of a CO₂:CS₂ mixed ice at 85 K. Moreover, the FWHM of the OCS band observed in Fig. 8.10 has a value of 11 cm⁻¹, which is good agreement with that reported by Ferrante *et al.* (2008) who measured it as being 15 cm⁻¹ at 70 K. It should be recalled that defining the FWHM value of the OCS absorption band is key to discriminating it from the CO₃ band, which is located at 2045 cm⁻¹ (Fig. 8.10) and has a narrower FWHM of 4 cm⁻¹.

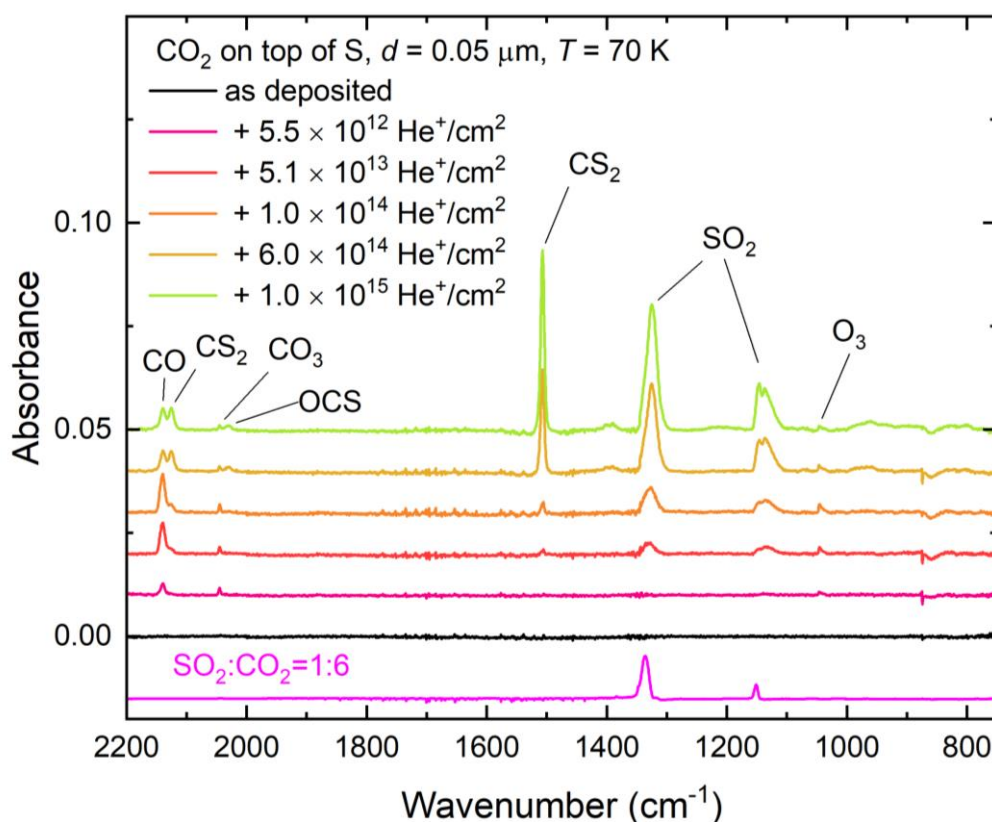


Fig. 8.10: Mid-infrared spectra of CO₂ ice deposited on top of a layer of elemental sulphur before and during its irradiation by 1 MeV He⁺ ions at 70 K. Included in the figure is the spectrum of an unirradiated CO₂:SO₂ (6:1) ice for comparative purposes. Note that spectra are vertically shifted for clarity.

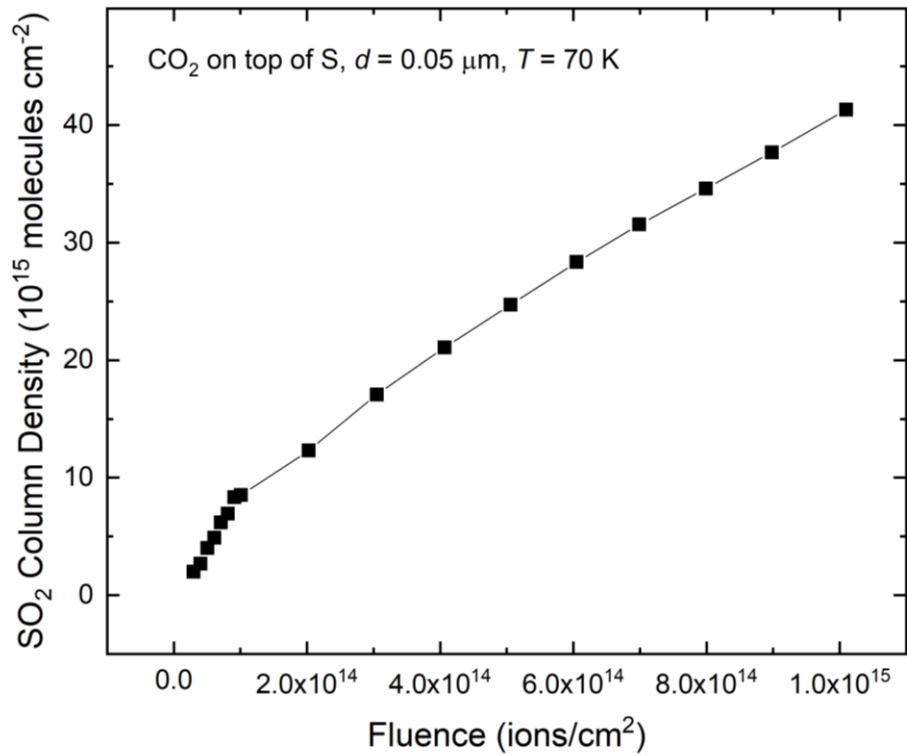


Fig. 8.11: Column density evolution of SO₂ formed as a result of the irradiation of CO₂ ice on top of a layer of elemental sulphur using 1 MeV He⁺ ions at 70 K. Note that the column density was calculated through measurement of the asymmetric stretching mode at 1327 cm⁻¹ using an integrated band strength constant of $1.47 \times 10^{-17} \text{ cm molecule}^{-1}$ (Garozzo *et al.* 2008).

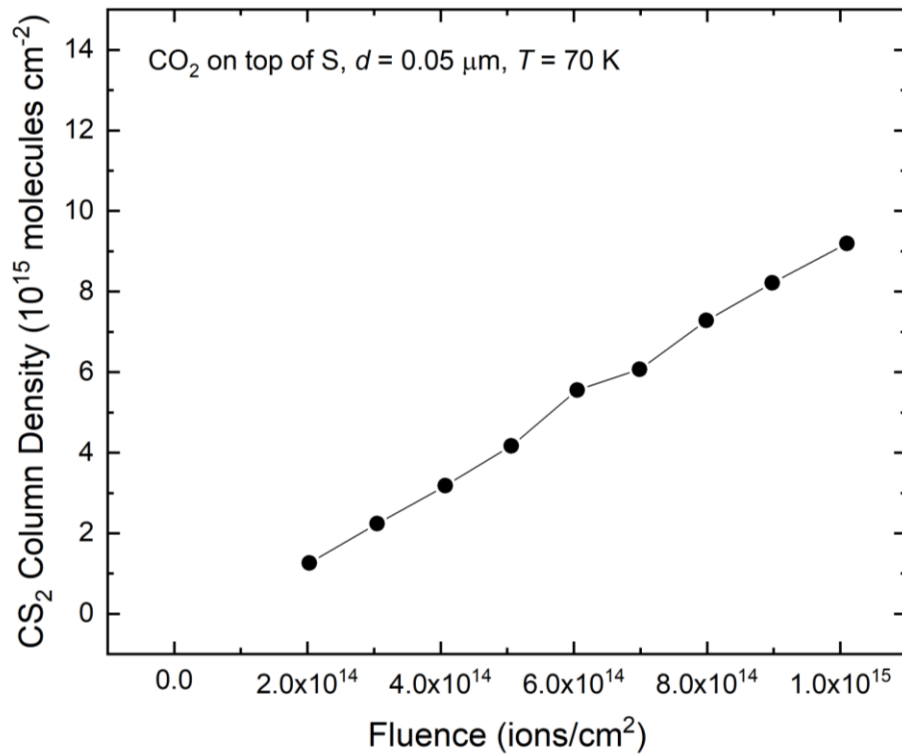


Fig. 8.12: Column density evolution of CS₂ formed as a result of the irradiation of CO₂ ice on top of a layer of elemental sulphur using 1 MeV He⁺ ions at 70 K. Note that the column density was calculated through measurement of the asymmetric stretching mode at 1507 cm⁻¹ using an integrated band strength constant of $9.1 \times 10^{-17} \text{ cm molecule}^{-1}$ (Pugh and Rao 1976).

However, as was demonstrated by Ferrante *et al.* (2008), OCS is not particularly stable when subjected to ionising radiation and therefore does not accumulate within the ice as inferred by its small absorption band (Fig. 8.10). A number of reaction routes are available for OCS in the ice, including the reaction with atomic oxygen to yield CO and SO (Jones and Taube 1973, Hsu *et al.* 1979, Chen *et al.* 1995), thus further contributing to the net SO₂ content of the ice *via* the subsequent oxidation of SO. Another possible reaction is that between OCS and sulphur atoms, for which two possible outcomes exist, both likely proceeding through a OCS₂ intermediate (Lo *et al.* 2004). The first process involves the dissociation of the intermediate to yield CO and S₂ (van Veen *et al.* 1983). Although S₂ is a volatile species (Moore *et al.* 1988), and thus represents one outcome of the volatilisation of the deposited sulphur layer, its formation could not be determined through mid-infrared spectroscopy due to it being a homonuclear diatomic molecule and thus lacking a dipole moment.

The second process also involves the dissociation of the OCS₂ intermediate, but yields an oxygen atom and CS₂ instead (Ferrante *et al.* 2008). Indeed, CS₂ was detected *via* the appearance of both its ν_3 mode at 1507 cm⁻¹ as well as its $\nu_1 + \nu_3$ combination band at 2125 cm⁻¹. It should be noted that, like the ν_3 mode, the wavenumber position of the CS₂ $\nu_1 + \nu_3$ combination band has also been reported to vary significantly depending on the chemical composition of the ice. For instance, studies of neat solid CS₂ by Maity *et al.* (2013) and Methikkalam *et al.* (2016) allowed them to identify this band at 2158 and 2145 cm⁻¹, respectively. Bahou *et al.* (2000) detected this band at 2177 cm⁻¹ in matrix isolation experiments using N₂ and argon, whilst Maity and Kaiser (2013) detected it at 2158 cm⁻¹ in their studies of CS₂:O₂ ice mixtures. The lower abundance of CS₂ accumulated within the ice compared to SO₂ is consistent with the proposed reaction scheme described above and summarised in Fig. 8.13, due to the greater number of shorter (i.e., involving fewer steps) chemical routes leading to the latter species.

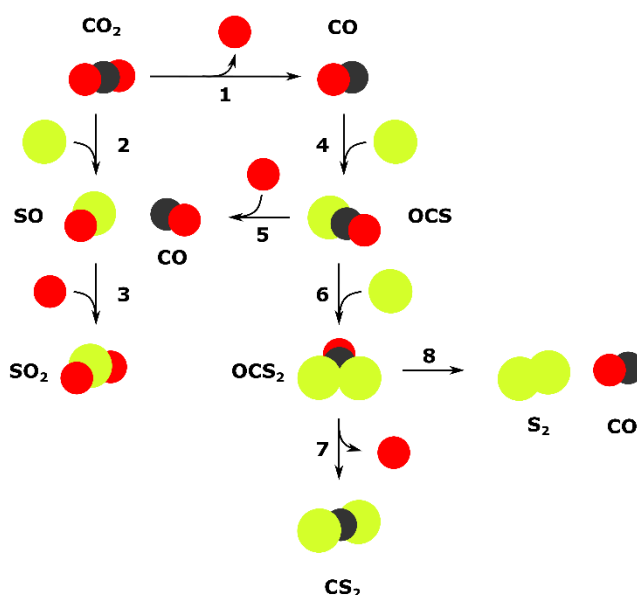


Fig. 8.13: The major reactions suggested to be taking place within the CO₂ ice on top of elemental sulphur irradiated by 1 MeV He⁺ ions at 70 K. In this scheme, CO₂ may undergo radiolytic dissociation to yield CO and an oxygen atom (1), or may alternatively react with a sulphur atom that has migrated from the underlying layer to produce CO and SO (2), the latter species subsequently being rapidly oxidised to SO₂ (3). Sulphur atom addition to CO results in the direct production of OCS (4) which, when reacted with an oxygen atom yields SO and CO (5). The addition of another sulphur atom to OCS yields the unstable intermediate OCS₂ (6), which decays to either CS₂ and an oxygen atom (7), or alternatively to S₂ and CO (8).

The increased migration of a large quantity of sulphur atoms within the solid CO₂ ice at 70 K induces a plethora of new reaction channels (Fig. 8.13) that were not available in the CO₂ ice into which a smaller number of sulphur ions had been implanted. These additional reactions include some that compete for the supra-thermal oxygen atoms yielded after the dissociation of the parent CO₂ molecule, thus rendering the formation of CO₃ and O₃ *via* oxygen atom addition reactions less efficient, consistent with the smaller absorption bands of these product molecules observed during the 70 K irradiation experiment (Fig. 8.10) compared to that conducted at 20 K (Fig. 8.8). The increased competition for oxygen atoms within the solid ice thus also reduces the likelihood of two oxygen atoms combining to produce O₂ (a preliminary step in the formation of O₃), which would efficiently sublime from the ice. This therefore significantly diminishes the depletion of oxygen within the ice compared to what was observed to occur after sulphur ion implantation, and thus helps explain the opposite trends reported with regards to the temperature dependence of the formation of sulphur-bearing products in the sulphur ion implantation processes described in Chapter 7 and the layered sulphur-ice experiments described in this chapter.

8.3.5 H₂O Ice on Top of Sulphur at 20 and 70 K

Previous works considering the radiation chemistry of elemental sulphur have been few and far between, and have typically only considered systems also involving H₂O. Early studies by Donaldson and Johnston (1968) and Donaldson and Johnston (1971) investigated the irradiation of colloidal suspensions of elemental sulphur in deaerated H₂O, and found evidence for the solubilisation of the sulphur and the subsequent formation of H₂SO₄. The mechanism by which this chemistry occurs was described by Della Guardia and Johnston (1980), who highlighted the important role played by OH radicals and H₂SO₂; a lower oxoacid of sulphur. The astrochemical importance of H₂SO₂ was expounded upon more recently by Góbi *et al.* (2021), who demonstrated its formation as a result of photochemical hydrogen addition to solid SO₂ at 3.1 K.

The first work to consider the irradiation of H₂O:S₈ mixtures in astrophysical ice analogues was conducted by Carlson *et al.* (2002), who investigated the chemical evolution of S₈ that was mixed with liquid H₂O and subsequently frozen prior to irradiation. Their work demonstrated that not only is H₂SO₄ efficiently formed by solid phase radiation chemistry, but that this synthesis is in fact more efficient at temperatures relevant to the surface of Europa than at higher temperatures. The only other study that has considered the radiation chemistry of a sulphur residue in an astrophysical ice analogue is that of Gomis and Strazzulla (2008) who, as discussed above, prepared a refractory sulphurous residue by irradiating SO₂ ice at 16 K using either 200 keV He⁺ ions or 200 keV Ar⁺ ions and subsequently warming it to room temperature. The remaining refractory sulphurous layer was then re-cooled to 80 K and a layer of H₂O ice was deposited on top of it, before being irradiated by 200 keV He⁺ ions. Irradiation resulted in the appearance of a very weak mid-infrared absorption band at around 1325 cm⁻¹ which could not be unambiguously identified. However, such a band does approximately coincide with the ν_3 mode of SO₂, thus tentatively suggesting its radiolytic formation (Gomis and Strazzulla 2008).

Despite providing an extensive characterisation of the formation of H₂SO₄ as a result of the irradiation of elemental sulphur mixed or layered with H₂O ice, the abovementioned studies have yet to provide any clear and unambiguous evidence for the formation of SO₂. As such, a systematic investigation of the irradiation of H₂O ice deposited on top of a layer of pure elemental sulphur is warranted. Extending the methodology used throughout this

chapter to prepare sulphur layers *via* the effusive evaporation of pure, solid sulphur to the study of the radiation chemistry occurring in a H₂O ice deposited on top of the sulphur layer presents at least two advantages over the method employed by Gomis and Strazzulla (2008). Firstly, it allows for a thicker sulphur layer to be readily prepared, thus increasing the number of sulphur atoms that may partake in the formation of sulphur-bearing product molecules. Secondly, it ensures that the resultant layer is purely composed of sulphur: this differs to the refractory residue produced by Gomis and Strazzulla (2008) which was more likely formed of polymers or oligomers composed of both sulphur and oxygen.

The mid-infrared spectra collected before and during the irradiation of H₂O ice on top of a layer of elemental sulphur by 1 MeV He⁺ ions at 20 K are shown in Fig. 8.14. It is possible to note that the irradiation does not result in many noticeable changes to the appearance of the spectra, other than the emergence of a weak but broad absorption band centred at 2863 cm⁻¹ which has been attributed to the formation of H₂O₂ (Giguère and Harvey 1959, Moore and Hudson 2000, Loeffler and Hudson 2015). Furthermore, two small absorption bands at 3696 and 3721 cm⁻¹ apparent in the mid-infrared spectrum of the H₂O ice upon its preparation at 20 K were observed to disappear very rapidly during irradiation. These bands were attributed to the hydroxyl dangling bonds that exist in microporous H₂O ices at low temperatures, and their disappearance was the result of the rapid compaction of the ice under the influence of ionising radiation (Baragiola 2003, Palumbo 2006, Boduch *et al.* 2015).

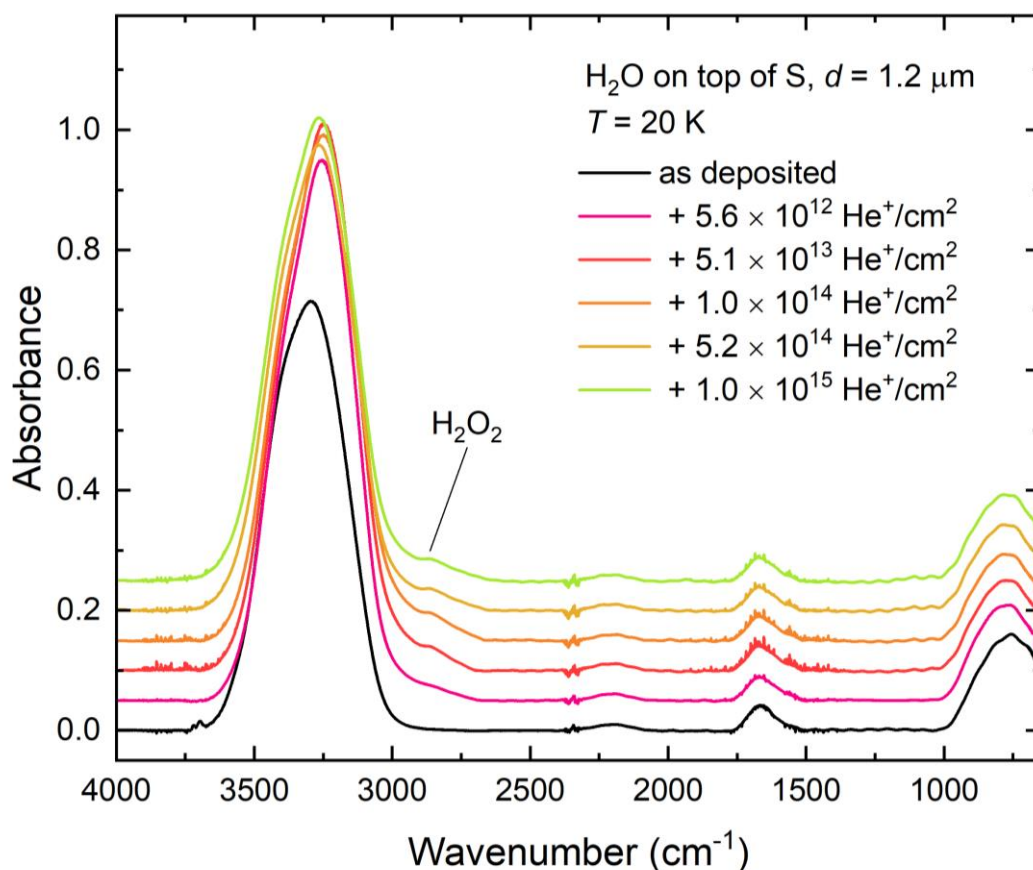


Fig. 8.14: Mid-infrared spectra of H₂O ice deposited on top of a layer of elemental sulphur before and during its irradiation by 1 MeV He⁺ ions at 20 K. Note that spectra are vertically shifted for clarity.

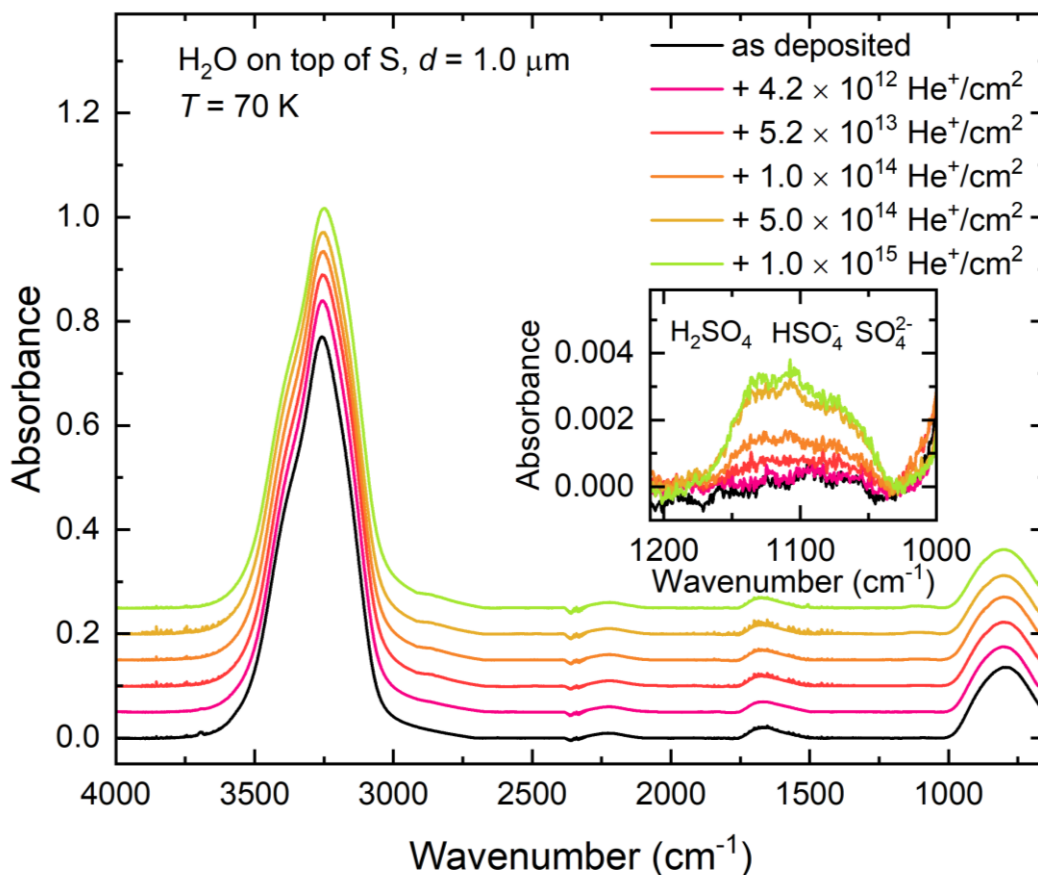


Fig. 8.15: Mid-infrared spectra of H₂O ice deposited on top of a layer of elemental sulphur before and during its irradiation by 1 MeV He⁺ ions at 70 K. Note that spectra are vertically shifted for clarity.

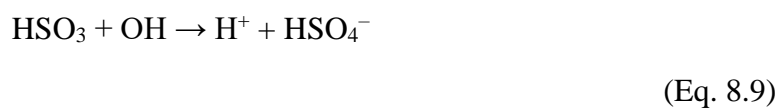
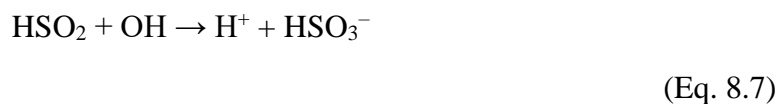
Of particular interest is the non-detection of mid-infrared bands attributable to any sulphur-bearing product species, including H₂SO₄ or any of its hydrates. Comparing this result to those previously published in the literature is not a straightforward task, as many experiments investigating sulphur ice astrochemistry have been aimed at characterising the surface chemistry of the icy Galilean satellites and have thus been performed at significantly higher temperatures. For instance, the sulphur ion implantations into H₂O ice performed by Strazzulla *et al.* (2007) and Ding *et al.* (2013) were conducted at 80 K, whilst the work of Carlson *et al.* (2002) on the irradiation of H₂O:S₈ ice mixtures was carried out at 77 K. Moore *et al.* (2007) performed their work on the irradiation of SO₂:H₂O ice mixtures at 86 K and also at higher temperatures.

Indeed, perhaps the only work that was carried out at a comparable temperature to that of the present experiment is that of Kaňuchová *et al.* (2017), who investigated the 30 keV He⁺ ion irradiation of a mixed SO₂:H₂O (2:1) ice at 16 K. Their work demonstrated that such energetic processing conditions are amenable to the formation of H₂SO₄ monohydrate and tetrahydrate as inferred from infrared absorption bands located at 1105 and 1070 cm⁻¹ respectively attributable to the HSO₄⁻ and SO₄²⁻ ions, as well as the broad H₃O⁺ band centred at approximately 1730 cm⁻¹ (Kaňuchová *et al.* 2017). This result contrasts strongly with that presented in Fig. 8.14, where no such mid-infrared absorption bands can be discerned. The reason for this difference may, however, be fairly mundane: it is possible that the sulphur chemistry occurring in the experiment of Kaňuchová *et al.* (2017) occurred to a greater extent than that of the present study due to the more homogeneous mixing of the SO₂ and H₂O thus allowing sulphur product formation to occur throughout their ice. Conversely, in

the present experiment, such chemistry could only occur at the interface of the H₂O ice and the elemental sulphur layer, thus reducing the abundance of sulphur-bearing products that could be produced.

The 1 MeV He⁺ ion irradiation of H₂O ice on top of a layer of elemental sulphur was also performed at 70 K. In this case, spectroscopic evidence for the formation of H₂SO₄, as well as its monohydrate and tetrahydrate forms (Fig. 8.15), was observed through the appearance of mid-infrared absorption bands at 1139, 1107, and 1060 cm⁻¹ respectively attributable to H₂SO₄, HSO₄⁻ (monohydrate), and SO₄²⁻ (tetrahydrate) (Loeffler *et al.* 2011, Kaňuchová *et al.* 2017). This result is in agreement with those reported by several other previous studies performed at similar temperatures, such as those by Carlson *et al.* (2002), Moore *et al.* (2007), Strazzulla *et al.* (2007), and Ding *et al.* (2013); who all reported the formation of H₂SO₄ acid hydrates.

The formation of H₂SO₄ as a result of the 1 MeV He⁺ ion irradiation of H₂O ice on top of elemental sulphur at 70 K, but not at 20 K, may simply be due to the higher diffusivities of sulphur moieties at this higher temperature, thus allowing for a higher degree of mixing and extending the relevant radiation chemistry to further beyond the ice-sulphur interface. A similar argument was invoked to explain the greater extent of sulphur chemistry observed after the irradiation of CO₂ ice on top of sulphur using 1 MeV He⁺ ions at 70 K compared to the analogous irradiation at 20 K (sub-section 8.3.4). Indeed, following from the previous work of Della Guardia and Johnston (1980), it is possible to propose a reaction scheme by which H₂SO₄ forms in the present experiment after the mobilisation of sulphur atoms from the underlying layer into the H₂O ice:



Once HSO₄⁻ has been formed in the ice, the reaction sequence diverges depending on whether the final radiation product is H₂SO₄, the monohydrate form, or the tetrahydrate form. In the case of H₂SO₄, the H⁺ and HSO₄⁻ ions simply undergo combination, while the monohydrate is formed *via* the combination of the H⁺ ion with a neutral H₂O molecule.

Finally, the tetrahydrate is produced in a two-step process in which the HSO_4^- first dissociates to H^+ and SO_4^{2-} , after which two H^+ ions combine with two neutral H_2O molecules to yield two H_3O^+ ions which are associated with the SO_4^{2-} anion together with another two neutral H_2O molecules.

Finally, it should be noted that neither the 20 K irradiation experiment nor the 70 K experiment considered here resulted in the formation of SO_2 or H_2S . This is in agreement with previous literature concerned with the implantation of reactive sulphur ions into H_2O ice (Strazzulla *et al.* 2007, Strazzulla *et al.* 2009, Ding *et al.* 2013) and with the irradiation of elemental sulphur mixed or layered with H_2O in either the aqueous or solid phases (Donaldson and Johnston 1968, Donaldson and Johnston 1971, Della Guardia and Johnston 1980, Carlson *et al.* 2002, Gomis and Strazzulla 2008). Indeed, combined with the results presented in this chapter, it is perhaps possible to state that the only sulphur chemistry of note to occur in irradiated H_2O ices containing some sulphurous species is the formation of H_2SO_4 hydrates. Although this statement may admittedly be viewed as somewhat hyperbolic, it is consistent with the overabundance of H_2SO_4 hydrates (compared to other sulphur-bearing species) on the surface of Europa, which is dominated by H_2O ice (Carlson *et al.* 2002). However, the production of SO_2 may occur as a result of the irradiation of H_2SO_4 itself, as has been shown in both the aqueous (Hochanadel *et al.* 1955) and solid (Loeffler *et al.* 2011, Loeffler and Hudson 2012) phases.

8.4 Astrochemical Implications

The results presented in this chapter carry significant implications for the astrochemistry of sulphur. It should be recalled that the dense ISM is characterised by an unexpected paucity of sulphur, where observed abundances of molecular sulphur in both the solid and gas phases are depleted (compared to their expected cosmic abundances) by two to three orders of magnitude (Tieftrunk *et al.* 1994, Ruffle *et al.* 1999). It has been proposed that this sulphur depletion phenomenon is at least partly caused by the Coulomb-enhanced freeze-out of S^+ ions onto negatively charged dust grains as diffuse clouds evolve into translucent ones, whereafter the ions are neutralised to atoms. The subsequent fate of the accreted atoms is not known for certain, although some models have suggested that they may be rapidly hydrogenated to H_2S on the surface of the dust grain (Caselli *et al.* 1994, Vidal *et al.* 2017).

However, the lack of a detection of solid H_2S is at odds with the results of these models (Boogert *et al.* 2015). More recent experimental and modelling efforts have alternatively proposed that allotropes of elemental sulphur composed of chains and rings of various geometries and molecular weights could form after the freeze-out of the S^+ ions, and should indeed constitute a major reservoir of the unobserved sulphur on the surfaces of interstellar dust grains (Anderson *et al.* 2013, Shingledecker *et al.* 2020, Cazaux *et al.* 2022). Such results provide a good motivation for understanding the chemistry of elemental sulphur allotropes under conditions relevant to the dense ISM, particularly with regards to the possible chemical transformations of elemental sulphur to the molecular forms of sulphur known to exist in interstellar icy grain mantles, namely SO_2 and OCS (Boogert *et al.* 1997, Palumbo *et al.* 1997). Such chemical transformations would largely occur at the interface of the surface of the dust grain with the polar ice layer (Fig. 2.7), where the abundances of elemental sulphur and sulphur-bearing residues would be highest. As such, the icy species of greatest importance are likely to be H_2O (the most abundant species in interstellar icy

grain mantles), along with smaller quantities of simple diatomic species (such as, for example, O₂) and CO₂ (Boogert *et al.* 2015, Öberg 2016).

The results obtained from the 1 MeV He⁺ ion irradiations of H₂O, CO₂, and O₂ ices on top of elemental sulphur at 20 K should therefore be discussed in the context of the potential roles of these processes in contributing to solid-phase interstellar sulphur chemistry. Perhaps the most relevant result is the non-detection of any sulphur-bearing radiolysis product after the irradiation of H₂O ice on top of sulphur at 20 K. Given that H₂O is the dominant species in interstellar icy grain mantles (Boogert *et al.* 2015, Öberg 2016), this result implies that the contribution to the presence of SO₂ within interstellar ices from the radiolytic conversion of elemental sulphur present at the surface of the dust grain should be minimal. Conversely, the irradiation of pure O₂ ice on top of elemental sulphur yielded an appreciable amount of SO₂, and so it is possible that this process could contribute to the presence of SO₂ in H₂O-poor interstellar icy grain mantles as long as a sufficient quantity of O₂ ice is maintained in contact with the underlying sulphur layer.

Although the irradiation of CO₂ on top of sulphur at 20 K yielded SO₂ and CS₂ as radiolysis products, these species were formed as minor productions of irradiation. Indeed, the major radiation chemistry occurring within this ice was the same as that occurring in irradiated pure CO₂ ices (Sivaraman *et al.* 2013, Martín-Doménech *et al.* 2015), with CO, CO₃, and O₃ comprising the major products formed. The decay of these products at higher irradiation fluences without any concomitant increase in the mid-infrared absorption bands of other molecules leads to the speculation that prolonged irradiation of a CO₂ ice on top of elemental sulphur at 20 K may lead to chemical modification of the sulphur layer rather than the overlaying ice. Future experiments dedicated to a complete chemical analysis of the molecular composition of any sulphurous residues left over after irradiation are warranted to confirm or refute this speculation. It is interesting to note that OCS was not detected as a product in this irradiation experiment, thus suggesting that OCS in real interstellar icy grain mantles is likely formed as a result of the processing of ice mixtures containing the necessary precursor atoms, as suggested by Ferrante *et al.* (2008).

The experiments described in this chapter are also relevant to the chemistry of comets, as all the species investigated in this present study have been detected in icy cometary nuclei (Huebner 2002, Läuter *et al.* 2022). Although a volatile element, sulphur may be present in cometary nuclei as refractory residues or minerals (Rietmeijer 1988, Calmonte *et al.* 2016), and could thus contribute to the formation of sulphur-bearing molecules in the cometary nucleus as a result of radiation chemistry mediated by the solar wind. These sulphur-bearing molecules may be subsequently released from the comet as a result of their sublimation as the comet approaches perihelion in its orbit around the sun, thus enriching the chemical composition of interplanetary space. H₂S is the most abundant sulphur-bearing species in a number of comets whose compositions have been studied in depth, such as 67P/Churyumov-Gerasimenko, C/1995 O1 Hale-Bopp, and C/2014/Q2 Lovejoy (Calmonte *et al.* 2016). The abundances of SO₂ and OCS are typically lower than that of H₂S, although they still represent some of the more common sulphur-bearing molecules in comets. Conversely, CS₂ is a trace component of the icy cometary nucleus and, indeed, has not been detected in all studied comets (Calmonte *et al.* 2016).

The results obtained from the 20 K irradiation experiments described in this chapter demonstrate that sulphur molecule formation as a result of the interaction of the cometary nucleus possessing refractory elemental sulphur with the solar wind is not an efficient process when the comet is positioned close to aphelion in the furthest reaches of the Solar

System. This may be concluded from the fact that the irradiation of H₂O ice on top of elemental sulphur at 20 K did not yield any sulphur-bearing products, while only small quantities of SO₂ or CS₂ could be detected after similar irradiations of CO, CO₂, or CH₃OH ice. Although the irradiation of O₂ ice on top of elemental sulphur did produce an appreciable yield of SO₂, it is important to note that none of the 20 K irradiation experiments considered in this chapter yielded H₂S or OCS as a radiolysis product. The non-detection of these species (which are meant to be among the most abundant in comets), combined with the low abundances of SO₂ produced as a result of irradiation, leads to the conclusion that sulphur residues in comets are most likely not the source of the volatile sulphur-bearing molecules distributed within the icy nucleus.

The 1 MeV He⁺ ion irradiations of solid H₂O and CO₂ on top of elemental sulphur at a temperature of 70 K are representative of the radiation chemistry occurring on the surface of Europa. The presence of allotropic forms of elemental sulphur and their participation in the European radiolytic sulphur cycle has long been discussed in the literature (Carlson *et al.* 2002, Gomis and Strazzulla 2008, Carlson *et al.* 2009). Indeed, allotropic sulphur is thought to be the second largest molecular reservoir of sulphur on the surface of Europa, after H₂SO₄ hydrates (Carlson *et al.* 2002). Given that H₂O and CO₂ ices are also known to be widespread across the surface of Europa (Hansen and McCord 2004, Hand *et al.* 2006, Hansen and McCord 2008), the 70 K irradiation experiments described in this chapter may provide a further insight into the radiation chemistry occurring on the surface of this Galilean moon.

The irradiation of H₂O ice on top of sulphur at 70 K was found to produce H₂SO₄ as a pure molecule, as well as in the monohydrate and tetrahydrate forms. This result is not only in agreement with previous works that have documented the formation of these acids after the irradiation of mixtures of H₂O and elemental sulphur in the liquid and solid phases (Donaldson and Johnston 1968, Donaldson and Johnston 1971, Della Guardia and Johnston 1980, Carlson *et al.* 2002), but also with their production after the implantation of reactive sulphur ions into H₂O ice at Europa-relevant temperatures (Strazzulla *et al.* 2007, Strazzulla *et al.* 2009, Ding *et al.* 2013). As such, the irradiation of H₂O ice layers deposited on top of elemental sulphur and sulphur-bearing residues is very likely to contribute to the presence of H₂SO₄ on the surface of Europa.

Lastly, the 70 K irradiation of CO₂ ice on top of elemental sulphur was shown to result in the efficient formation of SO₂ and CS₂, along with smaller abundances of OCS. Although CS₂ and OCS have yet to be identified on the surface of any of the Galilean moons of Jupiter, it is likely that these molecules are present on those icy satellites to at least some extent due to the sulphur-rich nature of their surfaces. The efficient synthesis of SO₂ in the present study is an interesting result, as it implies the existence of high concentrations of this species in those regions of the European surface where CO₂ ice is intermixed with allotropic sulphur. However, there is no evidence for any correlation in the spatial distributions of CO₂ and SO₂ on the surface of Europa (Hansen and McCord 2008). Therefore, this result may be interpreted in one of two ways: either the surface patches of CO₂ observed on Europa are not intermixed with allotropic sulphur, or the radiolytic formation of SO₂ from such a mixture is inhibited by some other unknown process.

8.5 Summary

This chapter presents results obtained during the 1 MeV He⁺ ion irradiation of various oxygen-bearing molecular ices deposited on top of a layer of elemental sulphur, which was

prepared *via* the effusive evaporation of a solid, pure sulphur powder. Among the oxygen-bearing ices investigated were O₂, CO, CO₂, and H₂O which were irradiated at a temperature of 20 K, as well as CH₃OH ice which was irradiated at 25 K. Furthermore, the irradiations of CO₂ and H₂O ice on top of an underlying layer of sulphur were also conducted at 70 K. The primary motivation of this study was to determine whether or not the irradiation of such icy configurations could give rise to volatile sulphur-bearing molecules, such as SO₂, OCS, or CS₂.

The irradiation of the O₂ ice on top of sulphur at 20 K resulted in an appreciable yield of SO₂. This contrasts with the results of a similar irradiation experiment conducted using CO, where no SO₂ was observed to form. Instead, a small quantity of CS₂ was produced together with several oxocarbon radicals and cumulene dioxides. CS₂ formation was also observed to result from the irradiation of CH₃OH ice on top of sulphur at 25 K, although this was a minor radiation product and the major products of irradiation were noted to be similar to those obtained after the irradiation of pure CH₃OH ice (Bennett *et al.* 2007, Schmidt *et al.* 2021). The irradiation of CO₂ at 20 K resulted in the formation of limited quantities of both SO₂ and CS₂; however, the yield of these products was significantly increased when the irradiation temperature was raised to 70 K and OCS was also detected as a radiation product at this temperature. The more extensive solid-phase sulphur chemistry occurring at 70 K compared to 20 K was attributed to the more extensive diffusivities of free sulphur atoms liberated from the underlying sulphur layer at higher temperatures. Finally, while the irradiation of H₂O ice deposited on a layer of sulphur did not yield any sulphur-bearing products at 20 K, the analogous irradiation process at 70 K was found to yield H₂SO₄ and its monohydrate and tetrahydrate forms, thus complementing previous results from studies investigating the irradiation of H₂O and elemental sulphur mixtures in both the solid and liquid phases (Donaldson and Johnston 1968, Donaldson and Johnston 1971, Della Guardia and Johnston 1980, Carlson *et al.* 2002), as well as those concerned with the implantation of reactive sulphur ions into H₂O ice (Strazzulla *et al.* 2007, Strazzulla *et al.* 2009, Ding *et al.* 2013).

The results presented in this chapter have also been discussed in the context of the astrochemistry of interstellar icy grain mantles within dense interstellar clouds, cometary nuclei, and the surface chemistry of Europa. Based on the results obtained, it has been possible to conclude that the SO₂ observed in interstellar icy grain mantles could be produced as a result of the irradiation of O₂ ices in contact with refractory sulphurous solids, as long as the abundance of O₂ within the icy mantle is sufficient and any H₂O which could otherwise trigger the formation of sulphur oxyanions *via* the oxidation of SO₂ by O₃ is absent. Conversely, based on the known relative abundances of sulphur-bearing species in cometary nuclei, it has been possible to conclude that the irradiation of oxygen-bearing species in proximity to allotropic forms of sulphur is not a significant contributor to the sulphur chemistry occurring on cometary surfaces. Lastly, the results presented herein suggest that the irradiation of H₂O ices intermixed with elemental sulphur on the surface of Europa could be an important additional contributor to the H₂SO₄ known to be present there.

9 CONCLUSIONS AND SCOPE FOR FUTURE WORK

In this final chapter of the thesis, a summative evaluation of the results presented throughout Chapters 5-8 is presented, with particular attention being given to how these results have contributed to answering the questions outlined in Section 1.6. Suggestions on how this work may be further developed in future experimental projects concerned with sulphur ice astrochemistry are also made. The chapter concludes with a discussion of proposed upgrades to the ICA set-up that would greatly expand its experimental capabilities, along with a brief discussion on the recommended commissioning of an ancillary facility that would allow for the improved simulation of interstellar dust grains and mineral surfaces.

9.1 Thesis Conclusions

Broadly speaking, this thesis is concerned with experimental work performed with the aim of addressing as yet unanswered questions in the field of sulphur ice astrochemistry, such as the sulphur depletion problem of dense molecular clouds in the ISM and the poorly constrained formation mechanisms of SO₂ ice on outer Solar System bodies such as the Galilean moon system of Jupiter. This research was guided by four specific questions that were posed in Chapter 1; each of which was addressed by the experiments described in a subsequent chapter. In this sub-section, a synopsis of the experimental results is provided together with a brief analysis on to what extent the results obtained answer the questions that were initially posed.

(i) Can improved and higher resolution infrared spectroscopy aid in the detection of H₂S and SO₂ in astrophysical ices?

The results obtained from experiments performed to address this question were presented in Chapter 5. Manuscripts are presently in preparation for publication.

The mid-infrared spectra of pure H₂S and SO₂ astrophysical ice analogues were acquired at a spectral resolution of 0.5 cm⁻¹ after their deposition at 20, 40, 70, and 100 K (the latter temperature having only been considered for SO₂) and during their thermal annealing to sublimation, which occurred at 90 and 120 K for solid H₂S and SO₂, respectively.

Thermal annealing of an amorphous H₂S ice deposited at 20 K resulted in the splitting of its broad ν_s band at 2551 cm⁻¹ into distinct ν_1 (E_u), ν_1 (A_{2u}), and ν_3 modes due to the crystallisation of the ice, with maximum splitting observed at 60 K. No ν_2 mode was apparent upon deposition, but sharp and identifiable absorption bands attributable to the ν_2 (A_{2u}) and ν_2 (E_u) modes were evident at 60 K. H₂S ices deposited at higher temperatures appeared to be largely crystalline, as evidenced by the splitting of their ν_s and ν_2 bands upon deposition and the fairly small variations in their band areas during thermal annealing. Thermal annealing of an amorphous SO₂ ice deposited at 20 K resulted in the splitting of its broad ν_1 , ν_3 , and $\nu_1 + \nu_3$ bands into individual contributions arising from infrared phonon modes and various isotopologues, indicative of ice crystallisation. The ice appeared to fully crystallise upon reaching a temperature of 80 K. The SO₂ ice deposited at 40 K was noted to be largely crystalline at a comparatively lower temperature of 70 K through the observation of the ³⁴S¹⁶O₂ ν_1 and ν_3 modes. However, the ³⁴S¹⁶O₂ $\nu_1 + \nu_3$ mode was not fully resolved at 70 K,

thus suggesting that the ice was not yet a fully crystalline solid but was rather a polycrystalline structure. Spectra of the ices deposited at 70 and 100 K demonstrate that the ices were crystalline.

The preparation of sulphur-poor H₂S:H₂O and SO₂:H₂O mixed ices at 20 K resulted in the formation of microporous ices which underwent compaction during subsequent thermal annealing. Thermal annealing also resulted in the crystallisation of the H₂O component of the ice. In the case of the H₂S:H₂O mixed ice, the H₂S ν_s band was red-shifted by 1.5 cm⁻¹ compared to its position in the analogous pure ice. Thermal annealing of this mixed ice did not result in either the crystallisation of the H₂S ice component, nor its segregation from the H₂O. Indeed, tentative spectroscopic evidence for the presence of H₂O...HSH...OH₂ hydrogen bonds was found throughout the thermal annealing process. No cryogenic thermal reactions occurred between H₂S and H₂O.

In the case of the SO₂:H₂O mixed ice, the SO₂ ν_1 and ν_3 modes were noted to be significantly blue-shifted by 6-8 cm⁻¹ compared to their positions in the analogous pure ice. Upon preparation of the mixed ice, mid-infrared absorption features attributed to the hydrogen bonding between H₂O and SO₂ were readily detected, although these features became weaker as a result of thermal annealing due to thermally induced segregation of the molecular ice components. Furthermore, thermal annealing promoted cryogenic thermal reactions leading to the formation of sulphur oxyanions, namely HSO₃⁻ and S₂O₅²⁻.

These spectroscopic results suggest that mid-infrared detections of H₂S in interstellar icy grain mantles may prove challenging due to the small absorptions of this species in H₂O-dominated ices. The results do, however, support the existence of amorphous H₂S on the surface of Io. Furthermore, they may be of use in confirming the existence of SO₂ on the surface of Europa *via* future mid-infrared spectroscopic measurements carried out by the *James Webb Space Telescope* or any of the forthcoming interplanetary missions, since detections made in the mid-infrared would be significantly more cogent than the ultraviolet spectroscopy upon which this detection has largely been based.

(ii) Is the radiation chemistry of H₂S and SO₂ influenced by changes in the phase of the ice, and how does this compare to other, more often considered species?

The results obtained from experiments performed to address this question were presented in Chapter 6. See also: Mifsud et al. (2022), Phys. Chem. Chem. Phys. 24, 10974; Mifsud et al. (2022), Eur. Phys. J. D: Atom. Mol. Opt. Plasma Phys. 76, 87; Mifsud et al. (2022), Front. Chem. 10, 1003163.

The phase of an irradiated molecular ice was found to play a key role in its electron-driven radiation chemistry. Studies of the 2 keV electron irradiation of solid CH₃OH and N₂O at 20 K demonstrated that the irradiation of the amorphous phase resulted in a more rapid decay of the parent species, as well as greater abundances of the radiolytic products, compared to the analogous irradiation of the crystalline phase. This relative radiolytic stability of the crystalline phase compared to its amorphous counterpart was attributed to the stability imparted to the latter by the solid lattice energy. However, this phenomenon was more pronounced in the case of CH₃OH due to the existence of strong and long-ranging hydrogen bonds in the crystalline phase which must be overcome before radiolytic decay can occur. Such a strong array of hydrogen bonds does not exist to the same extent in the amorphous ice, which therefore does not benefit from the same radiolytic stability. In

comparison crystalline N₂O is only characterised by the relative ordering of its molecular dipole. Since interacting dipole moments do not represent as strong a form of intermolecular bonding as do hydrogen bonds, the relative radiolytic stability of crystalline N₂O compared to its amorphous phase is not as great as in the case of CH₃OH.

Similar experiments were conducted with four phases of H₂O: amorphous solid water (ASW), restrained amorphous ice (RAI), cubic crystalline ice (Ic), and hexagonal crystalline ice (Ih). Results showed that the abundance of H₂O₂ formed after the 2 keV electron irradiation of these phases followed the order ASW > RAI > Ic > Ih, indicating the reverse trend with regards to stability of the ices against radiolytic decay. Once again, this increase in radiolytic stability with structural order was attributed to the stabilising effect of crystal lattice energies and the extensive hydrogen bonding regimes in the crystalline ice phases. The increased presence of micropores and structural defects in the amorphous ice phases also likely contributed to the greater abundance of H₂O₂ formed as a result of irradiation.

Similar results were also observed during the comparative 2 keV electron irradiation of amorphous and crystalline H₂S, with a more rapid decay of the parent species and greater abundances of radiolytic products being observed after irradiation of the amorphous ice. This was again likely due to stabilising contributions from lattice energies and extensive (although weak) hydrogen bonding systems in the crystalline phase. The 1.5 keV electron irradiation of amorphous and crystalline SO₂, however, presented significantly different results: the amorphous ice appeared to initially resist radiolytic decay, but was subsequently consumed at higher projectile electron fluences. Conversely, the crystalline SO₂ ice initially exhibited the anticipated rapid exponential decay, which subsequently slowed at higher electron fluences. Possible reasons behind these observations, such as the recombination of molecular fragments or changes in the integrated band strength constant as a result of radiation-induced ice compaction, were provided and discussed.

Such results may be applied to astrochemistry, as they suggest that the formation of product molecules as a result of the irradiation of astrophysical ices by galactic cosmic rays or stellar winds is more productive if the ice is amorphous. Therefore, it is entirely possible that those astrophysical environments in which crystallisation processes are out-competed by radiation-induced amorphisation are more conducive to the formation of molecules, which may possibly include complex organic species of direct relevance to the origins of life. Sulphur budgets for the irradiations of amorphous and crystalline H₂S and SO₂ were also constructed from which it was determined that a large percentage of the initially deposited sulphur is no longer spectroscopically observed after irradiation. Since electron-induced sputtering or desorption were discounted as efficient depletion mechanisms, this depletion of sulphur was instead ascribed to the sequestration of molecular sulphur to refractory sulphur residues. This result may therefore provide at least a partial explanation for the sulphur depletion problem in the dense ISM.

(iii) Does sulphur ion implantation into oxygen-bearing ices represent a reasonable mechanism by which SO₂ may form?

The results obtained from experiments performed to address this question were presented in Chapter 7. See also: Mifsud et al. (2022), Geophys. Res. Lett. 49, e2022GL100698.

High-energy sulphur ions were implanted into O₂, CO, and CO₂ ices at 20 K and, in the case of CO₂, also at 70 K with the aim of determining whether such a process could result

in the formation of sulphur-bearing volatile molecules, particularly SO₂. Results from the implantation experiment into solid O₂ at 20 K demonstrated that SO₂ is indeed among the products of irradiation, as is O₃. Conversely, no conclusive evidence for the formation of SO₂ could be found after sulphur ion implantation into CO ice at 20 K. Instead, the dominant radiolytic products were found to be CO₂, CO₃, O₃, and various cumulene dioxides and oxocarbon radicals. Although the ultimate fate of the implanted sulphur ions is not known for certain, it is possible to speculate that this was the formation of infrared inactive allotropic forms of sulphur.

The implantation of high energy, reactive sulphur ions into CO₂ ice at 20 and 70 K revealed a temperature dependence of the resultant sulphur chemistry. At 20 K, mid-infrared spectroscopic evidence for the formation of a small quantity of SO₂ was found, in agreement with the results of previously published studies. However, no SO₂ could be detected after the implantation of sulphur ions into CO₂ ice at 70 K. Indeed; the formation of all radiolytic products (such as CO, CO₃, and O₃) was significantly more limited at this higher temperature. This result was attributed to the efficient desorption of O₂ at this higher temperature, which would have significantly depleted the ice of its oxygen content thereby precluding the efficient formation of SO₂.

These results carry significant implications for the extra-terrestrial chemistry of solid-phase sulphur. Firstly, it demonstrates that the implantation of hot (>10 keV) sulphur ions from the Jovian magnetosphere into the surface ices of Europa is unlikely to be an efficient formation mechanism for the SO₂ ice observed on the surface. Previous studies have demonstrated that such implantations into H₂O ice (the dominant ice on the surface of Europa) do not result in the formation of SO₂: rather, it is H₂SO₄ and its hydrates that are formed. Although CO₂ ice is also known to exist on the surface of Europa, the lack of any SO₂ produced after sulphur ion implantation at 70 K (a temperature relevant to the European surface) as well as the lack of any correlation in the spatial distributions of the surface SO₂ and CO₂ components effectively rules out this mechanism as a formation pathway towards SO₂ ice on Europa.

O₂ ice is also a known surface component of Europa, where it may be found stabilised as clathrate hydrates. Despite the positive result demonstrated herein with regards to the formation of SO₂ after the implantation of sulphur ions into O₂, this mechanism is also unlikely to account for the presence of SO₂ on Europa. This is primarily due to the fact that, at higher temperatures, SO₂ is consumed in reactions with both O₃ and H₂O to yield various sulphur oxyanions and its accumulation on the surface will thus be largely precluded. Alternative mechanistic routes towards the formation of SO₂ on the surface of Europa of varying likelihoods have been discussed, including the radiolytic decay of various sulphate minerals, the implantation of cold (sub-keV) sulphur ions from the magnetosphere, and the exsolution of SO₂ from the putative subsurface global ocean.

The non-detections of OCS and CS₂ after the implantations of sulphur ions into either CO or CO₂ ice also carry important implications for astrobiology as both molecules may play a role in the formation of biomolecules in extra-terrestrial environments: OCS is a known catalyst for peptide bond formation while CS₂ irradiation is known to yield carbon- and sulphur-rich polymers that may serve as backbones for other, potentially prebiotic species. Their non-detections after the implantation of sulphur ions into both CO and CO₂ ices suggests, however, that the radiation-induced formation of OCS and CS₂ ices in extra-terrestrial environments is better explained by processes in which the necessary precursor atoms are already present in the ice prior to irradiation.

(iv) Can sulphur chemistry (including the formation of SO₂) be induced as a result of the irradiation of oxygen-bearing ices deposited above elemental sulphur layers?

The results obtained from experiments performed to address this question were presented in Chapter 8. Manuscripts are presently in preparation for publication.

The irradiation of oxygen-bearing ices (O₂, CO, CH₃OH, CO₂, and H₂O) on top of layers of elemental sulphur by 1 MeV He⁺ ions at different temperatures was probed to determine whether this represented a feasible mechanism of generating different sulphur-bearing volatile species, including SO₂. The layer of elemental sulphur was generated *via* the effusive evaporation of a powder sample and its subsequent condensation at the desired experimental temperature. Such a methodology represents a significant step forward compared to methods previously used to generate a refractory sulphur layer, as it allows for the rapid preparation of a relatively thick layer of pure sulphur.

Results demonstrated that the irradiation of O₂ ice on top of elemental sulphur at 20 K resulted in the efficient formation of SO₂. Indeed, more SO₂ was produced in this experiment than was during the implantation of sulphur ions into pure O₂ ice at the same temperature. This was likely due to the greater availability of sulphur atoms in the former experiment compared to the latter. Conversely, no SO₂ was observed to form after the irradiation of CO ice on top of elemental sulphur at 20 K, where CS₂ was observed to be the only sulphur-bearing radiolytic product molecule. Other product molecules, including most of the cumulene dioxides and oxoradical species observed after the implantation of reactive sulphur ions into CO ice, were also observed as a result of the 1 MeV He⁺ ion irradiation. The irradiation of CH₃OH ice on top of elemental sulphur at 25 K yielded very similar results to those observed after the proton irradiation of pure CH₃OH at 20 K (see Section 4.3), with the addition of a small quantity of CS₂ also being produced.

The irradiation of CO₂ ice on top of a layer of elemental sulphur by 1 MeV He⁺ ions at 20 K resulted in the formation of both SO₂ and CS₂. However, the abundances of these molecules produced after the corresponding irradiation at 70 K were significantly greater, and OCS was additionally produced. This result is the opposite of that observed after the implantation of reactive sulphur ions into CO₂ ice at 20 and 70 K, where a greater abundance of sulphur-bearing products (i.e., SO₂) was observed at lower temperatures. This result was attributed to the greater migration of sulphur atoms from the underlying layer into the ice structure at 70 K, where they would be able to participate in various reactions including those with carbon and oxygen atoms, thus increasing the yields of both SO₂ and CS₂ whilst simultaneously reducing the formation of O₂ within the ice (and, consequently, its subsequent sublimation to the gas phase).

The irradiations of H₂O ice on top of elemental sulphur proved to be less chemically productive. At 20 K, this irradiation only yielded H₂O₂ as a product while, at 70 K, small quantities of H₂SO₄ as well as its monohydrate and tetrahydrate forms were observed to form. Such results complement previous studies on the formation of H₂SO₄ hydrates both after the implantation of reactive sulphur ions into H₂O ice as well as after the irradiation of H₂O mixed with S₈.

These results are of great astrochemical significance as they imply that the formation of sulphur-bearing volatile species such as SO₂, CS₂, and OCS as a result of the irradiation of sulphur-free ices deposited on top of elemental sulphur layers is indeed favourable, and may thus contribute to the diversity of sulphur-bearing molecular species in extra-terrestrial environments. Indeed, the formation of H₂SO₄ hydrates after the irradiation of H₂O ice on top of sulphur at 70 K may constitute an additional source of these acidic species on the surface of Europa. Interestingly, no H₂S ice was detected throughout these experiments, suggesting that its existence in space must be due to other processes.

9.2 Scope for Future Work

The experiments presented in this thesis are merely the starting point for what is planned to be a rigorous and in-depth study of sulphur ice radiation astrochemistry. Indeed, a number of experiments that will build upon and extend the results described in previous chapters have already been planned for the future. A description of some of these planned experiments now follows.

9.2.1 Further Systematic Spectroscopic Characterisations

The need for more complete and systematic spectroscopic characterisations of sulphur-bearing cryogenic molecular ices to facilitate their detection in astrophysical environments such as the dense ISM or the outer Solar System was discussed in Chapter 1. The mid-infrared spectroscopic characterisations of H₂S and SO₂ ices deposited at various temperatures and thermally annealed to sublimation that were presented in Chapter 5 therefore represent a convenient starting point for a campaign of similar characterisations of other sulphur-bearing molecules of astrophysical relevance, including OCS, CS₂, several of the lower thiol homologues, and their mixtures with H₂O ice. This campaign is planned to take place using the ICA set-up in the near future.

Moreover, a systematic study is planned in which the mid-infrared spectra of SO₂:H₂O ice mixtures of different stoichiometric compositions will be acquired in order to study the influence of temperature and ice composition on the appearance and position of the absorption band at approximately 3595 cm⁻¹ due to hydrogen bonding between SO₂ and H₂O, as well as the influence of these experimental parameters on the thermally induced production of sulphur oxyanions. Such work is crucial in order to adequately constrain the composition and chemical productivities of such ice mixtures in environments where they are known to be present, such as on the surfaces of the icy Galilean moons of Jupiter.

Complementary spectroscopic characterisations of these species using other energies of the electromagnetic spectrum may also prove useful for their detection in astrophysical settings. Indeed, future work is planned with collaborators who have access to synchrotron facilities at the University of Aarhus (Denmark) and the National Synchrotron Radiation Research Centre (Taiwan) so as to carry out vacuum ultraviolet photoabsorption studies on condensed sulphur-bearing ices. Work on this project is already underway, with the spectra of SO₂, OCS, and CS₂ ices already having been recorded.

9.2.2 Radiolytic Formation of Thiols

The work presented in Chapters 7 and 8 focused on the potential formation of simple, volatile sulphur-bearing molecules such as SO₂ within astrophysical environments. However, similar methodologies to those used in those chapters may be adapted to study the formation of more complex organic species containing sulphur, such as thiols. Lower homologue thiols such as CH₃SH or CH₃CH₂SH are known to exist in interstellar space (Linke *et al.* 1979, Kolesniková *et al.* 2014, Rodríguez-Almeida *et al.* 2021), and may thus be available to participate in organic chemistry leading to the formation of more complex molecules of relevance to biochemistry or geochemistry.

Work is therefore planned to assess the possible radiolytic formation of such thiols in interstellar ice analogues. For example, experimental work on the irradiation of mixed ices containing hydrocarbons (such as CH₄ or C₂H₆) and SO₂ by energetic electrons is planned so as to gauge the potential formation of thiol molecules as a result of the insertion of sulphur atoms sourced from the dissociation of SO₂ into the molecular structure of the hydrocarbons.

Other potentially productive ices, such as hydrocarbon molecules deposited on top of elemental sulphur layers irradiated by either ions or electrons, will also be investigated. Of highest priority, however, is the implantation of reactive sulphur ions into various pure hydrocarbon ices such as CH₄ and C₂H₆, since such a project has successfully attracted funding in the form of a Europlanet Transnational Access Project grant.

The planned experimental work described above may also provide an insight into the possible radiolytic formation of H₂S in irradiated astrophysical ice analogues. Of all sulphur-bearing molecules of potential astrophysical interest, H₂S is arguably the least understood: although the molecule should readily form as a result of the hydrogenation of sulphur atoms on the surfaces of interstellar dust grains (Linnartz *et al.* 2015) and could potentially be one of the most abundant interstellar sulphur-bearing species, no conclusive evidence exists for its presence within interstellar icy grain mantles (Boogert *et al.* 2015, McGuire 2022). This apparent discrepancy between the ease of surface-catalysed hydrogenation reactions and the non-detection of solid H₂S in interstellar space thus warrants further investigation.

9.2.3 Reactivity of H₂S Ices

As described previously, the astrochemistry of solid H₂S is poorly constrained since, despite the apparent efficiency of hydrogenation reactions on the surfaces of interstellar dust grains (Linnartz *et al.* 2015), no evidence of its existence in dense interstellar clouds has been found (Boogert *et al.* 2015, McGuire 2022): instead, the only sulphur-bearing species known to exist in interstellar icy grain mantles are SO₂ and OCS. It is therefore possible to hypothesise that any H₂S formed within interstellar icy grain mantles is efficiently converted to SO₂ and OCS as a result of its radiation chemistry with carbon- and oxygen-bearing species. Experiments to test this hypothesis have been planned and will be carried out in the near future.

The experimental methodology that will be employed will not only seek to understand what radiolytic products are formed as a result of the irradiation of H₂S ices mixed with CO, CO₂, O₂, and H₂O at 20 K; but will also attempt to determine whether the structure of the ice plays an important role in the resultant radiation chemistry. To do this, three types of ices will be considered: (i) mixed ices formed by the co-deposition of H₂S and an oxygen-bearing species, (ii) layered ices formed as a result of the deposition of H₂S followed by the oxygen-bearing species, and (iii) inverse layered ices formed as a result of the deposition of the oxygen-bearing species followed by H₂S. Since the icy grain mantle compositions most amenable to the hypothetical formation of H₂S are not known and thus it is not known whether H₂S formation would occur in the polar or apolar layers of the icy grain mantle, on the surface of the bare dust grain, or on a layer of H₂O ice, consideration of these mixed and layered ice structures allows H₂S radiation chemistry following its formation in many of these molecular environments to be analysed.

9.2.4 Irradiation of Sulphur-Bearing Minerals

The irradiation of various sulphur-bearing minerals by galactic cosmic rays, stellar winds, and magnetospheric ions may also constitute an important route to the formation of sulphur-bearing molecules in astrophysical environments. Previous work on this subject is fairly sparse, with only a few minerals or ionic solids having been irradiated (Benninghoven 1969, Sasaki *et al.* 1978, Wiens *et al.* 1997, Johnson *et al.* 1998, McCord *et al.* 2001b). Given that a number of minerals (some of which contain sulphur) are thought to exist in radiation environments on the surfaces of the icy Galilean satellites (McCord *et al.* 2001a, McCord *et al.* 2001b) and that these moons are considered to be prime locations for the existence of

extra-terrestrial life, there is a strong motivation to better understand the radiation-induced decay of these minerals and the molecules that result from such a process.

An experimental project aimed at further elucidating the radiation chemistry of a selection of mineral species has therefore been proposed and has successfully attracted funding in the form of a Europlanet Transnational Access Project grant. The proposed project involves the irradiation of four mineral species with either 1 MeV proton or 1 MeV S^+ ion beams (or both) using the ICA set-up. The four minerals were selected on the basis of their relevance to different astrophysical environments: epsomite and halite ($MgSO_4 \cdot 7H_2O$ and $NaCl$) are hypothesised to be important mineral components of the surface of Europa (McCord *et al.* 2001b, Fox-Powell *et al.* 2019), while the silicates fayalite and berthierine (Fe_2SiO_4 and $(Fe^{2+}, Fe^{3+}, Al)_3(Si, Al)_2O_5(OH)_4$) may be representative of interstellar silicate dust grains (Chiar and Tielens 2006, Fogerty *et al.* 2016).

Due to the non-transparent nature of most of these minerals, no mid-infrared spectra can be collected *in situ* during irradiation, although the formation and sublimation of volatile molecules may be monitored *in situ* using quadrupole mass spectrometry. Instead, mid-infrared and ultraviolet-visible spectra of unirradiated mineral samples together with samples irradiated using different projectile ion fluences will be measured *ex situ* in collaboration with colleagues at the INAF Osservatorio Astrofisico di Catania (Italy), the Université Paris-Saclay (France), and the Institute of Technical Sciences of SASA (Serbia).

9.2.5 Radiation-Induced Sulphur Isotope Fractionations

Sulphur isotopic compositions in terrestrial rocks, shales, sediments, and mineral deposits have found use as biosignatures as they are able to trace metabolic pathways associated with biological sulphur cycling and isotope fractionations in past and present environments, such as sulphate reduction, sulphide oxidation, and sulphur disproportionation (Moreras-Marti *et al.* 2022). The extrapolation of processes known to result in isotope fractionations (i.e., the accumulation of a favoured isotope in the products of a chemical reaction) in terrestrial systems to extra-terrestrial settings, such as Mars and Europa, has long been proposed. However, in order to effectively make use of sulphur isotopes as potential biosignatures for sulphur-cycling in extra-terrestrial environments, it is necessary to determine whether abiotic processes in those environments also result in sulphur isotope fractionations and, if so, quantify the magnitude of discrimination.

A number of abiotic processes are known to result in sulphur isotope fractionations. For instance, thermochemical sulphate reduction has been demonstrated to discriminate against the ^{34}S and ^{36}S isotopes and in favour of the ^{32}S and ^{33}S isotopes (Machel *et al.* 1995, Oduro *et al.* 2011). Furthermore, the mass-independent fractionation of sulphur isotopes is known to occur as a result of the gas-phase photochemistry of SO_2 and other sulphur-bearing gases (Ono 2017). Biomass burning has also been experimentally demonstrated to result in small-magnitude mass-independent fractionation of sulphur isotopes (Lee *et al.* 2002, Shaheen *et al.* 2014, Lin *et al.* 2018), as have large stratospheric eruptions (Crick *et al.* 2021).

Despite this progress in understanding the abiotic drivers of sulphur isotope fractionations, no experimental studies have yet attempted to ascertain the potential influence of radiation chemistry on the fractionation of sulphur isotopes. The quantification of radiation-driven isotope fractionations is of crucial importance if the proposed use of sulphur isotopes measured from samples collected from Europa as potential biosignatures is to be realised. A project has thus been proposed in which an elemental sulphur layer of known isotopic composition is irradiated by various ion and electron beams at temperatures relevant to both the interstellar medium as well as the outer Solar System so as to determine whether any particular isotopes are favoured for incorporation into the resulting residue.

Accurate isotopic compositions would need to be measured *ex situ* by combustion in an elemental analyser connected in continuous flow mode to an isotope ratio mass spectrometer. Further work in which elemental sulphur layers deposited below ice layers (similarly as to what was performed in Chapter 8) are irradiated can also be performed with the aim of determining whether the presence of an overlaying ice (as may be the case on the surface of Europa or on the surface of interstellar dust grains) changes the fractionation of the irradiation process and, consequently, the isotopic composition of the resultant residue.

9.3 Proposed Upgrades to the ICA Set-Up

Although the ICA set-up in its present state is a versatile and highly useful piece of scientific equipment, it would benefit from future upgrades and modifications that would expand its experimental capabilities and thus allow for more complex work to be performed as well as avoid recurrent problems associated with the current set-up. A number of proposed upgrades to the ICA are briefly discussed below, along with a concise proposal regarding the commissioning of an ancillary facility aimed at better simulating interstellar dust grains and mineral surfaces.

9.3.1 Spectroscopic Range and Removal of Atmospheric Contaminants

The mid-infrared spectrophotometer currently attached to the ICA set-up is a Thermo Nicolet Nexus 670 FTIR spectrophotometer which offers a spectral range of $4000\text{-}650\text{ cm}^{-1}$ ($2.5\text{-}15.4\text{ }\mu\text{m}$) and a maximum spectral resolution of 0.5 cm^{-1} . Such a configuration allows for the mid-infrared spectroscopy of deposited and processed astrophysical ice analogues to be studied in detail, as has been demonstrated throughout this thesis. However, the optical components of the spectrophotometer are not maintained under vacuum, and thus the acquired mid-infrared spectra are susceptible to absorptions by infrared active gaseous species in the atmosphere of variable composition, particularly H_2O and CO_2 (see, as an example, the spectra depicted in Figs. 8.2 and 8.5). Although absorptions by these species may be mitigated by continually purging the MCT detector using purified dry air, it is not possible to totally exclude them. As such, instabilities in the purge flow of the detector or abrupt changes in the climate of the laboratory (such as changes in atmospheric humidity) may induce large, unwanted absorptions by atmospheric H_2O or CO_2 which decrease the quality of the acquired spectra and make their interpretation and quantification significantly more challenging.

In light of this, a new Bruker Vertex 70v FTIR spectrophotometer has been purchased and is expected to be installed in April or May 2023. The optical components of this new spectrophotometer, as well as the pathlength leading to its associated detector, may be readily evacuated and maintained under light vacuum (a few 10^{-2} mbar), thus removing atmospheric gases and excluding their absorptions from any acquired spectra. Furthermore, this new spectrophotometer offers an extended spectral range that may be investigated: the nominal spectral range of the spectrophotometer and its associated deuterated L-alanine doped triglycine sulphate (DLaTGS) detector is $8000\text{-}350\text{ cm}^{-1}$ ($1.25\text{-}28.57\text{ }\mu\text{m}$); however, additional optical components as well as a specialised DLaTGS detector covering the $700\text{-}10\text{ cm}^{-1}$ ($14.28\text{-}1000\text{ }\mu\text{m}$) range have also been included in the design of the spectrophotometer so as to enable studies of the far-infrared and terahertz absorption spectra of astrophysical ice analogues to be performed.

Far-infrared and terahertz spectroscopic studies of solid ices of astrophysical relevance allow for intermolecular bonding vibrational modes to be probed, and thus may offer increased information on the structure of an ice before and during its processing by ionising

radiation or thermal annealing. Such a technique may therefore yield complementary results to those obtained from the mid-infrared spectra presented in Chapter 6, wherein differences in the radiation chemistry and physics of amorphous and crystalline solid ices under otherwise equivalent experimental conditions were investigated. Despite its apparent utility in laboratory astrochemistry, far-infrared spectroscopy has only been used in a handful of studies (Moore and Hudson 1992, Moore and Hudson 1994, Hudson and Moore 1995, Allodi *et al.* 2014, Ioppolo *et al.* 2014, McGuire *et al.* 2016), none of which considered any sulphur-bearing species. The installation of this new spectrophotometer thus not only offers the opportunity for higher quality spectra to be acquired, but also opens many new avenues of spectroscopic research at higher wavelengths.

9.3.2 Ice Temperatures

Presently, the lowest temperature at which astrophysical ice analogues can be prepared using the ICA set-up is 20 K. In principle, the lowest temperature to which the deposition substrates may be cooled by the Leybold Coolpower 7/25 closed-cycle helium cryostat currently attached to the chamber is approximately 8 K, as detailed within the user manual provided by the manufacturer. In practice, however, this is limited to 20 K due to the proximity of the chamber side walls to the deposition substrates, which is about 80 mm at maximum. At this proximity, the chamber side walls are able to efficiently radiate heat to the deposition substrates such that the lowest maintainable temperature that can be reached is 20 K. Therefore, a larger chamber is required in order to reach a lower base temperature.

At 20 K, radicals formed as a result of the radiolytic dissociation of parent molecules are fairly mobile within the ice structure and are thus not easy to isolate, as evidenced by the paucity of open-shell species that were spectroscopically detected throughout this thesis. At 10 K, however, radical mobility would be significantly reduced and intermediate species in radiation chemistry would thus accumulate to a greater extent than at higher temperatures, thus facilitating their spectroscopic identification. A further motivation behind accessing lower base temperatures exists in the fact that quiescent molecular cores in dense interstellar clouds may reach temperatures of around 10 K (Tafalla *et al.* 2002), and so the ability to access such low temperatures would expand the range of astrophysical environments that may be simulated. Replacing the current chamber with a larger one would not only allow for lower base temperatures to be accessed, but would also allow for an increased number of ports in the chamber design to which new attachments (such as an ultraviolet photon lamp or a helium-neon laser interferometry system) could be installed. In this way, the experimental capabilities of the ICA would also be greatly expanded.

9.3.3 Determination of Ice Thicknesses and Optical Parameters

Throughout the experiments described in this thesis, the thicknesses of the deposited ice samples were determined on the basis of the magnitude of their mid-infrared absorptions by using the following equation:

$$d = 2.303 \times 10^4 \times \frac{P_a m}{\rho N_A A_s} \quad (\text{Eq. 9.1})$$

where P_a is the area of a characteristic mid-infrared absorption band of an ice component, m is the molecular mass of that component, ρ is its density, N_A is the Avogadro constant and A_s is the band strength constant for the absorption band over which Eq. 9.1 is integrated.

It is important to note, however, that the values of A_s quoted in the literature for various molecular ices are often valid only for pure ices at defined temperatures. Therefore, the use of these values in determining the thickness of a multi-component ice deposited at or annealed to a temperature different to that for which the utilised value of A_s was defined will introduce an uncertainty in the calculated thickness value that may be as high as 50% (Kaňuchová *et al.* 2017). It would therefore be desirable to be able to determine the thickness of a deposited astrophysical ice analogue in a manner that is independent of its spectroscopic absorptions.

Laser interferometry represents a technique with which the thickness of a deposited ice may be quantified without the need to assume any physical characteristics of the ice (such as its density or the integrated band strength constant of a particular mid-infrared absorption feature). This technique is based on monitoring the variations in the intensity of a helium-neon laser beam resulting from interference between laser light reflected from the surface of the ice and from the substrate-ice interface (Fig. 9.1). These variations, measured using a photodiode, result in the production of a fringe pattern such as those depicted in Fig. 9.2. The number of fringes N_{fr} observed in this pattern is related to the thickness of the ice d as follows (Gröner *et al.* 1973, Goodman 1978):

$$d = \frac{N_{fr}\lambda}{2\eta \cos \theta_1} \quad (\text{Eq. 9.2})$$

Or alternatively as (Heavens 1955):

$$d = \frac{N_{fr}\lambda}{2\sqrt{\eta^2 - \sin^2 \theta_0}} \quad (\text{Eq. 9.3})$$

where λ is the wavelength of the helium-neon laser *in vacuo* (0.6328 μm), η is the refractive index of the ice, θ_0 is the angle of reflection at the ice surface, and θ_1 is the angle of reflection at the substrate-ice interface (Fig. 9.1).

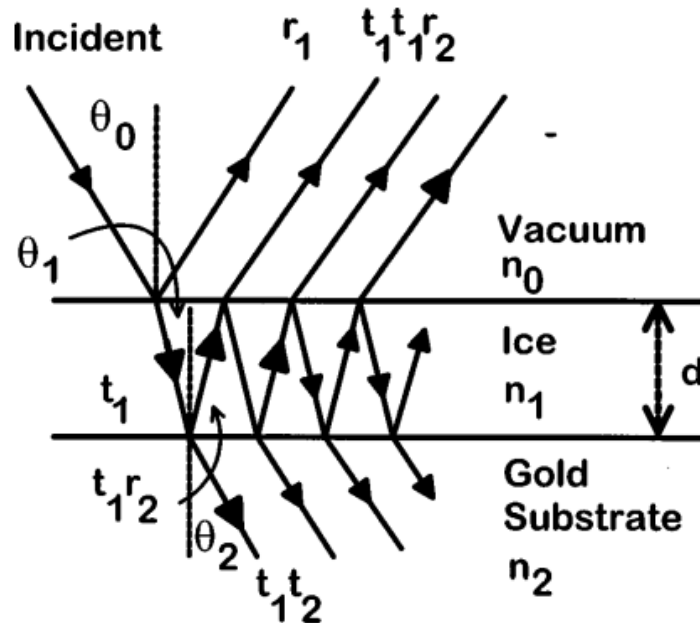


Fig. 9.1: Optical ray diagram exhibiting the various reflection and refraction processes leading to the detected interference of the helium-neon laser light. Image taken from Westley *et al.* (1998).

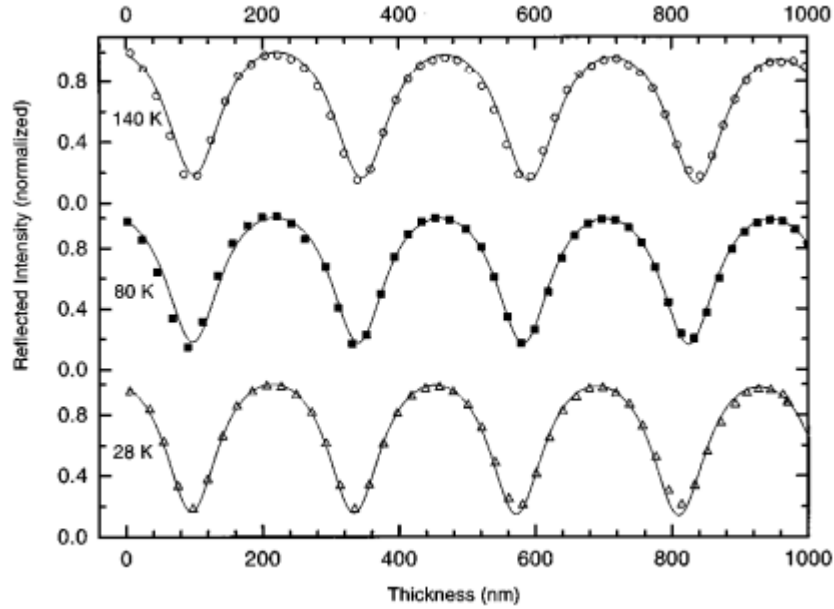


Fig. 9.2: Examples of typical fringe patterns observed during laser interferometry of H₂O ices deposited at different temperatures. Image taken from Westley *et al.* (1998).

It is possible to observe that the only variable in Eqs. 9.1 and 9.2 that is either not defined by the geometry of the chamber set-up or by the speed of light *in vacuo* is the ice refractive index η . However, this value may be either estimated or accurately calculated, depending on whether one or two helium-neon lasers are available for use. If one laser is available, then the refractive index may be estimated from the ratio of the maxima and minima of the fringe pattern: more information on this may be found in the works of Berland *et al.* (1994) and Westley *et al.* (1998). Conversely, if two laser beams are available and are impinging on the surface of the ice at two different angles to the normal (for the sake of this discussion, these angles shall be defined as θ_α and θ_β), then the refractive index of the ice can be calculated directly. This may be done by first plotting the ice deposition time (in seconds) against the number of fringes observed in the interferometric pattern measured by both laser beams: these plots result in straight lines having slopes l_α and l_β . From this information, the refractive index may be calculated through the following equation (Tempelmeyer and Mills 1968, Hudson *et al.* 2017):

$$\eta = \sqrt{\frac{\sin^2\theta_\beta - \left(\frac{l_\alpha}{l_\beta}\right)^2 \sin^2\theta_\alpha}{1 - \left(\frac{l_\alpha}{l_\beta}\right)^2}}$$

(Eq. 9.4)

Assuming that $\theta_\alpha < \theta_\beta$.

The ability to determine the thickness of a deposited ice *via* interferometry not only reduces the uncertainty with which it is associated, but also opens the possibility for a new type of study: the measurement of integrated band strength constants A_s . Such values are of paramount importance in gauging the column densities of ices observed in interstellar space, but are known to vary considerably with temperature and ice composition. Therefore, there exists a need for thorough and systematic quantifications of these constants for ices under various experimental conditions. This may be achieved by simply depositing an ice and

measuring the area of a particular mid-infrared absorption band as a function of the ice thickness as determined through laser interferometry. Rearranging Eq. 9.1 yields:

$$2.303 \times P_a = \frac{d\rho N_A A_s}{m} \quad (\text{Eq. 9.5})$$

Assuming that the ice thickness is measured in centimetres. To simplify this equation, it is possible to consider the molecular density of the ice ρ_{mol} :

$$\rho_{\text{mol}} = \frac{\rho N_A}{m} \quad (\text{Eq. 9.6})$$

Substituting Eq. 9.6 into Eq. 9.5 yields:

$$2.303 \times P_a = dA_s \rho_{\text{mol}} \quad (\text{Eq. 9.7})$$

Thus, a simple plot of $2.303 \times P_a$ against d yields a straight line having a slope of:

$$l = A_s \rho_{\text{mol}} \quad (\text{Eq. 9.8})$$

From which A_s is easily calculable if ρ_{mol} is known.

In the event that ρ_{mol} is not known, it is desirable to be able to experimentally quantify it. This parameter is evidently related to the density of the ice (Eq. 9.6), which may be measured if a quartz crystal microbalance (QCM) is available either alongside a deposition substrate or in place of one. The QCM is a microgravimetric device consisting of a quartz acoustic resonator whose frequency may be readily measured, and which is positioned beneath a flat surface of defined area which is typically made of a polished reflective material such as gold. This surface may be cooled in a similar fashion to the ZnSe deposition substrates present in the ICA, and is thus available to act as a surface onto which astrophysical ice analogues may be condensed. The deposition of an ice onto the cold surface of the QCM causes a damping of the resonance frequency. This frequency decrease is related to the mass of the deposited ice M through the Sauerbrey relation (Sauerbrey 1959):

$$\Delta\nu = -kM \quad (\text{Eq. 9.9})$$

where k is a constant (Hz g^{-1}) which takes into account the resonant frequency of the fundamental mode, the density and shear modulus of quartz, and the piezoelectrically active crystal area. The thickness of the ice deposited onto the QCM may be determined *via* laser interferometry as described above. As the surface area of the QCM onto which the ice was deposited is known, the volume of the ice may be easily calculated by multiplying this surface area by the measured thickness. The density is thus simply the ratio of the mass deposited to the volume of the ice.

It is therefore evident that the inclusion of two helium-neon lasers (and their respective photodiodes) as well as a QCM would greatly expand the experimental capabilities of the ICA by allowing independent measurements of the thicknesses of deposited ices, as well as the determination of mid-infrared integrated band strength constants, refractive indices, and ice densities. For this reason, these upgrades should be considered to be of high priority.

9.3.4 Quadrupole Mass Spectrometry

One notable feature of this thesis is the lack of mass spectrometric data presented. As described in Chapter 4, the ICA is equipped with a quadrupole mass spectrometer (QMS) which is able to provide a semi-quantitative indication of the gas-phase species within the chamber. Such information is particularly useful during ion irradiation and thermal annealing experiments, as it provides an important insight into the nature of those species sputtered or desorbed as a result of these respective processes. Despite this, no data collected by the QMS has been included in this thesis.

The reason for this is fairly mundane: during one of the major campaigns during which a significant amount of the data presented in this thesis was collected, the QMS developed a fault and had to be returned to the manufacturer for servicing for a number of weeks. In light of this unfortunate happenstance, it was decided that the focus of this thesis should be the radiation astrochemistry discerned through mid-infrared absorption spectroscopy, thus coherently linking the results presented in each chapter of the thesis. Future studies focusing on the nature and extent of radiation induced sputtering and desorption, as well as thermally induced sublimation, making extensive use of the QMS are planned.

It should be noted, however, that these planned future studies will not be performed using the Pfeiffer QME200 QMS that was initially installed to the ICA due to the fact that this device is only able to detect fragments with a mass-to-charge ratio of up to 200 amu and scans through this range of masses over a comparatively slow time-scale of a few minutes. A new QMS (Pfeiffer QMG250-F3) which is able to detect fragments with a mass-to-charge ratio of up to 300 amu and which is able to scan through this range of masses in about 2.5 seconds has very recently been installed to the ICA, and so future studies will be performed with this instrument.

9.3.5 Improved Simulation of Astrophysical Surfaces

The final suggested improvement to the experimental astrochemistry facility at Atomki is not an upgrade to the ICA itself, but is rather a recommendation in favour of commissioning an ancillary instrument tasked with better simulating the surface morphologies of interstellar dust grains and Solar System objects. The poor analogue provided by the ZnSe and metallic deposition substrates traditionally used in most experimental astrochemistry chambers was discussed in Section 4.4: however, recent progress has allowed for the design and development of novel set-ups able to levitate and spectroscopically characterise interstellar dust grain analogues in an ultrasonic trap (Mason *et al.* 2008, Brotton and Kaiser 2013, Dangi and Dickerson 2021).

Ultrasonic levitation is a specific example of the more generalised concept of acoustic levitation, in which a standing wave is generated in a gaseous medium (such as a noble gas or dry nitrogen) *via* the reflection of an ultrasonic wave of known frequency produced by a piezoelectric transducer. Given the known speed of sound in air (344 m s^{-1} at $20 \text{ }^\circ\text{C}$ and under atmospheric pressure), the wavelength of the standing wave may be estimated as the ratio of this speed to the oscillatory frequency. Knowledge of this wavelength allows the distance between the transducer and the reflector plate to be set to a specified distance within which a known number of nodal points exist. Any solid or liquid particles coincident in space with the standing wave are subjected to so-called acoustic radiation pressure resulting in a hydrodynamic force that counteracts gravity, thus suspending (i.e., levitating) the particles in the anti-nodal points of the standing wave which correspond to the pressure minima (Wang and Lee 1998, Brandt 2001, Xie and Wei 2001). It should be noted that, in order for a particle to be levitated in this way, it must have a maximum diameter that is smaller than the wavelength of the ultrasonic wave.

The main advantage of ultrasonic levitation is that solid dust particles of irregular (i.e., fractal) geometries and dimensions may be studied spectroscopically by incorporating the transducer and reflector into a chamber which is first evacuated before being filled to a desired pressure with a gaseous medium in which the standing wave is formed (Fig. 9.3). For example, Brotton and Kaiser (2013) successfully levitated epsomite ($\text{MgSO}_4 \cdot 7\text{H}_2\text{O}$) and gypsum ($\text{CaSO}_4 \cdot 2\text{H}_2\text{O}$) microparticles and studied their Raman spectroscopy both before and after heating using a CO_2 laser. They found that heating efficiently abstracts H_2O molecules from the crystal structure thus producing new mineral phases in varying stages of dehydration; most notably sanderite ($\text{MgSO}_4 \cdot 2\text{H}_2\text{O}$), bassanite ($\text{CaSO}_4 \cdot \frac{1}{2}\text{H}_2\text{O}$), and anhydrite (CaSO_4). Dangi and Dickerson (2021) used a similar set-up to demonstrate that the Raman spectra of small particles of polystyrene show evidence of efficient amorphisation as a result of their irradiation by ultraviolet photons, while the particles themselves undergo visible blackening after more prolonged irradiation.

Furthermore, the chemistry in which interstellar dust grain surfaces partake as a result of energetic processing may also be probed in the ultrasonic trap: if the gaseous medium in which the ultrasonic standing wave is generated is not an inert gas (e.g., CO_2 , SO_2 , N_2O), then gas molecules may react with the dust grain during its energetic processing *via* laser-induced heating, ultraviolet photon irradiation, or ion or electron beam irradiation. The resultant chemical changes may be studied *in situ* using various spectroscopic techniques, as well as *ex situ* after recovery of the particulate sample. Indeed, such an experimental methodology may lend itself to not only understanding chemical and mineralogical processes that occur in interstellar space, but may also provide an insight into processes occurring in terrestrial environments such as hydrothermal vents.

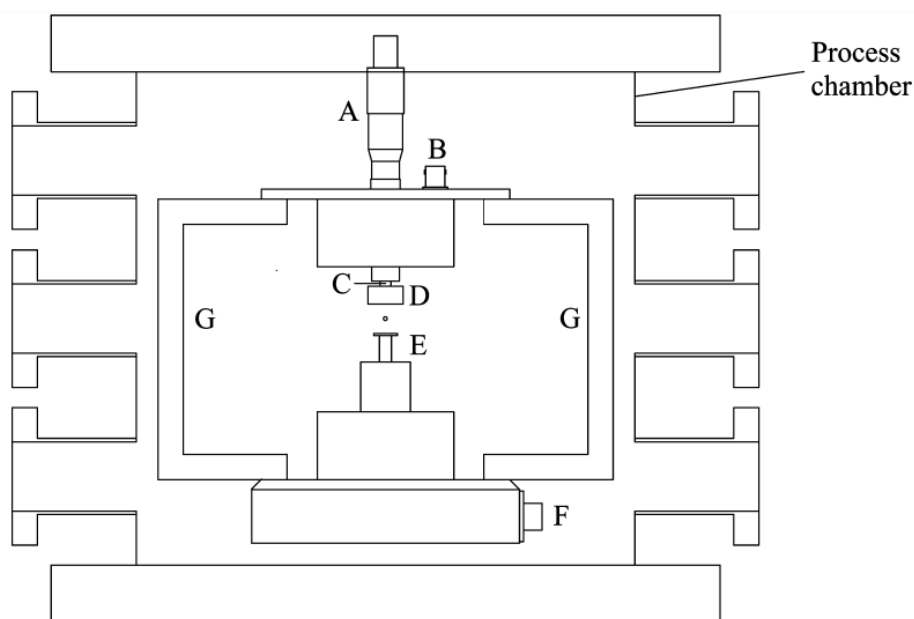


Fig. 9.3: Schematic diagram of a process chamber containing an ultrasonic levitator as constructed by Brotton and Kaiser (2013). Ultrasonic sound waves generated by the piezoelectric transducer (E) are reflected by a concave reflector (D), thus generating a standing wave. A linear manipulator (A) allows the distance between the transducer and reflector to be adjusted to accommodate a desired number of half-integer wavelengths. The pressure amplitude of the standing wave is monitored by connecting the output of the piezoelectric sensor (C) *via* a connector (B) to an oscilloscope. The radio frequency power to the transducer is supplied by a separate connector (F). A support structure (G) is also included.

By enclosing the ultrasonic levitator within a chamber, it is possible to control the humidity of the gaseous medium in which the standing wave is generated either by using a humidity controller or by mixing anhydrous and H₂O-saturated gas in different combinations (Schlegel *et al.* 2012). The introduction of H₂O to the gaseous medium would allow it to participate in chemical reactions and processes with the levitated dust particles, such as mineral rehydration (Brotton and Kaiser 2013). Furthermore, Mason *et al.* (2008) noted that H₂O from humid gaseous media may actually condense onto the dust particles, thus producing a realistic interstellar icy grain analogue. This phenomenon is the result of the decreased temperature at the pressure minima of the standing wave, in line with Amonton's Law (Bauerecker and Neidhart 1998).

From an astrochemical perspective, the cooling of the gaseous medium surrounding the levitated dust particles is highly desirable, as it allows for condensation processes and surface interactions relevant to interstellar chemistry and planetary science to be studied at relevant temperatures. There is, for example, a strong motivation to further characterise the mid-infrared spectra of various ices deposited onto levitated carbonaceous dust grains, as previous studies have suggested that these may differ in appearance to mid-infrared spectra of ices deposited onto flat optical windows serving as deposition substrates (Mason *et al.* 2008). Indeed, suggestions have been made with regards to incorporating closed-cycle helium cryostats or liquid nitrogen cooling systems into the overall design of the experimental set-up (Brotton and Kaiser 2013, Dangi and Dickerson 2021).

Lastly, it should be noted that some unwanted processes may occur within an ultrasonic trap, most notably microparticle coagulation and clumping (Mason *et al.* 2008). The probability of clumping is a function of the frequency of the generated standing wave and of the diameter of the particles. For instance, Mason *et al.* (2008) stated that the optimum frequency for the clumping of microparticles 0.1-10 μm in diameter is about 27 kHz. Therefore, if the oscillatory frequency of the standing wave is close to this value, microparticles in this size range will efficiently coagulate. Fortunately, the optimum frequency for clumping is also inversely related to the gas pressure, and so this problem may be easily circumvented by increasing the pressure of the gas within the process chamber thus driving the optimum clumping frequency to lower values.

The scientific advantages gained through the construction of an ultrasonic trap in more accurately modelling interstellar dust grain and planetary surfaces are therefore significant. The individual components of such a set-up are also commercially available and, with the exception of the spectrophotometers, are not particularly expensive. Once constructed, the set-up would be sufficiently versatile as to allow for studies to be conducted that may bear relevance to other fields of research, such as atmospheric chemistry and combustion science.

9.4 Summary

In this chapter, a summative overview of the outcomes of this thesis and suggestions for future research in this field have been provided. The chapter begins with a detailed evaluation of the experimental results obtained and to what extent these answer the questions that were initially posed in Chapter 1. A thorough discussion of possible future experiments that build off the results presented throughout this thesis has also been included, with a particular focus on further spectroscopic characterisations, radiation chemistry, and new experiments bridging the gap between astrochemistry and isotope geochemistry. The chapter concludes with a series of suggested upgrades to the ICA set-up which would greatly expand its experimental capabilities, as well as a concise but detailed discussion on the recommended commissioning of an ancillary ultrasonic trap that would allow for a more accurate study of interstellar dust grain and planetary surfaces.

APPENDIX A:

SRIM CALCULATION OUTPUT GRAPHS

In this appendix, the output graphs for the various SRIM calculations performed as part of this thesis are presented. The graphs depict the ion ranges for projectile ions impacting molecular ices for the ion irradiation experiments considered herein. Physical parameters considered in each simulation (e.g., ice thickness, density, temperature, etc.) are provided in each figure caption.

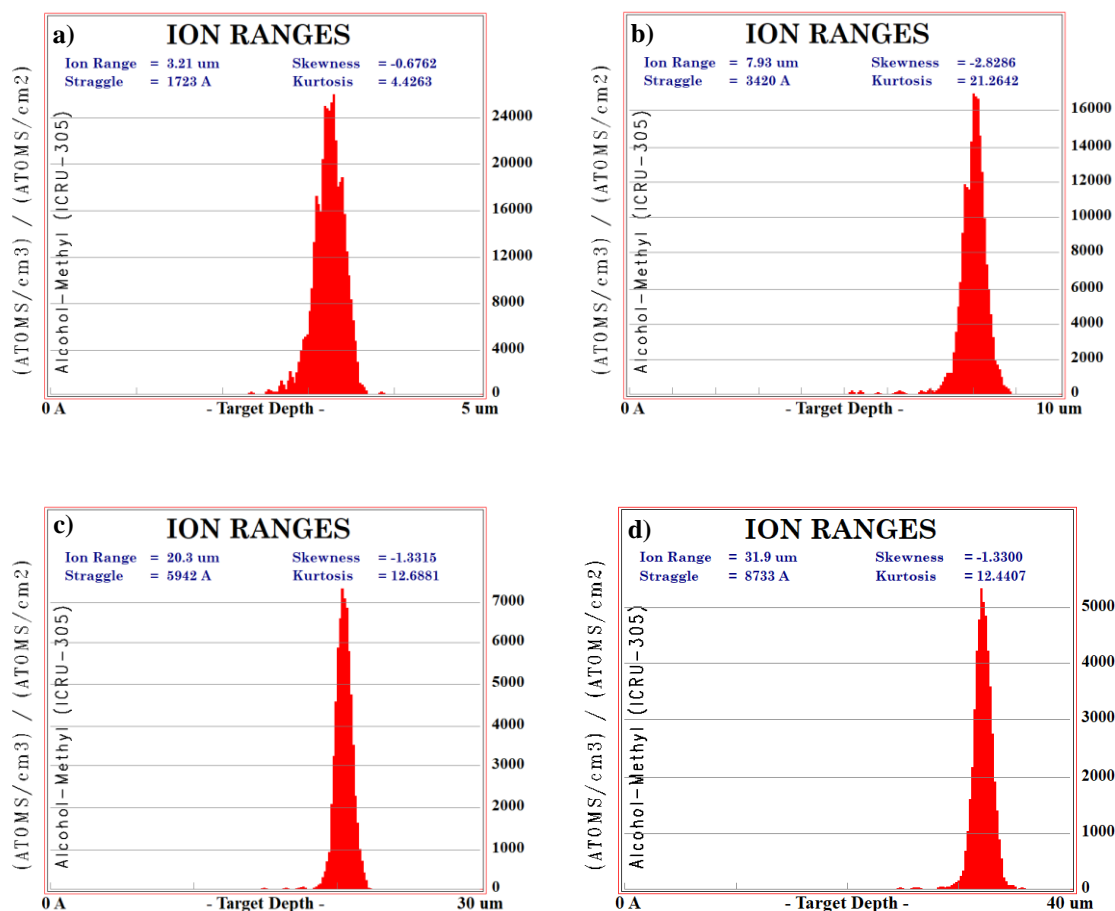


Fig. A.1: SRIM output graphs demonstrating the projectile ion penetration profile of *a*) 200 keV, *b*) 400 keV, *c*) 750 keV, and *d*) 1 MeV protons impacting an amorphous CH₃OH ice ($\rho = 0.636 \text{ g cm}^{-3}$) at 20 K and at an incidence angle of 36° to the normal. These irradiations were discussed in Chapter 4.

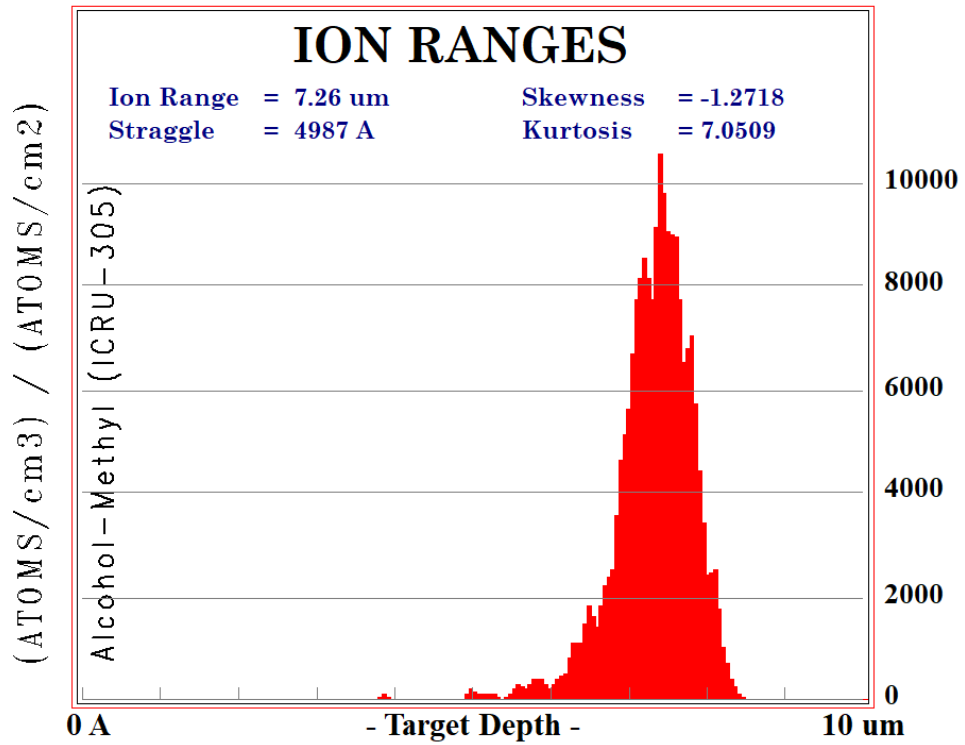


Fig. A.2: SRIM output graph demonstrating the projectile ion penetration profile of a 6 MeV S^+ ion beam impacting an amorphous CH_3OH ice ($\rho = 0.636 \text{ g cm}^{-3}$) at 20 K and at an incidence angle of 36° to the normal. The irradiation of this ice by a 6 MeV S^{2+} ion was discussed in Chapter 4; however, SRIM is not able to perform calculations for multiply charged projectile ions.

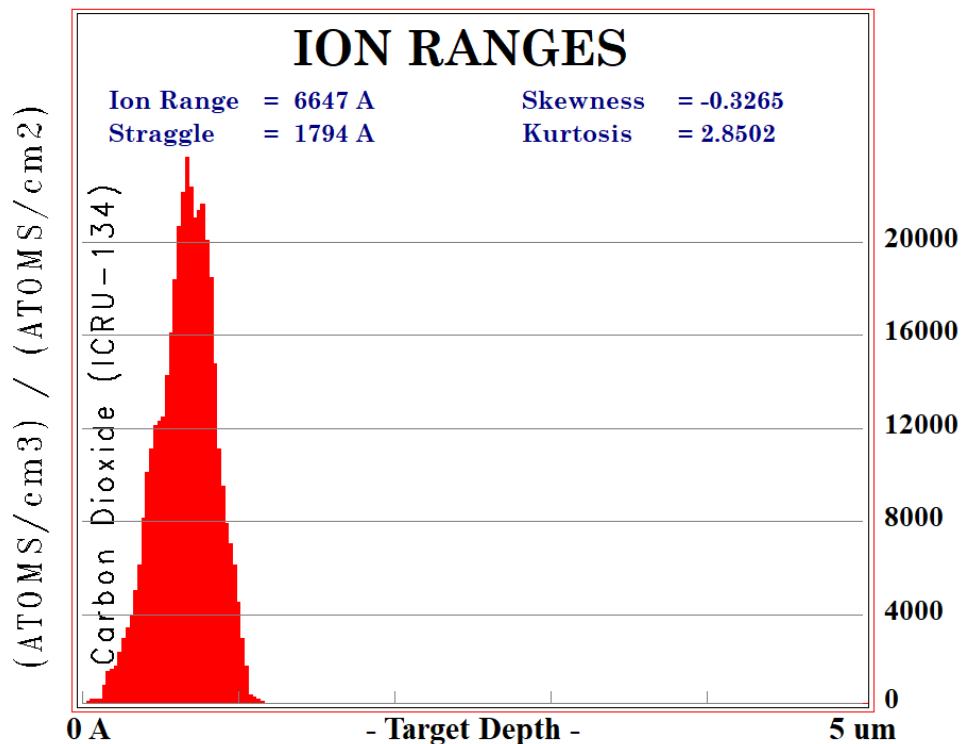


Fig. A.3: SRIM output graph demonstrating the projectile ion penetration profile of a 290 keV S^+ ion beam impacting an amorphous CO_2 ice ($\rho = 0.98 \text{ g cm}^{-3}$) at 20 K and at an incidence angle of 36° to the normal. This irradiation was discussed in Chapter 7.

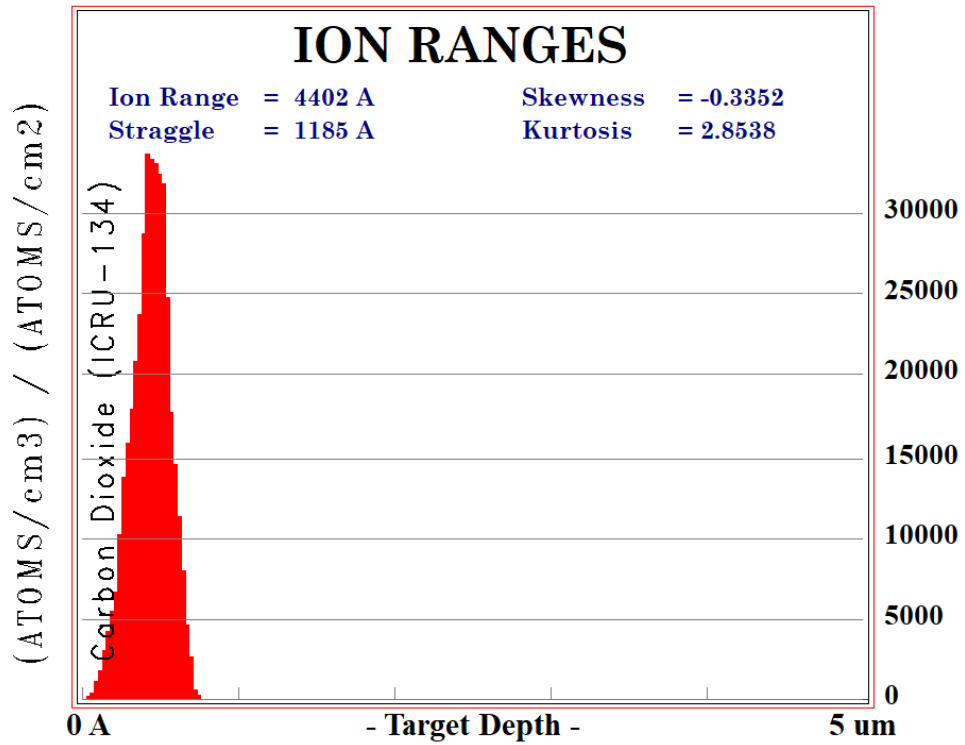


Fig. A.4: SRIM output graph demonstrating the projectile ion penetration profile of a 290 keV S^+ ion beam impacting a crystalline CO_2 ice ($\rho = 1.48 \text{ g cm}^{-3}$) at 70 K and at an incidence angle of 36° to the normal. This irradiation was discussed in Chapter 7.

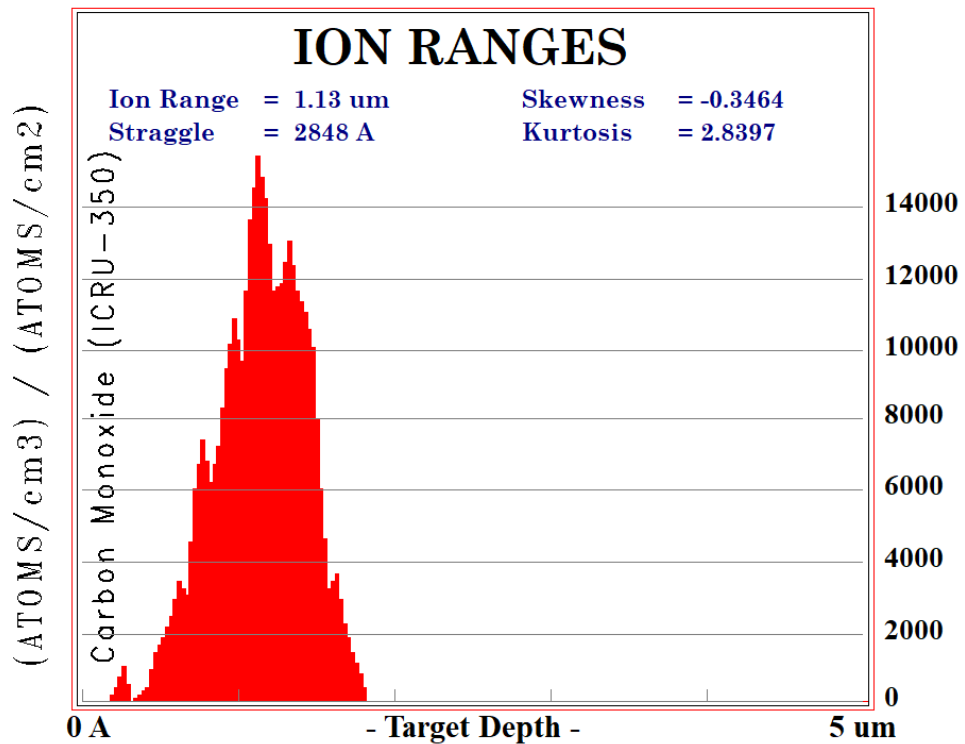


Fig. A.5: SRIM output graph demonstrating the projectile ion penetration profile of a 400 keV S^+ ion beam impacting a CO ice ($\rho = 0.8 \text{ g cm}^{-3}$) at 20 K and at an incidence angle of 36° to the normal. This irradiation was discussed in Chapter 7.

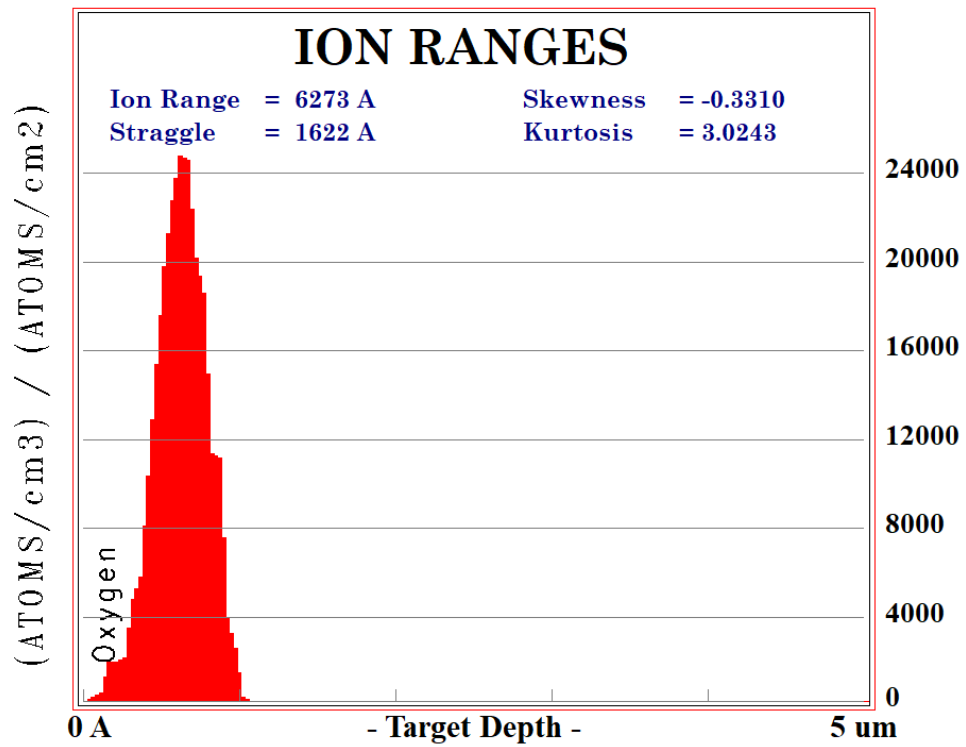


Fig. A.6: SRIM output graph demonstrating the projectile ion penetration profile of a 400 keV S^+ ion beam impacting a crystalline O_2 ice ($\rho = 1.54 \text{ g cm}^{-3}$) at 20 K and at an incidence angle of 36° to the normal. This irradiation was discussed in Chapter 7.

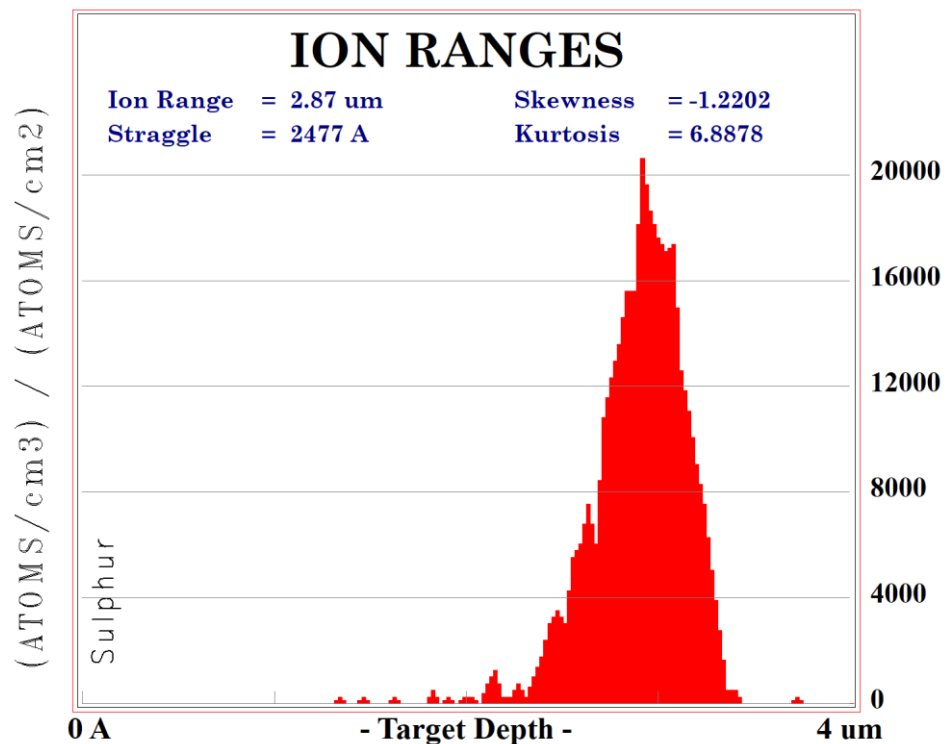


Fig. A.7: SRIM output graph demonstrating the projectile ion penetration profile of a 1 MeV He^+ ion beam impacting a pure elemental sulphur layer ($\rho = 2.07 \text{ g cm}^{-3}$) at 20 K and at an incidence angle of 36° to the normal. Although this irradiation was not performed, this information is useful for the interpretation of the data presented in Chapter 8.

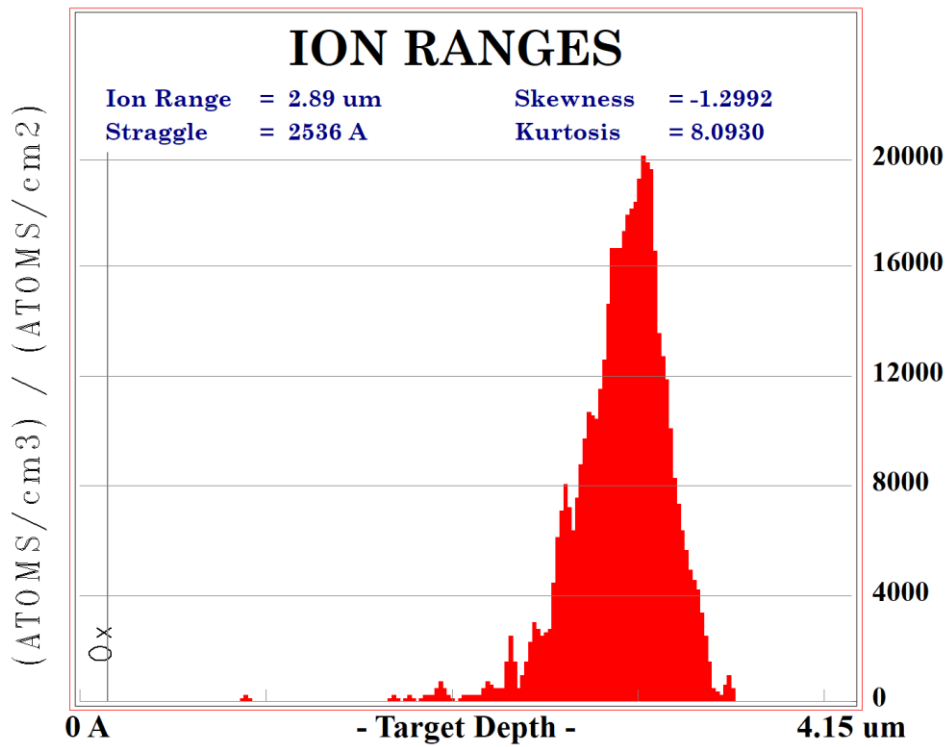


Fig. A.8: SRIM output graph demonstrating the projectile ion penetration profile of a 1 MeV He⁺ ion beam impacting a crystalline O₂ ice ($\rho = 1.54 \text{ g cm}^{-3}$) of thickness 0.20 μm deposited on top of a layer of elemental sulphur at 20 K and at an incidence angle of 36° to the normal. This irradiation was discussed in Chapter 8.

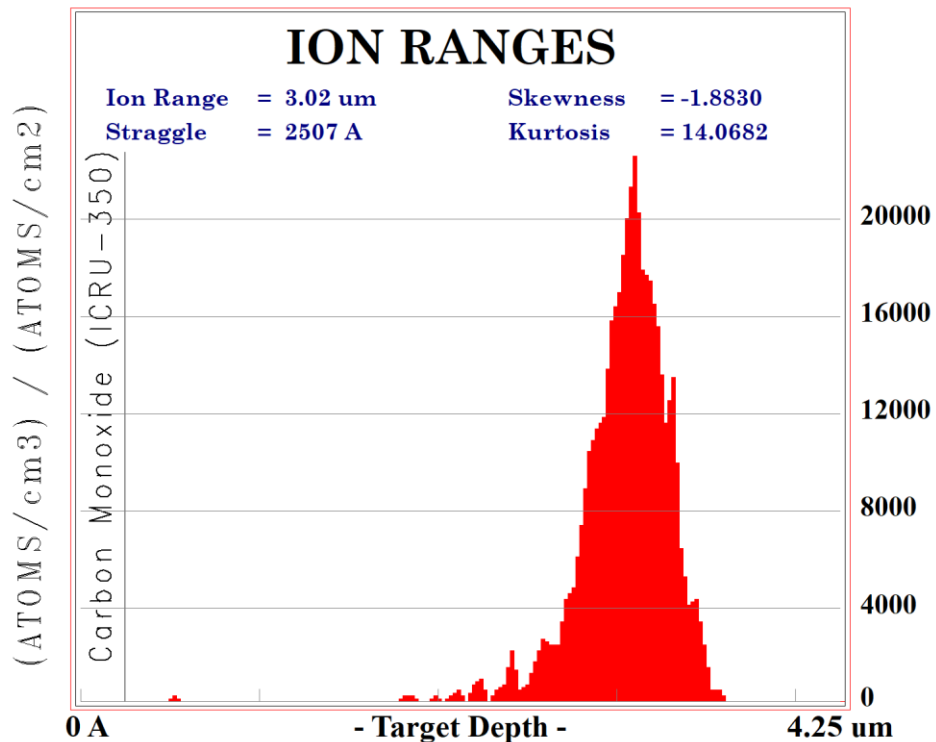


Fig. A.9: SRIM output graph demonstrating the projectile ion penetration profile of a 1 MeV He⁺ ion beam impacting a CO ice ($\rho = 0.8 \text{ g cm}^{-3}$) of thickness 0.20 μm deposited on top of a layer of elemental sulphur at 20 K and at an incidence angle of 36° to the normal. This irradiation was discussed in Chapter 8.

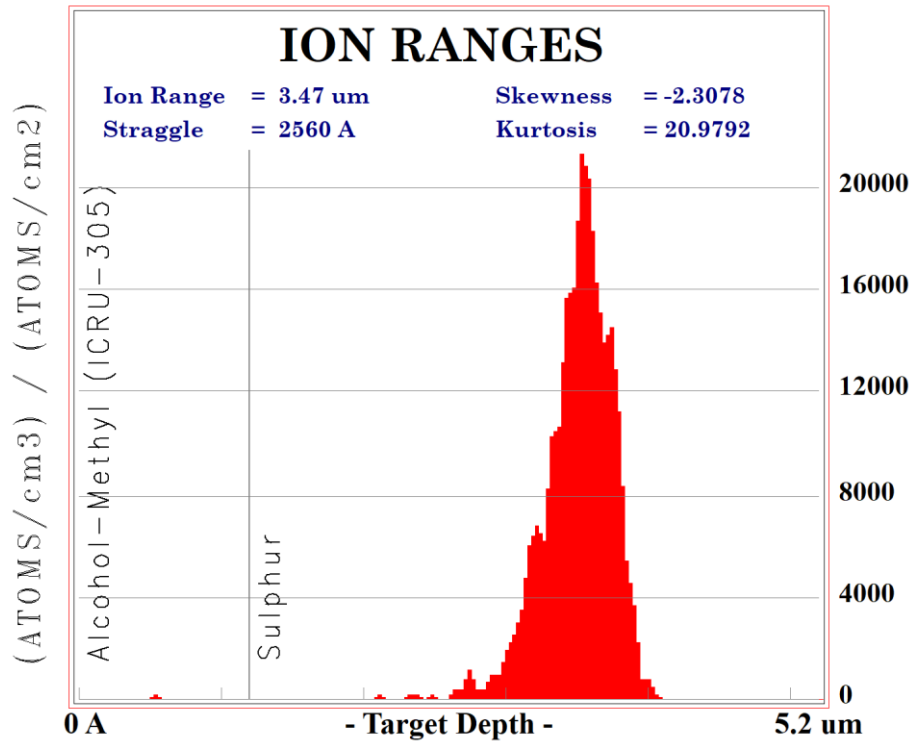


Fig. A.10: SRIM output graph demonstrating the projectile ion penetration profile of a 1 MeV He^+ ion beam impacting an amorphous CH_3OH ice ($\rho = 0.636 \text{ g cm}^{-3}$) of thickness $1.30 \text{ }\mu\text{m}$ deposited on top of a layer of elemental sulphur at 20 K and at an incidence angle of 36° to the normal. This irradiation was discussed in Chapter 8.

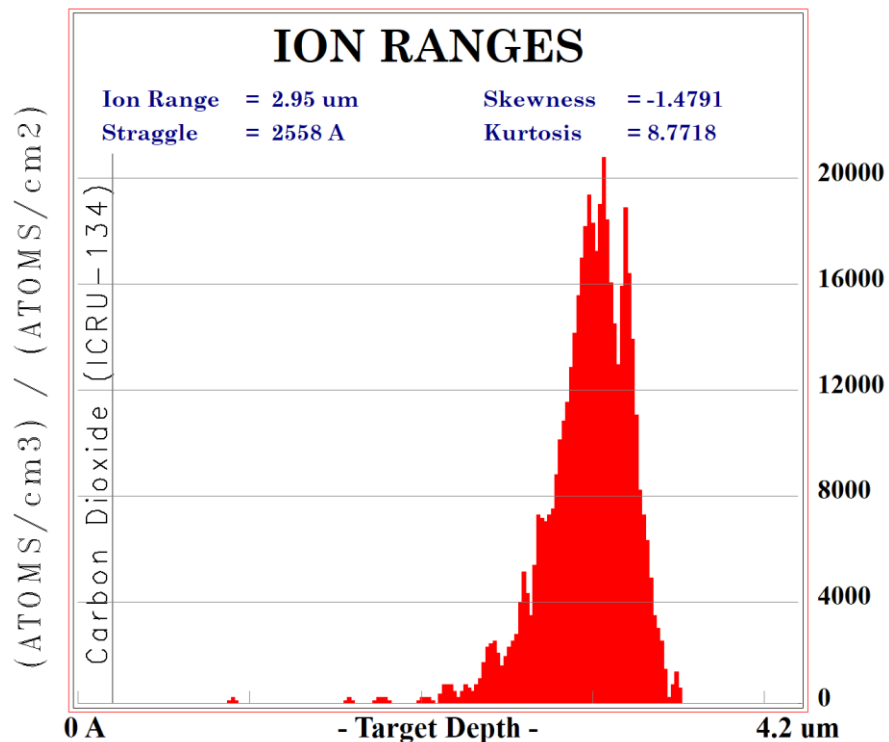


Fig. A.11: SRIM output graph demonstrating the projectile ion penetration profile of a 1 MeV He^+ ion beam impacting an amorphous CO_2 ice ($\rho = 0.98 \text{ g cm}^{-3}$) of thickness $0.07 \text{ }\mu\text{m}$ deposited on top of a layer of elemental sulphur at 20 K and at an incidence angle of 36° to the normal. This irradiation was discussed in Chapter 8.

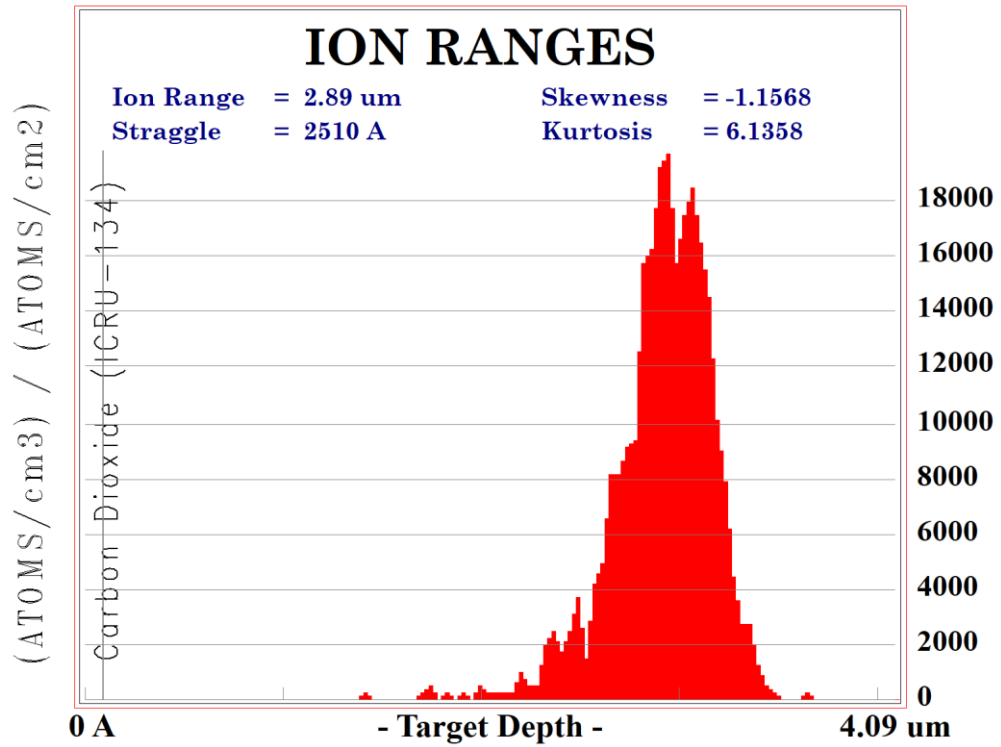


Fig. A.12: SRIM output graph demonstrating the projectile ion penetration profile of a 1 MeV He⁺ ion beam impacting a crystalline CO₂ ice ($\rho = 1.48 \text{ g cm}^{-3}$) of thickness 0.05 μm deposited on top of a layer of elemental sulphur at 70 K and at an incidence angle of 36° to the normal. This irradiation was discussed in Chapter 8.

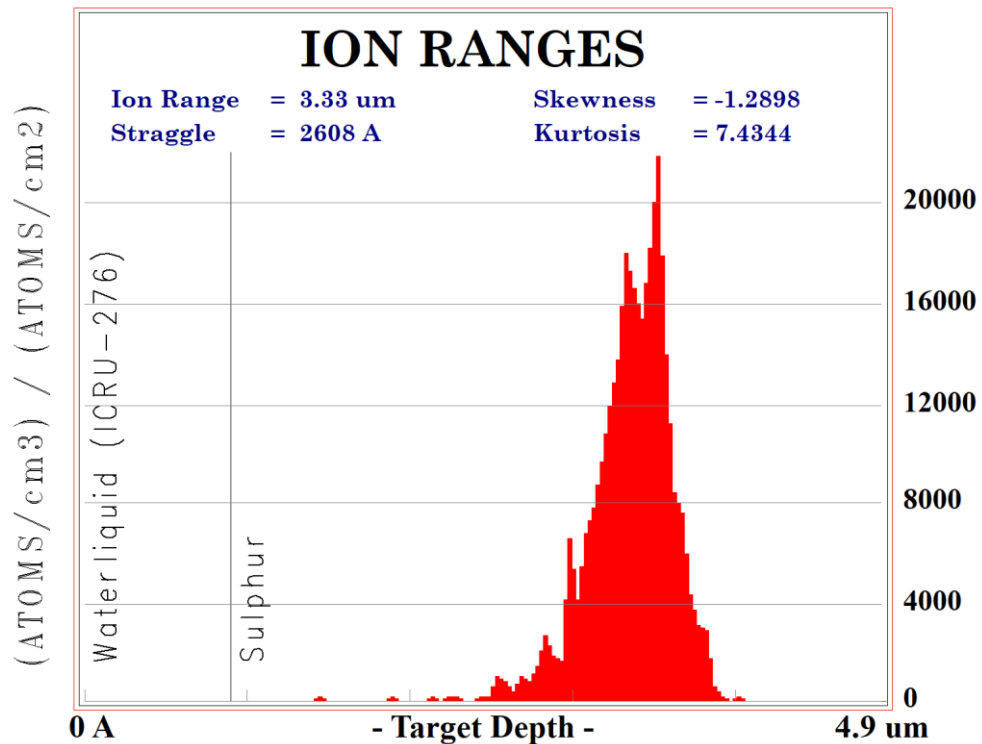


Fig. A.13: SRIM output graph demonstrating the projectile ion penetration profile of a 1 MeV He⁺ ion beam impacting an amorphous H₂O ice ($\rho = 0.94 \text{ g cm}^{-3}$) of thickness 1.20 μm deposited on top of a layer of elemental sulphur at 20 K and at an incidence angle of 36° to the normal. This irradiation was discussed in Chapter 8.

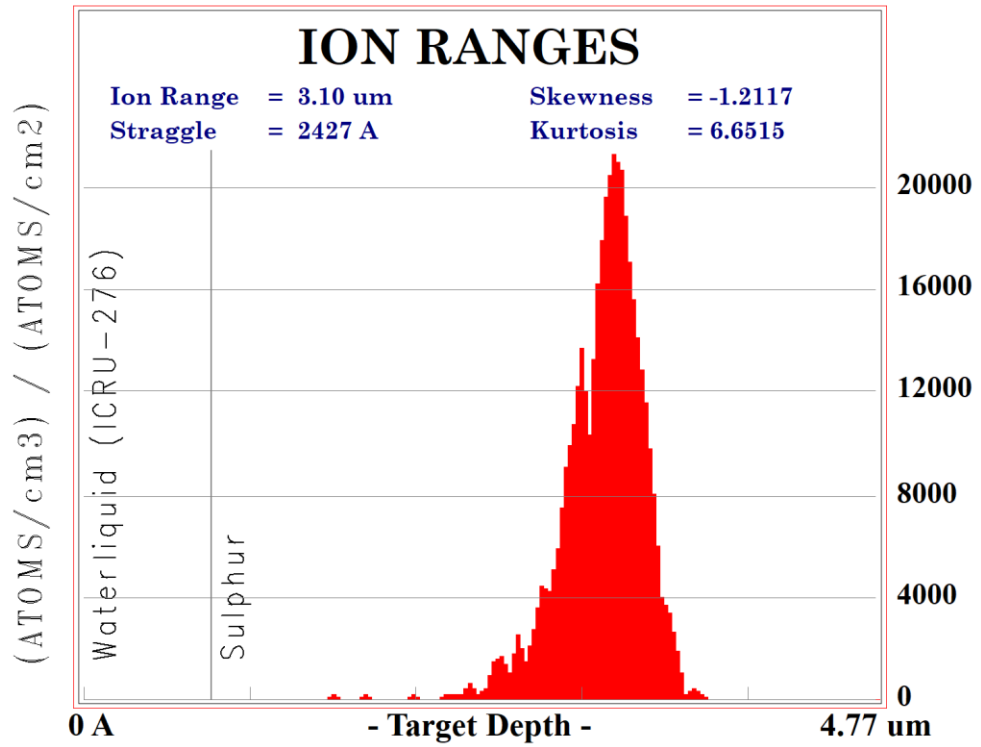


Fig. A.14: SRIM output graph demonstrating the projectile ion penetration profile of a 1 MeV He^+ ion beam impacting an amorphous H_2O ice ($\rho = 0.94 \text{ g cm}^{-3}$) of thickness $1.00 \mu\text{m}$ deposited on top of a layer of elemental sulphur at 70 K and at an incidence angle of 36° to the normal. This irradiation was discussed in Chapter 8.

APPENDIX B:

CASINO CALCULATION OUTPUT GRAPHS

In this appendix, the output graphs for the various CASINO calculations performed as part of this thesis are presented. The graphs depict the penetration depths for projectile electrons impacting molecular ices for the electron irradiation experiments considered herein. Physical parameters considered in each simulation (e.g., ice thickness, density, temperature, etc.) are provided in each figure caption.

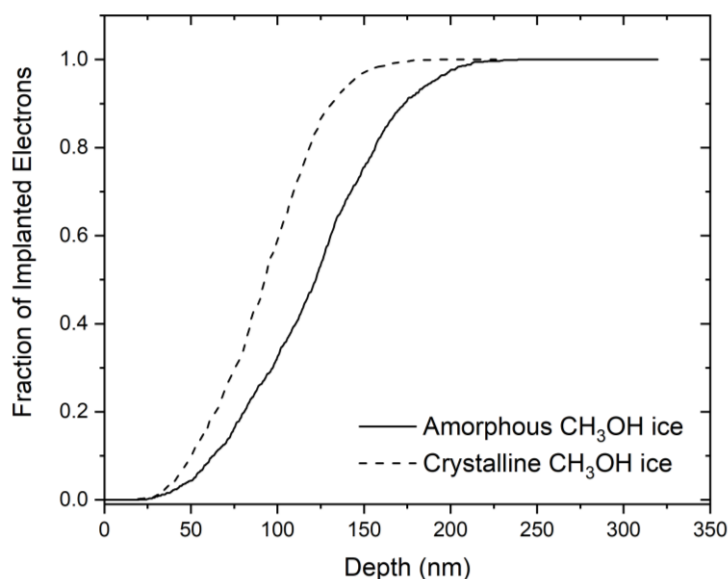


Fig. B.1: CASINO output graph demonstrating the projectile electron penetration profile of a 2 keV electron beam impacting an amorphous ($\rho = 0.636 \text{ g cm}^{-3}$) and a crystalline ($\rho = 0.838 \text{ g cm}^{-3}$) CH₃OH ice at 20 K and at an incidence angle of 36° to the normal. These irradiations were discussed in Chapters 4 and 6.

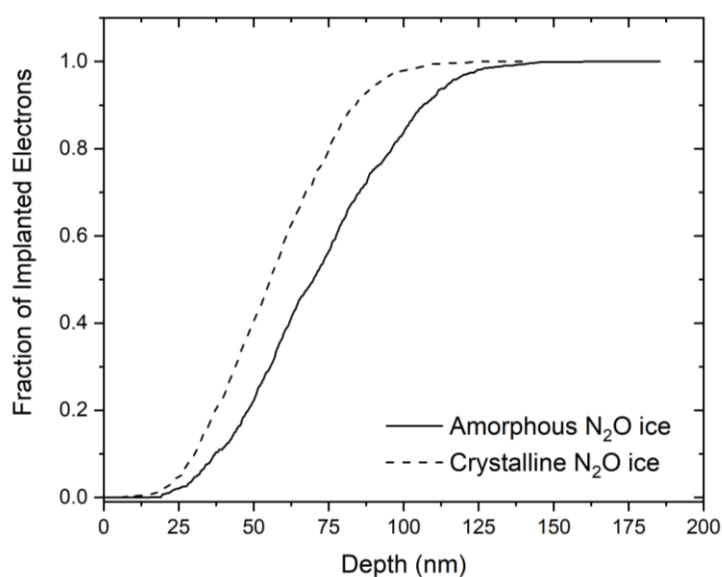


Fig. B.2: CASINO output graph demonstrating the projectile electron penetration profile of a 2 keV electron beam impacting an amorphous ($\rho = 1.263 \text{ g cm}^{-3}$) and a crystalline ($\rho = 1.591 \text{ g cm}^{-3}$) N₂O ice at 20 K and at an incidence angle of 36° to the normal. These irradiations were discussed in Chapter 6.

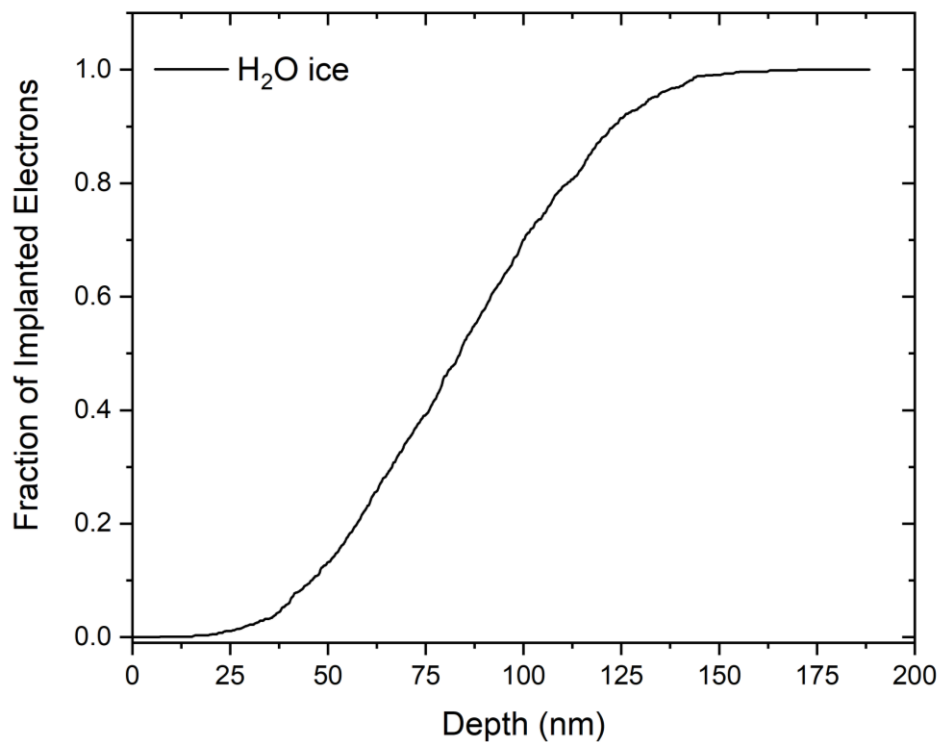


Fig. B.3: CASINO output graph demonstrating the projectile electron penetration profile of a 2 keV electron beam impacting a H₂O ice ($\rho = 0.94 \text{ g cm}^{-3}$) at 20 K and at an incidence angle of 36° to the normal. This irradiation was discussed in Chapter 6.

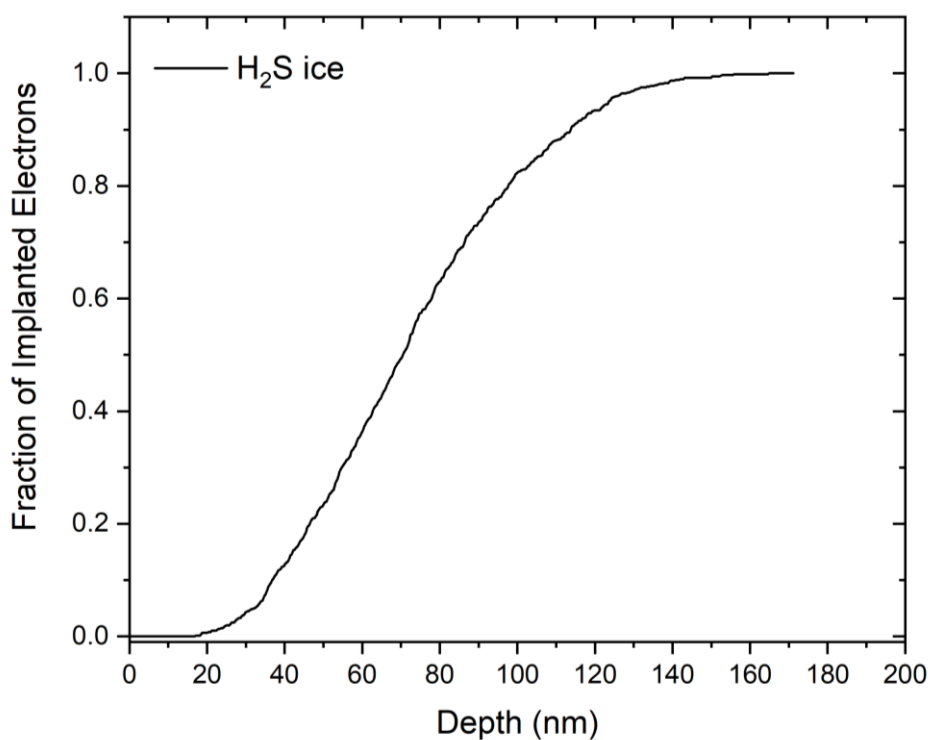


Fig. B.4: CASINO output graph demonstrating the projectile electron penetration profile of a 2 keV electron beam impacting a H₂S ice ($\rho = 1.22 \text{ g cm}^{-3}$) at 20 K and at an incidence angle of 36° to the normal. This irradiation was discussed in Chapter 6.

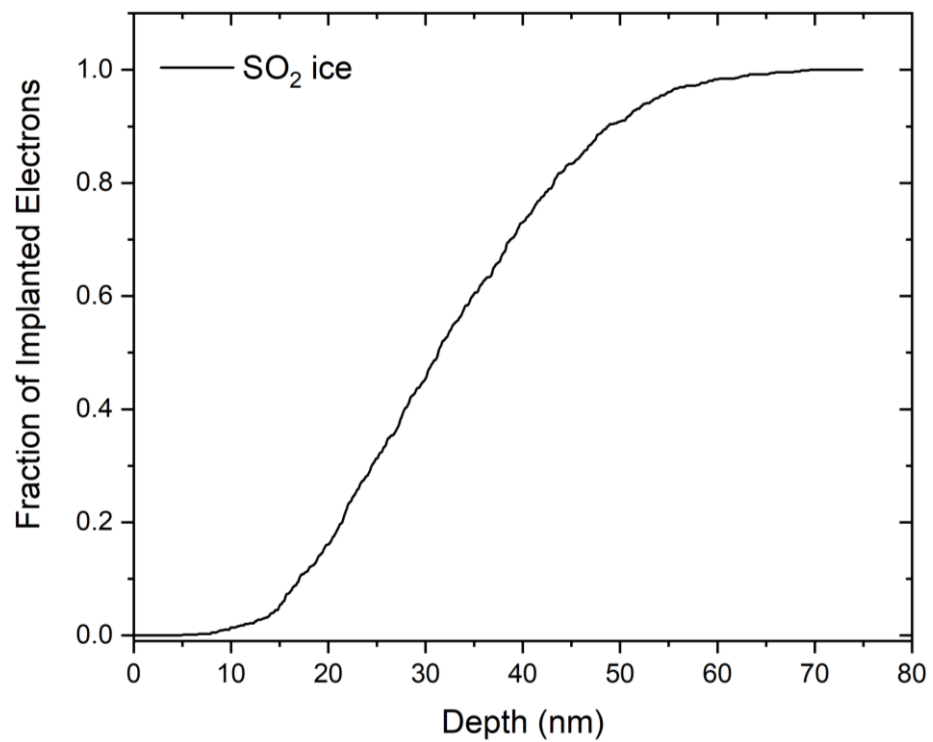


Fig. B.5: CASINO output graph demonstrating the projectile electron penetration profile of a 1.5 keV electron beam impacting a SO₂ ice ($\rho = 1.89 \text{ g cm}^{-3}$) at 20 K and at an incidence angle of 36° to the normal. This irradiation was discussed in Chapter 6.

Publications, Posters, and Presentations

Publications

1	Authors	DV Mifsud, Z Kaňuchová, P Herczku, S Ioppolo, Z Juhász, STS Kovács, NJ Mason, RW McCullough, B Sulik.
	Title	Sulphur Ice Astrochemistry: A Review of Laboratory Studies.
	Reference	<i>Space Science Reviews</i> , 2021 , 217, 14.
2	Authors	<u>DV Mifsud</u> , Z Juhász, P Herczku, STS Kovács, S Ioppolo, Z Kaňuchová, M Czentye, PA Hailey, A Traspas Muiña, NJ Mason, RW McCullough, B Paripás, B Sulik.
	Title	Electron Irradiation and Thermal Chemistry Studies of Interstellar and Planetary Ice Analogues at the ICA Astrochemistry Facility.
	Reference	<i>European Physical Journal D</i> , 2021 , 75, 182.
3	Authors	P Herczku, <u>DV Mifsud</u> , S Ioppolo, Z Juhász, Z Kaňuchová, STS Kovács, A Traspas Muiña, PA Hailey, I Rajta, I Vajda, NJ Mason, RW McCullough, B Paripás, B Sulik.
	Title	The Ice Chamber for Astrophysics-Astrochemistry (ICA): A New Experimental Facility for Ion Impact Studies of Astrophysical Ice Analogues.
	Reference	<i>Review of Scientific Instruments</i> , 2021 , 92, 084501.
4	Authors	S Biri, R Rácz, Gy Gyürky, F Fülöp, Z Juhász, B Sulik, <u>DV Mifsud</u> .
	Title	Astrophysics, Astrochemistry, and Laboratory Space Research with Particle Accelerators.
	Reference	<i>Gruppi Italiani di Astrofisica Nucleare e Sperimentale</i> , 2021 , 13, 9.
5	Authors	<u>DV Mifsud</u> , PA Hailey, A Traspas Muiña, O Auriacombe, NJ Mason, S Ioppolo.
	Title	The Role of Terahertz and Far-IR Spectroscopy in Understanding the Formation and Evolution of Interstellar Prebiotic Molecules.
	Reference	<i>Frontiers in Astronomy and Space Science</i> , 2021 , 8, 757619.
6	Authors	NJ Mason, PA Hailey, <u>DV Mifsud</u> , JS Urquhart.
	Title	Systems Astrochemistry: A New Doctrine for Experimental Studies.
	Reference	<i>Frontiers in Astronomy and Space Science</i> , 2021 , 8, 739046.
7	Authors	<u>DV Mifsud</u> , Z Kaňuchová, S Ioppolo, P Herczku, A Traspas Muiña, TA Field, PA Hailey, Z Juhász, STS Kovács, NJ Mason, RW McCullough, S Pavithraa, KK Rahul, B Paripás, B Sulik, SL Chou, JI Lo, A Das, BM Cheng, BN Rajasekhar, A Bhardwaj, B Sivaraman.
	Title	Mid-IR and VUV Spectral Characterisation of Thermally Processed and Electron Irradiated CO ₂ Astrophysical Ice Analogues.
	Reference	<i>Journal of Molecular Spectroscopy</i> , 2022 , 385, 111599.
8	Authors	<u>DV Mifsud</u> , PA Hailey, P Herczku, B Sulik, Z Juhász, STS Kovács, Z Kaňuchová, S Ioppolo, RW McCullough, B Paripás, NJ Mason.
	Title	Comparative Electron Irradiations of Amorphous and Crystalline Astrophysical Ice Analogues.
	Reference	<i>Physical Chemistry Chemical Physics</i> , 2022 , 24, 10974.
9	Authors	<u>DV Mifsud</u> , PA Hailey, P Herczku, Z Juhász, STS Kovács, B Sulik, S Ioppolo, Z Kaňuchová, RW McCullough, B Paripás, NJ Mason.
	Title	Laboratory Experiments on the Radiation Astrochemistry of Water Ice Phases.
	Reference	<i>European Physical Journal D</i> , 2022 , 76, 87.

10	Authors	<u>DV Mifsud</u> , Z Kaňuchová, S Ioppolo, P Herczku, A Traspas Muiña, B Sulik, KK Rahul, STS Kovács, PA Hailey, RW McCullough, NJ Mason, Z Juhász.
	Title	Ozone Production in Electron Irradiated CO ₂ :O ₂ Ices.
	Reference	<i>Physical Chemistry Chemical Physics</i> , 2022 , <i>24</i> , 18169.
11	Authors	S Pavithraa, R Ramachandran, <u>DV Mifsud</u> , JK Meka, JI Lo, SL Chou, BM Cheng, BN Rajasekhar, A Bhardwaj, NJ Mason, B Sivaraman.
	Title	VUV Photoabsorption of Thermally Processed Carbon Disulphide and Ammonia Ice Mixtures.
	Reference	<i>Spectrochimica Acta A</i> , 2022 , <i>283</i> , 121645.
12	Authors	<u>DV Mifsud</u> , P Herczku, R Rácz, KK Rahul, STS Kovács, Z Juhász, B Sulik, S Biri, RW McCullough, Z Kaňuchová, S Ioppolo, PA Hailey, NJ Mason.
	Title	Energetic Electron Irradiations of Amorphous and Crystalline Sulphur-Bearing Astrochemical Ices.
	Reference	<i>Frontiers in Chemistry</i> , 2022 , <i>10</i> , 1003163.
13	Authors	<u>DV Mifsud</u> , Z Kaňuchová, P Herczku, Z Juhász, STS Kovács, G Lakatos, KK Rahul, R Rácz, B Sulik, S Biri, I Rajta, I Vajda, S Ioppolo, RW McCullough, NJ Mason.
	Title	Sulphur Ion Implantations into Condensed CO ₂ : Implications for Europa.
	Reference	<i>Geophysical Research Letters</i> , 2022 , <i>49</i> , e2022GL100698.
14	Authors	Z Juhász, STS Kovács, V Vizcaíno, P Herczku, S Demes, R Rácz, B Sulik, S Biri, N Sens, <u>DV Mifsud</u> , JY Chesnel.
	Title	Molecular-Rotation-Induced Splitting of the Binary Ridge in the Velocity Map of Sub-eV H ⁺ Ions Ejected from H ₂ Molecules by Ion Impact.
	Reference	<i>Physical Review A</i> , 2023 , <i>107</i> , L010801.
15	Authors	AV Ivlev, BM Giuliano, Z Juhász, P Herczku, B Sulik, <u>DV Mifsud</u> , STS Kovács, KK Rahul, R Rácz, S Biri, I Rajta, I Vajda, NJ Mason, S Ioppolo, P Caselli.
	Title	Bombardment of CO Ice by Cosmic Rays: I. Experimental Insights into the Microphysics of Molecule Destruction and Sputtering.
	Reference	<i>Astrophysical Journal</i> , 2023 , <i>944</i> , 181.
16	Authors	<u>DV Mifsud</u> , P Herczku, B Sulik, Z Juhász, I Vajda, I Rajta, S Ioppolo, NJ Mason, G Strazzulla, Z Kaňuchová.
	Title	Proton and Electron Irradiations of CH ₄ :H ₂ O Mixed Ices.
	Reference	<i>Atoms</i> , 2023 , <i>11</i> , 19.
17	Authors	<u>DV Mifsud</u> , R Attard-Trevisan, NJ Mason.
	Title	The COPCA 2022 Conference: Report on its Objectives and Outcomes.
	Reference	<i>Xjenza Online</i> , 2023 , accepted for publication.
18	Authors	R Ramachandran, JK Meka, KK Rahul, W Khan, JI Lo, BM Cheng, <u>DV Mifsud</u> , BN Rajasekhar, A Das, H Hill, A Bhardwaj, NJ Mason, B Sivaraman
	Title	Ultraviolet Spectrum Reveals the Presence of Ozone on Jupiter's Fourth Moon Callisto.
	Reference	<i>Icarus</i> , 2023 , submitted for publication.
19	Authors	R Rácz, KK Rahul, STS Kovács, <u>DV Mifsud</u> , P Herczku, G Lakatos, HM Qutián-Lara, AH Corrigan, Z Juhász, B Sulik, Z Kaňuchová, S Ioppolo, NJ Mason, S Biri, RW McCullough.
	Title	AQUILA: A New Experimental Set-Up for keV Ion Irradiations of Astrophysical Ice Analogues.
	Reference	<i>ACS Earth and Space Chemistry</i> , 2023 , in preparation.

20	Authors	<u>DV Mifsud</u> , Z Kaňuchová, P Herczku, Z Juhász, STS Kovács, G Lakatos, KK Rahul, R Rácz, B Sulik, S Biri, I Rajta, I Vajda, S Ioppolo, RW McCullough, NJ Mason.
	Title	Sulphur Ion Implantations into O ₂ , CO, and CO ₂ Ices: Implications for the Surface Chemistry of the Galilean Moons.
	Reference	<i>Icarus</i> , 2023 , in preparation.
21	Authors	S Ioppolo, Z Kaňuchová, A Traspas Muiña, <u>DV Mifsud</u> , NC Jones, SV Hoffmann, NJ Mason, G Strazzulla.
	Title	VUV Photoabsorption Spectroscopy of Space-Related Ices: Formation of (Cyano)Polyyenes in 1 keV Electron Irradiated Ices Rich in Hydrocarbons.
	Reference	<i>Astronomy and Astrophysics</i> , 2023 , in preparation.
22	Authors	<u>DV Mifsud</u> , B Sivaraman, A Das, S Ioppolo, Z Kaňuchová, NJ Mason, SL Chou, JI Lo, BM Cheng.
	Title	VUV Photo-Absorption Spectroscopy of Astrochemical Ice Analogues Containing OCS and CS ₂ .
	Reference	<i>Journal of Molecular Spectroscopy</i> , 2023 , in preparation.
23	Authors	<u>DV Mifsud</u> , S Góbi, P Herczku, S Ioppolo, B Sulik, NJ Mason, Gy Tarczay.
	Title	The Influence of Temperature on the Electron Irradiation of Crystalline N ₂ O.
	Reference	<i>Journal of Physics B</i> , 2023 , in preparation.
24	Authors	<u>DV Mifsud</u> , P Herczku, B Dönczö, M Szarka, Z Juhász, STS Kovács, B Sulik.
	Title	Molecular Sulphur Depletion and Residue Formation as a Result of Ice Irradiation by Galactic Cosmic Ray Simulants.
	Reference	<i>Astronomy and Astrophysics</i> , 2023 , in preparation.
25	Authors	<u>DV Mifsud</u> , P Herczku, E Sinagra, S Ioppolo.
	Title	The Radiation Chemistry of H ₂ S Mixed and Layered with Oxygen-Bearing Molecules in Interstellar Ice Analogues.
	Reference	<i>ACS Earth and Space Chemistry</i> , 2023 , in preparation.
26	Authors	J Zhang, A Traspas Muiña, <u>DV Mifsud</u> , K Cielinska, P Herczku, KK Rahul, STS Kovács, JC Santos, AT Hopkinson, NC Jones, SV Hoffmann, L Craciunescu, H Linnartz, L Hornekær, Z Juhász, B Sulik, NJ Mason, F Fantuzzi, Z Kaňuchová, S Ioppolo.
	Title	A Systematic FTIR and VUV Investigation of the Ion, Electron, and Thermal Processing of Ethanolamine Ice.
	Reference	<i>Monthly Notices of the Royal Astronomical Society</i> , 2023 , in preparation.
27	Authors	A Traspas Muiña, <u>DV Mifsud</u> , F Fantuzzi, J Zhang, JC Santos, AT Hopkinson, JGM Schrauwen, D Ramsamoedj, K Cielinska, NC Jones, SV Hoffmann, L Hornekær, H Linnartz, NJ Mason, B Redlich, Z Kaňuchová, S Ioppolo.
	Title	Vacuum-Ultraviolet Photo-Absorption Spectroscopy of Molecular Ices: Applications to the Interstellar Medium and the Outer Solar System.
	Reference	<i>Monthly Notices of the Royal Astronomical Society</i> , 2023 , in preparation.
28	Authors	<u>DV Mifsud</u> , P Herczku, KK Rahul, Z Kaňuchová, S Ioppolo, R Ramachandran, S Pavithraa, B Sulik, Z Juhász, STS Kovács, R Rácz, S Biri, RW McCullough, B Sivaraman, NJ Mason.
	Title	Mid-IR Spectroscopic Characterisation of Sulphur-Containing Ices. I. SO ₂ Ices.
	Reference	<i>Astrophysics and Space Science</i> , 2023 , in preparation.

29	Authors	<u>DV Mifsud</u> , P Herczku, KK Rahul, Z Kaňuchová, S Ioppolo, R Ramachandran, S Pavithraa, B Sulik, Z Juhász, STS Kovács, R Rácz, S Biri, RW McCullough, B Sivaraman, NJ Mason.
	Title	Mid-IR Spectroscopic Characterisation of Sulphur-Containing Ices. II. H ₂ S Ices.
	Reference	<i>Astrophysics and Space Science</i> , 2023 , in preparation.
30	Authors	<u>DV Mifsud</u> , P Herczku, B Sulik, Z Juhász, Z Kaňuchová, S Ioppolo, G Strazzulla.
	Title	Emission of SiO and SO ₂ During the Irradiation of Epsomite and Berthierine.
	Reference	<i>Journal of Mass Spectrometry</i> , 2023 , in preparation.
31	Authors	<u>DV Mifsud</u> , P Herczku, B Sulik, Z Juhász, STS Kovács, D Jugović, Z Kaňuchová, S Ioppolo, NJ Mason, R Brunetto, G Strazzulla.
	Title	Proton and Sulphur Ion Irradiation of Minerals Relevant to the Surface of Europa.
	Reference	<i>Icarus</i> , 2023 , in preparation.
32	Authors	<u>DV Mifsud</u> , O Auriacombe, P Herczku, B Sulik, Z Juhász, S Ioppolo, NJ Mason, Z Kaňuchová.
	Title	1 MeV He ⁺ Ion Irradiation of CH ₃ OH Ice Deposited on Top of a Layer of Elemental Sulphur: Implications for Cometary and Interstellar Sulphur Chemistry.
	Reference	<i>Earth and Planetary Science Letters</i> , 2023 , in preparation.
33	Authors	<u>DV Mifsud</u> , P Herczku, O Auriacombe, B Sulik, STS Kovács, Z Juhász, R Rácz, S Biri, KK Rahul, S Ioppolo, NJ Mason, Z Kaňuchová.
	Title	Irradiation of H ₂ O, CO ₂ , CO, and O ₂ Ices on Top of Sulphur Layers.
	Reference	<i>Nature Astronomy</i> , 2023 , in preparation.
34	Authors	KK Rahul, P Herczku, <u>DV Mifsud</u> , STS Kovács, B Sulik, R Rácz, G Lakatos, PA Hailey, Z Kaňuchová, S Biri, S Ioppolo, RW McCullough, NJ Mason, Z Juhász.
	Title	Radiolytic Cyanide and Cyanate Formation in Astrophysical Ice Analogues.
	Reference	<i>Monthly Notices of the Royal Astronomical Society</i> , 2023 , in preparation.

Posters and Abstracts

1	Authors	P Herczku, Z Juhász, STS Kovács, B Sulik, S Ioppolo, NJ Mason, <u>DV Mifsud</u> , A Traspas Muiña, M Czentye, Z Kaňuchová, B Paripás, RW McCullough.
	Title	Ion and Electron Impact Studies on Astrophysically Relevant Ices: A New Laboratory at Atomki in Debrecen.
	Event	Europlanet Science Congress, 2020 , online.
2	Authors	<u>DV Mifsud</u> , PA Hailey, NJ Mason, P Herczku, Z Juhász, STS Kovács, B Sulik, S Ioppolo, Z Kaňuchová, RW McCullough, B Paripás.
	Title	Laboratory Ice Astrochemistry: A New Facility at Atomki.
	Event	University of Kent Graduate and Researcher College Colloquium, 2020 , online.
3	Authors	<u>DV Mifsud</u> , NJ Mason.
	Title	The Surface Chemistry of Europa: A Potential Abode for Extra-Terrestrial Life.
	Event	University of Kent Graduate and Researcher College Colloquium, 2021 , online.
4	Authors	A Traspas Muiña, S Ioppolo, P Herczku, Z Juhász, STS Kovács, <u>DV Mifsud</u> , Z Kaňuchová, NJ Mason, RW McCullough, B Sulik.
	Title	Spectroscopic Studies of Methyl Formate and its Formation in Space upon Ion Irradiation.
	Event	International Symposium on Molecular Spectroscopy, 2021 , online.

5	Authors	Z Juhász, V Vizcaíno, JY Chesnel, STS Kovács, P Herczku, S Demes, R Rácz, S Biri, N Sens, <u>DV Mifsud</u> , L Ábrók, B Sulik.
	Title	Rotational Excitation Followed by Collision-Induced Molecular Dissociation in 10-keV O ⁺ + H ₂ and O ⁺ + D ₂ Collisions.
	Event	International Conference on Photon, Electron, and Atom Collisions, 2021 , online
6	Authors	<u>DV Mifsud</u> , Z Kaňuchová, P Herczku, Z Juhász, STS Kovács, B Sulik, PA Hailey, A Traspas Muiña, S Ioppolo, RW McCullough, NJ Mason.
	Title	High-Fluence S ⁺ Implantation in Simple Oxide Astrophysical Ice Analogues.
	Event	International Conference on Photon, Electron, and Atom Collisions, 2021 , online.
7	Authors	P Herczku, <u>DV Mifsud</u> , Z Juhász, STS Kovács, B Sulik, PA Hailey, Z Kaňuchová, A Traspas Muiña, S Ioppolo, RW McCullough, B Paripás, NJ Mason.
	Title	A New Experimental Apparatus for Ion and Electron Impact Studies on Astrophysical Ice Analogues.
	Event	International Conference on Photon, Electron, and Atom Collisions, 2021 , online.
8	Authors	A Traspas Muiña, S Ioppolo, P Herczku, Z Juhász, STS Kovács, <u>DV Mifsud</u> , Z Kaňuchová, NJ Mason, RW McCullough, B Sulik.
	Title	Formation and Fate of Methyl Formate in Space Upon Ion Irradiation and its Astrophysical Relevance.
	Event	Europlanet Science Congress, 2021 , online.
9	Authors	<u>DV Mifsud</u> , Z Kaňuchová, P Herczku, Z Juhász, STS Kovács, B Sulik, PA Hailey, A Traspas Muiña, S Ioppolo, RW McCullough, NJ Mason.
	Title	S ⁺ Implantation in Oxide Ices: Relevance to Europa.
	Event	Europlanet Science Congress, 2021 , online.
10	Authors	A Traspas Muiña, V Spathis, S Ioppolo, J Tandy, <u>DV Mifsud</u> , P Herczku, Z Juhász, STS Kovács, J Zhang, Z Kaňuchová, NJ Mason, RW McCullough, B Sulik.
	Title	Investigating the Origin of Prebiotic Material in Space: 1 keV Electron Irradiation Processing vs Selective Infrared Photon-Induced Spectral Changes in Glycine-Rich Ices.
	Event	44 th COSPAR Scientific Assembly, 2022 , Athens (Greece).
11	Authors	<u>DV Mifsud</u> , Z Kaňuchová, P Herczku, Z Juhász, STS Kovács, B Sulik, KK Rahul, R Rácz, I Vajda, S Biri, PA Hailey, A Traspas Muiña, S Ioppolo, RW McCullough, NJ Mason.
	Title	S ⁺ Implantation into Condensed CO ₂ : Relevance for Europa.
	Event	Chemistry and Physics at Low Temperatures Conference, 2022 , Visegrád (Hungary).
12	Authors	<u>DV Mifsud</u> , PA Hailey, P Herczku, STS Kovács, B Sulik, Z Juhász, Z Kaňuchová, S Ioppolo, B Paripás, RW McCullough, NJ Mason.
	Title	The Role of Solid Phase in the Radiation Astrochemistry of Ices.
	Event	Chemistry and Physics at Low Temperatures Conference, 2022 , Visegrád (Hungary).
13	Authors	AH Corrigan, B Cavazzin, <u>DV Mifsud</u> , PA Hailey, NJ Mason.
	Title	Exploring the Prebiotic Chemistry of Europa.
	Event	Europlanet Science Congress, 2022 , Granada (Spain).
14	Authors	<u>DV Mifsud</u> , PA Hailey, P Herczku, Z Juhász, STS Kovács, B Sulik, KK Rahul, R Rácz, S Biri, S Ioppolo, Z Kaňuchová, B Paripás, RW McCullough, NJ Mason.
	Title	The Effect of Solid Phase Adopted by Astrophysical Ices on their Radiation Chemistry and Physics: Implications for the Synthesis of Prebiotic Molecules.
	Event	Europlanet Science Congress, 2022 , Granada (Spain).

15	Authors	KK Rahul, R Rácz, STS Kovács, P Herczku, B Sulik, Z Juhász, S Biri, <u>DV Mifsud</u> , S Ioppolo, Z Kaňuchová, TA Field, PA Hailey, RW McCullough, NJ Mason.
	Title	Astrochemistry Experimental Set-Up at Atomki-ECRIS: A Europlanet Facility.
	Event	Europlanet Science Congress, 2022 , Granada (Spain).
16	Authors	PA Hailey, <u>DV Mifsud</u> , P Herczku, KK Rahul, B Sulik, Z Juhász, STS Kovács, S Ioppolo, RW McCullough, NJ Mason
	Title	Energetic Processing of Astrochemical Ices and Formamide Ice Mixtures in Plausible Astrochemical Conditions: Prebiotic Chemistry in Space.
	Event	Europlanet Science Congress, 2022 , Granada (Spain).
17	Authors	<u>DV Mifsud</u> .
	Title	Implantations of Sulphur Ions into CO, CO ₂ , and O ₂ Ices: An Insight into the Surface Chemistry of Europa.
	Event	Collisions Physics and Chemistry and their Applications Conference, 2022 , Valletta (Malta).

Seminar Talks

1	Title	Astrophysical Chemistry: Current Work at the Atomki Institute for Nuclear Research.
	Seminar	University of Kent Centre for Astrophysics and Planetary Science Seminar.
	Date	19 th May 2020.
2	Title	Sulphur Ice Astrochemistry.
	Seminar	University of Kent Centre for Astrophysics and Planetary Science Seminar.
	Date	24 th November 2020.
3	Title	Transnational Access Projects.
	Seminar	Europlanet Society Outreach Division Workshop.
	Date	3 rd December 2020.
4	Title	Sulphur Astrochemistry: Current Problems and Future Solutions.
	Seminar	Physical Research Laboratory Seminar.
	Date	6 th May 2021.
5	Title	Radiochemical Molecular Synthesis in Astrophysical Ice Analogues.
	Seminar	Institute for Nuclear Research (Atomki) Young Researchers Colloquium.
	Date	14 th October 2021.
6	Title	Radiation-Induced Solid-Phase Astrochemistry: Recent Results from the ICA Apparatus in Debrecen.
	Seminar	University of Kent Centre for Astrophysics and Planetary Science Seminar.
	Date	9 th November 2021.
7	Title	The Prebiotic Potential and Molecular Diversity of Space Environments: Past Projects and Future Possibilities with SOFIA.
	Seminar	NASA-DLR SOFIA Community Forum Seminar.
	Date	19 th January 2022.
8	Title	From Simple Sulphur Molecules to Complex Organic Molecules: An Overview of My Research Interests in Space Chemistry.
	Seminar	Leiden University Seminar.
	Date	20 th October 2022.
9	Title	Studying Science: Why You Should Go for It!
	Seminar	St Martin's College Sixth Form Outreach Event.
	Date	10 th November 2022.
10	Title	Three Years of Sulphur – Lessons Learned in Laboratory Ice Astrochemistry.
	Seminar	University of Kent Centre for Astrophysics and Planetary Science Seminar.
	Date	17 th January 2023.

Conference Talks

1	Title	Sulphur Astrochemistry in the Laboratory: Techniques to Understand the Formation of Interstellar Sulphur-Bearing Molecules.
	Conference	Dynamics of Systems on the Nanoscale (DYSON).
	Dates	18 th -22 nd September 2021.
	Location	Santa Margherita Ligure, Italy.
2	Title	Laboratory Studies of Astrochemical Ices Using Mid-Infrared Spectroscopy.
	Conference	MultIChem Conference.
	Dates	16 th -18 th May 2022.
	Location	Boppard-am-Rhein, Germany.
3	Title	Exploring Radiation Ice Astrochemistry in the Laboratory: Ozone Formation from Irradiated Carbon Dioxide Ices.
	Conference	Network of Researchers on the Chemical Evolution of Life (NoRCEL) Conference
	Dates	9 th -11 th August 2022.
	Location	St Andrews, United Kingdom.
4	Title	The Seeds of Life in Space: Astrochemical Processes in Interstellar Ices.
	Conference	Collision Physics and Chemistry and their Applications Conference.
	Dates	30 th October – 4 th November 2022.
	Location	Valletta, Malta.
5	Title	Towards a Better Understanding of Sulphur Radiation Chemistry in Astrochemical Ices.
	Conference	Dust-Ice-Gas (DIG) Conference.
	Dates	17 th -18 th November 2022.
	Location	Online.

Biography

I was born on the 1st of May 1996 in the small town of Tal-Pietà on the Mediterranean island of Malta, where I spent my formative years attending St Michael Foundation for my primary and secondary level education. After successfully obtaining eleven O-Levels, I was awarded a High Aptitude Scholarship which permitted me to attend the prestigious St Martin's College Sixth Form, where I studied biology, chemistry, physics, pure and applied mathematics, classical philosophy and logic, and English literature. I completed my sixth form studies in 2014, achieving three A-Levels and five I-Levels as well as being awarded the school Prize for Academic Excellence.

I subsequently enrolled at the University of Malta, where I read for a BSc (Hons) degree in chemistry. As part of my studies, I performed an undergraduate dissertation project under the supervision of Prof. Robert M. Borg where I worked on one-pot photochemical organic synthesis reactions between alkenes, nucleophiles, and aromatic species (so-called photo-NOCAS reactions). I graduated with a first-class honours (summa cum laude) degree in 2018, having also been awarded the Medichem Prize for Organic Chemistry for my dissertation work as well as a Certificate for Academic Merit. Upon completion of my undergraduate studies, I was awarded an Endeavour Scholarship by the Government of the Republic of Malta that allowed me to pursue a MSc degree in geochemistry at the University of St Andrews. There, I was able to carry out research as part of my dissertation project on the use of organic carbon and nitrogen stable isotope ratios in tree-rings and foliage as bio-indicators for vehicular NO_x pollution in urban and residential areas under the supervision of Dr Eva E. Stüeken and Dr (now Prof.) Rob J. S. Wilson, which led to my first publication. For this work, I was awarded the global Prize for Best Masters Thesis by the Association for Tree-Ring Research. I graduated from the University of St Andrews with a distinction-grade (summa cum laude) MSc degree in 2019 and was also awarded the Deans' List Award.

In early 2020, I began my doctoral studies in astrophysical chemistry and molecular astrophysics at the University of Kent under the supervision of Prof. Nigel J. Mason OBE, funded by a Vice-Chancellor's Research Scholarship. Not long after my studies began, however, the Covid-19 global pandemic reached Europe and most British universities and laboratories were forced to shut down. In order to mitigate the resultant disruption to my research and studies, I embarked on an extended secondment to the Institute for Nuclear Research (Atomki) in Debrecen, Hungary where I spent the next two and a half years exploring the ion- and electron-induced radiation chemistry and cryogenic thermal chemistry of astrophysical ice analogues using the Ice Chamber for Astrophysics-Astrochemistry (ICA), in whose design and development I was able to assist. This work has led to the production and publication of a large number of research papers, with the main findings having been disseminated at several international scientific conferences over the past three years. During my time as a doctoral scholar, I was awarded the University of Kent Graduate and Researcher College Prize for Postgraduate Research Champion. At Atomki, I won three Paper of the Month Awards (May 2021, May 2022, and November 2022). Together with Prof. Mason, I also successfully organised an international conference between 30th October and 4th November 2022 in Malta, which was attended by nearly sixty delegates from fifteen countries. Following the conclusion of my doctoral studies, I shall pursue my scientific career at Atomki as a postdoctoral scientific research associate, where I intend to carry out many of the experiments and upgrades to the ICA described in Chapter 9 of this thesis.

References

A

- Abou Mrad, N., Duvernay, F., Theulé, P., Chiavassa, T., Danger, G. (2014). Development and Optimisation of an Analytical System for Volatile Organic Compound Analysis Coming from the Heating of Interstellar / Cometary Ice Analogues. *Anal. Chem.* **86**, 8391.
- Acharyya, K., Fuchs, G.W., Fraser, H.J., van Dishoeck, E.F., Linnartz, H. (2007). Desorption of CO and O₂ Interstellar Ice Analogues. *Astron. Astrophys.* **466**, 1005.
- Adams, W.S. (1941). Some Results with the COUDÉ Spectrograph of the Mount Wilson Observatory. *Astrophys. J.* **93**, 11.
- Adams, F.C., Laughlin, G., Graves, G.J.M. (2004). Red Dwarfs and the End of the Main Sequence. *Rev. Mex. Astron. Astrofis.* **22**, 46.
- Addison, P., Liuzzo, L., Arnold, H., Simon, S. (2021). Influence of Europa's Time-Varying Electromagnetic Environment on Magnetospheric Ion Precipitation and Surface Weathering. *J. Geophys. Res. Space Phys.* **126**, e2020JA029087.
- Allodi, M.A., Ioppolo, S., Kelley, M.J., McGuire, B.A., Blake, G.A. (2014). The Structure and Dynamics of Carbon Dioxide and Water Containing Ices Investigated *via* THz and Mid-IR Spectroscopy. *Phys. Chem. Chem. Phys.* **16**, 3442.
- Allred, A.L. (1961). Electronegativity Values from Thermochemical Data. *J. Inorg. Nucl. Chem.* **17**, 215.
- Altwegg, K. (2018). Chemical Highlights from the Rosetta Mission. *Proc. Int. Astron. Union* **13**, 153.
- An, D., Sellgren, K., Boogert, A.C.A., Ramírez, S.V., Pyo, T.-S. (2017). Abundant Methanol Ice Toward a Massive Young Stellar Object in the Central Molecular Zone. *Astrophys. J. Lett.* **843**, L36.
- Anders, C., Urbassek, H.M. (2019a). High-Energy Ion Impacts into the Sulphur-Bearing Ice Surface of Europa: An Atomistic Study of Chemical Transformations. *Astron. Astrophys.* **625**, 140.
- Anders, C., Urbassek, H.M. (2019b). Energetic Sulphur Ion Impacts into Cometary Ice Surfaces: A Molecular Dynamics Study. *Mon. Not. R. Astron. Soc.* **482**, 2374.
- Anderson, A., Savoie, R. (1965). Raman Spectrum of Crystalline and Liquid SO₂. *Can. J. Chem.* **43**, 2271.
- Anderson, A., Campbell, M.C.W. (1997). Infrared and Raman Spectra of Crystalline Sulphur Dioxide. *J. Chem. Phys.* **67**, 4300.
- Anderson, A., Binbrek, O.S., Tang, H.C. (1977). Raman and Infrared Study of the Low Temperature Phase of Solid H₂S and D₂S. *J. Raman Spectrosc.* **6**, 213.
- Anderson, J.D., Schubert, G., Jacobsen, R.A., Lau, E.L., Moore, W.B., Sjogren, W.L. (1998). Distribution of Rock, Metals, and Ices in Callisto. *Science* **280**, 1573.
- Anderson, D., Bergin, E.A., Maret, S., Wakelam, V. (2013). New Constraints on the Sulphur Reservoir in the Dense Interstellar Medium Provided by *Spitzer* Observations of S₁ in Shocked Gas. *Astrophys. J.* **779**, 141.
- Arnau, A., Aumayr, F., Echenique, P.M., Grether, M., Heiland, W., Limburg, J., Morgenstern, R., Roncin, P., Schippers, S., Schuch, R., Stolterfoht, N., Varga, P., Zouros, T.J.M., Winter, H.P. (1997). Interaction of Slow Multi-Charged Ions with Solid Surfaces. *Surf. Sci. Rep.* **27**, 113.
- Arumainayagam, C.R., Garrod, R.T., Boyer, M.C., Hay, A.K., Bao, S.T., Campbell, J.S., Wang, J., Nowak, C.M., Arumainayagam, M.R., Hodge, P.J. (2019). Extraterrestrial Prebiotic Molecules: Photochemistry vs. Radiation Chemistry of Interstellar Ices. *Chem. Soc. Rev.* **48**, 2293.
- Ashkenazy, Y. (2019). The Surface Temperature of Europa. *Heliyon* **5**, e01908.
- Asplund, M., Grevasse, N., Sauval, A.J., Scott, P. (2009). The Chemical Composition of the Sun. *Annu. Rev. Astron. Astrophys.* **47**, 481.

- Augé, B., Dartois, E., Engrand, C., Duprat, J., Godard, M., Delauche, L., Bardin, N., Mejía, C., Martinez, R., Muniz, G., Domaracka, A., Boduch, P., Rothard, H. (2016). Irradiation of Nitrogen-Rich Ices by Swift Heavy Ions: Clues for the Formation of Ultracarbonaceous Micrometeorites. *Astron. Astrophys.* **592**, A99.
- Augé, B., Been, T., Boduch, P., Chabot, T., Dartois, E., Madi, T., Ramillon, J.M., Ropars, F., Rothard, H., Voivenel, P. (2018). IGLIAS: A New Experimental Set-Up for Low Temperature Irradiation Studies at Large Irradiation Facilities. *Rev. Sci. Instrum.* **89**, 075105.

B

- Bag, S., Bhui, R.G., Pradeep, T. (2013). Distinguishing Amorphous and Crystalline Ice by Ultralow Energy Collisions of Reactive Ions. *J. Phys. Chem. C* **117**, 12146.
- Bagenal, F., Dols, V. (2020). The Space Environment of Io and Europa. *J. Geophys. Res. Space Phys.* **125**, e2019JA027485.
- Bahr, D.A., Famá, M., Vidal, R.A., Baragiola, R.A. (2001). Radiolysis of Water Ice in the Outer Solar System: Sputtering and Trapping of Radiation Products. *J. Geophys. Res. Planet.* **106**, 33285.
- Bahou, M., Lee, Y.-C., Lee, Y.-P. (2000). Production and IR Absorption of Cyclic CS₂ in Solid Ar. *J. Am. Chem. Soc.* **122**, 661.
- Baklouti, D., Schmitt, B., Brissaud, O. (2004). Infrared Study of Lower Sulphur Oxides on Io's Surface. *Bull. Am. Astron. Soc.* **36**, 16.07.
- Ballesteros-Paredes, J., André, P., Hennebelle, P., Klessen, R.S., Kruijssen, J.M.D., Chevance, M., Nakamura, F., Adamo, A., Vázquez-Semadeni, E. (2020). From Diffuse Gas to Dense Molecular Cloud Cores. *Space Sci. Rev.* **216**, 76.
- Bang, J., Shoaib, M.A., Choi, C.H., Kang, H. (2017). Efficient Thermal Reactions of Sulphur Dioxide on Ice Surfaces at Low Temperature: A Combined Experimental and Theoretical Study. *ACS Earth Space Chem.* **1**, 503.
- Banwell, C.N. (1983). *Fundamentals of Molecular Spectroscopy*. McGraw-Hill Book Company (Maidenhead, United Kingdom).
- Baragiola, R.A. (2003). Water Ice on Outer Solar System Surfaces: Basic Properties and Radiation Effects. *Planet. Space Sci.* **51**, 953.
- Baragiola, R.A., Loeffler, M.J., Raut, U., Vidal, R.A., Wilson, C.D. (2005). Laboratory Studies of Radiation Effects in Water Ice in the Outer Solar System. *Radiat. Phys. Chem.* **72**, 187.
- Baratta, G.A., Chaput, D., Cottin, H., Fernandez Cascales, L., Palumbo, M.E., Strazzulla, G. (2015). Organic Samples Produced by Ion Bombardment of Ices for the EXPOSE-R2 Mission on the International Space Station. *Planet. Space Sci.* **118**, 211.
- Barbe, A., Delahaigue, A., Jouve, P. (1971). Spectre Infrarouge à l'État Solide des Molecules Isotopique de SO₂. *Spectrochim Acta A: Mol. Spectrosc.* **27**, 1439.
- Barge, L.M., White, L.M. (2017). Experimentally Testing Hydrothermal Vent Origin of Life on Enceladus and Other Icy/Ocean Worlds. *Astrobiology* **17**, 1.
- Barnes, A.J., Bentwood, R.M., Wright, M.P. (1984). Molecular Complexes between Hydrogen Sulphide and Water Studied by Matrix Isolation Infrared Spectroscopy. *J. Mol. Struct.* **118**, 97.
- Bauerecker, S., Neidhart, B. (1998). Cold Gas Traps for Ice Particle Formation. *Science* **282**, 2211.
- Baxter, R.J., Hu, P. (2002). Insight into Why the Langmuir-Hinshelwood Mechanism is Generally Preferred. *J. Chem. Phys.* **116**, 4379.
- Bazsó, G., Csonka, I.P., Góbi, S., Tarczay, Gy. (2021). VISZLA – Versatile Ice Zigzag Sublimation Set-Up for Laboratory Astrochemistry. *Rev. Sci. Instrum.* **92**, 124104.
- Becker, T.M., Trumbo, S.K., Molyneux, P.M., Retherford, K.D., Hendrix, A.R., Roth, L., Raut, U., Alday, J., McGrath, M.A. (2022). Mid-Ultraviolet *Hubble* Observations of Europa and the Global Surface Distribution of SO₂. *Planet. Sci. J.* **3**, 129.

- Beinert, H. (2001). A Tribute to Sulphur. *Eur. J. Biochem.* **267**, 5657.
- Bennett, C.J., Kaiser, R.I. (2005). Laboratory Studies on the Formation of Ozone (O₃) on Icy Satellites and on Interstellar and Cometary Ices. *Astrophys. J.* **635**, 1362.
- Bennett, C.J., Chen, S.-H., Sun, B.-J., Chang, A.H.H., Kaiser, R.I. (2007). Mechanistic Studies on the Irradiation of Methanol in Extraterrestrial Ices. *Astrophys. J.* **660**, 1588.
- Bennett, C.J., Jamieson, C.S., Kaiser, R.I. (2010). Mechanical Studies on the Formation and Destruction of Carbon Monoxide (CO), Carbon Dioxide (CO₂), and Carbon Trioxide (CO₃) in Interstellar Ice Analogue Samples. *Phys. Chem. Chem. Phys.* **12**, 4032.
- Benninghoven, A. (1969). Die Emission Negativer Sekundarionen von Verbindungen mit Komplexen Anion (in German). *Z. Naturforsch. A* **24**, 859.
- Bergren, M.S., Schuh, D., Sceats, M.G., Rice, S.A. (1978). The OH Stretching Region Infrared Spectra of Low Density Amorphous Solid Water and Polycrystalline Ice Ih. *J. Chem. Phys.* **69**, 3477.
- Berland, B.S., Haynes, D.R., Foster, K.L., Tolbert, M.A., George, S.M., Toon, O. (1994). Refractive Indices of Amorphous and Crystalline HNO₃/H₂O Films Representative of Polar Stratospheric Clouds. *J. Phys. Chem.* **98**, 4358.
- Berland, B.S., Brown, D.E., Tolbert, M.A., George, S.M. (1995). Refractive Index and Density of Vapour-Deposited Ice. *Geophys. Res. Lett.* **22**, 3493.
- Bertie, J.E., Whalley, E. (1964). Infrared Spectra of Ices Ih and Ic in the Range 4000 to 350 cm⁻¹. *J. Chem. Phys.* **40**, 1637.
- Bhattacharjee, A., Matsuda, Y., Fujii, A., Wategaonkar, S. (2013). The Intermolecular S-H Y (Y = S, O) Hydrogen Bond in the H₂S Dimer and the H₂S-MeOH Complex. *Chem. Phys. Chem.* **14**, 905.
- Bijalwan, R.D., Ram, P.N., Tiwari, M.D. (1983). Lattice Thermal Conductivity of II-VI Compounds. *J. Phys. C: Sol. State Phys.* **16**, 2537.
- Billings, S.E., Kattenhorn, S.A. (2005). The Great Thickness Debate: Ice Shell Thickness Models for Europa and Comparisons with Estimates Based on Flexure at Ridges. *Icarus* **177**, 397.
- Biri, S. Vajda, I., Hajdu, P., Rácz, R., Csík, A., Kormány, Z., Perduk, Z., Kocsis, F., Rajta, I. (2021). The Atomki Accelerator Centre. *Eur. Phys. J. Plus* **136**, 247.
- Bjerrum, N. (1952). Structure and Properties of Ice. *Science* **115**, 385.
- Bland, M.T., Elder, C.M. (2022). Silicate Volcanism on Europa's Seafloor and Implications for Habitability. *Geophys. Res. Lett.* **49**, e2021GL096939.
- Blank, J.G., Miller, G.H., Ahrens, M.J., Winans, R.E. (2001). Experimental Shock Chemistry of Aqueous Amino Acid Solutions and the Cometary Delivery of Prebiotic Compounds. *Orig. Life Evol. Biosph.* **31**, 15.
- Blum, J., Wurm, G. (2008). The Growth Mechanisms of Macroscopic Bodies in Protoplanetary Discs. *Annu. Rev. Astron. Astrophys.* **46**, 21.
- Bockelée-Morvan, D., Colom, P., Crovisier, J., Despois, D., Paubert, G. (1991). Microwave detection of hydrogen sulphide and methanol in comet Austin (1989c1). *Nature* **350**, 318.
- Boduch, P., da Silveira, E.F., Domaracka, A., Gomis, O., Lv, X.-Y., Palumbo, M.E., Pilling, S., Rothard, H., Seperuelo Duarte, E., Strazzulla, G. (2011). Production of Oxidants by Ion Bombardment of Icy Moons in the Outer Solar System. *Adv. Astron.* **2011**, 327641.
- Boduch, P., Domaracka, A., Fulvio, D., Langlinay, T., Lv, X.-Y., Palumbo, M.E., Rothard, H., Strazzulla, G. (2012). Chemistry Induced by Energetic Ions in Water Ice Mixed with Molecular Nitrogen and Oxygen. *Astron. Astrophys.* **544**, A30.
- Boduch, P., Dartois, E., de Barros, A.L.F., da Silveira, E.F., Domaracka, A., Lv, X.-Y., Palumbo, M.E., Pilling, S., Rothard, H., Seperuelo Duarte, G., Strazzulla, G. (2015). Radiation Effects in Astrophysical Ices. *J. Phys. Conf. Ser.* **629**, 012008.
- Boduch, P., Brunetto, R., Ding, J.J., Domaracka, A., Kaňuchová, Z., Palumbo, M.E., Rothard, H., Strazzulla, G. (2016). Ion Processing of Ices and the Origin of SO₂ and O₃ on the Icy Surfaces of the Icy Jovian Satellites. *Icarus* **277**, 424.

- Boogert, A.C.A., Schutte, W.A., Helmich, F.P., Tielens, A.G.G.M., Wooden, D.H. (1997). Infrared Observations and Laboratory Simulations of Interstellar CH₄ and SO₂. *Astron. Astrophys.* **317**, 929.
- Boogert, A.C.A., Gerakines, P.A., Whittet, D.C.B. (2015). Observations of the Icy Universe. *Annu. Rev. Astron. Astrophys.* **53**, 541.
- Boogert, A.C.A. (2019). Questions About the Evolution of Ices, From Diffuse Clouds to Comets. *Proc. Int. Astron. Union* **15**, 15.
- Bossa, J.B., Theulé, P., Duvernay, F., Borget, F., Chiavassa, T. (2008). Carbamic Acid and Carbamate Formation in NH₃:CO₂ Ices – UV Irradiation versus Thermal Processes. *Astron. Astrophys.* **492**, 719.
- Bossa, J.B., Isokoski, K., de Valois, M.S., Linnartz, H. (2012). Thermal Collapse of Porous Interstellar Ice. *Astron. Astrophys.* **545**, A82.
- Bouilloud, M., Fray, N., Bénilan, Y., Cottin, H., Gazeau, M.-C., Jolly, A. (2015). Bibliographic Review and New Measurements of the Infrared Band Strengths of Pure Molecules at 25 K: H₂O, CO₂, CO, CH₄, NH₃, CH₃OH, HCOOH, and H₂CO. *Mon. Not. R. Astron. Soc.* **451**, 2145.
- Boyer, M.C., Rivas, N., Tran, A.A., Verish, C.A., Arumainayagam, C.R. (2016). The Role of Low-Energy (<20 eV) Electrons in Astrochemistry. *Surf. Sci.* **652**, 26.
- Brandt, E.H. (2001). Acoustic Physics – Suspended by Sound. *Nature* **413**, 474.
- Brimblecombe, P. (2013). *Treatise on Geochemistry*. Elsevier (Amsterdam, Netherlands).
- Brissaud, O., Schmitt, B., Bonnefoy, N., Douté, S., Rabou, P., Grundy, W., Fily, M. (2004). Spectrogonio Radiometer for the Study of Bidirectional Reflectance and Polarisation Functions of Planetary Surfaces. 1. Design and Tests. *Appl. Opt.* **43**, 1926.
- Brooker, M.H., Chen, J. (1991). Assignment of Transverse Optical-Longitudinal Optical Modes in the Vibration Spectrum of Solid Sulphur Dioxide. *Spectrochim. Acta A: Mol. Spectrosc.* **47**, 315.
- Brotton, S.J., Kaiser, R.I. (2013). *In Situ* Raman Spectroscopic Study of Gypsum (CaSO₄·2H₂O) and Epsomite (MgSO₄·7H₂O) Dehydration Utilising an Ultrasonic Levitator. *J. Phys. Chem. Lett.* **4**, 669.
- Brown, W.L., Lanzerotti, L.J., Poate, J.M., Augustyniak, W.M. (1978). Sputtering of Ice by MeV Light Ions. *Phys. Rev. Lett.* **40**, 1027.
- Brown, R.H., Cruikshank, D.P., Ververka, J., Helfenstein, P., Eluszkiewicz, J. (1995). Surface Composition and Photometric Properties of Triton. In: *Neptune and Triton*. Eds: Cruikshank, D.P., University of Arizona Press (Tucson, United States).
- Brown, M.E., Hill, R.E. (1996). Discovery of an Extended Sodium Atmosphere Around Europa. *Nature* **380**, 229.
- Brown, D.E., George, S.M., Huang, C., Wong, E.K.L., Rider, K.B., Smith, R.S., Kay, B.D. (1996). H₂O Condensation Coefficient and Refractive Index for Vapour-Deposited Ice from Molecular Beam and Optical Interference Measurements. *J. Chem. Phys.* **100**, 4988.
- Brown, R.H., Clark, R.N., Buratti, B.J., Cruikshank, D.P., Barnes, J.W., Mastrapa, R.M.E., Bauer, J., Newman, S., Momary, T., Baines, K.H., Bellucci, G., Capaccioni, F., Cerroni, P., Combes, M., Coradini, A., Drossart, P., Formisano, V., Jaumann, R., Langevin, Y., Matson, D.L., McCord, T.B., Nelson, R.M., Nicholson, P.D., Sicardy, B., Sotin, C. (2006). Composition and Physical Properties of Enceladus' Surface. *Science* **311**, 1425.
- Brown, M.E., Schaller, E.L., Fraser, W.C. (2012). Water Ice in the Kuiper Belt. *Astron. J.* **143**, 146.
- Brucato, J.R., Palumbo, M.E., Strazzulla, G. (1997). Carbonic Acid by Ion Implantation in Water/Carbon Dioxide Ice Mixtures. *Icarus* **125**, 135.
- Brunetto, R., Barucci, M.A., Dotto, E., Strazzulla, G. (2006). Ion Irradiation of Frozen Methanol, Methane, and Benzene: Linking to the Colours of Centaurs and Trans-Neptunian Objects. *Astrophys. J.* **644**, 646.
- Burchell, M.J. (2006). W(h)ither the Drake Equation? *Int. J. Astrobiology* **5**, 243.
- Burkhardt, A.M., Lee, K.L.K., Changala, P.B., Shingledecker, C.N., Cooke, I.R., Loomis, R.A., Wei, H., Charnley, S.B., Herbst, E., McCarthy, M.C., McGuire, B.A. (2021). Discovery of the Pure Polycyclic Hydrocarbon Indene (c-C₉H₈) with GOTHAM Observations of TMC-1. *Astrophys. J. Lett.* **913**, L18.

Butler, B.J., Muhleman, D.O., Slade, M.A. (1993). Mercury: Full-Disc Radar Images and the Detection and Stability of Ice at the North Pole. *J. Geophys. Res. Planet.* **98**, 15003.

C

Calmonte, U., Altwegg, K., Balsiger, H., Berthelier, J.J., Bieler, A., Cessateur, G., Dhooghe, F., van Dishoeck, E.F., Fiethe, B., Fuselier, S.A., Gasc, S., Gombosi, T.I., Hässig, M., Le Roy, L., Rubin, M., Sémon, T., Tzou, C.-Y., Wampfler, S.F. (2016). Sulphur-Bearing Species in the Coma of Comet 67P/Churyumov-Gerasimenko. *Mon. Not. R. Astron. Soc.* **462**, S253.

Campbell, E.K., Holz, M., Gerlich, D., Maier, J.P. (2015). Laboratory Confirmation of C_{60}^+ as the Carrier of Two Diffuse Interstellar Bands. *Nature* **523**, 322.

Campbell, E.K., Holz, M., Maier, J.P., Gerlich, D., Walker, G.A.H., Bohlender, D. (2016). Gas Phase Absorption Spectroscopy of C_{60}^+ and C_{70}^+ in a Cryogenic Ion Trap: Comparison with Astronomical Measurements. *Astrophys. J.* **822**, 17.

Carlson, H.G., Westrum, E.F. (1971). Methanol: Heat Capacity, Enthalpies of Transition and Melting, and Thermodynamic Properties from 5-300 K. *J. Chem. Phys.* **54**, 1464.

Carlson, R.W., Johnson, R.E., Anderson, M.S. (1999). Sulphuric Acid on Europa and the Radiolytic Sulphur Cycle. *Science* **286**, 97.

Carlson, R.W., Anderson, M.S., Johnson, R.E., Schulman, M.B., Yavrouian, A.H. (2002). Sulphuric Acid Production on Europa: The Radiolysis of Sulphur in Water Ice. *Icarus* **157**, 456.

Carlson, R.W., Anderson, M.S., Mehlman, R., Johnson, R.E. (2005). Distribution of Hydrate on Europa: Further Evidence for Sulphuric Acid Hydrate. *Icarus* **177**, 461.

Carlson, R.W., Kargel, J.S., Douté, S., Soderblom, L.A., Dalton, J.B. (2007). Io's Surface Composition. In: *Io After Galileo*. Eds: Lopes, R.M.C., Spencer, J.R., Praxis Publishing Company (Chichester, United Kingdom).

Carlson, R.W., Calvin, W.M., Dalton, J.B., Hansen, G.B., Hudson, R.L., Johnson, R.E., McCord, T.B., Moore, M.H. (2009). Europa's Surface Composition. In: *Europa*. Eds: Pappalardo, R.T., McKinnon, W.B., Khurana, K., University of Arizona Press (Tucson, United States).

Carr, M.H., Belton, M.J.S., Chapman, C.R., Davies, M.E., Giessler, P., Greenberg, R., McEwen, A.S., Tufts, B.R., Greeley, R., Sullivan, R., Head, J.W., Pappalardo, R.T., Klaasen, K.P., Johnson, T.V., Kaufman, J., Senske, D., Moore, J., Neukem, G., Schubert, G., Burns, J.A., Thomas, P., Veverka, J. (1998). Evidence for a Subsurface Ocean on Europa. *Nature* **391**, 363.

Carruthers, G.R. (1970). Rocket Observation of Interstellar Molecular Hydrogen. *Astrophys. J. Lett.* **161**, L81.

Caselli, P., Hasegawa, T.I., Herbst, E. (1994). The Production of Condensed Phase CO in Quiescent Molecular Clouds. *Astrophys. J.* **421**, 206.

Caselli, P., Walmsley, C.M., Tafalla, M., Dore, L., Myers, P.C. (1999). CO Depletion in the Starless Cloud Core L1544. *Astrophys. J.* **523**, L165.

Caselli, P., Ceccarelli, C. (2012). Our Astrochemical Heritage. *Astron. Astrophys. Rev.* **20**, 56.

Cassan, A., Kubas, D., Beaulieu, J.-P., Dominik, M., Horne, K., Greenhill, J., Wambsganss, J., Menzies, J., Williams, A., Jørgensen, U.G., Udalski, A., Bennett, D.P., Albrow, M.D., Batista, V., Brilliant, S., Caldwell, J.A.R., Cole, A., Coutures, C., Cook, K.H., Dieters, S., Dominis Prester, D., Donatowicz, J., Fouqué, P., Hill, K., Kains, N., Kane, S., Marquette, J.-B., Martin, R., Pollard, K.R., Sahu, K.C., Vinter, C., Warren, D., Watson, B., Zub, M., Sumi, T., Szymański, M.K., Kubiak, M., Poleski, R., Soszynski, I., Ulaczyk, K., Pietrzyński, G., Wyrzykowski, Ł. (2012). One or More Bound Planets per Milky Way Star from Microlensing Observations. *Nature* **412**, 167.

Cassidy, T.A., Paranicas, C.P., Shirley, J.H., Dalton, J.B., Teolis, B.D., Johnson, R.E., Kamp, L., Hendrix, A.R. (2013). Magnetospheric Ion Sputtering and Water Ice Grain Size at Europa. *Planet. Space Sci.* **77**, 64.

Castillo-Rogez, J. (2020). Future Exploration of Ceres as an Ocean World. *Nature Astron.* **4**, 732.

- Castillo-Rogez, J., Brophy, J., Miller, K., Sori, M., Scully, J., Quick, L., Grimm, R., Zolensky, M., Bland, M., Buczkowski, D., Raymond, C., Hendrix, A., Prettyman, T., Sekine, Y., Titus, T., Williams, D., Backes, P., Barge, L., Ermakov, A., Galassi, A., Moreland, S., Zacny, K. (2022). Concepts for the Future Exploration of Dwarf Planet Ceres' Habitability. *Planet. Sci. J.* **3**, 41.
- Cataldo, F. (1995). On the Photopolymerisation of Carbon Disulphide. *Inorg. Chim. Acta* **232**, 27.
- Cataldo, F., Heymann, D. (1998). Carbon Disulphide Sonopolymer: A Comparison with Other Carbon Disulphide Polymers. *Eur. J. Solid State Inorg. Chem.* **35**, 619.
- Cataldo, F. (2000). On the Radiopolymerisation of Carbon Disulphide. *Radiat. Phys. Chem.* **58**, 217.
- Cataldo, F., Heymann, D. (2001). Comparison of the Soluble Products from Radiolysis and Photolysis of CS₂. *Radiat. Phys. Chem.* **61**, 115.
- Cazaux, S., Carrascosa, H., Muñoz-Caro, G.M., Caselli, P., Fuente, A., Navarro-Almáida, D., Rivière-Marichalar, P. (2022). Photoprocessing of H₂S on Dust Grains: Building S Chains in Translucent Clouds and Comets. *Astron. Astrophys.* **657**, A100.
- Cernicharo, J., Cabezas, C., Agúndez, M., Tercero, B., Pardo, J.R., Marcelino, N., Gallego, J.D., Tercero, F., López-Pérez, J.A., de Vicente, P. (2021). The Sulphur Saga in TMC-1: Discovery of HCSCN and HCSCCH. *Astron. Astrophys.* **650**, L14.
- Chaabouni, H., Schriver-Mazzuoli, L., Schriver, A. (2000). Infrared Spectroscopy of Neat Solid Ozone and that of Ozone in Interaction with Amorphous and Crystalline Water Ice. *J. Phys. Chem. A* **104**, 6962.
- Chen, X., Wu, F., Weiner, B.R. (1995). Internal Energy Distributions of the SO(X)³Σ⁻ Product from the O(³P) + OCS Reaction. *Chem. Phys. Lett.* **247**, 313.
- Chen, Y.-J., Juang, K.-J., Nuevo, M., Jiménez-Escobar, A., Muñoz-Caro, G.M., Qiu, J.-M., Chu, C.-C., Yih, T.-S., Wu, C.-Y.R., Fung, H.-S., Ip, W.-H. (2015). Formation of S-Bearing Species by VUV/EUV Irradiation of H₂S-Containing Ice Mixtures: Photon Energy and Carbon Source Effects. *Astrophys. J.* **798**, 80.
- Chiar, J.E., Tielens, A.G.G.M. (2006). Pixie Dust: The Silicate Features in the Diffuse Interstellar Medium. *Astrophys. J.* **637**, 774.
- Chiar, J.E., Pendleton, Y.J., Allamandola, L.J., Boogert, A.C.A., Ennico, K., Greence, T.P., Geballe, T.R., Keane, J.V., Lada, C.J., Mason, R.E., Roelling, T.L., Sandford, S.A., Tielens, A.G.G.M., Werner, M.W., Whittet, D.C.B., Decin, L., Eriksson, K. (2011). Ices in the Quiescent IC 5146 Dense Cloud. *Astrophys. J.* **731**, 9.
- Christian, G.D., Dasgupta, P.K., Schug, K.A. (2014). Analytical Chemistry. Wiley (Hoboken, United States).
- Chuang, K.-J., Fedoseev, G., Ioppolo, S., van Dishoeck, E.F., Linnartz, H. (2016). H-Atom Addition and Abstraction Reactions in Mixed CO, H₂CO, and CH₃OH Ices – An Extended View on Complex Organic Molecule Formation. *Mon. Not. R. Astron. Soc.* **455**, 1702.
- Chyba, C.F. (1990). Impact Delivery and Erosion of Planetary Oceans in the Early Inner Solar System. *Nature* **343**, 129.
- Chyba, C.F., Hand, K.P. (2001). Life Without Photosynthesis. *Science* **292**, 2026.
- Chyba, C.F., Phillips, C.B. (2002). Europa as an Abode of Life. *Orig. Life Evol. Biosph.* **32**, 47.
- Cockcroft, J.K., Fitch, A.N. (1990). The Solid Phases of Deuterium Sulphide by Powder Neutron Diffraction. *Z. Kristall. Cryst. Mater.* **193**, 1.
- Collings, M.P., Dever, J.W., Fraser, H.J., McCoustra, M.R.S. (2003a). Laboratory Studies of the Interaction of Carbon Monoxide with Water Ice. *Astrophys. Space Sci.* **285**, 633.
- Collings, M.P., Anderson, M.A., Chen, R., Dever, J.W., Viti, S., Williams, D.A., McCoustra, M.R.S. (2003b). A Laboratory Survey of the Thermal Desorption of Astrophysically Relevant Molecules. *Mon. Not. R. Astron. Soc.* **354**, 1133.
- Congiu, E., Sow, A., Nguyen, T., Baouche, S., Dulieu, F. (2020). A New Multi-Beam Apparatus for the Study of Surface Chemistry Routes to Formation of Complex Organic Molecules in Space. *Rev. Sci. Instrum.* **91**, 124504.

- Consolmagno, G.J., Golabek, G.J., Turrini, D., Jutzi, M., Sirono, S., Svetsov, V., Tsiganis, K. (2015). Is Vesta an Intact and Pristine Protoplanet? *Icarus* **254**, 190.
- Cook, P.A., Langford, S.R., Dixon, R.N., Ashfold, M.N.R. (2001). An Experimental and *Ab Initio* Reinvestigation of the Lyman- α Photodissociation of H₂S and D₂S. *J. Chem. Phys.* **114**, 1672.
- Cooper, J.F., Johnson, R.E., Mauk, B.H., Garrett, H.B., Gehrels, N. (2001). Energetic Ion and Electron Irradiation of the Icy Galilean Satellites. *Icarus* **149**, 133.
- Cordiner, M.A., Linnartz, H., Cox, N.L.J., Cami, J., Najarro, F., Proffitt, C.R., Lallement, R., Ehrenfreund, P., Foing, B.H., Gull, T.R., Sarre, P.J., Charnley, S.B. (2019). Confirming Interstellar C₆₀⁺ Using the *Hubble Space Telescope*. *Astrophys. J. Lett.* **875**, L28.
- Covey, C., Thompson, S.L., Weissman, P.R., MacCracken, M.C. (1994). Global Climatic Effects of Atmospheric Dust from an Asteroid or Comet Impact on Earth. *Global Planet. Change* **9**, 263.
- Crawford, G.D., Stevenson, D.J. (1988). Gas-Driven Water Volcanism and the Resurfacing of Europa. *Icarus* **73**, 66.
- Crick, L., Burke, A., Hutchison, W., Kohno, M., Moore, K.A., Savarino, J., Doyle, E.A., Mahony, S., Kipfstuhl, S., Rae, J.W.B., Steele, R.C.J., Sparks, R.S.J., Wolff, E.W. (2021). New Insights into the ~74 ka Toba Eruption from Sulphur Isotopes of Polar Ice Cores. *Clim. Past* **17**, 2119.
- Cruikshank, D.P., Roush, T.L., Owen, T.C., Geballe, T.R., De Bergh, C., Schmitt, B., Brown, R.H., Bartholomew, M.J. (1993). Ices on the Surface of Triton. *Science* **261**, 742.
- Cruikshank, D.P., Roush, T.L., Moore, J.M., Sykes, M.V., Owen, T.B., Bartholomew, M.J., Brown, R.H., Tryka, K.A. (1997). The Surfaces of Pluto and Charon. In: *Pluto and Charon*. Eds: Stern, S.A., Tholen, D.J., University of Arizona Press (Tucson, United States).
- Cruikshank, D.P., Roush, T.L., Bartholomew, M.J., Geballe, T.R., Pendleton, Y.J., White, S.M., Bell, J.F., Davies, J.K., Owen, T.C., de Bergh, C., Tholen, D.J., Bernstein, M.P., Brown, R.H., Tryka, K.A., Dalle Ore, C.M. (1998). The Composition of Centaur 5145 Pholus. *Icarus* **135**, 389.

D

- Dalgarno, A. (2008). A Serendipitous Journey. *Annu. Rev. Astron. Astrophys.* **46**, 1.
- Dalton, J.B., Cruikshank, D.P., Stephan, K., McCord, T.B., Coustenis, A., Carlson, R.W., Coradini, A. (2010). Chemical Composition of Icy Satellite Surfaces. *Space Sci. Rev.* **153**, 113.
- Dalton, J.B., Shirley, J.H., Kamp, L.W. (2012). Europa's Icy Bright Plains and Dark Linea: Exogenic and Endogenic Contributions to Composition and Surface Properties. *J. Geophys. Res. Planet.* **117**, E03003.
- Dalton, J.B., Cassidy, T., Paranicas, C., Shirley, J.H., Prockter, L.M., Kamp, L.W. (2013). Exogenic Controls on Sulphuric Acid Hydrate Production at the Surface of Europa. *Planet. Space Sci.* **77**, 45.
- Dangi, B.B., Dickerson, D.J. (2021). Design and Performance of an Acoustic Levitator System Coupled with a Tuneable Monochromatic Light Source and a Raman Spectrometer for *In Situ* Reaction Monitoring. *ACS Omega* **6**, 10447.
- Das, A., Mandal, P.K., Lovas, F.J., Medcraft, C., Walker, N.R., Arunan, E. (2018). The H₂S Dimer is Hydrogen-Bonded: Direct Confirmation from Microwave Spectroscopy. *Ang. Chem. Int. Ed.* **57**, 15199.
- Davies, J.K., Roush, T.L., Cruikshank, D.P., Bartholomew, M.J., Geballe, T.R., Owen, T., de Bergh, C. (1997). The Detection of Water Ice in Comet Hale-Bopp. *Icarus* **127**, 238.
- Dawes, A. (2003). Spectroscopic Study of Photon, Ion, and Electron Stimulated Molecular Synthesis in Astrophysical Ices. PhD Thesis (University College London).
- de Barros, A.L.F., Domaracka, A., Andrade, D.P.P., Boduch, P., Rothard, H., da Silveira, E.F. (2011a). Radiolysis of Frozen Methanol by Heavy Cosmic Ray and Energetic Solar Particle Analogues. *Mon. Not. R. Astron. Soc.* **418**, 1363.
- de Barros, A.L.F., Seperuelo Duarte, E., Farenzena, L.S., da Silveira, E.F., Domaracka, A., Rothard, H., Boduch, P. (2011b). Destruction of CO Ice and Formation of New Molecules by Irradiation with 28 keV O⁶⁺ Ions. *Nucl. Instrum. Methods Phys. Res. B: Beam Interactions Mater. Atom.* **269**, 852.

- De Ley, H. (1968). Democritus and Leucippus: Two Notes on Ancient Atomism. *L'Antiquité Classique* **37**, 620.
- De Sanctis, M.C., Raponi, A., Ammannito, E., Ciarniello, M., Toplis, M.J., McSween, H.Y., Castillo-Rogez, J.C., Ehlmann, B.L., Carrozzo, F.G., Marchi, S., Tosi, F., Zambon, F., Capaccioni, F., Capria, M.T., Fonte, S., Formisano, M., Frigeri, A., Giardino, M., Longobardo, A., Magni, G., Palomba, E., McFadden, L.A., Pietersen, C.M., Jaumann, R., Schenk, P., Mugnuolo, R., Raymond, C.A., Russell, C.T. (2016). Bright Carbonate Deposits as Evidence of Aqueous Alteration on (1) Ceres. *Nature* **536**, 54.
- de Souza Bonfim, V., Barbosa de Castilho, R., Baptista, L., Pilling, S. (2017). SO₃ Formation from the X-Ray Photolysis of SO₂ Astrophysical Ice Analogues: FTIR Spectroscopy and Thermodynamic Investigations. *Phys. Chem. Chem. Phys.* **19**, 26906.
- Dehghani, M., Afshari, M., Abusara, Z., Moazzen-Ahmadi, N., McKellar, A.R.W. (2007). Nitrous Oxide Dimer: Observation of a New Polar Isomer. *J. Chem. Phys.* **126**, 164310.
- Delitsky, M.L., Lane, A.L. (1998). Ice Chemistry on the Galilean Satellites. *J. Geophys. Res. Planet.* **103**, 31391.
- Della Guardia, R.A., Johnston, F.J. (1980). Radiation-Induced Reaction of Sulphur and Water. *Radiat. Res.* **84**, 259.
- Ding, J.J., Boduch, P., Domaracka, A., Guillous, S., Langlinay, T., Lv, X.Y., Palumbo, M.E., Rothard, H., Strazzulla, G. (2013). Implantation of Multiply Charged Sulphur Ions in Water Ice. *Icarus* **226**, 860.
- Dixon-Warren, S.J., Legget, K., Matyjaszczyk, M.S., Polanyi, J.C., Young, P.A. (1990). Photochemistry of Adsorbed Molecules. VI. Ultraviolet Photoreaction of OCS on Li(001). *J. Chem. Phys.* **93**, 3659.
- Dobinski, W. (2006). Ices and Environment: A Technological Discussion. *Earth Sci. Rev.* **79**, 229.
- Dohnálek, Z., Kimmel, G.A., Ayotte, P., Smith, R.S., Kay, B.D. (2003). The deposition angle-dependent density of amorphous solid water films. *J. Chem. Phys.* **118**, 364.
- Donaldson, G.W., Johnston, F.J. (1968). The Radiolysis of Colloidal Sulphur. *J. Phys. Chem.* **72**, 3552.
- Donaldson, G.W., Johnston, F.J. (1971). The Radiolysis of Colloidal Sulphur. A Mechanism for Solubilisation. *J. Phys. Chem.* **75**, 756.
- Douglas, A.E., Herzberg, G. (1941). CH⁺ in Interstellar Space and in the Laboratory. *Astrophys. J.* **94**, 381.
- Douglas, A.E., Herzberg, G. (1942). Band Spectrum and Structure of the CH⁺ Molecule: Identification of Three Interstellar Lines. *Can. J. Res.* **A20**, 71.
- Douté, S., Schmitt, B., Lopes-Gautier, R., Carlson, R., Soderblom, L., Shirley, J., and the Galileo NIMS Team (2001). Mapping SO₂ Frost on Io by the Modelling of NIMS Hyperspectral Images. *Icarus* **149**, 107.
- Draine, B.T. (1978). Photoelectric Heating of Interstellar Gas. *Astrophys. J. Suppl. Ser.* **36**, 595.
- Draine, B.T. (2011). *Physics of the Interstellar and Intergalactic Medium*. Princeton University Press (Princeton, United States).
- Drouin, D., Couture, A.R., Joly, D., Tastet, X., Aimez, V., Gauvin, R. (2007). CASINO V2.42 – A Fast and Easy-to-Use Modelling Tool for Scanning Electron Microscopy and Microanalysis Users. *Scanning* **29**, 92.
- Druard, C., Wakelam, V. (2012). Polysulphanes on Interstellar Grains as a Possible Reservoir of Interstellar Sulphur. *Mon. Not. R. Astron. Soc.* **426**, 354.
- Dudley, T.J., Hoffmann, M.R. (2003). Theoretical Study of the Ground and First Excited Singlet State Potential Energy Surfaces of Disulphur Monoxide (S₂O). *Mol. Phys.* **101**, 1303.
- Dunham, T. (1937). Interstellar Neutral Potassium and Neutral Calcium. *Publ. Astron. Soc. Pac.* **49**, 26.
- Durie, R.A., Herzberg, G. (1960). Forbidden Transitions in Diatomic Molecules V: The Rotation-Vibration Spectrum of the Hydrogen Deuteride Molecule. *Can. J. Phys.* **38**, 806.

E

- Eberhardt, P., Meier, R., Krankowsky, D., Hodges, R.R. (1994). Methanol and Hydrogen Sulphide in Comet P/Halley. *Astron. Astrophys.* **288**, 315.
- Eddington, A.S. (1937). Interstellar Matter. *Observatory* **60**, 99.
- Ehrenfreund, P. (1999). The Diffuse Interstellar Bands as Evidence for Polyatomic Molecules in the Diffuse Interstellar Medium. *Bull. Am. Astron. Soc.* **31**, 880.
- Ehrenfreund, P., Charnley, S.B. (2000). Organic Molecules in the Interstellar Medium, Comets, and Meteorites: A Voyage from Dark Clouds to Early Earth. *Annu. Rev. Astron. Astrophys.* **38**, 427.
- Ehrenfreund, P., Fraser, H. (2003). Ice Chemistry in Space. In: *Solid State Astrochemistry*. Eds: Pirronello, V., Krelowski, J., Manico, G., Kluwer (Dordrecht, Netherlands).
- Ehrenfreund, P., Sephton, M.A. (2006). Carbon Molecules in Space: From Astrochemistry to Astrobiology. *Faraday Discuss.* **133**, 277.
- Ennis, C.P., Bennett, C.J., Kaiser, R.I. (2011). On the Formation of Ozone in Oxygen-Rich Solar System Ices via Ionising Radiation. *Phys. Chem. Chem. Phys.* **13**, 9469.
- Erickson, R.E., Yates, L.M., Clark, R.L., McEwen, D. (1977). The Reaction of Sulphur Dioxide with Ozone in Water and its Possible Atmospheric Significance. *Atmos. Environ.* **11**, 813.
- Esteban, C., Peimbert, M., García-Rojas, J., Ruiz, M.T., Peimbert, A., Rodríguez-M. (2004). A Reappraisal of the Chemical Composition of the Orion Nebula based on *Very Large Telescope* Echelle Spectrophotometry. *Mon. Not. R. Astron. Soc.* **355**, 229.
- Ernst, C.M., Chabot, N.L., Barnouin, O.S. (2018). Examining the Potential Contribution of the Hokusai Impact to Water Ice on Mercury. *J. Geophys. Res. Planet.* **123**, 2628.

F

- Fagents, S.A., Greeley, R., Sullivan, R.J., Pappalardo, R.T., Prockter, L.M., and the *Galileo* SSI Team (2000). Cryomagmatic Mechanisms for the Formation of Rhadamanthys Linea, Triple Band Margins, and Other Low-Albedo Features on Europa. *Icarus* **144**, 54.
- Famá, M., Bahr, D.A., Teolis, B.D., Baragiola, R.A. (2002). Ion Beam Induced Chemistry: The Case of Ozone Synthesis and its Influence on the Sputtering of Solid Oxygen. *Nucl. Instrum. Methods Phys. Res. B: Beam Interactions Mater. Atom.* **193**, 775.
- Famá, M., Loeffler, M.J., Raut, U., Baragiola, R.A. (2010). Radiation-Induced Amorphisation of Crystalline Ice. *Icarus* **207**, 314.
- Fathe, K., Holt, J.S., Oxley, S.P., Pursell, C.J. (2006). Infrared Spectroscopy of Solid Hydrogen Sulphide and Deuterium Sulphide. *J. Phys. Chem. A* **110**, 10793.
- Fayolle, E., Quirico, E., Schmitt, B., Jovanovic, L., Gautier, T., Carrasco, N., Grundy, W., Vuitton, V., Poch, O., Protopapa, S., Young, L., Cruikshank, D., Dalle Ore, C., Bertrand, T., Stern, A., and the New Horizons Surface Composition Science Theme Team. (2021). Testing Tholins as Analogues of the Dark Reddish Material Covering Pluto's Cthulhu Region. *Icarus* **367**, 114574.
- Ferrante, R.F., Moore, M.H., Spiliotis, M.M., Hudson, R.L. (2008). Formation of Interstellar OCS: Radiation Chemistry and IR Spectra of Precursor Ices. *Astrophys. J.* **684**, 1210.
- Ferraro, J.R., Fink, U. (1977). Near Infrared Reflectance Spectra and Analysis of H₂S Frost as a Function of Temperature. *J. Chem. Phys.* **67**, 409.
- Ferraro, J.R., Sill, G., Fink, U. (1980). Infrared Intensity Measurements of Cryodeposited Thin Films of NH₃, NH₄SH, H₂S and Assignments of Absorption Bands. *Appl. Spectrosc.* **34**, 525.
- Field, T.A., Slattery, A.E., Adams, D.J., Morrison, D.D. (2005). Experimental Observation of Dissociative Electron Attachment to S₂O and S₂O₂ with a New Spectrometer for Unstable Molecules. *J. Phys. B: Atom. Mol. Opt. Phys.* **38**, 255.

- Fitch, A.N., Cockcroft, J.K. (1990). A New Structure for the Lowest-Temperature Phase of Solid Hydrogen Sulphide. *J. Chem. Soc. Chem. Commun.* **1990**, 515.
- Fogerty, S., Forrest, W., Watson, D.M., Sargent, B.A., Koch, I. (2016). Silicate Composition of the Interstellar Medium. *Astrophys. J.* **830**, 71.
- Foing, B.H., Ehrenfreund, P. (1994). Detection of Two Interstellar Absorption Bands Coincident with Spectral Features of C₆₀⁺. *Nature* **369**, 296.
- Fortenberry, R.C. (2017). Quantum Astrochemical Spectroscopy. *Int. J. Quantum Chem.* **117**, 81.
- Fox-Powell, M.G., Osinski, G.R., Applin, D., Stromberg, J.M., Gázquez, F., Cloutis, E., Allender, E., Cousins, C.R. (2019). Natural Analogue Constraints on Europa's Non-Ice Surface Material. *Geophys. Res. Lett.* **46**, 5759.
- Frandsen, B.N., Farahani, S., Vogt, E., Lane, J.R., Kjaergaard, H.G. (2020). Spectroscopy of OSSO and Other Sulphur Compounds Thought to be Present in the Venus Atmosphere. *J. Phys. Chem. A* **124**, 7047.
- Frank, L.A., Paterson, W.R. (1999). Intense Electron Beams Observed at Io with the *Galileo* Spacecraft. *J. Geophys. Res.* **104**, 28657.
- Frankland, V.L., Rosu-Finsen, A., Lasne, J., Collings, M.P., McCoustra, M.R.S. (2015). Laboratory Surface Astrochemistry Experiments. *Rev. Sci. Instrum.* **86**, 055103.
- Frantseva, K., Nesvorný, D., Mueller, M., van der Tak, F.F.S., ten Kate, I.L., Pokorný, P. (2022). Exogenous Delivery of Water to Mercury. *Icarus* **383**, 114980.
- Frasco, D.L. (1964). Infrared Spectra of Ammonium Carbamate and Deuteroammonium Carbamate. *J. Chem. Phys.* **41**, 2134.
- Freiman, Y.A., Jodl, H.J. (2004). Solid Oxygen. *Phys. Rep.* **401**, 1.
- Froese, R.D.J., Goddard, J.D. (1993). *Ab Initio* Studies of the Lowest Singlet and Triplet Potential Energy Surfaces of CO₂S. *Mol. Phys.* **79**, 685.
- Fuchs, G.W., Acharyya, K., Bisschop, S.E., Öberg, K.I., van Broekhuizen, F.A., Fraser, H.J., Schlemmer, S., van Dishoeck, E.F., Linnartz, H. (2006). Comparative Studies of O₂ and N₂ in Pure, Mixed, and Layered CO Ices. *Faraday Discuss.* **133**, 331.
- Fuchs, G.W., Cuppen, H.M., Ioppolo, S., Romanzin, C., Bisschop, S.E., Andersson, S., van Dishoeck, E.F., Linnartz, H. (2009). Hydrogenation Reactions in Interstellar CO Ice Analogues. *Astron. Astrophys.* **505**, 629.
- Fulvio, D., Góbi, S., Jäger, C., Kereszturi, Á., Henning, T. (2017). Laboratory Experiments on the Low-Temperature Formation of Carbonaceous Grains in the ISM. *Astrophys. J. Suppl. Ser.* **233**, 14.
- Furuya, K., Oba, Y., Shimonishi, T. (2022). Quantifying the Chemical Desorption of H₂S and PH₃ from Amorphous Water-Ice Surfaces. *Astrophys. J.* **926**, 171.

G

- Gálvez, Ó., Maté, B., Martín-Llorente, B., Herrero, V.J., Escribano, R. (2009). Phases of Solid Methanol. *J. Phys. Chem. A* **113**, 3321.
- Garozzo, M., Fulvio, D., Gomis, O., Palumbo, M.E., Strazzulla, G. (2008). H-Implantation in SO₂ and CO₂ Ices. *Planet. Space Sci.* **56**, 1300.
- Garozzo, M., Fulvio, D., Kaňuchová, Z., Palumbo, M.E., Strazzulla, G. (2010). The Fate of S-Bearing Species After Ion Irradiation of Interstellar Icy Grain Mantles. *Astron. Astrophys.* **509**, A67.
- Gautier, T.N., Fink, U., Treffers, R.R., Larson, H.P. (1976). Detection of Molecular Hydrogen Quadrupole Emission in the Orion Nebula. *Astrophys. J. Lett.* **207**, L129.
- Ge, Y., Olsen, K., Kaiser, R.I., Head, J.D. (2006). The Potential Energy Surface of the H₂O₂ System. *AIP Conf. Proc.* **855**, 253.
- Geppert, W.D., Larsson, M. (2013). Experimental Investigations into Astrophysically Relevant Ionic Reactions. *Chem. Rev.* **113**, 8872.

- Gerakines, P.A., Schutte, W.A., Greenberg, J.M., van Dishoeck, E.F. (1995). The Infrared Band Strengths of H₂O, CO, and CO₂ in Laboratory Simulations of Astrophysical Ice Mixtures. *Astron. Astrophys.* **296**, 810.
- Gerakines, P.A., Moore, M.H. (2001). Carbon Suboxide in Astrophysical Ice Analogues. *Icarus* **154**, 372.
- Giammanco, C., Bochsler, P., Karrer, R., Ipavich, F.M., Paquette, J.A., Wurz, P. (2007). Determination of Sulphur Abundance in the Solar Wind. *Space Sci. Rev.* **130**, 329.
- Giguère, P.A., Falk, M. (1956). Infrared Spectrum of Solid Sulphur Dioxide. *Can. J. Chem.* **34**, 1833.
- Giguère, P.A., Harvey, K.B. (1959). An Infrared Study of Hydrogen Bonding in Solid H₂O₂ and H₂O:H₂O₂ Mixtures. *J. Mol. Spectrosc.* **3**, 36.
- Globus, N., Blandford, R.D. (2020). The Chiral Puzzle of Life. *Astrophys. J. Lett.* **895**, L11.
- Góbi, S., Csonka, I.P., Bazsó, G., Tarczay, Gy. (2021). Successive Hydrogenation of SO and SO₂ in Solid *para*-H₂: Formation of Elusive Small Oxoacids of Sulphur. *ACS Earth Space Chem.* **5**, 1180.
- Goldman, N., Reed, E.J., Fried, L.E., Kuo, I.-F.W., Maiti, A. (2010). Synthesis of Glycine-Containing Complexes in Impacts of Comets on Early Earth. *Nature Chem.* **2**, 949.
- Gomis, O., Leto, G., Strazzulla, G. (2004). Hydrogen Peroxide Production by Ion Irradiation of Thin Water Ice Films. *Astron. Astrophys.* **420**, 405.
- Gomis, O., Strazzulla, G. (2005). CO₂ Production by Ion Irradiation of H₂O Ice on Top of Carbonaceous Materials and its Relevance to the Galilean Satellites. *Icarus* **177**, 570.
- Gomis, O., Strazzulla, G. (2008). Ion Irradiation of H₂O Ice on Top of Sulphurous Solid Residues and its Relevance to the Galilean Satellites. *Icarus* **194**, 146.
- Goodman, A.M. (1978). Optical Interference Method for the Approximate Determination of Refractive Index and Thickness of a Transparent Layer. *Appl. Opt.* **17**, 2779.
- Goodman, J.C., Collins, G.C., Marhsall, J., Pierrehumbert, R.T. (2004). Hydrothermal Plume Dynamics on Europa: Implications for Chaos Formation. *J. Geophys. Res. Planet.* **109**, E03008.
- Goumans, T.P.M., Uppal, M.A., Brown, W.A. (2008). Formation of CO₂ on a Carbonaceous Surface: A Quantum Chemical Study. *Mon. Not. R. Astron. Soc.* **384**, 1158.
- Grasset, O., Dougherty, M.K., Coustenis, A., Bunce, E.J., Erd, C., Titov, D., Blanc, M., Coates, A., Drossart, P., Fletcher, L.N., Hussmann, H., Jaumann, R., Krupp, N., Lebreton, J.-P., Prieto-Ballesteros, O., Tortora, P., Tosi, F., Van Hoolst, T. (2013). *Jupiter Icy Moons Explorer (JUICE): An ESA Mission to Orbit Ganymede and to Characterise the Jupiter System.* *Planet. Space Sci.* **78**, 1.
- Grdanovska, S. (2015). Characterisation of Radiation Damage to a Novel Photonic Crystal Sensor. PhD Thesis (University of Maryland).
- Greenwood, N.N., Earnshaw, A. (1997). *Chemistry of the Elements.* Butterworth-Heinemann (Oxford, United Kingdom).
- Grieves, G.A., Orlando, T.M. (2005). The Importance of Pores in the Electron Stimulated Production D₂ and O₂ in Low Temperature Ice. *Surf. Sci.* **593**, 180.
- Groner, P., Stolkin, I., Gunthard, H.S. (1973). Measurement of Deposition Rate in Matrix Spectroscopy with a Small Laser. *J. Phys. E Sci. Instrum.* **6**, 122.
- Grundy, W.M., Binzel, R.P., Buratti, B.J., Cook, J.C., Cruikshank, D.P., Dalle Ore, C.M., Earle, A.M., Ennico, K., Howett, C.J.A., Lunsford, A.W., Olkin, C.B., Parker, A.H., Philippe, S., Protopapa, S., Quirico, E., Reuter, D.C., Schmitt, B., Singer, K.N., Verbiscer, A.J., Beyer, R.A., Buie, M.W., Cheng, A.F., Jennings, D.E., Linscott, I.R., Parker, J.W.M., Schenk, P.M., Spencer, J.R., Stansberry, J.A., Stern, S.A., Throop, H.B., Tsang, C.C.C., Weaver, H.A., Weigle, G.E., Young, L.A., the New Horizons Science Team (2016). Surface Compositions Across Pluto and Charon. *Science* **351**, aad9189.
- Guldán, E.D., Schindler, L.R., Roberts, J.T. (1995). Growth and Characterisation of Sulphuric Acid under Ultrahigh Vacuum. *J. Phys. Chem.* **99**, 16059.

H

- Habing, H.J. (1968). The Interstellar Radiation Density between 912 Å and 2400 Å. *Bull. Astron. Inst. Netherlands* **19**, 421.
- Hagen, W., Allamandola, L.J., Greenberg, J.M. (1979). Interstellar Molecule Formation in Grain Mantles: The Laboratory Analogue Experiments, Results, and Implications. *Astrophys. Space Sci.* **65**, 215.
- Hagen, W., Tielens, A.G.G.M., Greenberg, J.M. (1981). The Infrared Spectra of Amorphous Solid Water and Ice Ic between 10 and 140 K. *Chem. Phys.* **56**, 367.
- Hagen, W., Tielens, A.G.G.M. (1982). The Librational Region in the Spectrum of Amorphous Solid Water and Ice Ic between 10 and 140 K. *Spectrochim. Acta A: Mol. Biomol. Spectrosc.* **38**, 1089.
- Halfen, D.T., Ziurys, L.M., Brünken, S., Gottlieb, C.A., McCarthy, M.C., Thaddeus, P. (2009). Detection of a New Interstellar Molecule: Thiocyanic Acid HSCN. *Astrophys. J.* **702**, L124.
- Hallbrucker, A., Mayer, E. (1990). Unexpectedly Stable Nitrogen, Oxygen, Carbon Monoxide, and Argon Clathrate Hydrates from Vapour-Deposited Amorphous Solid Water: An X-Ray and Two-Step Differential Scanning Calorimetry Study. *J. Chem. Soc. Faraday Trans.* **86**, 3785.
- Hand, K.P., Chyba, C.F., Carlson, R.W., Cooper, J.F. (2006). Clathrate Hydrates of Oxidants in the Ice Shell of Europa. *Astrobiology* **6**, 463.
- Hand, K.P., Carlson, R.W., Chyba, C.F. (2007). Energy, Chemical Disequilibrium, and Geological Constraints on Europa. *Astrobiology* **7**, 1006.
- Hansen, G.B., McCord, T.B. (2004). Amorphous and Crystalline Ice on the Galilean Satellites: A Balance Between Thermal and Radiolytic Processes. *J. Geophys. Res. Planet.* **109**, E01012.
- Hansen, G.B., McCord, T.B. (2008). Widespread CO₂ and Other Non-Ice Compounds on the Anti-Jovian and Trailing Sides of Europa from *Galileo*/NIMS Observations. *Geophys. Res. Lett.* **35**, L01202.
- Hapke, B., Graham, F. (1989). Spectral Properties of Condensed Phases of Disulphur Monoxide, Polysulphur Oxide, and Irradiated Sulphur. *Icarus* **79**, 47.
- Harmon, J.K., Slade, M.A. (1992). Radar Mapping of Mercury: Full-Disc Images and Polar Anomalies. *Science* **258**, 640.
- Harrison, I., Polanyi, J.C., Young, P.A. (1988). Photochemistry of Adsorbed Molecules. IV. Photodissociation, Photoreaction, Photoejection, and Photodesorption of H₂S on LiF(001). *J. Chem. Phys.* **89**, 1498.
- Hauck, S.A., Aurnou, J.M., Dombard, A.J. (2006). Sulphur's Impact on Core Evolution and Magnetic Field Generation on Ganymede. *J. Geophys. Res. Planet.* **111**, E09008.
- Hawkins, M., Almond, M.J., Downs, A.J. (1985). Photochemistry of Low-Temperature Matrixes Containing Carbonyl Sulphide: Reactions of Sulphur Atoms with the Phosphorus Trihalides Phosphorus Trifluoride (PF₃) and Phosphorus Trichloride (PCl₃) and the Hydrocarbons Methane, Ethene, and Ethyne. *J. Phys. Chem.* **89**, 3326.
- Hayne, P.O., Aharonson, O. (2015). Thermal Stability of Ice on Ceres with Rough Topography. *J. Geophys. Res. Planet.* **120**, 1567.
- Heavens, O.S. (1955). *Optical Properties of Thin Solid Films*. Butterworths Scientific Publications (New York City, United States).
- Heger, M.L. (1922). Further Study of the Sodium Lines in Class B Stars. *Lick Observatory Bull.* **10**, 141.
- Heger, A., Fryer, C.L., Woosley, S.E., Langer, N., Hartmann, D.H. (2003). How Massive Single Stars End Their Life. *Astrophys. J.* **591**, 288.
- Heiselberg, H., Pandharipande, V. (2000). Recent Progress in Neutron Star Theory. *Annu. Rev. Nucl. Part. Sci.* **50**, 481.
- Hendrix, A.R., Cassidy, T.A., Johnson, R.E., Paranicas, C., Carlson, R.W. (2011). Europa's Disc-Resolved Ultraviolet Spectra: Relationships with Plasma Flux and Surface Terrains. *Icarus* **212**, 736.
- Hendrix, A.R., Vilas, F., Li, J.-Y. (2016). Ceres: Sulphur Deposits and Graphitised Carbon. *Geophys. Res. Lett.* **43**, 8920.

- Herbig, G. (1995). The Diffuse Interstellar Bands. *Annu. Rev. Astron. Astrophys.* **33**, 19.
- Herbst, E., van Dishoeck, E.F. (2009). Complex Organic Interstellar Molecules. *Annu. Rev. Astron. Astrophys.* **47**, 427.
- Hermann, R., Cocke, C.L., Ullrich, J., Haggmann, S., Stoekli, M., Schmidt-Boecking, H. (1994). Charge-State Equilibration Length of a Highly Charged Ion Inside a Carbon Solid. *Phys. Rev. A* **50**, 1435.
- Herron, J.T., Huie, R.E. (1980). Rate Constants at 298 K for the Reactions $\text{SO} + \text{SO} + \text{M} \rightarrow (\text{SO})_2 + \text{M}$ and $\text{SO} + (\text{SO})_2 \rightarrow \text{SO}_2 + \text{S}_2\text{O}$. *Chem. Phys. Lett.* **76**, 322.
- Hertel, N., Hoffmann, S.V. (2011). ASTRID-2: A New Danish Low-Emittance SR Source. *Synchrotron Radiat. News* **24**, 19.
- Herzberg, G. (1938). On the Possibility of Detecting Molecular Hydrogen and Nitrogen in Planetary and Stellar Atmospheres by their Rotation-Vibration Spectra. *Astrophys. J.* **87**, 428.
- Herzberg, G. (1949). Quadrupole Rotation-Vibration Spectrum of the Hydrogen Molecule. *Nature* **163**, 170.
- Herzberg, G. (1950a). Forbidden Transitions in Diatomic Molecules I: The Quadrupole Rotation-Vibration Spectrum of H_2 . *Can. J. Res.* **A28**, 144.
- Herzberg, G. (1950b). Rotation-Vibration Spectrum of the HD Molecule. *Nature* **166**, 563.
- Hess, S.L., Henry, R.M., Tillman, J.E. (1979). The Seasonal Variation of Atmospheric Pressure on Mars as Affected by the South Polar Cap. *J. Geophys. Res. Solid Earth* **84**, 2923.
- Hesse, M.A., Jordan, J.A., Vance, S.D., Oza, A.V. (2022). Downward Oxidant Transport Through Europa's Ice Shell by Density-Driven Brine Percolation. *Geophys. Res. Lett.* **49**, e2021GL095416.
- Heymann D., Cataldo, F., Thiemens, M.H., Fokkens, R., Nibbering, N.M.M., Vis, R.D. (2000). Formation of C_mS_n Compounds by Photopolymerisation of CS_2 in the Atmosphere of Jupiter. *Meteorit. Planet. Sci.* **35**, 355.
- Hibbitts, C.A., McCord, T.B., Hansen, G.B. (2000). Distributions of CO_2 and SO_2 on the Surface of Callisto. *J. Geophys. Res. Planet.* **105**, 22541.
- Hidaka, H., Watanabe, N., Shiraki, T., Nagaoka, A., Kouchi, A. (2004). Conversion of H_2CO to CH_3OH by Reactions of Cold Atomic Hydrogen on Ice Surfaces Below 20 K. *Astrophys. J.* **614**, 1124.
- Hidaka, H., Watanabe, M., Kouchi, A., Watanabe, N. (2011). FTIR Study of Ammonia Formation *via* the Successive Hydrogenation of N Atoms Trapped in a Solid N_2 Matrix at Low Temperatures. *Phys. Chem. Chem. Phys.* **13**, 15798.
- Hiroaka, K., Yamashita, A., Yachi, Y., Aruga, K., Sato, T., Muto, H. (1995). Ammonia Formation from the Reaction of H Atoms with N Atoms Trapped in a Solid N_2 Matrix at 10-30 K. *Astrophys. J.* **443**, 363.
- Hiroshi, S., Reiko, N., Masashi, I. (1968). γ -Radiolysis of a Binary Mixture of Methanol and Water. The Formation of Formaldehyde in the Radiolysis of Liquid Methanol. *Bull. Chem. Soc. Japan* **41**, 2877.
- Hirsch, T.K., Ojamäe, L. (2004). Quantum Chemical and Force-Field Investigations of Ice Ih: Computation of Proton-Ordered Structures and Prediction of their Lattice Energies. *J. Phys. Chem. B* **108**, 15856.
- Hochanadel, C.J., Ghormley, J.A., Sworski, T.J. (1955). The Decomposition of Sulphuric Acid by Cobalt γ -Rays. *J. Am. Chem. Soc.* **77**, 3215.
- Hodyss, R., Johnson, P.V., Meckler, S.M., Fayolle, E.C. (2019). Ultraviolet Spectroscopy and Photochemistry of $\text{SO}_2/\text{H}_2\text{O}$ Ices. *ACS Earth Space Chem.* **3**, 663.
- Hoey, W.A., Yeoh, S.K., Trafton, L.M., Goldstein, D.B., Varghese, P.L. (2017). Rarefied Gas Dynamic Simulation of Transfer and Escape in the Pluto-Charon System. *Icarus* **287**, 87.
- Hollenbach, D.J., Tielens, A.G.G.M. (1997). Dense Photo-Dissociation Regions (PDRs). *Annu. Rev. Astron. Astrophys.* **35**, 179.
- Hollenbach, D.J., Kaufman, M.J., Neufeld, D., Wolfire, M., Goicoechea, J.R. (2012). Chemistry of Interstellar OH^+ , H_2O^+ , and H_3O^+ : Inferring the Cosmic-Ray Ionisation Rates from Observation of Molecular Ions. *Astrophys. J.* **754**, 105.
- Holtom, P.D., Dawes, A., Mukerji, R.J., Davis, M.P., Webb, S.M., Hoffmann, S.V., Mason, N.J. (2006). VUV Photoabsorption Spectroscopy of Sulphur Dioxide Ice. *Phys. Chem. Chem. Phys.* **8**, 714.

- Honda, M., Inoue, A.K., Fukagawa, M., Oka, A., Nakamoto, T., Ishii, M., Terada, H., Takato, N., Kawakita, H., Okamoto, Y.K., Shibai, H., Tamura, M., Kudo, T., Itoh, Y. (2009). Detection of Water Ice Grains on the Surface of the Circumstellar Disc Around HD 142527*. *Astrophys. J.* **690**, L110.
- Hopkins, A.G., Brown, C.W. (1975). Infrared Spectrum of Sulphur Monoxide. *J. Chem. Phys.* **62**, 2511.
- Hornig, D.F., White, H.F., Reding, F.P. (1958). The Infrared Spectra of Crystalline H₂O, D₂O, and HDO. *Spectrochim Acta* **12**, 338.
- Housecroft, C.E., Sharpe, A.G. (2012). Inorganic Chemistry. Pearson Education Limited (Harlow, United Kingdom).
- Howell, S.M., Pappalardo, R.T. (2018). Band Formation and Ocean-Surface Interaction on Europa and Ganymede. *Geophys. Res. Lett.* **45**, 4701.
- Hsu, D.S.Y., Shaub, W.M., Burks, T.L., Lin, M.C. (1979). Dynamics of Reactions of O(³P) Atoms with CS, CS₂, and OCS. *Chem. Phys.* **44**, 143.
- Hudson, R.L., Moore, M.H. (1995). Far-IR Spectral Changes Accompanying Proton Irradiation of Solids of Astrochemical Interest. *Radiat. Phys. Chem.* **45**, 779.
- Hudson, R.L., Moore, M.H. (1999). Laboratory Studies of the Formation of Methanol and Other Organic Molecules by Water + Carbon Monoxide Radiolysis: Relevance to Comets, Icy Satellites, and Interstellar Ices. *Icarus* **140**, 451.
- Hudson, R.L., Moore, M.H., Dworkin, J.P., Martin, M.P., Pozun, Z.D. (2008). Amino Acids from Ion-Irradiated Nitrile-Containing Ices. *Astrobiology* **8**, 771.
- Hudson, R.L., Loeffler, M.J., Gerakines, P.A. (2017). Infrared Spectra and Band Strengths of Amorphous and Crystalline N₂O. *J. Chem. Phys.* **146**, 024304.
- Hudson, R.L., Gerakines, P.A. (2018). Infrared Spectra and Interstellar Sulphur: New Laboratory Results for H₂S and Four Malodorous Thiol Ices. *Astrophys. J.* **867**, 138.
- Huebner, W.F. (2002). Composition of Comets: Observations and Models. *Earth Moon Planet.* **89**, 179.

I

- Ikeda, A., Kawanaka, N., Yabushita, A., Kawasaki, M. (2008). Photodissociation Dynamics of OCS and CS₂ Adsorbed on Water Ice Films at 193 nm. *J. Photochem. Photobiol. A: Chem.* **195**, 330.
- Ingersoll, A.P., Svitek, T., Murray, B.C. (1992). Stability of Polar Frosts in Spherical Bowl-Shaped Craters on the Moon, Mercury, and Mars. *Icarus* **100**, 40.
- Ioppolo, S., Cuppen, H.M., Romanzin, C., van Dishoeck, E.F., Linnartz, H. (2008). Laboratory Evidence for Efficient Water Formation in Interstellar Ices. *Astrophys. J.* **686**, 1474.
- Ioppolo, S., van Boheemen, Y., Cuppen, H.M., van Dishoeck, E.F., Linnartz, H. (2011). Surface Formation of CO₂ Ice at Low Temperatures. *Mon. Not. R. Astron. Soc.* **413**, 2281.
- Ioppolo, S., Fedoseev, G., Lamberts, T., Romanzin, C., Linnartz, H. (2013). SURFRESIDE²: An Ultrahigh Vacuum System for the Investigation of Surface Reaction Routes of Interstellar Interest. *Rev. Sci. Instrum.* **84**, 073112.
- Ioppolo, S., McGuire, B.A., Allodi, M.A., Blake, G.A. (2014). THz and Mid-IR Spectroscopy of Interstellar Ice Analogues: Methyl and Carboxylic Acid Groups. *Faraday Discuss.* **168**, 461.
- Ioppolo, S., Kaňuchová, Z., James, R.L., Dawes, A., Jones, N.C., Hoffmann, S.V., Mason, N.J., Strazzulla, G. (2020). Vacuum Ultraviolet Photoabsorption Spectroscopy of Space-Related Ices: 1 keV Electron Irradiation of Nitrogen- and Oxygen-Rich Ices. *Astron. Astrophys.* **641**, A154.
- Ioppolo, S., Fedoseev, G., Chuang, K.-J., Cuppen, H.M., Clements, A.R., Jin, M., Garrod, R.T., Qasim, D., Kofman, V., van Dishoeck, E.F., Linnartz, H. (2021). A Non-Energetic Mechanism for Glycine Formation in the Interstellar Medium. *Nature Astron.* **5**, 197.
- Ip, W.-H. (1996). Europa's Oxygen Exosphere and its Magnetospheric Interaction. *Icarus* **120**, 317.

- Ip, W.-H., Williams, D.J., McEntire, R.W., Mauk, B. (1997). Energetic Ion Sputtering Effects at Ganymede. *Geophys. Res. Lett.* **24**, 2631.
- Ip, W.-H., Williams, D.J., McEntire, R.W., Mauk, B. (1998). Ion Sputtering and Surface Erosion at Europa. *Geophys. Res. Lett.* **25**, 829.
- Isokoski, K., Poteet, C.A., Linnartz, H. (2013). Highly Resolved Infrared Spectra of Pure CO₂ Ice (15-75 K). *Astron. Astrophys.* **555**, A85.
- Isokoski, K., Bossa, J.B., Triemstra, T., Linnartz, H. (2014). Porosity and Thermal Collapse Measurements of H₂O, CH₃OH, CO₂, and H₂O:CO₂ Ices. *Phys. Chem. Chem. Phys.* **16**, 3456.

J

- Jackson, S.M., Nield, V.M., Whitworth, R.W., Oguro, M., Wilson, C.C. (1997). Single-Crystal Neutron Diffraction Studies of the Structure of Ice XI. *J. Phys. Chem. B* **101**, 6142.
- James, R.L., Ioppolo, S., Hoffmann, S.V., Jones, N.C., Mason, N.J., Dawes, A. (2020). Systematic Investigation of CO₂:NH₃ Ice Mixtures Using Mid-IR and VUV Spectroscopy Part 1: Thermal Processing. *RSC Adv.* **10**, 37515.
- Jamieson, C.S., Mebel, A.M., Kaiser, R.I. (2006). Identification of the D_{3h} Isomer of Carbon Trioxide (CO₃) and its Implications for Atmospheric Chemistry. *Chem. Phys. Chem.* **7**, 2508.
- Jenkins, H.D.B. (2005). Thermodynamics of the Relationship between Lattice Energy and Lattice Enthalpy. *J. Chem. Educ.* **82**, 950.
- Jenkins, E.B. (2009). A Unified Representation of Gas-Phase Element Depletions in the Interstellar Medium. *Astrophys. J.* **700**, 1299.
- Jenniskens, P., Blake, D.F. (1994). Structural Transitions in Amorphous Water Ice and Astrophysical Implications. *Science* **265**, 753.
- Jenniskens, P., Mulas, G., Porceddu, I., Benvenuti, P. (1997). Diffuse Interstellar Bands Near 9600 Å: Not Due to C₆₀⁺ Yet. *Astron. Astrophys.* **327**, 337.
- Jheeta, S., Domaracka, A., Ptasinska, S., Sivaraman, B., Mason, N.J. (2013). The Irradiation of Pure CH₃OH and 1:1 Mixture of NH₃:CH₃OH Ices at 30 K Using Low Energy Electrons. *Chem. Phys. Lett.* **556**, 359.
- Jia, X., Kivelson, M.G., Khurana, K.K., Walker, R.J. (2010). Magnetic Fields of the Satellites of Jupiter and Saturn. *Space Sci. Rev.* **152**, 271.
- Jiménez-Escobar, A., Muñoz-Caro, G.M. (2011). Sulphur Depletion in Dense Clouds and Circumstellar Regions I. H₂S Ice Abundance and UV-Photochemical Reactions in the H₂O-Matrix. *Astron. Astrophys.* **536**, A91.
- Jiménez-Escobar, A., Muñoz-Caro, G.M., Ciaravella, A., Cecchi-Pestellini, C., Candia, R., Micela, G. (2012). Soft X-Ray Irradiation of H₂S Ice and the Presence of S₂ in Comets. *Astrophys. J. Lett.* **751**, L40.
- Jiménez-Escobar, A., Muñoz-Caro, G.M., Chen, Y.-J. (2014). Sulphur Depletion in Dense Clouds and Circumstellar Regions. Organic Products made from UV Photoprocessing of Realistic Ice Analogues Containing H₂S. *Mon. Not. R. Astron. Soc.* **443**, 343.
- Johari, G.P., Hallbrucker, A., Mayer, E. (1987). The Glass-Liquid Transition of Hyper-Quenched Water. *Nature* **330**, 552.
- Johnson, T.V., Fanale, F.P. (1973). Optical Properties of Carbonaceous Chondrites and their Relationship to Asteroids. *J. Geophys. Res.* **78**, 8507.
- Johnson, R.E., Killen, R.M., Waite, J.H., Lewis, W.S. (1998). Europa's Surface Composition and Sputter-Produced Ionosphere. *Geophys. Res. Lett.* **25**, 3257.
- Johnson, R.E., Quickenden, T.I., Cooper, P.D., McKinley, A.J., Freeman, C.G. (2003). The Production of Oxidants in Europa's Surface. *Astrobiology* **3**, 823.
- Johnson, R.E., Carlson, R.W., Cooper, J.F., Paranicas, C., Moore, M.H., Wong, M.C. (2004). Radiation Effects on the Surfaces of the Galilean Satellites. In: *Jupiter: The Planet, Satellites and Magnetosphere*. Eds: Bagenal, F., Dowling, T.E., McKinnon, W.B. Cambridge University Press (Cambridge, United Kingdom).

- Johnson, R.E., Sundqvist, B.U.R. (2018). Sputtering and Detection of Large Organic Molecules from Europa. *Icarus* **309**, 338.
- Johnson, P.V., Hodyss, R., Vu, T.H., Choukroun, M. (2019). Insights into Europa's Ocean Composition from its Surface Expression. *Icarus* **321**, 857.
- Johnston, F.J., Donaldson, G.W. (1971). Radiolysis of Colloidal Sulphur: Mechanism for Solubilisation. *J. Phys. Chem.* **75**, 756.
- Jones, P.R., Taube, H. (1973). Photochemical Studies on Ozone with Carbon Disulphide and with Carbonyl Sulphide in Low-Temperature Matrices. *J. Phys. Chem.* **77**, 1007.
- Jones, B.M., Kaiser, R.I. (2013). Application of Reflectron Time-of-Flight Mass Spectroscopy in the Analysis of Astrophysically Relevant Ices Exposed to Ionisation Radiation: Methane (CH₄) and D₄-Methane (CD₄) as a Case Study. *J. Phys. Chem. Lett.* **4**, 1965.
- Jones, B.M., Kaiser, R.I., Strazzulla, G. (2014). UV-Vis, Infrared, and Mass Spectroscopy of Electron Irradiated Frozen Oxygen and Carbon Dioxide Mixtures with Water. *Astrophys. J.* **781**, 85.

K

- Kalirai, J. (2018). Scientific Discovery with the *James Webb Space Telescope*. *Contemp. Phys.* **59**, 251.
- Kama, M., Shorttle, O., Jermyn, A.S., Folsom, C.P., Furuya, K., Bergin, E.A., Walsh, C., Keller, L. (2019). Abundant Refractory Sulphur in Protoplanetary Discs. *Astrophys. J.* **885**, 114.
- Kaňuchová, Z., Boduch, P., Domaracka, A., Palumbo, M.E., Rothard, H., Strazzulla, G. (2017). Thermal and Energetic Processing of Astrophysical Ice Analogues Rich in SO₂. *Astron. Astrophys.* **604**, A68.
- Kargel, J.S., Kaye, J.Z., Head, J.W., Marion, G.M., Sassen, R., Crowley, J.K., Prieto-Ballesteros, O., Grant, S.A., Hogenboom, D.L. (2000). Europa's Crust and Ocean: Origin, Composition, and the Prospects for Life. *Icarus* **148**, 226.
- Kerr, R.A. (2010). Magnetics Point to 'Magma Ocean' at Io. *Science* **327**, 408.
- Khanna, R.K., Zhao, G., Ospina, M.J., Pearl, J.C. (1988). Crystalline Sulphur Dioxide: Crystal Field Splittings, Absolute Band Intensities, and Complex Refractive Indices Derived from Infrared Spectra. *Spectrochim. Acta A: Mol. Spectrosc.* **44**, 581.
- Khriachtchev, L., Pettersson, M., Pehkonen, S., Isoniemi, E., Räsänen, M. (1999). Low-Temperature Thermoluminescence in Solid Argon: Short-Range Mobility of Atoms. *J. Chem. Phys.* **111**, 1650.
- Khurana, K.K., Kivelson, M.G., Stevenson, D.J., Schubert, G., Russell, C.T., Walker, R.J., Polansky, C. (1998). Induced Magnetic Fields as Evidence for Subsurface Oceans in Europa and Callisto. *Nature* **395**, 777.
- Kiljunen, T., Eloranta, J., Kunttu, H., Khriachtchev, L., Pettersson, M., Räsänen, M. (2000). Electronic Structure and Short-Range Recombination Dynamics of S₂ in Solid Argon. *J. Chem. Phys.* **112**, 7475.
- Kimmel, G.A., Stevenson, K.P., Dohnálek, Z., Smith, R.S., Kay, B.D. (2001). Control of Amorphous Solid Water Morphology Using Molecular Beams. I. Experimental Results. *J. Chem. Phys.* **114**, 5284.
- Kimura, J., Kamata, S. (2020). Stability of the Subsurface Ocean of Pluto. *Planet. Space Sci.* **181**, 104828.
- Kivelson, M.G., Khurana, K.K., Russell, C.T., Volwerk, M., Walker, R.J., Zimmer, C. (2000). *Galileo* Magnetometer Measurements: A Stronger Case for a Subsurface Ocean at Europa. *Science* **289**, 1340.
- Kleeberg, H., Luck, W.A.P. (1989). Experimental Tests of the H-Bond Cooperativity. *Z. Phys. Chem.* **270**, 613.
- Klinger, J. (1983). Extraterrestrial Ice: A Review. *J. Phys. Chem.* **87**, 4209.
- Köhler, M., Jones, A., Ysard, N. (2014). A Hidden Reservoir of Fe/FeS in Interstellar Silicates? *Astron. Astrophys.* **565**, L9.
- Kolasinski, K.W. (2008). *Surface Science: Foundations of Catalysis and Nanoscience*. Wiley (Hoboken, United States).

- Kolesnikov, A.I., Li, J., Parker, S.F., Eccleston, R.S., Loong, C.-K. (1999). Vibrational Dynamics of Amorphous Ice. *Phys. Rev. B* **59**, 3569.
- Kolesniková, L., Tercero, B., Cernicharo, J., Alonso, J.L., Daly, A.M., Gordon, B.P., Shipman, S.T. (2014). Spectroscopic Characterisation and Detection of Ethyl Mercaptan in Orion. *Astrophys. J. Lett.* **784**, L7.
- Kouchi, A., Kuroda, T. (1990). Amorphisation of Cubic Ice by Ultraviolet Irradiation. *Nature* **344**, 134.
- Kroto, H.W., Heath, J.R., O'Brien, S.C., Curl, R.F., Smalley, R.E. (1985). C₆₀: Buckminsterfullerene. *Nature* **318**, 162.
- Kroto, H.W. (1988). Space, Stars, C₆₀, and Soot. *Science* **242**, 1139.
- Kuchta, B., Eters, R.D., LeSar, R. (1992). The Influence of Molecular Shapes on the Relative Stability of Solid Phases: Application to N₂O. *J. Chem. Phys.* **97**, 5662.
- Kuo, Y.-P., Lu, H.-C., Wu, Y.-J., Cheng, B.-M., Ogilvie, J.F. (2007). Absorption Spectra in the Vacuum-Ultraviolet Region of Methanol in Condensed Phases. *Chem. Phys. Lett.* **447**, 168.
- Kuskov, O.L., Kronrod, V.A. (2005). Internal Structure of Europa and Callisto. *Icarus* **177**, 550.
- Kusumoto, T., Ngonon-Ravache, Y., Balanzat, E., Galindo, C., Ludwig, N., Raffy, Q., Yamauchi, T., Kodaira, S., Barillon, R. (2019). The Role of Molecular and Radical Mobility in the Creation of CO₂ Molecules and OH Groups in PADC Irradiated with C and O Ions. *Polym. Degrad. Stab.* **164**, 102.

L

- La Spisa, S., Waldheim, M., Lintemoot, J., Thomas, T., Naff, J., Robinson, M. (2001). Infrared and Vapour Flux Studies of Vapour-Deposited Amorphous and Crystalline Water Ice Films between 90 and 145 K. *J. Geophys. Res. Planet.* **106**, 33351.
- Laas, J.C., Caselli, P. (2019). Modelling Sulphur Depletion in Interstellar Clouds. *Astron. Astrophys.* **624**, A108.
- Lallement, R., Cox, N.L.J., Cami, J., Smoker, J., Fahrang, A., Elyajouri, M., Cordiner, M.A., Linnartz, H., Smith, K.T., Ehrenfreund, P., Foing, B.H. (2018): The EDIBLES Survey II: The Detectability of C₆₀⁺ Bands. *Astron. Astrophys.* **614**, A28.
- Lamers, H.J.G.L.M., Cassinelli, J.P. (1999). Introduction to Stellar Winds. Cambridge University Press (Cambridge, United Kingdom).
- Lane, A.L., Nelson, R.M., Matson, D.L. (1981). Evidence for Sulphur Implantation in Europa's UV Absorption Band. *Nature* **292**, 38.
- Larson, R.B. (2003). The Physics of Star Formation. *Rep. Prog. Phys.* **66**, 1651.
- Larsson, M., Geppert, W.D., Nyman, G. (2012). Ion Chemistry in Space. *Rep. Prog. Phys.* **75**, 066901.
- Lauck, T., Karssemeijer, L., Shulenberger, K., Rajappan, M., Öberg, K.I., Cuppen, H.M. (2015). CO Diffusion into Amorphous H₂O Ices. *Astrophys. J.* **801**, 118.
- Läuter, M., Kramer, T., Rubin, M., Altwegg, K. (2022). The Ice Composition Close to the Surface of Comet 67P/Churyumov-Gerasimenko. *ACS Earth Space Chem.* **6**, 1189-1203.
- Lee, C.C.-W., Savarino, J., Cachier, H., Theimens, M.H. (2002). Sulphur (³²S, ³³S, ³⁴S, ³⁶S) and oxygen (¹⁶O, ¹⁷O, ¹⁸O) isotopic ratios of primary sulphate produced from combustion processes. *Tellus B: Chem. Phys. Meteorol.* **54**, 193.
- Lee, K.L.K., Loomis, R.A., Burkhardt, A.M., Cooke, I.R., Xue, C., Siebert, M.A., Shingledecker, C.N., Remijan, A., Charnley, S.B., McCarthy, M.C., McGuire, B.A. (2021a). Discovery of Interstellar *trans*-Cyanovinylacetylene and Vinylcyanoacetylene in GOTHAM Observations of TMC-1. *Astrophys. J. Lett.* **908**, L11.
- Lee, K.L.K., Changala, P.B., Loomis, R.A., Burkhardt, A.M., Xue, C., Cordiner, M.A., Charnley, S.B., McCarthy, M.C., McGuire, B.A. (2021b). Interstellar Detection of 2-Cyanocyclopentadiene, C₅H₅CN, a Second Five-Membered Ring Toward TMC-1. *Astrophys. J. Lett.* **910**, L2.

- Leggett, K., Polanyi, J.C., Young, P.A. (1990). Photochemistry of Adsorbed Molecules. V. Ultraviolet Photodissociation of OCS on LiF(001). *J. Chem. Phys.* **93**, 3645.
- Leman, L., Orgel, L., Ghadiri, M.R. (2004). Carbonyl Sulphide-Mediated Prebiotic Formation of Peptides. *Science* **306**, 283.
- Leman, L., Huang, Z.-Z., Ghadiri, M.R. (2015). Peptide Bond Formation in Water Mediated by Carbon Disulphide. *Astrobiology* **15**, 709.
- Leto, G., Baratta, G.A. (2003). Ly- α Induced Amorphisation of Ic Water Ice at 16 Kelvin – Effects and Quantitative Comparison with Ion Irradiation. *Astron. Astrophys.* **397**, 7.
- Li, J., Gudipati, M.S., Mishra, Y.N., Liang, M.-C., Yung, Y.L. (2022). Oxidant Generation in the Ice Under Electron Irradiation: Simulation and Application to Europa. *Icarus* **373**, 114760.
- Lide, D.R. (2004). CRC Handbook of Chemistry and Physics: 84th Edition. CRC Press (Boca Raton, United States)
- Ligterink, N.F.W., Calcutt, H., Coutens, A., Kristensen, L.E., Bourke, T.L., Drozdovskaya, M.N., Müller, H.S.P., Wampfler, S.F., van der Wiel, M.H.D., van Dishoeck, E.F., Jørgensen, J.K. (2018). The ALMA-PILS Survey: Stringent Limits on Small Amines and Nitrogen-Oxides Towards IRAS 16293-2422B. *Astron. Astrophys.* **619**, A28.
- Lin, M., Zhang, X., Li, M., Xu, Y., Zhang, Z., Tao, J., Su, B., Liu, L., Shen, Y., Thiemens, M.H. (2018). Five-S-Isotope Evidence of Two Distinct Mass-Independent Sulphur Isotope Effects and Implications for the Modern and Archean Atmospheres. *Proc. Nat. Acad. Sci. USA* **115**, 8541.
- Linke, R.A., Frerking, M.A., Thaddeus, P. (1979). Interstellar Methyl Mercaptan. *Astrophys. J.* **234**, L139.
- Linnartz, H., Ioppolo, S., Fedoseev, G. (2015). Atom Addition Reactions in Interstellar Ice Analogues. *Int. Rev. Phys. Chem.* **34**, 205.
- Lissauer, J.J. (1993). Planet Formation. *Annu. Rev. Astron. Astrophys.* **31**, 129.
- Liu, X., Hwang, D.W., Yang, X.F., Harich, S., Lin, J.J., Yang, X. (1999). Photodissociation of Hydrogen Sulphide at 157.6 nm: Observation of SH Bimodal Rotational Distribution. *J. Chem. Phys.* **111**, 3940.
- Lo, W.-J., Chen, H.-F., Chou, P.-H., Lee, Y.-P. (2004). Isomers of OCS₂: IR Absorption Spectra of OSCS and O(CS₂) in Solid Ar. *J. Chem. Phys.* **121**, 12371.
- Loeffler, M.J., Baratta, G.A., Palumbo, M.E., Strazzulla, G., Baragiola, R.A. (2005). CO₂ Synthesis in Solid CO by Lyman- α Photons and 200 keV Protons. *Astron. Astrophys.* **435**, 587.
- Loeffler, M.J., Raut, U., Vidal, R.A., Baragiola, R.W., Carlson, R.W. (2006). Synthesis of Hydrogen Peroxide in Water Ice by Ion Irradiation. *Icarus* **180**, 265.
- Loeffler, M.J., Hudson, R.L. (2010). Thermally-Induced Chemistry and the Jovian Icy Satellites: A Laboratory Study of the Formation of Sulphur Oxyanions. *Geophys. Res. Lett.* **37**, L19201.
- Loeffler, M.J., Hudson, R.L., Moore, M.H., Carlson, R.W. (2011). Radiolysis of Sulphuric Acid, Sulphuric Acid Monohydrate, and Sulphuric Acid Tetrahydrate and its Relevance to Europa. *Icarus* **215**, 370.
- Loeffler, M.J., Hudson, R.L. (2012). Thermal Regeneration of Sulphuric Acid Hydrates After Irradiation. *Icarus* **219**, 561.
- Loeffler, M.J., Hudson, R.L. (2013). Low-Temperature Thermal Reactions Between SO₂ and H₂O₂ and their Relevance to the Jovian Icy Satellites. *Icarus* **224**, 257.
- Loeffler, M.J., Hudson, R.L. (2015). Descent Without Modification? The Thermal Chemistry of H₂O₂ on Europa and Other Icy Worlds. *Astrobiology* **15**, 453.
- Loeffler, M.J., Hudson, R.L. (2016). What is Eating Ozone? Thermal Reactions Between SO₂ and O₃: Implications for Icy Environments. *Astrophys. J. Lett.* **833**, L9.
- Lopes, R.M.C., Kamp, L.W., Smythe, W.D., Mougini-Mark, P., Kargel, J., Radebaugh, J., Turtle, E.P., Perry, J., Williams, D.A., Carlson, R.W., Douté, S., the Galileo NIMS and SSI Teams (2004). Lava Lakes on Io: Observations of Io's Volcanic Activity from Galileo NIMS During the 2001 Fly-Bys. *Icarus* **169**, 140.
- López-Isas, A., Colín-García, M., Negrón-Mendoza, A. (2019). Stability of Aqueous Formaldehyde under γ -Irradiation: Prebiotic Relevance. *Int. J. Astrobiology* **18**, 420.

- Lowder, J.E., Kennedy, L.A., Sulzmann, K.G.P., Penner, S.S. (1970). Spectroscopic Studies of Hydrogen Bonding in H₂S. *J. Quant. Spectrosc. Radiat. Transf.* **10**, 17.
- Lu, H.-C., Chen, H.-K., Cheng, B.-M., Kuo, Y.-P., Ogilvie, J.F. (2005). Spectra in the Vacuum-Ultraviolet Region of CO in Gaseous and Solid Phases and Dispersed in Solid Argon at 10 K. *J. Phys. B Atom. Mol. Opt. Phys.* **38**, 3693.
- Lu, H.-C., Chen, H.-K., Cheng, B.-M., Ogilvie, J.F. (2008). Absorption Spectra in the Vacuum-Ultraviolet Region of Small Molecules in Condensed Phases. *Spectrochim. Acta A Mol. Biomol. Spectrosc.* **71**, 1485.
- Lu, H.-C., Peng, Y.-C., Lin, M.-Y., Chou, S.-L., Lo, J.-I., Cheng, B.-M. (2013). Photoluminescence of a CVD Diamond Excited with VUV Light from a Synchrotron. *Opt. Photon. J.* **3**, 25.
- Lucas, S., Ferry, D., Demirdjian, B., Suzanne, J. (2005). Vapour Pressure and Solid Phases of Methanol Below Its Triple Point Temperature. *J. Phys. Chem. B* **109**, 18103.
- Luna, R., Molpeceres, G., Ortigoso, J., Satorre, M.Á., Domingo, M., Maté, B. (2018). Densities, Infrared Band Strengths, and Optical Constants of Solid Methanol. *Astron. Astrophys.* **617**, A116.
- Luspay-Kuti, A., Mousis, O., Lunine, J.I., Ellinger, Y., Pauzat, F., Raut, U., Bouquet, A., Mandt, K.E., Maggiolo, R., Ronnet, T., Brugger, B., Ozgurel, O., Fuselier, S.A. (2018). Origin of Molecular Oxygen in Comets: Current Knowledge and Perspectives. *Space Sci. Rev.* **214**, 115.
- Lv, X.Y., de Barros, A.L.F., Boduch, P., Bordalo, V., da Silveira, E.F., Domaracka, A., Fulvio, D., Hunniford, C.A., Langlinay, T., Mason, N.J., McCullough, R.W., Palumbo, M.E., Pilling, S., Rothard, H., Strazzulla, G. (2012). Implantation of Multiply Charged Carbon Ions in Water Ice. *Astron. Astrophys.* **546**, 81.
- Lv, X.Y., Boduch, P., Ding, J.J., Domaracka, A., Langlinay, T., Palumbo, M.E., Rothard, H., Strazzulla, G. (2014a). Sulphur Implantation in CO and CO₂ Ices. *Mon. Not. R. Astron. Soc.* **438**, 922.
- Lv, X.Y., Boduch, P., Ding, J.J., Domaracka, A., Langlinay, T., Palumbo, M.E., Rothard, H., Strazzulla, G. (2014b). Thermal and Energetic Processing of Ammonia and Carbon Dioxide Bearing Solid Mixtures. *Phys. Chem. Chem. Phys.* **16**, 3433.

M

- Machel, H.G., Krouse, H.R., Sassen, R. (1995). Products and Distinguishing Criteria of Bacterial and Thermochemical Sulphate Reduction. *Appl. Geochem.* **10**, 373.
- Mahjoub, A., Poston, M.J., Hand, K.P., Brown, M.E., Hodyss, R., Blacksberg, J., Eiler, J.M., Carlson, R.W., Ehlmann, B.L., Choukroun, M. (2016). Electron Irradiation and Thermal Processing of Mixed Ices of Potential Relevance to Jupiter Trojan Asteroids. *Astrophys. J.* **820**, 141.
- Mahjoub, A., Poston, M.J., Blacksberg, J., Eiler, J.M., Brown, M.E., Ehlmann, B.L., Hodyss, R., Hand, K.P., Carlson, R.W., Choukroun, M. (2017). Production of Sulphur Allotropes in Electron Irradiated Jupiter Trojans Ice Analogues. *Astrophys. J.* **846**, 148.
- Mahjoub, A., Hodyss, R. (2018). Thermal Reaction in Cometary and Pre-Cometary Ices: Formation of Thiocarbamate in OCS–CH₃NH₂ Mixed Ices. *Astrophys. J.* **869**, 98.
- Maity, S., Kaiser, R.I. (2013). Electron Irradiation of Carbon Disulphide-Oxygen Ices: Toward the Formation of Sulphur-Bearing Molecules in Interstellar Ices. *Astrophys. J.* **773**, 184.
- Maity, S., Kim, Y.S., Kaiser, R.I., Lin, H.M., Sun, B.J., Chang, A.H.H. (2013). On the Detection of Higher Order Carbon Sulphides (CS_x; x = 4-6) in Low Temperature Carbon Disulphide Ices. *Chem. Phys. Lett.* **577**, 42.
- Martin, W., Baross, J., Kelley, D., Russell, M.J. (2008). Hydrothermal Vents and the Origin of Life. *Nature Rev. Microbiol.* **6**, 805.
- Martín-Doménech, R., Manzano-Santamaría, J., Muñoz-Caro, G.M., Cruz-Díaz, G.A., Chen, Y.-J., Herrero, V.J., Tanarro, I. (2015). UV Photoprocessing of CO₂ Ice: A Complete Quantification of Photochemistry and Photon-Induced Desorption Processes. *Astron. Astrophys.* **584**, 14.

- Martins, Z. Price, M.C., Goldman, N., Sephton, M.A., Burchell, M.J. (2013). Shock Synthesis of Amino Acids from Impacting Cometary and Icy Planet Surface Analogues. *Nature Geosci.* **6**, 1045.
- Mason, N.J., Dawes, A., Holtom, P.D., Mukerji, R.J., Davis, M.P., Sivaraman, B., Kaiser, R.I., Hoffmann, S.V., Shaw, D.A. (2006). VUV Spectroscopy and Photo-Processing of Astrochemical Ices: An Experimental Study. *Faraday Discuss.* **133**, 311.
- Mason, N.J., Drage, E.A., Webb, S.M., Dawes, A., McPheat, R., Hayes, G. (2008). The Spectroscopy and Chemical Dynamics of Microparticles Explored Using an Ultrasonic Trap. *Faraday Discuss.* **137**, 367.
- Mason, N.J., Nair, B., Jheeta, S., Szymańska, E. (2014). Electron Induced Chemistry: A New Frontier in Astrochemistry. *Faraday Discuss.* **168**, 235.
- Mastascusa, V., Romano, I., Di Donato, P., Poli, A., Della Corte, V., Rotundi, A., Bussoletti, E., Quarto, M., Pugliese, M., Nicolaus, B. (2014). Extremophiles Survival to Simulated Space Conditions: An Astrobiology Mode Study. *Orig. Life Evol. Biosph.* **44**, 231.
- Mastrapa, R.M.E., Brown, R.H. (2006). Ion Irradiation of Crystalline H₂O Ice: Effect on the 1.65 μ m Band. *Icarus* **183**, 207.
- Mayer, E., Hallbrucker, A. (1987). Cubic Ice from Liquid Water. *Nature* **325**, 601.
- Mayer, E., Hallbrucker, A. (1989). Unexpectedly Stable Nitrogen and Oxygen Clathrate Hydrates from Vapour Deposited Amorphous Solid Water. *J. Chem. Soc. Chem. Commun.* **1989**, 749.
- McCord, T.B., Carlson, R.W., Smythe, W.D., Hansen, G.B., Clark, R.N., Hibbitts, C.A., Fanale, F.P., Granahan, J.C., Segura, M., Matson, D.L., Johnson, T.V., Martin, P.D. (1997). Organics and Other Molecules in the Surfaces of Callisto and Ganymede. *Science* **278**, 271.
- McCord, T.B., Hansen, G.B., Clark, R.N., Martin, P.D., Hibbitts, C.A., Fanale, F.P., Granahan, J.C., Segura, M., Matson, D.L., Johnson, T.V., Carlson, R.W., Smythe, W.D., Danielson, G.E. (1998a). Non-Water-Ice Constituents in the Surface Material of the Icy Galilean Satellites from the *Galileo* Near-Infrared Mapping Spectrometer Investigation. *J. Geophys. Res. Planet.* **103**, 8603.
- McCord, T.B., Hansen, G.B., Fanale, F.P., Carlson, R.W., Matson, D.L., Johnson, T.V., Smythe, W.D., Crowley, J.K., Martin, P.D., Ocampo, A., Hibbitts, C.A., Granahan, J.C., and the *Galileo* NIMS Team (1998b). Salts on Europa's Surface Detected by *Galileo*'s Near Infrared Mapping Spectrometer. *Science* **280**, 1242.
- McCord, T.B., Hansen, G.B., Matson, D.L., Johnson, T.V., Crowley, J.K., Fanale, F.P., Carlson, R.W., Smythe, W.D., Martin, P.D., Hibbitts, C.A., Granahan, J.C., Ocampo, A. (1999). Hydrated Salt Minerals on Europa's Surface from the *Galileo* Near-Infrared Mapping Spectrometer (NIMS) Investigation. *J. Geophys. Res. Planet.* **104**, 11827.
- McCord, T.B., Hansen, G.B., Hibbitts, C.A. (2001a). Hydrated Salt Minerals on Ganymede's Surface: Evidence of an Ocean Below. *Science* **292**, 1523.
- McCord, T.B., Orlando, T.M., Teeter, G., Hansen, G.B., Sieger, M.T., Petrik, N.G., Van Keulen, L. (2001b). Thermal and Radiation Stability of the Hydrated Salt Minerals Epsomite, Mirabilite, and Natron under Europa Environmental Conditions. *J. Geophys. Res. Planet.* **106**, 3311.
- McEwen, A.S. (1986). Exogenic and Endogenic Albedo and Colour Patterns on Europa. *J. Geophys. Res. Solid Earth* **91**, 8077.
- McGuire, B.A., Ioppolo, S., Allodi, M.A., Blake, G.A. (2016). THz Time-Domain Spectroscopy of Mixed CO₂-CH₃OH Interstellar Ice Analogues. *Phys. Chem. Chem. Phys.* **18**, 20199.
- McGuire, B.A. (2022). 2021 Census of Interstellar, Circumstellar, Extragalactic, Protoplanetary Disc, and Exoplanetary Molecules. *Astrophys. J. Suppl. Ser.* **259**, 30.
- McKellar, A. (1940a). Evidence for the Molecular Origin of Some Hitherto Unidentified Interstellar Lines. *Publ. Astron. Soc. Pac.* **52**, 187.
- McKellar, A. (1940b). Wavelengths of the CH Band Lines. *Publ. Astron. Soc. Pac.* **52**, 312.
- McKellar, A. (1941). The Problem of Possible Molecular Identification of Interstellar Lines. *Publ. Astron. Soc. Pac.* **53**, 233.
- McKinnon, W.B., Zolensky, M.E. (2003). Sulphate Content of Europa's Ocean and Shell: Evolutionary Consideration and Some Geological and Astrobiological Implications. *Astrobiology* **3**, 879.

- McMillan, J.A., Los, S.C. (1965). Vitreous Ice: Irreversible Transformations During Warm-Up. *Nature* **206**, 806.
- McMurray, J. (2012). Organic Chemistry. Brooks/Cole Publishers (Belmont, United States).
- Mejía, C.F., de Barros, A.L.F., Bordalo, V., da Silveira, E.F., Boduch, P., Domaracka, A., Rothard, H. (2013). Cosmic Ray-Ice Interaction Studied by Radiolysis of 15 K Methane Ice with MeV O, Fe, and Zn Ions. *Mon. Not. R. Astron. Soc.* **433**, 2368.
- Mejía, C.F., de Barros, A.L.F., Seperuelo Duarte, E., da Silveira, E.F., Dartois, E., Domaracka, A., Rothard, H., Boduch, P. (2015a). Compaction of Porous Ices Rich in Water by Swift Heavy Ions. *Icarus* **250**, 222.
- Mejía, C.F., Bender, M., Severin, D., Trautmann, C., Boduch, P., Bordalo, V., Domaracka, A., Lv, X.Y., Martinez, R., Rothard, H. (2015b). Radiolysis and Sputtering of Carbon Dioxide Ice Induced by Swift Ti, Ni, and Xe Ions. *Nucl. Instrum. Methods Phys. Res. B: Beam Interactions Mater. Atom.* **365**, 477.
- Mennella, V., Palumbo, M.E., Baratta, G.A. (2004). Formation of CO and CO₂ Molecules by Ion Irradiation of Water Ice-Covered Hydrogenated Carbon Grains. *Astrophys. J.* **615**, 1073.
- Mennella, V., Baratta, G.A., Palumbo, M.E., Bergin, E.A. (2006). Synthesis of CO and CO₂ Molecules by UV Irradiation of Water Ice-Covered Hydrogenated Carbon Grains. *Astrophys. J.* **643**, 923.
- Methikkalam, R.R.J., Pavithraa, S., Murali Babu, S.P., Hill, H., Rajasekhar, B.N., Pradeep, T., Sivaraman, B. (2016). Thio Residue from Thermal Processing of Cometary Ices Containing Carbon Disulphide and Ammonia. *Adv. Space Res.* **58**, 438.
- Mewaldt, R.A. (1994). Galactic Cosmic Ray Composition and Energy Spectra. *Adv. Space Res.* **14**, 10737.
- Migliorini, A., Kaňuchová, Z., Ioppolo, S., Barbieri, M., Jones, N.C., Hoffmann, S.V., Strazzulla, G., Tosi, F., Piccioni, G. (2022). On the Origin of Molecular Oxygen on the Surface of Ganymede. *Icarus* **383**, 115074.
- Milillo, A., Plainaki, C., De Angelis, E., Mangano, V., Massetti, S., Mura, A., Orsini, S., Rispoli, R. (2016). Analytical Model of Europa's O₂ Exosphere. *Planet. Space Sci.* **130**, 3.
- Millar, T.J. (2015). Astrochemistry. *Plasma Sources Sci. Technol.* **24**, 043001.
- Miller, R.E., Leroi, G.E. (1968). Raman Spectra of Polycrystalline H₂S and D₂S. *J. Chem. Phys.* **49**, 2789.
- Miller, R.E., Pedersen, L. (1997). The Structure of Nitrous Oxide Tetramer from Near Infrared Laser Spectroscopy. *Chem. Phys. Lett.* **275**, 307.
- Miller, R.E., Pedersen, L. (1998). The Infrared Spectrum and Structure of the Nitrous Oxide Trimer. *J. Chem. Phys.* **108**, 436.
- Minissale, M., Aikawa, Y., Bergin, E., Bertin, M., Brown, W.A., Cazaux, S., Charnley, S.B., Coutens, A., Cuppen, H.M., Guzman, V., Linnartz, H., McCoustra, M.R.S., Rimola, A., Schrauwen, J.G.M., Toubin, C., Ugliengo, P., Watanabe, N., Wakelam, V., Dulieu, F. (2022). Thermal Desorption of Interstellar Ices: A Review on the Controlling Parameters and their Implications from Snowlines to Chemical Complexity. *ACS Earth Space Chem.* **6**, 597.
- Monteux, J., Tobie, G., Choblet, G., Le Feuvre, M. (2014). Can Large Icy Moons Accrete Undifferentiated? *Icarus* **237**, 377.
- Moore, M.H. (1984). Studies of Proton-Irradiated SO₂ at Low Temperatures: Implications for Io. *Icarus* **59**, 114.
- Moore, M.H., Donn, B., Hudson, R.L. (1988). Vaporisation of Ices Containing S₂ – Implications for Comets. *Icarus* **74**, 399.
- Moore, M.H., Hudson, R.L. (1992). Far-Infrared Spectral Studies of Phase Changes in Water Ice Induced by Proton Irradiation. *Astrophys. J.* **401**, 353.
- Moore, M.H., Hudson, R.L. (1994). Far-Infrared Spectra of Cosmic-Type Pure and Mixed Ices. *Astron. Astrophys. Suppl. Ser.* **103**, 45.
- Moore, M.H., Ferrante, R.F., Nuth, J.A. (1996). Infrared Spectra of Proton Irradiated Ices Containing Methanol. *Planet. Space Sci.* **44**, 927.
- Moore, M.H., Hudson, R.L. (2000). IR Detection of H₂O₂ at 80 K in Ion-Irradiated Laboratory Ices Relevant to Europa. *Icarus* **145**, 282.

- Moore, M.H., Hudson, R.L., Carlson, R.W. (2007). The Radiolysis of SO₂ and H₂S in Water Ice: Implications for the Icy Jovian Satellites. *Icarus* **189**, 409.
- Moreras-Marti, A., Fox-Powell, M., Cousins, C.R., Macey, M.C., Zerkle, A.L. (2022). Sulphur Isotopes as Biosignatures for Mars and Europa Exploration. *J. Geol. Soc.* **179**, jgs2021-134
- Moses, J.I., Cavalié, T., Fletcher, L.N., Roman, N.T. (2020). Atmospheric Chemistry on Uranus and Neptune. *Phil. Trans. R. Soc. A* **378**, 20190477.
- Mozumder, A. (1999). Fundamentals of Radiation Chemistry. Academic Press (San Diego, United States).
- Muñoz Caro, G.M., Meierhenrich, U.J., Schutte, W.A., Barbier, B., Arcones Segovia, A., Rosenbauer, H., Thiemann, W.H.-P., Brack, A., Greenberg, J.M. (2002). Amino Acid from Ultraviolet Irradiation of Interstellar Ice Analogues. *Nature* **416**, 403.
- Muñoz Caro, G.M., Jiménez-Escobar, A., Martín-Gago, J.Á., Rogero, C., Atienza, C., Puertas, S., Sobrado, J.M., Torres-Redondo, J. (2010). New Results on Thermal and Photodesorption of CO Ice Using the Novel Interstellar Astrochemistry Chamber (ISAC). *Astron. Astrophys.* **522**, A108.
- Murray, N. (2011). Star Formation Efficiencies and Lifetimes of Giant Molecular Clouds in the Milky Way. *Astrophys. J.* **729**, 133.

N

- Nash, D.B. (1987). Sulphur in Vacuum: Sublimation Effects on Frozen Melts, and Applications to Io's Surface and Torus. *Icarus* **72**, 1.
- Nash, D.B., Howell, R.R. (1989). Hydrogen Sulphide on Io: Evidence from Telescopic and Laboratory Infrared Spectra. *Science* **244**, 454.
- Nash, D.B., Betts, B.H. (1995). Laboratory Infrared Spectra (2.3-23 μm) of SO₂ Phases: Applications to Io Surface Analysis. *Icarus* **117**, 402.
- Navarro-Almaida, D., Le Gal, R., Fuente, A., Rivière-Marichalar, P., Wakelam, V., Cazaux, S., Caselli, P., Laas, J.C., Alonso-Albi, T., Loison, J.C., Gerin, M., Kramer, C., Roueff, E., Bachiller, R., Commerçon, B., Friesen, R., García-Burillo, S., Goicoechea, J.R., Giuliano, B.M., Jiménez-Serra, I., Kirk, J.M., Lattanzi, V., Malinen, J., Marcelino, N., Martín-Domènech, R., Muñoz-Caro, G.M., Pineda, J., Tercero, B., Treviño-Morales, S.P., Roncero, O., Hacar, A., Tafalla, M., Ward-Thompson, D. (2020). Gas Phase Elemental Abundances in Molecular Clouds (GEMS) II. On the Quest for the Sulphur Reservoir in Molecular Clouds: The H₂S Case. *Astron. Astrophys.* **637**, A39.
- Navizet, I., Komiha, N., Linguerri, R., Chambaud, G., Rosmus, P. (2010). On the Formation of S₂O at Low Energies: An *Ab Initio* Study. *Chem. Phys. Lett.* **500**, 207.
- Nelander, B. (1978). Infrared Spectrum of the Water-Hydrogen Sulphide Complex. *J. Chem. Phys.* **69**, 3870.
- Nelson, M.L., McCord, T.B., Clark, R.N., Johnson, T.V., Matson, D.L., Mosher, J.A., Soderblom, L.A. (1986). Europa: Characterisation and Interpretation of Global Spectral Surface Units. *Icarus* **65**, 129.
- Nguyen, T., Baouche, S., Congiu, E., Diana, S., Pagani, L., Dulieu, F. (2018). Segregation Effect and N₂ Binding Energy Reduction in CO-N₂ Systems Adsorbed on Water Ice Substrates. *Astron. Astrophys.* **619**, A111.
- Noble, J.A., Cuppen, H.M., Coussan, S., Redlich, B., Ioppolo, S. (2020). Infrared Resonant Vibrationally Induced Restructuring of Amorphous Solid Water. *J. Phys. Chem. C* **124**, 20864.
- Noll, K.S., Weaver, H.A., Gonnella, A.M. (1995). The Albedo Spectrum of Europa from 2200 Å to 3300 Å. *J. Geophys. Res. Planet.* **100**, 19057.
- Nuevo, M., Chen, Y.-J., Yih, T.-S., Ip, W.-H., Fung, H.-S., Cheng, C.-Y., Tsai, H.-R., Wu, C.-Y.R. (2007). Amino Acids Formed from the UV/EUV Irradiation of Inorganic Ices of Astrophysical Interest. *Adv. Space Res.* **40**, 1628.

Nuevo, M., Milam, S.N., Sandford, S.A. (2012). Nucleobases and Prebiotic Molecules in Organic Residues Produced from the Ultraviolet Photo-Irradiation of Pyrimidine in NH₃ and H₂O+NH₃ Ices. *Astrobiology* **12**, 295.

O

Oba, Y., Tomaru, T., Lamberts, T., Kouchi, A., Watanabe, N. (2018). An Infrared Measurement of Chemical Desorption from Interstellar Ice Analogues. *Nature Astron.* **2**, 228.

Oba, Y., Tomaru, T., Kouchi, A., Watanabe, N. (2019). Physico-Chemical Behaviour of Hydrogen Sulphide Induced by Reactions with H and D Atoms on Different Types of Ice Surfaces at Low Temperature. *Astrophys. J.* **874**, 124.

Öberg, K.I. (2016). Photochemistry and Astrochemistry: Photochemical Pathways to Interstellar Complex Organic Molecules. *Chem. Rev.* **116**, 9631.

Öberg, K.I., Bottinelli, S., Jørgensen, J.K., van Dishoeck, E.F. (2010). A Cold Complex Chemistry Toward the Low-Mass Protostar B1-b: Evidence for Complex Molecule Production in Ices. *Astrophys. J.* **716**, 825.

Oduro, H., Harms, B., Sintim, H.O., Kaufman, A.J., Cody, G., Farquhar, J. (2011). Evidence of Magnetic Isotope Effects During Thermochemical Sulphate Reduction. *Proc. Nat. Acad. Sci. USA* **108**, 17635.

Ono, S. (2017). Photochemistry of Sulphur Dioxide and the Origin of Mass-Independent Isotope Fractionation in Earth's Atmosphere. *Annu. Rev. Earth Planet. Sci.* **45**, 301-329.

Orlando, T.M., Sieger, M.T. (2003). The Role of Electron-Stimulated Production of O₂ From Water Ice in the Radiation Processing of Outer Solar System Surfaces. *Surf. Sci.* **528**, 1.

Orlando, T.M., McCord, T.B., Grievies, G.A. (2005). The Chemical Nature of Europa Surface Material and the Relation to a Subsurface Ocean. *Icarus* **177**, 528.

Owen, T.C., Roush, T.L., Cruikshank, D.P., Elliot, J.L., Young, L.A., De Bergh, C., Schmitt, B., Geballe, T.R., Brown, R.H., Bartholomew, M.J. (1993). Surface Ices and the Atmospheric Composition of Pluto. *Science* **261**, 745.

P

Paige, D.A., Wood, S.E., Vasavada, A.R. (1992). The Thermal Stability of Water Ice at the Poles of Mercury. *Science* **258**, 643.

Palumbo, M.E., Geballe, T.R., Tielens, A.G.G.M. (1997). Solid Carbonyl Sulphide (OCS) in Dense Molecular Clouds. *Astrophys. J.* **479**, 839.

Palumbo, M.E., Castorina, A.C., Strazzulla, G. (1999). Ion Irradiation Effects on Frozen Methanol (CH₃OH). *Astron. Astrophys.* **342**, 551.

Palumbo, M.E. (2006). Formation of Compact Solid Water After Ion Irradiation at 15 K. *Astron. Astrophys.* **453**, 903.

Palumbo, M.E., Leto, P., Siringo, C., Trigilio, C. (2008). Detection of C₃O in the Low-Mass Protostar Elias 18. *Astrophys. J.* **685**, 1033.

Parks, G.S. (1925). Thermal Data on Organic Compounds I. The Heat Capacities and Free Energies of Methyl, Ethyl, and Normal-Butyl Alcohols. *J. Am. Chem. Soc.* **47**, 338.

Pavithraa, S., Lo, J.-I., Rahul, K.K., Rajasekhar, B.N., Cheng, B.-M., Mason, N.J., Sivaraman, B. (2017). Vacuum Ultraviolet Photoabsorption of Prime Ice Analogues of Pluto and Charon. *Spectrochim. Acta A: Mol. Biomol. Spectrosc.* **190**, 172.

Pellegrini, A., Ferro, D.R., Zerbi, G. (1973). Dynamics and Structure of Disordered Hydrogen-Bonded Crystals. *Mol. Phys.* **26**, 577.

Penkett, S.A., Jones, B.M.R., Brich, K.A., Eggleton, A.E.J. (1979). The Importance of Atmospheric Ozone and Hydrogen Peroxide in Oxidising Sulphur Dioxide in Cloud and Rainwater. *Atmos. Environ.* **13**, 123.

- Penteado, E.M., Boogert, A.C.A., Pontoppidan, K.M., Ioppolo, S., Blake, G.A., Cuppen, H.M. (2015). Spectroscopic Constraints on CH₃OH Formation: CO Mixed with CH₃OH Ices Towards Younger Stellar Objects. *Mon. Not. R. Astron. Soc.* **454**, 531.
- Perrero, J., Enrique-Romero, J., Martínez-Bachs, Ceccarelli, C., Balucani, N., Ugliengo, P., Rimola, A. (2022). Non-Energetic Formation of Ethanol via CCH Reaction with Interstellar H₂O Ices: A Computational Chemistry Study. *ACS Earth Space Chem.* **6**, 496.
- Perrin, D.D. (1982). Ionisation Constants of Inorganic Acids and Bases in Aqueous Solution. Pergamon Press (Oxford, United Kingdom).
- Pharr, C.R., Kopff, L.A., Bennett, B., Reid, S.A., McMahon, R.J. (2012). Photochemistry of Furyl- and Thienyldiazomethanes: Spectroscopic Characterisation of Triplet 3-Thienylcarbene. *J. Am. Chem. Soc.* **134**, 6443.
- Phillips, C.B., Pappalardo, R.T. (2014). *Europa Clipper* Mission Concept: Exploring Jupiter's Ocean Moon. *Eos* **95**, 165.
- Pichler, A., Fleissner, G., Hallbrucker, A., Mayer, E. (1997). FT-IR Spectroscopic Monitoring of Alkali Metal Disulphite and Hydrogensulphite in Freeze-Concentrated and Glassy Aqueous Solution. Implications for Atmosphere Chemistry. *J. Mol. Struct.* **408-409**, 521.
- Pilling, S., Bergantini, A. (2015). The Effect of Broadband Soft X-Rays in SO₂-Containing Ices: Implications on the Photochemistry of Ices Toward Young Stellar Objects. *Astrophys. J.* **811**, 151.
- Pilling, S., Carvalho, G.A., Rocha, W.R.M. (2022). Chemical Evolution of CO₂ Ices Under Processing by Ionising Radiation: Characterisation of Non-Observed Species and Chemical Equilibrium Phase with the Employment of PROCODA Code. *Astrophys. J.* **925**, 147.
- Platz, T., Nathues, A., Schorghofer, N., Preusker, F., Mazarico, E., Schröder, S.E., Byrne, S., Kneissl, T., Schmedemann, N., Combe, J.-P., Schäfer, M., Thangjam, G.S., Hoffmann, M., Gutierrez-Marques, P., Landis, M.E., Dietrich, W., Ripken, J., Matz, K.-D., Russell, C.T. (2017). *Nature Astron.* **1**, 0007.
- Plekan, O., Rosu-Finsen, A., Cassidy, A.M., Lasne, J., McCoustra, M.R.S., Field, D. (2017). A Review of Recent Progress in Understanding the Spontaneous State of Matter. *Eur. Phys. J. D: Atom. Mol. Opt. Plasma Phys.* **71**, 162.
- Ponciano, C.R., Martinez, R., Farenzena, L.S., Iza, P., Homem, M.G.P., Naves de Brito, A., Wien, K., da Silveira, E.F. (2008). Cluster Emission and Chemical Reactions in Oxygen and Nitrogen Ices Induced by Fast Heavy-Ion Impact. *J. Mass Spectrom.* **43**, 1521.
- Pontoppidan, K.M., Dartois, E., van Dishoeck, E.F., Thi, W.-F., d'Hendecourt, L. (2003). Detection of Abundant Solid Methanol Towards Young Low Mass Stars. *Astron. Astrophys.* **404**, L17.
- Pontoppidan, K.M. (2006). Spatial Mapping of Ices in the Ophiuchus-F Core: A Direct Measurement of CO Depletion and the Formation of CO₂. *Astron. Astrophys.* **453**, L47.
- Poteet, C.A., Megeath, S.T., Watson, D.M., Calvet, N., Remming, I.S., McClure, M.K., Sargent, B.A., Fischer, J., Furlan, E., Allen, L.E., Bjorkman, J.E., Hartmann, L., Muzerolle, J., Tobin, J.J., Ali, B. (2011). A *Spitzer* Infrared Spectrograph Detection of Crystalline Silicates in a Protostellar Envelope. *Astrophys. J. Lett.* **733**, L32.
- Potin, S., Brissaud, O., Beck, P., Schmitt, B., Magnard, Y., Correia, J.-J., Rabou, P., Jocu, L. (2018). SHADOWS: A Spectro-Gonio Radiometer for Bidirectional Reflectance Studies of Dark Meteorites and Terrestrial Analogues: Design, Calibrations, and Performances on Challenging Surfaces. *Appl. Opt.* **57**, 8279.
- Pugh, L.A., Rao, K.N. (1976). *Molecular Spectroscopy: Modern Research III*. Academic Press (New York City, United States).
- Puzzarini, C., Barone, V. (2020). The Challenging Playground of Astrochemistry: An Integrated Rotational Spectroscopy – Quantum Chemistry Strategy. *Phys. Chem. Chem. Phys.* **22**, 6507.

Q

- Qasim, D., Chuang, K.-J., Fedoseev, G., Ioppolo, S., Boogert, A.C.A., Linnartz, H. (2018). Formation of Interstellar Methanol Ice Prior to the Heavy CO Freeze-Out Stage. *Astron. Astrophys.* **612**, A83.

Qasim, D., Fedoseev, G., Chuang, K.-J., He, J., Ioppolo, S., van Dishoeck, E.F., Linnartz, H. (2020). An Experimental Study of the Surface Formation of Methane in Interstellar Molecular Clouds. *Nature Astron.* **4**, 781.

R

Rahul, K.K., Ambresh, M., Sahu, D., Meka, J.K., Chou, S.-L., Wu, Y.-J., Gupta, D., Das, A., Lo, J.-I., Cheng, B.-M., Rajasekhar, B.N., Bhardwaj, A., Hill, H., Janardhan, P., Mason, N.J., Sivaraman, B. (2020). N-Graphene Synthesised in Astrochemical Ices. arXiv: 2008.10011.

Rajta, I., Vajda, I., Gyürky, Gy., Csedreki, L., Kiss, Á.Z., Biri, S., van Oosterhout, H.A.P., Podaru, N.C., Mous, D.J.W. (2018). Accelerator Characterisation of the New Ion Beam Facility at MTA Atomki in Debrecen, Hungary. *Nucl. Instrum. Methods Phys. Res. A: Acceler. Spectrom. Detect. Assoc. Equip.* **880**, 125.

Raut, U., Teolis, B.D., Kammer, J.A., Gimar, C.J., Brody, J.S., Gladstone, G.R., Howett, C.J.A., Protopapa, S., Retherford, K.D. (2022). Charon's Refractory Factory. *Science Adv.* **8**, eabq5701.

Raza, Z., Alfè, D., Salzmann, C.G., Klimeš, J., Michaelides, A., Slater, B. (2011). Proton Ordering in Cubic Ice and Hexagonal Ice: A Potential New Ice Phase – XIc. *Phys. Chem. Chem. Phys.* **13**, 19788.

Reding, F.P., Hornig, D.F. (1957). Vibrational Spectra of Molecules and Complex Ions in Crystals. X. H₂S and D₂S. *J. Chem. Phys.* **27**, 1024.

Rietmeijer, F.J.M. (1988). Sulphides and Oxides in Comets. *Astrophys. J.* **331**, L137.

Rigby, E., Symonds, M., Ward-Thompson, D. (2004). A Comet Impact in AD 536? *Astron. Geophys.* **45**, 1.23.

Robitaille, T.P., Whitney, B.A. (2010). The Present-Day Star Formation Rate of the Milky Way Determined from *Spitzer*-Detected Young Stellar Objects. *Astrophys. J. Lett.* **710**, L11.

Rodríguez-Almeida, L.F., Jiménez-Serra, I., Rivilla, V.M., Martín-Pintado, J., Zeng, S., Tercero, B., de Vicente, P., Colzi, L. (2021). Thiols in the Interstellar Medium: First Detection of HC(O)SH and Confirmation of C₂H₅SH. *Astrophys. J. Lett.* **912**, L11.

Rolfes, T.R., Reeves, R.R., Harteck, P. (1965). The Chemiluminescent Reaction of Oxygen Atoms with Sulphur Monoxide at Low Pressures. *J. Phys. Chem.* **69**, 849.

Romano, R.M., Della Védova, C.O., Downs, A.J. (2001). (Bromocarbonyl)sulphenyl Bromide, BrC(O)SBr: A Novel Carbonyl Sulphenyl Compound Formed by the Photochemical Reaction between Br₂ and OCS Isolated Together in an Ar Matrix. *Chem. Commun.* 2001, 2638.

Rose, W.K. (1967). Pulsational Instability in Helium Shell-Burning Stars. *Astrophys. J.* **150**, 193.

Roth, L. (2018). Constraints on Water Vapour and Sulphur Dioxide at Ceres: Exploiting the Sensitivity of the *Hubble Space Telescope*. *Icarus* **305**, 149.

Rothard, H., Domaracka, A., Boduch, P., Palumbo, M.E., Strazzulla, G., da Silveria, E.F., Dartois, E. (2017). Modification of Ices by Cosmic Rays and Solar Wind. *J. Phys. B: Atom, Mol. Opt. Phys.* **50**, 062001.

Rowland, B., Fisher, M., Devlin, J.P. (1991). Probing Icy Surfaces with Dangling OH Mode Absorption: Large Ice Clusters and Microporous Amorphous Ice. *J. Chem. Phys.* **95**, 1378.

Rubin, M., Engrand, C., Snodgrass, C., Weissman, P., Altwegg, K., Busemann, H., Morbidelli, A., Mumma, M. (2020). On the Origin and Evolution of the Material in 67P/Churyumov-Gerasimenko. *Space Sci. Rev.* **216**, 102.

Ruf, A., Bouquet, A., Boduch, P., Schmitt-Kopplin, P., Vinogradoff, V., Duvernay, F., Urso, R.G., Brunetto, R., Le Sergeant d'Hendecourt, L., Mousis, O., Danger, G. (2019). Organosulphur Compounds Formed by Sulphur Ion Bombardment of Astrophysical Ice Analogues: Implications for Moons, Comets, and Kuiper Belt Objects. *Astrophys. J. Lett.* **885**, L40.

Ruf, A., Bouquet, A., Schmitt-Kopplin, P., Boduch, P., Mousis, O., Danger, G. (2021). Sulphur Ion Irradiation Experiments Simulating Space Weathering of Solar System Body Surfaces. *Astron. Astrophys.* **655**, A74.

Ruffle, D.P., Hartquist, T.W., Caselli, P., Williams, D.A. (1999). The Sulphur Depletion Problem. *Mon. Not. R. Astron. Soc.* **306**, 691.

- Rushdie, A.I., Simoneit, B.R.T. (2005). Abiotic Synthesis of Organic Compounds from Carbon Disulphide Under Hydrothermal Conditions. *Astrobiology* **5**, 749.
- Ryan, S.G., Norton, A.J. (2010). *Stellar Evolution and Nucleosynthesis*, Cambridge University Press (Cambridge, United Kingdom).

S

- Salama, F., Allamandola, L.J., Witteborn, F.C., Cruikshank, D.P., Sandford, S.A., Bregman, J.D. (1990). The 2.5-5.0 μm Spectra of Io: Evidence for H_2S and H_2O Frozen in SO_2 . *Icarus* **83**, 66.
- Salvail, J.R., Fanale, F.P. (1994). Near-Surface Ice on Mercury and the Moon: A Topographic Thermal Model. *Icarus* **111**, 441.
- Santoro, G., Sobrado, J.M., Tajuelo-Castilla, G., Accolla, M., Martínez, L., Azpeitia, J., Lauwaet, K., Cernicharo, J., Ellis, G.J., Martín-Gago, J.Á. (2020). INFRA-ICE: An Ultra-High Vacuum Experimental Station for Laboratory Astrochemistry. *Rev. Sci. Instrum.* **91**, 124101.
- Sasaki, T., Williams, R.S., Wong, J.S., Shirley, D.A. (1978). Radiation Damage Studies by X-Ray Photoelectron Spectroscopy. I. Electron Irradiated LiNO_3 and Li_2SO_4 . *J. Chem. Phys.* **68**, 2718.
- Salter, T.L., Stubbing, J.W., Brigham, L., Brown, W.A. (2021). Using Laboratory Investigations to Aid the Identification of Small Aromatic Molecules in Water-Containing Astrophysical Ices. *Front. Astron. Space Sci.* **8**, 644277.
- Satorre, M. Á., Palumbo, M.E., Strazzulla, G. (2000). CO/CO_2 Molecular Number Ratio Produced by Ion Irradiation of Ices. *Astrophys. Space Sci.* **274**, 643.
- Satorre, M.Á., Domingo, M., Milán, C., Luna, R., Vilaplana, R., Santonja, C. (2008). Density of CH_4 , N_2 , and CO_2 Ices at Different Temperatures of Deposition. *Planet. Space Sci.* **56**, 1748.
- Satorre, M.Á., Leliwa-Kopystynski, J., Santonja, C., Luna, R. (2013). Refractive Index and Density of Ammonia Ice at Different Temperatures of Deposition. *Icarus* **225**, 703.
- Sauerbrey, G. (1959). Verwendung von Schwingquarzen zur Wägung dünner Schichten und zur Mikrowägung (in German). *Z. Physik* **155**, 206.
- Schlegel, M.C., Wenzel, K.-J., Sarfraz, A., Panne, U., Emmerling, F. (2012). A Wall-Free Climate Unit for Acoustic Levitators. *Rev. Sci. Instrum.* **83**, 055101.
- Schmidt, B.E., Hughson, K.H.G., Chilton, H.T., Scully, J.E.C., Platz, T., Nathues, A., Sizemore, H., Bland, M.T., Byrne, S., Marchi, S., O'Brien, D.P., Schorghofer, N., Hiesinger, H., Jaumann, R., Pasckert, J.H., Lawrence, J.D., Buzckowski, D., Castillo-Rogez, J.C., Sykes, M.V., Schenk, P.M., DeSanctis, M.-C., Mitri, G., Formisano, M., Li, J.-Y., Reddy, V., LeCorre, L., Russell, C.T., Raymond, C.A. (2017). Geomorphological Evidence for Ground Ice on Dwarf Planet Ceres. *Nature Geosci.* **10**, 338.
- Schmidt, F., Swiderek, P., Bredehöft, J.H. (2021). Electron-Induced Processing of Methanol Ice. *ACS Earth Space Chem.* **5**, 391.
- Schmitt, B., de Bergh, C., Fesjou, M. (1995). *Solar System Ices*, Astrophysics and Space Sciences Library Volume 227. Kluwer (Dordrecht, Netherlands).
- Schmitt, B., Rodriguez, S. (2003). Possible Identification of Local Deposits of Cl_2SO_2 on Io from NIMS/*Galileo* Spectra. *J. Geophys. Res. Planet.* **108**, 5104.
- Schrader, B. (1995). *Infrared and Raman Spectroscopy: Methods and Applications*. VCH Publishers (Weinheim, Germany).
- Schriver-Mazzuoli, L., Schriver, A., Wierzejewska-Hnat, M. (1995). Fourier Transform Infrared Study of Sulphur Dioxide Dimer. II. Argon Matrix. *Chem. Phys.* **199**, 227.
- Schriver-Mazzuoli, L., Schriver, A., Chaabouni, H. (2003a). Photo-Oxidation of SO_2 and of SO_2 Trapped in Amorphous Water Ice Studied by IR Spectroscopy. Implications for Jupiter's Icy Satellite Europa. *Can. J. Phys.* **81**, 301.
- Schriver-Mazzuoli, L., Chaabouni, H., Schriver, A. (2003b). Infrared Spectra of SO_2 and $\text{SO}_2:\text{H}_2\text{O}$ Ices at Low Temperature. *J. Mol. Struct.* **644**, 151.

- Schubert, G., Stevenson, D.J., Ellsworth, K. (1981). Internal Structures of the Galilean Satellites. *Icarus* **47**, 46.
- Seperuelo Duarte, E., Boduch, P., Rothard, H., Been, T., Dartois, E., Farenzena, L.S., da Silveira, E.F. (2009). Heavy Ion Irradiation of Condensed CO₂: Sputtering and Molecule Formation. *Astron. Astrophys.* **502**, 599.
- Shaheen, R., Abaunza, M.M., Jackson, T.L., McCabe, J., Savarino, J., Thiemens, M.H. (2014). Large Sulphur-Isotope Anomaly in Nonvolcanic Sulphate Aerosol and its Implications for the Archean Atmosphere. *Proc. Nat. Acad. Sci. USA* **111**, 11979.
- Shingledecker, C.N., Lamberts, T., Laas, J.C., Vasyunin, A., Herbst, E., Kästner, J., Caselli, P. (2020). Efficient Production of S₈ in Interstellar Ices: The Effects of Cosmic-Ray-Driven Radiation Chemistry and Nondiffusive Bulk Reactions. *Astrophys. J.* **888**, 52.
- Shirley, J.H., Dalton, J.B., Prockter, L.M., Kamp, L.W. (2010). Europa's Ridged Plains and Smooth Albedo Plains: Distinctive Compositions and Compositional Gradients at the Leading Side-Trailing Side Boundary. *Icarus* **210**, 358.
- Shoemaker, E.M. (1983). Asteroid and Comet Bombardment of the Earth. *Annu. Rev. Astron. Astrophys.* **11**, 461.
- Silverstein, T.P., Heller, S.T. (2017). pK_a Values in the Undergraduate Curriculum: What is the Real pK_a of Water? *J. Chem. Educ.* **94**, 690.
- Simpson, J.A. (1983). Elemental and Isotopic Composition of the Galactic Cosmic Rays. *Annu. Rev. Nucl. Part. Sci.* **33**, 323.
- Sivaraman, B., Jamieson, C.S., Mason, N.J., Kaiser, R.I. (2007). Temperature-Dependent Formation of Ozone in Solid Oxygen by 5 keV Electron Irradiation and Implications for Solar System Ices. *Astrophys. J.* **669**, 1414.
- Sivaraman, B., Ptasinska, S., Jheeta, S., Mason, N.J. (2008). Electron Irradiation of Solid Nitrous Oxide. *Chem. Phys. Lett.* **460**, 108.
- Sivaraman, B., Rajasekhar, B.N., Fulvio, D., Hunniford, A., McCullough, R.W., Palumbo, M.E., Mason, N.J. (2013). Ozone and Carbon Trioxide Synthesis by Low Energy Ion Implantation onto Solid Carbon Dioxide and Implications to Astrochemistry. *J. Chem. Phys.* **139**, 074706.
- Sivaraman, B. (2016). Electron Irradiation of Carbon Dioxide-Carbon Disulphide Ice Analogue and its Implication for the Identification of Carbon Disulphide on the Moon. *J. Chem. Sci.* **128**, 159.
- Slade, M.A., Butler, B.J., Muhleman, D.O. (1992). Mercury Radar Imaging: Evidence for Polar Ice. *Science* **258**, 635.
- Smith, I.W.M. (2011). Laboratory Astrochemistry: Gas-Phase Processes. *Annu. Rev. Astron. Astrophys.* **49**, 29.
- Smith, L.R., Gudipati, M.S., Smith, R.L., Lewis, R.D. (2021). Isotope Effect on the Sublimation Curves and Binding Energies of ¹²CO and ¹³CO Interstellar Ice Analogues. *Astron. Astrophys.* **656**, A82.
- Snow, T.P., McCall, B.J. (2006). Diffuse Atomic and Molecular Clouds. *Annu. Rev. Astron. Astrophys.* **44**, 367.
- Snow, T.P., Bierbaum, V.M. (2008). Ion Chemistry in the Interstellar Medium. *Annu. Rev. Anal. Chem.* **1**, 229.
- Sodeau, J.R., Lee, E.K.C. (1980). Photooxidation of Sulphur Dioxide in Low-Temperature Matrices. *J. Phys. Chem.* **84**, 3358.
- Sofia, U., Cardell, J.A., Savage, B.D. (1994). The Abundant Elements in Interstellar Dust. *Astrophys. J.* **430**, 650.
- Sojo, V., Herschy, B., Whicher, A., Camprubi, E., Lane, N. (2016). The Origin of Life in Alkaline Hydrothermal Vents. *Astrobiology* **16**, 181.
- Sori, M.M., Sizemore, H.G., Byrne, S., Bramson, A.M., Bland, M.T., Stein, N.T., Russell, C.T. (2018). Cryovolcanic Rates on Ceres Revealed by Topography. *Nature Astron.* **2**, 946.
- Spencer, J.R., Calvin, W.M., Person, M.J. (1995). Charge-Coupled-Device Spectra of the Galilean Satellites: Molecular-Oxygen on Ganymede. *J. Geophys. Res. Planet.* **100**, 19049.

- Spencer, J.R., Calvin, W.M. (2002). Condensed O₂ on Europa and Callisto. *Astrophys. J.* **124**, 3400.
- Spieler, S., Kuhn, M., Postler, J., Simpson, M., Wester, R., Scheier, P., Ubachs, W., Bacalla, X., Bouwman, J., Linnartz, H. (2017). C₆₀⁺ and the Diffuse Interstellar Bands: An Independent Laboratory Check. *Astrophys. J.* **846**, 168.
- Stechauer, G., Kozeschnik, E. (2014). Self-Diffusion in Grain Boundaries and Dislocation in Pipes in Al, Fe, and Ni and Application to AlN Precipitation in Steel. *J. Mat. Eng. Perform.* **23**, 1576.
- Steinacker, J., Linz, H., Beuther, H., Henning, T., Bacmann, A. (2016). Mass Estimates for Very Cold (<8 K) Gas in Molecular Cloud Cores. *Astron. Astrophys.* **593**, L5.
- Stephan, K., Jaumann, R., Krohn, K., Schmedemann, N., Zambon, F., Tosi, F., Carrozzo, F.G., McFadden, L.A., Otto, K., De Sanctis, M.C., Ammannito, E., Matz, K.-D., Roatsch, T., Preusker, F., Raymond, C.A., Russell, C.T. (2018). *Geophys. Res. Lett.* **44**, 1660.
- Stuedel, R., Holdt, G., Young, A.T. (1986). On the Colours of Jupiter's Satellite Io: Irradiation of Solid Sulphur at 77 K. *J. Geophys. Res. Solid Earth* **91**, 4971.
- Stuedel, R., Eckert, B. (2003). Solid Sulphur Allotropes. *Top. Curr. Chem.* **230**, 1.
- Stuedel, R., Stuedel, Y. (2004). The Thermal Decomposition of S₂O Forming SO₂, S₃, S₄, and S₅O: An *Ab Initio* MO Study. *Eur. J. Inorg. Chem.* **2004**, 3513.
- Stevenson, D.J. (1982). Volcanism and Igneous Processes in Small Icy Satellites. *Nature* **298**, 142.
- Stevenson, K.P., Kimmel, G.A., Dohnálek, Z., Smith, R.S., Kay, B.D. (1999). Controlling the Morphology of Amorphous Solid Water. *Science* **283**, 1505.
- Strazzulla, G., Baratta, G.A., Leto, G., Foti, G. (1992). Ion Beam-Induced Amorphisation of Crystalline Water Ice. *Eur. Phys. Lett.* **18**, 517.
- Strazzulla, G., Brucato, J.R., Palumbo, M.E., Satorre, M.Á. (1997). Is It Possible to Detect Frozen O₂ and N₂ on Interstellar Grains? *Astron. Astrophys.* **321**, 618.
- Strazzulla, G., Baratta, G.A., Leto, G., Gomis, O. (2007). Hydrate Sulphuric Acid After Sulphur Implantation in Water Ice. *Icarus* **192**, 623.
- Strazzulla, G., Garozzo, M., Gomis, O. (2009). The Origin of Sulphur-Bearing Species on the Surfaces of Icy Satellites. *Adv. Space Res.* **43**, 1442.
- Strazzulla, G. (2011). Cosmic Ion Bombardment of the Icy Moons of Jupiter. *Nucl. Instrum. Methods. Phys. Res. B: Beam Interact. Mater. Atom.* **269**, 842.
- Strazzulla, G., Brunetto, R. (2017). Particle Accelerators as Tools to Investigate Astrochemistry. *Nucl. Phys. News* **27**, 23.
- Strömgren, B. (1939). The Physical State of Interstellar Hydrogen. *Astrophys. J.* **89**, 526.
- Stuart, B.H. (2004). *Infrared Spectroscopy: Fundamentals and Applications*. Wiley (Chichester, United Kingdom).
- Stubbs, T.J., Wang, Y. (2012). Illumination Conditions at the Asteroid 4-Vesta: Implications for the Presence of Water Ice. *Icarus* **217**, 272.
- Sullivan, K.K., Boamah, M.D., Shulenberger, K.E., Chapman, S., Atkinson, K.E., Boyer, M.C., Arumainayagam, C.R. (2016). Low-Energy (<20 eV) and High-Energy (1000 eV) Electron-Induced Methanol Radiolysis of Astrochemical Interest. *Mon. Not. R. Astron. Soc.* **460**, 664.
- Sum, A.K., Sandler, S.I. (2000). *Ab Initio* Calculations of Cooperativity Effects on Clusters of Methanol, Ethanol, 1-Propanol, and Methanethiol. *J. Phys. Chem. A* **104**, 1121.
- Sunshine, J.M., A'Hearn, M.F., Groussin, O., Li, J.-Y., Belton, J.S., Delamere, W.A., Kissel, J., Klaasen, K.P., McFadden, L.A., Meech, K.J., Melosh, H.J., Schultz, P.H., Thomas, P.C., Veverka, J., Yeomans, D.K., Busko, I.C., Desnoyer, M., Farnham, T.L., Feaga, L.M., Hampton, D.L., Lindler, D.J., Lisse, C.M., Wellnitz, D.D. (2006). Exposed Water Ice Deposits on the Surface of Comet 9P/Tempel 1. *Science* **311**, 1453.
- Swings, P., Rosenfeld, L. (1937). Considerations Regarding Interstellar Molecules. *Astrophys. J.* **86**, 483.

T

- Tafalla, M., Myers, P.C., Caselli, P., Walmsley, C.M., Comito, C. (2002). Systematic Molecular Differentiation in Starless Cores. *Astrophys. J.* **569**, 815.
- Tauer, K.J., Lipscomb, W.N. (1952). On the Crystal Structures, Residual Entropy and Dielectric Anomaly of Methanol. *Acta Crystall.* **5**, 606.
- Tempelmeyer, K.E., Mills, D.W. (1968). Refractive Index of Carbon Dioxide Cyrodeposit. *J. Appl. Phys.* **39**, 2968.
- ten Kate, I.L., Reuver, M. (2016). PALLAS: Planetary Analogues Laboratory for Light, Atmosphere, and Surface Simulations. *Ned. J. Geosci.* **95**, 183.
- Tevault, D.E., Smardzewski, R.R. (1978). Chemiluminescent Reactions of Sulphur Atoms and Oxygen Atoms in Solid Argon Matrices. SO Chemiluminescence. *J. Chem. Phys.* **69**, 3182.
- Theulé, P., Duvernay, F., Danger, G., Borget, F., Bossa, J.B., Vinogradoff, Mispelaer, F., Chiavassa, T. (2013). Thermal Reactions in Interstellar Space: A Step Towards Molecular Complexity in the Interstellar Medium. *Adv. Space Res.* **52**, 1567.
- Thomas, N., Bagenal, F., Hill, T.W., Wilson, J.K. (2004). The Io Neutral Clouds and Plasma Torus. In: *Jupiter: The Planet, Satellites and Magnetosphere*. Eds: Bagenal, F., Dowling, T., McKinnon, W., Cambridge University Press (Cambridge, United Kingdom).
- Tieftrunk, A., Pineau des Forêts, G., Shilke, P., Walmsley, C.M. (1994). SO and H₂S in Low Density Molecular Clouds. *Astron. Astrophys.* **289**, 579.
- Tielens, A.G.G.M. (2005). *The Physics and Chemistry of the Interstellar Medium*. Cambridge University Press (Cambridge, United Kingdom).
- Titus, T.M., Kieffer, H.H., Christensen, P.R. (2003). Exposed Water Ice Discovered Near the South Pole of Mars. *Science* **299**, 1048.
- Tobón, Y.A., Nieto, L.I., Romano, R.M., Della Védova, C.O., Downs, A.J. (2006). Photochemical Reaction Channels of OCS with Cl₂, ICl, or IBr Isolated Together in an Argon Matrix: Isolation of Syn-Iodocarbonylsulphenyl Bromide. *J. Phys. Chem. A* **110**, 2674.
- Tobón, Y.A., Romano, R.M., Della Védova, C.O., Downs, A.J. (2007). Formation of New Halogenothiocarbonylsulphenyl Halides, XC(S)SY, Through Photochemical Matrix Reactions Starting from CS₂ and a Dihalogen Molecule XY (XY = Cl₂, B₂, or BrCl). *Inorg. Chem.* **46**, 4692.
- Torrie, B.H., Weng, S.-X., Powell, B.M. (1989). Structure of the α -Phase of Solid Methanol. *Mol. Phys.* **67**, 575.
- Torrie, B.H., Binbrek, O.S., Strauss, M., Swainson, I.P. (2002). Phase Transitions in Solid Methanol. *J. Solid State Chem.* **166**, 415.
- Tosi, F., Mura, A., Lopes, R.M.C., Filacchione, G., Ciarniello, M., Zambon, F., Adriani, A., Bolton, S.J., Brooks, S.M., Noschese, R., Sordini, R., Turrini, D., Altieri, F., Cicchetti, A., Grassi, D., Hansen, C.J., Migliorini, A., Moriconi, M.L., Piccioni, G., Plainaki, C., Sindoni, G. (2020). Mapping Io's Surface Composition with *Juno/JIRAM*. *J. Geophys. Res. Planet.* **125**, e2020JE006522.
- Traspas Muiña, A., Burchell, M.J. (2021). Tardigrade Survival Limits in High-Speed Impacts – Implications for Panspermia and Collection of Samples from Plumes Emitted by Ice Worlds. *Astrobiology* **21**, 845.
- Tribbett, P.D., Loeffler, M.J. (2022). Thermal Reactions between H₂S and O₃: Implications for Europa Surface Chemistry. *Planet. Sci. J.* **3**, 233.
- Trofimov, B.A., Sinegovskaya, L.M., Gusarova, N.K. (2009). Vibrations of the S–S Bond in Elemental Sulphur and Organic Polysulphides: A Structural Guide. *J. Sulphur Chem.* **30**, 518.
- Trottier, A., Brooks, R.L. (2004). Carbon-Chain Oxides in Proton-Irradiated CO Ice Films. *Astrophys. J.* **612**, 1214.
- Tucker, O.J., Johnson, R.E., Young, L.A. (2015). Gas Transfer in the Pluto-Charon System: A Charon Atmosphere. *Icarus* **246**, 291.

Tyler, R.H., Henning, W.G., Hamilton, C.W. (2015). Tidal Heating in a Magma Ocean within Jupiter's Moon Io. *Astrophys. J. Suppl. Ser.* **218**, 22.

V

van der Tak, F.F.S., Boonman, A.M.S., Braakman, R., van Dishoeck, E.F. (2003). Sulphur Chemistry in the Envelopes of Massive Young Stars. *Astron. Astrophys.* **412**, 133.

van Dishoeck, E.F., Black, J.H. (1989). Interstellar C₂, CH, and CN in Translucent Molecular Clouds. *Astrophys. J.* **340**, 273.

van Dishoeck, E.F., Herbst, E., Neufeld, D.A. (2013). Interstellar Water Chemistry: From Laboratory to Observations. *Chem. Rev.* **113**, 9043.

van Dishoeck, E.F. (2014). Astrochemistry of Dust, Ice and Gas: Introduction and Overview. *Faraday Discuss.* **168**, 9.

van Veen, N., Brewer, P., Das, P., Bersohn, R. (1983). The Adiabatic and Diabatic Reactions of S(¹D) Atoms with OCS: Internal State Distribution of the S₂ Products. *J. Chem. Phys.* **79**, 4295.

Vance, S., Brown, M.J. (2013). Thermodynamic Properties of MgSO₄ to 800 MPa at Temperatures from –20 to 100 °C and Concentrations to 2.5 mol kg⁻¹ from Sound Speeds, with Applications to Icy World Oceans. *Geochim. Cosmochim. Acta* **110**, 176.

Vance, S., Bouffard, M., Choukroun, M., Sotin, C. (2014). Ganymede's Internal Structure Including Thermodynamics of Magnesium Sulphate Oceans in Contact with Ice. *Planet. Space Sci.* **96**, 62.

Vasavada, A.R., Paige, D.A., Wood, S.E. (1999). Near-Surface Temperatures on Mercury and the Moon and the Stability of Polar Ice Deposits. *Icarus* **141**, 179.

Vidal, T.H.G., Loison, J.-C., Jaziri, A.Y., Ruaud, M., Gratier, P., Wakelam, V. (2017). On the Reservoir of Sulphur in Dark Clouds: Chemistry and Elemental Abundance Reconciled. *Mon. Not. R. Astron. Soc.* **469**, 435.

Vincendon, M., Forget, F., Mustard, J. (2010). Water Ice at Low to Midlatitudes on Mars. *J. Geophys. Res. Planet.* **115**, E10001.

Vollhardt, K.P.C., Schore, N.E. (2011). Organic Chemistry: Structure and Function. W.H. Freeman and Company (New York City, United States).

von Steiger, R., Zurbuchen, T.H., McComas, D.J. (2010). Oxygen Flux in the Solar Wind: Ulysses Observations. *Geophys. Res. Lett.* **37**, L22101.

W

Wada, A., Mochizuki, N., Hiraoka, K. (2006). Methanol Formation from Electron-Irradiated Mixed H₂O/CH₄ Ice at 10 K. *Astrophys. J.* **644**, 300.

Wakelam, V., Bron, E., Cazaux, S., Dulieu, F., Gry, C., Guillard, P., Habart, E., Hornekær, L., Morisset, S., Nyman, G., Pirronello, V., Price, S.D., Valdivia, V., Vidali, G., Watanabe, N. (2017). H₂ Formation on Interstellar Dust Grains: The Viewpoints of Theory, Experiments, Models and Observations. *Mol. Astrophys.* **9**, 1.

Walker, G.A.H., Bohlender, D.A., Maier, J.P., Campbell, E.K. (2015). Identification of More Interstellar C₆₀⁺ Bands. *Astrophys. J. Lett.* **812**, L8.

Wallner, M., Jarraya, M., Olsson, E., Ideböhn, V., Squibb, R.J., Ben Yaghlane, S., Nyman, G., Eland, J.H.D., Feifel, R., Hochlaf, M. (2022). Abiotic Molecular Oxygen Production – Ionic Pathway from Sulphur Dioxide. *Science Adv.* **8**, eabq5411.

Wang, T.G., Lee, C.P. (1998). Nonlinear Acoustics. Eds: Hamilton, M.F., Blackstock, D.T., Academic Press (San Diego, United States).

Ward, P.D., Brownlee, D. (2000). Rare Earth: Why Complex Life is Uncommon in the Universe. Springer Verlag (Berlin, Germany).

- Watanabe, N., Kouchi, A. (2002). Efficient Formation of Formaldehyde and Methanol by the Addition of Hydrogen Atoms to CO in H₂O-CO Ice at 10 K. *Astrophys. J.* **571**, L173.
- Wells, C.H.J. (1972). Introduction to Molecular Photochemistry. Chapman and Hall (London, United Kingdom).
- Westley, M.S., Baratta, G.A., Baragiola, R.A. (1998). Density and Index of Refraction of Water Ice Films Vapour Deposited at Low Temperatures. *J. Chem. Phys.* **108**, 3321.
- Whalley, E. (1977). A Detailed Assignment of the O–H Stretching Bands of Ice I. *Can. J. Chem.* **55**, 3429.
- Whittet, D.C.B., Poteet, C.A., Chiar, J.E., Pagani, L., Bajaj, V.M., Horne, D., Shenoy, S.S., Adamson, A.J. (2013). Ice and Dust in the Pre-Stellar Dar Cloud Lynds 183: Pre-Planetary Matter at the Lowest Temperatures. *Astrophys. J.* **774**, 102.
- Wiens, R.C., Burnett, D.S., Calaway, W.F., Hansen, C.S., Lykke, K.R., Pellin, M.J. (1997). Sputtering Products of Sodium Sulphate: Implications for Io's Surface and for Sodium-Bearing Molecules in the Io Torus. *Icarus* **128**, 386.
- Wierzejewska-Hnat, M., Schriver, A., Schriver-Mazzuoli, L. (1994). FT Infrared Study of Sulphur Dioxide Dimer. I. Nitrogen Matrix. *Chem. Phys.* **183**, 117.
- Winter, H.P., Aumayr, F. (1999). Hollow Atoms. *J. Phys. B: Atom. Mol. Opt. Phys.* **32**, R39.

X

- Xie, W.J., Wei, B. (2001). Parametric Study of Single-Axis Acoustic Levitation. *Appl. Phys. Lett.* **79**, 881.

Y

- Yabushita, A., Hama, T., Kawasaki, M. (2013). Photochemical Reaction Processes During Vacuum-Ultraviolet Irradiation of Water Ice. *J. Photochem. Photobiol. C: Photochem. Rev.* **16**, 46.
- Yamamoto, S. (2017). Introduction to Astrochemistry: Chemical Evolution from Interstellar Clouds to Star and Planet Formation. Springer (Tokyo, Japan).
- Yanoff, M., Duker, J.S. (2009). Ophthalmology. Mosby Elsevier (Amsterdam, Netherlands).
- Yarnall, Y., Hudson, R.L. (2022a). A New Method for Measuring Infrared Band Strengths in H₂O Ices: First Results for OCS, H₂S, and SO₂. *Astrophys. J. Lett.* **931**, L4.
- Yarnall, Y., Hudson, R.L. (2022b). Crystalline Ice – Densities and Comparisons for Planetary and Interstellar Applications. *Icarus* **373**, 114799.
- Yocum, K.M., Smith, H.H., Todd, E.W., Mora, L., Gerakines, P.A., Milam, S.N., Widicus Weaver, S.L. (2019). Millimetre/Submillimetre Spectroscopic Detection of Desorbed Ices: A New Technique in Laboratory Astrochemistry. *J. Phys. Chem. A* **123**, 8702.
- Yoneda, M., Nozawa, H., Misawa, H., Kagitani, M., Okano, S. (2010). Jupiter's Magnetospheric Change by Io's Volcanoes. *Geophys. Res. Lett.* **37**, L11202.
- Yoshikawa, I., Suzuki, F., Hikida, R., Yoshioka, K., Murakami, G., Tsuchiya, F., Tao, C., Yamazaki, A., Kimura, T., Kita, H., Nozawa, H., Fujimoto, M. (2017). Volcanic Activity on Io and its Influence on the Dynamics of the Jovian Magnetosphere Observed by EXCEED/Hisaki in 2015. *Earth Planet. Space* **69**, 110.
- Yoshioka, K., Tsuchiya, F., Kagitani, M., Murakami, G., Fukuyama, D., Yamazaki, A., Yoshikawa, I., Fujimoto, M. (2018). The Influence of Io's 2015 Volcanic Activity on Jupiter's Magnetospheric Dynamics. *Geophys. Res. Lett.* **45**, 10193.
- Young, L.A., Braga-Ribas, F., Johnson, R.E. (2020). Volatile Evolution and Atmospheres of Trans-Neptunian Objects. In: *The Trans-Neptunian Solar System*. Eds: Prrialnik, D., Barucci, M.A., Young, L.A., Elsevier (Amsterdam, Netherlands).

Z

- Zanchet, A., Rodríguez-Lazcano, Y., Gálvez, Ó., Herrero, V.J., Escribano, R., Maté, B. (2013). Optical Constants of NH₃ and NH₃:N₂ Amorphous Ices in the Near-Infrared and Mid-Infrared Regions. *Astrophys. J.* **777**, 26.
- Zapała, J., Custer, T., Guillemin, J.-C., Gronowski, M. (2019). Photochemistry of XCH₂CN (X = -Cl, -SH) in Argon Matrices. *J. Phys. Chem. A* **123**, 3818.
- Zeng, W.Y., Anderson, A. (2001). Vibrational Spectra of Solid Hydrogen Sulphide: A Lattice Dynamics Study. *J. Raman. Spectrosc.* **32**, 9.
- Zhang, Z., Ewing, G.E. (2002). Infrared Spectroscopy of SO₂ Aqueous Solutions. *Spectrochim. Acta A: Mol. Biomol. Spectrosc.* **58**, 2105.
- Zhang, J.A., Paige, D.A. (2009). Cold-Trapped Organic Compounds and the Poles of the Moon and Mercury: Implications for Origins. *Geophys. Res. Lett.* **36**, L16203.
- Zhang, X., Liang, M.C., Mills, F.P., Belyaev, D.A., Yung, Y.L. (2012). Sulphur Chemistry in the Middle Atmosphere of Venus. *Icarus* **217**, 714.
- Zheng, W., Jewitt, D., Kaiser, R.I. (2006a). Formation of Hydrogen, Oxygen, and Hydrogen Peroxide in Electron-Irradiated Crystalline Water Ice. *Astrophys. J.* **639**, 534.
- Zheng, W., Jewitt, D., Kaiser, R.I. (2006b). Temperature Dependence of the Formation of Hydrogen, Oxygen, and Hydrogen Peroxide in Electron-Irradiated Crystalline Water Ice. *Astrophys. J.* **648**, 753.
- Zheng, W., Jewitt, D., Kaiser, R.I. (2007). Electron Irradiation of Crystalline and Amorphous D₂O Ice. *Chem. Phys. Lett.* **435**, 289.
- Zhou, J., Zhao, Y., Hansen, C.S., Yang, J., Chang, Y., Yu, Y., Cheng, G., Chen, Z., He, Z., Yu, S., Ding, H., Zhang, W., Wu, G., Dai, D., Western, C.M., Ashfold, M.N.R., Yuan, K., Yang, X. (2020). Ultraviolet Photolysis of H₂S and its Implications for SH Radiation Production in the Interstellar Medium. *Nature Commun.* **11**, 1547.
- Ziegler, J.F., Ziegler, M.D., Biersack, J.P. (2010). SRIM – The Stopping and Range of Ions in Matter (2010). *Nucl. Instrum. Methods. Phys. Res. B: Beam Interact. Mater. Atom.* **268**, 1818.
- Zimmer, C., Khurana, K.K., Kivelson, M.G. (2000). Subsurface Oceans on Europa and Callisto: Constraints from *Galileo* Magnetometer Observations. *Icarus* **147**, 329.
- Ziurys, L.M., Apponi, A.J., Hollis, J.M., Snyder, L.E. (1994). Detection of Interstellar N₂O: A New Molecule Containing an N–O Bond. *Astrophys. J.* **436**, L181.
- Zysman-Colman, E., Leste-Lassere, P., Harpp, D.N. (2008). Probing the Chemistry of Rare Sulphur Allotropes: S₉, S₁₂, and S₂₀. *J. Sulphur Chem.* **29**, 309.